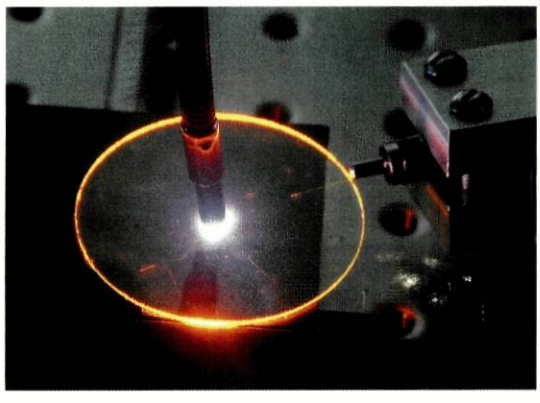
U.PORTO

FACULDADE DE CIÊNCIAS
UNIVERSIDADE DO PORTO

Luminescence Based Optical Fiber Systems for Biochemical Sensing Applications





Pedro Alberto da Silva Jorge

Departamento de Física da Faculdade
de Ciências da Universidade do Porto

Porto 2006


Biblioteca
Faculdade de Ciências
Universidade do Porto
D000109103

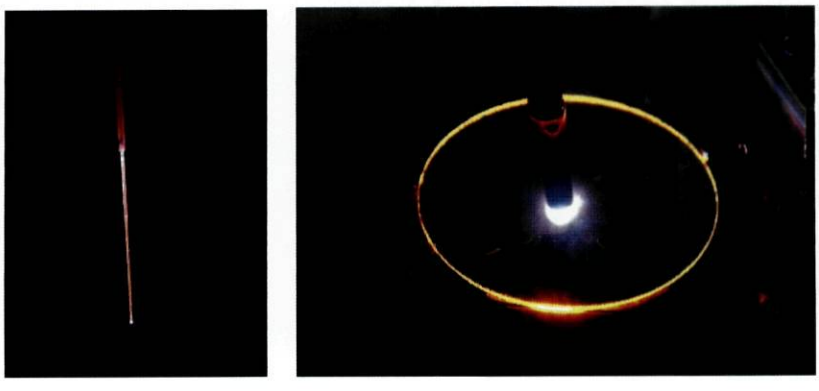
QC 476.5 JDR p.1 2006

EQOQ

U.PORTO

FACULDADE DE CIÊNCIAS
UNIVERSIDADE DO PORTO

Luminescence Based Optical Fiber Systems for Biochemical Sensing Applications



Dissertação submetida à Faculdade de Ciências da Universidade do Porto
para obtenção do grau de Doutor em Física

Faculdade de Ciências do Porto
14577
Biblioteca do Departamento de Física

Pedro Alberto da Silva Jorge
Departamento de Física da Faculdade
de Ciências da Universidade do Porto

Porto 2006

Dissertação realizada sob a supervisão do
Doutor José Luís Campos de Oliveira Santos,
Professor Associado do Departamento de Física da
Faculdade de Ciências da Universidade do Porto

Dedicatória

À **Nocas**

À minha **família**

Ao meu amigo **Tomazini** e à sua busca pela perfeição

[In the initial phase of the process (. . .), the scientist works through the imagination, as does the artist. Only afterwards, when critical testing and experimentation come into play, does science diverge from art . . .]

F. Jacob, 1997

Agradecimentos

Em primeiro lugar, gostaria de agradecer ao meu orientador Doutor José Luís Santos pela motivação e entusiasmo que soube transmitir, sempre com a maior amizade. Ao professor Faramarz Farahi pelas brilhantes discussões científicas e por tão abertamente partilhar a sua visão filosófica da vida. Ao Professor Joaquim Esteves pela paciente supervisão das minhas incursões no fascinante mundo da Química.

Não posso deixar de dirigir uma palavra especial de carinho à Luísa pela sua fantástica diligência, simpatia e amizade. A todos os meus colegas e amigos da UOSE pelas ajudas prestadas e pela boa disposição partilhada. Um agradecimento especial ao Paulo Caldas, companheiro constante desta aventura, pelo trabalho realizado. E também uma menção honrosa ao doutor Paulo "Sol-gel" Moreira pelos seus sábios conselhos nesta área.

Aos colegas da Química, pelo precioso esforço efectuado no meio dos reagentes, sem o qual grande parte do trabalho não seria possível, à Paula, à Andreia, ao Ricardo e ao Ricarte e ao Ben, nos Estados Unidos. Aos restantes amigos que tornaram a vida na Carolina não só suportável como extremamente agradável e divertida. Obrigado, Mona, Ernesto, Wim e Marion & Zeneck.

Finalmente à minha família, namorada e amigos pela amizade e encorajamento transmitidos e pela paciência em aturar as minhas fases mais negras.

Não posso ainda deixar de agradecer ao INESC Porto pelo apoio logístico e institucional sem o qual o trabalho realizado nunca seria possível. E ainda à FCT, à FLAD e à Gulbenkian pelos apoios financeiros prestados.

A associação de técnicas de luminescência com a tecnologia de fibras ópticas tem enorme potencial para o desenvolvimento de instrumentação analítica avançada para determinação de parâmetros bioquímicos. No presente trabalho, várias aplicações desta tecnologia são exploradas.

No primeiro capítulo é feita uma breve descrição do actual estado da arte desta área de investigação. O objectivo do capítulo dois é enquadrar as aplicações práticas exploradas nos restantes capítulos. Assim, são abordados assuntos fundamentais, como princípios da espectroscopia de fluorescência, tipos de marcadores luminescentes e membranas de imobilização. Além disso, são também descritos algum problemas tecnológicos, como o acoplamento de luz à fibra e os diferentes tipos de configurações sensoras em fibra óptica.

No capítulo três é relatado algum trabalho exploratório enquadrado na determinação do pH por métodos de luminescência. Foram testadas e comparadas várias técnicas de imobilização de indicadores na fibra óptica. Algumas das membranas resultantes foram utilizadas para medir pH usando diferentes técnicas de interrogação: detecção da intensidade, detecção de dois comprimentos de onda, medição de deslocamento espectral e interrogação no domínio das frequências.

No quarto capítulo é descrito o desenvolvimento de um sensor óptico de oxigénio baseado na inibição de fluorescência de complexos de ruténio imobilizados em membranas sol-gel. É feita uma descrição do actual estado da arte, identificando os problemas mais actuais. É apresentado um sistema em fibra óptica para interrogação de compostos luminescentes no domínio da frequência, que foi utilizado para testar várias geometrias de cabeças sensoras. O resultados obtidos fornecem pistas valiosas para a optimização do sistema sensor. É ainda apresentada uma configuração para determinação simultânea de oxigénio e temperatura. Os resultados obtidos demonstram a viabilidade do sistema proposto para utilização em qualquer sensor baseado em luminescência.

No capítulo cinco as aplicações de nanopartículas semicondutoras em sensores luminescentes são exploradas. As suas extraordinárias propriedades de luminescência, tais como altos rendimentos quânticos, fotoestabilidade elevada, reduzida largura espectral da emissão, capacidade de sintonização espectral, etc., têm um enorme potencial de aplicação. Neste capítulo é dada uma perspectiva actual desta nova área de investigação. São apresentados resultados, no contexto de sensores ópticos de oxigénio, que demonstram a possibilidade de usar nanocristais como referência de temperatura ou de intensidade em sensores luminescentes. São ainda demonstradas várias possibilidades de multiplexagem usando estes materiais. Finalmente, o capítulo seis apresenta um resumo das principais conclusões do trabalho realizado e fornece algumas pistas de trabalho futuro.

Summary

The goal of the present work is to explore the potential of optical fiber systems to develop luminescence-based biochemical sensors. A general overview of the present state of the art is provided in chapter one. The aim of chapter two is to provide an adequate background for the practical applications explored in the remaining chapters. In this context, a brief outline of the main physical principles and technologies involved in the implementation of optical fiber luminescence-based sensors is presented. Fundamental themes of luminescence spectroscopy, sensing dyes and immobilization membranes are addressed. The discussion of technical aspects includes the different types of sensing geometries and the optimization of the optical excitation/detection systems.

In chapter three some exploratory experimental work is presented in the framework of optical pH sensing. Different immobilization techniques were tested and compared. An optical fiber system was implemented and used to interrogate some of the resulting sensing membranes. Results are presented showing the possibility of measuring pH based on intensity detection, ratiometric detection of two wavelengths, wavelength shift detection and also frequency domain interrogation.

In chapter four, the development of a luminescence based oxygen sensor is addressed. An overview of the present state of this technology is given. In addition, an interrogation system for luminescence measurements in the intensity and phase domains is presented. The system was used to evaluate oxygen sensing fiber probes based on luminescence quenching of ruthenium complexes, immobilized in sol-gel membranes. Several fiber probe geometries were tested and characterized. Experimental results were obtained providing valuable clues towards the implementation of an ideal sensing system. A scheme for simultaneous determination of temperature and oxygen concentration, with applicability in many luminescence based sensors, is proposed. Preliminary results are presented showing the viability of oxygen measurements independent of temperature and optical power drifts.

In chapter five, the application of semiconductor nanoparticles, or quantum dots, in luminescence-based sensors is explored. Quantum dots, with high quantum yields, narrow emission, outstanding photostability and the ability to tune their optical properties, are ideal for biological tagging and a powerful tool for chemical sensing applications. In this chapter, an overview of this rapidly expanding area of research is presented. Additionally, results are shown, with emphasis on applications in optical oxygen sensing, which establish quantum dots as suitable temperature and intensity references for application in luminescence based chemical sensors. The possibility of wavelength multiplexing applications using luminescent nanocrystals is also explored. This concept is demonstrated in a system for multipoint measurement of oxygen and temperature. Finally, in chapter six, an outline of the main conclusions is given together with some hints for future work.

Sommaire

Cette thèse décrit le travail qui a eu pour but explorer le potentiel des systèmes en fibres optiques en utilisant les phénomènes de luminescence pour développer des senseurs biochimiques.

Le premier chapitre présente l'état de l'art de la recherche de ces technologies. Le deuxième chapitre introduit les concepts nécessaires pour comprendre les applications pratiques qui seront explorés dans les chapitres suivants. Les principes spectroscopiques de la luminescence sont présentés ainsi comme les technologies basées sur les colorants et les membranes d'immobilisations. Les problèmes techniques associés au couplage de la lumière dans la fibre optique et aux différentes configurations pour les systèmes senseurs en fibres optiques sont discutés.

Le troisième chapitre présente quelques expériences exploratoires dans le cadre des capteurs optiques de pH. Des techniques d'immobilisations différentes ont été testées et sont comparées. Un système en fibre optique a été implémenté et utilisé pour interroger des membranes senseurs. Les résultats sont présentés et montrent la possibilité de mesurer le pH en utilisant différentes techniques d'interrogation : détection d'intensité, détection de deux longueurs d'onde, mesure de déplacement spectral et interrogation utilisant le domaine des fréquences.

Le quatrième chapitre s'adresse au développement d'un senseur optique d'oxygène. Une révision des derniers développements de cette technologie est présentée. Un système d'interrogation en fibre optique a été développé pour mesurer la réponse luminescente d'un composite dans les domaines d'intensité et fréquence. Ce système a été utilisé pour tester plusieurs têtes senseurs en fibre optique avec des différentes géométries. Les résultats expérimentaux ont donné des pistes précieuses pour l'implémentation d'un système idéal. Un schéma pour mesurer simultanément la température et la concentration de l'oxygène est proposé. Les résultats obtenus démontrent la viabilité de cette solution et renforcent son applicabilité en plusieurs senseurs luminescents.

Dans le cinquième chapitre, l'application des nanoparticules semiconductrices luminescentes pour les senseurs biochimiques est explorée. Les propriétés extraordinaires des nanoparticules semiconductrices, telles qu'une rendement quantique et une photo-stabilité élevées, capacité de syntonisation spectrale, etc., sont utiles pour de nombreuses applications. Ce chapitre donne une perspective actuelle de ce nouveau champ de recherche. Les résultats montrés, dans le contexte des applications comme senseurs optiques d'oxygène, démontrent la validité des points quantiques comme références de température et d'intensité. La possibilité d'applications des nano-cristaux luminescents pour le multiplexage en longueur d'onde est explorée. Finalement, le sixième chapitre présente les conclusions générales de ce travail et évoquera les perspectives ouvertes par ce travail.

Agradecimentos 7
Sumário 9
Summary 11
Sommaire 13
Contents 15

Chapter 1 Optical Fiber Sensors for Biochemical Sensing 19

1.1 Introduction 19
1.2 Overview 21
1.3 Motivation 28
1.4 Thesis structure 29
1.5 References 31

Chapter 2 Technological Aspects of Optical Fiber Biochemical Sensors 35

2.1 Introduction 35
2.2 Principles of luminescence spectroscopy 36
2.2.1 Photoluminescence 37
2.2.2 Luminescence quenching 48
2.2.3 Intensity based spectroscopy 63
2.2.4 Time domain spectroscopy 72
2.2.5 Frequency domain spectroscopy 78
2.3 Luminescent sensing dyes 86
2.3.1 Intrinsic luminophores and organic dyes 87
2.3.2 Long lived transition metal complexes 88
2.4 Membranes for optical chemical sensing 92
2.4.1 Polymers 93
2.4.2 Sol-gel technology 95
2.5 Optical fiber systems for luminescence sensing 104
2.5.1 Optoelectronics for fiber sensing 106
2.5.2 Launching light into the fiber system 118
2.5.3 Coupling light from an LED into a multimode fiber 137
2.5.4 Sensor design 142
2.6 References 161

Chapter 3 Optical Fiber pH Sensors 169

3.1 Introduction 169
3.2 Luminescent pH sensing 171
3.2.1 Definition of pH 171
3.2.2 Optical pH indicators 172
3.2.3 Optical fiber pH sensors 177
3.3 Membranes for pH sensing 187
3.3.1 pH indicator 187
3.3.2 PVA 190
3.3.3 Polyacrylamides 193
3.3.4 Sol-gel 196
3.4 Intensity Based pH sensing 201

3.4.1 Sensing system 201
3.4.2 Intensity based pH and ion sensors 202
3.4.3 Ratiometric pH sensor 209
3.4.4 Wavelength pH sensor 211
3.5 Lifetime based pH sensors 215
3.5.1 Combination of indicators with different lifetimes 216
3.5.2 Frequency domain interrogation of NIR pH indicators 217
3.6 Conclusions 223
References 226

Chapter 4 Luminescence Based Oxygen Sensors 231

4.1 Introduction 231
4.2 Oxygen sensing by luminescence quenching 234
4.2.1 Sensing mechanism 234
4.2.2 Frequency domain interrogation 244
4.2.3 Luminescent indicators and polymers for oxygen sensing 249
4.2.4 Optical fiber oxygen sensors 257
4.3 Implementation of an optical fiber oxygen sensor 263
4.3.1 Interrogation system 264
4.3.2 Sensing films 270
4.3.3 Fabrication and testing of different fiber probe geometries 281
4.4 Temperature reference scheme for Optical O_2 sensors. 295
4.4.1 Proposed configuration 297
4.4.2 Self referenced temperature measurements 298
4.5 Conclusion 303
4.6 References 304

Chapter 5 Application of Quantum Dots to Optical Oxygen Sensing 309

5.1 Introduction 309
5.2 Semiconductors 310
5.2.1 Interband absorption 312
5.2.2 Interband luminescence 321
5.3 Quantum confined semiconductor structures 324
5.3.1 Infinite square potential well 325
5.3.2 Infinite potential well with spherical symmetry 328
5.3.3 Confinement in real quantum dots 329
5.3.4 Interband transitions in quantum structures 332
5.3.5 Technology 337
5.4 Semiconductor nanocrystals 338
5.4.1 Colloidal chemistry 339
5.4.2 Optical properties 341
5.4.3 Commercial products 346
5.5 Optical sensing applications of quantum dots 347
5.5.1 Physical sensors 347
5.5.2 Chemical sensors 348
5.5.3 Biosensors 351
5.6 Quantum dots as auxiliary tools in biochemical sensors 354
5.6.1 Samples preparation and characterization 357
5.6.2 Quantum dots as temperature probes 367
5.6.3 Quantum dots as an intensity reference 372

5.7 Multiplexing applications of quantum dots 377
5.7.1 Multipoint temperature sensing with quantum dots 378
5.7.2 Quantum dots as oxygen sensors with unique spectral signature 382
5.8 Conclusion 387
5.9 References 390

Chapter 6 395

Conclusions and Future Perspectives 395

6.1 Introduction 395
6.2 Luminescence based pH sensing - main achievements 395
6.3 Luminescence based oxygen sensors - main achievements 396
6.4 Application of semiconductor nanoparticles - main achievements 397
6.5 Conclusions and future perspectives 397
6.6 List of publications resulting from this work 404

Appendix - List of Abbreviations 407

Chapter 1

Optical Fiber Sensors for Biochemical Sensing

1.1 Introduction

The health of ecosystems and the survival of living organisms rely on the delicate balance of a diversity of biochemical parameters. In the present world, this balance is being continuously challenged by human action, putting both Man and Nature constantly at risk. In this context, the real-time determination of biochemical parameters is a critical need in many applications. Optical methods are specially attractive for sensing applications. In particular, luminescence based techniques are powerful analytical tools [1, 2]. Traditionally, luminescence methods are associated with very expensive and bulky equipments, very useful in the laboratory but unpractical for everyday life applications. In this regard, the combination of luminescence based techniques with optical fiber technology and modern optoelectronics has a great potential. High sensitivity, fast response times, immunity to electromagnetic interference, real-time remote measurements, high miniaturization and multiplexing capabilities are some of the most appealing characteristics which are associated to optical fiber luminescence based biochemical sensors [3].

Optical fiber sensing of physical parameters, like temperature or strain, is already a mature technology. It is not only the subject of study for many scientists but also a growing industry [4]. Conversely, in spite of its appealing characteristics, sensing of biochemical parameters with optical fibers is comparatively less advanced [5]. The main reason is that this particular field faces some additional challenges which demand a highly specialized yet multidisciplinary approach. Specific molecular indicators need to be immobilized in host materials, which should allow interaction with the analyte while simultaneously preventing loss of sensing dye and diffusion of interfering species. Each particular case requires highly specific solutions demanding the development of tailored chemical procedures. This requires dealing with Chemistry and Material Science. Compatibility of the sensing chemistry with suitable detectors and optical sources, and development of suitable interrogation techniques, on the other hand, involve both optics and optoelectronics. All of this should be combined in the tip of an optical fiber, with the final product usually facing extra demands. Biocompatibility, chemical and mechanical stability, ease of fabrication and compatibility

with mass production are challenging issues requiring a great deal of medical and engineering knowledge.

In spite of all difficulties, major developments took place over the last twenty years and today optical fiber biochemical sensing is a fast expanding research area with some products making their first appearance in the commercial market [6, 7]. Behind these advances are several technological developments which have concurred to create a more favorable scenario. From the optoelectronics point of view, the development of new light sources spanning from the UV to the near infra red (NIR) have been a decisive factor. Blue LEDs and laser diodes are efficient excitation sources for many indicator dyes. This fact, together with their compatibility with optical fibers and capability of pulsed or modulated operation, have contributed to the development of the first low cost optical fiber luminescent sensors. In this regard, the increasing availability of highly sensitive photodiodes and CCD detectors in a wide spectral range has also been extremely favorable. Fiber optic devices, on the other hand, have left their telecom cradle and are now being developed for sensing purposes, and have become available in a wide variety of materials and shapes. Large core multimode fibers, with relatively low loss from blue to NIR and with suitable characteristics for luminescence applications, can now be acquired commercially. Relatively low cost lock-in amplifiers and oscilloscopes have made possible the implementation of novel interrogation techniques in the time and frequency domain [8, 9].

The use of these tools, however, became possible only thanks to great progress in the development of new sensing dyes and immobilization polymer materials [10]. In particular, the exploration of metal-organic luminescent indicators has been quite fruitful. High quantum yields, long lifetimes, relatively high photostability and the possibility of tailoring their sensing properties without significantly changing their photophysical properties are some of the characteristics with most impact. The combination of these dyes with new polymer and sol-gel based materials has allowed the development of new sensing membranes whose application potential is just starting to unfold [11].

Perhaps the last frontiers of optical fiber sensing lie in the biological applications. In the field of biotechnology, great developments have also taken place. From genetic engineering to the creation of synthetic biomolecular receptors, the control of biological processes at the molecular level is now a reality. This has allowed, in the recent years, to use extremely powerful methods, like enzyme based techniques or immunoassays, for sensing purposes. With these techniques, the ultimate degree of specificity can be achieved in the tip of an optical fiber. Anything from biological agents to food or explosives can be recognized at the molecular level [12].

As the technology advances, the number of applications multiplies but so does the number of technological challenges. Therefore, this is presently an exciting area of research with increasingly growing activity both in the academic and in the industrial world. In the following lines a brief overview of the most exciting advances in this research field are provided. In addition, the main motivations for the research presented in this work are given, followed by a brief outline of the thesis structure.

1.2 Overview

Optical fibers have made possible the use of conventional spectroscopy techniques in sites otherwise inaccessible. In addition, their unique characteristics have provided new possibilities like multiplexing capability and evanescent wave sensing. These features, along with the technological advances just described, have allowed the establishment of a mature optical fiber biochemical sensing technology. Presently, with many fundamental proof of principle sensing schemes already demonstrated, a growing number of more practical applications is being explored in a wide range of situations [13-15]. Major areas currently explored include medical and chemical analysis, molecular biotechnology, marine and environmental analysis, industrial production monitoring and bioprocess control, and the automotive industry. In this context, a comprehensive discussion of the present state-of-the art is an overwhelming task. Any attempt at a full description will inevitably be incomplete. Nevertheless, an outline of some of the more fundamental techniques and applications, together with a description of some representative applications, will provide a good perspective of the present state and of the tremendous potential of optical fiber sensors for biochemical sensing. In addition of the insight provided in this introduction, throughout the remaining of this document a variety of examples of sensing schemes, interrogation techniques and applications will be given, framed in the specific subject of each chapter.

In spite of luminescence based techniques being probably the most widely used in sensing applications, a broad range of other optical techniques are being explored in the context of biochemical sensing with optical fibers. Absorption or Raman spectroscopy, refractive index measurements, surface plasmon resonance or polarization effects are some areas where current research is also very active. Nevertheless, these techniques are out of the scope of this work and special focus will be given to sensing methods based on luminescence spectroscopy.

Chemical sensors and biosensors

Although such a broad theme can be the subject of many different classifications, it is worth mentioning some basic distinctions. This way, two major classes can be identified: chemical sensors and biosensors. Chemical sensors are usually aimed at measuring the concentration of chemical species like ions, pH and metabolites. They can be based on direct measurements of the intrinsic absorption or luminescence of the analyte; more frequently, however, the sensing mechanism relies on the interaction between the analyte and a luminescent indicator. Biological sensors, on the other hand, are usually based on the interaction of biological elements, like enzymes, antibodies or nucleic acids, and rely on very specific catalytic or affinity reactions. Some of these reactions are irreversible. Therefore, a distinction is usually made between a biosensor which is able to continuously monitor the analyte concentration, providing quantitative information, and a bioprobe which is usually disposable after one measurement, and, although it can also provide quantitative analysis, it is typically used to assess the presence or absence of a certain biological agent. The distinction between chemical and biological sensors is merely a guideline as the two fields usually overlap in many applications. It is often the case that chemical sensors of pH or oxygen provide the basis for some sensor based on a biological reaction. Therefore, the term biochemical sensor can also be applied in a more broad perspective.

Interrogation techniques

A tremendous variety of bi-molecular indicator-analyte interactions can provide suitable luminescence based sensing mechanisms. Independently of the particular details, however, the actual measurements usually rely on the detection of a luminescent signal. The simplest approach to luminescence sensing is based on intensity measurements. However, several problems associated with intensity based techniques make them unsuitable or demand complex referencing schemes [16]. Leaching and photobleaching of the dye, drift of detection electronics or aging of the optical source are some of the more critical fragilities of intensity based measurements. This way, a currently active area of research includes the development and improvement of advanced methods of interrogation, such as time-resolved or spatially resolved spectroscopy. Time resolved measurements are particular attractive due to their self reference capability. Their use in low cost applications, however, requires relatively long lived dyes which are not always available for a specific analyte. This way, efforts have been made to develop new interrogation techniques which allow to use faster luminophores. Successful examples include the combination of indicators with different lifetimes, use of an absorbing dye in combination with a luminescent one and dual-lifetime referencing [17, 18]. These

techniques allow for low cost frequency domain and time domain interrogation to be applied to a broad selection of indicators.

Immobilization of dyes

Immobilization of the sensing dyes is a key step towards the development of a sensor capable of continuous and reversible measurement. However, this subject is also one of the most challenging problems of biochemical sensing technology.

This is particularly true in aqueous media where the membrane must encapsulate the dye while maintaining an equilibrium with the surrounding media, allowing the circulation of the analyte but preventing the diffusion of interfering species. Its mechanical and chemical robustness are also important parameters. In the end, it is the sensing membrane resulting from the dye-matrix combination which determines the sensor properties The development of efficient and reproducible immobilization procedures is critical for a successful application, but it is particularly difficult because each sensing application has its particular requirements depending on the sensing media or specific analyte-indicator pair. Biosensing applications pose additional difficulties of fulfilling biocompatibility and maintaining the biological activity of bioreceptors. Fortunately, many advances have been made in this regard. A variety of techniques has been used to encapsulate luminescent indicators in different polymeric materials. Chemical or physical adsorption, covalent binding or physical entrapment in a porous host are some of the methods explored, each having its advantages and drawbacks. Recently, sol-gel materials are being explored by many authors. By quite simple ambient temperature chemical methods, porous glass matrices can be developed capable of physically entrapping luminescent indicators without significant interference with their properties [19-21].

pH and ion sensors

pH is an essential parameter in a diversity of biological and chemical applications. The need for its monitorization spans from patient care in clinical applications to process control in food industry or surveillance of environmental quality. The protonation of many molecular dyes can deeply affect their absorption and/or emission properties. For this reason, there is a wide availability of indicator dyes suitable to monitor different pH ranges at different wavelengths. Absorption methods are simple and extensively used, but luminescence based techniques are comparatively much more sensitive and are therefore preferred in critical applications. The interaction of these excited dyes with different ionic species can also provide very sensitive sensing mechanisms for

ionic analytes or particular gases. In this framework, pH sensors are an important class of biochemical sensors [22].

A large number of luminescent pH dyes are very short lived (nanosecond range). Although time resolved measurements are still possible, the associated instrumentation becomes increasingly costly. Fortunately, many indicators have dual emission allowing the implementation of ratiometric detection schemes. Acidic and basic forms of the indicator usually emit at different bands and have different behaviors with pH. This way, detection at two different wavelengths, and a subsequent ratio of the detected signals allows measurements which are independent of optical power drifts and loss of indicator molecules. However, the use of simple frequency domain detection schemes is more desirable for low cost applications. This way, the development of strategies to design pH sensors with luminescence decay times in the microsecond range is a special focus of present research [18].

An increasing number of fiber sensors have been reported for measurement of pH in different fields of application; monitoring of pH in the biomedical field is of particular importance. pH microoptodes using tapered fiber tips in the sub-micron range have been used to perform intracellular measurements [23]. Imaging fiber sensors based in fiber bundles and pH indicators have been used to obtain images of cancer cells [24]. Monitoring of pH in the gastric cavity or in the blood of patients using optical fiber sensors is the goal of many researchers. Many prototypes have been demonstrated with suitability for *in vivo* applications. In this particular case, however, increased difficulties are at stake with important issues like biocompatibility and patient safety making the creation of true products harder. In the environment field, application of pH sensing devices has been demonstrated for groundwater monitoring and for measurements in seawater [25, 26]. Many industrial processes depend critically on pH level. In this context, many fiber sensors have been developed in the laboratory which demonstrated potential for different industrial applications but are still being put to test in real applications. Distributed pH sensors, based on time-domain reflectometry, seem to be suitable for corrosion monitoring in metal structures such as planes and bridges [27]. Optical sensors for high acidic or alkaline environments have been developed which can be very useful in many manufacturing plants, photographic developers and waste treatment facilities.

A popular scheme for ion sensing is based on ion exchange (cation in-proton out) with a polymeric membrane having an immobilized pH indicator dye. Problems of cross-sensitivity to pH can be overcome by making use of coextraction mechanisms. Sensors for alkaline metals and alkaline earth metal ions, of interest for use in clinical chemistry, have been reported using these

methods [15]. Luminescence quenching is a sensing mechanism which is used with a variety of analytes. In particular, this technique is recognized as the standard method for determination of halides [28]. The sensitive detection of these elements is of particular importance and highly desirable in many applications involving human physiology, chemical industry and the environment. Several luminescence based halide sensing systems have been reported. Still, several problems have to be addressed for successful practical applications, involving ionic analytes in general, such as cross-sensitivity to other ions, immobilization issues and development of suitable reference schemes.

Gas sensors

In addition to measuring acidity, or ionic species, pH sensors can also be used to detect some particular gases. Numerous optical fiber sensors for gases, like CO_2 or NH_3, have been developed on the basis of pH sensors. For this purpose the indicator dyes together with a gas sensitive buffer are usually immobilized in a gas permeable membrane, which, however, is impermeable to H^+. The diffusion of the gas to the membrane causes the change in the buffer pH and therefore induces the response of the sensing dye [22].

Oxygen is a particularly important gas for life itself. Therefore, its measurement is mandatory in many medical, environmental and even industrial applications. Optical oxygen sensors based on luminescence quenching have been successfully demonstrated over the last decade, in particular. These sensors are among the few biochemical optical sensors which have made the breakthrough from the research laboratory into commercial products. The combination of several technological advances, like the development of long-lived oxygen sensing dyes, the appearance of cheap LEDs in the blue range of the spectrum and reports of major progress in immobilization materials, have surely contributed to the high degree of maturity of oxygen sensing technology. All this would not have been possible without the powerful driving forces of a huge potential market and the urgent need for an alternative to conventional oxygen sensing technologies.

Most oxygen sensors reported are based on the luminescence quenching of metal-organic ruthenium complexes [29, 30]. These dyes have very suitable features for all-purpose oxygen sensing. Nevertheless, and more recently, a growing interest is being devoted to oxygen sensitive phosphorescent mettaloporphyrins. With much higher sensitivity, they are suitable for application in lower concentration ranges, like in pressure sensitive paints or studies of anaerobic stress in cellular cultures. Photostability and quantum yield of these dyes need further improvements for practical applications to succeed, though [31, 32].

Several applications of oxygen fiber sensors have been reported in many different areas. Monitoring of dissolved oxygen (DO) was successfully demonstrated in seawater. Optical oxygen sensors application in waste water treatment plants has been demonstrated. Such treatment plants usually rely on microorganisms to decompose water pollutants. However, an efficient process relies on the treatment pool being adequately aerated in order to ensure the survival of microorganisms. Online monitoring of DO with highly sensitive fiber sensors is very desirable as it allows a much more efficient control of the whole process. One particularly important feature of optical oxygen sensors is the fact that no oxygen is consumed. This way, measurements can be performed without interference in delicate media. In these conditions, ppb sensitivity at micro-scale spatial resolution can be achieved. Oxygen microoptodes with these characteristics are typically based on tapered fiber tips and are suitable to perform detailed studies of biological sediments or cellular cultures. Presently, many applications have been reported using these devices, some of which are commercially available. Some of these products offer the possibility of simultaneous interrogation of an array of up to eight sensors with the same processing unit [33]. Prototypes of multiparameter sensors including oxygen, carbon dioxide and pH, have been reported for blood gas analyses and gastric monitoring [34, 35].

Luminescence based sensors for many other gases have also been reported. The development of most of them, however, is still at the laboratory proof-of-principle stage, and many problems remain unsolved. Some examples include monitoring of important pollutants like NO_x, SO_x, CO_x and ozone [15].

Biosensors

Biological sensors rely on biological agents that interact specifically and reversibly. Usually these interactions result in changes of the physicochemical properties. Catalytic based interactions, for instance, may result in changes in the local proton concentration or electron density, release or uptake of gases like O_2, NH_3 or specific ions, changes in optical density, etc. The measurement of these changes is made through suitable transducers which will determine the final sensing mechanisms. Different types of transduction mechanisms are used which result in electrochemical, optical, piezoelectric and even colorimetric devices. Among these, schemes relying on luminescent indicators are among the most powerful and sensitive techniques. Major challenges in biosensing applications include the immobilization of the bioreceptors on the fiber surface and their conjugation with luminescent indicators without loosing biological activity. A common strategy

includes immobilizing the bioreceptors within their cells of origin. While this allows to maintain bioactivity for longer periods, it also affects the sensor selectivity and response time [12, 36].

Evanescent wave sensing is a particularly powerful tool in biological assays. It allows selective excitation of the biological sensing membrane on the surface of an unclad fiber. This avoids the excitation of molecules in the solution from creating strong background noise and allows to perform traditionally multi-step immunoassays (probing, washing, detecting) directly in the probed medium [37].

Although biosensors rely, by definition, on biological receptors like enzymes and antibodies, they can be used to detect virtually any analyte. From metabolic parameters to toxins and water pollutants, many applications have been reported. An algal biosensor using alkaline phosphatase for determination of heavy metals was described. It exploits the inhibitory action of heavy metals on the alkaline phosphatase present in the membrane of Chlorella vulgaris microalgae. The microalgal cells were immobilized on removable membranes placed in front of the tip of an optical fiber bundle. A portable optical fiber sensor for on-site analyses of explosive trinitrotoluene (TNT) in ground water was successfully tested in the field.

The fact that the action of many enzymes results in changes of the oxygen concentration (oxidase enzymes) was used to implement sensors of different metabolic parameters, which are based in luminescent oxygen sensing technology. Main examples of demonstrated applications include glucose, cholesterol, urea and different pesticides.

Multiparameter sensing

The multiplexing capability of optical fiber systems is a promising characteristic to be applied in the implementation of multi-parameter sensors or the determination of the same analyte simultaneously at different locations. Existing practical systems, however, rely mostly on solutions that demand a single fiber per sensing point/parameter and often require multiple sources and detectors. Few examples of single fiber used for multiplexed sensing have been reported, most of these being based on time domain reflectometry with colorimetric indicators. The main difficulties of multiplexing luminescence-based sensors include limited spatial resolution of time domain multiplexing due to the finite lifetime of sensing dyes, and the relatively broad spectra, severely hindering wavelength multiplexing. In spite of all these great challenges, the need for multiplexed systems makes this subject one of the currently hot research topics in the field [38-40].

Commercial products

Great progress has been made over the last twenty years in the field of optical fiber based biochemical sensors. This is presently a highly attractive and active field of research. In spite of all the efforts, very few examples of successful products available commercially can be found. A few pH and oxygen sensors are among the most developed items in this regard, with many companies offering products suitable for different applications [6, 7, 14].

Many reasons contribute to the rather slow pace of technology transfer into companies. The most important ones are related to some challenges that need to be overcome. These include improving long term stability, reduce cross-sensitivity with other analytes, develop reproducible immobilization methods compatible with mass production and easy and stable calibration, and establish of standard methods for comparison of results of different techniques, and comply with existing industry standards. Many advances are presently being made in these fields, however. New materials arising from nanothecnology and biotechnology are allowing a previously unseen control over material properties. A variety of nanoparticles, nanowires and nanotubes made of widely different materials and with surprising properties are contributing to the improvement of many traditional sensing techniques and also creating the opportunity for completely new approaches [41-43].

The continuous effort of the scientific community, the will of many companies to acquire these new technologies, together with an increased awareness of the need for multidisciplinary collaborations and teaching in universities will surely contribute to keep increasing the rate of new achievements and to establish a solid transfer of technology in the near future.

1.3 Motivation

This work was performed in a research group having a long tradition in optical fiber sensors and integrated optics technologies for the measurement of physical parameters like strain, temperature or electrical current. In this group there is the possibility to fabricate optical fiber and integrated optics devices for sensing purposes, like fiber Bragg gratings, fiber couplers or integrated optical circuits, and a vast experience in addressing the associated processing techniques (like interferometric and multiplexing techniques). Consequently, the potential of applying this knowledge in the field of biochemical sensors is certainly appealing. In this context, the primary goal of this work is to explore the field of luminescence based biochemical sensing and to identify opportunities of application of optical fiber devices, processing and multiplexing techniques in this exciting new area.

The difficulties of addressing a completely new area must be taken seriously. Therefore, within the wide range of possible applications, there was the need to address a subject where a substantial amount of information and scientific achievements were already established.

From the previous discussion it became clear that optical oxygen sensors based on luminescence quenching are particularly in an advanced technological state. In spite of great advances, however, like in all new technologies, a great deal of problems subsists and there is still much room for improvement. Long term stability, temperature dependence and cross-sensitivity to other chemical species are only a few of the many challenges remaining. This way, optical oxygen sensing is a research field with many established and well documented achievements, but with still a great deal of challenges to be addressed. Therefore, this makes it the perfect subject to approach the much broader world of biochemical optical sensing.

1.4 Thesis structure.

The subject under study is very broad and multidisciplinary. This way, although some common branches link the work presented in the different chapters, a wide variety of subjects is addressed. In this context, each chapter was designed to be, to some extent, a self-contained document, providing fundamental information on the specific topic, description of the state of the art, along with the experimental work developed. This way, the knowledgeable reader can easily address each one of the experimental chapters independently. However, the less prepared reader could find it difficult to fully understand these contents without further study. Although the fundamentals of many of the subjects addressed are available in the literature, due to the variety of topics this information is highly scattered in different sources. Therefore, in order to provide a unity to the work presented and to facilitate the introduction to this exciting area of research, an extra chapter was added containing more fundamental information.

Consequently, chapter two addresses the principles of luminescence spectroscopy and provides the basis to all the sensing techniques explored in this work. Particular attention is paid to the basic interrogation techniques and sensing mechanisms. In addition, some technological aspects of optical fibers in the context of sensing applications are addressed.

Due to the lack of any previous experience in luminescence based sensing techniques, there was the need, at an initial stage, to perform a great deal of laboratory work, based on previously published results, addressing the primary interrogation techniques, immobilization methods and general sensor design. This work is presented in chapter three and is focused on pH sensing. pH sensors were chosen as the subject for the first experimental chapter because the great variety of

luminescent pH indicators available is suitable to explore widely different detection techniques and immobilization methods. In addition, pH sensors are a very important class of biochemical sensors by themselves and also provide the basis for many sensing solutions for other chemical species like gases and metal ions. In chapter three the immobilization of sensing dyes in different solid matrices is addressed. Results obtained with different polymeric hosts are compared and discussed. The interrogation of pH sensing indicators is performed using different techniques. Detection of luminescent intensity, ratiometric detection of two emission wavelengths and frequency domain interrogation are some of the techniques explored.

Chapter four contains experimental work regarding an optical oxygen sensor based on quenching of the luminescence. Particular focus is given to the study of the optical fiber sensing head geometry. Some hints towards the optimization of the sensing probe are discussed. A temperature reference scheme is also proposed and demonstrated in the context of oxygen sensing, which is applicable to virtually any luminescence based sensor.

Chapter five also presents experimental work. In this chapter the applications of semiconductor nanocrystals in the field of luminescence sensors are explored. Several results are presented, in the context of an optical oxygen sensor, which demonstrate the great potential of these new materials. Quantum dots are very well suited to provide luminescent biochemical sensors with temperature and intensity reference signals. In addition, they introduce the possibility to explore wavelength multiplexing of luminescence based sensors by using the adequate combination of nanocrystals and sensing dye.

Finally, in chapter six an outline of the main conclusions is given together with some hints for future work.

1.5 References

[1] S. Kulmala and J. Suomi, *Current status of modern analytical luminescence methods.* Analytica Chimica Acta 2003. **500**: p. 21-69.

[2] Orellana, G., *Luminescent optical sensors.* Anal Bioanal Chem, 2004. **379**: p. 344–346.

[3] F. Baldini, A. N. Chester, J. Homola, and S. Martellucci, eds. *Optical Chemical Sensors.* NATO Science Series II. Mathematics, Physics and Chemistry. Vol. 224. 2004, Springer.

[4] Grattan, K.T.V. and T. Sun, *Fiber optic sensor technology: an overview.* Sensors and Actuators a-Physical, 2000. **82**(1-3): p. 40-61.

[5] Gerhard Holst and B. Mizaikoff, *Fiber Optic Sensors for Environmental Applications*, in *Handbook of Optical Fibre Sensing Technology.* 2002, John Wiley & Sons, LTD. p. 729-755.

[6] *Ocean Optics, Inc. www.oceanoptics.com.* [cited 2006].

[7] *PreSens - Precision Sensing GmbH . http://www.presens.de.* [cited 2006].

[8] Gerard O'Keeffe, Brian D. MacCraith, Aisling K. McEvoy, Colette M. McDonagh, and J.F. McGilp, *Development of LED-based phase fluorimetric oxygen sensor using evanescent wave excitation of a sol-gel immobilized dye.* Sensors and Actuators B, 1995. **29**: p. 226-230.

[9] Zhiyi Zhang, K. T. V. Grattan, and A.W. Palmer, *Phase-locked detection of fluorescence lifetime.* Review of Scientific Instruments, 1993. **64**: p. 2531-2540.

[10] Amao, Y., *Probes and polymers for optical sensing of oxygen.* Microchimica Acta, 2003. **143**(1): p. 1-12.

[11] Brian D. MacCraith, Colette M. McDonagh, Gerard O'Keeffe, Aisling K. McEvoy, T. Butler, and F.R. Sheridan, *Sol-gel coatings for optical chemical sensors and biosensors.* Sensors and Actuators B, 1995. **29**: p. 51-57.

[12] Mehrab Mehrvar, Chris Bis, Jeno M. Scharer, Murray Moo-Young, and J.H. Luong, *Fiber-Optic Biosensors - Trends and Advances.* Analytical Sciences, 2000. **16**: p. 677-692.

[13] Otto S. Wolfbeis, *Fiber Optic Chemical Sensors and Biosensors.* Anal. Chem., 2002. **72**: p. 81R-89R.

[14] R. Narayanaswamy and O.S. Wolfbeis, eds. *Optical Sensors - Industrial Environmental and diagnostic Applications.* Springer Series on Chemical Sensors and Biosensors, ed. O.S. Wolfbeis. 2004, Springer: Berlin.

[15] Otto S. Wolfbeis, *Fiber Optic Chemical Sensors and Biosensors.* Anal. Chem., 2004. **76**: p. 3269-3284.

[16] Antonius Song, Stephen Parus, and Raoul Kopelman, *High-Performance Fiber-Optic pH Microsensors for Practical Physiological Measurements Using a Dual-Emission Sensitive Dye.* Anal. Chem., 1997. **69**(5): p. 863-867.

[17] Christian Huber, Ingo Klimant, Christian Krause, and O.S. Wolfbeis, *Dual Lifetime Referencing as Applied to a Chloride Optical Sensor.* Anal. Chem., 2001. **73**: p. 2097-2103.

[18] Ute Kosch, Ingo Klimant, and O.S. Wolfbeis, *Long-lifetime based pH micro-optodes without oxygen interference.* Fresenius J Anal Chem, 1999. **364**(48–53).

[19] Harsányi, G., *Polymer films in sensor applications: a review of present uses and future possibilities.* Sensor Review, 2000. **20**(2): p. 98-105.

[20] Mohr, G.J., *Polymers for Optical Sensors*, in *Optical Chemical Sensors*, F. Baldini, et al., Editors. 2004, Springer. p. 297-321.

[21] Podbielska, H., Agnieszka Ulatowska-Jarza, Gerhard Muler, and H.J. Eichler, *Sol-Gels for Optical Sensors*, in *Optical Chemical Sensors*, F. Baldini, et al., Editors. 2004, Springer. p. 353-385.

Faculdade de Ciências do Porto

Biblioteca do Departamento de Física

[22] Lin, J., *Recent development and applications of optical and fiber-optic pH sensors.* Trends in Analytical Chemistry, 2000. **19**(9): p. 541-552.

[23] Deepak Uttamchandani and S. McCulloch, *Optical nanosensors - towards the development of intracellular monitoring.* Advanced Drug Delivery Reviews, 1996(21): p. 239-247.

[24] Walt, D.R., *Imaging optical sensor arrays.* Current Opinion in Chemical Biology, 2002. **6**(5): p. 689-695.

[25] Jones, T.P., S.J. Coldiron, W.J. Deninger, and M.D. Porter, *A Field-Deployable Dual-Wavelength Fiberoptic Ph Sensor Instrument Based on Solid-State Optical and Electrical Components.* Applied Spectroscopy, 1991. **45**(8): p. 1271-1277.

[26] Maher, M.H. and M.R. Shahriari, *A Fiber Optic Chemical Sensor for Measurement of Groundwater Ph.* Journal of Testing and Evaluation, 1993. **21**(5): p. 448-452.

[27] Browne, C.A., D.H. Tarrant, M.S. Olteanu, J.W. Mullens, and E.L. Chronister, *Intrinsic sol-gel clad fiber-optic sensors with time-resolved detection.* Analytical Chemistry, 1996. **68**(14): p. 2289-2295.

[28] Geddes, C.D., *Optical halide sensing using fluorescence quenching: theory, simulations and applications-a review.* Measurement Science and Technology, 2001. **12**: p. R33-R88.

[29] Ingo Klimant and O.S. Wolfbeis, *Oxygen-sensitive Luminescent materials basead on silicone-soluble ruthenium diimine complexes.* Analytical Chemistry, 1995. **67**: p. 3160-3166.

[30] Andrew Mills and F.C. Williams, *Chemical influences on the luminescence of ruthenium diimine complexes and its response to oxygen.* Thin Solid Films, 1997. **306**: p. 163-170.

[31] Sang-Kyung Lee and I. Okura, *Porphyrin-doped sol-gel glass as a probe for oxygen sensing.* Analytica Chimica Acta, 1997. **342**: p. 181-188.

[32] Sang-Kyung Lee and I. Okura, *Photostable Optical Oxygen Sensing Material: Platinum Tetrakis(pentafluorophenyl)porphyrin Immobilized in Polystyrene.* Analytical Communications, 1997. **34**: p. 185-188.

[33] Holst, G., R.N. Glud, M. Kuhl, and I. Klimant, *A microoptode array for fine-scale measurement of oxygen distribution.* Sensors & Actuators B, 1997. **38-39**: p. 122-129.

[34] Guillermo Orellana and D. Garcia-Fresnadillo, *Environmental and Industrial Optosensing with Tailored Luminescent Ru(II) Polypyridyl Complexes*, in *Optical Sensors - Industrial Environmental and diagnostic Applications*, R. Narayanaswamy and O.S. Wolfbeis, Editors. 2004, Springer: Berlin. p. 309-357.

[35] Mignani, A.G. and F. Baldini, *Biomedical sensors using optical fibres.* Rep. Prog. Phys., 1996. **59**: p. 1-28.

[36] María Dolores Marazuela and M.C. Moreno-Bondi, *Fiber-optic biosensors – an overview.* Anal Bioanal Chem, 2002. **372**: p. 664-682.

[37] Anderson, G.P., J.P. Golden, L.K. Cao, D. Wijesuriya, L.C. Shriverlake, and F.S. Ligler, *Development of an Evanescent-Wave Fiber Optic Biosensor.* Ieee Engineering in Medicine and Biology Magazine, 1994. **13**(3): p. 358-368.

[38] Epstein, J.R. and D.R. Walt, *Fluorescence-based fibre optic arrays: a universal platform for sensing.* Chemical Society Reviews, 2003. **32**(4): p. 203-214.

[39] Campbell, M., Y.T. Yang, P.A. Wallace, and A.S. HolmesSmith, *A multipoint quasi-distributed optical fiber pH sensor.* Optical Review, 1997. **4**(1A): p. 111-113.

[40] Lieberman, R.A., L.L. Blyler, and L.G. Cohen, *A distributed fiber optic sensor based on cladding fluorescence.* Journal of Lightwave Technology, 1990. **8**(2): p. 212-220.

[41] Sharron G. Penn, Lin He, and Michael J. Natan, *Nanoparticles for bioanalysis.* Current Opinion in Chemical Biology, 2003. **7**(5): p. 609-615.

[42] Liang, S., D.T. Pierce, C. Amiot, and X.J. Zhao, *Photoactive nanomaterials for sensing trace analytes in biological samples.* Synthesis and Reactivity in Inorganic Metal-Organic and Nano-Metal Chemistry, 2005. **35**(9): p. 661-668.

[43] Ozkan, M., *Quantum dots and other nanoparticles: what can they offer to drug discovery?* Drug Discovery Today, 2004. **9**(24): p. 1065-1071.

Chapter 2

Technological Aspects of Optical Fiber Biochemical Sensors

Summary

The aim of this chapter is to provide an adequate background for the practical applications explored in the remaining part of this work. In this context, a brief outline of the main physical principles and technologies involved in the implementation of optical fiber luminescence-based chemical sensors is presented. The fundamental themes of luminescence spectroscopy, sensing dyes and immobilization membranes are addressed. The discussion of technical aspects includes the different types of sensing geometries and the optimization of the optical excitation/detection systems.

2.1 Introduction

Luminescence based techniques are very powerful tools frequently used in a range of applications, from material characterization to the study of molecular dynamics. Although very sensitive and versatile, luminescent methods are usually associated with very complex and expensive instrumentation and, therefore, its use was for long restricted to research laboratories. In the last twenty years, however, revolutionary developments in many different areas have concurred to change this picture [1]. The developments in optoelectronics, with the advent of solid state optical sources including the blue range of the spectrum, together with contributions from organic chemistry, with the creation of long lived, photostable, metal-organic luminescent complexes, have made possible the implementation of highly sensitive frequency domain techniques in low-cost sensing applications [2-6]. Great advances in materials science contributed to the development of sophisticated immobilization techniques, with polymer and sol-gel chemistry, allowing the number of possible applications to multiply even further [7-9]. All these advances have made possible to associate the potentialities of luminescence-based techniques with the intrinsic capability of optical fibers for performing remote, on-line motoring, free of electromagnetic interferences and with minimum intrusion. Presently, optical fiber luminescence based chemical sensing is a strongly expanding area of research and development, with commercial systems already making its first

appearances[10-13]. This is a demanding area of research, however, as it encompasses a wide range research fields. A successful approach to such challenge is necessarily multidisciplinary [14].

In this context, when conceiving and implementing a luminescence based chemical sensing system, a wide range of fundamental principles and technological aspects, which are intimately interrelated, must be thoroughly considered. Understanding the physical principles involved in luminescence processes is essential to choose the appropriate sensing mechanism and the adequate interrogation technique for a given application. For each specific analyte, a luminescent sensing dye with suitable photophysical and photochemical properties must be used. Dye immobilization in an adequate solid membrane is also of critical importance. Ideally, such membrane should encapsulate the sensing dye without changing its properties and it should be in equilibrium with the surrounding environment, being permeable to the analyte but impermeable to any interfering species. All of these choices will have implications on the instrumentation, such as the excitation optical source and the detection and processing electronics. In the particular case of optical fiber applications, the compatibility of the sensing systems with low-cost standard optoelectronic devices, like solid state emitters and detectors, silica waveguides etc., is highly desirable. In this perspective, since luminescent signals traveling in the optical fiber are usually very weak, a great deal of effort is directed towards the optimization of sensing head geometries and coupling systems efficiencies.

In order to provide the adequate background to understand the specific applications of optical fiber chemical sensors that are explored in the remaining part of this work, this chapter provides an overview of the relevant topics that were just described. Further details are reported to adequate bibliography. In addition, in the subsequent chapters, some of the subjects will be explored in more detail, framed in specific applications.

2.2 Principles of luminescence spectroscopy

The ancient fascination felt by our ancestors when contemplating natural luminescent phenomena, like northern lights and fire-flies, is still present in the modern observer. After all, now that their causes are scientifically known, understanding those phenomena makes them even more striking. Derived from the Latin *lumen* and *essentia*, luminescence means literally 'made of light'[1]. Luminescence happens whenever an electronically excited species is deactivated by emission of ultra-violet, visible or infra-red radiation. Depending on how the material was excited in the first place, the luminescent event can fit into different categories. If high energy photons, from UV to

[1] First introduced as *luminescenz* by the physicist and science historian Eilhardt Wiedemann in 1888, to describe 'all those phenomena of light which are not solely conditioned by the rise in temperature', as opposed to incandescence.

blue, are used to provide excitation, the emission is called photoluminescence. Conversely, when the excitation mechanism is a chemical reaction, chemiluminescence is obtained. A variety of excitation mechanisms can be used, a list of the most important ones is given in Table 2-1.

Phenomenon	Excitation mechanism
Photoluminescence (fluorescence, phosphorescence)	Absorption of light (photons)
Radioluminescence	Ionizing radiation (X-rays, α, β, γ)
Cathodoluminescence	Cathode rays (electron beams)
Electroluminescence	Electric field
Thermoluminescence	Heating after prior storage of energy (e.g. radioactive irradiation)
Chemiluminescence	Chemical process (e.g. oxidation)
Bioluminescence	Biochemical process
Triboluminescence	Frictional and electrostatic forces
Sonoluminescence	Ultrasounds

Table 2-1 Different excitation mechanisms for obtaining luminescence [15].

Although most of these methods are often used as analytical tools in a diversity of domains, photoluminescence is, by far, the most widely used and studied technique. This is particularly true in the field of optical sensing. For these reasons the fundamentals of photoluminescence spectroscopy will be discussed in the following sections [15-18].

2.2.1 Photoluminescence

Photoluminescent phenomena can be roughly divided in two different sub-categories, fluorescence and phosphorescence. In fluorescence the transitions between the excited state and the fundamental state are spin allowed and, therefore, highly probable. Spin allowed transitions occur between levels having electrons with opposite spins, such levels are called singlet states. Because the spin remains unchanged after transition, the resulting electron pair obeys Pauli's principle, and the transition is highly probable. It thus results that fluorescence emission presents, typically, high transition rates and characteristic lifetimes in the nanosecond range. Phosphorescence, on the other hand, results from transitions involving levels with electrons having the same spin orientation, usually called triplet states. These are quantum mechanically forbidden transitions, with a very small but non-zero probability of occurrence, resulting in low transition rates and much slower time scales (ranging from few microseconds to several milliseconds or even longer).

The border, in the time domain, between these two processes is ill-defined but it can be roughly set around $1\,\mu s$. Such time scale is amenable to the implementation of time domain and frequency domain analytical techniques with relatively simple optoelectronics. Transition metal-ligand complexes (MLC's), containing a metal and one or more organic ligands, display mixed singlet-triplet states and present lifetimes ranging from $400\,ns$ to few microseconds, bridging the gap between fluorescence and phosphorescence. This new family of luminescent dyes, besides operating in an adequate time scale, presents high quantum yields and good photostability, characteristics that make them particularly interesting for sensing applications [19]. In addition to organometallic compounds, from which ruthenium and lanthanide complexes are representative examples, luminescence can be found in a variety of other materials, both organic and inorganic. Some examples of luminescent organic compounds are aromatic hydrocarbons (naphthalene, anthracene, pyrene), fluorescein and amino acids (tryptophan, tyrosine). Conversely, luminescent inorganic compounds include lanthanide ions (Eu^{3+}, Tb^{3+}), doped glasses (with Nd, Mn, Sn, Ag...) and semiconductor crystals (ZnS, CdS, ZnSe).

Molecular Orbitals

The covalent bonds that link together the different atoms of most polyatomic molecules result from the mutual sharing of electrons. In this process the atomic orbitals of single atoms overlap to form molecular orbitals. The absorption and emission of radiation observed in most luminescent dyes result from transitions between different molecular energy levels, involving these orbitals.

Depending on the shape of the initial atomic orbitals and on the degree of overlap, different kinds of molecular orbitals arise. Sigma orbitals can be formed from the overlap of two s atomic orbitals or from one s and one p atomic orbital. The σ bonds can also result from the overlap of two p orbitals, provided they have a collinear axis of symmetry. In both cases there is a strong orbital overlap which corresponds to strong molecular binding. Sigma bonds are the strongest type of covalent bonds. If, on the other hand, p orbitals overlap laterally, the degree of overlap will be smaller and the resulting bonds weaker. These bonds are formed by pi orbitals and usually arise in molecules having multiple bonds. Typically, in molecules with double and triple bonds, one is a sigma bond and the others are pi. In formaldehyde (H_2CO), for example, the double bond between carbon and oxygen is formed by a π and a σ orbital. The structural formula of formaldehyde is depicted in Figure 2.1 where the bonds are indicated. Due to the presence of heteroatoms like oxygen and nitrogen, dye molecules can also have electrons that do not contribute to bonding. The corresponding molecular orbitals are called n orbitals and are also represented in the figure.

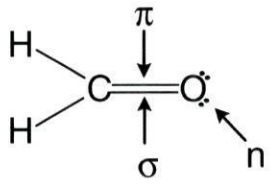


Figure 2.1 Structural formula of formaldehyde indicating different types of molecular orbitals.

The promotion of electrons in π orbitals to antibonding orbitals, designated π^*, can be achieved by absorption of photons with appropriate energy. The same is true for sigma orbitals. Transitions between non-bonding n orbitals and antibonding orbitals are also possible. However, while $\pi \rightarrow \pi^*$ and $n \rightarrow \pi^*$ transitions occur by absorption of UV and visible photons (in the $200 - 700\,nm$ region), $\sigma \rightarrow \sigma^*$ demand for much higher energies, only obtained with deep UV radiation (below $150\,nm$). This way, only the former are usually relevant for luminescence applications. The energy magnitudes of the different kinds of transitions are usually scaled as follows:

$$n \rightarrow \pi^* < \pi \rightarrow \pi^* < n \rightarrow \sigma^* < \sigma \rightarrow \pi^* < \sigma \rightarrow \sigma^*. \tag{2.1}$$

Considering a molecule in the fundamental state, the highest occupied molecular orbital (HOMO) and the lowest unoccupied molecular orbital (LUMO), are particularly important for spectroscopy applications. The difference in energy between these two orbital corresponds to the minimum necessary to optically excite the molecule and establishes the onset of absorption[2]. In formaldehyde the HOMO is a n orbital and the LUMO is a π^* orbital.

If one of a pair of electrons in the fundamental state is promoted to a higher energy orbital its spin will, in principle, remain unchanged. This way, the electron in the ground level and the electron in the excited level will have opposite spins. The total spin quantum number will then be zero, and the spin multiplicity[3] will be 1. Because the spin multiplicities of both ground and excited state are equal to 1, both states are called singlet states. Ground level singlet state is denoted by S_0 and excited singlet states by $S_1, S_2 \ldots$ and so on. Transitions between these levels are called singlet transitions and are usually associated with fluorescence. Through internal processes, usually

---

[2] To those more familiar with semiconductor physics, the HOMO and LUMO orbitals can, by analogy, be compared with valence and conduction bands respectively. In this context, the HOMO/LUMO energy difference is comparable to the semiconductor energy gap.

[3] Spin multiplicity is the number of possible orientations of the spin angular momentum for the same spatial electronic wave function. It is calculated by $(M = 2S + 1)$ where S is the total spin quantum number. A sate of singlet multiplicity has $S = 0$ and $M = 1$, in a triplet state $S = 1$ and $M = 3$.

associated with spin-orbit coupling, there is a non-zero probability that excited singlet molecules can undergo conversion to a state where the excited electron changes its spin. Spin-orbit coupling results from the interaction between the electronic spin and the magnetic dipole associated with the 'electronic cloud'. With two electrons having the same spin (one of them in the ground level) the excited state total spin number will be 1 and its multiplicity equal to 3. Such levels are usually called triplet states, have lower energy than the corresponding singlet states[4], and are associated with phosphorescence processes. Excited triplet states are usually denoted by $T_1, T_2 \ldots$and so on. The relative spin orientation of an electron pair in ground state and in singlet and triplet excited states is shown schematically in Figure 2.2. The conversion of excited singlet states into excited triplet states is called intersystem crossing. The singlet and triplet states that occur in formaldehyde are shown as an example in Figure 2.3. The different molecular levels are labeled according to the original and final orbital involved in each transition.

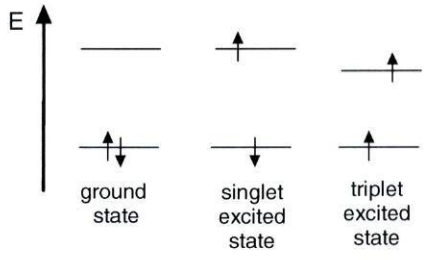


Figure 2.2 Schematic representation of electronic spin orientations in the ground level and in excited singlet and triplet states.

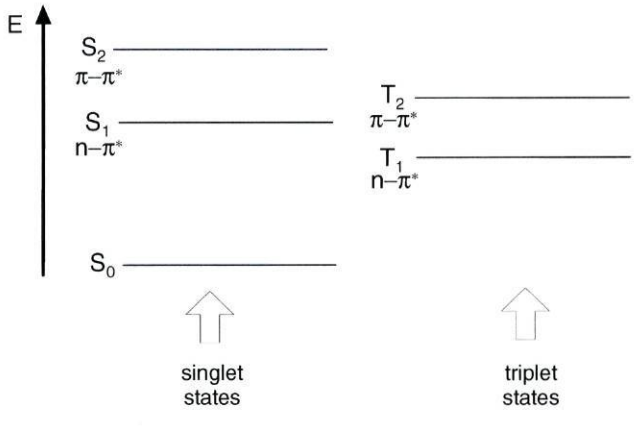


Figure 2.3 Singlet and triplet states in formaldehyde. The spectroscopic levels are labeled according to the original and final orbital.

[4] According to Hund's rules, states with higher multiplicity are usually more stable and correspond to a lower energy configuration. This is thought to be due to reduced screening of nuclear attraction when the electrons are further apart.

In molecules like formaldehyde with a single double bond, the orbitals are localized between pairs of atoms. Such localization confines the electronic wave function and also happens for single σ bonds and for π orbitals in isolated double bonds. In longer molecules, however, where double and single carbon-carbon bonds alternate, the overlap of different π orbitals allows for electrons to spread over the whole molecule. The reduced confinement of the electronic wave function results in lower energies for the $\pi \rightarrow \pi^*$ transitions and in a corresponding shift of the absorption to longer wavelengths. This way, the absorption and emission properties of molecular dyes are strongly dependent on the molecular structure and will be defined by the orbitals arrangements. This provides a mechanism for chemical engineers to control the luminescent properties of dyes, which can be tailored to a specific application [18].

Non radiative processes

Fluorescence and phosphorescence are only two of many possible mechanisms through which an excited molecule can return to the fundamental state. Both internal and external processes can deactivate the excited state of a molecular luminophore. Intrinsic processes include internal conversion (non-emissive return to lower energy states without photon emission, usually by vibrational relaxation), intersystem crossing (conversion from singlet to triplet states, which have higher probability of non-radiative deactivation), intramolecular charge transfer and conformational changes. Extrinsic processes, on the other hand, involve interaction of the excited luminophores with other molecules. Through these interactions, the excited states can be quenched by electron transfer, proton transfer, energy transfer, or excimer formation.

Whether the absorption of a photon by a luminescent molecule ultimately results in the emission of a photon or in some other energy transfer, will depend on the relative time scales of all the processes involved. For instance, phosphorescence is seldom observed in solutions because, at ambient temperature, many relaxation and quenching processes, faster than the long lived emissive state, compete for deactivation. Fluorescence, on the other hand, being much faster than many non-radiative processes, is easily observed. This way, the emission properties of most luminescent dyes is highly sensitive to the micro environment surrounding the excited molecule. Factors like temperature, pH level, pressure, presence of ions and polarity, can strongly impact the luminescence output. Many of the luminescence parameters, like quantum yield, lifetime and spectral distribution can thus be used to probe the environment with extreme sensitivity, providing both spatial and time information. Depending on the lifetime of the molecular probes, dynamic processes with different time scales can be monitored (eg. diffusion, chemical reactions, biological process). The high

sensitivity and specificity (different molecular probes have different susceptibilities) of luminescence to environmental parameters (at micro and macro scale) explain its success as an analytical tool and provides the basis for its application in optical sensing [20].

Usually, the spectroscopic properties of a molecule are determined by the intra-molecular processes. The effect of the external inter-molecular processes over these properties can then be used as a probe of the molecular environment.

Absorption and emission of radiation

The absorption and emission spectra of a molecular dye are primarily established by the possible electronic transitions. However, a molecule can also acquire or loose energy through vibrations and collisions with other molecules. The amount of energy associated with vibrational modes is smaller by an order of magnitude when compared with electronic transitions. As a consequence, a very closely spaced, almost continuous set of vibrational energy sublevels is associated to each electronic state. This multiplies even further the number of possible transitions causing homogeneous broadening of the absorption (and emission) spectra. Fluctuations in the microenvironment of individual molecules, on the other hand, cause inhomogeneous broadening. This way, molecular dyes usually present broad absorption bands instead of the discrete spectral lines that correspond to pure electronic transitions.

The spectral distributions of both absorption and luminescent emission are, in this way, defined by a multitude of possible transitions, which in turn depend on the physical configuration of the molecule. The study of such complex processes is usually performed in a simplified way using Perrin-Jablonsky diagrams [17]. In Figure 2.4 (a) an example of such diagram is represented, showing the radiative and non-radiative transitions involved in luminescent processes. External mechanisms, like quenching by other molecules, will be addressed later, and are not shown for simplification purposes. Processes in which photons are involved include absorption, fluorescence and phosphorescence and are represented by straight arrows. The non-radiative processes, like vibrational relaxation, internal conversion (IC) and intersystem crossing (ISC), are represented by curly arrows. The singlet and triplet states are labeled according to the notation previously defined and are represented by thick horizontal lines. The thin horizontal lines represent the vibrational levels associated with each electronic state.

At room temperature, most electrons are in the lowest vibrational level of the fundamental state. They follow a Boltzmann distribution which shows that, in this temperature range, thermal energy is not sufficient to significantly populate the excited vibrational levels of ground state. In

order for luminescence to be observed, however, the higher energy electronic levels must be populated by absorption of visible or UV radiation. Depending on the energy of the absorbed photons, electrons in the ground level can be promoted to different vibrational levels of the excited singlet states (S_1 or S_2). In comparison to the other processes involved (see Table 2-2), however, photon absorption can be considered instantaneous ($10^{-15} s$). In such timescale, nuclear displacement can be neglected, meaning that electronic transitions tend to occur with higher probability between vibrational levels where the nuclear configuration is the same in both states (Franck Condon principle). As a consequence, following absorption, electrons are usually promoted to higher vibrational levels of the electronic excited state. As the nuclear configuration eventually accommodates and releases the excess energy, electrons rapidly relax to the lowest vibrational level of S_1. This usually takes place by vibrational relaxation, heat release and collision with other molecules.

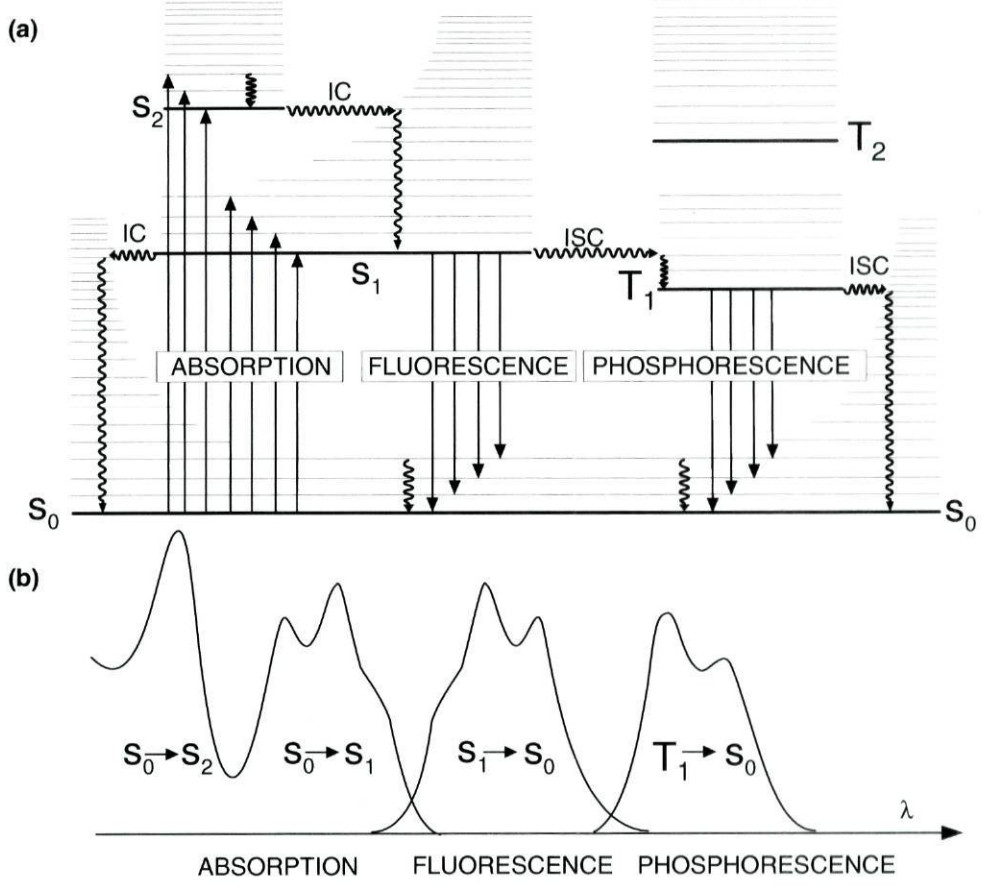


Figure 2.4 (a) Perrin-Jablonsky diagram illustrating the different transitions involved in luminescent processes. IC – internal conversion; ISC – intersystem crossing. Straight arrows represent radiative transitions and curly arrows non-radiative processes (b) Corresponding absorption and emission spectra. Adapted from [15].

The structure of the molecular absorption spectrum will therefore reflect the structure of the excited vibrational levels. The relative strength of each vibrational absorption line will depend on the molecular configuration and is proportional to the overlap of the wave functions of the two states involved in the transition. In Figure 2.4 (b) the absorption spectrum that results from the transitions represented in the respective Jablonsky diagram is shown. In the band corresponding to the $S_0 \rightarrow S_1$ transition, different vibrational peaks can be clearly identified. Due to inhomogeneous broadening, the vibrational structure is smoothed and can sometimes become unnoticeable.

Because internal conversion processes are usually faster than the lifetimes associated with fluorescence, emission tends to occur from the lowest vibrational level of the excited state. This way, the energy of the emitted photons is always smaller than the energy of the absorbed photons. The measure of the wavelength difference between the main absorption and emission peaks is called the Stokes' shift. This is an important parameter to consider when designing a practical system. The smaller its value, the harder will be to discriminate between the excitation radiation and the emitted fluorescence. This can greatly increase the complexity of the filtering and detection instrumentation. A small overlap between the emission and absorption spectra can sometimes be observed contradicting Stokes' rule. However, such transitions (not represented in the diagram) are explained by the fact that, according to Boltzmann's distribution, a small fraction of electrons is always in excited vibrational levels (both in the fundamental and excited electronic states). As a consequence, this effect tends to disappear at lower temperatures.

Transition	**Characteristic times (s)**
Absorption	10^{-15}
Vibrational relaxation	$10^{-12} - 10^{-10}$
S_1 excited state lifetime	$10^{-10} - 10^{-7} \rightarrow$ fluorescence
Intersystem crossing	$10^{-10} - 10^{-8}$
Internal conversion	$10^{-11} - 10^{-9}$
T_1 excited state lifetime	$10^{-6} - 1 \rightarrow$ phosphorescence

Table 2-2 Characteristic time scales of the different radiative and non-radiative transitions involved in luminescence processes [15].

The return to the ground state usually occurs to excited vibrational levels. Further vibrational relaxation will then restore the system to thermal equilibrium, placing almost all the electrons in the fundamental state. This way, the vibrational level structure can also be seen in the emission spectrum. In fact, the emission spectrum is usually a mirror image of the absorption spectrum (see

Figure 2.4 (b) and corresponding transitions in the diagram of Figure 2.4(a)). This happens because the structure of the vibrational levels depends on the nuclear configuration which is very similar in the fundamental and excited singlet states[5]. The same homogeneous and inhomogeneous broadening processes that affect absorption will also impact the resulting emission spectrum. This way, molecular dyes usually present relatively broad emission spectra.

Intersystem crossing is also represented in the diagram of Figure 2.4 (a). Trough this process an electron in the short lived excited singlet level, S_1, can have its spin inverted being transferred to a long lived excited triplet state, T_1. Radiative transitions rates of molecules in excited triplet states, correspond to phosphorescence and are orders of magnitude smaller than those of fluorescence. Because triplet states are of lower energy, phosphorescence occurs at longer wavelengths. With the longer radiative lifetimes associated with phosphorescence, the probability of non-radiative return to the ground state, trough vibrational relaxation, greatly increases. These processes are particularly favored in solutions and at ambient temperature due to collisions with solvent molecules. Under these conditions radiative quantum yields are usually very low and phosphorescence is seldom observed. Conversely, at low temperatures or in solid state, phosphorescence can be detected. In such cases, the lifetime of T_1 can be greatly increased and phosphorescence observed in timescales of milliseconds or even minutes. In addition, in molecules containing heavy atoms, there is higher spin-orbit coupling and intersystem crossing is favored. In such compounds phosphorescence quantum yields can be greatly enhanced.

The luminescence emission spectrum observed is usually independent of the wavelength of the excitation radiation. This happens because, even when the absorbed energy exceeds that of the HOMO/LUMO gap, due to the fast relaxation processes electrons always end up in the lowest energy vibrational levels of S_1 or T_1. This way, the intensity of the luminescent signal observed, at a fixed wavelength, is proportional to the incident excitation power and to the absorbance at that particular wavelength. The plot of the luminescent intensity as a function of the incident wavelength is called the excitation spectrum. If corrections are made to compensate for variation of the excitation source spectral distribution, the excitation spectrum will have the same shape as the absorption spectrum. The excitation spectrum is often a valuable tool used for spectroscopic characterization.

---

[5] Although the mirror rule is generally observed there are many exceptions. Deviations to the mirror rule usually indicate different nuclear arrangements for the molecule in the excited state as compared to the ground state.

Excited state lifetime

Although by itself the emission process is very fast ($10^{-15}\ s$), the average time a molecule stays in the excited state before returning to the fundamental state can be much longer. The magnitude of such time interval will determine the way the luminescence is affected by the environment and depends on the rate constants associated with all the radiative and non-radiative mechanisms involved. The simplified Jablonsky diagram in Figure 2.5 shows a representation of these mechanisms and their respective rate constants.

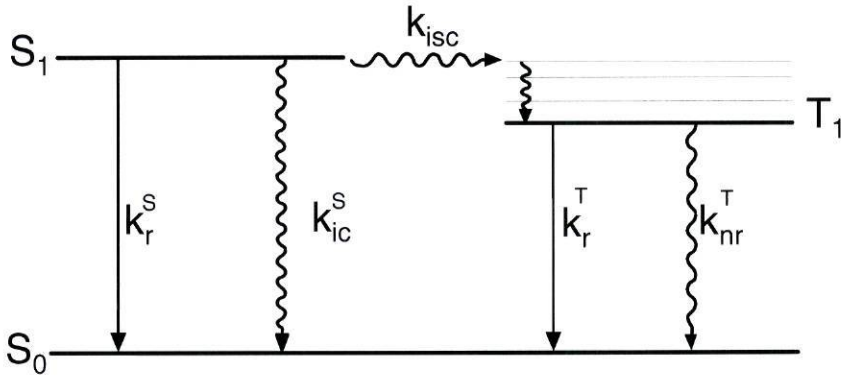


Figure 2.5 Representation of radiative and non radiative decay rates involved in fluorescence and phosphorescence processes. Adapted from [15].

The radiative rate constant of fluorescence, associated with the $S_1 \rightarrow S_0$ transition is labeled k_r^S. The non-radiative rates associated with internal conversion, k_{IC}^S, and intersystem crossing, k_{ISC}, can be grouped into a single non-radiative decay rate given by

$$k_{nr}^S = k_{IC}^S + k_{ISC}\,. \tag{2.2}$$

Similarly, rate constants, k_r^T and k_{nr}^T, are defined for the triplet radiative and non–radiative transitions, respectively. Decay rates associated with deactivation due to interaction with other molecules will be considered later, for simplicity.

Given these constants, the lifetime of a specified fluorescent molecule can be estimated by

$$\tau_0 = \frac{1}{k_r^S + k_{nr}^S}, \tag{2.3}$$

where τ_0 is the average time the molecules remain in the excited state after absorption. After excitation of a fluorescent dye solution, not all the molecules emit precisely at the same instant. Spontaneous emission is a random process and all the molecules have the same probability of emitting in a certain time interval. When a fluorescent sample is excited by a δ-function like pulse of

light, a given concentration of excited molecules, $[M^*]_0$, is initially obtained. This population will then decrease at a rate described by

$$\frac{d[M^*]}{dt} = -(k_r^S + k_{nr}^S)[M^*]. \tag{2.4}$$

By integration of this equation, it is possible to obtain the concentration of excited molecules, $[M^*]$, at any given time. The number of excited molecules will decrease exponentially according to

$$[M^*] = [M^*]_0 \, e^{-t/\tau_0}. \tag{2.5}$$

Because the intensity of the luminescent signal, I, is proportional to the concentration of excited molecules, following a pulsed excitation, the output luminescence intensity will also decrease in an exponential fashion with a time constant given by τ_0. The proportionality constant between $[M^*]$ and I is the radiative decay rate constant. This way, it can be written:

$$I(t) = k_r^S[M^*] = k_r^S[M^*]_0 \, e^{-t/\tau_0} = I_0 \, e^{-t/\tau_0}, \tag{2.6}$$

where I_0 is the luminescence intensity immediately after excitation. This way, τ_0 can be defined as the time it takes for the fluorescence intensity to decrease by $1/e$ of its initial value. The function $I(t)$ is the impulse response of the system. The response of the luminescence output to more complicated excitation patterns can be obtained by convolution of this function with the exciting impulse. In a practical situation, the detected luminescent signal is proportional to the effectively emitted luminescent intensity, but it depends on many experimental factors, some of which will be described later.

In the absence of non-radiative recombination mechanisms, the lifetime of the fluorophore would be given by $\tau_r = 1/k_r^S$. This time constant is called the radiative or 'natural' lifetime of the material and it can be theoretically calculated from the emission and absorption spectra. It is an intrinsic characteristic of the fluorophore.

In the case where intersystem crossing is favored, phosphorescence will be obtained instead. Similar expressions can be obtained for this process using the corresponding rate constants. For this reason, in the remaining of the text, when referring generically to luminescent processes, the labels S or T will be dropped from the rate constants.

The single exponential decay just described is valid assuming a homogeneous solution of a single molecular dye. The combination of different fluorophores or coexistence of the same fluorophore in different environments will result in more complex multi-exponential or non-exponential decays.

Quantum yield

The quantum yield of a luminescent dye can also be estimated from its rate constants. This parameter is a measure of the efficiency of the luminescence process. It is defined as the ratio between the number of emitted photons by the number of absorbed photons and it can be calculated from

$$\Phi = \frac{k_r}{k_r + k_{nr}}. \tag{2.7}$$

The quantum yield can be nearly unit depending on the relative magnitudes of the radiative and the non-radiative rate constants. Nevertheless, the energy efficiency of the luminescence process will always be less than unit, on account of the Stokes' shift. In practice, the value of Φ results from the summation of all the photons emitted during the whole decay interval divided by the number of absorbed photons, which is equal to the number of initially excited molecules, $[M^*]_0$, i.e.:

$$\Phi_F = \frac{1}{[M^*]_0}\int_0^\infty I(t)\,dt\,. \tag{2.8}$$

Considering the same incident excitation optical power, the higher the quantum yield the easier it will be to detect the luminescent signal of a given sample. The quantum yield can also be related with the lifetime of the fluorophore by

$$\Phi = \frac{\tau_0}{\tau_r}.$$

Depending on the nature of the deactivation mechanisms to which the fluorophore is subjected, the quantum yield can remain, or not, proportional to the excited state lifetime.

The lifetime and the quantum yield are two fundamental parameters of luminescent emission. They determine the intensity of the luminescent signal and its temporal behavior. In addition to the intrinsic deactivation mechanisms described above, the interaction with other molecular species introduces further non-radiative decay routes which can have a strong impact in both these parameters. Monitoring the lifetime and/or quantum yield, under the influence of such mechanisms, provides the basis for very sensitive sensing techniques and is widely used in many luminescence sensing applications.

2.2.2 Luminescence quenching

Sensing applications based on luminescence can be extremely sensitive. Unlike absorption, where measurements are performed comparing two light intensities which, sometimes, differ less than 1%, luminescence measurements are performed against a dark background. This way, signal-to-

noise ratios in luminescence can be very high, even when faint signals are being measured. Under certain conditions, even the luminescence of a single molecule can be measured. Luminescence, on the other hand, can be very sensitive to the external medium. This way, it is the perfect probe to perform a wide variety of measurements.

In most sensing applications, the luminophore is in fact used as a probe, and the goal is to measure the concentration of some analyte, through the influence it has on the luminescent indicator. Depending on the combination luminophore-analyte, different detection schemes can be used. The analyte concentration can impact the luminescent intensity, the lifetime, the spectral characteristics of the luminescent emission, etc. Conversely, this influence can take place through a variety of interaction mechanisms, namely, resonant energy transfer, photo induced electron transfer, proton transfer, and so on. Many of these phenomena have been used successfully as sensing mechanisms, each of them with advantages and disadvantages depending on the specific application. The detection of the concentration of an analyte trough collisional quenching of luminescence, in which the analyte is usually the quencher, is a particularly successful approach that has been used for sensing of many chemical and biological analytes [21]. This technique is often compatible with both intensity or lifetime detection; furthermore, several models are available, describing different quenching mechanisms, that provide simple calibration functions. In this work, some sensing applications based on the quenching of luminescence will be explored. For this reason special attention is given to quenching phenomena in the following lines. Other sensing mechanisms will be addressed shortly in some examples given throughout the text. For further details adequate references are provided [15, 22, 23].

Luminescence quenching

The term quenching refers, broadly, to any decrease in the luminescence intensity due to the presence of an external agent. Depending on the deactivation mechanism, the excited state lifetime of the luminophore is often decreased as well. Quenching is a bimolecular process involving the interaction between an excited luminescent molecule, M^*, and the external quencher molecule, Q. The result of this interaction is the non-radiative deactivation of the luminophore. This can be achieved by a variety of mechanisms such as electron transfer, proton transfer, energy transfer, molecular rearrangements or even formation of new molecular compounds [24, 25]. A generic representation of the quenching process is shown in the diagram of Figure 2.6, in which k_q

represents the observed rate constant of the bimolecular interaction[6]. τ_0 is the excited state lifetime in the absence of the quencher and results from the reciprocal of the sum of all intrinsic decay rates ($\tau_0 = (k_r + k_{nr})^{-1}$). The presence of a quenching agent, in a given concentration, introduces an additional external non-radiative decay rate in the luminescence process. As a consequence of the competition between intermolecular processes and the intrinsic deactivation mechanisms, both the quantum yield and the lifetime of luminescence can be decreased.

Quenching mechanisms are photophysical processes meaning that, after all the de-excitation steps, the luminophore gets back into the ground state, M, unaltered. These are reversible processes and a reduction in the quencher concentration results in an increase of the luminescent signal.

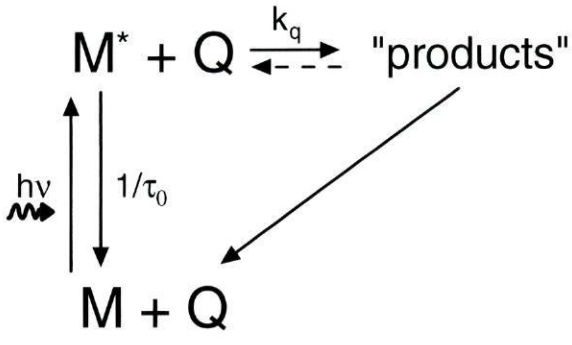


Figure 2.6 Simplified diagram illustrating the competition between the radiative emission and the quenching process. Adapted from [24].

Because most quenching processes demand for the interacting molecules to be in close contact, this can be a very sensitive sensing mechanism and a valuable tool with potential to provide information about the kinetics of many chemical and biochemical processes. For the later application, the lifetime of the fluorophore will determine the timescale of the dynamic processes that can be observed. In order for quantitative data to be extracted from experimental observations, theoretical models describing the quenching mechanisms must be developed. Depending on the kinetics of the processes involved, different approaches must be considered. When the quenching event is a consequence of a collisional encounter between the quencher and the fluorophore, a dynamic quenching model can be applied. Conversely, if the quencher and the luminophore associate to form a new non-emissive molecular compound, a static quenching model must be used instead.

---

[6] Usually expressed in units of $mol^{-1}s^{-1}$, this constant, together with the molar concentrations of quencher, $[Q]$, and excited luminophore, $[M^*]$, determines the rate at which the non-luminescent 'products' are formed: $rate\ of\ reaction = k_q \times [Q] \times [M^*]$. It depends on many factors, including temperature and viscosity.

Dynamic quenching

Dynamic quenching results from a collisional encounter between the excited fluorophore, M^* and the quencher molecule, Q. It happens when the mutual approach of the two molecules involved can occur in timescales smaller than the excited state lifetime of the luminophore. In this type of quenching there is no chemical change of the molecules. In dynamic, or collisional, quenching the bimolecular interaction is a diffusion-limited process. This means that the rate constant associated to the intrinsic quenching mechanism is much faster than the diffusion process. In such conditions, the observed rate constant of quenching, k_q, is determined by the diffusion rate, and can present a time dependent behavior. Such transient effects can be observed because the quenching rate depends on the initial distance between Q and M^*. At low to moderate concentrations, however, these effects are not noticeable, k_q can be considered approximately constant, and quenching can be adequately described by Stern-Volmer kinetics [26].

Examples of collisional quenchers include oxygen, amines, halogens and acrylamide. The actual quenching mechanism can vary with the luminophore-quencher pair. For instance, while acrylamide quenches indole by electron transfer processes, quenching by halogens is usually due to spin-orbit coupling inducing intersystem crossing to triplet states. Oxygen is an efficient collisional quencher of almost all known luminophores and it has often to be removed from solutions in order for other quenching processes to be studied. On the other hand, the quenching of luminescence is a preferred method for the optical detection of oxygen. This topic will be addressed in chapter 4, where further details will be given about the particular quenching mechanism and sensing technique.

When a homogeneous solution of a luminescent dye is excited by a δ-like radiation impulse, an initial concentration of excited molecules, $[M^*]_0$, is obtained. According to the scheme in Figure 2.6, in the presence of a quencher, the concentration of excited molecules will then decay at a rate given by

$$\frac{d[M^*]}{dt} = -(1/\tau_0 + k_q[Q])[M^*]. \tag{2.9}$$

Integration of this equation yields the time evolution of $[M^*]$:

$$[M^*] = [M^*]_0 \, e^{-(1/\tau_0 + k_q[Q])t}, \tag{2.10}$$

which, at any instant, is proportional to the emitted luminescence intensity[7]. According to equation (2.6), it can then be written

$$I(t) = I_0\, e^{-(1/\tau_0 + k_q[Q])t}. \tag{2.11}$$

This way, the luminescence intensity will follow a single-exponential decay with a time constant given by

$$\tau = \frac{1}{1/\tau_0 + k_q[Q]} = \frac{\tau_0}{1 + k_q\tau_0[Q]}. \tag{2.12}$$

This equation can then be written to read

$$\frac{\tau_0}{\tau} = 1 + k_p\tau_0[Q]. \tag{2.13}$$

This relation provides a way to monitor the concentration of a given quencher by comparing the quenched lifetime, τ, with the lifetime in the absence of the quencher, τ_0.

A similar relation can be obtained for the luminescence intensities, considering that the quantum yield in the presence of the quencher is

$$\Phi = \frac{k_r}{k_r + k_{nr} + k_q[Q]} = \frac{k_r}{1/\tau_0 + k_q[Q]}, \tag{2.14}$$

whereas in the absence of the quencher it is given by

$$\Phi_0 = k_r\tau_0. \tag{2.15}$$

The ratio between equations (2.14) and (2.15) leads to the Stern-Volmer equation:

$$\frac{\Phi_0}{\Phi} = \frac{I_0}{I} = 1 + k_q\tau_0[Q] = 1 + K_{SV}[Q]. \tag{2.16}$$

Here, I and I_0 represent the steady-state luminescence intensities (obtained for a given pair of excitation and emission wavelengths) and $K_{SV} = k_q\tau_0$ is the Stern-Volmer constant for dynamic quenching. Comparing equations (2.13) and (2.16) it is found that

$$\frac{I_0}{I} = \frac{\tau_0}{\tau}. \tag{2.17}$$

This is a very distinct characteristic of purely dynamic quenching processes where, in the presence of the quencher, both the lifetime and the luminescence intensity are reduced. The

[7] The luminescence output is usually proportional to the luminophore concentrations; however, this is true only for low to moderate luminophore concentrations; at higher concentrations self-quenching effects can take place and a non-linear dependence may be observed.

decrease in the lifetime occurs because the quencher introduces an additional decay rate that depopulates the excited state. Because the deactivation process is non-radiative, the quantum yield is decreased as well. That is not the case of static quenching where, for reasons that will be explained later, only the luminescence intensity is decreased whereas the lifetime remains constant.

Quenching data is usually obtained in the form of a Stern-Volmer (SV) plot where I_0 / I or τ_0 / τ is represented as a function of quencher concentration, $[Q]$. If only purely dynamic quenching is present, a linear behavior will be observed as described by equations (2.13) and (2.16). In such case, the slope of the SV plot corresponds to $K_{SV} = k_q \tau_0$ (Figure 2.7 (a)).

Overall, the observation of a linear variation in the Stern-Volmer plot is a good indication that a single class of luminophore, homogeneously distributed and with equal access to the quencher, is present in the solution. In rigid media, it is often the case that different environments are created in which the quencher has different accessibility. In such situation the observed SV plot departs from linearity presenting a downward curvature .

Obtaining a linear SV plot from intensity data, however, is not proof of pure dynamic quenching. Linear dependence of I_0 / I can also be observed with static quenching phenomena. Static and dynamic quenching can be distinguished by lifetime measurements (τ_0 / τ) or by their differing dependence on viscosity and temperature.

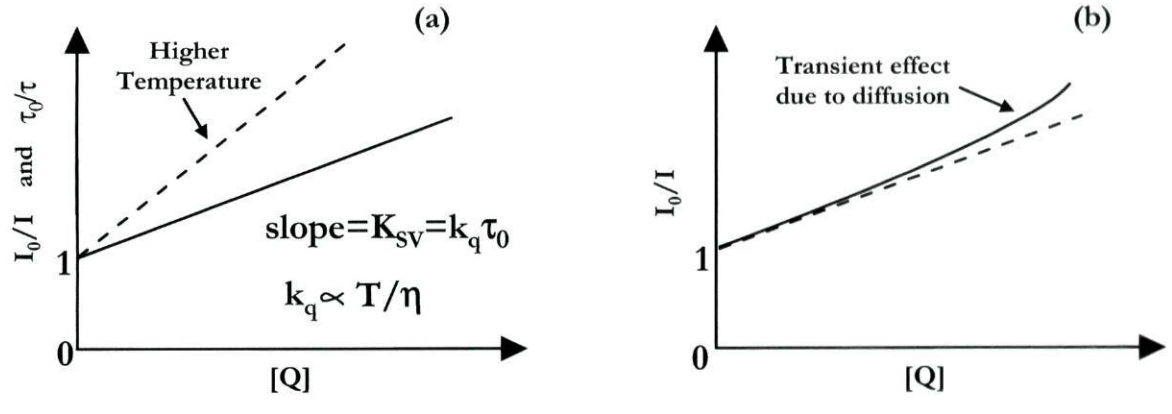


Figure 2.7 (a) Schematic representation of a typical Stern-Volmer plot as obtained for pure dynamical quenching processes. The dashed line illustrates the effect of an increase in the temperature. (b) At higher quenching concentrations or in viscous media transient effects due to diffusion cannot be neglected and can be identified by an upward curvature in the SV plot. Adapted from [21].

When the unquenched lifetime, τ_0, is known, the bimolecular quenching rate constant, k_q, can be obtained from the slope of the SV plot. This parameter allows the evaluation of the efficiency of the quenching process and it is a measure of the accessibility of the quencher to the luminophore, providing useful information about the quencher diffusion process. For diffusion-limited quenching

mechanisms, values of k_q around $10\,M^{-1}s^{-1}$ are typically observed. Lower values may indicate shielding of the luminophore while higher apparent values may arise from some binding interactions. Generically, the bimolecular quenching rate constant can be expressed as the product of the quenching efficiency , γ , with the diffusion rate constant k :

$$k_q = \gamma k . \tag{2.18}$$

For diffusion limited processes, γ is approximately equal to unit, meaning that practically every collisional encounter results in deactivation of the excited luminophore. Oxygen and acrylamide are examples of very efficient quenchers. The value of k depends on the properties of both the medium and the interacting molecules and it can be calculated by the Smoluchowsky formula

$$k = 4\pi D R_c N^{1000} , \tag{2.19}$$

where R_c is the collision radius, usually calculated by summing the molecular radii of the luminophore and the quencher. Similarly, the parameter D results from the sum of their individual diffusion coefficients. N^{1000} is Avogadro's number divided by 1000 , the division being performed so that the value of k can be expressed in terms of molarity. The diffusion coefficient of each molecular species can be estimated by the Stokes-Einstein formula

$$D = \frac{K_B T}{6\pi R \eta} \tag{2.20}$$

where K_B is Boltzmann's constant, η is the solvent viscosity, R is the molecular radius and T is the absolute temperature. This relation describes the diffusion coefficients of molecules that are larger than the solvent molecules. This way, it tends to underestimate D for smaller molecules, like oxygen. Nevertheless, it shows that an increase in temperature will result in a more efficient diffusion coefficient and that increasing the medium viscosity, on the other hand, has the opposite effect. This way, the efficiency of a collisional quencher will increase with temperature and decrease with the medium viscosity. The increase in the quenching rate constant due to temperature is illustrated in the plot of Figure 2.7 (a), where the dashed curve obtained at higher T presents a higher slope. These dependencies can have a strong impact on the quencher performance and are particularly important to consider when choosing rigid supports for sensing luminophores.

Excited luminophores, M^*, that are closer to quencher molecules, Q, at the time of excitation, will react, on average, faster than those that are further away, and whose reaction is dependent on mutual approach through diffusion. This way, the diffusion rate constant will show a time dependent behavior and should be written as $k(t)$. Several models have been developed to

express this time dependence where generically the diffusion rate constant is expressed by a constant term given by equation (2.19) plus a transient term containing the time dependence. While for a medium of low viscosity the transient term is only significant at very short time scales ($< 100\,ps$) and can be neglected, in media with moderate to high viscosity its effect cannot be ignored, and the observed luminescence decay is no longer a single exponential. This effect is stronger in luminophores with shorter lifetimes. The influence of the transient term in the luminescence steady state response can be described by a modified Stern-Volmer equation

$$\frac{I_0}{I} = \frac{1 + 4\pi N^{1000} R_c D \tau_0 [Q]}{Y}, \tag{2.21}$$

in which Y is a correction factor that accounts for the transient term and leads to a slight upward curvature of the Stern-Volmer plot (Figure 2.7 (b)). Although to a lesser extent, the plot of lifetime data may also present an upward curvature (it will depend on the relative scales of the lifetime and the transient term). Depending on the nature of the quenching process, different transient models can provide better fitting to experimental data. The analysis of the quenching data in terms of the various models can provide valuable information on the molecular dynamics of the quenching process [27].

Static quenching

The combination of luminescent dyes, in the ground state, with quencher molecules to form non-luminescent complexes can also take place. When excited by light absorption, the new complex returns to its ground state by non-radiative processes. This mechanism is referred to as static quenching, as opposed to dynamic quenching, and it is not dependent on diffusion or collisions. Static quenching can often be an interfering process hindering the analysis of dynamic quenching data. On the other hand, it can also provide valuable information about binding of the luminophore with quencher molecules.

When a quencher, Q, and the ground state luminophore, M, combine in a $1:1$ proportion, equilibrium is established according to the relation

$$M + Q \rightleftharpoons MQ, \tag{2.22}$$

where MQ is the non-luminescent complex. In this situation, the association constant for the complex formation is given by

$$K_S = \frac{[MQ]}{[M][Q]}. \tag{2.23}$$

With $[M]_0$ being the total (initial) concentration of uncomplexed luminophore, and considering the mass conservation law, it can be written that

$$[M]_0 = [M] + [MQ]. \tag{2.24}$$

The fraction of uncomplexed luminophore can then be obtained from

$$\frac{[M]}{[M]_0} = \frac{1}{1 + K_S[Q]}. \tag{2.25}$$

Considering that, for dilute solutions, the luminescent intensity is proportional to the concentrations, this equation can be written as

$$\frac{I_0}{I} = 1 + K_S[Q], \tag{2.26}$$

and describes a linear dependence of I_0 / I with $[Q]$. This is a similar behavior to that observed with dynamic quenching; in this particular case, however, the quenching constant is the association constant, K_S. This way, quenching data based on intensity measurements, alone, can be explained either by a dynamic or static quenching model. Additional information is needed to identify the actual quenching mechanism, and usually this is done by performing lifetime measurements. The formation of the non-emissive complexes affects only the ground state population of the luminophore, M, as the excited state population, M^*, is not affected. This way, static quenching reduces the luminescence intensity because it reduces the concentration of luminophore, M, available for excitation. The observed luminescence, however, arises from the remaining excited state population, M^*, which is not influenced by the formation of the complex, presenting a constant lifetime, τ_0.

A typical SV plot for static quenching is shown schematically in Figure 2.8, where (I_0 / I) is shown to change linearly with concentration, while the lifetime remains constant in the whole range $(\tau_0 / \tau = 1)$. In this scheme another property is illustrated that distinguishes dynamic and static processes, namely, the temperature behavior. The increase in temperature reduces stability and can cause break-up of the non-luminescent complexes. This will translate in a decrease of the association constant, K_S, and, therefore, in a decrease of the static quenching efficiency (dashed line in Figure 2.8). This is in opposition to what happens with dynamic processes where diffusion, and hence the quenching efficiency, is favored by increased temperatures. In addition to these methods, the formation of non-emissive ground state complexes can often be confirmed by observation of changes in the absorption spectrum.

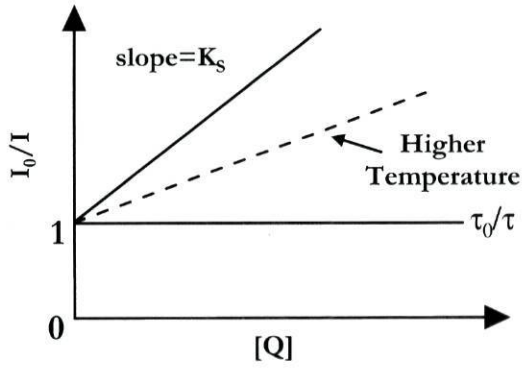


Figure 2.8 Typical SV plot obtained with static quenching. The dashed line indicates the effect of an increase in temperature. Lifetime is not affected by static quenching. Adapted from [21].

When high quencher concentrations are present, another type of static quenching can arise, without the formation of non-luminescent complexes. With increasing quencher concentrations, a growing number of closely spaced quencher-luminophore pairs are formed. This way, many of the excited molecules can be instantaneously quenched after excitation, which is perceived as an apparent static quenching.

This mechanism can be modeled considering an interaction sphere of volume V around the luminophore, M. If a quencher molecule, Q, is within this volume, then the quenching process will be complete. If, conversely, the quencher is outside the sphere of action, it will have no effect on the luminophore. This way, this type of static quenching will decrease the luminescence intensity, but it will have no effect on the luminescence lifetime. The volume V usually defines a sphere with a diameter only slightly bigger than the sum of the molecular radii of the quencher and luminophore.

Assuming a random distribution of quencher in the solution, the probability of having n quenchers inside the sphere can be calculated considering a Poisson distribution. Following this model, it is possible to demonstrate that the 'sphere of action' static quenching can then be described by

$$\frac{I_0}{I} = e^{VN[Q]} \tag{2.27}$$

where N is Avogadro's number. This equation expresses a non-linear dependence of I_0/I on quencher concentration. A plot of Equation (2.27) will present an upward curvature in the high concentration range. For low quenching concentrations, however, $e^{VN[Q]} \approx 1 + VN[Q]$, and the concentration dependence is approximately linear. Nevertheless, the two types of static quenching just described can be distinguished because the 'sphere of action' quenching does not impact the ground state luminophore, having no effect on the observed absorption spectrum.

Simultaneous static and dynamic quenching

The simultaneous presence of dynamic and static quenching can also cause deviations from linearity that can be described by a modified form of the SV equation. If the luminophore is quenched both by collisions and by complex formation with the same quencher, the luminescence steady-state response to changes in $[Q]$ is given by the product of equations (2.16) and (2.26):

$$\frac{I_0}{I} = (1 + K_{SV}[Q])(1 + K_S[Q]). \tag{2.28}$$

The resulting equation is second order in $[Q]$, and the corresponding SV plot (Figure 2.9 (a)) presents an upward curvature at higher quencher concentrations. In this situation, it is possible to discriminate the static and dynamic components of the quenching data using different methods. The most straight-forward method is to use lifetime measurements. A plot of (τ_0 / τ) as a function of $[Q]$, also represented in Figure 2.9 (a), will account only for the dynamic component, and provides a way to obtain K_{SV}. Alternatively, equation (2.28) can be expanded, and K_S and K_{SV} can be obtained by curve fitting of the following equation:

$$\frac{I_0}{I} = 1 + (K_{SV} + K_S)[Q] + K_{SV}K_S[Q]^2. \tag{2.29}$$

Conversely, if an apparent quenching constant defined by $K_{app} = (I_0 / I - 1)/[Q]$ is calculated for each value of quencher concentration, a linear plot should be obtained, described by

$$\frac{I_0}{I} = 1 + K_{app}[Q], \tag{2.30}$$

having an intercept at $I = K_S + K_{SV}$ and a slope given by $G = K_{SV}K_S$. An example of such situation is schematically represented in Figure 2.9 (b). The information obtained graphically allows the two rate constants to be obtained from the solutions of the second degree equation

$$K_S^2 - K_S I + G = 0. \tag{2.31}$$

In order to assign K_S and K_{SV} to each of the solutions obtained, extra information, like behavior with temperature and viscosity or magnitude of diffusion coefficients, must be addressed.

The 'sphere of action' static quenching can also take place together with dynamic quenching. Such combination was already observed, for instance, in data regarding the quenching of perylene by oxygen at high oxygen pressures. In fact, this is a situation most likely to be observed at very high quencher concentrations. In these cases, the modified SV equation should read

$$\frac{\mathrm{I_0}}{\mathrm{I}} = (1 + K_{SV}[Q])e^{VN[Q]}. \tag{2.32}$$

This equation describes a SV plot with an upward curvature in the high concentration range, similar to the one illustrated in Figure 2.9(a). Although equation (2.28) and equation (2.32) describe distinct phenomena, quenching data can often fit both models. However, in the absence of the formation of non-luminescent ground state complexes, the values obtained for K_S are usually small, indicating weak association and meaning that static quenching is more likely to be due to the close proximity of luminophore and quencher at the time of excitation. In such case, the 'sphere of action' quenching model will provide a more adequate description. The observation of the absorption spectrum, only affected when ground state complexes are formed, can also be used to identify the type of static quenching causing the non-linear behavior.

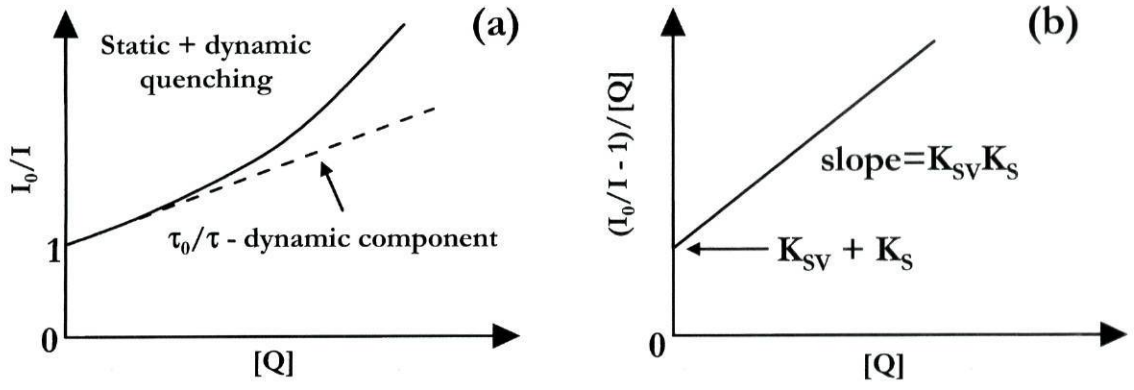


Figure 2.9 . (a) When dynamic and static quenching are simultaneously present the SV plot presents an upward curvature. The dynamic component can be obtained from the lifetime plot. (b) Alternatively, K_{SV} and K_S can be obtained graphically from the plot of $(I_0/I-1)/[Q]$. Adapted from [21].

It should be taken into consideration that the upward curvature of the SV plots may not be exclusively due to the presence of a static quenching component. It was already described that the presence of transient effects, characteristic of diffusion based processes, can lead to a similar behavior. In fact, the two effects can sometimes be superimposed. In such cases, for an accurate description, a more general expression can be used,

$$\frac{I_0}{I} = (1 + K_{SV}[Q])\frac{e^{VN[Q]}}{Y}, \tag{2.33}$$

including the parameter Y which accounts for the transient effects. In practical situations, however, equation (2.32) usually provides a very good fit of the experimental data, regardless of the mechanism actually causing the upward curvature. In such cases, an increased apparent value may be obtained for V, having contributions from both the transient term and true static quenching.

Quenching in heterogeneous emitting systems

In all the quenching models just described, a homogeneous distribution of a single luminophore in the solution or supporting medium was generally assumed. However, when the system observed has different populations of luminophores, the previous models are no longer valid and should be modified. A non-homogeneous luminophore distribution can arise either from the coexistence of more than one luminescent species, or from a heterogeneous distribution of a single luminophore in different sites of the solution or host matrix. When the multiple dyes have no overlapping emission spectra, the homogeneous quenching models can still be used, with the individual responses being spectrally discriminated. Most often, however, absorption and emission characteristics of the different populations are very similar, or exactly the same, as in the case of heterogeneous distribution of the same dye.

In sensing applications, it is often necessary for a single luminescent sensing dye to be immobilized in a solid support, usually provided by a polymer or sol-gel matrix. In such cases, the distribution of the sensing dye in the solid host, obtained after the immobilization procedures, is frequently not homogeneous [28, 29]. In this context, even in the presence of pure dynamic quenching alone, deviations from the linear SV equation can be observed. The non-linear behavior arises from the existence of different micro-environments within the solid matrix, where the quencher has different accessibility to the luminophore. In practice, the same dye can then behave like a population of different luminophore species, having the same spectral characteristics, but displaying a combination of multiple quenching rate constants, usually corresponding to distinct lifetimes. In this situation, for a population of n species undergoing only dynamic quenching, the steady state luminescence response, considering a certain pair of excitation and emission wavelengths, can be described by the weighted sum of the individual contributions from each species in the sample:

$$\frac{I_0}{I} = \left[\sum_{i=1}^{n} \frac{f_i}{\{1 + K_{SVi}[Q]\}} \right]^{-1}. \tag{2.34}$$

Each species has an associated SV constant, K_{SVi}, and contributes to the total luminescence intensity observed, I, with a given intensity fraction f_i. By definition $\sum f_i = 1$. The values of f_i are determined by the concentration, quantum yield, absorption and emission spectrum of each individual luminescent species. Furthermore, in this model it is assumed that each species acts independently and there is no mutual interference.

Very often, for a sensing dye immobilized in a sol-gel or polymer matrix, a good description of the quenching behavior can be obtained considering two luminophore populations. In this two site model, generally a fraction of the sensing dye, will be most accessible to the quencher presenting a higher SV constant. The remaining fraction of the luminophore, with a higher degree of inaccessibility, will present a much lower K_{SVi} value. When the values of the different Stern-Volmer constants differ significantly, usually a downward curvature will be observed in the resulting SV plot. This happens because the initial slope of the intensity ratio is determined by the largest K_{SVi} value. As the quencher concentration increases, however, the effect of the smaller K_{SVi} terms starts being noticed and the average apparent slope will be smaller. When, on the other hand, both populations present similar quenching constants the resulting plot will be approximately linear. The different populations usually present distinct lifetimes; this way, the lifetime data (τ_0/τ) can mimic the behavior of the intensity plot. Using equation (2.34), plots describing the two extreme situations could be simulated. The results are shown in Figure 2.10. In both cases the following population distribution was considered: $f_1 = 0.7$ and $f_2 = 0.3$. It can be observed that, when similar SV constants are considered ($K_{SV1} = 7\,M^{-1}$ and $K_{SV1} = 5\,M^{-1}$), the resulting quenching data is apparently linear. Conversely, the combination of two quenching constants with very distinct values ($K_{SV1} = 9\,M^{-1}$ and $K_{SV1} = 1\,M^{-1}$), results in a SV plot with a strong downward curvature.

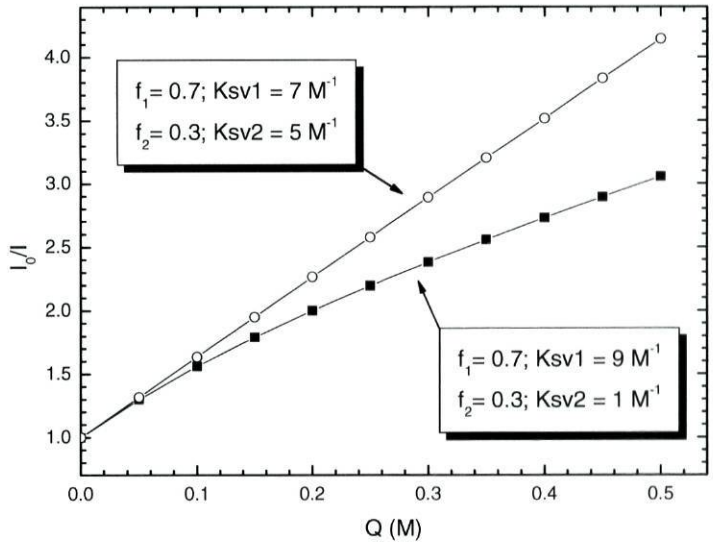


Figure 2.10 Simulated data showing SV plots obtained with two distinct populations of luminophores, subjected to dynamic quenching. The white circles plot was obtained with similar values of K_{SV}; the black squares represent two sites with very different values of K_{SV}.

If an increasing number of luminophore populations is considered, the analysis of the results becomes even more complex. For instance, the plot resulting from a three site model, will present very subtle curvature changes and will very often have an apparent linear behavior.

It is also possible that a dynamically quenched heterogeneous luminophores population can undergo simultaneously static quenching, described by any of the models considered previously. In such cases, a multi-site model can still be used, just by replacing the SV equation in the denominator of equation (2.34) by the respective static quenching model (Equations (2.28) or (2.32)). If, for instance, the 'sphere of action' static quenching takes place in combination with dynamic quenching, the measured intensity ratio I_0 / I, resulting from a population of n species, would be described by

$$\frac{I_0}{I} = \left[\sum_{i=1}^{n} \frac{f_i}{\{1 + K_{SVi}[Q]\} e^{ViN[Q]}} \right]^{-1}, \tag{2.35}$$

where different values of f_i, K_{SVi} and V_i are assigned to each luminescent species. As discussed previously, these static quenching phenomena usually result in an upward curvature of the Stern-Volmer plot. The degree of curvature, in this case, will depend on the fractional contribution from each species. The static quenching component can, in some situations, counteract the downward curvature that arises from different K_{SV} values. This way, the resulting plot can present either a linear behavior or an upward curvature, or even a combination of both.

Photochemical processes

When a luminescent dye is illuminated by energetic excitation radiation, besides the photophysical processes just described, photochemical processes may be induced as well. Photochemical de-excitation of excited molecules is usually non-radiative and involves the breaking of chemical bonds or creation of new bonds; this way, the ground state molecules are not recovered. This leads to an irreversible and gradual decrease in the number of dye molecules available for excitation, and thus, to a decrease in the observed luminescence intensity. The stronger the incident optical power, the faster the photo-degradation process will be. This process is also referred to as photobleaching and can be assisted by the quencher. Oxygen quenching of luminescent ruthenium complexes is a representative example of irreversible photo-degradation [30]. Although photobleaching also takes place in the absence of oxygen, it is stronger in the presence of this reactive gas.

The presence of photobleaching further complicates the analysis of intensity based quenching data and hinders its use in sensing applications. In face of a constant decrease in the observed luminescence intensity, a sensor calibration using one of the quenching models described would

have very limited validity. Lifetime data, on the other and, is practically unaffected by these processes, because it is an intrinsic characteristic of the remaining luminescent molecules.

Luminescence quenching can be a powerful tool, both for the analysis of systems at the molecular level and for biochemical sensing applications. A large number of different processes may be involved, however, that demand careful analysis of the quenching data. It is often the case that a particular model adequately fits the experimental data without being physically correct. This could lead to false conclusions about the subject under study (the quenching mechanism, structural information, molecular dynamics etc.). For the successful identification of the quenching mechanisms, and use of the adequate quenching models, usually different tests must be performed. In this regard, important tools like use of lifetime data, monitoring of the temperature behavior or observation of absorption spectra should be employed in combination with the luminescence intensity information. Although this can be a complex task, a wealth of information regarding a system, at the molecular level, can often be obtained.

For the particular case of sensing applications, however, data analysis can be greatly simplified. Most of the times, the quencher is the analyte under study and the goal is simply to determine its concentration. In this context, the simplest quenching models can still be used, and the choice should be made based on the fitting quality. The sensing of chemical species by luminescence quenching techniques has been used successfully in many applications, where very simple models were used, but still taking advantage of the very high sensitivity which is intrinsic to luminescence techniques [21, 31-33].

2.2.3 Intensity based spectroscopy

In order to implement a practical luminescence-based sensing system using, for instance, the quenching mechanisms just described, measurements of the luminescent properties must be performed. Luminescence detection techniques can be broadly classified in two main types of measurements, steady-state and time resolved measurements [34]. The former will be described first.

Steady-state measurements are those performed under continuous illumination and observation. This is the most commonly used technique and consists of recording the luminescence spectrum or the luminescence intensity (corresponding to a specified spectral range), while submitting the sample to continuous illumination with an adequate excitation source. These measurements can either serve the purpose of evaluating the luminophore intrinsic properties, like quantum yield or emission spectrum, or of assessing the influence of a given external parameter on these properties. The later is the basis of any sensing application. In either case, a vast number of

both intrinsic and experimental parameters should be thoroughly considered. In this regard, although simple in principle, the experimental measurement of luminescence intensity can be a complex task in practice.

Absorbance

For the purpose of obtaining a luminescent signal, optical excitation must first be achieved. A successful excitation depends on the spectral overlap of the exciting radiation with the dye absorption spectrum. Therefore, the choice of excitation source is of primary importance. In order to make a good decision, the luminophore absorption characteristics should be well known. Besides the quantum mechanical factors defining the strength of absorption at each particular wavelength, the efficiency of absorption will depend also on several experimental parameters. Macroscopically, the absorption efficiency of a sensing dye can be evaluated by the transmittance of a sample

$$T(\lambda) = \frac{I_T(\lambda)}{I_0(\lambda)}, \tag{2.36}$$

where $I_0(\lambda)$ and $I_T(\lambda)$ are the excitation light intensities entering and leaving the absorbing medium, respectively. For accurately measuring the transmittance of luminescent samples, only the transmitted excitation intensity should be measured and care has to be taken in order to avoid detection of the luminescent emission. A plot of equation (2.36) is a transmission spectrum and it will show a minimum at the wavelength where the absorption of the dye is maximum. From the transmittance, the absorbance

$$A(\lambda) = \log\frac{I_0(\lambda)}{I_T(\lambda)} = -\log T(\lambda), \tag{2.37}$$

can be calculated. The absorbance is proportional to the dye concentration, c, and to the sample thickness, l, following the Beer-Lambert law,

$$A(\lambda) = \varepsilon(\lambda) lc, \tag{2.38}$$

where ε is the molar decadic absorption coefficient, commonly expressed in $L\,mol^{-1}cm^{-1}$. A decadic absorption coefficient, $a(\lambda)$, can be calculated by dividing the absorbance obtained by the sample thickness

$$a(\lambda) = \frac{A(\lambda)}{l}. \tag{2.39}$$

From this relation it can also be written that

$$I_T = I_0 10^{-a(\lambda)l}. \tag{2.40}$$

Physicists usually prefer to use the natural logarithm instead of the decadic logarithm in the definitions just given. This way, in the literature the Napierian absorption coefficient, $\alpha(\lambda)$, is also frequently defined leading to

$$I_T = I_0 e^{-\alpha(\lambda)l} . \tag{2.41}$$

The SI unit of both a and α is m^{-1}, but for practical reasons cm^{-1} is commonly used. While these parameters are a characteristic of a given sample and depend on the dye concentration, the molar absorption coefficient is an intrinsic characteristic of the luminophore. The two can be related by:

$$a(\lambda) = \varepsilon(\lambda) c , \tag{2.42}$$

and

$$\alpha(\lambda) = 2.303\, \varepsilon(\lambda) c . \tag{2.43}$$

According to the Beer-Lambert law, the sample absorbance increases linearly with increasing dye concentration. Consequently, the more concentrated the sample, or the thicker the sensing medium, the more efficient will be the excitation process. However, although linear behavior is observed in dilute solutions, for very high luminophore concentrations deviations are often observed. This may be due to saturation effects leading to the formation of dye aggregates, which scatter light or may have modified absorption. Sample turbidity and light scattering can also impact the measured absorbance. The accurate application of the Beer-Lambert law, in an experimental situation, must also take into account reflections at the sample interfaces, detection solid angle, etc. In practice, it is not straightforward to determine the optical power actually reaching the sample, or the luminescent power actually leaving the sample. Absorbance also increases with the sample thickness; however, for practical reasons, l cannot be made too large as it will impact sensor miniaturization and it will increase its response time. All these factors should be carefully considered when preparing a luminescent sensing sample.

Steady-state luminescence

Considering a luminescent sample under continuous illumination, the number of photons incident, per unit volume and per unit time, will correspond to a constant excitation intensity I_0 (in moles of photons per liter per second). The number of absorbed photons would then be given by

βI_0, where β can be defined as the efficiency of absorption. Considering that the absorbed intensity is given by the difference , $I_A = I_0 - I_T$, it can be easily shown that $\beta = I_A / I_0 = 1 - 10^{-\varepsilon c l}$.

This excitation process creates a population of luminophores in the excited state which will decrease, by radiative and non-radiative mechanisms, at a rate given by equation (2.3). In steady-state, equilibrium is achieved between the excitation and the deactivation mechanisms, and the concentration of excited luminophores, $[M]^*$, remains constant. This means that the rate of change of the excited state population is zero and thus

$$\frac{d[M]^*}{dt} = 0 = \beta I_0 - (k_r + k_{nr})[M]^* . \tag{2.44}$$

In these conditions, the constant concentration of excited luminophores is given by

$$[M]^* = \frac{\beta I_0}{k_r + k_{nr}}, \tag{2.45}$$

and the corresponding steady-state luminescence intensity, I_L, can thus be expressed as

$$I_L = k_r [M]^* = \beta I_0 \frac{k_r}{k_r + k_{nr}} . \tag{2.46}$$

Considering the definition of quantum yield given in equation (2.7), I_L can also be written as

$$I_L = \beta I_0 \Phi = I_0 (1 - 10^{-\varepsilon c l}) \Phi , \tag{2.47}$$

where Φ is the luminophore quantum yield. This equation shows that, in addition to the dependence on the excitation efficiency, the luminescent output will depend also on the quantum yield. The quantum yield is an intrinsic parameter of the luminescent material, proportional to the relative magnitudes of the radiative and non-radiative decay rates. This way, for obtaining a strong luminescence output, materials with high quantum yields should be chosen. Although a smaller quantum yield could be compensated by increasing the incident excitation intensity, this is not a desirable situation. Photobleaching becomes stronger at high intensities, rapidly degrading the sensor performance.

Emission spectrum

In the previous discussion, the photon energy of the absorbed and emitted radiation was not considered, for simplicity. In practice the photons emitted follow a certain energy distribution which defines the luminophore emission spectrum. In this context, it is useful to express the steady-state luminescence intensity per absorbed photon as a function of the wavelength of the emitted photons. Such function can be denoted by $F_\lambda(\lambda_L)$, and should satisfy the relationship

$$\int_0^\infty F_\lambda(\lambda_L)\,d\lambda_L = \Phi\,. \tag{2.48}$$

$F_\lambda(\lambda_L)$ reflects the distribution of the probability of the different transitions involved in the luminescent decay and, in practice, it defines the emission spectrum. The luminescent emission spectrum is a characteristic of each luminophore. Experimentally, together with the associated Stokes' shift, it will determine the characteristics of the necessary detection instrumentation (filtering, detector spectral range, etc.).

In an experimental situation, the luminescence intensity detected at a given emission wavelength, $I_L(\lambda_L)$, will be proportional to $F_\lambda(\lambda_L)$ and to the number of absorbed photons at the excitation wavelength λ_E which correspond to a certain absorbed intensity $I_A(\lambda_E)$. The absorbed intensity can, in turn, be defined as the difference between the incident excitation intensity, $I_0(\lambda_E)$, and the transmitted excitation intensity, $I_T(\lambda_E)$:

$$I_A(\lambda_E) = I_0(\lambda_E) - I_T(\lambda_E)\,. \tag{2.49}$$

Taking this into consideration, the detected luminescent intensity can then be written

$$I_L(\lambda_E,\lambda_L) = kF_\lambda(\lambda_L)I_A(\lambda_E)\,, \tag{2.50}$$

where k is a proportionality factor depending on many experimental parameters. The parameter k accounts for a diversity of other factors affecting the detected signal (detection geometry, wavelength dependence of detector sensitivity, system spectral resolution, polarization effects, filtering, electronic gain, etc.), some of which can hardly be quantified. This way, the numerical value of a luminescence intensity measurement has no direct physical meaning and is usually expressed in arbitrary units or simply normalized to a reference value.

The absorbed intensity can also be expressed in terms of the sample absorption characteristics (concentration, molar absorption) through the Beer-Lambert law. For this purpose, using equations (2.41), (2.42) and (2.49), the luminescent intensity can also be written as

$$I_L(\lambda_E,\lambda_L) = kF_\lambda(\lambda_L)I_0(\lambda_E)\left\{1 - e^{-2.3\varepsilon(\lambda_E)lc}\right\}. \tag{2.51}$$

For low concentrations, the term in brackets can be expanded and approximated to $2.3\varepsilon lc$, leading finally to

$$\begin{aligned} I_L(\lambda_E,\lambda_L) &= 2.3\,k\,F_\lambda(\lambda_L)\,I_0(\lambda_E)\,\varepsilon(\lambda_E)\,l\,c \\ &= 2.3\,k\,F_\lambda(\lambda_L)\,I_0(\lambda_E)\,A(\lambda_E) \end{aligned} \tag{2.52}$$

This equation demonstrates that the detected luminescent signal depends on a great number of intrinsic and experimental parameters, which should be considered thoroughly for an accurate

interpretation of the obtained data. Conversely, it also provides a good insight into the many ways the signal detection, and thus the sensor sensitivity, can be optimized.

It should be remembered that equation (2.52) was approximated for low luminophore concentrations. Deviations from linearity are readily observed with increasing absorbance. Furthermore, when the concentration of the luminescent dye is very high, inner filtering effects may take place that can reduce the observed signal. These effects can have geometrical causes; for thick samples, the excitation intensity can be significantly attenuated before it gets through the sample, and this can greatly reduce the detected luminescence signal if detection is made in a transmission configuration. Moreover, when an overlap exists between the dye absorption and emission spectra, self-absorption may take place. The presence of impurities providing scattering centers or background luminescence can further complicate the observed behavior.

When I_L is measured as a function of λ_L, for a fixed excitation wavelength, λ_E, the emission spectrum can be obtained (i.e., a signal proportional to $F_\lambda(\lambda_L)$). If, on the other hand, the luminescent intensity is measured at a fixed wavelength, λ_L, while the excitation wavelength, λ_E, is being changed, the excitation spectrum can be obtained instead (i.e., a signal proportional to $A(\lambda_E)$).

Spectral measurements are usually performed using a spectrofluorometer. These instruments usually consist of a broadband optical source, followed by a monochromator to select the excitation wavelength. The selected radiation is then shined upon the luminescent sample and detection is usually made at 90° with the incident beam. In order to perform wavelength discrimination of the luminescence emission, a second monochromator is placed before the detector, usually a photomultiplier. An ideal spectrofluorometer would have an optical source with a constant photon output at all wavelengths ($I_0(\lambda_E) = const$), monochromators with polarization and wavelength independent efficiency and a detector with equal sensitivity at all wavelengths. Unfortunately, such components are not available and, in practice, corrections must be performed in order to account for these variable parameters.

Instrumentation

The instrumentation used in practice introduces a series of wavelength dependencies that cause distortion of the measured spectra if no corrective measures are taken [35]. High pressure xenon arc lamps are widely used as excitation sources. Except for a few sharp lines near $450\,nm$ and $800\,nm$, these lamps provide a relatively continuous light output in a broad wavelength range ($250\,nm$ to $700\,nm$), which can be used to excite most luminophores. Nevertheless, its emission spectrum is not flat and the wavelength dependent output of these lamps will distort the measured

spectra. Due to the need to select the excitation wavelength using a monochromator, the optical power reaching the sample is usually low. It is possible to use other lamps that provide higher intensities in the UV region, like mercury lamps or mercury-xenon lamps. In these cases, however, the optical power is further concentrated in sharp spectral lines.

In addition to the optical source wavelength dependence, the monochromators also have a wavelength dependent efficiency. This dependence arises mostly from their dispersive element, typically a diffraction grating, which usually has a maximum diffraction efficiency at a given wavelength. Also, scattering and higher order diffraction can increase the levels of stray light reaching the detector and further distort the measured spectra. On top of this, the efficiency of monochromators is typically dependent on the polarization of the incident radiation. This can be a problem because the luminescent emission is often anisotropic and can be partially polarized[8] [36]. In order to avoid polarization dependence, the excitation radiation is usually linearly polarized, and detection is performed through a second polarizer at 54.7° with the input polarization (called magic angle). In these conditions, it can be demonstrated that the signal detected is always proportional to the total luminescent intensity[9].

Typically, photomultiplier tubes are used for detection in steady-state measurements due to their high sensitivity. More recently, linear and 2-D CCD detectors are also being used in many devices and practical applications. Unfortunately, all these detectors have a wavelength dependent sensitivity that must be accounted for.

---

[8] Luminescence anisotropy arises from the fact that both absorption and emission have associated transition moments that lie along specific directions of the molecular structure of the luminophore. The probability of absorption is proportional to the relative orientation of the incident electric field and the absorption transition moment. This way, those molecules aligned with the electric field, at the time of excitation, will be preferentially excited. In these conditions the luminescent emission that follows can be totally or partially polarized. Usually, in solutions, where molecules are free to rotate, the molecular rearrangement causes the emission anisotropy to decrease very fast towards zero (depolarized light) or to some fixed value. The anisotropy decay, however, depends strongly on the medium viscosity, lifetime, temperature, etc.

[9] When the fluorescence emission is polarized, the use of polarizers with appropriate orientations allows detection of a signal proportional to the total fluorescence intensity. The disposition of the polarizers is based on the fact that the total intensity is proportional to $I_T = I_{\parallel} + 2I_{\perp}$ where $I_{\parallel}$ and $I_{\perp}$ are the intensities of vertically and horizontally polarized emission, respectively. For a typical set-up, where observation is made at right angles with excitation (see [15] for details), it can be shown that, if the angle θ of the excitation polarizer (placed before the sample) and the angle ϕ of the detection polarizer (placed after the sample) obey the relation $2\cos^2\theta\cos^2\phi = \sin^2\phi + \sin^2\theta\cos^2\phi$, the detected signal will always be proportional to the total intensity, independent of the original luminescence polarization. Therefore, if the excitation polarizer is in the vertical position $\theta = 0$, the emission polarizer must be set at the 'magic angle' $\phi = 54.7^{\circ}$ ($\cos^2\phi = 1/3$). If, on the other hand the emission polarizer is in the vertical position $\phi = 0$, the excitation polarizer must be set at the magic angle $\theta = 54.7^{\circ}$ ($\cos^2\theta = 1/3$).

Due to the wavelength dependence of the optical source, most of the time the only way to obtain accurate spectral measurements is to provide for a reference channel. For this purpose, in spectrofluorometers, a few per cent of the excitation radiation is usually deviated towards a second detection channel. Generally this light is detected by a photodiode with an approximately spectrally-flat response; alternatively, a quantum counter is used. A quantum counter usually consists of a concentrated solution of a dye with a quantum yield that does not depend on λ_E. This way, all the incident photons are absorbed and the emitted luminescent signal detected by the reference detector is proportional to the photon flux incident in the sample under study. In principle, ratiometric detection of the signal from the main detector with the signal from the reference detector will allow to compensate for the wavelength dependences of the excitation optical source, excitation monochromator efficiency and detector sensitivity. In addition, any fluctuations of the output intensity of the excitation source over time will be compensated as well.

Most of the time, however, because the optical path of both channels is not exactly the same, full compensation cannot be achieved. In addition, with this method, the detection monochromator is not accounted for. In the cases where very accurate measurements are needed, usually a standard dye is used with known emission and excitation spectra. The spectra of this dye are then measured and compared with the expected spectra, allowing the calculation of adequate correction factors. Alternatively, instrument correction factors can also be obtained by measuring the spectrum of a calibrated light source transmitted trough a transparent scattering solution. The determination of quantum yields is an example of a measurement only possible using accurately corrected spectra. For this particular application, the use of standard dyes with known quantum yield must be considered for accurate calibration of the system.

In summary, the main difficulty associated with intensity based measurements arises from the fact that the detected intensity is not an intrinsic parameter of the luminescent dye. It depends on intrinsic properties of the luminophore, like the quantum yield, but also on a great diversity of external parameters. The control of all these variables is critical when aiming to obtain accurate information on the dye intrinsic properties, like quantum yield, emission and absorption spectra.

Sensing systems

All of these parameters should also be thoroughly considered when designing a practical sensing system. In such cases, the aim is often to detect a luminescence intensity signal proportional to the concentration of the luminophore or, in alternative, to the concentration of a given quencher. In this context, many of the factors just described do not affect the sensor performance so critically.

For instance, in many applications spectral discrimination is not necessary and detection is made by a photodetector which sums up all the photons in a given spectral range. In this case, it would not be necessary to correct for the spectral dependence of the detector sensitivity or excitation source intensity. Usually, a limited spectral range is used for a given sensor application. Consequently, filters can be used instead of monochromators to select excitation and emission wavelengths. In addition, optical sources like laser diodes or LEDs can be chosen to closely overlap the absorption spectrum of the dye being used. In these conditions, higher signal-to-noise ratios can be achieved, leading to higher sensitivities.

On the other hand, additional external parameters come into play. For instance, while in the laboratory the sample temperature can be easily controlled, in field applications this parameter should be monitored and accounted for when evaluating the measured intensity; in some cases the dye is immobilized in a solid host and it tends to leach out when the sensor is used in aqueous media; the use of optical fibers may introduce other sources of intensity fluctuations, like changes in the coupling conditions due to vibrations and microbending, etc..

In any case, intensity based measurements will always require the use of some reference scheme in order to separate the effect of the parameter being measured from the effect of external factors like temperature, optical source drift, change in coupling conditions, etc.. Some schemes have been conceived, trying to provide intensity based sensors with adequate reference. A successful method consists of performing ratiometric detection at two different emission wavelengths [37]. For this purpose the luminophore to be used must display a shift in its absorption or emission bands in the presence of the analyte. The analyte concentration can then be determined by the ratio of two luminescent intensities detected at two distinct excitation or emission wavelengths. This is a simple scheme capable of ruling out the influence of many external parameters. However, although these spectral features are common to many pH sensitive dyes, they are rare otherwise. In alternative, two luminescent dyes can be used, one of them being insensitive to the analyte.

Nevertheless, such schemes will often increase system complexity and cost. In addition, few of them will fully compensate for photochemical degradation of the sensing dye. Photobleaching is, in fact, one of the biggest pitfalls of intensity based luminescence sensors. A sensor suffering from this problem will have its useful life greatly decreased and it will require constant recalibration. Although some dual wavelength detection schemes can partially avoid this problem, the simplest way to get around it, without compromising the system sensitivity (by greatly decreasing the excitation optical power or limiting the quencher damaging effect), is to perform time resolved measurements [38].

2.2.4 Time domain spectroscopy

Time resolved measurements of the luminescence intensity are a powerful alternative to steady-state measurements. The different techniques of time resolved detection aim to measure the excited state lifetime or, more precisely, to determine the parameters associated with the luminescent decay of a given sample [34, 39].

Lifetime is an intrinsic characteristic of the luminophore; therefore, unlike steady-state detection, measurements are not so susceptible to system changes such as optical alignment, source intensity fluctuations, dye concentration or even photobleaching. On the other hand, the excited state lifetime can be very sensitive to certain molecular interactions, like those observed between luminophore and quencher. In this context, a sensing system based on lifetime detection could provide, in principle, very sensitive, self-referenced measurements, with very stable calibration, suitable for long term use. The observation of luminescent decay, which occurs in very short time scales, provides the opportunity to monitor many transient behaviors of molecular systems, which sometimes become unnoticeable under steady state excitation. For these reasons, time resolved detection of the luminescent intensity can frequently provide much more information about the system being studied than it is possible to achieve with steady-state data. For instance, two species having similar spectral properties but different lifetimes would be distinguished by decay time measurements but not by steady-state detection. In the analysis of quenching experiments, lifetime data is an essential tool for identification and discrimination of static and dynamic quenching mechanisms. In general, the study of the dynamics of excited states has a fundamental role in the study of the kinetics of many photophysical, photochemical and photobiological processes.

Time resolved measurements can be made in the time domain, where the sample is excited with a short pulse of light, or in the frequency domain, where the sample is excited by radiation with sinusoidal amplitude modulation. The two methods are widely used nowadays both in laboratory environment and in sensing applications. Time domain techniques are the preferred method for direct determination of lifetimes, and will be described first. Frequency domain techniques, on the other hand, are being explored in many sensing applications and will be addressed in the next section.

Pulsed fluorometry

The basic principle of time-domain techniques is the excitation of the sample with a short pulse of light, and the observation of the subsequent luminescent decay. The pulse width should be made as short as possible, preferably much shorter than the lifetime of the dye under study.

In the simplest case, the δ-pulse response of a luminescent sample, $I(t)$, is a single exponential with a time constant equal to the excited state lifetime (equation (2.6)). A representation of the data obtained in this ideal situation is shown in the diagrams of Figure 2.11. If the time dependent intensity is measured as a function of time, the decay time can then be estimated from the slope of the linear plot of $\log I(t)$ (Figure 2.11 (b)), or from the time at which the intensity drops to $1/e$ of its initial maximum value at $t = 0$ (Figure 2.11 (a)).

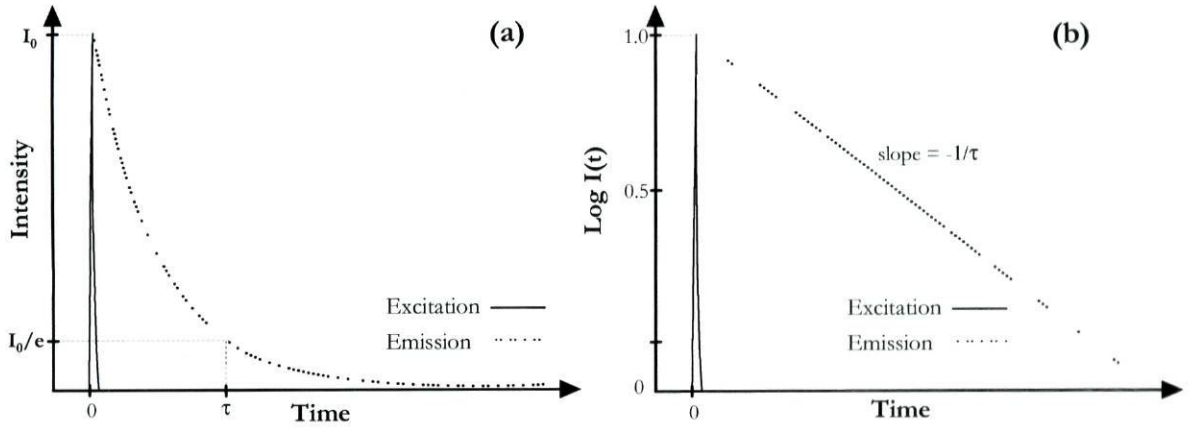


Figure 2.11 Principles of time resolved measurements. (a) After an excitation impulse, the luminescent intensity decays exponentially with a time constant given by the lifetime. (b) The decay time can be calculated from the slope of the plot $\log I(t)$ vs. time. Adapted from [39].

In practical circumstances, however, the situation is never so simple. Usually, the excitation pulse has a short but finite time width, not negligible in comparison with the lifetime to be measured. In addition, the response time of the detection system can introduce further broadening in the measured signals. In such cases, the luminescent response will be given by the convolution of the ideal δ-pulse response, $I(t)$, with a function, $E(t)$, describing the real excitation impulse as perceived by the detection system:

$$R(t) = E(t) \otimes I(t) = \int_{-\infty}^{t} E(t')I(t-t')dt' . \tag{2.53}$$

In order to obtain the lifetime of the luminophore from the measured data, the impulse response of the excitation/detection system ($E(t)$) must be known very accurately, and a deconvolution must be performed. Much of the complexity of lifetime data analysis comes from the difficulty in extracting the true luminophore impulse response from the measured signals. For this reason, a great effort is placed in the optimization of the deconvolution process. Nevertheless, interpretation of data arising from single exponential decays is relatively straightforward. The real challenge comes from the fact that most samples display more than one decay time.

Multiple exponential decays

Multiple lifetimes can arise from the presence of different luminescent species in the same sample. However, a single luminophore may also present a complex multi-exponential or non-exponential decay. If, for instance, a luminescent dye has a heterogeneous distribution in a solid matrix, existing in different environments where it is shielded or exposed to a quencher, then different lifetimes may be assigned to each one of these populations. In general, more complex decay functions can be fitted by a multi-exponential model described by

$$I(t) = \sum_i \alpha_i \, e^{(-t/\tau_i)}, \tag{2.54}$$

where α_i are called the pre-exponential factors which determine the amplitudes of each component at $t = 0$, and τ_i are the respective lifetimes. Depending on the system being studied the meaning of these parameters may differ. For a single dye existing in different environments, usually the various populations have the same radiative decay rate; in such case, α_i represents the fraction of luminophore in each of the environments. For a mixture of different luminescent species, however, the relative values of α_i depend on many parameters, like the quantum yield and concentration of the different luminophores, and assigning a molecular meaning to each α_i is not straight-forward.

In any case, it is possible to calculate the fractional luminescent intensity contribution, f_i, of each lifetime component to the total steady-state luminescent intensity, using the parameters α_i and τ_i. The values of f_i are given by:

$$f_i = \frac{\alpha_i \tau_i}{\sum_j \alpha_j \tau_j}, \tag{2.55}$$

with $\sum_{i=1}^{n} f_i = 1$. The product $\alpha_i \tau_i$ is proportional to the area under the decay curve for each decay time. For a mixture of luminescent species, f_i represents the contributions of each luminophore to the total intensity.

The simplest case to consider is the presence of two different populations. Usually, the presence of a second lifetime will introduce a curvature in the plot of $\log I(t)$. Fitting the obtained data with equation (2.54), will then allow to recover the decay parameters. However, depending on the relative magnitudes of the different parameters, the change in the decay data can be very small, may be present only in the end of the decay tail and sometimes is barely noticed by simple observation. For this reason it is important to capture the whole decay function, which demands a high signal to noise ratio. As the number of fractional contributions increases, the interpretation of lifetime data becomes increasingly complex, and to extract the values of f_i, α_i and τ_i from the

observed decay measurements is not a trivial task. This happens because the parameters α_i and τ_i are correlated. This means that the same decay data may fit different combinations of α_i and τ_i. In practice it is not possible to resolve two distinct lifetimes if they differ from less than 20%.

For these reasons, evaluation of the fitting quality is a critical step of lifetime measurements, and is usually done with the help of dedicated software. Many models have been explored to evaluate the quality of fitting: methods of least squares, moments, Fourier transforms, Laplace transforms, and others. The most widely used method is based on non-linear least squares [40]. The basic principle of this technique is to minimize a quantity that represents the mismatch between the theoretical model and the experimental data. This correlation parameter, χ^2, is usually defined as the weighted sum of the squares of the deviations of the experimental response $R(t_i)$ from the calculated function $R_C(t_i)$,

$$\chi_r^2 = \frac{1}{\nu}\sum_{i=1}^{N}\left[\frac{R(t_i) - R_C(t_i)}{\sigma(i)}\right]^2 = \frac{1}{\nu}\chi^2, \tag{2.56}$$

where N is the total number of data points and $\sigma(i)$ is the standard deviation associated to the ith data point. ν is the number of degrees of freedom defined by $N - p$, where p is the number of fitting parameters. Dividing χ^2 by the number of degrees of freedom, a reduced value is obtained (χ_r^2) that is independent of N and p. For a good fit the value obtained for χ_r^2 should be close to unit. Although these mathematical tools provide valuable help, careful analysis and a lot of experience is necessary for accurate interpretation of lifetime data.

Regardless of the number of exponential terms considered, it is always possible to define an average decay time, $\langle\tau\rangle$. This value can be obtained by averaging the time t over the intensity decay of the luminophore

$$\langle\tau\rangle = \frac{\int_0^\infty tI(t)dt}{\int_0^\infty I(t)dt}. \tag{2.57}$$

For a single exponential decay, equation (2.57) should yield the luminescence lifetime τ. For the particular case of a double exponential decay, the average decay time can also be expressed as

$$\overline{\tau} = \frac{\alpha_1\tau_1^2 + \alpha_2\tau_2^2}{\alpha_1\tau_1 + \alpha_2\tau_2} = f_1\tau + f_2\tau. \tag{2.58}$$

In this definition, the average decay time results from the sum of the different lifetimes weighted by the corresponding fractional intensities. The interpretation of these parameters in terms

of molecular properties can sometimes be very difficult when performing analyses of complex systems, as they do not provide a complete description of the intensity decay. On the other hand, the use of an average value can be very useful and straightforward in many practical situations. For instance, the intensity weighted lifetime can be used to calculate an average collisional quenching constant. Such average parameters are of particular interest for sensing applications, where most of the times an apparent lifetime is measured as a function of the concentration of some analyte. In this context, the analysis of lifetime data can be greatly simplified.

Techniques and instrumentation

There are many ways to record lifetime data, such as streak cameras, boxcar integrators, and so on. Nevertheless, most instruments used for the determination of lifetimes are based on the time-correlated single photon counting (TCSPC) method, also called single-photon timing (SPT). This technique is based on the fact that the probability of detecting a single photon at the time t after excitation is proportional to the luminescence intensity at that time. This way, measuring the time between the excitation pulse and the first arriving photon, at different times and for a large number of excitation impulses, it is possible to reconstruct the intensity decay curve, based on the obtained histogram of photon counts per time channel. Because only a single photon is detected by measurement cycle, this technique requires a large number of measurements in order to completely reconstruct the decay function. SPT can be very sensitive but, although conceptually simple, it is associated with very complex instrumentation, which, ultimately, will determine the sensitivity and time resolution that can be achieved.

The excitation source is of primary importance and it should provide narrow pulses with a relatively high repetition rate. Initially, the excitation was provided mainly by flash lamps, which delivered low intensity nanosecond pulses with repetition rates in the $10\,kHz$ to $100\,kHz$ range, in a limited spectral range ($200\,nm - 400\,nm$). Flash lamps are relatively inexpensive and by using de-convolution it is possible to measure lifetimes in the hundreds of picoseconds range. However, low repetition rates demand for long acquisition times where lamp drift can become a problem. Nowadays, although much more expensive, lasers are used as the preferred excitation source. A mode-locked laser, associated with a dye-laser or Ti:Sapphire laser can easily provide picosecond pulses, at high repetition rates (MHz) and in a wide range of wavelengths.

The time resolution of the instrument is also critically determined by the sampling and detection electronics. While standard dynode chain photomultiplier tubes (PMT) can provide response times in the nanosecond range, nowadays microchannel plate (MCP) PMTs are available

capable of operating $10-20$ times faster. Nevertheless, this new generation of PMTs is considerably ore expensive. Although photodiodes are much cheaper and can respond faster than MCP PMTs, they lack sensitivity. Avalanche photodiodes (APDs) have adequate gain, but their fast response is dependent on a very small size active area ($10\mu m \times 10\mu m$) on which the luminescent signal must be focused. This way, APDs do not have the necessary sensitivity for most measurements. With mode-locked lasers and microchannel plate photomultipliers, widths of the instrument pulse response in the range $30\,ps - 40\,ps$ can be achieved. This allows the measurement of decay times as short as $10\,ps - 20\,ps$.

Although source and detector are the key elements in lifetime measurements, these techniques rely also on a variety of sophisticated electronic devices, like synchronization electronics, time to amplitude converters, filtering, delay lines, etc., which add to the cost and complexity of the measurement system. In addition, several problems in data collection can arise that must be considered, like polarization effects, scattering in turbid solutions, and wavelength dependence of the measurement system. Solving these problems often demands additional data processing, use of filtering or even using a reference channel.

Generally, the shorter the lifetime to be measured the more expensive and complex the measurement system becomes. Consequently, the use of standard organic fluorophores, with lifetimes in the nanosecond range, can be a serious obstacle to the implementation of low cost sensing applications using time resolved detection techniques. In this regard, the advent of long lived luminescent probes, like organometallic complexes, can provide interesting solutions. Because these sensing dyes present lifetimes in the microsecond range, the instrumentation can be greatly simplified. In these time scales, system impulse responses tens of nanoseconds wide are acceptable, which can be achieved by laser diodes or even low cost LEDs in combination with photodiodes. Initially limited to the infrared region of the spectrum, these light sources are now available in a wide spectral range including blue and violet. High brightness blue LEDs, with emission spectra suitable for the excitation of many sensing dyes, are now available at low cost. In addition, in many sensing applications it is just necessary to determine the change in the apparent lifetime induced by the analyte; this way, the measurement procedure can be greatly simplified.

In summary, the direct measurement of lifetimes is the basis of extremely sensitive techniques, which can provide a wealth of information about many molecular systems or be used in extremely sensitive sensing applications. Although these techniques are usually associated to complex and expensive instrumentation, recent developments in solid-state optoelectronics, together with new long lived luminescent probes, have the potential for allowing the implementation of self-referenced,

lifetime based sensors, at low cost. Although some examples of life-time based sensing and imaging systems using time resolved measurements have been explored [41-43], and are even part of some commercial systems, due to their intrinsic simplicity, frequency domain measurements are preferred for this kind of applications. Nevertheless, the constant evolution of optoelectronics will surely contribute to further lowering the cost and complexity of time domain instrumentation, making it attractive for a wide range of practical applications.

2.2.5 Frequency domain spectroscopy

The measurement of excited state lifetimes can also be performed in the frequency domain, as an alternative to the time domain techniques just described [44, 45]. Both techniques are widely used nowadays and, although they differ in method and associated instrumentation, their goal is the same, to determine the decay parameters of complex luminescent responses.

Frequency domain or phase modulation fluorometry

In frequency domain spectroscopy the excitation optical source is modulated in amplitude at high frequency. Typically, sinusoidal modulation is applied at frequencies that should be in the range of the reciprocal of the decay time. In these circumstances, the obtained luminescent emission is also modulated in amplitude at the same frequency. Due to the time lag between excitation and emission, however, the luminescent signal is delayed in phase relative to the excitation. This way, the phase delay, ϕ, can be used to calculate the lifetime. The scheme in Figure 2.12 shows the typical response of a luminophore submitted to amplitude modulated excitation.

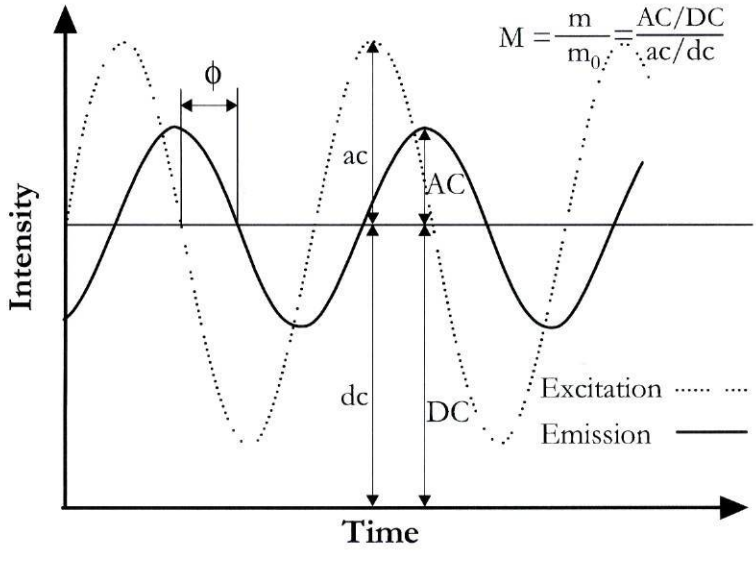


Figure 2.12 Response of luminescence emission to intensity modulated excitation, showing the relative phase delay, ϕ, and modulation ratio, M.

This scheme also shows that, in addition to the phase delay, the resulting signal can present a decreased modulation depth, $m = AC/DC$, in comparison to the excitation signal, $m_0 = ac/dc$. The decrease in modulation depth is also called demodulation and it happens because the luminescent response is given by the convolution of the impulse response with the sinusoidal modulation. This way, for a fixed modulation frequency, the longer the decay tail of the luminophore impulse response, the greater the extent of the demodulation will be. Evaluation of the modulation ratio, $M = m/m_0$, can also be used to calculate the lifetime.

Typically, the relative phase, ϕ, and modulation ratio, M, are evaluated in a range of frequencies and the curves obtained characterize the harmonic response of the system. It is possible to demonstrate that the harmonic response corresponds to the Fourier transform of the δ-pulse response. This way, the two techniques are theoretically equivalent, in the sense that they analyze the same physical phenomenon although operating in different domains (frequency domain and time domain). However, they differ in the measurement methods and necessary instrumentation. In the particular case of frequency domain interrogation, because the data is evaluated directly in the frequency domain, no deconvolution is necessary.

Calculation of the lifetime

In order to extract the decay information, from the frequency domain data, it is necessary to relate ϕ and M with the lifetime τ. Assuming a single exponential decay, the δ-impulse response of the luminophore can be described by

$$I = I_0 e^{(-t/\tau)}. \tag{2.59}$$

In such case, the differential equation describing the time dependent luminescent intensity is given by

$$\frac{dI(t)}{dt} = -\frac{1}{\tau} I(t) + E(t). \tag{2.60}$$

where $E(t)$ is the function describing the excitation radiation. In the particular case of sinusoidally modulated excitation, this function can be described by

$$E(t) = a + b \operatorname{sen} \omega t \tag{2.61}$$

where ω is the angular modulation frequency, and a and b correspond to the dc and ac components, respectively, of the incident intensity. This way, the modulation depth of the excitation function is given by $m_0 = a/b$. The luminescent dye will respond to this excitation with a

luminescent output at the same frequency, but shifted in phase and presenting a different modulation depth. Then, it can be assumed that the time dependent luminescent intensity, $I_L(t)$, is described by a function like

$$I_L(t) = A + B\sin(\omega t - \phi). \tag{2.62}$$

When the sample is submitted to the sinusoidal excitation described by equation (2.61), equation (2.62) should be a solution to the differential equation (2.60). The substitution of $I_L(t)$ and $E(t)$ into equation (2.60) yields

$$\omega B\cos(\omega t - \phi) = -\frac{1}{\tau}[A + B\sin(\omega t - \phi)] + a + b\sin\omega t. \tag{2.63}$$

For the proposed solution to hold, this equation should be valid at all times. The relation between the excitation/emission parameters and the lifetime can be obtained by expansion of the trigonometric functions followed by equating the constant terms, and the terms in $\sin\omega t$ and $\cos\omega t$. This procedure yields the equations that follow:

$$a - \frac{1}{\tau}A = 0, \tag{2.64}$$

$$\omega\cos\phi - \frac{1}{\tau}\sin\phi = 0, \tag{2.65}$$

and

$$\omega\sin\phi + \frac{1}{\tau}\cos\phi = b/B. \tag{2.66}$$

From equation (2.65), a relation between the lifetime and the phase delay can be obtained

$$\tan\phi = \omega\tau = 2\pi f\tau. \tag{2.67}$$

Squaring and then adding equations (2.65) and (2.66), yields the expression

$$\omega^2 + \left(\frac{1}{\tau}\right)^2 = \left(\frac{b}{B}\right)^2, \tag{2.68}$$

which, after division by equation (2.64) squared ($(A/a)^2 = \tau^2$), yields a relation between the lifetime and the modulation ratio

$$M = \frac{B/A}{b/a} = \frac{1}{\sqrt{1+\omega^2\tau^2}}. \tag{2.69}$$

Experimental measurements of the phase angle, ϕ, and the modulation ratio, M, can be used to calculate the lifetime through equation (2.67) or equation (2.69), respectively.

Frequency domain data

In practice, these parameters are usually evaluated in a range of frequencies, and the corresponding theoretical equations are then fitted to the measured data. A typical set of frequency domain data was calculated using equations (2.67) and (2.69), assuming a single exponential decay with a time constant of $\tau = 1.0\,\mu s$. The results obtained are shown in Figure 2.13.

For low modulation frequencies, the decay tail is negligible in comparison with the modulation period; this way, the emission closely follows the excitation, the phase delay is very small and the relative modulation depth is nearly unit. However, as the modulation frequency approaches values near the reciprocal of the lifetime $(1/\tau)$, the phase delay rapidly increases, and the modulation starts to fade. This is the frequency range where the rates $\partial\phi/\partial f$ and $\partial M/\partial f$ are higher and which contains more information about the sample parameters[10]. For higher frequencies, as the decay tail starts to overlap several modulation periods, the modulation depth decreases towards zero and the luminescent emission becomes continuous. Simultaneously, the phase delay grows very fast, and it converges asymptotically to 90° as the modulation vanishes. For samples with shorter lifetimes, the frequency range of interest (where the two curves cross) is shifted for higher frequencies.

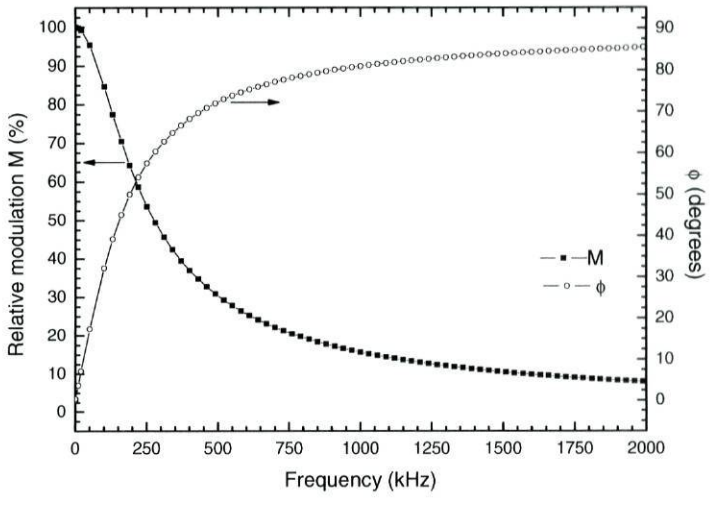


Figure 2.13 Simulated data showing the relative phase, ϕ, and the modulation ratio, M, as a function of the modulation frequency, for a single exponential decay with $\tau = 1.0\,\mu s$.

[10] The calculation of the optimal modulation frequency, where the phase has maximum sensitivity to lifetime changes, yields a frequency given by the reciprocal of the luminophore lifetime ($f_{opt} = 1/2\pi\tau$). This calculation is given in chapter 4, for determination of the optimal modulation frequency of an oxygen sensing scheme.

Frequency domain data provides two independent measurements of the lifetime (equations (2.67) and (2.69)), which can be evaluated from phase measurements

$$\tau_\phi = \frac{1}{\omega}\tan^{-1}\phi \tag{2.70}$$

or by the determination of the relative modulation

$$\tau_M = \frac{1}{\omega}\left(\frac{1}{M^2} - 1\right)^{1/2}. \tag{2.71}$$

If the decay is a single exponential, the values obtained from the two measurements should be the same, identical to the sample lifetime ($\tau_\phi = \tau_M = \tau$), and independent of the modulation frequency. In such cases, measurements can be performed at a single frequency and the determination of the sample lifetime can be very fast.

Multiple exponential decays

Most of the time, however, the two independent measurements of the lifetime yield different values, indicating a multiple-exponential decay. In such cases the values observed for τ_ϕ and τ_M are just apparent and result from a complex weighting of the various decay parameters. Usually the value obtained by phase measurements is smaller than the value obtained through the modulation parameter, $\tau_\phi < \tau_M$. In addition, the measured values are dependent of the modulation frequency, decreasing for higher frequencies. Although these parameters are characteristic of the system under study, they are not true molecular parameters. Nevertheless, it can be useful to monitor the apparent lifetime, at a fixed frequency, using one of these techniques. Many sensing applications have been reported where the apparent lifetime was monitored in order to determine changes in the quencher concentration, using frequency domain techniques.

In general, for determination of the parameters of a complex decay, measurements should be performed in the widest possible frequency range, centered at a frequency near the reciprocal of the lifetime. The data obtained must then be fitted to a theoretical curve. The frequency domain data for a multiexponential decay can be calculated from the sine and cosine transforms of the δ-impulse response $I(t)$, which are given by

$$P = \frac{\int_0^\infty I(t)\sin(\omega t)\,dt}{\int_0^\infty I(t)\,dt} \tag{2.72}$$

and

$$Q = \frac{\int_0^\infty I(t)\cos(\omega t)\,dt}{\int_0^\infty I(t)\,dt}. \tag{2.73}$$

In the case where the impulse response is described by a sum of exponentials (equation (2.54)) these transforms can be expressed as

$$P = \omega\sum_{i=1}^{n}\frac{f_i\tau_i}{1+\omega^2\tau^2} \tag{2.74}$$

and

$$Q = \sum_{i=1}^{n}\frac{f_i}{1+\omega^2\tau^2}, \tag{2.75}$$

where f_i represents the fractional contribution of each luminophore population for the steady-state luminescence intensity, defined in equation (2.55). The frequency dependent values of ϕ and M can then be finally calculated from

$$\tan\phi_c = \frac{P}{Q} \tag{2.76}$$

and

$$M_c = \left[P^2 + Q^2\right]^{1/2}, \tag{2.77}$$

where the subscript 'c' stands for calculated. By adjusting the parameters α_i and τ_i, equations (2.76) and (2.77) can be fitted to the experimental data. Judgment of the fitting quality is a critical step in frequency domain measurements. Evaluation is usually done by non-linear least squares analysis, seeking to obtain a correlation parameter, χ_r^2, near unit. χ_r^2 can be evaluated simultaneously for the phase and modulation measurements, in which case it is defined by

$$\chi_r^2 = \frac{1}{\nu}\sum_{i=1}^{N}\left[\frac{\phi(\omega)-\phi_c(\omega)}{\sigma_\phi(\omega)}\right]^2 + \frac{1}{\nu}\sum_{i=1}^{N}\left[\frac{M(\omega)-M_c(\omega)}{\sigma_M(\omega)}\right]^2, \tag{2.78}$$

where σ_ϕ and σ_M, are the uncertainties associated with the phase and modulation measurements, respectively. These uncertainty values are also frequency dependent; however, in most experiments, global parameters independent of frequency are estimated and used instead. The values used for σ_ϕ and σ_M impact the value obtained of χ_r^2, but usually do not affect the obtained fitting parameters α_i and τ_i. This way, more importance is given to the relative changes observed in χ_r^2 when some fitting parameter is changed than to its absolute value.

Instrumentation

In addition to all the instrumentation associated with steady-state measurements, frequency domain spectrofluorometers require a modulated light source and the associated RF electronics. The light source can be an arc-lamp followed by a monochromator, in which case the modulation can be achieved by an electro-optic (EO) modulator, usually a Pockels cell. Typically, a high driving voltage is required to operate these devices. In addition, careful optimization is needed in these set-ups because EO modulators have small active areas and work best with collimated light. This way, the excitation optical power obtained with this configuration is usually low. Nevertheless, commercial systems are available using this arrangement, in which arc-lamps can be modulated up to $200\,MHz$. In applications where higher excitation powers are needed, the EO modulators can be used with a variety of cw laser sources. These sources, however, are more expensive and cover only limited wavelength ranges. Intrinsically modulated light sources, like laser diodes and LEDs, can overcome most of these problems. However, although these sources are now available in the blue range of the spectrum, they still lack emission in the UV needed for most biological applications. Nevertheless, many frequency domain sensing applications of chemical species have been reported where low cost LEDs were used as the light source.

In order to perform measurements of phase angles and achieve modulation at such high frequencies, special techniques must be used. Presently, most frequency domain instruments are based on a multi-frequency cross-correlation detection technique (MFCC). This technique requires that the gain of the photomultiplier tube should be modulated at the same frequency as the excitation beam, f_m, plus a small frequency offset Δf, i.e. at a frequency $f_m + \Delta f$. With adequate electronic filtering, this system yields a signal at the difference frequency, Δf, usually in the $100Hz - 1000Hz$ range, that contains the same phase and modulation information as the original high frequency signal. This way, all the measurements can be performed in a low frequency range, using a zero-crossing detector and a ratio digital voltmeter, independently of the modulation frequency. With this method, high frequency harmonics and other sources of noise are rejected, allowing measurements at lower frequencies to be performed with high accuracy. For instruments using a cw laser, standard deviations of $0.1^{\circ} - 0.2^{\circ}$ for the phase shift and $0.002 - 0.004$ for the modulation ratio can be obtained.

Similarly to time domain techniques, detectors with short impulse responses are also needed in frequency domain measurements, in order to avoid signal demodulation due to the instrumentation. The necessary bandwidth will depend on the lifetimes to be measured. For a given luminophore, the frequency range of interest is approximately given by $\omega = 1/\tau$. Typically, for luminophores with

lifetimes around $10\,ns$, modulation frequencies in the $2MHz - 200MHz$ are adequate. Picosecond lifetimes, on the other hand, will require modulations in the GHz range. Due to their fast response, PMTs and MCP PMTs are also widely used in frequency domain spectrofluorometers. The gain of regular PMTs can be easily modulated by injection of the RF signal in one of its dynodes. Typical bandwidths are in the $200MHz - 300MHz$ range. With MCP PMTs much higher bandwidths can be achieved ($2\,GHz - 5\,GHz$); with these devices, however, cross correlation must be performed using an external circuit. Although they are seldom used in laboratory instrumentation because of their limited gain, photodiodes are increasingly used for frequency domain measurements, particularly in sensing applications based on long-lived luminophores.

A frequency domain spectrofluorometer usually has two detectors, one for the sample and another to serve as reference. The reference PMT usually measures part of the reflected or scattered excitation light. On the other hand, the sample detector is alternatively exposed to luminescence from the sample or to excitation light from a scattering solution. This way, for every frequency, two sets of measurements are performed. First, the phase delay ϕ_R and the modulation ratio m_R of the light emitted by the scattering solution are measured with respect to the signal detected by the reference PMT. The relative phase obtained, ϕ_R, is an arbitrary phase angle due to the unavoidable delays in cables and electronic circuits, and provides a reference phase value. Then, the phase delay, ϕ_S, and the modulation ratio, m_S, of the luminescent sample are measured with respect to the signal detected by the reference photomultiplier. The phase, ϕ_S, contains also the arbitrary phase term ϕ_R added to the phase shift of interest ϕ_ω, i.e., $\phi_S = \phi_\omega + \phi_R$. This way, absolute phase shift and modulation ratio, accounting only for the luminophore lifetime, can then obtained from $\Phi = \phi_S - \phi_R = \phi_\omega$ and $M = m_S / m_R$.

Although this referencing technique allows the compensation of the influence of many external parameters, some problems common to time domain devices may still be observed, such as wavelength dependence of detector sensitivity, polarization effects, etc..

Presently, from the instrumental point of view, laboratory devices for time domain and frequency domain measurements are very similar in cost and performance. Nevertheless, differences exist that may be important in specific applications. For the particular case of low cost sensing applications, frequency domain measurements present some considerable advantages. Frequency domain measurements are usually faster; the sinusoidal signals are easier to measure than the very short decay signals characteristic of time domain measurements; no deconvolution is necessary, saving computation time and money in complex software analyses. Overall, considering specific applications, frequency domain systems can usually be implemented with simpler electronics and at

lower cost than time domain systems. Nevertheless, luminescent emission can sometimes be too weak for frequency domain detection, where the signal must be strong enough to make zero crossing detection. In these cases, time domain SPT with longer acquisition times is extremely sensitive and can still be used.

Low cost frequency domain measurements for sensing applications.

In specific sensing applications, all the instrumentation associated with frequency domain measurements can be greatly simplified. Usually, for a particular sensing dye only a limited spectral range must be considered; thus, filters in combination with a suitable optical source can be used instead of a monochromator. In addition, it is often more convenient to evaluate an apparent lifetime, as a function of the fluorophore or quencher concentration, regardless of the complex decay parameters; this way, single frequency measurements can be performed, and the modulation and detection electronics can be very simplified.

Recent developments in solid state optical sources have made available LEDs and laser diodes with emission in the blue range of the spectrum. These sources are perfectly suited to be used with new families of metal-organic complexes, which display strong absorption bands in this spectral region. In addition, because these luminophores are long lived (μs) and have high quantum yields, they are suitable to perform frequency domain measurements at low frequencies (kHz), where standard photodiodes and phase sensitive lock-in amplifiers can be used for detection. In addition, using a combination of a short lived sensitive dye, with a long lived reference luminophore, it is possible to use low frequency instrumentation to interrogate luminophores with very fast lifetimes [46].

All these developments have made possible the emergence of a new generation of low cost frequency domain instruments, compatible with optical fibers and suitable for in-field sensing applications [47-49]. Many sensing devices have been demonstrated based on these principles, some of which are available commercially [10].

2.3 Luminescent sensing dyes

The luminescent probe is the most critical component of any luminescence-based sensing system. Ultimately, the photophysical and photochemical properties of the sensing dye will determine the characteristics of the whole sensing system. The luminophore absorption and emission spectra will establish the spectral range of the optical source and detector; modulation frequencies or pulse widths, on the other hand, will be determined by the probe lifetime. In addition,

the properties of the dye will determine which sensing mechanisms can be used, and which analytes can be studied, etc.. For this reason, a great deal of research has been devoted to the development of luminescent dyes with adequate characteristics for a range of applications. As a result, in addition to many substances which are naturally luminescent, many other synthesized organic and inorganic compounds are available nowadays. Overall, thousands of luminescent probes are currently known.

2.3.1 Intrinsic luminophores and organic dyes

A distinction can be made between intrinsic and extrinsic luminescent probes. Intrinsic luminophores are those occurring naturally and include aromatic amino acids, NADH[11], and chlorophyll, among others. These probes are ideal in the sense that they are already part of the environment being studied, and measurements can be performed with minimum interference with the biological process or chemical reactions taking place. For instance, the presence of tryptophan and tyrosine residues (two luminescent amino-acids) in proteins is often used to study the shape or the biological function of enzymes. However, such examples are limited, and most of the time the molecule of interest is non-luminescent and an extrinsic luminescent probe must be introduced.

In addition, most of the naturally occurring luminescent bio-probes have absorption and emission spectra in the UV/blue region of the spectrum. In the particular case of amino acids absorption usually occurs in the $260\,nm - 300\,nm$ range and emission spans from $280\,nm$ to $350\,nm$. Such energetic radiation can have a harmful effect when studying living systems. In addition, these wavelengths are out of the range of cheaper solid state sources and detectors and require the use of quartz optics. Moreover, the fast lifetimes usually associated with these molecules ($3\,ns - 5\,ns$) require more expensive instrumentation.

Thousands of synthesized luminophores, mostly organic, are now available for labeling of biological systems or for sensing applications [20, 50]. Usually, they are either covalently bound to the molecule of interest or are simply associated with it (by polarity or some other chemical affinity). Most of these dyes have adequate sensitivity, through quenching or some other mechanism, to be used as sensors of some analyte (pH, ions, oxygen). It is usually desirable that these luminophores have longer absorption and emission wavelengths. Primarily, the aim is to avoid interference with or from the intrinsic biological luminescence which can act as background luminescent noise. In addition, it is desirable, from the instrumental point of view (sources, detectors, optical fibers transmission properties), to work with visible and near infrared wavelengths instead. Although this

[11] Nicotinamide adenine dinucleotide (NAD) is an important coenzyme found in cells. NADH is the reduced form of NAD.

has been accomplished to some extent, as nowadays luminophores are available covering the whole visible spectrum and some options are even available in the near infrared, still the majority of dyes available require UV or blue excitation.

Two representative examples of these organic dyes, widely used as biological labels, are fluorescein and rodhamine. They are used due to their high quantum yields and their relatively strong absorption maxima, which occur respectively at $480\,nm$ and $560\,nm$. These dyes can be combined with a variety of functional groups that provide them with specific sensitivities or binding abilities. Nevertheless, they present very short lifetimes (around $4\,ns$), which can still be useful for the study of dynamic process but are associated with expensive instrumentation. In addition, their Stokes' shift is very small, their emission spectra peak respectively at $510\,nm$ and $570\,nm$. This characteristic is common to most organic dyes and causes problems of self-quenching (inner filter effects), and they need high quality optical filtering in order to separate excitation from emission. With some exceptions, these properties are common to most organic luminophores. In addition, it should be considered that each of these dyes usually presents different chemical properties. This further complicates their combined use and demands the development of dedicated protocols for synthesis, functionalization and immobilization. Also, most organic dyes present a high degree of photodegradation, hindering their use in long term sensing applications. In this context, the advent of a family of long-lived and photostable dyes, with more homogeneous spectral and chemical properties and large Stokes' shifts, suitable for sensing of chemical and biological species, is highly desirable. Presently, this gap is being filled by hybrid metal-organic luminescent complexes.

2.3.2 Long lived transition metal complexes

Originally developed for solar-energy conversion applications, transition metal complexes (TMC) are now being extensively explored in a wide range of sensing applications. These complexes are characterized by a transition-metal containing one or more organic ligands (typically diimines). Special attention is being devoted to those complexes with platinum metals (Ru, Os, Re, Rh and Ir), from which ruthenium is by far the most studied case [5, 19, 51-53].

Ruthenium complexes have very desirable features for sensing applications. They are long lived, with lifetimes ranging from $100\,ns$ to $7\,\mu s$, making them suitable for simpler and less expensive time domain and frequency domain measurements. They present relatively high quantum yields, independent of the excitation wavelength and that can reach up to 0.5 (although values in the range $0.04 - 0.2$ are more usual). Most ruthenium complexes display strong absorption bands in the visible range (around $470\,nm$) which overlap perfectly with the emission of low cost blue LEDs. In

addition, they present large Stokes' shifts, with emission typically occurring in the red range of the spectrum (around $600\,nm$). The absorption and emission spectra of a ruthenium dye, dissolved in methylene chloride, is shown in Figure 2.14.

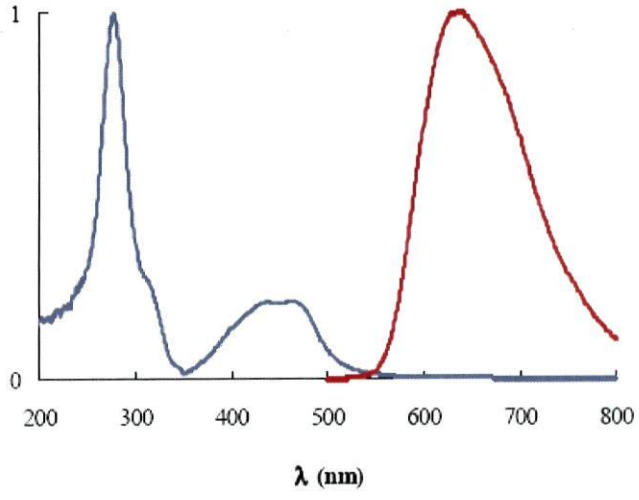


Figure 2.14 Absorption (blue) and emission (red) spectra of $Ru(dpp)_3^{2+}$ dissolved in methylene chloride.

In comparison with traditional organic dyes, TMC are photochemically and thermally very stable. Chemically, they are extremely versatile due to the organic ligands. One or more of these ligands can be chemically modified to: adjust the net electrical charge of the complex; provide functional groups in order to attach the dye to a polymer support; neutralize or enhance the interaction of the dye with a given analyte; alter the dye solubility; and adjust its spectroscopic properties. The structure of some ligands typically used in TMC is shown in Figure 2.15.

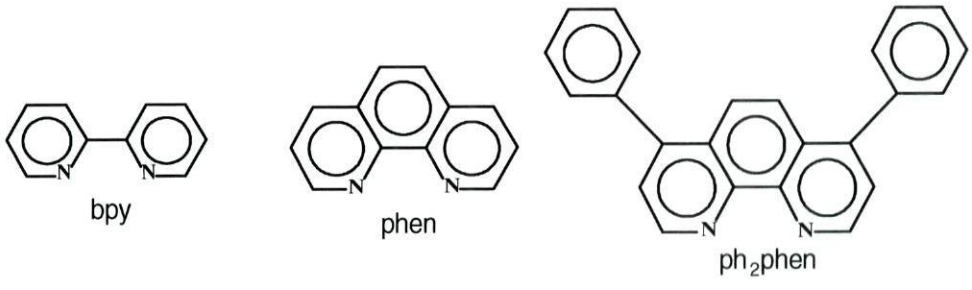


Figure 2.15 Structure of organic ligands and respective abbreviations commonly used in transition metal complexes [54].

Many of the interesting photophysical and photochemical properties of these complexes derive mostly from their unique electronic states. Most of these complexes are characterized by a central metallic atom with partially filled d-orbitals, in particular some of the most studied and

promising cases have six d-electrons, d^6. The energetic arrangement and filling within these orbitals determines to a great extent the emissive properties of the resulting complex. Such an energy distribution will be determined by the type, number, and spatial arrangement of the ligands. The scheme of Figure 2.16 shows the orbitals and state diagram corresponding to a d^6 complex of the form ML_6, with an octahedral arrangement, in which M stands for the metal and L for the ligand.

The π orbitals are associated with the ligands and the d orbitals with the metal. The presence of the ligands splits the five degenerate d orbitals of the metal by an amount, Δ, into a triply degenerate t level and a doubly degenerate e level. The amount of splitting Δ is determined by the crystal field strength of the ligands and central metal ion. The electronic distribution in these levels, and thus the luminescent properties of the resulting complex, are determined to a great extent by the magnitude of Δ. In this particular case, Δ is large and pairing electrons in the t levels is energetically favorable in comparison to distributing unpaired electrons through t and e. Changes in the ligands geometry and metal ion will impact Δ and provide a way to control these properties. In the scheme shown, spectroscopic levels are labeled according to the original and final orbitals involved in the transition. Three types of excited states are possible in the resulting complex. Metal-centered $d-d$ states, ligand based $\pi-\pi^*$ states, and charge transfer states, i.e. states involving transitions between metal orbitals and ligand orbitals ($t-\pi^*$). In each of these categories there are singlet and triplet states (denoted by ^{1} and ^{3}), with the triplets always having lower energies with respect to the corresponding singlet states.

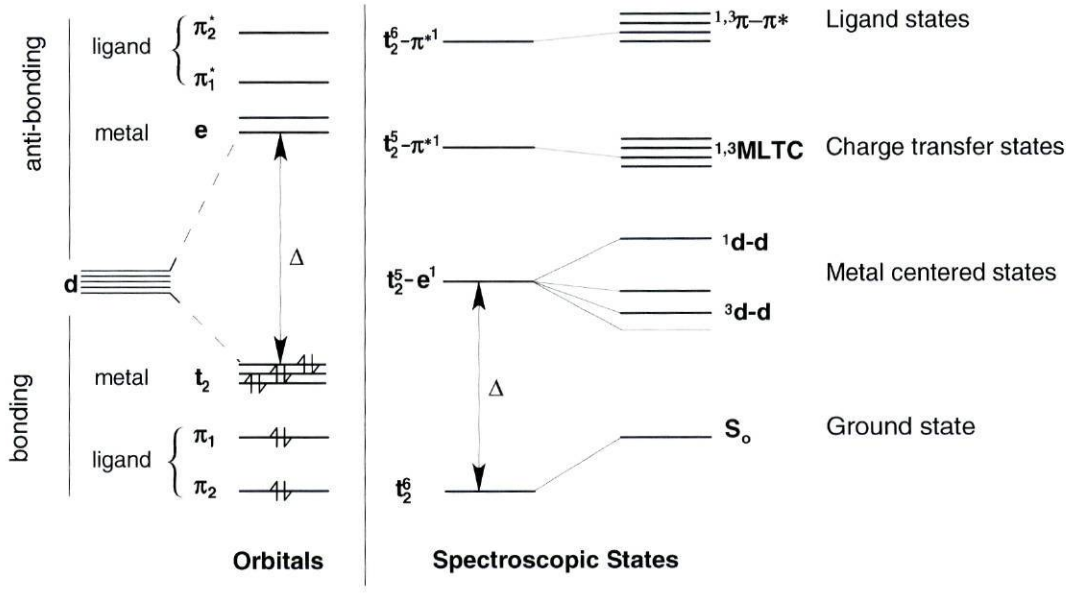


Figure 2.16 Simplified orbital and states diagram for a d^6 metal in an octahedral environment, showing d and π bonding and π^* antibonding orbitals. The spectroscopic state denomination is determined by the original and final orbitals involved. Adapted from [19].

The intra-ligand $\pi - \pi^*$ transitions have similar energies to those observed in the free ligands and are responsible for intense absorption bands in the UV range ($250\,nm - 300\,nm$), typically observed in ruthenium complexes (see example in Figure 2.14). The metal centered $d - d$ transitions, occurring between t-bonding and e-anti-bonding levels, are formally forbidden. This way, although $d - d$ absorption can take palace, radiative rates are very low and no luminescence is actually observed. In addition, because e electrons are antibonding, the resulting excited state is very unstable and can lead to decomposition by ligand displacement. Charge transfer states, CT, may include transitions from metal orbitals to ligand orbital or from ligand orbitals to metal orbitals. In ruthenium complexes of interest, the ligands are easily reduced and electrons are promoted from the metal to the ligand. These states are also called metal-to-ligand charge transfer, MLCT, and are the most remarkable feature of TMC, being responsible for their characteristic absorption bands in the visible range, peaking between $440\,nm - 500\,nm$ (also shown in Figure 2.14). These absorption bands are attributed to spin allowed $d - \pi^{*1}$ MLCT transitions.

After a fast and efficient intersystem crossing process, electrons rapidly relax to the MLCT triplet states. Emission from these triplet states is responsible for the characteristic orange-red luminescence associated with ruthenium dyes, and is formally classified as phosphorescence. Nevertheless, the presence of the heavy metallic atom favors spin-orbit coupling, thus resulting that these states have shorter lifetimes (μs) than typical phosphorescence compounds (ms or longer). This way, emission can occur prior to total quenching and these dyes usually display strong luminescence.

The understanding of the above parameters is the key for the synthetic control of the spectroscopic characteristics of these dyes, and thus of the luminescence properties, through alteration of the ligands, geometry, and central metal ion. Due to strong active research dedicated to the photophysical and photochemical properties of these complexes, a great deal of this knowledge is now available, enabling further expansion of the already impressive list of applications of these dyes. Some examples include applications as quantum counters, DNA probes, study of membranes and proteins, immunoassays, and ion sensing.

In the context of this work, the oxygen sensing properties of some ruthenium complexes will be explored. Due to their long lifetimes, most ruthenium dyes are very sensitive to collisional quenching by oxygen. The ruthenium complexes represented in Figure 2.17, Ru(dpp) and Ru(bpy), where bpy stands for 2,2 –bypiridyne and dpp for 4,7-diphenyl-1,10-phenanthrolin, are two of the most widely used compounds for oxygen sensing applications. A long list of applications of these

dyes as oxygen sensors has been reported [33, 48, 53, 55]. Some of the few commercially available optical oxygen sensors are based in such dyes [10, 11].

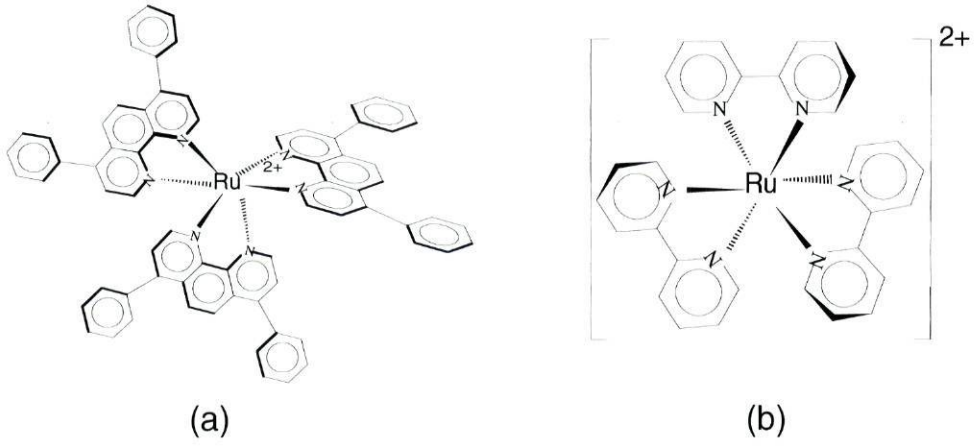


Figure 2.17 Representation of the structure of ruthenium complexes commonly used as oxygen sensing dyes. (a) Ru(dpp); (b) Ru(bpy) [54].

In addition to oxygen sensing, the use of complexes with modified ligands has also been reported where the dye luminescence was made sensitive to humidity, pH or CO_2. These applications demonstrate the possibility of developing a homogeneous set of sensing dyes, with identical photophysical and photochemical properties, based on a single family of coordination compounds [56]. Although this versatility may rise some concern about cross sensitivities, in particular to oxygen, the combination of the dye with adequate solid membranes can greatly enhance sensor selectivity. This way, conditions are created for the development of a family of chemical sensors, suitable for a wide variety of analytes, and with similar enough characteristics to be operated with the same basic instrumentation.

2.4 Membranes for optical chemical sensing

One of the most critical steps for the implementation of an optical fiber biochemical sensor is the immobilization of the luminescent indicator in a solid matrix. In order to fabricate a sensing probe capable of continuous measurement, the indicator chemistry must be immobilized in the fiber tip. This is usually done by encapsulating the luminophores in a solid host. The resulting sensing membrane can either be directly bound to the fiber surface, in an intrinsic approach, or attached to it by some physical support in an extrinsic configuration. Ultimately, the properties of the sensing membrane will determine the sensor performance [57-59]. An ideal immobilization membrane would effectively entrap the indicator and preserve its optical and chemical properties, avoiding leaching and photobleaching. Simultaneously, it should allow the establishment of a fast and

reversible equilibrium with the aqueous environment or gaseous atmosphere being probed. While permeability to the analyte is a highly desirable feature, penetration of potentially interfering chemical species into the sensing membrane should be avoided. On top of these requirements, a good adhesion to the fiber surface, together with mechanical and chemical stability, are particularly important features for long term practical applications.

Simultaneous fulfillment of all these requirements is extremely difficult to be achieved, especially considering that every analyte/luminophore combination may have specific chemical properties. Traditionally, polymers are materials of choice for this task due to their chemical versatility and great variety available [8]. Although many successful sensing applications using polymers doped with luminescent indicators have been reported, the sensing membranes are far from ideal and some problems subsist. Major issues are leaching of the sensor from the solid host, poor chemical resistance and modification of the properties of the sensing dye.

In this context, sol-gel glasses are a particular kind of polymeric material which have very suitable properties for sensing applications [7]. With this technique porous silica matrices can be formed which are highly compatible with the fiber surface. In addition, the sensing dye is physically encapsulated in the micro porous structure, avoiding leaching while preserving the indicator chemical properties. These features have been demonstrated with a variety of sensing dyes in widely different applications. However, there is no universal solution, since each application has its specific chemistry, and many challenging applications still require a great deal of research.

In the following sections some of the key topics regarding the main types of immobilization membranes for sensing applications will be addressed. Particular attention will be given to the basic notions of the sol-gel process and to the properties of the materials it produces, since these will be applied in different experiments developed throughout this work.

2.4.1 Polymers

Polymer technology is very well established in modern industry and polymeric materials are all around us. Their versatility makes them useful in a wide variety of applications and new uses are constantly arising. Polymers offer many favorable characteristics for applications, in sensor technologies [60]. They are relatively low cost materials and are usually associated with simple fabrication techniques, avoiding the need for a clean-room environment. Their suitability to serve as hosts for sensing indicators arises from the low temperatures associated with the polymerization processes and from the fact that organic and inorganic dyes can be dissolved in polymeric matrices. In addition, they are available in a variety of different compositions whose chemical and physical

properties can be tailored. Polymers can be made hydrophilic or hydrophobic, elastic or rigid, and their permeability can be adjusted to block some interfering species. Their versatility makes them suitable to be deposited on a variety of substrates. A doped polymer can be easily deposited over an optical fiber during its drawing process. This way, fibers with luminescent cladding or core can be produced which are suitable for implementation of distributed sensing schemes [61].

In spite of many advantages, polymer sensing membranes also suffer from some problems. For applications in aqueous environments, leaching of the dye from the polymer host matrix can seriously limit the sensor performance. If a hydrophobic dye is immobilized in a hydrophobic polymer this problem can be avoided. However, such membranes are ion-impermeable and this approach is only suitable for neutral analytes. Ionic permeability of hydrophobic polymers is only possible through ionic exchange between the polymer matrix and the surrounding environment. This exchange can happen only after doping the matrix with adequate ion donors. Such processes, however, are only compatible with a limited number of indicator dyes and usually result in an increased cross sensitivity to pH. Most organic dyes are water soluble and, therefore, their immobilization in hydrophobic polymers is only possible if the dye is chemically modified. For detection of ionic species using luminescent dyes, hydrophilic polymers should be used instead. In this case, to avoid leaching, the luminophore must be covalently bonded to the polymer host. This process often involves the chemical modification of the sensing dye. Nevertheless, extremely stable sensors can be obtained by this method, which are able to operate for long periods and with shelf lives that can go up to several years. However, the chemical processes required for covalent immobilization are typically quite elaborated and fastidious.

Another common problem associated with polymer membranes arises from the interactions between the polymer chemistry and the luminophore molecules. These interactions can result in spectral shifts or in more profound changes in the dye sensing properties that can seriously compromise the system performance.

The physical properties of a polymer material may vary widely from elastic to extremely rigid, and are also very important for practical applications. Although some polymeric membranes can be mechanically robust, most hydrophilic polymers are relatively fragile. Usually hydrophilic polymers can absorb a great deal of water (from $10\% - 1000\%$ of its original volume). This can cause considerable swelling of the sensing membranes, which can affect the sensing dye properties. Besides favoring leaching, it can also compromise the physical integrity of the membrane, which becomes very soft. Adhesion to the fiber glass surface is also an important parameter but it varies

widely depending on the polymer used, and sometimes chemical treatment of the fiber surface must be performed prior to coating.

For intrinsic sensing configurations, where the sensing membrane can become part of the waveguide, the refractive index of the sensing medium can have an important role. Typically, organic polymers have higher refractive indexes than silica based materials. This way, it is not feasible to use sensing membranes based on polymeric materials for replacing the cladding of silica waveguides, while maintaining guiding conditions. As a result, the collection efficiency of the luminescent signals can be significantly reduced. Special fluorinated polymers can be used for the purpose of obtaining lower refractive index, or else low refractive index dilutants may be added prior to polymerization. Polymers can be made transparent to a wavelength range of interest, usually in the visible spectrum. Although they can present much higher losses than silica based materials, the path lengths involved are usually very small and this fact does not impact the membrane performance.

In spite of some difficulties, polymer materials have been successfully used in many luminescent based sensing systems. In addition, each application has its specificities, like sensing dye chemistry, characteristics of the substrate (glass fiber, plastic fiber...), environmental conditions, etc. This way, the search for adequate host materials is a continuous effort and new materials are constantly arising. Sol-gel materials, for instance, are a particular class of polymeric materials that present very promising characteristics for sensing applications.

2.4.2 Sol-gel technology

Sol-gel derived materials have been attracting the attention of many researchers working in the immobilization of sensing luminophores in solid supports. In comparison with some polymers, these materials can be mechanically robust and chemically very resistant. In addition, by choosing the right ingredients and adjusting the process parameters, properties like polarity and porosity can be tailored to the specific needs of an application [62, 63]. Furthermore, they are usually optically transparent, and their refractive index can be tuned within a wide range. The simplicity and low temperatures associated with the fabrication process, along with the compatibility with a variety of coating processes (spin coating, dip coating, casting, spraying) make them suitable for use in very specific laboratory applications as well as in large-scale industrial processes. For these reasons, this technology is being used not only for sensing membranes but also in a wide range of applications, from fabrication of optical components to food packaging.

The sol-gel process

The sol-gel process can be used to produce a variety of materials, organic and inorganic, with very different properties, and as films, powders, fibers or even in bulk form. Of particular interest for optical fiber sensing applications is the fabrication of metal oxide based materials from metal alkoxide precursors, both organic and inorganic. The overall reaction starts with a metal alkoxide, i.e. a molecule which has a metal atom in the middle and alkoxy groups[12] around it. In optical fiber applications, silica based alkoxides are the most used ones for the purpose of producing porous glass materials. Tetraethoxysilane (or tetraethyl ortosilicate, TEOS) is one of the most extensively applied and studied materials and it will be used as an example for the description of the main stages of the sol-gel process. The structural formula of TEOS is depicted in Figure 2.18. This precursor is a transparent liquid at ambient temperature and it is widely available from many suppliers.

The sol-gel process can be divided in four principal stages: hydrolysis and condensation, gelation, aging and drying. When the metal alkoxide is mixed with water, hydrolysis reactions start taking place. In this reaction, water molecules replace the alkoxy groups with hydroxyl groups (OH). The result is a metal hydroxide and an alcohol, in this case silicon hydroxide and ethanol. This first step is represented in Figure 2.19.

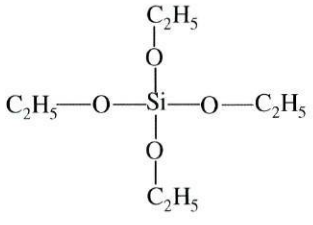


Figure 2.18 Structural formula of tetraethoxysilane (TEOS). A central silicon atom sharing single bonds with four ethoxy group.

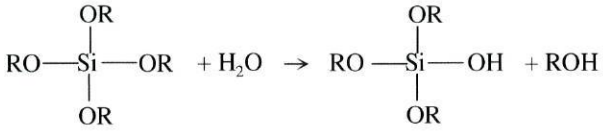


Figure 2.19 Hydrolysis: substitution of alkyl group by an hydroxyl and formation of alcohol.

[12] An alkane is a molecule containing only carbon and hydrogen atoms linked exclusively by single bonds (eg. ethane C_2H_6). If an hydrogen atom is removed from an alkane molecule the corresponding alkyl is obtained, having an electron available to establish a single bond (eg. ethyl $-C_2H_5$). When an hydroxyl group (OH) bonds with an alkyl the corresponding alcohol is obtained (eg. ethanol C_2H_5OH). Finally, removing the proton form the hydroxyl group in an alcohol an alkoxy ligand is obtained (eg. ethoxy $-OC_2H_5$).

In this scheme the alkoxy ligands are represented in its generic form, $-OR$, where R stands for the alkyl groups. In the particular case of TEOS, the alkyls are ethyl ligands (C_2H_5). As soon as they are formed, the metal hydroxides will start reacting with each other and with free alkoxide groups. Water and alcohol are released as a product of these reactions from which results the formation of oxide links between metal atoms. This part of the process is called polycondensation and is schematically represented in Figure 2.20.

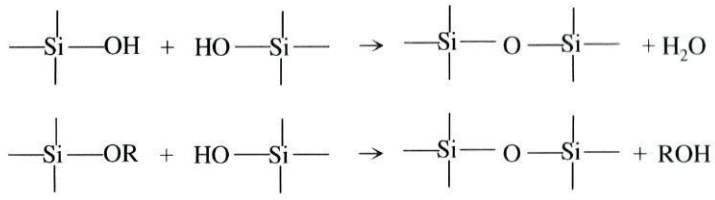


Figure 2.20 Polycondensation: formation of silica oxide bonds through condensation of water (top) and alcohol (bottom).

The two reactions, hydrolysis and condensation, cannot be separated from one another as condensation starts when hydrolysis is not complete, and both processes continue to occur even during the later stages of gelation and aging of the gel.

In the initial phase of the hydrolysis and condensation process, the solid products of these reactions start aggregating and a sol is formed. A sol is a colloidal suspension of solid particles in a liquid[13]. Adding a doping material, like a sensing luminophore, usually takes place at this early stage. As reactions continue, colloidal particles and condensed silica link to form a gel. This is the gelation stage where an interconnected rigid network, with pores of sub-micrometer dimensions and polymeric chains with average length below one micrometer, filled with a continuous liquid phase, is formed. The physical characteristics of the gel network depend upon the size of the particles and the extent of cross-liking prior to gelation. These factors, in turn, depend on several processing parameters like pH, catalyst, precursor concentration, temperature, aging and drying conditions. Among these, two of the most important variables affecting the gel pore structure and polarity are the solution pH and the drying conditions. After the sol-gel transition, the solvent is removed from the interconnected solid network by evaporation, resulting in a dry porous matrix, a 'xerogel'. The resulting material is then simply a metal oxide network. In this case each silicon atom has four siloxane bonds, i.e., it is bonded to four oxygen atoms. With each oxygen atom being shared by two

[13] In a colloidal suspension the dispersed particles are so small ($\sim 1\,nm - 1000\,nm$) that gravitational forces are negligible. Interactions are dominated by short-range forces and there is no precipitation even if the solution is left still.

silicon atoms, a SiO_2 glass polymer is formed whose mechanical properties may vary widely. A diagram representing the main steps in the sol-gel process is shown in Figure 2.21.

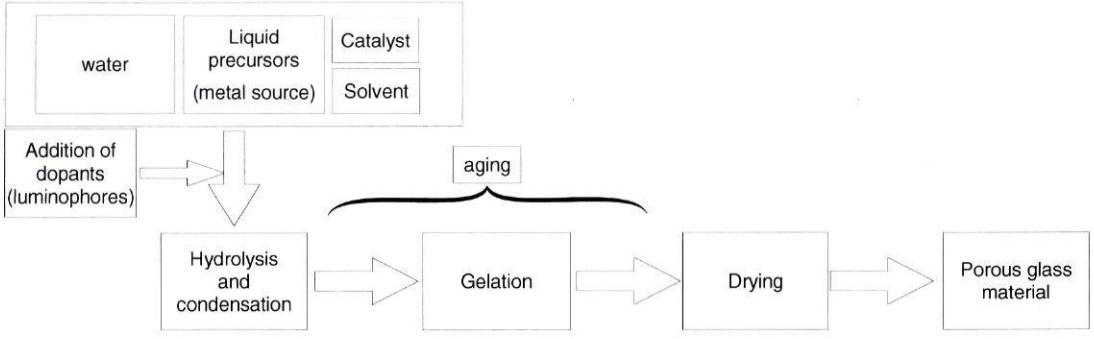


Figure 2.21 Schematic representation of the main stages of the sol-gel process.

Depending on the reaction rates and other process parameters, the resulting inorganic polymer may be in the form of powder, small spheres, films, or even bulk monoliths. In all these forms the porosity of these materials may vary in a wide range. The rate of the chemical processes is adjusted primarily by changing the ratio of the precursors and by using acid or basic catalysis. A solvent, usually an alcohol, can also be added. The catalyst and the solvent are not strictly necessary but they provide an extra way of controlling the reaction rates, allowing to fine tune the material properties. The drying process may also be adjusted by controlling the physical environment in which drying takes place, its temperature and possibly a solvent atmosphere. All these parameters play an important role in determining the properties of the final product. Depending on the precursor type and the relative concentration of the various components, the whole process can either be very slow, as in solutions with excess water where the formation of the xerogel can take months, or relatively fast, with a monolith being formed in some minutes. For thin film production the desired substrate, usually an optical fiber, is dipped in the solution somewhere in between the sol and the gel phase. After removal from the solution, the material sticking to the substrate will undergo gelation and drying processes, eventually resulting in a thin porous glass film. Due to the reduced amount of material produced, the whole process is much faster for thin film than for monolith formation.

While there is a very large number of possible variables in the process, from which the thin film properties will depend, there are some basic rules which apply. This way, it is possible to tailor the material properties in order to make them more suitable for specific applications [64, 65]. The structure and porosity of the material are particularly important to consider since they will determine

the degree of immobilization of the sensing dye and its accessibility by the analyte, two critical features for a successful sensing application.

Process parameters and their influence

Typically, polycondensation reactions can be rather slow as they have relatively high threshold energies. However, these reactions can be made faster by adding catalysts to the initial solution. The catalysis is performed by adjusting the pH of the solution so that given polycondensation and hydrolysis rates are achieved. For instance, a given volume of a $0.01M$ HCl solution can be added to the initial mixture in order to increase its acidity. The distinction between acid and basic catalysis, however, depends on the precursors used. When silica-based materials are considered, the sol pH is defined with respect to the isoelectric point of silica. This is the pH value at which electron mobility and surface charge are zero, and occurs at pH ~ 2. This pH value establishes a boundary between acid catalysis and basic catalysis. Acid-catalysis is characterized by fast hydrolysis, where condensation is thus inhibited, and leads to a more polymeric form of gel with linear chains as intermediates, resulting in weakly branched microporous structures. With base catalysis, on the other hand, hydrolysis is slow and condensation rates are faster. This yields colloidal gels where gelation occurs by cross-linking of the colloidal particles, giving rise to more highly branched particulate structures with large average pore size. It should be borne in mind that each material will have a given pH interval outside of which no stable films can be formed. For silica based materials, for instance, pH higher than 6 can lead to the formation of negatively charged silica nanoparticles that repel each other. This way, gelation will not take place and a stable sol is formed. In addition, many other parameters influence the reaction rates. Nevertheless, assuming that all other parameters are favorable to film formation, and considering a limited pH interval, higher pH values yield films with enhanced porosity

One of the parameters that most influences sol-gel synthesis is the water-to-alkoxide molar ratio (usually denoted by R). When there is an excess of water, which for TEOS will correspond to having $R > 2$, the hydrolysis process is faster. This way, almost all alkoxy groups are replaced by hydroxides before polycondensation. However, this does not mean that the whole process becomes faster. In fact, under these conditions condensation becomes slower (if there is a large excess of water a reverse reaction to polycondensation may occur as the metal-oxide bonds start to hydrolyze). The amount of excess water also impacts the viscosity of the sol, as does the excess solvent. By using excess water the time before gelation can be greatly increased due to very slow condensation. This provides the solution with much longer storage times which can be useful for some

applications. Overall, for a fixed pH value, increased amounts of water in the solution result in films of higher density. This way, the smaller the value of R , the higher the porosity of the resulting film. Once again, depending on the precursor used, this parameter can only be changed in a limited interval outside of which film formation is compromised.

The presence of a solvent is not strictly necessary, but generally solvents are added in order to help mixing and to produce a more homogeneous sol. Their use will also reduce the reactions rates as dilution of the sol reduces the concentration of the other components. This leads to retardation in the gelation process which results in slower particle growth processes and reduced crosslinking in the sol. As a consequence, high solvent content will cause a reduction of porosity. The choice of solvent also affects the drying time of the gels. Increasing the amount of solvent leads to longer drying times. In addition, larger molecules tend to evaporate more slowly, and thus produce longer drying times. Slow drying is often desirable in thin film fabrication in order to avoid internal tensions and crack formation. The effect of the solvent in the overall solution viscosity can also be used to control the film thickness.

To produce a sol of sufficient viscosity for coating and to tailor the porosity for a particular application, a sol–gel aging or pre-polymerization step is usually carried out. During this step, the sol is allowed to stand either at room temperature or at an elevated temperature for a period of time during which hydrolysis and condensation reactions cause further aggregation and crosslinking. This process can enhance the stability as well as the porosity of the films. Usually extended aging times yield films with higher porosity. Aging is a particularly important process when using precursors that have relatively slow reaction rates, like TEOS. Some other precursors can be used, having much higher reaction rates, where the gelation can be achieved in just a few minutes. In such cases aging is not performed.

To obtain the final product the solvent has to be removed from the gel. The rate at which the evaporation takes place affects the physical properties of the end product very significantly. During drying, significant shrinking of the solid structure takes place. Evaporation first happens at the surface of the gel. When the pores get exposed, capillary tension develops as the liquid flows to prevent exposure of the solid phase. The critical point arises when the solid network gets too stiff to follow capillary stress and the liquid stars to recede into the interior of the glass structure. This is the stage where cracking is most likely to develop. After this the evaporation rate decreases, the pores start filling with air but their walls are still covered with liquid that flows to the outside and evaporates. At a later stage, further drying is only possible by evaporation and vapor diffusion to the outside. This process eventually stops, or at least an equilibrium is established with the outer

medium, meaning that some humidity can remain inside the porous matrix. While the structure shrinks, non-uniform shrinking tends to break it. This is one of the main obstacles to obtain a stable sol-gel material, particularly monolithic samples. Films shrink in a more uniform manner, as their small thickness facilitates evaporation of the solvents. However, films tend to shrink in all three dimensions, whereas the substrate allows shrinkage only in one direction (thickness). This causes stress both at the film-substrate interface and into the film itself, and thick films tend to crack or tear off the surface. This process is more critical for films with increased thickness, and a given material tends to have a critical thickness below which cracks can be prevented. In order to avoid cracking of the film, the drying conditions must be carefully controlled. For instance, increased solvent contents lead to a slower drying process and can increase the film stability. Addition of some organic solvents can also help stabilizing the gel, thus improving the mechanical strength and stability of the resulting films. Although drying can take place at ambient temperature, usually it is advisable to do it at increased temperatures in order to ensure that most of the solvent and water are removed from within the porous structure. In addition, slow curing at controlled temperatures can provide annealing of the structure, reducing its internal stress. Higher drying temperatures usually yield glasses of higher density with a more homogeneous structure. While this can increase the material mechanical and chemical stability (lower surface area per unit volume), and its overall durability, it also reduces the film porosity. This way, a compromise must usually be established according to the desired sensor properties.

Sol-gels for sensing

If a sensing luminophore is added to the sol-gel initial solution, its molecules will stay encapsulated in the resulting porous structure of the thin film. Doping is also possible by introducing a dry film in a solution containing the dye. This alternative, however, is more prone to dye leaching when sensing is performed in aqueous media. In either case, dye encapsulation can be done without chemical modification of the sensing dye structure which, in this way, will have its sensing properties virtually unchanged. Although some particular luminophores do present some spectral shift upon immobilization, usually the sensing properties are maintained [66, 67].

Possible leaching of the dye can be avoided by adjusting the characteristics of the pore structure. The pore sizes, however, can also influence the way the analyte diffuses in and out of the sensing membrane, greatly influencing sensor response time and sensitivity. In the particular case of sensing by luminescence quenching, if different micro environments coexist in the same membrane where the luminophore has variable accessibility by the analyte, non-linear responses can arise.

Usually some thermal treatments can be performed that increase the sensing membrane homogeneity. Some chemical additives can also help in this process, although they must be carefully chosen in order to avoid interaction with the sensing dye. Nevertheless, even when non-linear quenching responses are present, several models exist that allow for correct sensor calibration.

Besides porosity, the polarity of the sol-gel material will also influence the sensing membrane selectivity. TEOS based materials are usually hydrophilic. This means they are permeable to ions, and this makes them suitable matrices to pH sensing and ion sensing. Unlike hydrophilic polymers, water soluble dyes can still be immobilized in these materials, without chemical modifications, as the entrapment inside the pore structure prevents leaching. These materials, however, are not adequate for gas sensing in aqueous environments since the presence of water inside the pores hinders diffusion of the analyte. Polarity and other characteristics of sol-gel glasses can be further modified by using organically modified siloxanes (Ormosils)[63, 68]. These are hybrid systems whose precursors have organic components. Typically these hybrid precursors are of the form $R'Si(OR)_3$ or $R_2'Si(OR)_2$, in which R' represents a non-hydrolysable organic substitute. This substitute can also be a reactive species which will allow subsequent covalent binding with sensing indicators. Ormosils glasses are not as hydrophilic and brittle as glasses made from purely inorganic precursors. As the organic component increases, the material will turn hydrophobic and ion-impermeable. Nevertheless, because it is still gas permeable, it has good characteristics to implement gas sensing in both gaseous and aqueous media. The organic component also provides the solid matrix with further elasticity, allowing the formation of much thicker films without cracking.

A major advantage of sol-gel materials is the large extent to which their optical properties can be tailored. The intrinsic refractive index of silica is approximately 1.46 (at $\lambda = 600\,nm$); as the porosity of the structure increases, however, the effective refractive index of the material will become lower. For extremely porous structures, called aerogels, the effective refractive index can be as low as 1.01. On the other hand, the refractive index of titania, another popular sol-gel material, is above 2.2 in its amorphous (glass) form. This way, sol-gel glasses are suited for applications in optical waveguides either for cladding formation or to be used as core material. The optical properties of sol-gel glasses are generally good. Indeed, many sol-gel materials are virtually transparent in the visible range of the spectrum. However, even the small pores may scatter light at very short wavelengths, and very porous aerogels tend to have yellowish transmission. Also, organic substances in the material may turn yellow during drying at elevated temperatures and transmission losses at telecom wavelengths are still relatively high. Nevertheless, several efforts are being applied

in order to solve these potential problems which, in spite of all, do not significantly impact the performance of sol-gel as sensing membranes.

Coating techniques

Due to the characteristics of the sol, a low viscosity liquid at ambient temperature, sol-gel materials are compatible with different coating processes. Overall, the aim of any coating technique is to produce a uniform layer of sol which then gels and forms a uniform thin film after drying. Dip coating and spin coating are two of the most popular techniques. In the spinning process the substrate is submitted to high speed rotation in order to uniformly spread the sol on its surface. The dipping technique, on the other hand, consists of withdrawing the substrate from the sol at a controlled rate. The choice of the coating method has an impact on the final properties of the thin film. For instance, the evaporation rate during spinning is higher than that during dip coating. This way, films produced by spin coating are thinner and less porous than equivalent dipped films.

Spin coating produces homogeneous films with constant thickness, for this reason it is the preferred method for integrated optics applications. However, this method works best with substrates having rotational symmetry. Although it can be used to produce sensing membranes on flat substrates, it cannot be applied to direct coating of optical fibers. For this reason, dip coating is used instead.

Dip coating is performed by immersing the substrate in the sol followed by withdrawal at a fixed speed [69]. Typically, this is done with the substrate being displaced in the direction of the normal of the liquid surface. As the substrate is drawn away from the solution, it captures some of the liquid with it. The liquid surface is bent upwards to join the surface of the substrate tangentially. A part of the liquid drawn with the substrate returns to the bath. The thickness of the dipped layer is mainly a function of the viscosity of the sol and of the withdrawal speed. In practice, increasing the withdrawal speed or the sol viscosity both increase film thickness.

The evaporation rate will also influence the film thickness and the material properties, and it will depend greatly on the atmosphere surrounding the substrate. In still environments, the air around the film will be saturated with alcohol, lowering the drying speed. Controlling temperature, humidity, working in still environments or under a draught will all influence film properties and should be carefully controlled to obtain reproducible results.

Dip coating can produce uniform thin films on large substrates, yet there is a tendency for increased thickness at the film borders due to surface tension effects. On flat substrates this is not a problem, as the majority of the film surface will be uniform. However, this behavior introduces

some difficulties when coating the tip of optical fibers. Although very high quality smooth thin films can be deposited on the fiber lateral walls, surface tension creates a 'drop' effect at the fiber tip. This translates in an excess of solution sticking to the fiber tip, having a drop like shape. This makes it very difficult to obtain uniform thin films at the fiber tip; thicker films with non-uniform thickness are obtained instead. When using inorganic precursors, the increased thickness can lead to crack formation and even detachment of the film from the substrate. In spite of all this, with careful control of all processing parameters it is possible to obtain usable coatings at the fiber tip, and most applications reported use dipping as the deposition method. In some cases, high-pressure spraying nozzles can be used as an alternative method for deposition of sol-gel materials. This method can achieve good thickness uniformity and its use was already demonstrated for fiber optic coatings.

The application of sol-gel materials as immobilization membranes in luminescence sensing systems has been demonstrated in a wide variety of contexts. The characteristics of sol-gel thin films were shown to be very favorable to the encapsulation of different sensing dyes (organic, inorganic, luminescent, colorimetric), for detection of many analytes (gas, pH, ions, biomarkers) in a variety of environments (gaseous, aqueous, biological). As the potential of these materials was already fully recognized, many efforts are been applied not only in specific applications but also in studying, modifying and creating new capabilities. In this context, it is expected that sol-gel technology will have an increasingly growing contribution for the establishment of a mature luminescence sensing technology.

2.5 Optical fiber systems for luminescence sensing

The primary drive for the development of optical fiber technology has been, for a long period of time, the implementation of large bandwidth telecommunications systems. In this framework, the fiber materials and the associated optoelectronics evolved naturally for wavelengths where transmission loss and material dispersion are minimal. This way, most of the available low cost fiber systems were optimized to operate in the infrared region of the spectrum, at $1.3\,\mu m - 1.5\,\mu m$. Nevertheless, the intrinsic capabilities of optical fibers to transmit information through long distances, with minimum intrusion and immunity to electromagnetically interferences, were early recognized as being very attractive for sensing applications. At the present, besides being an appealing and active research field, optical fiber sensing is also a growing industry. This is particularly true for sensors of physical observables like temperature, pressure or deformation, in which standard fiber technology is commonly used [70]. The measurement of chemical and biological parameters using optical fibers, in combination with luminescence techniques, faces some

additional challenges that somewhat delayed the development of biochemical fiber sensing technology and its arrival in the market.

Currently, however, the situation has changed and biochemical fiber sensing is a fast developing area. New types of fibers, optical sources and detectors are being developed and explored in sensing applications. A wider variety of optical fibers is now commercially obtainable: fibers with transmission over a wide spectral range compatible with luminescence applications, large core diameters, plastic optical fibers, micro-structured optical fibers, etc. Simultaneously, great advances are being reported in the associated optoelectronics, with semiconductor sources (laser diodes and LEDs) now being available with emission in the blue or UV. These advances, together with the development of new sensing dyes and associated immobilization chemistry, have contributed to a relatively recent outburst of luminescence based fiber sensor technology [71]. In spite of all the achievements, this is still a particularly challenging field of application and all the stages of the sensing system must be thoroughly optimized for a good performance to be obtained.

In Figure 2.22, the scheme of a prototypical luminescent chemical fiber sensor, in a reflection configuration, is represented, indicating some of the specific problems concerning the implementation of these systems. One of the main concerns for sensor design is the spectral compatibility of the different system elements. These spectral requirements are primarily defined by the absorption and emission spectra of the sensing luminophore. The optical source should match the dye absorption while the detector should be optimized for its luminescence output. The optical fiber, on the other hand, should have low attenuation in both spectral regions. Most of the time some compromises must be addressed.

Other important issues include the need for low cost excitation sources, capable of high launching efficiencies into optical fibers; the optimization of the sensing head design in order to maximize the capture of the luminescent signals and the interaction with the analyte; the development of advanced detection and signal processing techniques in order to reject background noise and accurately interpret the luminescent information. In all these issues, the characteristics of the optical fiber used in the sensing system will play a critical role. These and other important problems that should be considered when designing an optical fiber system for luminescence sensing applications will be addressed in the remaining part of this chapter.

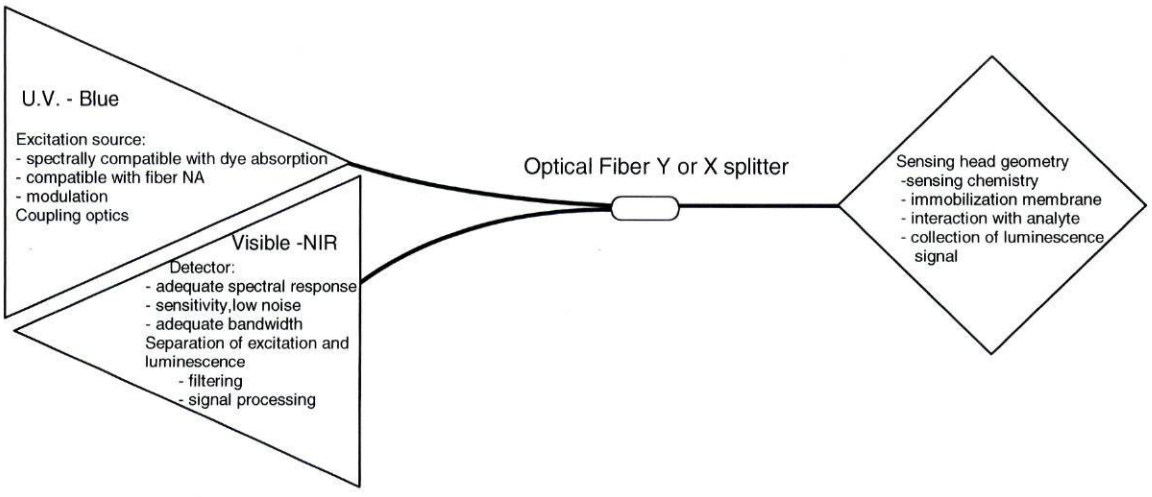


Figure 2.22 Scheme of a prototypical optical fiber system for biochemical luminescence based sensing. In the diagram, critical aspects of sensor optimization are indicated for the excitation, sensing and detection stages.

2.5.1 Optoelectronics for fiber sensing

Optical fibers are waveguides capable of transmitting light over large distances with very small loss. Therefore, they possess a great potential for sensor applications in general and for biochemical sensing in particular. Different techniques have been explored for biochemical sensing using optical fibers: absorption measurements, refractive index changes, scattering and luminescence. In particular, the combination of luminescence spectroscopy techniques with the intrinsic capabilities of optical fibers is very attractive. This combination paves the way for a new generation of very sensitive analytical instruments capable of remote, real-time monitorization of biochemical parameters, with minimum intrusion, and with a wide range of applications for environmental and biomedical purposes. In order to take full advantage of the optical fiber potential, a good knowledge of its operating principles and intrinsic properties is necessary [72-74].

Optical fiber fundamental properties

An optical fiber can be defined as a cylindrical dielectric waveguide made of low loss materials, such as silica glass. It has a central core with high refractive index, n_{co}, through which the light is guided, surrounded by a cladding of slightly lower refractive index, n_{cl}. The refractive index difference is achieved by selectively doping the silica core or cladding with different materials.

According to Snell's law, light rays incident in the core/cladding interface at angles exceeding the critical angle suffer total internal reflection and are guided through the fiber core. Conversely, rays incident at angles lower than the critical angle are refracted and loose part of their power to the

cladding. These rays, also called leaky rays, are not guided and its power is eventually lost by absorption and scattering.

This way, not all the light incident upon the fiber end face will be guided. Only rays within a certain acceptance angle, θ_a, will, after refraction at the air/core interface, satisfy the guidance conditions. This situation is represented schematically in Figure 2.23 . From this figure, and using Snell's law, it can be easily shown that

$$\theta_a = \sin^{-1}[NA], \tag{2.79}$$

where NA is called the numerical aperture of the fiber, defined by

$$NA = \left(n_{co}^2 - n_{cl}^2\right)^{1/2}. \tag{2.80}$$

The numerical aperture and the associated acceptance angle are a fundamental characteristic of an optical fiber, and are essentially determined by its refractive index profile. These parameters determine the fiber capability of gathering light and are thus critical when designing systems for coupling light into and out of the optical fiber.

Another determinant property of an optical fiber is its core size. Standard telecommunication optical fibers have very small cores, typically less than $10\,\mu m$ in diameter, surrounded by a cladding of $125\,\mu m$ diameter. In this size range, geometrical optics is no longer adequate to describe the propagation of light. Instead, electromagnetic theory is used to derive the electromagnetic field distribution of light propagating along the fiber. Each possible solution corresponds to a propagation mode, with particular spatial, temporal and polarization properties, which are determined by the waveguide geometry. In terms of geometrical optics, each mode can be thought off as a ray propagating at a giving angle with the fiber axis. Higher order modes travel through the fiber at larger angles with the fiber axis. Due to the reduced core size and to very small difference between the core and cladding refractive indices (typically less than 1%), in standard telecommunication fibers only a single mode is guided. This is called the fundamental mode and has a Gaussian profile spatial power distribution. Fibers with larger core diameters and larger refractive index differences are also available in which several modes can propagate. These are termed multimode fibers and can be found in a wide range of core/cladding diameters and numerical apertures. Standard multimode fibers, also used for short range telecom applications, typically have core/cladding dimensions of $50/125\,\mu m$ or $62.5/125\,\mu m$.

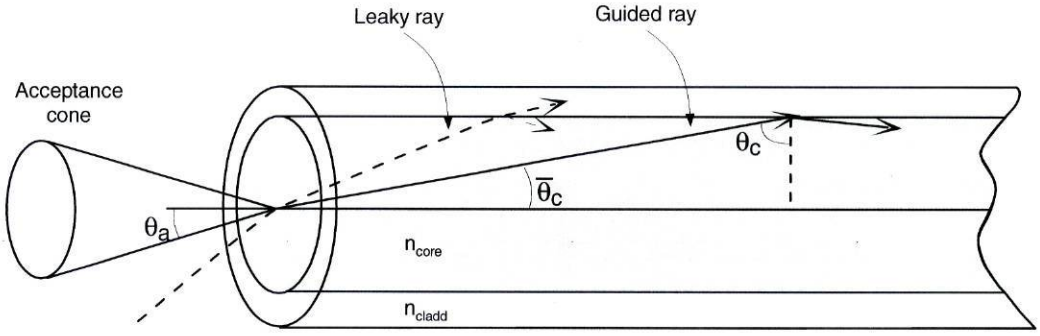


Figure 2.23 Scheme showing the acceptance angle, θ_a, of the optical fiber. Light rays within the acceptance cone are guided by total internal reflection. Adapted from [72].

Due to their small size and reduced numerical aperture (~ 0.13), it can be a difficult task to launch a significant amount of optical power into single mode fibers. Nevertheless, they have special characteristics that can be important in time resolved measurements. Besides the chromatic dispersion intrinsic to the fiber material, multimode fibers also suffer from modal dispersion. Each mode of a multimode fiber propagates at a different speed, causing pulse spreading and limiting the transmission bandwidth. Single mode fibers do not suffer from this problem and have the smallest possible temporal dispersion. Pulse spreading is thus minimized; this can be an important feature when performing time resolved measurements with very short-lived luminophores over long fiber lengths. Typically, single mode fibers can transmit signals modulated at several *GHz* over many kilometers. Multimode fibers, on the other hand, are limited to the *MHz* range. Nevertheless, if in place of the step–index profile, common to most fibers, a graded index profile is used instead, the bandwidth of multimode fibers can be substantially increased.

In spite of all this, for small lengths multimode fibers can still be used in most time resolved experiments. In addition, the capacity of light collection of multimode fibers is far superior to that of single mode fibers. For this reason, large core multimode fibers are usually preferred for most luminescence sensing applications. The multimode properties of a fiber, i.e., how many modes it will propagate, depend on the waveguide characteristics but also on the radiation wavelength. In order to evaluate these properties, a fiber parameter, the V-number, is usually defined by

$$V = 2\pi \frac{a}{\lambda} NA, \tag{2.81}$$

where a is the core radius and λ is the radiation wavelength. A step-index fiber with a V-number of 2.405 or less will typically be single mode. Because this is a wavelength dependent parameter, a fiber which is single mode in the infrared can usually propagate a few modes in the visible range. The larger the V-number, the higher will be the light collection capability of the optical fiber.

The presence of a cladding in optical fibers is necessary if long range transmission is to be achieved. In the absence of cladding, because the external medium, usually air, has a lower refractive index, guiding still occurs. However, in this case the cladding material would be the external environment with its changing parameters (humidity, gases, dirt). Such conditions would result in an increased loss by absorption at the interface. This happens because, in total internal reflection, a fraction of the optical power penetrates the external medium. This is called the evanescent field and it has appealing properties for sensing applications. For a multimode waveguide, the penetration depth, d_p, of the evanescent field into the external medium of refractive index n, assuming the cladding was removed, is given by

$$d_p = \frac{\lambda}{2\pi\sqrt{n_{co}^2 \sin^2\theta - n^2}}. \tag{2.82}$$

The penetration depth is usually polarization dependent, and for optical guides propagating few modes this expression is no longer valid. Nevertheless, it can be used to give some insight into the dependence of d_p on the different propagation parameters. Equation (2.82) shows that d_p increases with wavelength and decreases with increasing numerical aperture. It can be shown that the optical power of the evanescent field decreases exponentially with penetration distance. Typically, penetration depths do not exceed distances in the range of a few wavelengths $(2\lambda - 5\lambda)$. While in multimode fibers only higher order modes (with high θ) significantly penetrate into the second medium, in single mode fibers an important part of the optical power propagates in the cladding.

If the cladding of an optical fiber is partially removed, this feature provides an alternative way to excite luminophores on the outer surface. In addition, the emitted luminescence can be coupled into the fiber core for detection. Because the excitation field penetrates a very small distance into the outside medium, evanescence sensing can be a very sensitive and selective detection mechanism. Only those luminophores near the surface are excited, and this avoids background luminescent noise and minimizes inner filter effects. Also, this mechanism is compatible with a transmission configuration and can be used to address multiple points along the same optical fiber, which is an attractive feature for multiplexing applications.

Another important parameter to consider when choosing an optical fiber is the attenuation at the wavelengths of interest. This is particularly critical in luminescence applications, where a large wavelength span is typically used and luminescence signals are usually very low. The attenuation coefficient, α, can be expressed in dB/km and depends on the fiber material; it is defined in terms of the input and output intensities as

$$\alpha = \frac{1}{L} 10 \log\left(\frac{I_{in}}{I_{out}}\right), \tag{2.83}$$

where L is the fiber length in kilometers. Attenuation in optical fibers is caused mainly by fundamental scattering processes and absorption. The wavelength dependent attenuation of a typical silica optical fiber is shown in Figure 2.24.

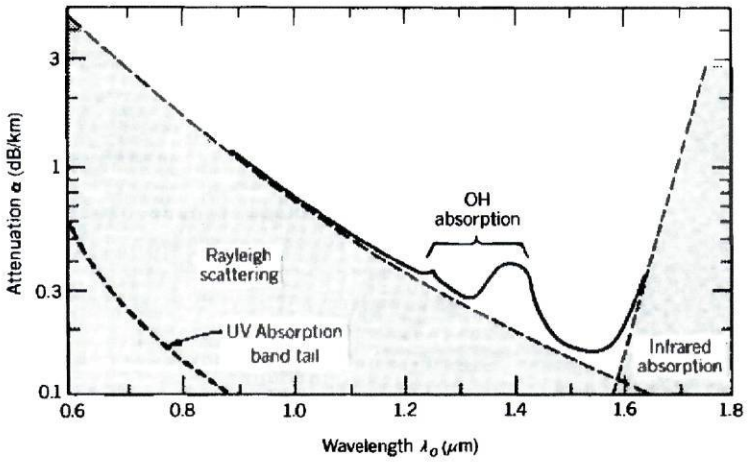


Figure 2.24 Attenuation characteristics of a typical silica optical fiber, with indication of main loss mechanisms. Adapted from [72].

Absorption can be due to intrinsic absorption from the fiber material or from impurities. Silica has two strong absorption bands, an UV band due to electronic and molecular transitions and a mid-infrared band arising from vibrational transitions. OH and other impurities can introduce additional extrinsic absorption peaks. Although hydroxyl groups are difficult to remove, presently fibers are available with low OH content, having reduced absorption in the near-infrared.

In addition to absorption, Rayleigh back-scattering, which is caused mainly by refractive index heterogeneities, induces further transmission losses. The scattering intensity is proportional to $1/\lambda^4$; therefore, at lower wavelengths, in the visible to UV range, Rayleigh scattering is usually the main source of loss. This way, although some changes in fiber composition can slightly reduce attenuation in some wavelength range of interest, in the UV to visible range most fibers present attenuation profiles similar to that shown in Figure 2.24. While in the near infrared the propagation loss can be as low as $0.2 dB/km$, as the wavelength is reduced loss values increase steadily and can reach hundreds of dB/km in the UV and visible range. Thus, for practical reasons and in this wavelength range, loss is also expressed in dB/m. The UV and visible parts of the spectrum are of particular interest to luminescence applications, and such strong attenuations can hinder applications where long fiber lengths are necessary. For small fiber lengths, however, where only a few meters are

needed, this problem is not so critical. Nevertheless, efforts are being made in order to produce sensing dyes with absorption and emission further into the near-infrared where fiber loss and dispersion are minimal and laser sources and photodetectors, more adequate for fiber applications, are available at low cost.

Fibers for sensing

Nowadays, a wide variety of optical fibers is commercially available with appealing characteristics for sensing applications [11, 75]. Single mode fibers are no longer restricted to the traditional telecom wavelength range ($1.3\,\mu m - 1.55\,\mu m$). Today, it is possible to find single mode fibers spanning the whole visible range and near infrared as well, from $400\,nm$ up to $1620\,nm$. The attenuation grows steadily as the wavelength is reduced, reaching $10\,dB/km - 30\,dB/km$ in the visible range (while it can be as low as $0.2\,dB/km$ at $1.55\,\mu m$). Nevertheless, this is not a critical problem for applications where only a few meters are necessary. Single mode fibers in the visible range are attractive because they can be very useful for time-resolved measurements where a large bandwidth is needed. In addition, some of these fibers are available with high birefringence, i.e., they can be used as polarization maintaining fibers. This property provides the opportunity to use single mode optical fibers in applications involving fluorescence anisotropy, where polarization properties are analyzed to obtain information on molecular dynamics and structure. Due to the reduced dimension of their core, single mode fibers can be used to probe the medium with very high spatial resolution. Also, typically, single mode waveguides propagate a higher percentage of the optical power in the cladding, making them suitable for evanescent sensing applications.

In spite of many favorable characteristics, single mode fibers, with small core radius and reduced numerical aperture, have a very limited light collecting capability. Launching light into a single mode fiber is not an easy task, particularly if broadband excitation sources like lamps or LEDs are used; therefore, laser sources must be used instead. On the other hand, the interaction with the sample occurs in a very small volume and the collected luminescence signals can be very small. Low signal levels demand for more sensitive detectors like PMTs and expensive electronics. In this context, the high numerical aperture and core diameter of multimode fibers are very appealing for low cost sensing applications.

Presently, the offer of multimode fibers is very broad. Typical core diameters can vary from $50\,\mu m$ up to $1\,mm$, or higher. Because the refractive index difference between core and cladding is usually larger in multimode fibers, numerical apertures are higher and can range from 0.22 to 0.50. This makes it much easier to couple light from extended broadband sources like lamps and LEDs,

or to collect light from a luminescent sample. Nevertheless, multimode fibers typically present higher attenuation. This happens because different modes, in particular higher order modes, usually travel longer distances through the fiber as compared to the fundamental mode in single mode fibers. This way, the higher the V-number of a fiber the higher the propagation losses will be. Nevertheless, this is compensated by the larger amount of optical power propagating in multimode fibers; this is especially true for small distances. In Table 2-3 the order of magnitude of loss values for different types of available multimode fibers is shown. It can be seen that, from visible to near-infrared, losses can range from tenths to hundreds of dB/km depending on the fiber material. Ultra-violet radiation below $300\,nm$ degrades transmission in standard silica (losses increase with exposure time) and even when special silica fibers are used with increased resistance to UV exposure, attenuation in this wavelength range can exceed $10^3\,dB/km$.

Table 2-3 also shows that multimode fibers are available in different materials [61, 76]. Besides silica glass, other optical glasses can be used depending on the intended application. Multimode fibers made of polymer materials are particularly appealing for low cost applications and their use in short range telecom and sensing applications is growing very fast. Silica-core/plastic-cladding fibers are also available. In spite of the fact that they present higher attenuation values and are limited to the visible-infrared range (UV/blue induced aging alters their transmission properties), plastic fibers offer some interesting advantages over glass fibers. These include, first of all, low cost, but also simple coupling to detectors and emitters, and ease of termination and processing. The physical characteristics of plastic fibers, like geometrical shape and surface polishing, can be modified using inexpensive techniques as compared to glass technology.

Multimode step index fibers	UV-silica	Silica	Optical Glass	Plastics
Transparency	From $170\,nm$	$400-2000\,nm$	$400-1000\,nm$	$500-1500\,nm$
Min. optical losses (dB/km)	10^3	10^1	10^2	10^2-10^3
Refractive Index	1.55 @ $200\,nm$	$1.45-1.49$ @ $633\,nm$	$1.50-1.95$ @ $588\,nm$	$1.35-1.60$ @ $588\,nm$
Typical core radius (μm)		$50-1000$		$1000-1500$

Table 2-3 Properties of some multimode fibers currently available in the marketplace.

Due to lower processing temperatures, organic dyes can be incorporated in the core or the cladding of plastic optical fibers during their fabrication process. This is not possible with silica

fibers, which are manufactured at temperatures in the range $1800\,^{\circ}C - 2100\,^{\circ}C$, while most organic dyes deteriorate at temperatures exceeding $300\,^{\circ}C - 500\,^{\circ}C$. On the other hand, plastic fibers can only be operated at relatively low temperatures, usually below $85\,^{\circ}C$. Nevertheless, dye-doped plastic fibers have been successfully used in many physical and chemical sensing applications. They are specially promising for distributed luminescence sensing.

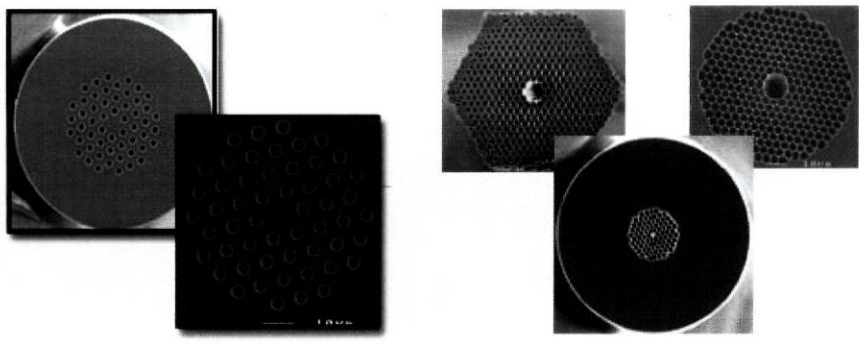
In applications where light collection is the most critical parameter, fiber bundles can be used instead of single fibers. Fiber bundles are usually assembled from hundreds or thousands of small diameter optical fibers ($40\,\mu m - 50\,\mu m$), with very thin cladding, which are glued together with an optical epoxy and result in an optical waveguide which can have from a few hundred microns to several millimeters in diameter. Fiber bundles can be coherent, meaning that the fibers are arranged in an ordered array which will transport imaging information in a pixilated form, or incoherent, meaning that they are randomly arranged. Imaging bundles can be very useful to interrogate multi-parameter sensing arrays [77, 78].

Based on a concept proposed more than a decade ago, a new optical fiber technology has recently become available in the market which has large potential for sensing applications. Photonic crystal fibers (PCF) contain an array of roughly wavelength-sized holes running along the fiber axis (see examples in Figure 2.25). These fibers are available in two fundamentally different types: solid core (figure (a)) and hollow core (figure (b)).

In solid core fibers, guiding is performed by total internal reflection but, unlike standard fibers, the refractive index difference necessary for this to happen is provided by the holes in the cladding. The presence of the holes lowers the effective, or average, refractive index, providing the necessary guiding conditions. Changing the arrangement of the holes, or the core shape, allows tailoring some of the fiber fundamental optical properties like mode shape, dispersion, or birefringence. In addition, it is easy to incorporate more than one core in a single fiber, forming arrays of independent or coupled waveguides. This is particularly attractive for luminescence applications where a core can be used to provide excitation, and a second core can be used to collect the luminescent signal.

A similar versatility is also possible with the hollow core PCF. In this type of waveguide, however, light propagates through a hollow core [79]. Guidance is provided by a fundamentally different mechanism. In this case, the hole matrix in the cladding forms a silica-air lattice that creates a photonic bandgap analogous to an electronic bandgap in crystalline solids, which prevents light within a certain wavelength range from propagating in the cladding. The hollow core acts as a defect through which wavelengths within the gap can propagate by practically loss-free reflection in the

core cladding boundary. This makes it possible to create low loss waveguides with gas filled or even evacuated cores at virtually any optical wavelength. Although PCF losses are presently still relatively high ($\geq 10^2\, dB/km$), theoretically hollow core fibers can be made with lower loss than traditional fibers.



(a) (b)

Figure 2.25 Some examples of photonic crystal fibers available commercially. (a) solid core; (b) hollow core. Available from [75].

The versatility of these new optical fibers is very attractive for sensing applications and, in particular, for those based on spectroscopy. The fiber optical properties can be tailored to improve guidance, reduce loss or improve evanescent interaction in the wavelength of interest. In addition, the holes in the fibers can be used as sensing micro-chambers where a gas, or a liquid, can interact with light or with a sensing luminophore. Although some sensing applications have already been demonstrated, this is a very recent technology, and most of its potential remains unexplored. Presently they are extremely expensive, but, as their potential to telecom applications starts to unveil, this is bound to change with mass production. In addition, their compatibility with standard fibers was already demonstrated, which allows for very small lengths of sensing PCF to be incorporated in a conventional system [80-83].

The many fiber types just described are a sample of the wide variety available either commercially or in research labs all over the world. The availability of most of these fibers in the marketplace, plays a key role in the establishment of optical fiber sensing as a mature technology, and will surely contribute to the growth of successful applications.

Tools and devices

The use of fibers in practical situations involves a great deal of technical skills in order to properly cut, polish or connect them to sources, detectors or other fibers. Fortunately, besides the fiber itself, a whole range of associated tools and accessories is also available from most

manufacturers that make these procedures much easier. These include cutting and polishing tools and special connectors for fiber to fiber or fiber to source easy alignment, splicing machines, etc.. Although these techniques or tools may differ significantly depending on the fiber type, the basic principles are essentially those used with telecom fibers. Most of the time, the fiber manufacturer provides excellent technical notes about fiber preparation and recommendations of the adequate tools. This way, the description of these techniques and tools will not be addressed in detail, unless where absolutely necessary. Nevertheless, it should be stressed that the preparation of a perfectly clean and smooth fiber end face which is perpendicular to the fiber axis is an essential first step, for any successful fiber application [75, 84, 85].

Sources and detectors for luminescent fiber sensing

In addition to the fiber itself, optical sources and detectors are crucial for any luminescence sensing system [1, 74]. For implementation of luminescence fiber sensors, the optical excitation source, besides providing adequate excitation of a specific dye, should be capable of high launching efficiencies into the fiber system. Furthermore, time resolved measurements demand pulsed or modulated outputs. With broadband sources traditionally used in spectroscopy applications, like mercury and xenon arc lamps, coupling efficiencies are extremely small. These are extended and diffuse light sources that usually generate large amounts of heat. This way, both fiber and coupling optics cannot be too close to the lamp. These characteristics make it particularly difficult to focus and couple a reasonable amount of power into the fiber systems. Also, modulation of the lamp output is only possible with external electro-optic modulation or a chopper. In addition, due to their broadband emission, these sources usually require some wavelength selecting device. Absorption filters, interference filters and even monochromators must be used. Such systems can greatly reduce the available optical power. Lamp based configurations can easily become expensive and cumbersome and are incompatible with low cost and compact sensing applications.

On the other hand, using standard laser sources, which are characterized by a very small angular divergence and reduced spectral bandwidth, it is rather simple to focus and couple relatively high optical power levels even into single mode fibers. Some of these sources can provide very fast pulsed outputs, and are already widely used in laboratory spectroscopy applications. Nevertheless, lasers traditionally used in spectroscopy applications, like dye lasers or gas-lasers, are usually very expensive and sometimes demand bulky power supplies and refrigeration systems.

The most suitable optical sources for optical fiber applications are by far semiconductor laser diodes and, to a less extent, LEDs. Based on an emissive semiconductor junction, these optical

sources were developed primarily for telecom applications (presently, they can be found in a variety of consumer products from image displays to CD players). For this reason, they are readily available with emissions from the mid visible ($600\,nm$) to the infrared region of the spectrum. The semiconductor junction material determines the wavelength range of emission. Infrared emitting diodes are usually based on compound semiconductors like GaAlAs ($820\,nm - 870\,nm$) or GaInAsP ($\sim 1300\,nm$). However, most dyes presently used in luminescence sensing applications demand excitation in the blue/UV range of the spectrum. Although semiconductor sources based on Gallium Nitride compounds became recently available with emission in this wavelength range, they are still relatively expensive, and present a limited choice of wavelengths (typically $470\,nm$, $400\,nm$ and $375\,nm$). Still, this is a fast developing technology, and lower prices and wider wavelength choice should soon be available as demand and the range of possible applications rapidly increases.

Laser diodes have excellent characteristics to be used in combination with optical fibers. Although their output usually presents a high angular divergence, using laser diodes in combination with micro-lenses or graded index lenses, it is possible to couple high amounts of power into the fiber core. Currently it is possible to acquire laser diodes with a fiber lead, with optimized coupling efficiency. Usually called pigtailed sources, they are mostly available in the telecom wavelengths range with standard single mode or multimode fiber. Pigtails with large core multimode fibers are also available but usually they are custom made, and thus can be very expensive. Semiconductor sources can be intrinsically modulated at very high frequencies, or pulse rates, by simply modulating the semiconductor junction injection current.

In spite of their relatively high angular divergence and lower optical output powers, the use of LEDs provides a much cheaper alternative in comparison with laser diodes. Available in the same wavelength ranges as laser diodes, they have much broader emission spectra (typical FWHM of $20\,nm - 50\,nm$). This way, they can overlap completely the absorption bands of many dyes. It is now possible, indeed, to cover the whole visible and near UV spectral range with just a few LEDs. In spite of being slower than laser diodes, their output can be modulated at several MHz with simple electronics. Moreover, they are comparatively more robust and easy to operate than lasers. All these characteristics make it worth the effort of dealing with much lower launching efficiencies. Nevertheless, although traditionally associated with much smaller output powers than laser diodes, a new generation of high brightness LEDs is now available [3]. The application of these small devices goes far beyond telecom and sensing applications. Presently, their use is also being explored in imaging and illumination applications. Such a huge potential market provides a strong drive towards

low price and fast technological development. This way, it is expected that LEDs with more suitable characteristics for a wider range of luminescence applications will soon be available.

Although the output of an optical fiber usually has a high divergence angle, it is fairly simple to detect this energy with virtually any kind of detector. The only limitation regards the small signals transmitted by the fiber, which demand a highly sensitive response. This way, many luminescence fiber sensing applications have been reported where PMTs were used for detection. Although this is not a problem in laboratory conditions, the high price and somewhat bulky housing of PMTs are not compatible with low cost and portable applications. The detectors of choice to be used with optical fibers are based on semiconductor junctions. Like laser diodes and LEDs, these detectors can be acquired with a pigtail, thus ensuring maximum coupling efficiency. Although regular PIN diodes sometimes lack the necessary sensitivity to detect faint luminescent signals, much higher sensitivities can be obtained with the more expensive avalanche photodiodes. Although these photodetectors can provide very fast responses, compatible with time resolved measurements, the bandwidth decreases with an increasing detector area, therefore with increasing detection sensitivity. Consequently, a compromise must be established between sensitivity and bandwidth. Even though there is a range of photodiodes available which are responsive in a wide spectral range (from $150\,nm$ to $2600\,\mu m$), their sensitivity is much higher in the infrared. Typically, the responsivity obtained in the UV can be smaller by an order of magnitude. Nevertheless, most dyes used nowadays in sensing applications have their emission in the visible range of the spectrum, where the photodiodes responsivity is still reasonably high.

CCD arrays, linear or matrix type, can also be used for detection of luminescent signals. Although their slow response times make them unsuitable for time resolved experiments, they can be extremely sensitive light detection devices. Widely used in imaging applications, CCD technology has registered major developments in the last few years and is now available at relatively low price. Presently, extremely sensitive spectrofluorometers based on this technology, operating from UV to near infrared, are available. This way, the use of CCD detection has great potential for steady state applications, particularly when spectral discrimination is needed. Moreover, relatively inexpensive miniature CCD spectrometers, which are compatible with compact fiber sensing applications, are now commercially available [11].

Although the use of semiconductor technology faces some challenges when standard organic dyes are used, requirements are more relaxed if long lived metal organic complexes are used instead. Due to their long lifetimes and high quantum yields, lower sensitivities and bandwidths are acceptable. In addition, the absorption spectra of these dyes are compatible with the new generation

of blue LEDs. For these reasons, the successful use of long lived luminophores, in combination with LEDs and standard photodiodes, has been reported in many biochemical sensing applications. Indeed, some of the first commercially available instruments for detection of chemical species are based on these technologies. This successful example indicates the right strategy for the development of optical fiber luminescence sensing technology. Efforts should be applied simultaneously in many fronts: the sensing dye properties, the optical sources and detectors characteristics, and the fiber itself should be optimized, having in mind their matching properties and the final application.

2.5.2 Launching light into the fiber system

From a practical point of view, the theoretically best choices cannot always be implemented. A narrow budget, geometrical or environmental constraints, restricted selection of sensing dyes are some examples of practical limitations. In this context, from the previous discussion it becomes clear that maximization of the launching efficiency is a critical step in sensing system implementation. Many factors are determined by the amount of optical power launched into the optical fiber, like the adequate excitation of the sensing dye and the resulting luminescent signal, which, in turn, establish the necessary detector sensitivity. Ultimately, the possibility of using a particular excitation source will be determined by the amount of power that can be coupled into the optical fiber system. Therefore, it is reasonable that a considerable amount of effort should be dedicated to this matter [86-89].

The launching of power from a radiation source into an optical fiber involves the consideration of many parameters from both elements. The amount of radiated energy that will be successfully coupled into the optical fiber will depend critically on characteristics like its numerical aperture, core size and refractive index profile, but also on the optical source size and angular power distribution. The coupling efficiency is defined by

$$\eta = \frac{P_f}{P_s}, \tag{2.84}$$

where P_s is the total power emitted by the optical source and P_f is the amount of power actually launched into the optical fiber. Depending on the type of fiber used, and optical source properties, different schemes for maximizing η can be applied. These include the use of auxiliary focusing and collimating optics, micro lenses, direct butt-coupling, etc.. Coupling light into multimode or single mode fibers are actually two separate problems. While the former can be addressed with geometrical optics, with the fiber being fully described by its core size and numerical aperture, single mode

coupling can only be understood using electromagnetic theory. Coupling light into a single mode fiber is a problem of matching the incident field distribution with that of the fiber fundamental mode. Because the applications explored in this work deal essentially with multimode fibers, multimode coupling will be explored in the following lines; single mode coupling will not be addressed.

When lasers are used, due to the favorable characteristics of the emitted radiation (narrow spectral bandwidth, coherence, easy focusing) it is reasonably simple to introduce a high amount of power into the fiber system. Laser diodes, for instance, can be acquired with a pigtail or with collimating optics, greatly facilitating this task. In such cases, the fiber is usually placed in contact with the emitting surface, either directly or using micro lenses, and then glued with some optical epoxy. With this scheme, high efficiencies are usually achieved, and the problem of light coupling is reduced to a simpler one of just connecting two optical fibers.

LEDs, on the other hand, with their broadband spectrum and high divergence are usually poor fiber emitters. Although pigtailed LEDs can be found at the telecom wavelengths, in the visible range they are only available by custom order, which can greatly increase cost. This way, because they have many characteristics which are highly attractive for low cost luminescence sensors, it is desirable to develop techniques which allow maximizing the launching efficiencies using standard LEDs. In the context of the sensing applications explored in this work, the problem of maximizing the launching efficiency of an LED into a multimode fiber is a particularly important one.

Coupling light from an LED into a multimode optical fiber

In order to evaluate the different coupling schemes, it is instructive to calculate the efficiency of a direct butt coupling configuration, in which the optical fiber end-face is placed in close proximity to the semiconductor emitting surface. To perform this calculation, the optical source radiative pattern must first be known. This property can be assessed by evaluating the source radiance, which is defined as the optical power radiated per unit projected area, per unit solid angle and can be expressed as

$$L = \frac{d^2\Phi}{d\Omega \cdot dA \cdot \cos\theta} \approx \frac{\Phi}{\Omega \cdot A \cdot \cos\theta}, \tag{2.85}$$

where Φ is the radiant flux or optical power, Ω is the solid angle, A is the emitting area of the source and θ is the angle between the emissive surface normal and a specified direction of observation/detection (the approximation holds for small values of A and Ω) [90]. Radiance is usually expressed in units of $W\,cm^{-2}sr^{-1}$. A spherical coordinate system, like the one represented in

Figure 2.26, is best suited for the description of the emission pattern. Usually, the optical source radiance can be a function of both angular variables, θ and ϕ, and also vary from point to point of the emitting area.

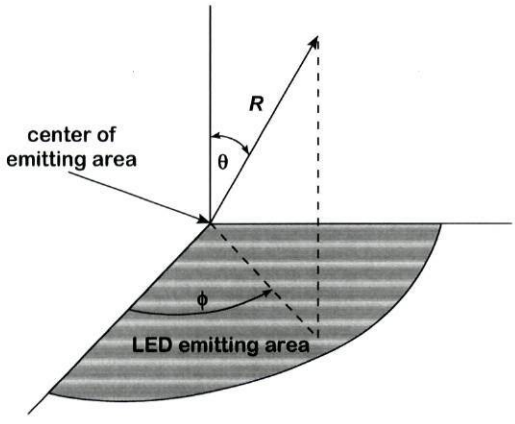


Figure 2.26 Spherical coordinate system used for description of the optical source emission pattern. Adapted from [88].

However, it is reasonable to assume, for the sake of simplicity, that emission across the source area is uniform. Furthermore, in the particular case of surface emitting LEDs, the emission pattern is approximately lambertian, meaning that the source is equally bright when viewed from any direction, i.e. it has a constant radiance. Under these conditions, the power delivered at an angle θ, measured relative to the normal to the emitting surface, varies as $\cos\theta$. The cosine factor arises from the projection of the area of the emission surface into the direction of observation. This way, the emission pattern of a lambertian source can be described by the angular dependence of its radiant intensity, which is given by

$$I(\theta,\phi) = I_0 \cos\theta, \tag{2.86}$$

where I_0 is the source radiant intensity (given in W/sr) along the normal to the radiating surface[14]. In practice, a clipped Lambertian or limited Lambertian distribution is more commonly observed. These are distributions that appear to be Lambertian but only on a limited range of angles. Outside that range of angles there is no energy flux. Such a distribution can arise, for instance, when a true Lambertian source is observed over a limited planar aperture.

When compared to surface emitting LEDs, edge emitting LEDs or laser diodes typically present more complex emission patterns having different radiances in the normal and parallel planes ($\phi = 90°$, and $\phi = 0°$).

[14] Irradiance I, and radiance, L, are related by $I = L\,dA\cos\theta$.

The configuration considered for calculation of the coupling efficiency is represented in Figure 2.27. The LED is assumed to be a Lambertian source with a circular emitting surface of radius r_s, placed in close proximity to the fiber end-face, and centered to its core of radius a.

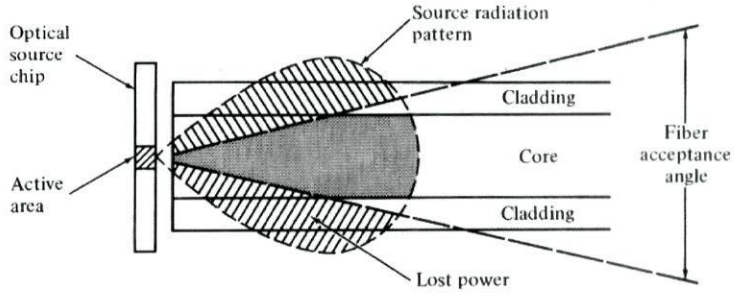


Figure 2.27 Schematic representation of source to fiber coupling. Taken from [88].

In this situation, and considering a source of radiance $L(A_s,\Omega_s)$, where A_s and Ω_s are, respectively, the area and emission solid angle of the source, the coupled power can be found using the relationship

$$P_f = \int_{A_f} dA_s \int_{\Omega_f} d\Omega_s \cos\theta \cdot L(A_s,\Omega_s) \tag{2.87}$$

where the area and solid acceptance angle of the fiber, A_f and Ω_f, respectively, define the integration limits. This calculation can be performed by first integrating the radiant intensity $I(\theta,\phi)$, from an individual radiating point source on the emitting surface, over the acceptance solid angle of the fiber:

$$P_i = \int_0^{2\pi} \int_0^{\theta_a} I(\theta,\phi) \sin\theta \, d\theta \, d\phi \, . \tag{2.88}$$

In this equation $\sin\theta \, d\theta \, d\phi = d\Omega$, and θ_a is the acceptance angle of the fiber. The total coupled power can then be determined by summing up the contributions from each individual point source over the emitting area and is thus given by

$$P_f = \int_0^{r_{\max}} \int_0^{2\pi} P_i \, d\theta_s r \, dr \, , \tag{2.89}$$

where $d\theta_s \, r \, dr = dA_s$. The upper integration limit $r_{\max}$ will be determined by the relative size of the fiber and source. If the fiber core is larger than the LED emitting area, then $r_{\max} = r_s$; if, on the other hand, the source area is bigger than the fiber, then $r_{\max} = a$.

With these simple expressions, and considering a Lambertian emitter with radiant intensity given by equation (2.86), it is straight-forward to calculate the optical power coupled from the LED into the fiber core. Conversely, the total power emitted from the optical source can also be found using the same equation but considering, as integration limits, the total emitting area (A_s) and solid

angle ($2\pi\, sr$) of the source. From these calculations it can be shown that the launching efficiency from a Lambertian source of small dimensions compared to the fiber diameter is given by

$$\eta = (NA)^2 \qquad for \qquad r_s \leq a\,. \tag{2.90}$$

If, on the other hand, the source dimensions exceed the core diameter, the launching efficiency in given instead by

$$\eta = \left(\frac{a}{r_s}\right)^2 (NA)^2 \quad for \qquad r_s > a\,. \tag{2.91}$$

For a source smaller than the fiber core, the fundamental limitation in the launching efficiency is set by the fiber numerical aperture. For extended sources, in addition to the NA limitation, the launching efficiency is decreased by the ratio $\left(a/r_s\right)^2$. Therefore, an ideal source should have approximately the same dimensions as the fiber core and its radiation pattern should match the fiber numerical aperture. In the particular case of surface emitting LEDs such conditions are never met, as being lambertian sources their emission solid angle always exceeds the fiber NA. The size of the emissive area, on the other hand, can vary from a few tens of microns to millimeters, depending on the particular LED technology. Nevertheless, the use of lenses allows some manipulation of the source parameters that can, in some cases, improve the launching efficiency.

The efficiencies calculated above were obtained assuming that the refractive index of the medium separating the source and the fiber matched the core refractive index. However, even when the fiber and the source are in direct contact, any refractive index difference causes Fresnel reflections to occur at the interfaces. This way, considering a perpendicular fiber end-face and normal incidence, the launching efficiencies specified in equations (2.90) and (2.91) are usually decreased by a factor given by the surface reflectivity

$$R = \left(\frac{n_{co} - n}{n_{co} + n}\right)^2, \tag{2.92}$$

in which n is the refractive index of the medium surrounding the fiber core. For an air/glass interface this factor is approximately 4%. This problem can be reduced by using index matching material between the interfaces. When lenses are involved, antireflection coatings are used instead.

Sources with a broad angular distribution tend to launch light into all the fiber modes, guided modes and leaky modes alike. As the propagating modes reach equilibrium, however, the power in the non-propagating modes will eventually be lost by radiation/absorption out of the fiber. Typically, the equilibrium condition will be reached after a few tens of meters. This way, the apparent numerical aperture at the fiber input will generally exceed the fiber equilibrium numerical

aperture. The difference between these two parameters is usually a function of the refractive index difference and will vary according to the fiber type. When using short lengths of fiber, accurate measurement of the numerical aperture can only be performed if mode scrambling devices are used to force the equilibrium condition.

Optical invariant

In light launching applications, lenses can be used to image the optical source emitting surface on the fiber end-face. This procedure can be useful when the emissive surface is not accessible for direct butt coupling. In addition, it provides a mechanism through which the apparent size and emission solid angle of the source can be changed to match that of the optical fiber being used. Unfortunately, these two parameters cannot be changed independently, limiting the maximum launching efficiencies achievable.

This limitation arises from the conservation of the *étendue* or *throughput*, which is defined by the product of the refractive index of the media surrounding the source, n, the source size, A_s, and its emission solid angle Ω[15]. The value of that product remains the same in the image plane regardless of the optical system used; an optical system with a different magnification can change the size of the image or the converging angle of the light cone, but it will not change the value of the product of these parameters. For these reasons the *etendue* is also called the optical invariant or the Lagrange invariant. Considering the definition of radiance (equation (2.85)), and the conservation of optical power, it can be seen that, in an ideal system, radiance is also conserved. In practical situations, however, the radiance can decrease due to losses by reflection, absorption or scattering. This invariance property is related to fundamental energy conservation principles but it can be easily understood by simple geometrical optics [91, 92].

In the scheme of Figure 2.28, the fundamental parameters necessary to understand the imaging process using an ideal thin lens are represented. A paraxial approximation is used in which only small angles are considered ($\sin\theta \approx \theta$). In order to obtain the image of an object of height y_1, at a distance s_1 from the lens surface, two rays with special properties can be used. A ray leaving the object, and propagating parallel to the optical axes of the lens, will be refracted crossing the optical axis at the focus, f, on the image side of the lens. Another ray, passing through the center of the

[15] More precisely , considering a bundle of rays intersecting a constant z plane in a small region of size $dxdy$ and having a small range of angles $d\alpha\, d\beta$, then as the light propagates through a lossless system, the following quantity, called the *etendue*, remains constant: $\int n^2 dx\, dy\, d\alpha\, d\beta = \int n^2 dA \cos\theta\, d\Omega$. Here $dA = dx\, dy$ is the differential area, $d\Omega$ is the solid angle, and θ is the angle between the normal to the emitting surface and the direction of observation .

lens, goes through it with practically no deflection. This happens because, at this particular point, both lens surfaces are normal to the optical axis and the lens is considered thin. The intersection of these two rays determines univocally the image of the selected object point. By this method the image height y_2, and distance from the lens, s_2, are thus obtained.

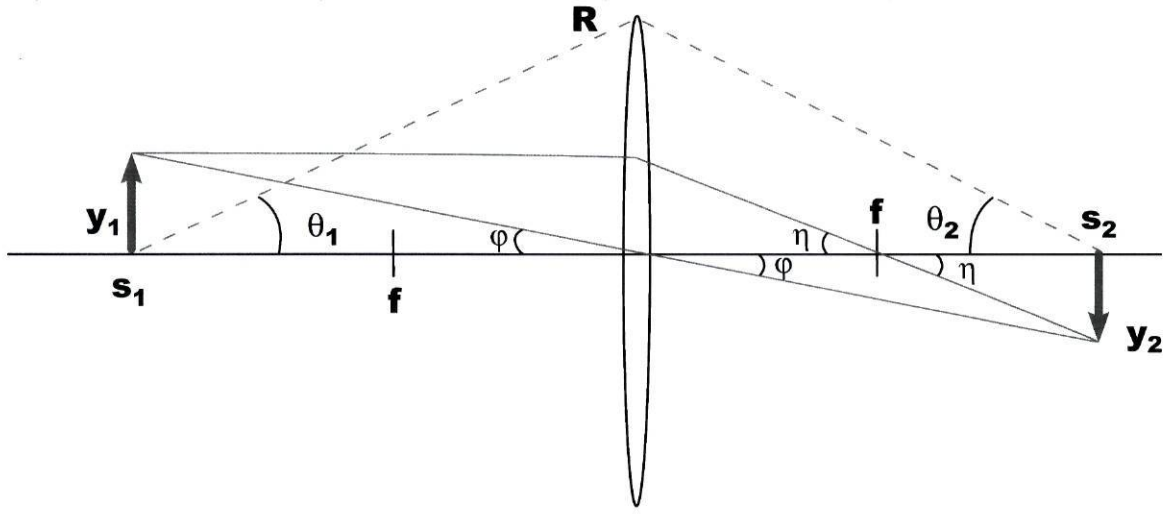


Figure 2.28 Imaging by an ideal thin lens.

The magnification provided by the lens can then be calculated from the scheme represented in Figure 2.28, using the relations between the angle φ, and the sides of the triangles defined by y_1, s_1 and y_2, s_2:

$$\frac{y_2}{y_1} = \frac{s_2}{s_1} = M\,. \tag{2.93}$$

The magnification, M, is given by the ratio of the image/object heights or distances to the lens. These relations impose some limitations on the optical system dimensions. For a given system geometry, there is only a single lens position, or object/image positions, that will provide the desired magnification. By using the angles η, and the corresponding triangles, in the scheme of Figure 2.28, it is also possible to relate the lens focal length to the object and image distances

$$\frac{1}{f} = \frac{1}{s_1} + \frac{1}{s_2}. \tag{2.94}$$

This relationship is called the paraxial lens equation, and together with equation (2.93) provides a way to design the optical system. In a practical light coupling application, usually the sizes of the optical source and of the optical fiber core are known. In order to match them, the necessary magnification can them be calculated. Usually, as an additional geometrical constraint in practical

applications, s_1, s_2 or $s_1 + s_2$, will be kept as small as possible. These conditions, together with equation (2.94) will allow full specification of the optical system.

However, it was already discussed that, in order for effective light coupling to take place, besides adjusting the relative sizes of the source and fiber, the emission solid angle of the source should not exceed the fiber numerical aperture. In order to assess the influence of the lens system on the angular distribution of the radiation, a marginal ray was represented in Figure 2.28. This ray leaves the object making the maximal angle, θ_1, with the optical axis, and crosses the lens at the limit of its aperture, at a distance R from the optical axis. Again making use of simple geometrical relations and using the definition of magnification it can be shown that

$$y_2\theta_2 = y_1\theta_1 . \tag{2.95}$$

This relationship is the geometrical optics equivalent of the Lagrange invariant. In any optical system comprising only lenses, the product of the image size and ray angle is a constant, or invariant, of the system. This is valid for the paraxial approximation and for aberration free lenses. Deviation from these ideal conditions in a practical situation will translate in the replacement of the equal sign by a greater-than-or-equal sign in equation (2.95). That is, aberrations could increase the product but nothing can make it decrease.

The marginal ray also shows that the lens itself may impose some limitation on the amount of radiation that is collected from the optical source. In this particular example any ray leaving the source with an angle exceeding θ_1 would not be collected. For this reason it is important to choose a lens system with a large enough clear aperture so that it collects the highest possible amount of light from the source. This feature of the lens is usually given by its f-number, or f#, which is defined as the ratio between the lens focal distance and its diameter or, in terms of lens radius, $f\# = f/2R$. The minimum possible value of f# is 1, meaning that all the lens surface is clear, it corresponds to the maximum aperture and, therefore, to the maximum light collecting capability. In practice, the useful lens surface is limited to a fraction of its total area, in order to avoid aberrations, resulting in higher f-numbers. Considering the geometry of Figure 2.28, choosing a lens with $f\# < 1/(2\theta_1)$, θ_1 being the highest emission angle of the optical source, ensures that the maximum amount of light will be collected by the lens. However, in practice, reducing y_2 in order to image a larger emission area into the fiber core can only be accomplished by increasing the distance s_1 or decreasing the lens radius R [16]. However, both of these actions will decrease the light collected by the lens. This way,

[16] Using simple geometrical relations it can be shown that for $s_2 \approx f$, the image size is given by $y_2 = 2y_1(R/s_1)f\#$.

when collecting light from an extended source, a compromise must be taken between the achievable magnification and the lens aperture.

Ideally, for maximum coupling efficiency, the optical source invariant should not exceed the 'optical fiber invariant' (given by its core size times its acceptance solid angle), and the lens aperture should be such that it does not block any of the emitted radiation. In practice these conditions are seldom met and compromises must be considered. In view of equations (2.93) and (2.94), and the optical invariant principle, it is easy to verify that, when the optical source is smaller than the fiber core, the use of lens can, in fact, improve the launching efficiency. When the emission area is magnified to fit the core area, i.e., when y_2 is increased, equation (2.95) shows that the apparent emission solid angle must become smaller, i.e. θ_2 must decrease in order to keep $y_2\theta_2$ constant and equal to $y_1\theta_1$. This way, θ_2 will become a closer match to the fiber numerical aperture further improving the light coupling efficiency.

If, on the other hand, the optical source emission area exceeds that of the fiber core, reducing the image size in order to fit the fiber diameter will result in an increase of the apparent emission solid angle. I.e. if y_2 is reduced, θ_2 must increase in order to keep $y_2\theta_2$ constant. Considering the object side of the lens, increasing y_1 will result in a decrease of θ_1, i.e., although light is being collected from an increased area, the decrease in collection angle prevents any improvement. If for instance, a lens is used to condense light onto the fiber end-face from an area of the source with $y_1 = 5\,y_2$, the system will be collecting light from an area that is $25\times$ larger than the area of the fiber (assuming a circular area of radius y_1). However, the optical invariant constraint implies that θ_1 must now be decreased by a factor of 5, so the system will be collecting light from a solid angle that is reduced by the same factor of 25 [17]. Hence, the total light collected, irradiance $\times$ area $\times$ solid angle, is a constant. Therefore, in this particular situation, the use of lenses cannot improve the launching efficiency. An imaging system collecting light from an extensive diffuse source into a fiber cannot collect more power than could be collected by direct butt-coupling. In this particular situation, equation (2.91) gives the maximum launching efficiency achievable. For LEDs with large emission areas exceeding the fiber core diameter, the best launching efficiency is achieved by bringing the fiber end as close as possible to the emitting semiconductor junction. Nevertheless, very often the source emissive surface is not directly accessible to the fiber end. In such cases, lenses can be used to retrieve the efficiency that could be obtained in a direct butt coupling configuration.

---

[17] In order to achieve the $1/5$ magnification, the distance s_1 must be increased in order to equal $5\,s_2$. This way, considering that $\theta_1 \approx R/s_1$, this angle is decreased by a factor of 5. Because the corresponding solid angle is given by $\Omega = A/s_1^2$ it will be reduced by a factor of 25.

Coupling with lenses

Although in the example of Figure 2.28 a single lens is considered, in practical situations more complex lens systems must be used, in order to provide high magnification and compensate for aberrations. In the context of practical applications, in addition, the size of the coupling system must be kept as small as possible. This way, the use of discrete lens elements is usually avoided. Traditionally, launching light from laser sources into optical fibers is done using microscope objectives [84, 85]. These compound optical elements provide high magnifications ($10\times$, $20\times$, $60\times$), and high numerical apertures (0.25, 0.40), in order to cope with the high divergence of laser diodes and allow for very small working distances ($s_1 \approx 10\,mm$). All of this is provided in a very compact solution and with high quality at a considerably low price. Available from most fiber dealers, they are compatible with a whole set of precision positioning mechanical devices that allow to accurately align the optical fiber with the lens focal plane. An optical system with the same characteristics using discrete optical elements would be bulky and costly.

The use of these optical elements with standard surface emitting LEDs, as an alternative to laser diodes, faces, however, some additional difficulties. Being Lambertian, these sources have a much broader emission solid angle than lasers; in addition, the size of the emissive area can be much larger. This way, taking into consideration the fundamental limitations imposed by the optical invariant, launching efficiencies can be much smaller with LEDs. This is true independently of the optical system used for coupling. Furthermore, these sources are traditionally provided with a plastic lens-shaped encapsulation which, although it reduces their divergence to $15^\circ - 20^\circ$, increases their size to $3\,mm - 5\,mm$. This can exceed the clear aperture of some of the objectives typically used, leading to an increased insertion loss. Consequently, although microscope objectives make a good combination with laser diodes, even when single mode fibers are used, they are not particularly efficient when used with standard LEDs.

Micro spheres and GRIN lenses

In modern telecommunication systems, micro-optic components are used to couple light between fibers, from laser diodes to fibers and from fibers to detectors. Both ball lenses and graded index (GRIN) lenses may be employed in these roles [93]. Besides providing a major decrease in package size, these coupling systems are usually associated with reduced insertion loss. This improvement is due to the decrease in the number of optical interfaces (usually a single element is used). Also, their small surface areas can be anti-reflection (AR) coated with high quality and at much lower cost than larger standard optics. Even with reduced number of interfaces, AR coatings

are very important to minimize losses due to reflection which, depending on the refractive indices, can be fairly high (see equation (2.92)).

Ball lenses are spherical in shape; they are made of standard glasses and usually have a constant refractive index. They work, as a standard lens, by refraction at the air/glass interfaces, and inside the lens rays propagate in straight lines. GRIN lenses, on the other hand, are cylindrical in shape, and have a refractive index distribution varying radially with a parabolic profile, with its maximum on the lens axis. This way, unlike the ray trajectory in standard lens, the light path curves gradually as it propagates trough the lens. By choosing the adequate refractive index profile and lens length, GRIN lenses can be used to focus collimated or diverging beams into the optical fiber.

GRIN lenses are widely used in the telecom industry and are readily available from many vendors. Their design takes into consideration the need for a reduced package size and the small dimensions of the emission area of telecom lasers. In accordance with these constraints, typical GRIN lens radius values are in the $0.5\,mm - 1.0\,mm$ range, while their lengths can vary from $3\,mm - 6\,mm$. This way, the use of a standard GRIN lens with large extended sources is somewhat limited. Ball lenses, on the other hand, are available from a number of dealers and can have much larger sizes, with diameters up to $10\,mm$; this gives them an increased light collecting capability, more suitable for use with extended sources. Conversely, they can also be much smaller (as small as $250\,\mu m$) than GRIN lenses, leading to reduced package sizes. The cost of ball lenses is also less than that of GRIN lenses.

Although ball lenses present some advantages, either for telecom applications or for use with extended sources, up to this point GRIN lenses have been heavily favored, being employed in practical telecom systems more frequently. One of the main reasons for this is the fact that their simpler geometry makes them easier to manufacture, without worrying about of accurately polished curved surfaces. Their flat surfaces are also easier to coat uniformly with AR-thin films. In addition, aberration corrections can be achieved by tailoring the refractive index profile with no need for multi element systems or aspheric lenses.

On the contrary, when coating ball lenses with traditional technologies, like evaporation or sputtering, it is not possible to ensure uniform deposition over the whole surface. The deposition rate of these techniques is highly dependent upon the angular orientation between surface and source, as well as on their distance. Spheres coated by evaporation must be turned to coat both sides. In addition, while the North and South Poles of the sphere are covered, the equators remain bare, unprotected. This way, a sphere coated by these processes will have its useful optical axis along the poles, introducing an additional alignment requirement. Recently, however, new coating

technologies started being used, based on chemical vapor deposition, which allow uniform coating of the whole sphere surface. AR-coated ball lenses are uniformly covered, and can have losses less than $0.01\,dB$ (99.75% transmission) per surface, over broad wavelength ranges.

These new generation ball lenses are less expensive than GRIN lenses, and can be fabricated from a wide range of glasses with a diversity of refractive indexes. Also, alignment requirements are dramatically reduced when using these lenses, as no rotational orientation is required. For all these reasons, ball lenses promise to be very valuable devices to perform coupling between fibers, sources and detectors. Having high numerical apertures and low insertion losses, particularly when coated with adequate materials, they can achieve relatively high launching efficiencies, even when extended sources are used.

For proper choice of the ball lens adequate for a given application, some of its basic features must be known. The focal length of ball lenses depends only on their diameter, D, and refractive index, n (Figure 2.29). Using the paraxial lens equation [94] it can be shown that the focal length, f, as measured from the center of the sphere, is given by

$$f = \frac{nD}{4(n-1)}. \tag{2.96}$$

From this equation, the working distance or back focal length, BFL, can be easily calculated from

$$BFL = f - \frac{D}{2}. \tag{2.97}$$

The numerical aperture of a ball lens depends on its focal length and on the input diameter, d. Considering a paraxial approximation, the ball lens NA can be estimated from

$$NA = \frac{2d(n-1)}{nD}. \tag{2.98}$$

The choice of the adequate lens to couple light from a source into a given fiber will be determined by the source output diameter (d), and the fiber numerical aperture. The numerical aperture of the lens should be less or equal to that of the fiber. Because aberrations were not considered, the NA value yielded by equation (2.98) is a minimum value, only achievable with an ideal lens. This way, it is good practice to assume that the theoretical numerical aperture of the coupling optics should not exceed 70% of the fiber numerical aperture. After establishing the value of the desired numerical aperture, the output diameter of the optical source can be used to calculate the ball lens minimum diameter (D). In practice, most of the time, a compromise is established between the desired NA and the available lens diameters.

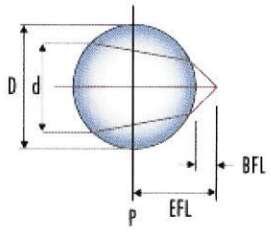


Figure 2.29 Scheme representing a ball lens and its relevant geometrical parameters. Taken from [93]

Ball lenses are available in a wide range of diameters, from $200\,\mu m$ to $10\,mm$. Smaller diameters are difficult to handle but provide an excellent compact solution to be used in pigtails with laser diodes and even LEDs. Larger diameters, on the other hand, are easily handled and, due to increased light collecting capability, are compatible with extended sources of larger dimensions. In this regard they provide an interesting solution to be used with large diameter LEDs and multimode optical fibers. In addition, as their use increases, a wider choice of diameters and lens materials will become available, facilitating the best fit for each application.

Non-imaging optics

The primary purpose of a coupling system is to transform a given energy distribution, radiated from the source with a certain area and angular spread, into a different distribution, with a different area and angular spread, that better matches the fiber acceptance parameters. The systems described previously for performing this task were imaging systems. They fulfill the above requirements by providing, in the plane of the fiber end-face, an exact image of the source with the adequate magnification. An image is formed because each point of the object has an exact correspondence to a point in the image plan. As discussed above, image formation involves many geometrical constraints that limit the system design. In addition, particularly when high angular spreads are involved, imaging systems are strongly affected by aberrations or have limited entrance pupils. This translates into a decrease of radiance at the image plane and, this way, from the point of view of power transfer, imaging systems may not be the most efficient solution.

The field of non-imaging optics deals with the design of optical devices with the purpose of transforming a light distribution *a* into a light distribution *b*, while maximizing the energy throughput. A generic representation of such a transformer can be seen in Figure 2.30.

While an imaging optical system maintains a strict relationship between points belonging to two conjugate planes, such that an exact image of the source is formed at the receiver, a non-imaging system relaxes the requirement for image formation and instead requires only that all the

flux leaving the source gets redirected to the receiver, regardless of any mixing of the light rays that may occur during the process. This way, energy transfer can be maximized at the cost of image quality.

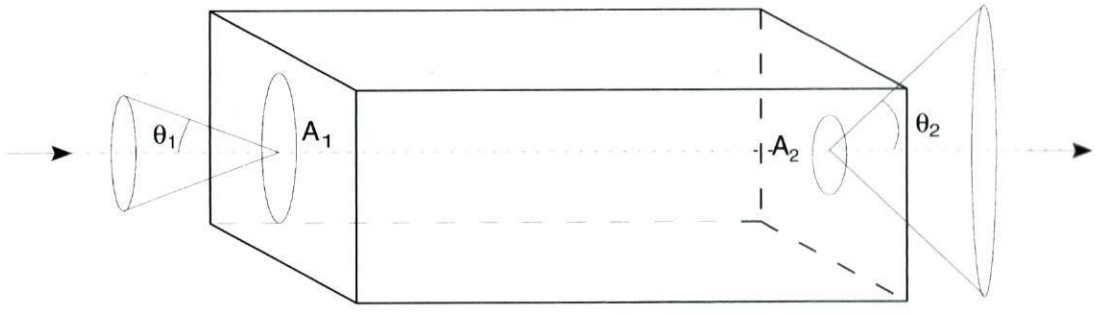


Figure 2.30 Generic representation of a non-imaging device which transforms an input light distribution with area A_1 and angular spread θ_1 into a different output light distribution with area A_2 and angular spread θ_2.

Non-imaging devices have many applications, from Cerenkov counters to detection of very weak astronomical signals, but their major development was achieved in the context of illumination applications and solar energy concentration [92, 95, 96]. In solar energy applications the goal is to attain the maximum possible concentration of solar radiation. The concentration achieved with a particular device is given by the ratio of the system output area to the input area. Thus, considering the device of Figure 2.30, the concentration would be given by

$$C = \frac{A_1}{A_2}. \tag{2.99}$$

Because the conservation of *étendue* derives from fundamental thermodynamic principles, non-imaging devices are also constrained by the optical invariant. This way, concentration of energy into a smaller area is only achievable by increasing the angular divergence of the output radiation. Hence, it can be shown that the highest possible concentration achievable is given by

$$C = \frac{y_1}{y_2} = \frac{n_2 \sin\theta_2}{n_1 \sin\theta_1}, \tag{2.100}$$

for a 2D geometry and by

$$C = \frac{A_1}{A_2} = \frac{n_2^2 \sin\theta_2^2}{n_1^2 \sin\theta_1^2}, \tag{2.101}$$

for a 3D geometry [97]. In both expressions, n_1 and n_2 represent the refractive indices of the media in which the input and output of the non-imaging device is immersed. Both these equations are a consequence of the conservation of *etendue* (note that equation (2.100) is a more generic expression

of the geometrical optical invariant given by equation (2.95), which was derived within the paraxial approximation). The maximum values of C are achieved when $\theta_2 = 90°$, in which case the device is termed an ideal concentrator. For situations where the angular output must be limited to a certain value $\theta_2 < 90°$, like in some fiber optic applications, the device is termed a θ_1 / θ_2 transformer[98].

A number of methods exist for designing non-imaging optical systems. The simplest and most intuitive of these is known as the edge-ray method or the method of strings [95, 97, 99, 100]. The main concept behind the edge-ray method is that extreme rays at the input aperture are also extreme rays at the output aperture. Rays in between the edge rays also strike the receiver, although the path they take may involve no reflections or multiple reflections. A model system of an ideal 2D concentrator is the compound parabolic concentrator, or CPC. An example of the construction of a CPC by the string method is shown in Figure 2.31.

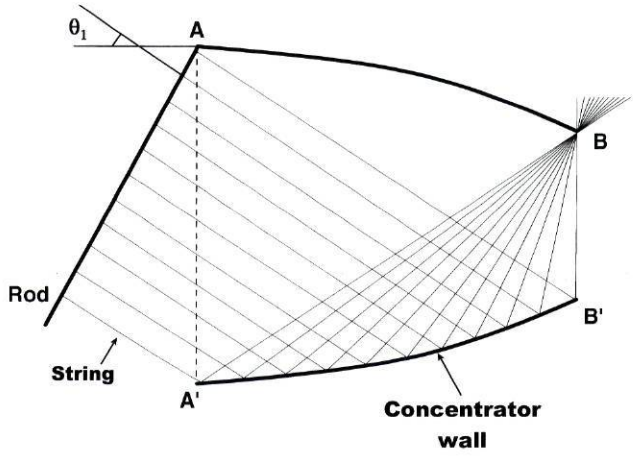


Figure 2.31 Construction of CPC by the edge ray method.

According to the edge-ray method, the reflector walls should be constructed in such a way that all rays incident upon the input aperture, AA', at the limiting acceptance angle, $\pm\theta_1$, be reflected directly to the edge of the output aperture to points B and B'. According to the edge-ray principle, when these conditions are satisfied rays incident at smaller angles will also get through to the concentrator output.

The necessary reflector shape can then be obtained by considering a rod inclined at an angle θ_1 to the entrance aperture AA', and imagining a piece of string attached via a slip ring and positioned at point A on the rod, such that the string is taut and stretched following the path of ray $AB'B$. According to Fermat's principle, all input rays parallel to this edge ray should possess identical optical path lengths. Therefore, assuming a constant string length (or optical path), and slipping the ring to move along the rod such that the string (ray) is parallel to the preceding ray in

every successive position, the concentrator wall $A'B'$ can be traced out as shown in the scheme of Figure 2.31. This construction defines the concentrator profile for the non-imaging device. In this particular case, each concentrator wall consists of a segment of a parabolic profile (AB and $A'B'$), hence the name CPC. The axes of the parabolas are inclined by $\pm\theta_1$ relative to the concentrator optical axis, and their foci are located at the edge of the opposite wall (at A' and A respectively). This way, rays incident at the maximum acceptance angle are indeed focused at these extreme points. This method can be extended to dielectric optical devices and to more sophisticated objects. For this particular concentrator geometry, it can be shown that the device length is given by [92]

$$L = \frac{(\overline{AA'} + \overline{BB'})}{\tan\theta_1}. \tag{2.102}$$

This formula provides the minimum length needed to achieve maximum concentration; falling short of this minimum value will result in a decreased concentration ratio. It can also be seen that the device length will grow very fast as the acceptance angle becomes smaller.

The CPC configuration was shown to behave as an ideal concentrator in a 2D geometry. Rotation of this structure about the symmetry axis yields a cone-like structure which is the 3D version of the CPC. This new device, however, is not ideal in the sense that it does not transmit all available radiation within the nominal acceptance range to the exit aperture and, therefore, does not reach the thermodynamic limit for concentration of radiation [101]. Fortunately, in many cases, rotation of an ideal 2D structure yields almost perfect 3D concentrators, where only a small fraction of energy is lost by skew rays. Nevertheless, the performance of 3D concentrators can be improved by slight variations of their shape.

The CPC profile was derived considering a Lambertian source at infinity, subtending a limited solid angle (the sun). For different practical applications, however, with sources at finite distance, the edge ray principle can still be used to obtain the concentrator shape. Although in these cases the profiles obtained are not parabolic, these devices are sometimes termed CPC-type concentrators. For a source at finite distance form the concentrator input wall, for instance, the yielded profile is elliptical (compound elliptical concentrator - CEC). If, on the other hand, rays cross the concentrator appearing to come from a virtual source located at the device output, (this can happen when a lens is used between the source and the device input), the ideal concentrator will have walls describing a hyperbolic profile (compound hyperbolic concentrator - CHC). In this particular case, the hyperboloid of revolution is also an ideal 3D concentrator often called a 'trumpet' [92, 102].

When θ_1 is small, CPC-type concentrators can turn out with long geometries. To avoid an excessively long system, these devices can be used in combination with other optical elements like

lenses or mirrors. Many examples can be found in the literature in which a lens is placed at the concentrator finite aperture. The device can then be illuminated with relatively narrow angular distributions. The lens produces higher angles which are then further concentrated by the non-imaging device. This combination results in shorter devices as compared to pure CPC type devices. The combination of a lens with a CHC is particularly attractive because the non-imaging device is placed between the lens and the lens focal plane, resulting in the most compact solution. In addition, both lens and CHC can be tailored in order to minimize aberrations and sometimes the combination can be adjusted so that the CHC can be approximated by a cone with straight sides [103].

It is also possible to "fill' the concentrator with solid dielectric material and replace the inner reflective surface by total internal reflection (TIR)[104]. This has the advantage of avoiding mirror losses since TIR is 100% effective. In addition, if the exit medium is made of the same dielectric material, Fresnel reflections at the output are avoided and the concentration ratio can be enhanced by a factor of n^2. The length of the resulting device can be slightly larger than hollow concentrators. The design of dielectric devices is subjected to the additional constraint that any ray striking the input face of the CPC at the maximum acceptance angle, in order to undergo TIR, should strike the inner wall at an angle equal or higher than the critical angle. It can be demonstrated that a standard CPC design will comply with the TIR requirement as long as the dielectric material has the adequate refractive index. The necessary refractive index will be determined by the specified acceptance angle. For acceptance angles between $0°$ and $90°$, the refractive indices will range from $\sqrt{2}$ to 2, which falls within the choice of available glasses. Using a value other than the ideal refractive index is also possible as long as the profile slope is modified to accommodate for TIR. A combination of a dielectric material with a curved entrance surface (a lens) was proposed where very compact and nearly ideal 3D concentrators were demonstrated [105].

All the non-imaging configurations discussed so far, for ideal concentrators, can be modified to implement θ_1/θ_2 transformers by simply introducing the additional constraint of keeping θ_2 from exceeding a specified value. Such a concentrator converts a limited-angle Lambertian distribution with maximum angle θ_1 into another limited-angle Lambertian distribution with maximum angle θ_2. Among many other applications, such a device can be particularly useful for fiber coupling. The combination of an ideal $\theta_1/90°$ concentrator with a second ideal $\theta_2/90°$ concentrator can be used to produce an ideal θ_1/θ_2 transformer, simply by disposing the two devices 'neck' to 'neck'. First a θ_1 distribution is transformed to a full Lambertian distribution by the $\theta_1/90°$ device. If the second concentrator is then used in a reverse fashion ($90°/\theta_2$), the full Lambertian output of the first device will be transformed in a θ_2 distribution by the second device. This design, however, has some

disadvantages. Physically, the transformer can be very long for small input and output angles; in addition, rays reaching the 'neck' of the device with large angles can undergo multiple reflections. Alternatively, one of the simplest versions for a transformer can be obtained by replacing part of the small end of a regular CPC by a cone with straight sides. The slope and length of this linear segment will determine the intended value for θ_2. Transformers can also be fabricated with dielectric materials in which case the critical angle constraint must be accounted for. In addition, possible Fresnel reflections at the interfaces should be considered. These dielectric devices can also incorporate lenses both at the entrance and exit apertures, resulting in very compact solutions. A 3D θ_1 / θ_2 configuration, in which a portion of a hyperbolic concentrator was combined with two lenses (positive lens at the input and a negative lens at the output), was demonstrated to be an ideal transformer with no loss of throughput if perfect lenses were used [98]. The practical implementation of this device using real lenses, however, will introduce deviations from ideal performance. Nevertheless, for high f# lenses, the system performance is nearly perfect. The configurations proposed are valid for 'hollow' devices as well as for dielectric devices. In both cases, for small input and output angles, the hyperbolic section can be approximated to a cone with straight sides with no significant loss of performance. This feature can greatly simplify the manufacture process of a practical device.

The practical use of non-imaging solutions has been reported in many fields. Solar energy collection is a particularly successful case where these devices have been demonstrated to outperform imaging optics by a factor of four [95]. Overall, it is not unusual for a non-imaging solution to obtain efficiencies increased by 50% to 150% over corresponding imaging optical systems, while remaining typically four to twelve times mores compact [106]. Although the differences in performance decrease as output angles get progressively smaller, in many cases non-imaging devices still provide more efficient and compact solutions. In some instances, like in illumination applications, they provide the only possible solution.

From the point of view of optical fiber applications the non-imaging devices just described have very appealing characteristics. Their use as multimode fiber-to-fiber couplers has already been demonstrated successfully [107]. By bonding the narrow tip of a θ_1 / θ_2 transformer to an optical fiber, the fiber output can be expanded and collimated. Two similar fibers can then be coupled with high efficiency by using the scheme depicted in Figure 2.32. Transformers with a hyperbolic profile and a lens shaped end were designed for this purpose. The devices were fabricated by injection molding, which is compatible with low cost mass production, and tested with multimode fibers with diameters ranging from $100\,\mu m - 400\,\mu m$. Coupling was demonstrated to have a high efficiency and a

greatly increased tolerance to lateral misalignment. The tolerance to tilting was less than that obtained with direct fiber coupling but still manageable; nevertheless, the design can be optimized to improve this feature. By using index matching fluid between the two transformers, to minimize Fresnel reflections, losses of $0.38\,dB$ were measured that were very close to the theoretical limit ($0.25\,dB$). Although some standard fiber couplers can present lower losses ($< 0.25\,dB$), these non-imaging devices have comparatively a lower cost, and are easier to manufacture and handle.

Source-to-fiber coupling is also a potential application for non-imaging devices. As previously discussed, a major source of difficulty arises from the highly divergent beam emitted by many light sources, which requires the use of optical elements with large numerical apertures. If the fiber tip is shaped as a non-imaging device with the narrow end facing the optical source, as shown schematically in Figure 2.32 (b), it is possible to increase its numerical aperture to unit. This way, it becomes theoretically possible to achieve a 100% coupling efficiency. To attain such performance, however, this configuration requires that the source emitting area should not exceed the area of the transformer tip. This constraint excludes the application of this scheme to most high brightness LEDs and other large area extended sources. Nevertheless, these devices could still be used with most lasers diodes and some LEDs. In such applications, maximization of the fiber numerical aperture indicates that this configuration could outperform direct butt coupling with standard fiber or even coupling with micro lenses.

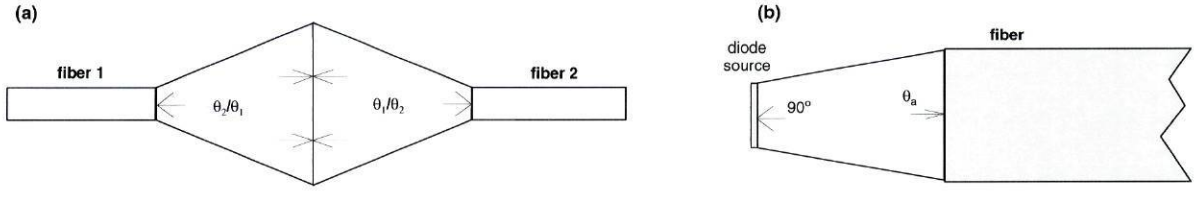


Figure 2.32 Conceptual designs of non-imaging devices for fiber-optic applications. (a) Fiber-to-fiber coupler; (b) Source-to-fiber coupler. Adapted from [98].

It was numerically demonstrated that a CPC shaped fiber tip would indeed have a maximum numerical aperture [108]. Shaping the fiber with a parabolic profile, however, can present some fabrication difficulties. Nevertheless, it was already discussed that, in some particular configurations, the shape of the concentrator can be approximated by a cone with straight sides, with little loss in performance. This means that tapering the fiber end to a conical shape can be sufficient to obtain a great increase in coupling efficiency. Indeed, the use of fiber tapers to couple light from small area sources has been demonstrated successfully and is presently used by many manufacturers to supply pigtailed sources. Presently, fibers with tapered ends, simple or with special AR coatings, and with

lens shaped tips, can be purchased by special order. In spite of all this, a rigorous CPC-type design, although it presents increased fabrication difficulties, may be required for optimal performance.

The same configuration used for coupling can, with adequate modification, also be useful when the fiber is intended to deliver a specified radiance pattern at its tip. For instance, in laser fiber optic contact surgical procedures, high irradiance levels are required at the fiber tip; in addition, light must be emitted uniformly over a wide angular range. A number of fiber tip configurations designed using non-imaging optics principles were proposed for laser surgery applications. It was shown that the modified CPC geometries presented a significant improvement in performance as compared to traditionally used tapered fibers, showing that in critical applications rigorous design of the tip geometry can be mandatory [109].

In the context of luminescence sensing applications, the use of non-imaging designs can also be a powerful tool to optimize the sensing head geometry. The increase of the sensing tip numerical aperture using CPC-type designs can dramatically improve the collection capacity of the luminescent signal. In fact, simply tapering the fiber end can greatly improve the sensor performance in this regard. The successful use of fiber tapers as sensing heads in luminescence applications has been reported by many authors [110]. Although this simpler approach provides satisfactory results in many instances, the use of rigorous CPC shaped fiber tips has a great potential, still to be explored, not only in increasing the light collecting capability of the sensing head but also in providing a controlled and more efficient delivery of the excitation radiation to the fluorophore.

In conclusion, although a great number of interesting solutions exists for coupling light into the optical fiber, most of them are most effective only when the emitting source area is smaller than the fiber core. For extensive lambertian sources, like LEDs, the best coupling efficiency is achieved by direct butt coupling. Therefore, improvement in the amount of light launched into the fiber can only be achieved with fibers with larger cores, increased numerical apertures, or by using sources with increased brightness.

2.5.3 Coupling light from an LED into a multimode fiber

In face of the critical importance of efficient coupling of light into the optical fiber system, some tests were performed using an LED and a multimode optical fiber, seeking an optimized configuration. In most applications explored in this work, a multimode silica fiber with core/cladding diameters of $550\,\mu m / 600\,\mu m$ was used in combination with a blue LED. The fiber had two additional coatings, over core and cladding: a thin hard cladding for extra physical strength with an approximate thickness of $30\,\mu m$, and a protective plastic buffer which made the total

diameter of the fiber $1\,mm$. According to the manufacturer specifications, the numerical aperture was 0.22. The transmission properties of this fiber, which has a very low OH content, were optimized for visible to near infrared transmission. This choice was made in order to minimize losses of the luminescence from the dyes used throughout this work, at visible to near-infrared wavelengths. Although this implied increased loss at the excitation wavelengths, for small fiber lengths the differences between this fiber and the UV to visible fiber (with high OH content) were not significant. The transmission spectra of both fibers can be compared in Figure 2.33.

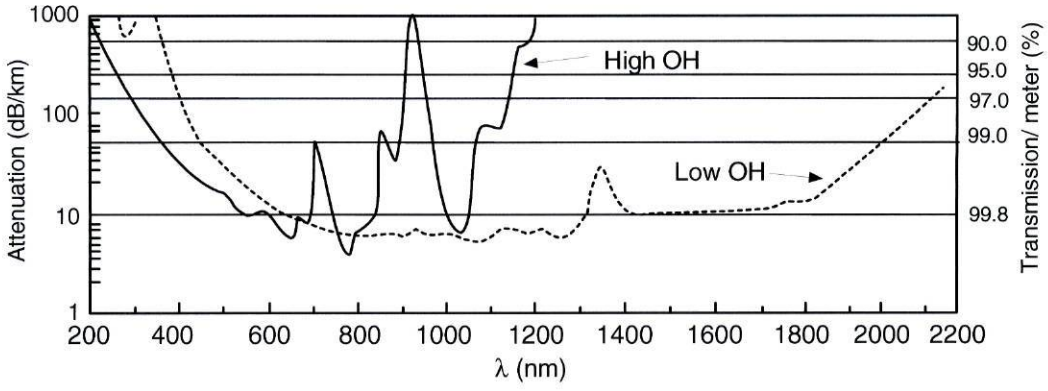


Figure 2.33 Transmission spectra of multimode optical fibers with different OH content. Taken from [75].

The optical source used in most experiments was a blue LED from Nichia (NSPB500S) with emission centered at $470\,nm$. The emitting semiconductor diode was housed in an acrylic lens-shaped dome with $5\,mm$ diameter. The measured divergence half-angle was approximately $15°$, which was according the manufacturer specifications. At the recommended operation current ($20\,mA$) the measured output optical power was of approximately $5\,mW$.

According to what was discussed earlier, about coupling light from an extended diffuse source whose dimensions exceed those of the fiber core, best results are achieved by direct butt coupling. However, due to the LED encapsulation, the emitting surface was not directly available to be placed in contact with the fiber core. This way, seeking to maximize the injection of LED radiation into the fiber system, different coupling configurations were tested using the optical elements available in the laboratory. Three different systems were used in which several configurations were tested. Figure 2.34 shows the basic setups used: (a) standard optics represented by microscope objectives; (b) miniature spherical ball lens; and (c) direct butt coupling. Although it is not apparent in the scheme, both fiber and optical source could be moved relatively to the lens system, or to each other, with micrometric precision in all three directions.

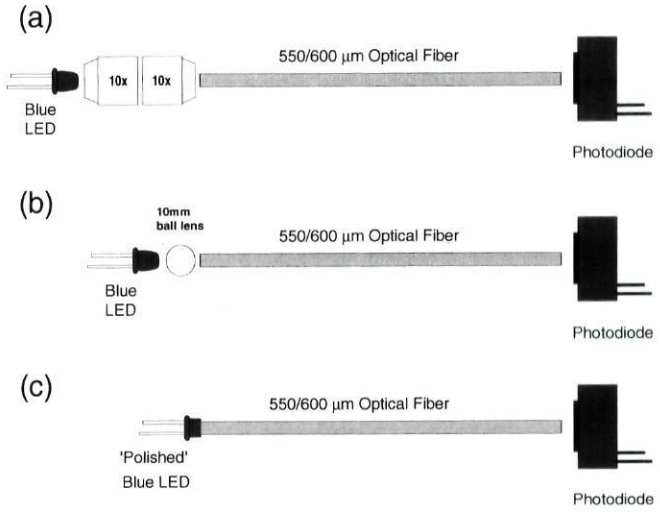


Figure 2.34 Schematic representation of the different coupling configurations tested. (a) Microscope objective; (b) ball lens; (c) direct butt coupling.

Two $10\times$ microscope objectives, with numerical apertures of 0.25, were used to collimate and focus the LED output in the fiber core. This collimating and focusing scheme is standard practice with laser diodes and single mode fibers and allows for more precise alignment. With this configuration an efficiency of approximately 2% was obtained. This very poor figure was mainly due to very high insertion losses of the lens system, which resulted from back reflections and from part of the LED radiation being blocked by the entrance pupil. After crossing the lens system, the measured optical power was reduced by 85% from the original LED output. Because the LED acrylic lens already provided a relatively low angular divergence, a single microscope objective was used to directly focus the source output into the fiber core. Due to a reduction in insertion loss (which now was $\sim 70\%$), this configuration presented an increased efficiency of approximately 3%. In addition to the very low efficiency, both configurations were very sensitive to the alignment of the fiber relatively to the focal plane.

Some spherical lenses (Tech Spec™ BK7-uncoated ball lens) were also tested. According to equation (2.98), and considering an input diameter $d = 5mm$, in order to match the numerical aperture of the fiber (0.22) the ball lens should have a diameter of $15mm$. However, the largest diameter available was $10mm$, which resulted in $NA = 0.33$. Using this lens, the system sensitivity to alignment was slightly more relaxed. In addition, the insertion loss was greatly reduced, as almost 90% of the LED output optical power could be detected after the lens. As a result, the coupling efficiency was increased to approximately 8%. A ball lens of $8mm$ diameter, theoretically having an increased numerical aperture (~ 0.4) was also tested. Nevertheless, very similar results were obtained in this case, indicating that the lens-fiber NA mismatch was not significantly impacting the

results. This was probably due to the fact that some of the radiation was being coupled into the fiber cladding, resulting in a higher apparent numerical aperture. The fiber lead was only $2\,m$ in length, which was not enough to completely loose radiation coupled into the cladding. In addition, because the fiber had a secondary hard clad, and an external plastic cladding, inducing losses by bending was not an easy task, specially in such a short length. This way, although some efforts were made to attenuate the cladding radiation, by bending the fiber, no effect was observable in the measured fiber output.

Theoretically, with an extended source the highest possible efficiency should be obtained with direct butt-coupling of the fiber to the LED surface. This configuration was also tested but the measured efficiency was very small in comparison with the previous schemes. With direct butt coupling only 1.2% of the radiation was launched into the optical fiber. However, taking into consideration that the LED acrylic housing acts as a lens, the present configuration cannot be considered a direct butt-coupling. Instead, the fiber is being coupled to an enlarged version of the semiconductor junction, imaged by the lens, and thus the efficiency is reduced. In order to perform true direct butt- coupling, the acrylic housing of the LED should be removed. The removal procedure was carried out by carefully polishing the LED surface with smooth sand paper. Using microscope observation the hard polishing was halted when the semiconductor junction was only $\sim 100\,\mu m$ away from the surface. The now flat LED surface was then polished to optical quality using progressively smoother fiber polishing paper.

At the end of this process the LED emitting surface could be clearly observed under the microscope. Figure 2.35 shows a scheme of the observed configuration. The main source of radiation was a square area with approximately $400\,\mu m$ side. In addition, a very bright ring-shaped area, having $900\,\mu m$ diameter and a few microns wide, could be observed as well. This radiation is originated from a reflector placed beneath the semiconductor junction that collects some of the downward emission.

It was numerically demonstrated that a CPC shaped fiber tip would indeed have a maximum numerical aperture [108]. Shaping the fiber with a parabolic profile, however, can present some fabrication difficulties. Nevertheless, it was already discussed that, in some particular configurations, the shape of the concentrator can be approximated by a cone with straight sides, with little loss in performance. This means that tapering the fiber end to a conical shape can be sufficient to obtain a great increase in coupling efficiency. Indeed, the use of fiber tapers to couple light from small area sources has been demonstrated successfully and is presently used by many manufacturers to supply pigtailed sources. Presently, fibers with tapered ends, simple or with special AR coatings, and with

lens shaped tips, can be purchased by special order. In spite of all this, a rigorous CPC-type design, although it presents increased fabrication difficulties, may be required for optimal performance.

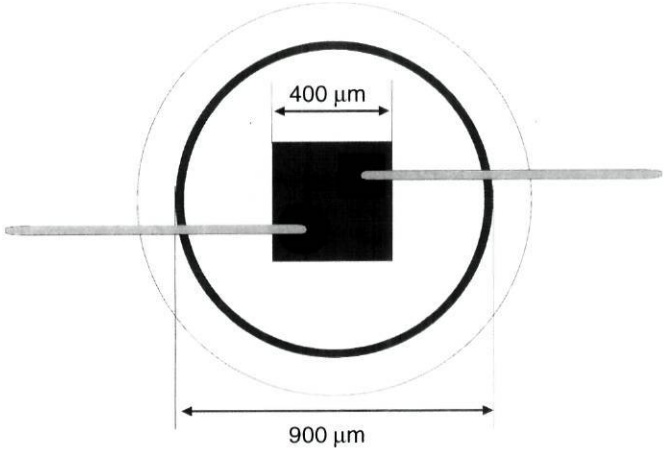


Figure 2.35 Representation of the LED emission area as observed with an optical microscope. The circular area arises from a reflector that is placed under the semiconductor junction to collect part of the radiation emitted backwards.

Because the acrylic lens was removed, the measured angular divergence increased to $45°$. In spite of this, direct but coupling resulted in a launching efficiency of approximately 8%. This result is very similar to what was previously obtained with the ball lenses. This indicates that, in principle, with the ball lens the semiconductor junction was being imaged in the plane of the fiber end. Because the emitting area is slightly bigger than the fiber core (although they differ in shape) no improvement was observed in comparison with direct butt coupling. Instead, the ball lens simply retrieved the efficiency of direct butt coupling.

Theoretically, due to the conservation of radiance, an improvement in the coupling efficiency using standard optics or non-imaging optics is not possible. The only way to improve the launching efficiency is to use a multimode fiber with increased numerical aperture or core radius. In fact, it was verified that using a fiber with a $1mm$ core, a launching efficiency of 20% could easily be obtained with direct butt coupling. A summary of the best results achieved is shown in Table 2-4.

The fiber core area and the LED emitting area differ by roughly 25%. According to equation (2.91), considering a numerical aperture of 0.22, and neglecting Fresnel losses, the direct butt coupling scheme should present a coupling efficiency of approximately 3%. However, the efficiency achieved in practice (8%) greatly exceeds the predicted value. As already mentioned, this is due to the fact that the apparent numerical aperture of the fiber for short lengths usually exceeds the equilibrium numerical aperture. Indeed, an efficiency of 8% indicates an apparent numerical aperture of 0.40. This value is in accordance with typical values of apparent NA of large core

multimode fibers. In addition, it explains the fact that very similar efficiencies were obtained with the $10\,mm$ and $8\,mm$ ball lens diameters (with NA of 0.3 and 0.4, respectively). This way, it is expected that for applications where the fiber length exceeds a few meters, the coupling efficiencies shall meet the predicted values.

Coupling system	Coupling efficiency	Alignment
Microscope	2.6 %	Very Sensitive
Ball Lens	8 %	Sensitive
Butt coupling 550 μm core fiber	8%	Straightforward
Butt coupling 1 mm core fiber	20%	Straightforward

Table 2-4 Power launching efficiencies of the different coupling schemes.

2.5.4 Sensor design

The combination of optical fiber technology with luminescence sensing techniques has great potential for the development of advanced analytical instruments, capable of remote monitoring of biochemical parameters with very high sensitivity, and able to operate in hazardous or sensitive environments with minimal intrusion. Once the intrinsic sensing mechanism is defined, it will determine the necessary spectral and electronic characteristics of the sensing system components. After these choices are made, the implementation of a successful application depends essentially on the careful design of the sensing scheme. Usually, the fiber has a double function, to transport light and to interact with the environment at some point. The fiber can be used to deliver the excitation radiation to the sensing site and/or to collect the luminescent emission back to detection. In addition, at the sensing site, the fiber tip or a small fiber segment interacts with the analyte, either by means of an external membrane which contains the sensing dye (extrinsic sensor) or by modification of the fiber structure to include the sensing chemistry (intrinsic sensor). In this context, sensor design can be roughly divided in two major stages: the definition of the sensing probe configuration, and the arrangement of the light guiding fiber system. The choices made in either of these steps are not independent and are usually determined by the specific application, considering the number of sensing points/parameters, the physical constraints, etc.. For instance, choosing between a transmission or reflection configuration will immediately limit the options of the possible sensing probe designs. A very large number of configurations and interesting solutions for optical fiber luminescence sensing have been reported in the literature. Nevertheless, a smaller number of

fundamental approaches can easily be identified which allow to understand more complex solutions and provide the basis for the creation of new arrangements. In the following sections an overview of the basic sensing configurations will be given, and the more relevant design issues will be addressed.

Sensing probe geometry

The implementation of practical sensing devices for the determination of biochemical parameters using luminescence methods requires, in most cases, the immobilization of a luminophore in a solid host. In an intrinsic configuration, in addition to containing the sensing dye, the resulting membrane needs to be bonded to the fiber surface. If, on the other hand, the membrane is independent from the fiber, the resulting configuration is called extrinsic. Each of these alternatives has its own merits and drawbacks. In intrinsic configurations the fiber itself becomes the sensor, providing the most compact solutions. For this to be achieved, however, the support matrix has to fulfill the extra requirement of having good adhesion to the fiber surface. Moreover, eventual substitution of the sensing head is somewhat hindered. Extrinsic membranes, on the other hand, are easily substituted and are more compatible with mass production. For these reasons, they are more suitable to be used as disposable sensing probes. However, the construction of a compact solution becomes more difficult since some sort of physical envelope must be added in order to support the sensing membrane, keeping it coupled to the fiber tip, without interfering with the sensing process.

In the simplest configuration of a luminescence sensing head, the distal fiber tip is used as a single point probe of the surrounding environment. The excitation light is guided to the fiber tip where the sensing chemistry is either immobilized on the flat end surface, or attached to it in an external membrane. The luminescent signal emitted by the transducer chemistry is collected and guided back to detection by the same fiber. This configuration provides the most compact and miniaturized solutions. However, it comprises some important restrictions. The volume of the sensing sample is usually very small, particularly in the intrinsic configurations, and is limited by the size of the fiber core. For this reason, the collected luminescent signals can be very weak. In order to overcome this limitation, large core multimode fibers must frequently be used. Such fibers are widely available, but they are generally more expensive than standard fibers (except for some plastic fibers). In addition, other accessories like fiber couplers and connectors are usually obtainable but can be much more expensive for non-standard fiber. Nevertheless, usually short fiber lengths are needed. In addition, their larger light collecting capability frequently results in less expensive systems with better performance. This way, around 70% of the reported sensing applications use large core

multimode fibers. Still, in situations where the use of smaller core fibers is advantageous or even mandatory, measurements can be performed even through single mode fibers, at the expense of using laser sources in combination with very sensitive and expensive detection instrumentation. This way, single mode fibers are used in about 5% of sensor applications. The remaining 25% corresponds to applications where planar waveguide sensing structures are used [74].

A variety of reported applications can be found where instead of one fiber, two or more fibers, or even fiber bundles, are used to separately illuminate and collect the luminescence. These solutions can be very practical for some applications, and are particularly suited for multi analyte interrogation; however, they usually add to the complexity, cost and physical dimensions of the sensing probe. Ultimately, constraints associated with each specific application, like size of the sensing sample or required spatial resolution, will determine the optimal sensing head configuration [78, 111].

Increasing the optical power of the excitation source can, to some extent, improve the luminescence output. However, increased excitation levels have the downside of accelerating the photodegradation of the sensing dye, limiting the useful life of the sensor. Because the sensing area is so small, very high energy densities can be attained, even with moderate optical powers, and photobleaching can be a serious problem. In practice, a compromise must be established considering the luminescent signal level and the luminophore photostability.

Although coating the flat fiber tip is a simple procedure, the resulting sensing probe is usually not very robust and can suffer mechanical damage. Additional protective coating can be added but care has to be taken in order not to interfere with the sensor sensitivity and response time. An alternative providing some mechanical protection is to place the sensing membrane inside of a micro-chamber produced at the fiber tip by chemical etching [112]. Filling such a chamber with a doped polymer or sol-gel solution, however, can be a challenging procedure. Generally, dip coating produces good quality thin films on the fiber lateral walls; at the flat tip, however, it can be very tricky to obtain films with constant thickness. As an alternative, the fiber tip can be sprayed using an air-brush. When using external membranes this problem is not as serious, films can be produced by either spin coating or dip coating on flat substrates and usually good quality reproducible results can be obtained.

Two examples of the distal tip configuration using large core fibers can be seen in Figure 2.36 (a) and (b). Figure (a) shows a silica fiber with a $440\,\mu m$ core diameter, with a sol-gel sensing layer ($100\,\mu m$ thickness) bonded to its end-face. The sol-gel film was doped with a luminescent ceramic material (Cu-ZSM-5), which was used to measure gaseous oxygen, through luminescence quenching,

in a high temperature gas stream [113]. Figure (b), on the other hand, shows the scheme of an extrinsic configuration where a $250\,\mu m$ core plastic fiber was used to interrogate a pH sensitive external membrane. The sensing medium consists of polyacrylamide microspheres which contain a covalently bonded pH indicator, was attached to the fiber tip using a cellulose dialysis tube. This sensor configuration was effectively used to determine blood acidity in different *in vivo* applications [13].

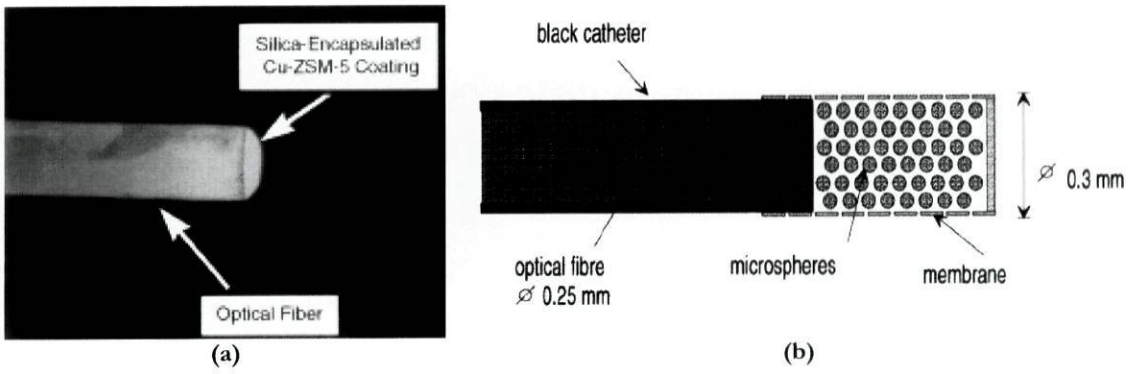


Figure 2.36 Examples of single point fiber tip design. (a) Intrinsic configuration for gas sensing at high temperatures. A luminescent ceramic material (Cu-ZSM-5) is immobilized on the tip of a silica fiber by the sol-gel process [113]. (b) Extrinsic configuration for blood pH determination. An acid-base indicator is covalently bonded to polyacrylamide microspheres which are contained in a dialysis tubing coupled to the tip of a plastic fiber [13].

Independently of the specific applications, the strict comparison of both geometries clearly shows that the intrinsic approach is indeed much simpler in design. Nevertheless, although it involves a stronger engineering effort, the extrinsic configuration is more versatile and could be used successfully in most demanding *in vivo* applications, where biocompatibility imposes extra requirements. In spite of all this, in many instances intrinsic fiber probes provide unique solutions and a great deal of the research effort is presently applied to the improvement of their design.

A representative example, where intrinsic probes are desirable, is the measurement of biochemical parameters with high spatial resolution in biological and environmental samples. Knowledge of the microscale distribution of these parameters is of great importance to understand the function and regulation of living systems. In this particular field, small diameter ($< 100\,\mu m$) intrinsic fiber tips provide a unique solution and a simpler alternative to presently used microelectrode sensors. Such optical sensing heads are sometimes called micro-optrodes. Usually the micro-optrode is fabricated by tapering the fiber tip to the desired diameter. Typically, fiber tip diameters in the range of $5\,\mu m - 10\,\mu m$ are able to provide the necessary spatial resolution while performing the measurement without perturbing the biological system. Core diameters varying from

$300\,\mu m$ or higher down to standard multimode fibers ($50\,\mu m$) can be used. Some applications using single mode fibers were also reported. Graded index fibers, $100\,\mu m / 140\,\mu m$, are a popular choice since they allow for relatively high coupling efficiencies even when LEDs are used as excitation sources.

The details of a sensing head using this particular fiber can be seen in Figure 2.37. Tapering of the fiber tip was performed by placing it under a micro-torch while mechanical tension was applied. The final diameter of the fiber tip could be controlled by changing the temperature of the torch or by adjusting the applied tension. The micro-optrode was then produced by coating the tip of the resulting fiber taper with an ormosil sol-gel glass doped with an oxygen sensitive ruthenium complex [68]. The coated fiber tips were fixed in a glass capillary for increased mechanical robustness and for better handling during the measurements. This reminds that, as the sensing scheme steps out of the lab and approaches practical applications, even intrinsic sensing configurations require some degree of engineering. Besides providing an increased spatial resolution, fiber tapering was also found to favor the collection of the luminescent signal. Because fiber tapers approach the profile of some non-imaging devices, the numerical aperture of the fiber probe is increased.

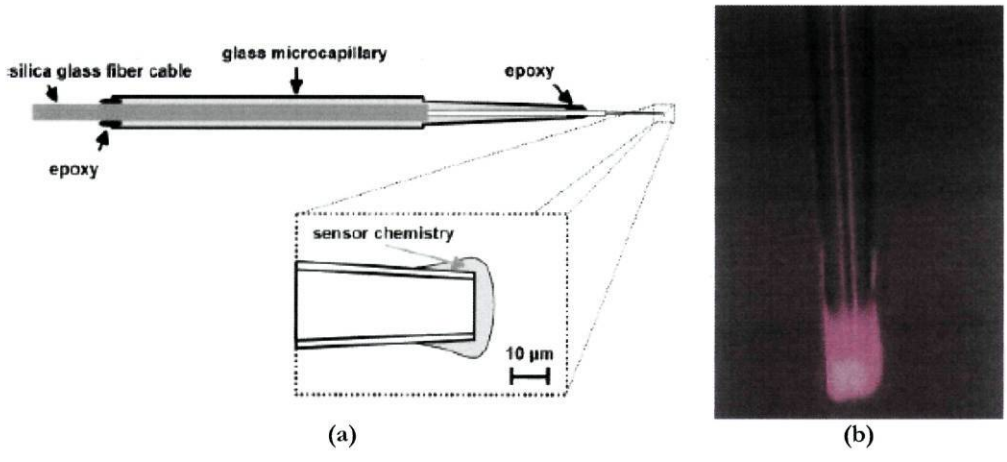


Figure 2.37 Example of micro-optrode using a tapered fiber configuration [68]. (a) Scheme of the sensing head; (b) picture of the luminescent tapered fiber ($20\,\mu m$ at the tip).

Nanometer sized sensing tips were also reported using tapered single mode fibers. In this case the fiber was used to illuminate a pH sensitive dye immobilized at the fiber tip. Detection of the luminescent emission was performed by collecting the radiation directly at the sensing site. This configuration was shown to be compatible with intracellular measurements [114, 115].

Other techniques can be used for reshaping the fiber tip. The heat and pulling method can be applied using alternative energy sources, like a CO_2 laser or an electric arc. Chemical etching is also a very popular technique which is often used to fabricate fiber tips with special profiles for near field

microscopy applications. Typically, a solution of hydrofluoric acid (HF) is used as the etching agent. The fiber profile can then be defined by selective etching (core and cladding usually have different etching rates) and by controlled immersion in the acid solution. If a length of fiber is gradually introduced into the acid, the fiber tip will remain in the etching solution for a longer period of time than the rest of the fiber length, which, therefore, acquires a tapered shape. By controlling the immersion rate and the fiber length, the slope of the fiber walls can be specified [116, 117].

While thermal techniques tend to preserve the core/cladding refractive index distribution, chemical methods completely remove the fiber cladding. For this reason chemical etching is the preferred method to design sensing heads based on evanescent wave detection. If the fiber cladding is partially or totally removed, the excitation radiation will interact with the external medium through the evanescent field. Because the penetration depth of the evanescent wave is roughly one wavelength, only a very thin slice of the external medium is probed, thus preventing the detection of background luminescence. A prototypical evanescent-wave tip configuration for use in immunoassays is represented in Figure 2.38 (a) where recognition antibodies were immobilized on the surface of the bare fiber core. These antibodies bind to fluorophore-labeled antigens keeping them in the range of the evanescent wave and enabling their selective excitation. I.e., because of the limited scope of the evanescent excitation, only those fluorophores bound to the fiber surface are excited. The fiber end-face is usually covered with an absorbing coating, in order avoid direct excitation of the luminophores in the solution, ensuring that only evanescent excitation takes place.

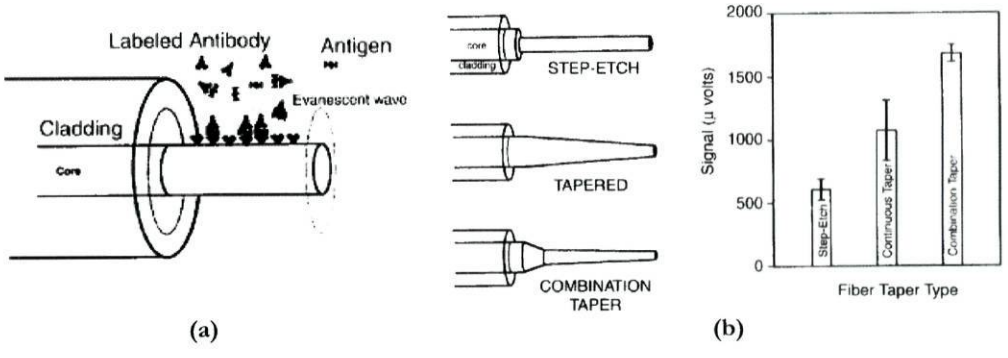


Figure 2.38 Prototypical evanescent wave configurations. (a) Recognition antibodies are bound to the bare core surface. A luminescent signal is obtained only when the fluorophore-labeled antigens are bound to the fiber surface. (b) Different geometries for the evanescent tip configuration and corresponding luminescence collection efficiencies [118].

Unfortunately, the collection efficiency of the luminescent signal can be very small in evanescent configurations, limiting the potential of this technique. In the absence of the original cladding, the biological solution acts as a cladding of much lower refractive index; as a result, the

unclad section of the fiber propagates a higher number of modes than the original fiber. Because part of the luminescent signal is coupled into these extra modes, which will not propagate into the clad fiber, loss is introduced. To make things worse, typically the luminescent signal is preferentially coupled into these higher order modes. The weak coupling can be partially compensated by extending the length of etched fiber. For practical reasons, however, the length of the sensing tip should not exceed a few centimeters. Some modifications of the shape of the bare fiber core can decrease the modal mismatch. Anderson et. al [110, 118] showed that reducing the diameter of the unclad region, in a step etch fashion, can reduce the number of propagating modes, which can eventually match that of the fiber, improving the collection of the luminescence signal. In doing so, however, the loss of the excitation optical power at the transition point (from intact fiber to etched fiber) increased significantly. This way, more radiation was directly coupled to the solution increasing the background luminescence. The authors showed that with a smoother transition, obtained by tapering the fiber tip, total internal reflection could be maintained while still reducing modal mismatch. Figure 2.38 (b) shows the three geometries proposed by the authors, step-etched, continuous taper and combined taper; in all three the etched fiber length was the same ($12\,cm$). Their respective collection efficiencies are also presented. The two stage taper was shown to establish the best compromise between modal matching and total internal reflection, presenting an almost three fold improvement over the step-etched configuration.

Other examples can be found in the literature where the unclad fiber tip is coated with a thin membrane containing a sensitive dye. MacCraith et. al [33] demonstrated an evanescent fiber tip configuration for determination of gaseous oxygen. In this example the unclad fiber tip was dip coated with a sol-gel solution, doped with a ruthenium complex. By this process, after drying, the evanescent tip was coated with a permeable porous-glass thin film with luminescent properties and with a thickness of $300\,nm$. In order to avoid direct excitation of the sensing film at the fiber tip, the fiber end-face was covered with an absorbing material prior to the coating process. Measurements of the oxygen concentration, based on quenching of the luminescence of the sensing membrane, were successfully performed. A similar scheme was used to demonstrate a pH sensor using a plastic optical fiber and a sol-gel coating [119].

A particularly attractive feature of these evanescent configurations, in comparison with the simple tip probe, is their greater versatility in controlling sensitivity determining parameters such as the length, the thickness, and the refractive index of the sensing film. The latter is particularly important because adjusting the coating to an adequate refractive index can significantly reduce mode mismatch problems. Furthermore, due to the enlarged area of the sensing film,

photobleaching problems are greatly reduced. It is also worth of mention that, with dip coating, high quality reproducible thin films can be produced on the lateral walls of the fiber.

From the previous examples it becomes clear that, in general, fiber tapering introduces improvement in the sensing head performance. By coating the fiber taper with an adequate sensing membrane, these configurations can be used to implement virtually any luminescence based chemical sensor. Advantages can be taken from the control of the refractive index of the sensing film which can be used to improve guiding and reduce mode mismatch. With adequate design a coated fiber taper can provide an enlarged sensing area and more efficient excitation and collection of the luminescent signal, introducing a significant improvement in sensor performance. Thinner films can be used which translates into much faster response times. Although several authors have presented sensing configurations using tapered fibers, there is still room for further improvements. In particular, knowledge of principles of non-imaging optics can be of great usefulness in designing fiber tips with very specific properties. In addition, the study of glass substrates coated with luminescent thin films showed that, under certain conditions, the emission of luminescence into the substrate can be strongly anisotropic [120]. This way, coated fiber tapers can present coupling improvements that exceed what would be expected strictly from ray optics. If these radiation distributions are taken into consideration when designing the fiber profile, increased performance can be obtained.

All the geometries described so far were single point probes on the distal end of the fiber. Because the luminescent signal propagates backward through the same path of the excitation radiation, these can be classified as reflective type configurations. Such configurations provide the most compact and elegant solutions for single probe measurements. However, transmission or in-line configurations, more suitable for multipoint measurements using a single fiber, are also possible [121]. In these cases the luminescent sensing probe is a small fiber segment located somewhere along the fiber. The most typical transmission design uses an evanescent configuration, where the cladding of a length of fiber is removed and substituted by a sensing membrane. Alternatively, the core of a fiber segment can be substituted by a dye doped sensitive core section. This is often called an interrupted fiber configuration. Each of these schemes has its strengths and pitfalls.

The properties of the evanescent transmission configuration are very similar to those discussed previously for the evanescent reflection probes. The major difference lies in the fact that forward propagating luminescence is usually detected instead. As a result, stronger efforts have to be applied in order to properly separate the excitation and luminescence signals at the detection stage. Nevertheless, and upon excitation, equal parts of luminescent power will propagate in both

directions. This way, detection can also be performed in a reflection configuration. Using this method, excitation and detection can be performed at the same location and the need for a 'closed loop' configuration is avoided. The fabrication of in-line sensing probes is usually a more complicated process as compared to that of tip configurations. This is due to the fact that removal of the cladding must be performed at some point along the fiber and not at the fiber tip.

Single mode fibers usually carry a significant amount of the guided optical power in the fiber cladding. For this reason, they are particularly suited for evanescent sensing configurations. However, partial removal of their cladding results in very fragile sensing probes. Multimode fibers, on the other hand, usually have small evanescent fields. Nevertheless, due to the increased core radius and numerical aperture, they provide superior mechanical strength and improved signal to noise ratios. Furthermore, the fraction of power in the evanescent field can be greatly enhanced by tapering the optical fiber. Tapering of the fiber can be performed by chemical etching or by the heating and pulling method. For transmission tapers the latter method is much easier to implement. In either case, in order to allow the luminescent signal of the sensing membrane to be guided by the fiber, removal of the cladding is a necessary step.

Some authors demonstrated that a significant amount of the evanescent field still penetrates the outer medium when the fiber taper is made without cladding removal [122]. Besides being much easier to fabricate, the resulting device has enhanced mechanical stability and is, therefore, easier to handle. Such configuration, however, is only adequate for absorption measurements, since the presence of the cladding could prevent efficient coupling of the luminescent signal. Nevertheless, Villatoro et. all presented some interesting results regarding the geometry of a cladded taper that could be interesting for luminescence based applications [123]. These authors showed that the sensor sensitivity could be improved by extending the taper waist with a constant diameter region. Figure 2.39 (a) shows an example of a taper with an uniform waist of length L_0. The authors measured absorption spectra by submerging the taper in an absorbing liquid. With this scheme they demonstrated that the uniform waist region of the fiber taper was the main responsible for its sensitivity and that the sensor dynamic range could be controlled by adjusting the taper diameter. Although this was an absorbing configuration, it could be applied to luminescence sensing provided that the cladding of the uniform waist was removed and replaced by a luminescent sensing membrane. This shows that geometrical variations of the taper shape provide a way to control the sensor characteristics.

An alternative to the evanescent transmission configuration can be implemented by substitution of a segment of the fiber core by an active core made of porous glass and containing the

sensing dye. Unlike the evanescent configuration where only a small fraction of the guided excitation power interacts with the luminophore, in the interrupted fiber configuration almost all the guided light interacts with the sensing material. It can be shown that, for the same fiber length, the interaction path length of the interrupted fiber configuration is several thousand times higher than for the evanescent configuration (where the interaction path length is given by the penetration depth times the number of reflections). This way, the sensitivity can be greatly enhanced by using active fiber cores. A schematic representation of an interrupted fiber configuration is shown in Figure 2.39 (b).

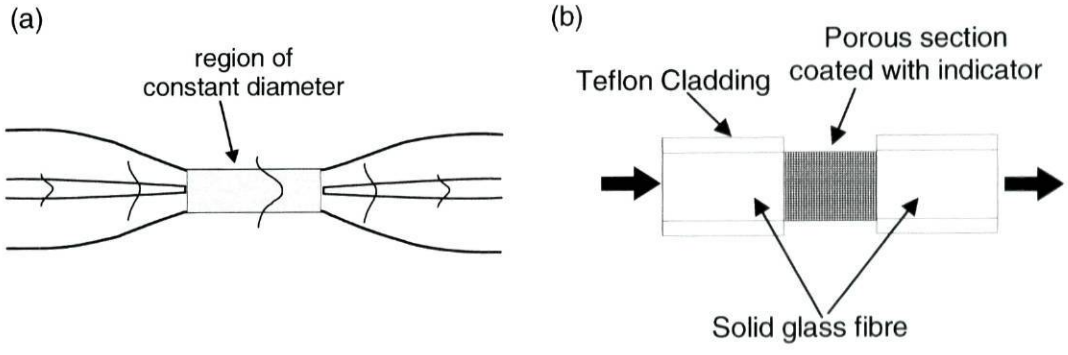


Figure 2.39 Transmission type sensing probe configurations. (a) Evanescent type with tapered fiber [123]; (b) interrupted fiber type with porous glass active core [124].

Besides containing the sensing chemistry, however, the active core should also interact with the surrounding environment, being permeable to the analyte. Such characteristics usually demand for a porous structure. Quan Zhou et. al [125], reported for the first time the fabrication of a porous fiber structure suitable for implementing interrupted fiber sensing configurations. For this purpose, the authors used high-transparency alkali borosilicate glass optical fibers with diameters ranging from $150\,\mu m - 300\,\mu m$. In order to produce the porous core, a small section of the fiber $(0.5\,cm)$ was phase separated by heat treatment at about $500^{\circ}C$, one phase being an alkali borate rich phase, another being a silica rich phase. The soluble alkali borate phase was leached away with a suitable acid solution to leave a silica rich porous skeleton. The resulting porous core was then impregnated with humidity sensitive dye by immersion in a cobalt chloride solution followed by drying. Humidity measurements were then successfully performed by absorption spectroscopy. These results established a new sensing configuration which can be used either for absorption or luminescence applications, simply by changing the sensing dye properties. The major source of loss was scattering at the porous structure. Because porosity will determine the sensor sensitivity, which depends on the analyte diffusion, a compromise must be established between permeability and induced loss.

Nevertheless, the measured loss was relatively small ($0.7\,dB/cm$) considering the small length of the sensing sections.

More recently, the fabrication of a porous glass fiber using the sol-gel technique was reported. The porosity of sol-gel glass can be tailored to meet the specific needs of the sensor. In addition, the low processing temperatures allow for the sensing dye to be incorporated during the fabrication process, resulting in more efficient encapsulation as compared to impregnation, more resistant to leaching. Introducing the sol-gel solution into a tube with adequate diameter, a porous glass sensing fiber with a diameter of $390\,\mu m$ could be obtained after gelation and drying. A segment with $0.2\,cm$ was glued with epoxy between two multimode silica fibers with $300\,\mu m$ diameter. The authors only presented a very rough estimate of the fiber transmission properties, which nevertheless showed to be adequate for visible and infrared applications. Furthermore, due to the versatility of the sol-gel process, it is possible to fine tune the glass spectral properties. In this particular application, major losses were introduced by the core diameter mismatch. This problem, however, can by easily solved by fine tuning the fibers diameter [126].

Plastic fibers are particularly suited to implement in-line configurations, either evanescent or interrupted fiber. With a silica core/plastic cladding fiber, for instance, cladding removal is much easier than with all-silica fibers. In addition, due to the low processing temperatures, doping of the core or cladding with a luminescent dye can be easily implemented during the fabrication process. Consequently, using this method, much longer fiber lengths can be easily doped. Such luminescent fibers can then be used to implement a truly distributed sensor [61].

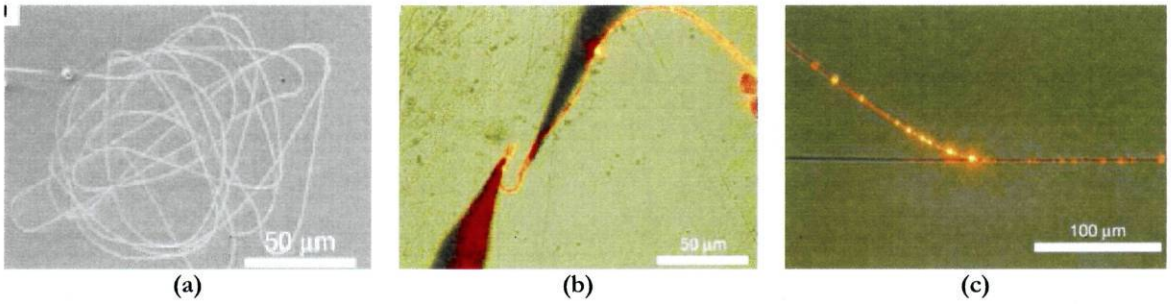
The configurations described so far are representative examples of the main tendencies in fiber probe design. Most of these configurations have been tested in many different ways, and besides being used in many proof-of-principle laboratory demonstrations, they are actually used as tools by many scientists. Some were also incorporated in advanced prototypes capable of field measurements and even in commercial products [10]. In addition to these fundamental examples, many exploratory variations can be found in the literature. The potential of a variety of non-conventional fibers is being explored [76]. For instance, D-shaped fibers with the core near the flat fiber surface have very suitable characteristics for evanescent sensing. Fibers with special refractive index profile to improve evanescent coupling have also been fabricated [127]. The use of standard single mode fibers is also little explored, mainly due to some of the difficulties discussed previously. A wide variety of fiber devices, like fiber Bragg gratings, tunable filters, optical circulators, etc., is available for this type of fiber, which has a tremendous potential for luminescent sensing applications. Surely the great advances verified in semiconductor laser sources, along with the

production of highly photostable luminescent sensing dyes, will contribute to a wider use of single mode technology. Also, new fiber technologies are arising with enormous potential for luminescence sensing application. Such is the case of photonic crystal fibers which were described in a previous section. Their holey structure has very promising characteristics for being used as a micro-chamber where sensing takes place. Although some proof-of-principle examples of sensing applications can already be found in the literature, their potential is just starting to unveil.

Another exciting example which promises to reveal totally new sensing configurations is the recent demonstration of light guiding nano-wires with low loss ($0.1 dB/mm$). Silica nano-wires with sub-wavelength diameters were produced by carefully drawing a fiber heated by a flame with closely controlled temperature. The stabilization of the flame temperature was critical for the production of good quality waveguides. By this method, wires with diameters as low as $50 nm$ and lengths of several millimeters were produced with very smooth walls and with almost constant diameter. The resulting wires were easily manipulated without breaking, presenting surprising mechanical properties [128]. Figure 2.40 (a) shows a $260 nm$ diameter silica wire with approximately $4 mm$ length coiled in a random manner. They could be bent to a very tight radius of a few microns without breaking. In addition, because of the large index contrast between silica and air, silica nano-wires can be bent sharply without introducing significant bending losses. Simulated data showed that a bending loss of less than $0.3 dB$ would be obtained for a $90°$ turn with a bending radius of $5 \mu m$ in an air-clad $450 nm$ diameter silica wire (for light of $633 nm$ wavelength). This feature provides nano-wires with a great potential for applications with very limited space. Figure 2.40 (b) shows light traveling trough a very sharp bend ($5.6 \mu m$) in a $510 nm$ diameter silica wire with no apparent major loss.

As their diameter is reduced, the amount of power traveling in the evanescent field greatly increases. This way, evanescent coupling can be easily performed between different nano-wires (Figure 2.40 (c)). Furthermore, their evanescent distribution greatly increases the sensitivity to the external medium, making them very suitable for sensing applications.

Although, so far, no sensing devices using this technology have been reported, it is easy to imagine that the interesting guiding and mechanical properties of silica nano-wires will allow to implement totally new sensing configurations.



(a) (b) (c)

Figure 2.40 Silica nano-wires with sub-wavelength diameters were successfully fabricated, and present low losses and surprising mechanical properties. (a) A coiled $260\,nm$ diameter silica wire with a total length of about $4\,mm$. (b) 633-nm light traveling through a sharp bend with a radius of $5.6\,\mu m$ in a $510\,nm$ diameter silica wire. (c) A $390\,nm$ diameter taper coupling light into a $450\,nm$ diameter silica wire [128].

Sensor topology

In addition to the definition of the design of the sensing probes, the configuration of the light guiding fiber system is also of critical importance for sensor performance. A schematic representation of the basic arrangements is shown in Figure 2.41. The simplest possible configuration involves a single fiber to deliver the excitation and collect the luminescent signal. Single fiber design (Figure 2.41 (a)) can be implemented with reflection or transmission configurations involving tip or in-line fiber probes. In either case, some scheme has to be implemented in order to provide discrimination between the luminescent signal and the excitation optical power. Although this task can be fairly simple in a transmission design, where an absorbing filter with adequate cut-off can eliminate the remaining power of the excitation signal, it greatly complicates reflection type configurations. Usually bulk optics elements like filters, dichroic mirrors, or diffractive elements must be used for this purpose. The set-up can get quite complex as signal separation must be performed without interfering with proper coupling of light into the fiber system. In general, for compact sensing applications, the use of bulk optics should be avoided as it involves additional alignment requirements, which usually result in increased signal loss and greatly hinder mechanical stability and miniaturization. Nevertheless, such systems are very versatile and can be adapted to a variety of sensing purposes. For this reason they are typically used in laboratory environments.

The use of separate fibers for excitation and detection is also a possibility (Figure 2.41 (b)). Although this can greatly simplify some aspects of design (it becomes much easier to separate excitation from emission, and allows tailoring each fiber for a specific wavelength), it also introduces some important drawbacks. The receiving fiber can easily collect scattered excitation radiation, it excludes the use of evanescent configurations, and it complicates the design of a compact sensing

head. Usually it implies the use of external membranes or, alternatively, the membrane must be bonded to the two fibers. In either case, it is difficult to ensure that the excited sample volume is the same that the receiving fiber is capable of viewing. This usually involves careful alignment procedures at the distal fiber end which can become quite unpractical. This way, although many examples can be found using such configuration, single fiber designs are more popular for practical applications. Nevertheless, with careful design this arrangement can ensure a better rejection of background noise and stray excitation radiation, and can provide a good solution when these factors are critical. This way, assemblies with two different fibers, bonded side by side in one end and separated at the other end, can be purchased from different dealers, being provided with protective coatings and standard connectors [111].

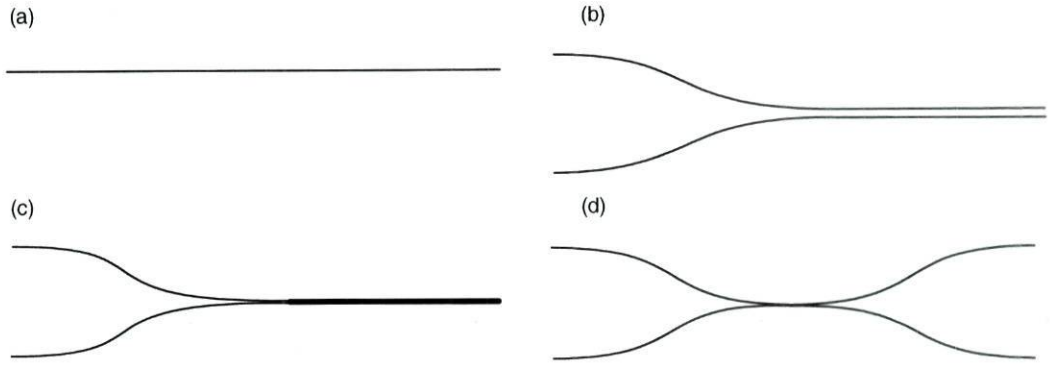


Figure 2.41 Different schemes for sensor excitation/interrogation. (a) single fiber; (b) separate excitation and detection fibers; (c) Y splitter; (d) 2×2 **fiber coupler.**

In reflection type configurations, the use of fiber devices like Y splitters and fiber couplers can provide very practical solutions. With these devices it is possible to use a single fiber at the sensing site while still employing different fibers for excitation and detection. The separation of optical paths is made in the fiber device, avoiding the use of complex bulk optics schemes (Figure 2.41 (c) and (d)). These devices are widely used in practical applications as they are suited for designing very compact systems. Y splitters are typically made of three distinct fibers: an input and an output fiber with the same diameter are bonded at one end with a third fiber, which can have the same or a larger diameter and leads to the sensing tip. In spite of the design advantages this configuration implies some power loss at the fiber junction which depends on the relative fiber diameters. Nevertheless, the system design is greatly simplified, alignment requirements are reduced and mechanical stability is enhanced. The Y configuration can also be implemented with optical fiber bundles, in which case the excitation and collection optical paths can be fully separated. This way, Y splitters are presently very popular and are commercially available. Different dealers provide these fiber devices in a wide

variety of fiber types, with appropriate protective coatings and with standard connectors which allow them to be incorporated in more complex fiber systems [11].

Fiber couplers are very similar to Y splitters, the main difference arising from the mechanism by which the optical power is shared by the different fibers. In addition, while a 2×2 configuration is more typical (see Figure 2.41 (d)), any $n \times m$ configuration is possible in principle. Fiber couplers can be fabricated by different methods. Using the technique that produces the best results, two or more fibers are fused together along part of their lengths, in order to allow an exchange of optical power between the fiber cores. By adjusting the processing parameters, the coupling ratio can be controlled. A $50/50$ power split is the most common configuration. With such device, the excitation optical power injected in one of the fiber inputs will by split in half, with each output fiber receiving 50% of the optical power. By reciprocity, only 50% of the optical power emitted at the sensing probe tip will reach the detection fiber. In spite of the losses introduced, fiber couplers provide a way to design very compact and robust systems. In addition, the extra output fiber gives these devices greater versatility than Y splitters. The second output fiber can be used to provide a reference channel that partially compensates for optical power drift. Alternatively, a second sensor, which can, for instance, provide temperature measurements, can be connected to this fiber. Perhaps the most important advantage of this extra output is the possibility it gives to design more complex fiber systems, with multiple sensors or even sources and detectors. Fiber couplers are widely used in the telecom field where they are an essential element in practically any fiber system. Presently couplers using different kinds of large core multimode fibers can also be obtained, and are extensively used for sensing applications. In most cases their cost is still much higher than that of standard components. Nevertheless, this is partially due to the small market and prices will surely go down as the chemical sensing industry starts to develop.

The sensing probe geometries and layouts just discussed are the building blocks from which more complex multipoint systems can be implemented.

Multiplexing and multiparameter sensors

In many applications involving living organisms or complex ecosystems it is often necessary to perform the real time determination of different biochemical parameters at multiple sites. The association of optical fiber technology with luminescence sensing techniques has great potential for the implementation of such multiplexed sensing systems. The fiber multiplexing capabilities have been thoroughly and successfully explored both in telecom and physical sensing applications [70]. The implementation of similar systems for chemical sensors, however, faces some additional

challenges. Nevertheless, many of the classical techniques and architectures can be applied in this field. Figure 2.42 show examples of four basic multiplexing schemes that could be used for chemical sensing.

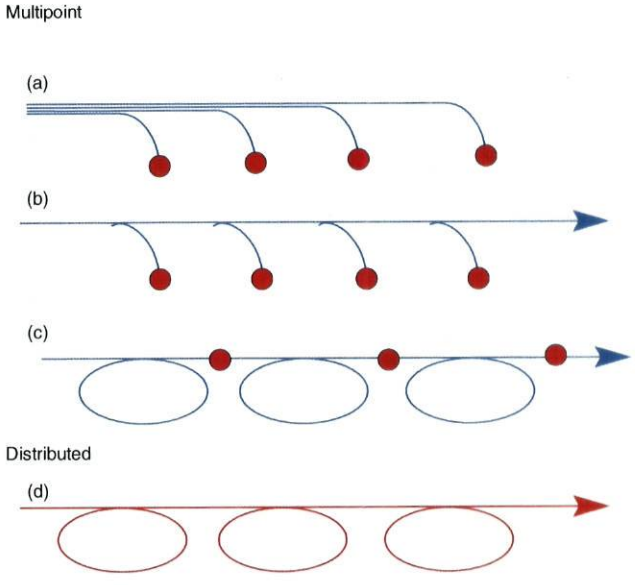


Figure 2.42 Examples of multiplexed sensing architectures. (a) Star, multiple fibers connected to a central unit; (b) tree, multiple sensing fibers branch from a central 'trunk' fiber; (c) Line, multiple sensing points are embedded along a single fiber; (d) distributed.

In the basic star topology, shown in Figure 2.42 (a), multiple fibers, usually one per sensing point, converge in a common processing unit. With this scheme any single point sensor can be used without any extra requirement. Instead, all the complexity is laid in the processing unit. For this reason this scheme can be easily applied to luminescence fiber sensors. Excitation and detection of multiple sensing signals can either be performed using multiple excitation sources and/or detectors or, in alternative, some switching system must be implemented. Main disadvantages of this scheme arise from increased cost and complexity due to the larger number of optoelectronic components and the fiber length used. In addition, depending on the mechanism by which the individual sensors are discriminated, the system addressing time can hinder fast response times. On the other hand, all the complexity is packed in a single processing unit, making this system very practical. Individual sensors can be easily substituted and their distribution in the sensing environment can be rearranged with no danger of mutual interference. Many examples can be found in the literature where a star configuration was used to interrogate arrays of luminescent sensors [129, 130].

If a common fiber is used to perform excitation and collection of luminescence from individual sensors located in secondary fiber branches, a tree architecture can be implemented similar to the one depicted in Figure 2.42 (b). Connection of the sensing fibers to the main fiber can

be done using 2×2 couplers. With this scheme multiple fiber tip probes can be interrogated through a single fiber [112]. If in-line fiber probes are used instead, all the sensors can be located in the same fiber, avoiding the use of several couplers (Figure 2.42 (c)). Both in-line sensing probe designs, evanescent and interrupted fiber, are compatible with multipoint sensing along the same fiber.

In order for these configurations to be implemented, however, some mechanism for addressing independently the individual sensors must be employed. Because all the signals are traveling in the same fiber this requires some intrinsic multiplexing techniques. Spectral multiplexing is one of the most obvious solutions. However, such scheme requires that each sensor has a different spectral signature imposing wavelength discriminating detection. This implies, usually, that each sensor will have different absorption spectrum and chemical behavior. Such distinct properties can greatly complicate system implementation. In addition, due to the very large spectrum of organic dyes, this scheme is limited to a few sensors per fiber. Although all these limitations make this configuration unpractical for multipoint interrogation of the same parameter, it can be worth implementing for multiparameter systems, where the sensor chemistry and spectra are already different anyway [121]. In the line configuration, care has to be taken in order to avoid mutual absorption of the different sensor signals and also excessive attenuation of the excitation radiation. In this regard, with evanescent probes it is easier to ensure a uniform excitation of all the sensors. Using in-line probes, on the other hand, this is a much more difficult task. Substitution of the different sensors along the fiber is still feasible in the tree topology but it can be tricky for line configurations. For all these reasons, wavelength multiplexing of fiber based chemical sensors is a solution of limited applicability and is mostly used for simultaneous detection of different parameters.

Time resolved excitation and detection provide a more feasible approach for the tree and line configurations. This technique is based on optical time-domain reflectometry (OTDR). First used to locate faults in optical fibers, it has come into use for distributed fiber-optic sensors. This scheme is based on coupling excitation light pulses into the fiber which, upon encountering a sensor region, produce light scattered back and detected at the input end of the fiber with a characteristic time delay. The use of luminescent species at the sensing sites has the potential to provide much larger signals, since the quantum efficiencies for fluorescence may be orders of magnitude higher than those for scattering. Evanescent probes allow the use of a larger number of sensing sites than interrupted fiber probes, which induce more loss of excitation radiation. A multipoint luminescent pH sensor was successfully interrogated using time domain techniques. In a typical application using

this scheme, pulsed optical excitation ($0.5\,ns$) and time-resolved emission detection were used to simultaneously monitor several multiplexed sensor cladded regions along a single optical fiber. Time-resolved detection was also demonstrated to provide information on both the spatial location and the fluorescence kinetics of the individual sensors along the fiber-optic waveguide [131, 132].

For both core and cladding doping, the spatial resolution of the multipoint fiber sensor is limited roughly by the luminescence lifetime of the sensing dye. This way, better spatial resolution, i.e., smaller lengths of fiber between consecutive sensors, is only attainable by using very fast lifetime luminophores. This, in turn, requires very short excitation pulses and fast detection electronics. Nevertheless, even when short-lived luminophores ($\sim 10\,ns$) are used, sensor spacing still has to exceed a few meters. Although this can be acceptable for many environmental applications, much higher spatial resolution is required in many biomedical tests.

Prince et al [133] proposed the use of two separate fibers in order to decrease the space between consecutive sensors greatly increasing spatial resolution. The use of a second fiber, serving as an optical delay line, is the key to this problem. One fiber contains the sensing regions that can be spaced within fractions of a millimeter. The second fiber periodically contacts the sensor regions, either (depending on the preferred configurations) providing evanescent excitation of the sensing dye or evanescently collecting the emitted luminescence. A scheme of this set-up is shown in Figure 2.43.

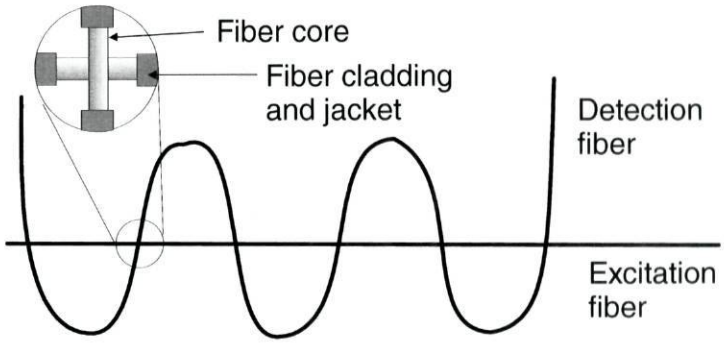


Figure 2.43 Dual fiber scheme used to improve the spatial resolution of multi-point sensing configurations based on time-resolved excitation/detection [133].

For this scheme to work, the separation between two adjacent contact points along the second fiber has to be sufficiently large to create the required temporal separation. That is, the second fiber causes a delay in either the excitation pulse or the emitted fluorescence with respect to adjacent sensor regions of the first fiber. With this scheme, even for a large number of sensors, one of the fibers can be arranged in a compact fashion, allowing easy handling. The authors reported the successful interrogation of several sensors through this fiber-to-fiber evanescent coupling scheme.

The response of up to 6 individual sensors, separated by very short fiber lengths (from $5\,mm - 10\,mm$), was spatially discriminated. Four different luminescent dyes were used on a single fiber to show that wavelength discrimination could be combined with this technique. Although the results presented are very promising, the use of this configuration for practical applications poses some challenging engineering problems that were not addressed by the authors. Packaging of both fibers in a single cable and mechanical stability of the sensing regions may be difficult to solve while maintaining a compact solution.

All the configurations discussed so far considered multipoint measurements. For many applications, however, the ideal configuration must provide continuous measurement along all the fiber length. For this purpose the fiber itself has to become a sensor. The fabrication of special fibers, having active luminescent core or cladding, or both, has already been reported, and some of them are commercially available. Plastic fibers are specially suited for this purpose.

Some sensing applications were reported using these fibers, where the excitation was performed externally, in the vicinity of the sensing fiber [134]. Although this configuration has many interesting applications, it is not suitable for most remote environmental applications. Although excitation and detection through the luminescent fiber itself is possible, discrimination of signals coming from specific points along the fiber is a problem with no obvious solution. Nevertheless, intrinsic sensing fibers have great potential that continues to be explored. Their use was reported for detection of radiation (the fiber was externally excited by radioluminescence). A similar configuration could be used for biochemical sensing making use, for instance, of chemiluminescent reactions between the luminophore and the analyte.

Multiplexing of luminescence based optical fiber chemical sensors is a particularly challenging research field. Although many proof-of-principle applications have been reported, very few practical system are presently in use. Nevertheless, new technologies are becoming available that could provide new tools for luminescence multiplexing. Photonic crystals fibers, with their highly versatile guiding properties, and luminescent semiconductor nanoparticles, with narrow band tunable emission, are just two examples of new developments with great potential in this field.

2.6 References

[1] S. Kulmala and J. Suomi, *Current status of modern analytical luminescence methods.* Analytica Chimica Acta 2003. **500**: p. 21-69.

[2] *www.nichia.com.* [cited 2006].

[3] *www.lumileds.com.* [cited 2006].

[4] J. N. Demas and B.A. DeGraff, *Applications of luminescent transition metal complexes to sensor technology and molecular probes.* Journal of Chemical Education, 1997. **74**: p. 690-695.

[5] A. Juris, V. Balzani, F. Barigalletti, S. Campagna, P. Belser, and A.v. Zelewsky, *Ru(II) polypyridine complexes: photophysics, photochemistry, electrochemistry, and chemiluminescence.* Coordination Chemistry Reviews, 1988. **84**: p. 85-277.

[6] Otto S. Wolfbeis, Ingo Klimant, Tobias Werner, Christian Huber, Ute Kosch, Christian Krause, Gerhard Neurauter, and A. Durkop, *Set of luminescence decay time based chemical sensors for clinical applications.* Sensors and Actuators B, 1998. **51**: p. 17-24.

[7] Podbielska, H., Agnieszka Ulatowska-Jarza, Gerhard Muler, and H.J. Eichler, *Sol-Gels for Optical Sensors*, in *Optical Chemical Sensors*, F. Baldini, et al., Editors. 2004, Springer. p. 353-385.

[8] Mohr, G.J., *Polymers for Optical Sensors*, in *Optical Chemical Sensors*, F. Baldini, et al., Editors. 2004, Springer. p. 297-321.

[9] Brian D. MacCraith, Colette M. McDonagh, Gerard O'Keeffe, Aisling K. McEvoy, T. Butler, and F.R. Sheridan, *Sol-gel coatings for optical chemical sensors and biosensors.* Sensors and Actuators B, 1995. **29**: p. 51-57.

[10] *PreSens - Precision Sensing GmbH . http://www.presens.de.* [cited 2006].

[11] *Ocean Optics, Inc. www.oceanoptics.com.* [cited 2006].

[12] Gerhard Holst and B. Mizaikoff, *Fiber Optic Sensors for Environmental Applications*, in *Handbook of Optical Fibre Sensing Technology.* 2002, John Wiley & Sons, LTD. p. 729-755.

[13] Mignani, A.G. and F. Baldini, *Biomedical sensors using optical fibres.* Reports on Progress in Physics, 1996. **59**(1): p. 1-28.

[14] F. Baldini, A. N. Chester, J. Homola, and S. Martellucci, eds. *Optical Chemical Sensors.* NATO Science Series II. Mathematics, Physics and Chemistry. Vol. 224. 2004, Springer.

[15] Valeur, B., *Molecular Fluorescence: principles and applications.* 2002, Weinheim: Wiley VCH.

[16] Orellana, G., *Luminescent optical sensors.* Anal Bioanal Chem, 2004. **379**: p. 344–346.

[17] Joseph R. Lakowicz, *Principles of Fluorescence Spectroscopy.* 2 ed. 1999, New York: Kluwer-Plenum.

[18] Kuhn, H. and H.-D. Forsterling, *Principles of Physical Chemistry.* 2000, New York: John Wiley & Sons.

[19] J. N. Demas and B.A. DeGraff, *Design and applications of highly luminescent transition metal complexes.* Analytical Chemistry, 1991. **63**: p. 829A-837A.

[20] Wolfbeis, O.S., *Chemical Sensing Using Indicator Dyes*, in *Optical Fiber Sensors: Applications, Analysis and Future Trends.* 1997, Artech House: Boston-London. p. 53-107.

[21] Geddes, C.D., *Optical halide sensing using fluorescence quenching: theory, simulations and applications-a review.* Measurement Science and Technology, 2001. **12**: p. R33-R88.

[22] Clapp, A.R., I.L. Medintz, J.M. Mauro, B.R. Fisher, M.G. Bawendi, and H. Mattoussi, *Fluorescence resonance energy transfer between quantum dot donors and dye-labeled protein acceptors.* Journal of the American Chemical Society, 2004. **126**(1): p. 301-310.

[23] Orellana, G., *Fluorescence based sensors*, in *Optical Chemical Sensors*, F. Baldini, et al., Editors. 2004, Springer. p. 99-116.

[24] Valeur, B., *Effects of intermolecular photophysical processes on fluorescence emission*, in *Molecular Fluorescence: principles and applications*. 2002, Wiley VCH: Weinheim. p. 72-124.

[25] Eftink, M.R., *Fluorescence Quenching: Theory and Applications*, in *Topics in Fluorescence Spectroscopy: Principles*, J.R. Lakowicz, Editor. 1991, Plenum Press: New York-London. p. 53-120.

[26] Joseph R. Lakowicz, *Quenching of fluorescence*, in *Principles of Fluorescence Spectroscopy*. 1999, Kluwer-Plenum: New York. p. 237-265.

[27] Harold Boaz and G.K. Rollefson, *The quenching of fluorescence: Deviations from the Stern-Volmer law*. Journal of American Chemical Society, 1950. **72**: p. 3435-3443.

[28] E. R Carraway, J. N. Demas, and B.A. DeGraff, *Luminescence quenching mechanism for microheterogeneous systems*. Analytical Chemistry, 1991. **63**: p. 332-336.

[29] J. N. Demas, B. A. DeGraff, and W. Xu, *Modeling of luminescence quenching-based sensors: comparison of multisite and nonlinear gas solubility models*. Analytical Chemistry, 1995. **67**: p. 1377-1380.

[30] Paul Hartmann, Marc J. P. Leiner, and P. Kohlbacher, *Photobleaching of ruthenium complex in polymers used for oxygen optodes and its inhibition by singlet oxygen quenchers*. Sensors and Actuators B, 1998. **51**: p. 196-202.

[31] Han Chuang and M.A. Arnold, *Linear calibration function for optical oxygen sensors based on quenching of ruthenium fluorescence*. Analytica Chimica Acta, 1998. **368**: p. 83-89.

[32] Li-Li Zhoua, Hao Suna, Xiao-Hong Zhang, and Shi-Kang Wu, *An effective fluorescent chemosensor for the detection of copper(II)*. Spectrochimica Acta Part A, 2004. **61**: p. 61–65.

[33] Brian D. MacCraith, Colette M. McDonagh, Gerard O'Keeffe, Emmetine T. Keyes, Johannes V. Vos, Brendan O'Kelly, and J.F. McGilp, *Fibre optic oxygen sensor based on fluorescence quenching of evanescent-wave excited ruthenium complexes in sol-gel derived porous coatings*. Analyst, 1993. **118**: p. 385-388.

[34] Valeur, B., *Principles of steady-state and time-resolved fluorometric techniques*, in *Molecular Fluorescence: principles and applications*. 2002, Wiley VCH: Weinheim. p. 155-199.

[35] Joseph R. Lakowicz, *Instrumentation for fluorescence spectroscopy*, in *Principles of Fluorescence Spectroscopy*. 1999, Kluwer-Plenum: New York. p. 25-62.

[36] Valeur, B., *Fluorescence polarization. Emission anisotropy*, in *Molecular Fluorescence: principles and applications*. 2002, Wiley VCH: Weinheim. p. 125-154.

[37] Antonius Song, Stephen Parus, and Raoul Kopelman, *High-Performance Fiber-Optic pH Microsensors for Practical Physiological Measurements Using a Dual-Emission Sensitive Dye*. Anal. Chem., 1997. **69**(5): p. 863-867.

[38] B. Hannemann, A. Tamachkiarowa, and C. Radehaus. *Comparison between stationary intensity and lifetime luminescence measurements with fiber optic oxygen sensores, containaing $[Ru\ (4.7\ Ph_2\ phen)_3]^{2+}$ in silicone polymer*. 1995 Vol. 2508, p. 291-302.

[39] Joseph R. Lakowicz, *Time-Domain Lifetime Measurements* in *Principles of Fluorescence Spectroscopy*. 1999, Kluwer-Plenum: New York. p. 95-141.

[40] Oconnor, D.V., W.R. Ware, and J.C. Andre, *Deconvolution of Fluorescence Decay Curves - Critical Comparison of Techniques*. Journal of Physical Chemistry, 1979. **83**(10): p. 1333-1343.

[41] T. Sun, Z. Y. Zhang, K. T. V. Grattan, A. W. Palmer, and S.F. Collins, *Temperature dependence of the fluorescence lifetime in Pr^{3+}: ZBLAN glass for fiber optic thermometry*. Review of Scientific Instruments, 1997. **68**: p. 3447-3451.

[42] Henryk Szmacinski and J.R. Lakowicz, *Fluorescence lifetime-based sensing and imaging*. Sensors and Actuators B, 1995. **29**: p. 16-24.

[43] Peter C. Schneider and R.M. Clegg, *Rapid acquisition, analysis, and display of fluorescence lifetime-resolved images for real-time applications.* Review of Scientific Instruments, 1997. **68**: p. 4107-4119.

[44] Zhiyi Zhang, K. T. V. Grattan, and A.W. Palmer, *Phase-locked detection of fluorescence lifetime.* Review of Scientific Instruments, 1993. **64**: p. 2531-2540.

[45] Joseph R. Lakowicz, *Frequency-Domain Lifetime Measurements* in *Principles of Fluorescence Spectroscopy.* 1999, Kluwer-Plenum: New York. p. 142-184.

[46] Christian Huber, Ingo Klimant, Christian Krause, and O.S. Wolfbeis, *Dual Lifetime Referencing as Applied to a Chloride Optical Sensor.* Anal. Chem., 2001. **73**: p. 2097-2103.

[47] Gerard O'Keeffe, Brian D. MacCraith, Aisling K. McEvoy, Colette M. McDonagh, and J.F. McGilp, *Development of LED-based phase fluorimetric oxygen sensor using evanescent wave excitation of a sol-gel immobilized dye.* Sensors and Actuators B, 1995. **29**: p. 226-230.

[48] Brian D. MacCraith, Gerard O'Keeffe, Aisling K. McEvoy, and C. McDonagh. *Development of a LED-based fibre optic oxygen sensor using a sol-gel-derived coating.* 1994 Vol. 2293, p. 110-120.

[49] P. Herman, B. P. Maliwal, H.-J. Lin, and J.R. Lakowicz, *Frequency-domain fluorescence microscopy with the LED as a light source.* Journal of Microscopy, 2001. **203**: p. 176-181.

[50] Joseph R. Lakowicz, *Fluorophores*, in *Principles of Fluorescence Spectroscopy.* 1999, Kluwer-Plenum: New York. p. 63-94.

[51] Andrew Mills and F.C. Williams, *Chemical influences on the luminescence of ruthenium diimine complexes and its response to oxygen.* Thin Solid Films, 1997. **306**: p. 163-170.

[52] R. J. Watts and G.A. Crosby, *Spectroscopic characterization of complexes of ruthenium(II) and iridium(III) with 4,4'-diphenyl-2,2'-bipyridine and 4,7-diphenyl-1,10-phenanthroline.* Journal of the American Chemical Society, 1971. **93**: p. 3184-3188.

[53] E. R Carraway, J. N. Demas, B. A. DeGraff, and J.R. Bacon, *Photophysics and photochemistry of oxygen sensors based on luminescent transition-metal complexes.* Analytical Chemistry, 1991. **63**: p. 337-342.

[54] Demas, J.N. and B.A. DeGraff, *Applications of luminescent transition platinum group metal complexes to sensor technology and molecular probes.* Coordination Chemistry Reviews, 2001. **211**: p. 317-351.

[55] Aisling K. McEvoy, Colette M. McDonagh, and B.D. MacCraith, *Dissolved oxygen sensor based on fluorescence quenching of oxygen-sensitive ruthenium complexes immobilized in sol-gel-derived porous silica coatings.* Analyst, 1996. **121**: p. 785-788.

[56] Guillermo Orellana and D. Garcia-Fresnadillo, *Environmental and Industrial Optosensing with Tailored Luminescent Ru(II) Polypyridyl Complexes*, in *Optical Sensors - Industrial Environmental and diagnostic Applications*, R. Narayanaswamy and O.S. Wolfbeis, Editors. 2004, Springer: Berlin. p. 309-357.

[57] B. A. DeGraff and J.N. Demas. *Luminescent Sensors: Sensor Suport.* 1996 [cited 2002].

[58] Heather M. Rowe, Wenying Xu, J. N. Demas, and B.A. DeGraff, *Metal ion sensors based on a luminescent ruthenium(II) complex: the role of polymer support in sensing properties.* Applied Spectroscopy, 2002. **56**: p. 167-173.

[59] Sonja Draxler, Max E. Lippitsch, Ingo Klimant, Heinz Kraus, and O.S. Wolfbeis, *Effects of polymer matrices on the time-resolved luminescence of a ruthrnium complex quenched by oxygen.* Journal of Physical Chemistry, 1995. **195**: p. 3162-3167.

[60] Harsányi, G., *Polymer films in sensor applications: a review of present uses and future possibilities.* Sensor Review, 2000. **20**(2): p. 98-105.

[61] Rebecca J. Bartlett, Rekha Philip-Chandy, Piers Eldridge, David F. Merchant, Roger Morgan, and P.J. Scully, *Plastic optical fibre sensors and devices.* Transactions of the Institute of Measurement and Control 2000. **22**(5): p. 431-457.

[62] Larry L. Hench and J.K. West, *The sol-gel process.* Chemical Reviews, 1990. **90**: p. 33-72.

[63] Colette .M. McDonagh, B.D. MacCraith, and A.K. McEvoy, *Tailoring of sol–gel films for optical sensing of oxygen in gas and aqueous phase.* Anal. Chem., 1998. **70**: p. 45–50.

[64] Colette M. McDonagh, P. Bowe, K. Mongey, and B.D. MacCraith, *Characterisation of porosity and sensor response times of sol-gel-derived thin films for oxygen sensor applications.* Journal of Non-Crystalline Solids, 2002. **306**: p. 138-148.

[65] Voipio, V., *Instrument for Measuring pH with Optical indicator thin film*, in *Department of Electrical and Communications Engineering.* 2001, Helsinki University of Technology: Helsinki. p. 194.

[66] P. Innocenzi, H. Kozuka, and T. Yoko, *Fluorescence properties of the $Ru(bpy)_3^{2+}$ complex incorporated in sol–gel-derived silica coating films.* J. Phys. Chem. B, 1997. **101**(2285–2291).

[67] K. Maruszweski et al., *Physicochemical properties of $Ru(bpy)_3^{2+}$ entrapped in silicate bulks and fiber thin films prepared by the sol–gel method.* Chem. Phys. Lett., 1999. **314**: p. 83–90.

[68] Klimant, I., F. Ruckruh, G. Liebsch, C. Stangelmayer, and O.S. Wolfbeis, *Fast response oxygen micro-optodes based on novel soluble ormosil glasses.* Mikrochimica Acta, 1999. **131**(1-2): p. 35-46.

[69] C. Jeffrey Brinker and A.J. Hurd, *Fundamentals of sol-gel dip-coating.* J. Phys. III France, 1994. **4**: p. 1231-1242.

[70] Grattan, K.T.V. and T. Sun, *Fiber optic sensor technology: an overview.* Sensors and Actuators A - Physical, 2000. **82**(1-3): p. 40-61.

[71] Otto S. Wolfbeis, *Fiber Optic Chemical Sensors and Biosensors.* Anal. Chem., 2002. **72**: p. 81R-89R.

[72] Bahaa E.A. Saleh and M.C. Teich, *Fundamental of Photonics.* 1991: John Wiley & Sons.

[73] Thompson, R.B., *Fluorescence-Based Fiber-Optic Sensors*, in *Topics in Fluorescence Spectroscopy: Principles.* 1991, Plenum Press: New York-London. p. 345-363.

[74] Dybko, A., *Fundamentals of Optoelectronics*, in *Optical Chemical Sensors*, F. Baldini, et al., Editors. 2004, Springer. p. 47-58.

[75] *Thor Labs Inc. www.thorlabs.com.* [cited 2006].

[76] Ivan Kasik, Vlastimil Matejec, Miroslav Chomat, Milos Hayer, and D. Berkova, *Optical Fibers for Optical Sensing*, in *Optical Chemical Sensors*, F. Baldini, et al., Editors. 2004, Springer. p. 59-76.

[77] Walt, D.R., *Imaging optical sensor arrays.* Current Opinion in Chemical Biology, 2002. **6**(5): p. 689-695.

[78] Szunerits, S. and D.R. Walt, *The use of optical fiber bundles combined with electrochemistry for chemical Imaging.* Chemphyschem, 2003. **4**(2): p. 186-192.

[79] R. F. Cregan, B.J.M., J. C, Knight, T. A. Birks, J. Russel, P. J. Roberts and D. C. Allan, *Single-mode photonics band gap guidance of light in air.* Science 1999. **285**: p. 1537-1539.

[80] T. M. Monro, D. J. Richardson, and P.J. Bennett, *Developing holey fibres for evanescent filed devices.* Electronics Letters, 1999. **35**(14): p. 1188-1189.

[81] David Monzón-Hernández, Vladimir P. Minkovich, and J. Villatoro, *High-Temperature Sensing With Tapers Made of Microstructured Optical Fiber.* IEEE Photonics Technology Letters, 2006. **18**(3): p. 511-513.

[82] T. M. Monro, W. Belardi, K. Furusawa, J. C. Baggett, N. G. R. Broderick, and D.J. Richardson, *Sensing with microstructured optical fibres.* Meas. Sci. Technol. , 2001. **12**: p. 854-858.

[83] Fini, J., *Microstructure fibres for optical sensing in gases and liquids.* Meas. Sci. Technol., 2004. **15**: p. 1120-1128.

[84] *www.newport.com.* [cited 2006].

[85] *www.mellesgriot.com.* [cited 2006].

[86] Garland Best and O.M. Sezerman. *Shedding Light on Hybrid Optics: A tutorial in coupling*, in *Optics & Photonics News*, February, 1999.

[87] Sunak, H.R.D., *Measurement of Launching Efficiency Into Multimode Optical Fibers Using Semiconductor Laser Diodes.* IEEE Transactions on Instrumentation and Measurement, 1988. **37**(4): p. 561-563.

[88] Keiser, G., *Optical fiber communications.* 2001: Mc Graw Hill.

[89] Sead Doric and M. Tubic. *Fiber-coupling of LEDs depends on emitter type*, in *Laser Focus World*, October, 2004.

[90] Ohno, Y., *Radiometry and Photometry Review for Vision Optics*, in *Handbook of optics: Classical, vision, & X-ray optics*, M. Bass, Editor. 2001, McGraw-Hill: New York. p. 14.1-14.14.

[91] Goodman, D.S., *General Principles of Geometric Optics* in *Handbook of optics: devices, measurements and properties*, M. Bass, Editor. 1995, McGraw-Hill: New York. p. 1.3-1.109.

[92] Cassarly, W., *Non-imaging Optics: Concentration and Illumination*, in *Handbook of optics: Classical, vision, & X-ray optics*, M. Bass, Editor. 2001, McGraw-Hill: New York. p. 2.1-2.53.

[93] Clark, T. and K. Wanser. *Choosing Ball or GRIN Lenses*, in *Photonics Spectra*, February, 2001.

[94] Born, M. and E. Wolf, *Principles of Optics.* 1959, New York: Pergamon Press. 190-196.

[95] Winston, R., *Nonimaging optics.* Scientific American, 1991: p. 52-57.

[96] Walter T. Welford and R. Winston, *The Optics of Nonimaging Concentrators Light and Solar Energy.* 1978, New York: Academic Press.

[97] W. T. Welford and R. Wiston, *The Optics of Non-imaging Concentrators.* 1978, New York: Academic.

[98] Ning, X., *Three-dimensional ideal θ_1/θ_2 angular transformer and uses in fiber optics.* Applied Optics, 1988. **27**: p. 4126-4130.

[99] Cassarly, W. *Taming Light*, in *SPIE OE magazine*, December, 2002.

[100] Gordon, J.M., *Simple String Construction Method for Tailored Edge-Ray Concentrators in Maximum-Flux Solar Energy Collectors.* Solar Energy, 1996. **56**(3): p. 279-284.

[101] Harald Ries, Narkis Shatz, John Bortz, and W. Spirkl, *Performance limitations of rotationally symmetric nonimaging devices.* Journal of Optical Society of America A, 1997. **14**: p. 2855-2862.

[102] Ari Rabl and R. Winston, *Ideal concentrators for finite sources and restricted exit angles.* Applied Optics, 1976. **15**: p. 2880-2883.

[103] Manuel Collares-Pereira, Ari Rabl, and R. Winston, *Lens-mirror combinations with maximal concentration.* Applied Optics, 1977. **16**: p. 2677-2683.

[104] Winston, R., *Dielectric compound parabolic concentrators.* Applied Optics, 1976. **15**: p. 291-292.

[105] Xiaohui Ning, Roland Winston, and J. O'Gallagher, *Dielectric totally internally reflecting concentrators.* Applied Optics, 1987. **26**: p. 300-305.

[106] Pelka, D. *Lighting by Design*, in *SPIE's oe magazine*, August, 2005.

[107] Behzad Moslehi, Joel Ng, Ivan Kasimoff, and T. Jannson, *Fiber-optic coupling based on non-imaging expanded-beam optics.* Optics Letters, 1989. **14**(23): p. 1327-1329.

[108] Lee C. Chen, Andy L. Y. Low, and S.F. Chien, *Compound parabolic tapered fiber for fiber coupling with a highly divergent source.* Applied Optics, 2004. **43**(32): p. 5923-5925.

[109] Thanassis Papaioannou, Norris W. Preyer, Qiyin Fang, Adam Brightwell, Michael Carnohan, Greg Cottone, Russel Ross, Linda R. Jones, and L. Marcu, *Effects of fiber-optic probe design and probe-to-target distance on diffuse reflectance measurements of turbid media: an experimental and computational study at 337 nm.* Applied Optics, 2004. **43**(14).

[110] Shriverlake, L.C., G.P. Anderson, J.P. Golden, and F.S. Ligler, *The Effect of Tapering the Optical Fiber on Evanescent Wave Measurements.* Analytical Letters, 1992. **25**(7): p. 1183-1199.

[111] Louch, J. and J.D. Ingle, *Experimental Comparison of Single-Fiber and Double-Fiber Configurations for Remote Fiber-Optic Fluorescence Sensing.* Analytical Chemistry, 1988. **60**(22): p. 2537-2540.

[112] V. Murphy, B.D. MacCraith, T. Butler, C. McDonagh, and B. Lawless, *Quasi-distributed fiber optic chemical sensing using telecom optical fiber.* Electronics Letters, 1997. **33**(7): p. 618-619.

[113] Jeffrey T. Remillard, Jeffrey R. Jones, Ben D. Poindexter, Chaitanya K. Narula, and W.H. Weber, *Demonstration of a high-temperature fiber-optic gas sensor made with a sol-gel process to incorporate a fluorescent indicator.* Applied Optics, 1999. **38**(25): p. 5306-5309.

[114] McCulloch, S. and D. Uttamchandani, *Development of micro-optrodes using sol-gel immobilisation.* IEE Proc. Sci. Meas. Technol., 1997. **144**(6): p. 241-246.

[115] Uttamchandani, D. and S. McCulloch, *Optical nanosensors - towards the development of intracellular monitoring.* Advanced drug Delivery Reviews, 1996. **21**: p. 239-247.

[116] Pak Kin Wong, Tza-Huei Wang, and C.-M. Ho. *Optical fiber tip fabricated by surface tension controled etching.* in *Solid-state sensor, Actuator and Microsystems Workshop.* 2002. Hilton Head Island, South Carolina, p. 94-97.

[117] R.K. Kenny, T.A. Birks, and K.P. Oakley, *Control of optical fiber taper shape.* Electron. Lett., 1991. **77**: p. 1654-1656.

[118] Anderson, G.P., J.P. Golden, L.K. Cao, D. Wijesuriya, L.C. Shriverlake, and F.S. Ligler, *Development of an Evanescent-Wave Fiber Optic Biosensor.* Ieee Engineering in Medicine and Biology Magazine, 1994. **13**(3): p. 358-368.

[119] Gupta, B.D. and D.K. Sharma, *Evanescent wave absorption based fiber optic pH sensor prepared by dye doped sol-gel immobilization technique.* Optics Communications, 1997. **140**(1-3): p. 32-35.

[120] Blue, R., N. Kent, L. Polerecky, H. McEvoy, D. Gray, and B.D. MacCraith, *Platform for enhanced detection efficiency in luminescence-based sensors.* Electronics Letters, 2005. **41**(12): p. 682-684.

[121] Irina B. Bakaltcheva, Frances S. Ligler, Charles H. Patterson, and L.C. Shriver-Lake, *Multi-analyte explosive detection using a fiber optic biosensor.* Analytica Chimica Acta, 1999. **399**: p. 13-20.

[122] Shangping Guo and S. Albin, *Transmission property and evanescent wave absorption of cladded multimode fiber tapers.* Optics Express, 2003. **11**(3): p. 215-223.

[123] Villatoro, J., D. Monzon-Hernandez, and D. Luna-Moreno, *In-line optical fiber sensors based on cladded multimode tapered fibers.* Applied Optics, 2004. **43**(32): p. 5933-5938.

[124] J. Y. Ding, M.R. Shahriari, and G.H. Sigel, *Fibre Optic pH Sensor Prepared by Sol-gel Immobilisation Technique.* Electron. Lett., 1991. **27**(17).

[125] Zhou, Q., M.R. Shahriari, D. Kritz, and G.H. Sigel, *Porous Fiber-Optic Sensor for High-Sensitivity Humidity Measurements.* Analytical Chemistry, 1988. **60**(20): p. 2317-2320.

[126] Tao, S.Q., C.B. Winstead, R. Jindal, and J.P. Singh, *Optical-fiber sensor using tailored porous sol-gel fiber core.* Ieee Sensors Journal, 2004. **4**(3): p. 322-328.

[127] Vlastimil Matejec, Miroslav Chomát, Ivan Kasík, Jirí Ctyroký, Daniela Berková, and M. Hayer, *Inverted-graded index fiber structures for evanescent-wave chemical sensing.* Sensors and Actuators B, 1998. **51**: p. 340-347.

[128] Limin Tong, Rafael R. Gattass, Jonathan B. Ashcom, Sailing He, Jingyi Lou, Mengyan Shen, Iva Maxwell, and E. Mazur, *Subwavelength-diameter silica wires for low-loss optical wave guiding.* NATURE, 2003. **426** (18): p. 816-819.

[129] Holst, G., R.N. Glud, M. Kuhl, and I. Klimant, *A microoptode array for fine-scale measurement of oxygen distribution.* Sensors & Actuators B, 1997. **38-39**: p. 122-129.

[130] Artur Dybko, Wojciech Wroblewski, Ewa Rozniecka, Krzysztof Pozniak, Janusz Maciejewski, Ryszard Romaniuk, and Z. Brzozka, *Assessment of water quality based on multiparameter fiber optic probe.* Sensors and Actuators a-Physical, 1998. **51**: p. 208–213.

[131] Browne, C.A., D.H. Tarrant, M.S. Olteanu, J.W. Mullens, and E.L. Chronister, *Intrinsic sol-gel clad fiber-optic sensors with time-resolved detection.* Analytical Chemistry, 1996. **68**(14): p. 2289-2295.

[132] Campbell, M., Y.T. Yang, P.A. Wallace, and A.S. HolmesSmith, *A multipoint quasi-distributed optical fiber pH sensor.* Optical Review, 1997. **4**(1A): p. 111-113.

[133] Barry J. Prince, Alan W. Schwabacher, and P. Geissinger, *A Readout Scheme Providing High Spatial Resolution for Distributed Fluorescent Sensors on Optical Fibers.* Anal. Chem., 2001. **73**: p. 1007-1015.

[134] Robert A. Lieberman, L. L. BLyler, and L.G. Cohen, *A Distributed Fiber Optic Sensor Based on Cladding Fluorescence.* Journal of Lightwave Technology, 1990. **8**(2): p. 212-220.

Chapter 3

Optical Fiber pH Sensors

Summary

The determination of pH is an essential analytical tool in many fields of application. Although electrochemical methods are well established standards in this field, there are many instances where optical pH sensors offer considerable advantages over traditional techniques. In this chapter, a brief overview of the present state of luminescence based optical fiber pH sensing technology is presented. An essential step towards the implementation of any optical fiber luminescence sensor comprises the immobilization of the pH indicator in a solid host material. Therefore, in a first stage of this work, different methods of sensing dye immobilization were tested and compared. In addition, using some of the resulting sensing membranes, several interrogation techniques were addressed. Using the same optical fiber system, pH measurements were performed using luminescence intensity detection, dual wavelength ratiometric detection, wavelength shift detection and frequency domain interrogation. From the results presented the obvious advantages of frequency domain interrogation become apparent. In the final work presented in this chapter, new pH indicators based on osmium(II) complexes were characterized. The new complexes can be excited by red laser diodes and present pH dependent infrared luminescence emission. The sensitivity of their lifetime to pH points to the possibility of using these indicators in frequency domain based systems.

3.1 Introduction

The acidity of a medium is of critical importance for many biochemical processes. For this reason, the pH level is a fundamental parameter in many biomedical and environmental applications, which can greatly influence reaction rates and even the type of products resulting from different chemical synthesis procedures. Many chemical reactions can only take place within a narrow pH range. In the human body, for instance, the chemistry of life is only possible if the pH of blood is strictly maintained between 7.35 and 7.45. Therefore, the determination of pH is of critical importance in a wide range of applications. In the medical field, continuous and real-time knowledge of blood pH, together with blood gas analysis, is of vital importance in operating rooms and

intensive-care units [1-3]. Also, the determination of pH of ground water is a good indicator of ecosystems health. In fact, the success of waste water treatment is often assessed by evaluating the neutrality of treated industrial waste waters [4]. As a process parameter in chemical industry, measuring and controlling pH is essential to find and maintain the optimum reaction conditions. In the food industry, on the other hand, pH level must be accurately controlled in different fermentation processes. In addition, the acidity level is also used to assess the freshness of different food products [5, 6].

From these few examples, it immediately becomes apparent that the determination of pH is probably one of the most used analytical procedures in a modern technological society. The economical value of a reliable technology, capable of online pH measurements, with fast response, high sensitivity and long term stability is, therefore, unquestionable. Presently, most analytical methods for pH determination rely on electrochemical sensors and glass electrodes are, in particular, the most commonly used devices. Although the use of glass electrodes is a well established technology, offering high sensitivity and a wide dynamic range, in some situations their application is impossible or can cause severe problems. The operation of potentiometric sensors in hazardous electromagnetic environments is seriously compromised. In addition, glass electrodes show poor performance at extreme pH values. In highly alkaline media, for instance, the glass membrane can be damaged irreversibly. This way, continuous monitoring of pH level in many industrial processes often requires the daily substitution of the sensing device, greatly increasing operational costs.

In this context, the development of new technologies for pH monitoring is highly desirable. Optical methods for determination of pH have many appealing characteristics which make them a promising alternative to conventional technologies. Insensitive to electromagnetic interferences, they are suitable for remote monitoring in hazardous environments when used in combination with optical fibers. In addition, the ease of miniaturization and compatibility with multi-analyte systems makes optical sensors a very versatile option in comparison with electrodes. Although optical pH sensors usually operate in a smaller dynamic range, they do so with increased sensitivity. These advantages, together with the prospect of a huge potential market, have contributed to justify a significant effort of the scientific community and the interest of many companies to focus on optical sensing technologies [7, 8]. As a result, major developments have been achieved over the last twenty years and presently optical pH sensors are already available as commercial products [9].

In spite of numerous advantages, and of many technological breakthroughs, the measurement of pH by optical methods still faces some unavoidable technological challenges. The vast majority of pH sensing solutions rely on colorimetric or luminescent indicators, with the latter producing the

most sensitive devices. The application of these techniques in practical systems, however, is only possible following immobilization of the indicator chemistry in a suitable solid membrane [10]. Ideally, such membranes should be proton permeable, and should provide effective encapsulation of the sensing dye while preserving its sensing properties and avoiding the diffusion of interfering species. This task often requires complex chemical procedures and is not always successful. In practice, many pH sensors have their long term operation compromised by leaching or photobleaching of the sensing dye [11, 12]. The effects of interfering species and of temperature also limit the number of successful applications. This way, at present, optical pH sensing is still an active and exciting area of research [13]. Strong research efforts are also directed towards multipoint and multiparameter sensing using optical techniques [5, 14-16]. In addition, the search for increased reliability, long term stability, reproducibility and compatibility with mass production is also being thoroughly pursued, aiming at large scale commercialization.

3.2 Luminescent pH sensing

3.2.1 Definition of pH

The pH scale provides a measure of the acidity of a solution and was originally defined by Soren Sorensen, a Danish biochemist, as the negative of the base ten logarithm of the hydrogen ion concentration, $[H^+_{(aq)}]$[18], i.e.

$$pH = -\log[H^+_{(aq)}]. \tag{3.1}$$

The application of a logarithmic scale removed the need for using an unpractical negative power notation for hydrogen ion concentrations, which can range over several orders of magnitude from about $\sim 1M$ at the high end to $\sim 10^{-14}M$ at the low end. Instead, using Sorensen scale, the extremes of acidity and alkalinity correspond, respectively, to pH values of 0 and 14. In aqueous systems the hydrogen ion concentration is dictated by the dissociation constant of water and interactions with other ions in the solution. At $25^{\circ}C$, pure water naturally dissociates in $H^+_{(aq)}$ and $OH^-_{(aq)}$ ions, with equal concentrations of $[H^+_{(aq)}] = [OH^-_{(aq)}] = 10^{-7} mol/L$[19]. This particular

[18] In practice, in aqueous solution, hydrogen ions do not exist in a free state as they are immediately solvated by water, becoming surrounded by an hydration shell of polar water molecules. As the same ion can exist in different solvation configurations (e.g. $H_3O^+(H_2O)_6$ or $H_3O^+(H_2O)_{20}$), an hydrated hydrogen ion is generally represented by $H^+_{(aq)}$, where the subscript stands for *aqueous*. The same notation is used for any other ion in an aqueous solution.

[19] The auto ionization of pure water can be described by the reaction $H_2O_{(l)} \rightleftharpoons OH^-_{(aq)} + H^+_{(aq)}$. The equilibrium constant of this reaction is given by $K_a = ([OH^-_{(aq)}][H_3O^+_{(aq)}])/[H_2O_{(l)}]$. Because the self-ionization process does not change significantly the concentration of water, the number of ionized molecules is actually very small, the value of $[H_2O_{(l)}]$ can be considered approximately constant, therefore $K_w = [OH^-_{(aq)}][H^+_{(aq)}] = K_a[H_2O_{(l)}]$ can be written.

situation corresponds to pH 7 and indicates neutrality. High acidity, on the other hand, corresponds to a predominance of $H^+_{(aq)}$ ions in the solution and, therefore, to low pH values ($pH < 7$). Conversely, as the number of hydrogen ions in the solution decreases, the pH value increases. Solutions with $pH > 7$ will have decreased $H^+_{(aq)}$ concentration and will present alkaline behavior.

Although the Sorensen definition is valid for dilute solutions, it becomes inaccurate when the ion concentration is high. In such cases, inter ionic interactions and other phenomena will decrease the number of hydrogen ions available for reaction. Therefore, the modern definition of pH is based on the activity of hydrogen ions, instead. This way, a more accurate definition of pH is given by

$$pH = -\log a_{H^+_{(aq)}} \tag{3.2}$$

where the hydrogen ion activity, $a_{H^+_{(aq)}}$, is a measure of the concentration of hydrogen ions that is effectively available for reaction in the solution. The ion activity depends on the solutions' ionic strength[20]. In solutions of low ionic strength, the activity of an ion can be approximated to its concentration. In this situation Sorensen's definition for pH is still valid and can be applied. At high, ionic strengths, however, the activity of hydrogen ions can strongly differ from its actual concentration. In this situation, calculated pH values based on concentrations can be very different from the real values, which must be calculated using the ion activity, equation (3.2).

3.2.2 Optical pH indicators

The observation of color changes displayed by certain substances in the presence of acid or alkaline solutions is one of the oldest analytical methods in chemistry. Indeed, pH indicator strips based on color changes are routinely used in different applications. However, the association of this principle with modern optoelectronics is now responsible for new powerful techniques. Modern methods for optical determination of pH typically involve the use of colorimetric or luminescent indicators whose spectral properties are dependent on the medium acidity. The chemical transduction of pH relies either on changes in the absorption spectrum or in the luminescent properties of the indicator. pH indicators are, therefore, molecular probes which have different spectral properties in their protonated or non-protonated forms. Several applications can be found

---

K_w is the dissociation constant of water and its value at 25 $^{\circ}C$ is approximately $K_w \simeq 1.011 \times 10^{-14} M^2$. Because there is only water in the solution, the number of $H^+_{(aq)}$ and $OH^-_{(aq)}$ ions must be the same, therefore $[H^+_{(aq)}] = [OH^-_{(aq)}] = \sqrt{K_w} \approx 10^{-7} M$.

[20] The ionic strength of a solution is a measure of the concentration of ions in the solution and is defined by $I = 1/2 \sum c_i z_i^2$, where c_i is the molarity concentration of each ion, z_i is the charge of that ion, and the sum is taken over all ions in the solution.

where pH was measured by monitoring optical parameters like absorption, reflectance or luminescence. Absorption methods are simple and easy to use but they are not very sensitive and often require high dye concentrations or very thick sensing membranes. Such features can strongly hinder miniaturization. Luminescence based techniques, on the other hand, are typically much more sensitive than absorption based methods. With luminescent indicators it is easier to implement highly miniaturized sensing probes. Due to their increased sensitivity, such indicators are preferred in critical applications. Although some examples of applications using absorbing dyes will be addressed, luminescence based pH sensing will be the focus of this chapter.

Sensing mechanism

While pH determination based on electrochemical methods yields a response that is directly related to the activity of protons, the same is not true for optical methods (colorimetric or luminescent). pH indicators have acid-base properties and, typically, they exist predominantly in an acid form or a base form, depending on the pH level of the surrounding environment. Each of the corresponding molecular species can then have different spectral properties, thus providing a mechanism to measure pH using spectroscopic techniques. These techniques rely on the optical determination of the concentrations of the acidic form and/or basic form of the indicator.

The changes in the luminescence output of a pH indicator in a given aqueous solution result from an acid-base equilibrium which can be described by the reaction

$$HA_{(aq)} \rightleftharpoons H^{+}{}_{(aq)} + A^{-}{}_{(aq)} \tag{3.3}$$

where the two forms of the indicator coexist. In this expression, $HA_{(aq)}$ is an acid indicator and $A^{-}{}_{(aq)}$ is its conjugated base. Similar equilibrium reactions can be described for basic indicators. The reaction represented in equation (3.3) has an associated ionization constant, K_a, which, for a weak acid indicator, can be calculated using the law of mass action

$$K_a = \frac{[H^{+}{}_{(aq)}][A^{-}{}_{(aq)}]}{[HA_{(aq)}]}, \tag{3.4}$$

where the terms in brackets stand for the concentration corresponding to each species. K_a is also called the acidity constant. High values of this parameter indicate that the reaction equilibrium is shifted towards the products side ($[H^{+}{}_{(aq)}]$ and $[A^{-}{}_{(aq)}]$), resulting in a strong ionization of the acid indicator. Stronger acids have larger acidity constants. For weaker acids, on the other hand, there is little ionization and the equilibrium is shifted towards the reactants side, $[HA_{(aq)}]$, corresponding to

smaller values of K_a. Taking the logarithm of both sides of the equation and rearranging, it can be written that

$$pH = pK_a + \log\frac{[HA_{(aq)}]}{[A^-_{(aq)}]}, \tag{3.5}$$

where pK_a is defined as the negative of the logarithm of the equilibrium constant K_a and $[AH_{(aq)}]$ and $[A^-_{(aq)}]$ are, respectively, the concentration of the indicator in its acidic and alkaline forms. The pK_a value is also a measure of the strength of an acid, defined in a logarithmic scale. Stronger acids will therefore display a low pK_a and weaker acids will be characterized by higher pK_a values. From this equation, called the Henderson-Hasselbalch equation, it can be predicted that in a solution with 50% ionization (where $[A^-_{(aq)}] = [AH_{(aq)}]$) the pH will equal the pK_a. It is in this region, where $pH \approx pK_a$, that the indicators' spectral properties will show stronger dependence on the sample pH level. For much higher or much lower pH values, however, either the acidic form or the basic form of the indicator will be predominant and, therefore, the spectral properties of the sensor will display little response to changes in the pH level. Usually this region of reduced response takes place within ± 2 pH units from the pK_a value of the indicator. While the response in an extended pH range follows a characteristic sigmoidal curve, in the limited range around the pK_a the concentration changes display an approximately linear behavior with pH (see example in Figure 3.1). The acidity constant is therefore an essential parameter which establishes the useful pH range for a given molecular indicator. For physiological applications, for instance, it is desirable to have an indicator with a pK_a around 7.4.

In most applications, the luminescent indicators are then employed in a pH range around the ground state pK_a, where their absorption spectrum shows strong dependence on pH level. This happens due to the fact that the protonation/deprotonation of the indicator molecules cause changes in its electronic π-system which, in turn, can introduce modifications in their absorption spectra. Therefore the acidic and basic forms will have different absorption properties. In addition, depending on the nature of the molecular pH indicator, different photophysical processes will take place upon optical excitation (photoinduced proton transfer, photoinduced electron transfer) that will define the luminescent behavior of the sensor. This way, the emitting form of some indicators is always the basic form and the fluorescence spectrum remains unchanged as the pH of the solution is modified. This type of indicators (e.g. pyranine, hydroxycoumarins) will display luminescence intensity changes as a function of pH. With other types of indicators (e.g. fluorescein, eosin Y), however, both forms, acidic and basic, display luminescent properties, either in similar or distinct spectral regions. This way, when increasing the pH, the absorption and emission bands of the acidic

form should decrease, and an increase should be observed in the absorption and emission bands of the basic form. As a result, the detected luminescence can present both intensity and spectral changes as a function of pH. In either case, if the concentration of the indicator is kept low enough, a linear relationship between absorbance or luminescence intensity and concentration is fulfilled. Consequently, optical measurements can be made which relate linearly with the concentrations of the acid and alkaline indicator species.

The Henderson-Hasselbalch equation [17] describes the relation between the pH of a solution and the concentration of the indicator and is typically used in the calibration of optical pH sensors. However, it should be mentioned that equation (3.5) neglects the fact that the true value of pH must be calculated from ion activities and not concentrations[21]. While in very dilute solutions the concentrations and the activity of an ion are nearly the same, in solutions of high ionic strength they can differ strongly. This way, because optical methods usually relate to concentrations, significant errors can take place. Nevertheless, in many applications the sensor operates in media of constant ionic strength (e.g. blood). Therefore, equation (3.5) can still be used, as long a calibration is performed in a solution under very similar conditions, and adequate corrections are made.

In order to relate the measurement of luminescent signals with the concentrations of the two indicator species, the more generic case where both the acidic and alkaline forms are emissive will be described. In this situation, considering a wavelength where both species emit, the detected luminescence intensity will be given by

$$I(\lambda_E,\lambda_L) = I = a[AH_{(aq)}] + b[A^-_{(aq)}]. \tag{3.6}$$

where $I(\lambda_E,\lambda_L)$ is the luminescent intensity at a given pair of excitation (λ_E) and emission (λ_L) wavelengths, and a and b are constants proportional to the absorption coefficients and to the quantum yields of $AH_{(aq)}$ and $A^-_{(aq)}$ respectively. For extreme pH values, where the indicator exists only in its acidic form or in its basic form, the luminescent intensities are given, respectively, by

$$I_{AH} = a\,c_0 \tag{3.7}$$

---

[21] The Henderson-Hasselbalch equation comprises several approximations. Indeed, the true value of the ionization constant of the acid/base reaction must be calculated based on activities (a_x) instead of concentrations, $[x]$, i.e. $K = (a_{H^+}\, a_{A^-})/a_{AH}$. This way, in a more accurate approach, the Henderson-Hasselbalch equation should be written instead as $pH = pK + \log(a_{A^-}/a_{AH})$ or $pH = pK + \log([A^-]/[AH]) + \log(f_{A^-}/f_{AH})$, where f_x stands for the activity coefficient of each corresponding ion. Comparison with equation (3.5) shows that $pK_a = pK + \log(f_a/f_b)$ and, therefore, K_a should be considered as an 'apparent' constant that depends not only on temperature, but also on factors able to modify the activity coefficients, such as ionic strength of the solutions, specific interactions depending on the chemical nature of the indicator and the surrounding medium, type of encapsulating matrix, etc. While in dilute solutions the activity coefficients are nearly unit, and equation (3.5) can still be used, in more general approaches the influence of ionic strength should be accounted for during sensor calibration.

and

$$I_{A^-} = b\,c_0\,, \tag{3.8}$$

where c_0 is the total concentration of the indicator such that

$$c_0 = [AH_{(aq)}] + [A^-_{(aq)}]\,. \tag{3.9}$$

Combination of the previous equations yields

$$\frac{[A^-_{(aq)}]}{[AH_{(aq)}]} = \frac{I - I_{AH}}{I_{A^-} - I} \tag{3.10}$$

Therefore, the Henderson-Hasselbalch equation can then be written as a function of the detected luminescence signals

$$pH = pK_a + \log\frac{I - I_{AH}}{I_{A^-} - I}\,. \tag{3.11}$$

This new form of the Henderson-Hasselbalch equation provides a way to calibrate optical pH sensors. Recording experimentally the detected luminescence intensities of the indicator as a function of the solution pH, a titration curve is obtained which can be accurately described by equation (3.11) and can then be used for calibration purposes.

Figure 3.1 shows a practical example of this procedure, based on data obtained by Willoughby et al., where the luminescent indicator 8-hydroxy-1,3,6-pyrene trisulfonic acid trisodium salt (HPTS) was used [18]. When excited at $457\,nm$, the alkaline form of HPTS emits strong luminescence around $500\,nm$. Conversely, in its acidic form, HPTS is non-emissive. Therefore, in this particular case, in acidic environments the observed luminescence intensity approaches zero. The detected luminescence intensity of HPTS in solutions of different pH (from $pH\,3.8$ to $pH\,8.9$) was registered. The experimental data obtained could then be fitted by equation (3.11), which provides a calibration function, using the following parameters: $I_{A^-} = 3164$, $I_{AH} = 0$, and $pK_a = 7.15$.

While simple in principle, intensity based luminescent pH sensors suffer from several problems. Like any intensity based system, such sensors require the use of some reference mechanism in order to clearly distinguish intensity changes due to pH from power fluctuations originating from any other source (optical source or detector drift, optical fiber bending losses, etc.). In the particular case of luminescent indicators immobilized in a solid host, leaching and photobleaching of the dye are very common problems which can cause severe drift of the optical signals and even limit the useful lifetime of the optical sensor. This way, several techniques have

been used trying to minimize these problems, from ratiometric detection at two distinct wavelengths to time resolved measurements.

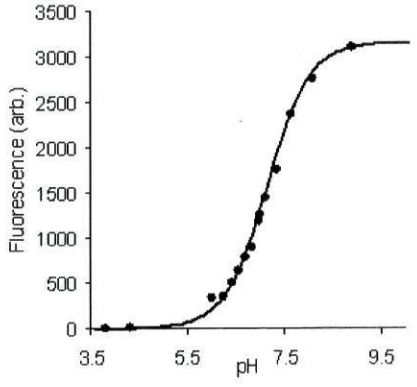


Figure 3.1 Calibration of $500\,mM$ HPTS in $110\,mM$ CsCl. Solutions of $pH\,3.8$ to $pH\,8.9$ were excited at $458\,nm$ and fluorescence $> 505\,nm$ was collected from a $1\,mm$ thick optical slice [18].

Although the calibration procedure presented previously was illustrated with changes in the luminescence intensity, the Henderson-Hasselbalch equation can be rewritten using any parameter which is proportional to the concentrations of the conjugated acid-base indicator pair. Thus, an equation similar to (3.11) can be written using the absorbance of the different indicator species, luminescence intensity ratios at two different excitation or detection wavelengths, or even lifetime values.

3.2.3 Optical fiber pH sensors

The great developments in optoelectronics and optical fiber technology, together with highly motivated research in the fields of indicator and immobilization chemistry, have concurred to important developments in the area of optical fiber biochemical sensing over the last twenty years. Presently, this is an highly developed research field and also a new growing industry. This is particularly true for the specific case of optical pH sensors. Several factors have contributed to this particular success, as the need for new pH sensing technologies in many applications, the wide availability and versatility of luminescent/colorimetric pH indicators, and the prospect of a huge potential market. Although some pH sensors are commercially available, many problems still defy the practical implementation of this optical technology. This way, at present, this is still a very active research field. A vast range of publications can be found on a variety of subjects, from fundamental improvements of sensor performance to state-of-the-art applications in biomedical and environmental fields [2, 13, 19]. In this context, a complete description of the present state of pH sensing technology would be a massive task. Nevertheless, a brief description is given in the

following sections, addressing the most relevant topics of pH optical sensing, which should provide a reasonable overview of the present state-of-the-art.

Immobilization in solid membranes

One of the key steps for the implementation of a luminescence based optical fiber sensor is the successful immobilization of the indicator dye in a solid substrate. In the particular case of pH sensors, this task is particularly challenging since the sensor should establish an equilibrium with an aqueous solution while avoiding the loss of indicator dye and the interference of other ionic species.

There are several methods for immobilization of pH indicators which can be roughly classified in three different categories: adsorption, covalent binding and entrapment.

The adsorption method is the simplest one but probably the least effective. Through electrostatic or hydrophobic interactions, the indicator dye is incorporated in a polymeric solid host. The main problem of this technique is usually a high degree of leaching, where the indicator is lost into the sample solution. Nevertheless, different adsorption-based deposition methods have been developed showing improved features [20, 21]. Layer-by-layer electrostatic self-assembly, for instance, has been demonstrated in the deposition of very thin films (nanometer range) in non planar surfaces [22, 23]. Also, recently, Narayanaswamy et al. [13] have developed a new technique in which the pH indicator is first adsorbed in a resin and then encapsulated in a poly(vinyl chloride) (PVC) porous membrane. The combination of the adsorption and entrapment methods has resulted in a large reduction or even elimination of the leaching of the indicator dye. Leaching can also be avoided using lipophilic polymers. However, since most indicator molecules are hydrophilic, a successful immobilization procedure often requires rendering the indicator lipophilic as well (which demands for further chemical synthesis), or, in alternative, to use ion pairing techniques conjugating the dye with a surfactant or a ionic polymer [24].

In what concerns dye leaching, covalent binding is the most effective immobilization technique, providing the sensor with high stability and superior shelf life. However, chemical procedures associated with these techniques are very often complex and fastidious and most of the time require chemical modification of the sensing dye, which inevitably leads to changes in its spectral properties. In spite of all this, leaching is usually not a problem in covalent membranes. Cellulose based membranes have been widely used for pH sensors based on covalent binding. In addition to being biocompatible, these materials also allow physical entrapment of the dye, making it a very versatile solution [1, 25].

In the entrapment method, the luminescent indicator is physically retained in a polymeric porous substrate. For this to be achieved the indicator dye is usually added to the substrate prior to its polymerization. This is a simple and reliable technique but slow leaching of the dye can be a problem. The porosity of the solid matrix can usually be tailored by controlling the process parameters. However, a compromise must usually be established between sensitivity and degree of leaching [11]. Lobnik et al. [3] compared the performance of aminofluorescein (AF) as a pH indicator using both covalent binding and physical entrapment in sol-gel based membranes. The membrane obtained by entrapment was shown to be an adequate material for sensing pH in terms of response time, relative signal change and stability. However, a small degree of leaching was observed which could become a problem under continuous operation. The covalent membrane, on the other hand, showed an unsurpassed long term stability. However, in comparison with the previous results, sensors based on covalently bound AF displayed relatively smaller signal changes and rather long response times. Improvement of these features would require further modification of the matrix microstructure.

Several different solutions can be found in the literature, using any of the techniques described, some of which have been mentioned in chapter two. Although many of these techniques are effective, there is no universal solution. The optimum parameters of a given immobilization technique are usually dependent on the dye/host combination. In addition, each application has its specific requirements. This way, strong research efforts are still directed towards this particular subject. An example of recent developments can be found in the sol-gel technique. This method allows to fabricate very thin porous glass films which can be used to physically entrap indicator dyes. The high versatility of the process, together with the high compatibility of the optical properties of sol-gel films with optical fibers, made its use in sensing applications increasingly popular [26-28].

Sol-gel is a process by which porous glass materials can be produced at ambient temperature (details of this technique are given in chapter two). The fabrication process is simple and highly versatile, allowing to tailor the properties of the resulting membrane through control of the process parameters. Sol-gel materials can be easily doped with indicator dyes by simply introducing the desired luminophore in the precursor solution. This way, the dye molecules will be physically entrapped in the porous structure of the glass matrix. Membranes produced by the sol-gel method can be used to coat optical fibers and other solid substrates by a variety of techniques (dip-coating, spin-coating, casting). The resulting films are highly compatible with the fiber glass surface, showing very favorable optical properties for sensing applications (refractive index, transmission spectrum). These characteristics have drawn the attention of an increasing numbers of researchers and,

presently, the use of sol-gel based membranes has been reported in a variety of successful luminescence based sensing applications [22-24, 28, 29].

A clear distinction can be made between purely inorganic sol-gel materials, which can produce very thin films with an highly porous structure and hydrophilic properties, and hybrid sol-gel materials where organic and inorganic precursors are mixed. Inorganic based membranes are very effective for use in gas sensing applications, but behave poorly in aqueous environments. In addition, they are usually brittle and crack easily with increased thickness. On the other hand, the use of different ratios of organic and inorganic precursors can produce hybrid materials, also called ormosils (organically modified silicates), with very interesting properties for sensing in aqueous environments. Namely, by controlling the initial composition of this material it is possible to tailor the polarity of the resulting sol-gel surface. Also the mechanical and optical properties of hybrid materials can be modified in a broad range. It is then feasible to produce membranes with different hydrophilic/hydrophobic properties, with tailored mechanical and optical properties which can be controlled to suite the specific applications. The use of these materials was reported to provide very stable pH sensing membranes with minimum leaching [29-31].

Referencing techniques

From the previous discussion it becomes clear that leaching is a common problem of many pH sensing membranes. In addition to this difficulty, photobleaching of the sensing dye is also very frequent in luminescence sensors in general. Both phenomena can strongly hinder the long term application of a luminescence based sensor. In addition, when simple intensity measurements are performed, any change in the luminescent output can introduce serious measurement errors. This way, in order minimize the impact of leaching and photobleaching of the dye, drifts of the optical source/detector and any other variable losses in the fiber system, some sort of referencing scheme must usually be applied.

Due to their acid-base properties, pH indicators typically present dual absorption and/or emission bands; for this reason, ratiometric detection schemes are very popular in this field. Depending on the sensing dye properties, different configurations are possible. One possibility is to use one emission and two excitation wavelengths [32]. This method can be used with most indicator dyes; however, it requires the excitation at two different wavelengths (with the dye showing different absorption responses to pH in each spectral region). This demands the use of two excitation sources and some switching scheme in order to obtain the two signals with a single detector. This scheme is also popular for use with absorption dyes; in such case the reference source is used in a region

where the dye is non absorptive. Although it requires some additional complexity in the excitation/detection scheme, the ratio of the two signals is usually independent of any optical power drift, allowing for long term operation [33].

In alternative, for those sensing dyes displaying different emission bands in alkaline/acidic media, a scheme using one excitation and two emission wavelengths can be implemented. With this technique a single excitation source is needed. On the other hand, detection must be performed using spectral discrimination. As long as photobleaching affects both species (acid and alkaline) in the same way, this scheme is also very effective in eliminating dependence on the optical power level. Recently, Song et al. have demonstrated the possibility of performing drift free pH measurements, in biological fluids, using optical fiber microoptodes coated with a dual-emission sensing dye and ratiometric detection [34].

In spite of providing some stability to the sensor calibration, any ratiometric schemes will only work as long as a measurable signal is available. This way, severe photobleaching and leaching will gradually degrade the sensor signal-to-noise ratio (SNR) limiting its useful lifetime of application. Time resolved measurements are an appealing alternative to ratiometric schemes. Lifetime is an intrinsic property of the excited luminophores and it is independent of both the indicator concentration and the intensity of the excitation light. In addition, the use of pulsed or modulated excitation usually allows operation with lower levels of excitation optical power, reducing the degree of photobleaching.

While direct lifetime measurements require very expensive instrumentation, frequency domain detection can often be implemented using lower cost optoelectronics. This technique requires excitation with a sinusoidally modulated optical source. In this situation, the luminescence output of the sensing dye will be a sinusoidal signal, with the same frequency as the excitation signal, but presenting a time delay which is proportional to the excited state lifetime and, therefore, proportional to the analyte. With adequate instrumentation, the time delay can be measured as a phase shift which will be proportional to the pH level[22]. For this to happen, however, it is required that both acidic and alkaline forms of the indicators emit and that their decay times are different so that the change in pH will change the relative contribution of each form to the overall decay. If only one form emits, then the measured lifetime would be that of the emitting species, independent of the pH. In addition, long lived dyes must be used as they allow interrogation using relatively low modulation frequencies. Typically, the dye lifetime should be in the hundreds of nanoseconds range

[22] Further details of frequency domain spectroscopy are given in chapter two

in order to allow the use of modulation frequencies under $1\,MHz$ [23]. While such frequency range can be implemented using relatively low cost optoelectronics, higher modulation frequencies will greatly increase system complexity. Unfortunately, such constraints strongly reduce the number of available pH sensing dyes suitable to apply frequency domain interrogation.

In this context, there is presently a substantial research effort directed towards the synthesis of new long lived and more photostable pH indicators. Recently, highly luminescent metal organic complexes have been shown to have highly suitable characteristics for luminescence sensing applications (high quantum yields, relatively high photostability and very long lifetimes - microsecond range)[35]. In particular, ruthenium based dyes have been used extensively in intensity based and frequency domain luminescence oxygen sensors [8, 36]. While these dyes are readily quenched by molecular oxygen, they are generally insensitive to pH. However, by attaching a pH sensitive group to a metal complex its emissive properties can become responsive to changes in the acidity level. This was demonstrated by Clarke et al. [37], by introducing a dicarboxy ligand in a ruthenium complex. The authors demonstrated that both the luminescence intensity (peak at $625\,nm$) and the excited state lifetime ($\tau \sim 600\,ns$) of the new dye are highly sensitive to pH changes in the $pH\,2 - pH\,5$ acidity range. Murtaza et al. produced a similar ruthenium dye with a pK_a around 7.5, therefore suitable for biological applications [38]. A common problem with ruthenium based dyes, however, is their cross sensitivity to oxygen. This means that for univocal determination of pH, the oxygen concentration must be known as well. Nevertheless, in many biomedical applications, pH, oxygen, and other parameters must be measured simultaneously. In this context, the need for an additional oxygen sensor together with the pH sensing device is not a major disadvantage. In alternative to synthesize new pH indicators, long lived pH insensitive dyes can have their lifetime become dependent on acidity level when used in combination with a colorimetric indicator. In such case the lifetime change is induced by resonant energy transfer between the long lived luminescent indicator and the absorbing dye [39]. Also Wolfbeis et al. have developed a technique where the combination of a short lived luminescent indicator with a long lived luminescent reference dye allows to perform time domain interrogation at relatively low frequencies [40].

[23] Typically, the ideal modulation frequency, f, is approximately given by $f = 1/2\pi\tau$, where τ is the excited state lifetime of the luminescent dye.

pH range and ionic strength

Comparatively to electrochemical sensors, which have a linear response in practically the full pH scale, optical sensors have a limited operation range (typically ± 2 pH units around pK_a). Although this limitation is somewhat compensated by increased sensitivity, in many applications a broad operation range is mandatory. Therefore, many attempts have been made to increase the dynamic range of optical pH sensors.

Several authors have demonstrated that the combination of different pH indicators with different pK_a can be used to obtain an optical response to pH in an increased acidity range. Different solutions were reported where the different indicators were either used as an array of sensors or were co-immobilized in the same sensing matrix. However, in early approaches to this method, the response of the obtained sensor was sometimes highly non-linear.

More recently, Lin and Liu [41] reported a linear operation in an extend pH range. In their method, the requirements on the different pH indicators, such as ΔpK_a between the indicators and color of the indicators, were carefully considered. In addition, the ratio between the indicators concentrations was optimized by computation. The authors used this technique to develop a sol-gel glass pH sensor by co-entrapping three pH indicators (bromocresol green, bromocresol purple and phenol red), which had linear response over a range of 3.5 pH units, from $pH\,6.3$ to $pH\,9.8$ [42]. In a similar approach, different authors obtained linear response for a dynamic range of 8.5 pH units from $pH\,4.5$ to $pH\,13$.

A set of new pH indicators based on ruthenium complexes has been characterized which, upon immobilization in sol-gel membranes, displayed an increased dynamic range [43]. Trying to avoid the use of multiple sensing dyes, Barragán and coworkers [44] explored the fact that the pK_a of the sensing dyes is affected by the host matrix properties. Using the sol-gel technique, several membranes were produced suitable for operation at different pH ranges. This was achieved by co-immobilization of the same mercurochrome based luminescent indicator with different kinds of surfactants. Using three of such mercurochrome pH sensing membranes, each of them covering a different range of acidity, reversible sensing between $pH\,1$ and $pH\,9$, with response times in the order of about $1\,\mathrm{min}$, could be accomplished.

Unlike electrochemical sensors which are based on changes in ion activity, the response of optical pH sensors is correlated to changes in indicator concentrations. While in dilute solutions this poses no problems, using optical pH sensors in media of high ionic content can introduce serious errors. At high ionic strengths the concentration can differ strongly from ion activity, changing the apparent pK_a of optical indicators. If the sensor is used in media of constant ionic strength (IS),

appropriate corrections can be made, provided calibration is performed in similar conditions. However, in many real samples the electrolyte concentration is not constant and cross sensitivity towards ionic strength must be accounted for. In spite of this problem, papers addressing this problem are very rare. Sensitivity towards ionic strength is dependent on the ionic nature of the indicator itself and also on the immobilization material. Highly charged indicators are more sensitive to changes in IS. Using a charged indicator in a neutral host environment provides a strong response to IS. If, on the other hand, the indicator is immobilized in an highly charged environment, its cross sensitivity towards IS will be minimal. Using the combined response of two such sensors, some authors have been able to monitor IS and pH simultaneously. However, this was achieved at the expense of higher complexity and additional calculations [45, 46].

More recently, Weidgans et al. [47] have proposed several schemes where the same dye, or two different dyes, were immobilized in differently charged microenvironments within the same host matrix. The combined response of the resulting sensing membrane showed a remarkable independence towards IS, in a broad range of ion concentrations.

One of the attractive features of optical pH sensors is the possibility of operation in very acidic and basic ranges, either between pH $10-14$ where glass electrodes suffer from errors and chemical deterioration, or at $pH < 1$ where there are also large errors. Cellulose and sol-gel glass have been used in the development of pH sensors for high acidity and alkalinity by several groups of researchers [13, 48].

Applications

In spite of many problems, the intrinsic advantages of optical pH sensors are being explored in a wide range of practical applications, from medical instrumentation and industrial process monitoring to environmental surveillance.

In the work of Kopelman and colleagues [49], nanometer scaled sensing probes were constructed by heating an optical fiber using a focused CO_2 laser beam, and then pulling the heated region until the fiber acquired a tapered shape and eventually the tip narrowed down to nanometer dimensions. A pH sensitive dye was then immobilized on the tip of the fiber probe by photopolymerization of an appropriate polymer precursor solution. The developed nanosensors were later used to perform pH measurements of 10 and 12 day rat embryos [50]. Similar technology was adapted by different authors for application in high resolution intracellular microscopy [51].

The determination of pH in different clinical applications was already demonstrated. Although the application of optical sensors in this field faces some additional challenges, like the need for

biocompatibility, the use of materials which can withstand sterilization, etc., some successful examples can be found. The first intravascular sensor for pH determination was demonstrated as a multiparameter sensor, where pH, pO_2, and pCO_2 were simultaneously measured using three optical fibers ($125\,\mu m$ diameter). This sensor was developed for commercial application by CDI-3M Health Care (Irvine CA, USA) on the basis of a system designed and tested by Gehrich et al. [35]. The three fibers were encapsulated in a polymer host having a thermocouple embedded for temperature monitoring. The pH measurement was carried out by means of the luminescent indicator, hydroxypyrene trisulphonic acid (compatible with ratiometric detection), covalently bonded to a cellulose matrix attached to the fiber tip [52]. Although pH could be measured, showing a good correlation with standard electrochemical sensor, major biocompatibility problems were detected (a thrombus formed around the sensor tip interfering with the response of all the three sensors). The problem could be avoided using the sensor in an external blood circuit. Also in the medical field, gastric pH measurements in real patients were performed by Baldini et al. using similar technology [1, 53].

Monitoring and controlling pH level of cultured biological fluids is a critical step for the successful operation of bioreactors. Measurements of pH in the cell culture should be performed without compromising the system sterility, preferably without sensor recalibration or substitution during the whole operation period. In a very simple approach, the suitability for optical pH sensors to perform such tasks was demonstrated by Jeevarajan et al. [54]. pH was monitored continuously in a perfused bioreactor system using an optical fiber system. In this particular case, the pH indicator, phenol red, was not immobilized in a solid host, instead, it was dissolved in the culture medium. The system was initially calibrated and then used continuously for 124 days during which it showed adequate performance.

Optical fiber pH sensors are also very attractive for environmental monitoring due to their ability of in situ, remote and underground sensing. The suitability of optical pH sensors to monitor the acidity of groundwater was demonstrated successfully in the laboratory and in many field applications [55, 56].

The possibility to perform quasi-distributed pH sensing is also very appealing for monitoring the pH level in extended areas, either in environmental applications, like acidity control in pools or lakes, or in industrial environments for corrosion control at multiple points of complex structures. Distributed optical fiber pH sensors are usually evanescent wave sensors fabricated by coating a pH sensing layer on sections of exposed fiber core spaced over the length of the fiber. Different systems were developed using either luminescent or absorption based indicators. In both cases the position

information is determined from the propagation delay of the returning signals. Although luminescence based signals operate with increased sensitivity, usually the finite lifetime of the luminophore limits the spatial resolution of the system [14-16].

Due to their versatility, pH indicators are also used for determination of different analytes. Numerous optical sensors for gases, such as CO_2 and NH_3, have been developed on the basis of pH sensors. The sensing principle is based on the fact that these gases change the media acidity level. This way, using appropriate membranes which are gas permeable but do not allow proton diffusion, measurements of gas concentration can be performed based on changes of the spectral properties of the pH indicator [57, 58]. In addition, because these particular gases are the product of some enzymatic reactions, pH indicators could be used to monitor enzyme activity. Because pH is also modified by other biological processes, other metabolites of clinical interest, such as penicillin, creatinine, glucose, and urea, have been determined by use of multianalyte optical sensors based on pH-transduction [59].

Due to their proton donor ability, pH indicators have often been used for determination of other ionic species like heavy metal ions. The detection of metal ions can be performed using ionophores[24], molecules that bind selectively to some ionic species. However, the immobilization of ionophores is often performed in lipophilic membranes to avoid leaching. In this situation, in order to establish equilibrium with the sample solution, the ionic analyte can only be driven into the host membrane if either a counter ion is inserted into the membrane, or if an ion of equal charge is released from it. Frequently, protons are involved within this process and pH indicators are integrated into the membrane acting as transducers [60, 61]. Although cross sensitivity to pH can become a problem, this can be overcome by simultaneous measuring the sample pH. More recently, pH-independent sensing schemes based on co-extraction of a colored counter ion were developed [62].

In spite of the many challenges it still faces, the usefulness of optical pH sensing technology is clear in a diversity of domains. The versatility of many pH indicators allow developments which go beyond simple pH measurements and allow sensing applications of metal ions and biological species. For these reasons, an approach to the field of optical fiber biochemical sensing would not be complete without addressing some practical aspects of this technology. Thus, in the following sections, several results obtained in the context of optical pH sensing are described. The work

[24] The term ionophores is used to describe ligands that selectively bind ions. Typically, ionophores are macrocyclic molecules with an ion binding cavity. These molecules are often called metal chelators. Some of these chelators where designed to change color when they bind to the metal ion. In this case they are also called chromo-ionophores.

presented was performed on an purely exploratory basis, in order to obtain experience on the implementation of luminescence based sensors, to become aware of the main problems associated with this technology and to identify potential innovation opportunities. This way, a sample of results is shown referring to different problems addressed, from test and comparison of different immobilization techniques to several intensity and lifetime based detection schemes.

3.3 Membranes for pH sensing

Despite some particular situations where the sensing indicator can be dissolved in the sample solution, the practical implementation of an optical fiber pH sensor requires prior immobilization of the optical indicator in a solid host material. From the earlier discussion it becomes clear that a wealth of different materials for optical sensor immobilization is presently available. The choice of the most adequate dye/host combination depends on the particular application and it must be carefully considered as, very often, the indicator properties are affected by the host environment. In the end, each dye/host arrangement results in a sensing membrane with unique characteristics. Therefore, this is a critical step in sensor implementation. Because this is true for all luminescence based optical fiber sensors in general, there was the need, in an initial stage, to acquire some experience in different methods of immobilization of indicator dyes. Therefore, with the collaboration of the Chemistry Department of FCUP, different immobilization methods were tested and compared, using luminescent pH indicators. Some of the most important results obtained are presented in the following sections.

3.3.1 pH indicator

Although different luminescent pH indicators were used in the present work, for the initial characterization of the different sensing membranes a single luminescent indicator was used. This way, all immobilization materials tested were doped with 5(6)-carboxynaphtofluorescein (CNF), purchased from Fluka (ref. 21932). This dye belongs to a group of indicators called semi-naphthofluoresceins (SNARF). These indicators were designed to have pKa values in the physiological range, and exhibit distinct emission bands for the protonated and deprotonated forms, so that emission ratio measurements are possible. CNF, in particular, was obtained by addition of an extra phenyl ring to the original SNARF structure, which results in a red shift of the absorption/emission spectra and is conjugated with a carboxyl group, which increases retention in cells making it suitable for *in vivo* applications. The structural formula of CNF can be observed in Figure 3.2.

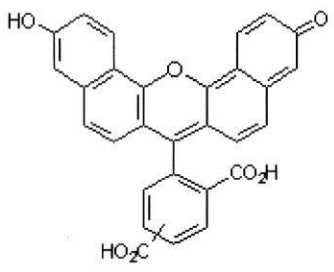


Figure 3.2 Chemical structure of the luminescent pH indicator 5(6)-carboxynaphthofluorescein (CNF).

CNF has a pK_a of 7.6 and, therefore, its luminescence response to pH is maximum around the physiological range ($pH\,6.0$ to $pH\,8.0$). It has strong absorption bands at $500\,nm$ (acid) and $600\,nm$ (alkaline), making it suitable to LED and diode laser excitation. In this particular dye, both the acid and alkaline forms fluoresce, but in different spectral regions. In its acidic form, CNF presents an emission band with its peak at $570\,nm$. When in alkaline environments, however, it displays strong luminescence emission around $670\,nm$. Since both acid and alkaline forms of the dye suffer similar degree of photobleaching, in this particular case, performing ratiometric detection can minimize the effect of dye photodegradation. The use of CNF as ratiometric indicator was already demonstrated, with measurements performed in biological samples with good reproducibility [34].

In all the results presented in this chapter, the response to pH was always tested using standard buffer solutions[25] with acidity ranging from $pH\,2$ to $pH\,10$. These solutions of constant ionic strength were prepared following standard procedures which will not be described. By dilution of CNF in such solutions it was possible to measure the response of the sensing dye to changes in acidity level. A He-Ne laser was used to excite the alkaline band of CNF. Excitation was performed through an optical fiber and detection of the luminescence emission was achieved using a CCD spectrometer (Spex-3D Horiba-Jobin Yvon). The results obtained, after correcting for backscattered laser radiation, can be observed in Figure 3.3.

---

[25] Buffer solutions are solutions which resist changes in pH level, upon addition of small amounts of acid or base, or upon dilution. Typically, buffer solutions consist of a weak acid and its conjugate base. The steady response is the result of the equilibrium between this acid/base pair ($HA_{(aq)} \rightleftharpoons H^{+}_{(aq)} + A^{-}_{(aq)}$). Any other base added to the solution is consumed by hydrogen ions. These ions are then mostly regenerated as the equilibrium moves to the right and some of the acid dissociates into hydrogen ions and the conjugate base. If a strong acid is added, the conjugate base is protonated, and the pH is almost entirely restored. Therefore, by definition, buffer solutions have a constant ionic strength. Buffer solutions play an important role in Nature as they are necessary to keep the right pH for enzymes, which typically operate in a very narrow pH range. For instance, in the human body a buffer of carbonic acid (H_2CO_3) and bicarbonate (HCO_3^-) is present in the blood plasma, to maintain a pH between 7.35 and 7.45.

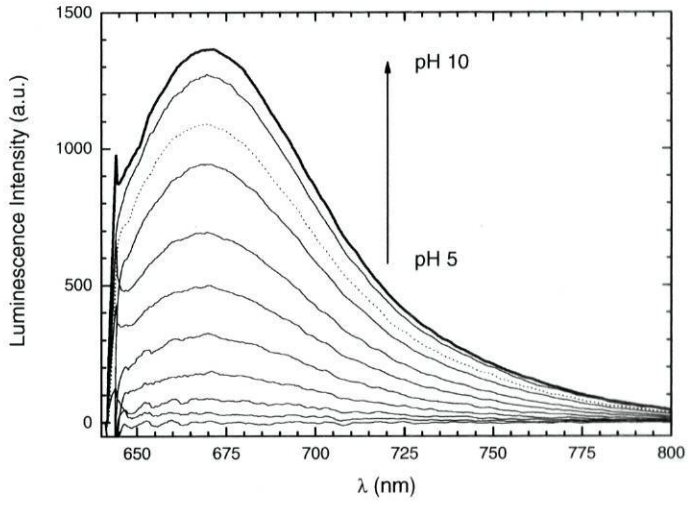


Figure 3.3 Alkaline band of CNF at different acidity levels. Excitation performed at $633\,nm$ **.**

The emission spectra obtained from buffer solutions with pH changing from $pH\,5$ to $pH\,10$ show a clear dependence on the acidity level. Because this is the alkaline band of CNF, the intensity of luminescence, which has its maximum at $670\,nm$, strongly increases as pH is increased. Plotting the integrated luminescence intensity as a function of pH, the typical sigmoidal response, described by the Henderson-Hasselbalch equation, could be obtained, as shown in Figure 3.4 (a).

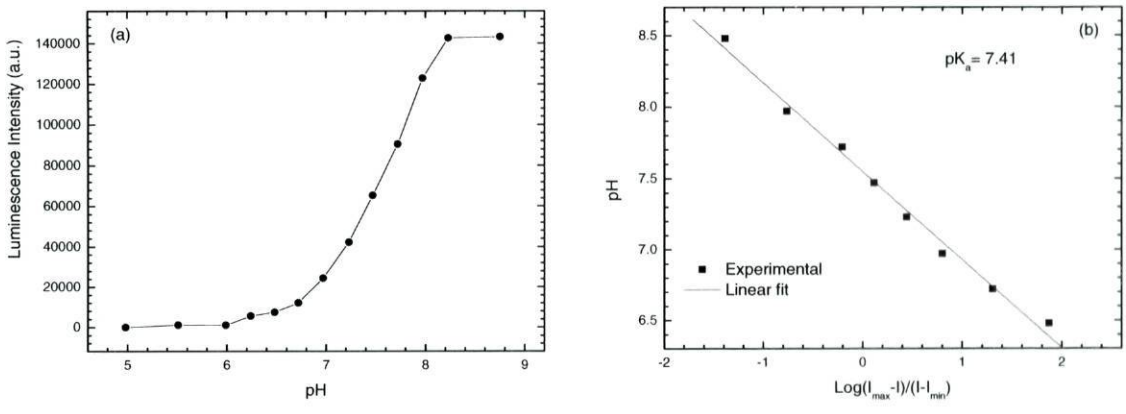


Figure 3.4 (a) Luminescence intensity response of CNF alkaline band as a function of solution pH. (b) Linearization plot used to estimate the pKa **of the luminescent indicator.**

The graphical representation of pH as function of $\log[(\mathrm{I_{max}} - I)/(I - \mathrm{I_{min}})]$, shown in Figure 3.4 (b), was then used to estimate the pKa value. From the obtained data $pK_a = 7.41$ could be estimated, which is in agreement with values reported by the manufacturer. Similar results could be obtained with the CNF acid band as long as the excitation was performed at lower wavelengths ($400\,nm - 500\,nm$). In this particular case, however, the luminescence emission (peak at $580\,nm$) was maximum at low pH and decreased strongly as the acidity decreased. During some tests performed

using the excitation lamp of the CCD spectrometer (Xenon), it was observed that the yellow luminescence band of CNF had much lower quantum yield than its alkaline counterpart. In spite of this, in some of the membranes tested, pH measurements were performed using both emission bands.

3.3.2 PVA

Polyvinyl alcohol (PVA) is a polymer with hydrophilic characteristics, which is therefore suitable for pH and ion sensing. Due to its ability to form high quality homogeneous films, it can be applied as a solid support for luminescent indicator dyes. The properties of PVA based membranes depend on its molecular weight and degree of hydrolysis. In order to maintain stability in aqueous solutions, PVA must be cross-linked. Some of the common cross-linking agents that have been used for PVA membrane preparation include glutaraldehyde, acetaldehyde and formaldehyde.

In order to evaluate the properties of PVA as an immobilization membrane for optical fiber sensing, a procedure reported in the literature to prepare PVA based membranes (cross-linked with glutaraldehyde) was followed [63, 64]. In the original paper cyanuric chloride was used to couple the luminescent indicator, fluoresceinamine, to PVA which was then cross-linked with glutaraldehyde in the presence of an acid (HCl), which acted as a catalyst. By this method the indicator was covalently bonded to PVA prior to the cross-linking step. In addition, the rate of the crosslinking reaction could be controlled by varying the amount of acid catalyst. This way, the process could be adjusted so that the rate of cross-linking was sufficiently slow to allow the glutaraldehyde/PVA solution to be manipulated as a liquid prior to the deposition step. In the particular case reported here, however, some adjustments were made in order to immobilize CNF as the pH indicator.

Membrane fabrication

The first step in the preparation of the PVA membrane was to dissolve $5\,g$ of PVOH [poly(vinylalcohol)] (Fluka, ref. 51438) in $50\,mL$ of H_2O. The resulting solution was then placed in a bath at a constant temperature of $80\,^{\circ}C$. Stirring was applied for $2\,h$. The stock solution was filtered and $0.5\,mL$ were then combined with $50\,\mu L$ of 2% aqueous $C_5H_8O_2$ (glutaraldehyde) (Fluka, ref. 49629) and $50\,\mu L$ of HCl $4\,M$. Doping of the membrane was achieved by addition of a $50\,\mu L$ solution of CNF dissolved in acetone. Following this procedure the indicator was physically encapsulated in the polymeric host matrix.

Variations of this procedure were applied trying to assess the influence of some process parameters like the amount of glutaraldehyde used or the concentration of sensing dye. Some

membranes were produced without indicator in order to evaluate the material's physical characteristics. Small moulds were used to produce disk shaped membranes ($5\,mm$ diameter, $1\,mm$ thick). Attempts were made to fabricate pH sensing fiber probes by dipping the fiber tip into the precursor solution.

Some physical properties of the membranes produced, like elasticity, robustness, and degree of doping (color) were evaluated by direct observation. The response to pH was tested by immersing the membranes in buffer solutions with different degrees of acidity. In a first stage, the response to pH was evaluated by visual observation of the membrane color when placed in solutions of extreme pH ($pH\,4$ or $pH\,9$). The degree of leaching was also evaluated by immersion of the membranes in the buffer solution for periods of up to $24\,h$. Following this period the buffer solutions were checked for traces of indicator dye.

At a later stage, deposition of PVA sensing membranes on the tip of optical fibers was also tested. Using an optical fiber system, the luminescent response of some of the membranes with best characteristics was evaluated as a function of the pH of several buffer solutions.

Results

Following addition of glutaraldehyde and HCl the polymerization process was very fast (4 min to 8 min) and a clear transparent gel was formed. Any deposition process aiming to produce a sensing film would then had to be concluded within this time window. The PVA membranes obtained following the described procedure were generally very robust and elastic and were not easily damaged, even though some swelling was observed in aqueous environments. It was observed that the amount of glutaraldehyde had influence on the solidification time and degree of cross-linking of the resulting membrane. Higher contents of glutaraldehyde lead to faster solidification, and reduced the swelling of the membranes in aqueous environments, indicating increased cross-linking.

Doped membranes presented strong blue color when in alkaline media and a pink coloration in acidic media (Figure 3.5). A reversible color change was observed when the membranes were placed alternatively in acid and alkaline buffer solutions.

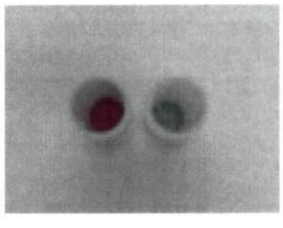


Figure 3.5 PVA+CNF membranes in equilibrium with acidic (pink) and alkaline (blue) media.

The strong change in the color of the membrane indicates a clear change in its absorption spectrum which, in this particular indicator, will translate into different luminescence emissions.

While some leaching was observed in membranes with a smaller degree of cross-linking, the problem could be fixed by increasing the amount of glutaraldehyde. This resulted in membranes with higher degrees of cross-linking, where there was no apparent leaching of the sensor into the buffer solutions even after the sensor was left in alkaline or acid buffer solutions for periods of several days.

The luminescence response of the PVA membranes was also tested. The same membrane was successively immersed in buffer solutions of different pH, while it was excited by a HeNe laser ($632.8\,nm$). Because the excitation was performed in this region of the spectrum, only the alkaline band of CNF could be observed ($670\,nm$). The luminescent emission was recorded using a CCD spectrometer. As expected, it was observed that the luminescence intensity was strongly enhanced as the pH of the buffer solutions was increased. The response time of the sensors produced was evaluated by monitoring the luminescence intensity of CNF alkaline band while changing the pH between $pH\,5$ and $pH\,10$. It was observed that while leaching membranes responded very fast ($1\,\text{min} - 2\,\text{min}$) to these pH changes, in membranes with higher degree of cross-linking response times could go up to $30\,\text{min}$. Therefore a compromise must be established between sensitivity/response time and degree of leaching.

The doping concentration of the dye was changed between $0.1\,mM$ to $1.6\,mM$. It was verified that in the lower range of this interval the increase in sensor concentration resulted in a linear increase of the luminescence intensity (at a fixed pH). However, in the upper range inner filter effects produced a decrease on the luminescence output with increased concentration. Otherwise, the concentration of the dye had no noticeable influence in the polymerization process.

In spite of some appealing characteristics, this immobilization material had a serious problem regarding its implementation in a fiber optic system. The adhesion of the solid membrane to the fiber core was weak. No uniform films could be formed on the fiber surface by dip coating. In addition, immersion of the fiber in buffer solutions often resulted in detachment of the sensing membrane from the fiber surface. In spite of these difficulties, several tests were performed using extrinsic membranes interrogated by an optical fiber system. Some of the results obtained will be presented in section 3.4.

3.3.3 Polyacrylamides

Photochemical or photo-initiated polymerization occurs when radicals are produced by ultraviolet and visible light irradiation of a reaction system. In general, light absorption results in radical production when a given compound in the system undergoes excitation by energy absorption and sub-sequent decomposition into radicals; conjugation of these free radicals with a monomer molecule will produce a chain initiating radical which will originate polymer fibers by successive addition of monomer molecules. Photo-initiation offers several advantages. Polymerization can be spatially directed being confined to specific regions, or turned on and off by switching the polymerization light source. Such systems are widely used in industry for a variety of applications and present interesting characteristics for design of optical sensing membranes [65].

Photo-polymerization of acrylamide in the presence of triethylamine (the photo-initiator) results in a highly cross-linked polymer with highly hydrophilic characteristics. When the polymerization process is initiated in the presence of a previously silanized glass surface, the resulting polymeric membrane can be covalently linked to the glass surface. pH sensitive membranes were produced using such system by Song and coworkers [34]. Photo-polymerization was performed through the optical fiber using a laser source (Argon laser line $488\,nm$). The radiation was guided to the distal fiber end, which was dipped in the polymer solution. This way, a polymer membrane could be formed on the fiber tip. The membrane was rendered pH sensitive by doping a polyacrylamide solution with CNF prior to the photo-polymerization process. The resulting fiber optodes were successfully used to monitor pH in some biological samples.

In order to evaluate the immobilization system just described and compare it with the other techniques tested, some membranes were prepared following the procedure described in Songs' work.

Membrane fabrication

The polymerization solution was prepared mixing $2.70\,g$ acrylamide (Fluka, ref. 01696) and $0.30\,g$ of N,N-methylenebis(acrylamide) (Aldrich, ref. 148326) in $7\,mL$ $0.1\,M$ phosphate buffer ($pH\,6.5$). $1\,mL$ of the solution obtained was then combined with $40\,\mu L$ $C_6H_{15}N$ (triethylamine) (Fluka, ref. 90335). In the presence of this photo-initiator the polymerization of polyacrylamide gel could then be photo-induced by a blue light source ($430\,nm$) (Hilux Curing Light 200). In different assays, different amounts of CNF (between $2.20\,mg$ and $14.00\,mg$) were added to the polymerization solution producing membranes with different degrees of doping.

Immobilization of CNF using the acrylamide membranes was tested both in extrinsic and in fiber probe configurations. For the extrinsic membranes the polymerization process was executed in small disk shaped molds (the same ones used for the PVA membranes). The curing light source was then applied to both sides of the mold until full polymerization was achieved.

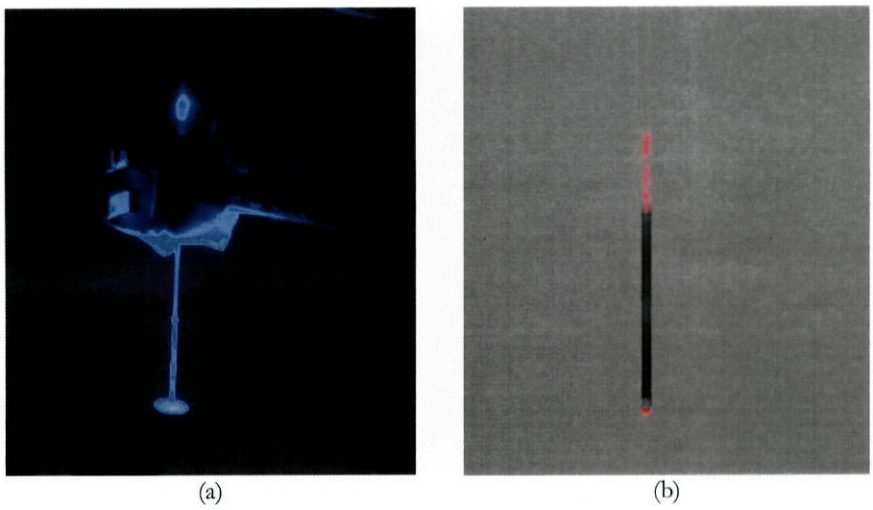
In the case of immobilization in the fiber probes an additional procedure was necessary in order to obtain adhesion of the polymer membrane to the surface of the optical fiber. The sensing fiber tips were carefully polished and cleaned. In some of the probes the cladding of a section of the fiber tip was removed by chemical etching using hydrofluoric acid. This way, excitation/detection could be performed in an extended surface of the fiber.

The prepared glass surfaces of the fiber were then silanized for $75\,\text{min}$ in a 2% solution of 3-(trimethoxysilyl) propyl methacrylate (Sigma, ref. $M6514$) in $pH\,3.45$ water and then dried overnight in a nitrogen atmosphere. Undergoing hydrolysis and condensation reactions, the 3-(trimethoxysilyl) molecules were covalently bonded to the glass surface. In addition, at a later stage during the polymerization process the free ligands of these molecules established covalent bonds with the polyacrylamide molecules. Following this procedure the polyacrylamide membranes could be covalently bonded to the silica surface of the fibers.

In order to produce the sensing membranes on the fiber surface, the fibers were immersed into a glass capillary, with internal diameter of $1\,mm$, filled with polymerization solution and illuminated with the curing light. After photo-induced polymerization the membrane was bound to the silanized core but not to the glass capillary, which was easily removed. Figure 3.6 shows a fiber probe being submitted to the photo-polymerization process (Figure 3.6 (a)), and the resulting fiber probe being excited by a HeNe laser (Figure 3.6 (b)).

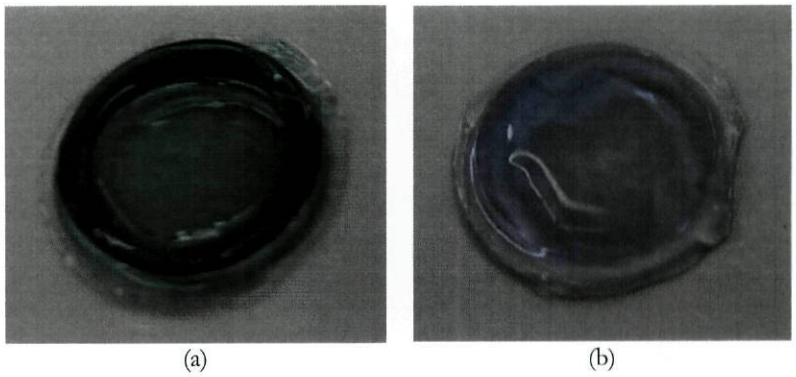
Results

When immersed into different buffer solutions, the polyacrylamide sensing membrane showed a fast ($< 1\,\text{min}$) and reversible response to pH changes in the surrounding medium. Both the color and the fluorescent emission of CNF changed according to pH. A little leaching was observed and it occurred mainly when the sensor was immersed in alkaline solutions. Due to the covalent bonds, adhesion to the fiber core was relatively strong. However, in its hydrated form, the membrane was soft and could be easily damaged. The gel consistency of the sensing membranes and their response to pH changes can be observed in pictures taken right after the membrane fabrication (Figure 3.7 (a)), and after the membrane established an equilibrium with an alkaline buffer solution (Figure 3.7 (b)).



(a) (b)

Figure 3.6 (a) Photopolymerization of acrylamide membranes on an optical fiber using a blue curing lamp. (b) resulting fiber probe excited by a HeNe laser.



(a) (b)

Figure 3.7 Acrylamide membranes doped with CNF. (a) after fabrication; (b) in equilibrium with alkaline buffer solution.

By increasing the amount of acrylamide in the initial solution, from the original 27% to 35% (molar percentage), the degree of leaching could be greatly reduced. After an initial washing step where any unbound indicator was removed, no leaching was apparent even after several days storage in alkaline buffer solutions. In addition, after this period the membrane still responded reversibly to changes in the solution pH. Nevertheless, probably due to an increased degree of cross-linking, response times were slower (minutes). It was also verified that the duration of irradiation and the amount of photo-initiator interfered in the membrane properties. If the amount of added triethylamine was reduced below $30\,\mu L$, no stable membrane could be formed even after very long irradiation times. By adding $40\,\mu L$ of the photo-initiator solution, however, it was found that membranes with optimized properties could be obtained after 10 min total irradiation time. Reduced irradiation times resulted in fragile membranes with high degree of leaching; conversely, increased

exposure times resulted in brittle membranes with poor hydration and very slow response to acidity changes.

Although some external membranes with very good characteristics for pH sensing could be fabricated by molding, their deposition on the surface of the optical fiber faced some difficulties. Using the fabrication procedure described above, good quality films were obtained on the lateral surface of the fiber (see Figure 3.6 (b)). However, the end of the fiber tip could not be efficiently coated. In an attempt to coat the fiber end face, the radiation from a blue laser ($473\,nm$) was guided into the fiber. By this method a small polymeric membrane could be formed on the fiber end face. However, its adhesion to the glass surface was poor and the sensing layer could be easily removed by accident during the tests. Another problem arising from the fabrication procedure of this membrane was that photo-polymerization with blue radiation contributed to premature photo-degradation of the sensing dye. As a result of these difficulties, the luminescent signals detected through the fiber were very faint, resulting in poor signal-to-noise ratio.

In spite of all these problems, some tests could be performed using some of the external membranes. Several measurements of the luminescent response as a function of pH indicated that the sensing membranes pK_a was around 7.2. Although this value is slightly lower than the one obtained in solution, this result is probably due to the reduced SNR of the acrylamide probes, which increased data dispersion. However, the spectral response of CNF when immobilized in acrylamide membranes was found to be very similar to the response observed with the PVA based probes.

3.3.4 Sol-gel

The suitability of sol-gel based materials for optical sensing applications has long been recognized. Besides being a simple and versatile process, allowing to tailor many of the properties of the resulting porous glass, these materials can present optical and physical properties which are highly compatible with optical fibers. In this work, different sol-gel materials were used to produce several pH sensing membranes. Both inorganic and ormosil precursors were used. A brief description of the results obtained is given in the following subsections. Additional results, where these pH sensing membranes were used to implement different interrogation techniques, will be described in the next section.

Membrane fabrication

For fabrication of inorganic sol-gel membranes the following procedures were applied.

TEOS solution: Sol-gel solutions were prepared by mixing $2\,mL$ of tetraethoxysilane (TEOS) (Aldrich, ref. 23,620-9), $25\,\mu L$ of phenyltriethoxysilane (Ph-TriEOS) (Aldrich, ref. 17,560-9), $2.5\,mL$ of deionized water and $0.80\,mL$ of $0.1\,M$ HCl. The mixture was stirred at room temperature for $25\,\text{min}$. A specified amount of the pH indicator was then dissolved in ethanol and added to the sol-gel solution prior to the coating and gelation processes.

TMOS solution: A different solution was prepared by combining $1\,mL$ of tetramethoxysilane (TMOS) (Fluka, ref. 87680), $1.2\,mL$ of methanol, $0.74\,mL$ of deionized water and $0.16\,mL$ of $0.1\,M$ NaOH. The mixture was stirred at room temperature for $40\,\text{min}$. An ethanol solution with a specified amount of a pH indicator was then added to the sol-gel precursor solution.

Different hybrid materials were also used where a wide diversity of precursors combinations were tested. Some of the best results were obtained with the following procedures. The organic precursor TEOS was combined in a $1:1$ molar ratio with different hybrid sol-gel precursors containing an organic component. Different solutions were produced combining TEOS and one of the following ormosils: methyltrimethoxysilane (MTMOS), isobutyltrimethoxysilane (BTMOS) or phenyltrimethoxysilane (PTMOS). All ormosils were acquired from Aldrich (ref. 246174, 444065, 104744, respectively). In all cases the sensing dye (CNF or others) was dissolved in ethanol and was incorporated in $85\,\mu L$ of a TEOS solution. The volume ratio of the silanol solution and the doped ethanol solution was always $1:3.6$. The addition of $29\,\mu L$ of HCl $0.1\,M$ and $40\,\mu L$ of H_2O would then start the polycondensation/hydrolysis process, which eventually lead to polymer formation. Stirring was applied for at least $20\,\text{min}$ in order to obtain a homogeneous precursor solution.

Thin films were produced by casting or spin coating on glass slides using solutions with different aging times. Different optical fiber probes were also produced by dip-coating.

Results

The membranes fabricated with inorganic sol-gel precursors produced very poor results. Although a porous glass material could be obtained which was adequately doped with the sensing dye and presented a relatively good adhesion to the optical fiber surface, in most cases the resulting membrane showed very poor properties for sensing applications.

It was observed that both TEOS and TMOS matrices could produce very thin films. Increasing the film thickness, however, invariably resulted in cracking of the glass films. Indeed, both materials were very brittle and cracked very easily when hydrated. As result of their highly

porous nature, in the case of TEOS some leaching of sensing dye into the buffer solutions was observed. As a consequence of their poor mechanical stability when in aqueous environments, no reproducible results could be obtained with these materials and no further tests were performed.

Although some of the problems reported were also found in some of the produced hybrid sol-gel materials, the majority of the procedures resulted in membranes with good characteristics for sensing. After tuning some of the fabrication parameters (solution aging time, doping method, curing process) best results could be obtained with the TEOS and MTMOS combination.

With these materials, membranes with good adhesion to the optical fiber could be produced. Doping of the sol-gel solutions with CNF could be successfully implemented. The resulting membranes showed no apparent leaching and displayed a fast ($< 1\,\mathrm{min}$) and reversible response to changes in the sample solutions acidity level. Figure 3.8 shows an optical fiber sensing probe produced by dip coating of a TEOS and MTMOS membrane doped with CNF. The sensing membrane is being excited by a blue laser and yellow luminescence emission, characteristic of CNF when in acidic media, can be clearly observed.

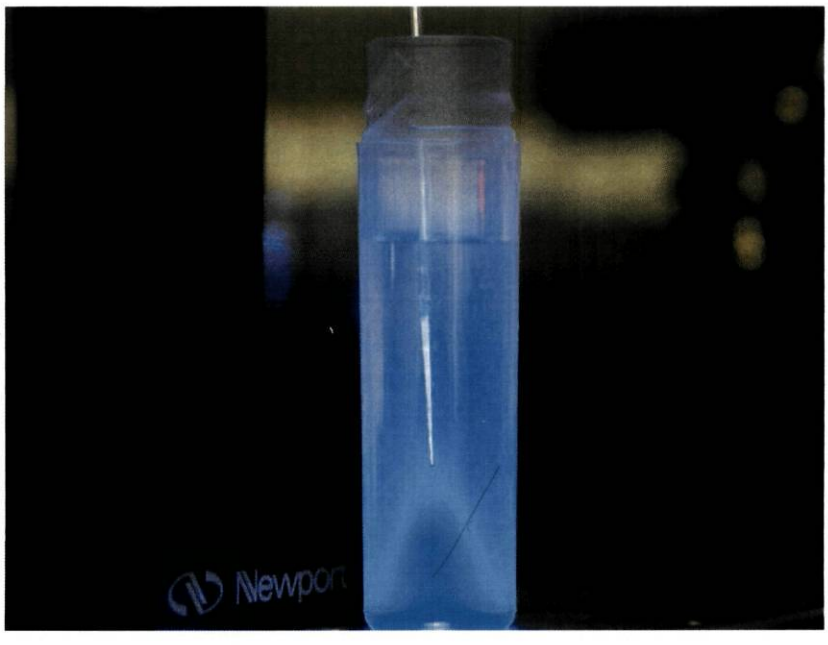


Figure 3.8 Fiber probe coated with a CNF doped sol-gel membrane immersed in acid buffer solution. Excitation was performed using a blue laser ($473\,nm$).

The major problem encountered with the membranes produced was the high degree of photobleaching observed. This problem, however, was mainly an intrinsic property of the sensing dye and was common to all membranes tested. Nevertheless, due to the fact that the sol-gel membranes were very thin glass films, the amount of sensing dye deposited on the fiber surface was reduced in comparison with other membranes. This way, the density of excitation radiation was

much higher, resulting in faster photo-degradation of the sensor. Nevertheless, membranes doped with metal-organic complexes, like ruthenium and osmium complexes, which were produced at a later stage, showed a very much increased photostability as compared with CNF doped membranes.

Although leaching was not apparent with most sensing dyes tested, it was observed that prolonged exposure to highly alkaline media ($pH \approx 10$) resulted in slow degradation of the sensing film. Nevertheless, in most biological applications these pH levels will not be reached. In addition, some sol-gel procedures are available which can produce membranes for extreme pH applications, which could be adapted for the sensors tested [13].

In spite of these difficulties, the sol-gel based membranes were shown to be the most compatible ones with optical fiber applications in terms of adhesion to the fiber surface and response time. Different pH sensing techniques were implemented using an excitation/detection fiber system in combination with some of the sensing probes produced by the sol-gel method. These results are given in the next section, where further characterization of the membranes obtained is provided.

Qualitative comparison of the different immobilization methods

From the different methods tested it becomes clear that the production of an ideal sensing membrane is not an easy task. Although many of the techniques tested produced membranes with very favorable characteristics, none of them was free of problems. Some of the techniques investigated are quite versatile and allow to change some of the membrane properties by controlling specific process parameters. However, most often a given fabrication parameter affects more than one membrane property and, therefore, usually some kind of compromise must be established.

Table 3-1 shows a summary of the qualitative evaluation performed with the different membranes doped with CNF. With the exception of the inorganic sol-gel membranes which were generally very brittle and showed a poor interaction with the probed solution, all the other methods presented some interesting characteristics.

The PVA membrane showed very good overall characteristics regarding leaching, response time and reversibility. In addition, this material was very elastic and resistant to mechanical pressure. However, the adhesion of the PVA membranes to the fiber surface was very poor, and this somewhat hinders the use of these materials in optical fiber applications. Nevertheless, they are still quite suitable to implement sensing heads based on extrinsic membranes, which in some situations can present considerable advantages. For instance, the sensing membrane can be easily substituted without interfering with the remaining fiber sensing system.

The acrylamide membrane, on the other hand, presented very good adhesion to the fiber surface. This characteristic, however, was only achieved after silanization of the glass surface of the fiber. Although good quality membranes could be obtained in the fiber lateral surface, coating of the fiber end face was very difficult. In addition, although this membrane was very elastic (it had a gel consistency), its resistance to mechanical hazards was very poor. Also, it was verified that the photo-polymerization process, necessary for membrane formation, strongly decreased the useful lifetime of the sensing dye because it caused its premature photo-degradation.

Membrane properties	**PVA**	**Acrylamide**	**TEOS**	**TMOS**	**Hybrid sol-gel**
Adhesion to fibre surface	Poor	Very good	Regular	Poor	Very good
Film thickness (multiple dip coating)	Thick	Thick	Very thin	Very thin	Thin
Elasticity /robustness	Very Good	Regular	Poor	Poor	Good
Leaching observed	Little	Little	High	Very little	Very little
Sensor response time	Fast	Fast	Slow	Slow	Very Fast
Sensor reversibility	Very good	Very good	Poor	Poor	Very good

Table 3-1 Qualitative comparison of the properties of the different sensing membranes produced.

Finally, very interesting results were obtained with the hybrid sol-gel membranes, with most of the sensors produced showing good reversibility, fast response times and reduced leaching. The combination of organic and inorganic precursors produced hybrid materials still with good adhesion to the fiber surface, but with increased elasticity (compared to inorganic sol-gel membranes). Therefore, the resulting membranes showed a good compromise between adhesion and mechanical robustness. In addition, the increased elasticity allowed the formation of thicker films without crack formation. However, films produced by this method were still very thin and produced fast responses to pH changes. On the other hand, because the amount of sensing dye was relatively small, these membranes were very susceptible to photobleaching of the sensing dye. Although this is an intrinsic problem of the luminescent indicator, this shows that no material presents an universal solution for dye immobilization. Each situation demands careful analysis, with evaluation of the advantages and disadvantages of each host material being an important step in choosing the final solution.

In the following section, the evaluation of some of the produced sensing membranes in an optical fiber sensing system is described. Different interrogation techniques were explored, from simple intensity detection to frequency domain interrogation.

3.4 Intensity Based pH sensing

The suitability of some of the membranes obtained to be used in optical fiber sensing applications was addressed. For this purpose, an optical fiber system was assembled which was employed to interrogate different intrinsic and extrinsic fiber sensing probes using different signal processing techniques.

3.4.1 Sensing system

The system implemented and used to test the sensing membranes is schematically represented in Figure 3.9. Excitation could be performed using different optical sources. A HeNe laser ($633\,nm$) was available to provide excitation of the red absorption band of CNF. Alternatively, a blue LED ($470\,nm$) was available, which was able to excite both acidic and alkaline bands of this dye. In addition, the LED source could be modulated in order to implement a frequency domain interrogation scheme. The excitation radiation was launched into the fiber system using either a microscope objective (for the laser) or a small diameter ball lens (for the LED).

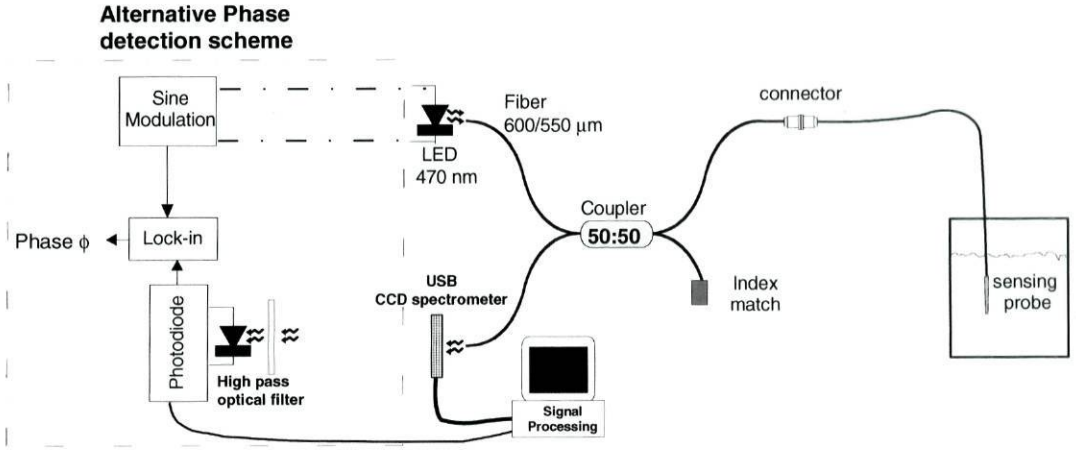


Figure 3.9 Experimental set-up of the fiber system used to interrogate the pH sensitive membranes. At the detection stage it was possible to choose between intensity based detection using a CCD spectrometer, and frequency domain interrogation using a photodetector and a lock-in amplifier. This last option demanded for modulation of the excitation optical source which could be implemented using a blue LED.

In order to obtain luminescent signals of higher magnitude at the detection stage, large diameter multimode silica fibers were used with core/cladding diameters of $550\,\mu m / 600\,\mu m$. An optical fiber coupler (50/50 coupling ratio) allowed excitation and detection of the sensing membranes using the same fiber probe (which was connected to one of the distal arms of the coupler). Detection of luminescence signals could be performed using alternative systems. For intensity based detection, and wavelength discrimination, the fiber output was directed towards a

miniature CCD spectrometer (USB2000 Ocean Optics). If frequency domain interrogation was to be applied instead, the fiber output was then connected to a photodetector. The use of a lock-in amplifier and a reference signal (from the optical source modulation) allowed to retrieve, from the photodetector output, a phase signal which was proportional to the lifetime of the sensing dye.

Using the system implemented, different techniques for interrogation of pH indicators were then tested applying some of the sensing membranes described previously.

3.4.2 Intensity based pH and ion sensors

Intensity based pH sensor

Although the PVA membranes could not be successfully attached to the fiber surface, it was possible to perform some tests using an external membrane configuration. In this scheme, the distal end of the fiber probe was simply put into contact with the PVA membrane, which was attached to the bottom of a cuvette containing the buffer solutions.

In order to investigate the suitability of the sensing membrane to be used as pH sensor, its luminescence emission was monitored using the fiber system, while the pH of the buffer solution was changed. Excitation was performed through the same fiber using a HeNe laser. In Figure 3.10 the spectral response of CNF immobilized in PVA can be seen, when the membrane was immersed into solutions of different acidity in the range $pH\,4.98 - pH\,8.48$.

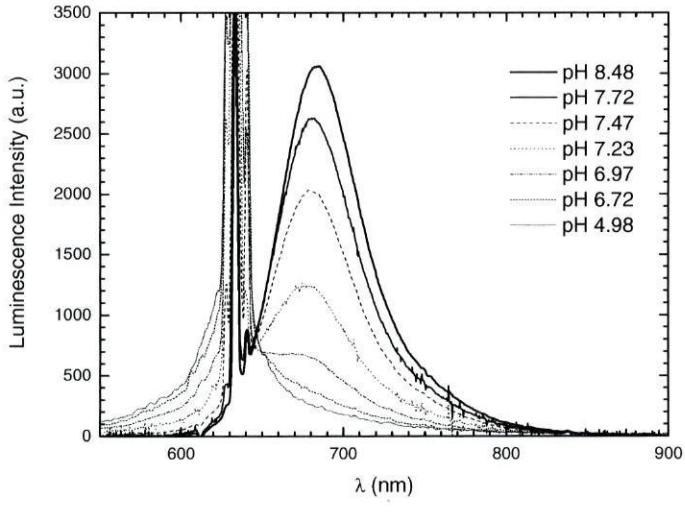


Figure 3.10 Spectral response of a PVA/CNF membrane when immersed in different pH buffer solutions. Excitation performed using a HeNe laser ($633\,nm$).

The resulting spectra indicate an increase in the luminescence signal as the pH of the buffer solution increases. The luminescence emission can be easily discriminated from the laser emission.

However, it can be seen that the back reflection of the laser is stronger than the CNF fluorescence signal. In practical applications, the use of an optical high pass filter is needed in order to increase noise rejection and improve the sensor signal-to-noise ratio. The emission peak of the CNF fluorescence corresponds to its alkaline band and is around $685\,nm$. There is a red shift of $15\,nm$ relative to what was observed in solution. Such spectral shifts upon immobilization are very common and have been reported in different dye/host combinations. They can have different causes, from interference of the rigid support with the relaxation dynamics of the dye excited molecules to inner filter effects. Nevertheless, the effect upon the dye sensing properties is usually not significant.

In order to confirm that the dye preserves its sensitivity to pH changes, the intensity of the fluorescence peak was plotted as a function of the solution pH. The results are shown in Figure 3.11 (a), where the sensor response in the pH range of $3.9 - 9.9$ can be seen. The data obtained follows a typical behavior which can be described by equation (3.11). This way, the graphical representation of pH as a function of $\log[(\mathrm{I_{max}} - I)/(I - \mathrm{I_{min}})]$ yields a linear plot whose zero intercept gives the pK_a of the luminescent indicator. Applying this procedure to the data obtained resulted in the plot of Figure 3.11 (b), from which it can be estimated that $pK_a \approx 7.4$.

These results are in reasonable agreement to what was observed in buffer solutions doped with CNF. This indicates that the process of physical entrapment did not interfere significantly with the properties of the indicator, demonstrating good compatibility between this sensing dye and PVA as immobilization membrane. Efforts are in course to improve adhesion of this material to the surface of the optical fiber which will allow the implementation of intrinsic fiber probe configurations. One possible solution is the use of plastic fibers where PVA adhesion should be improved.

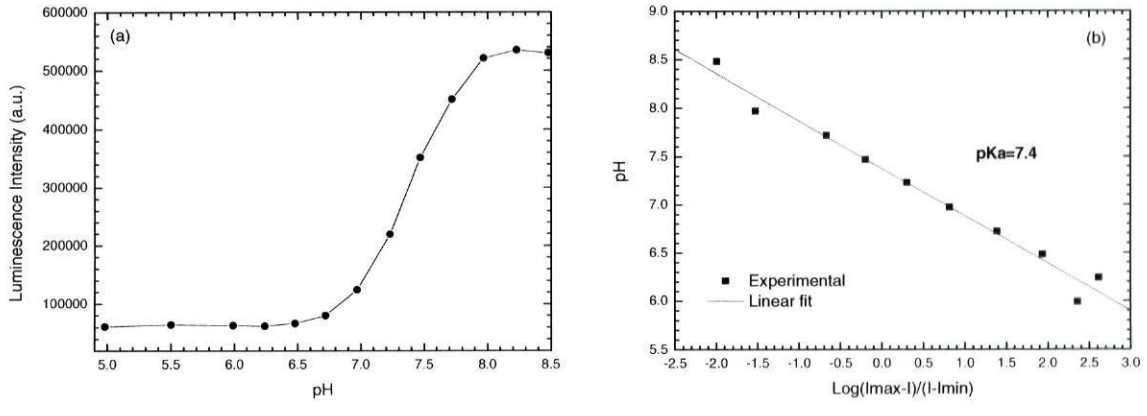


Figure 3.11 (a) Titration curve obtained from the luminescence response of a PVA membrane doped with CNF. (b) Linearization plot used to estimate the pK_a of the luminescent indicator.

In spite of showing favorable characteristics for pH sensing, like good compatibility with the sensing dye, reduced or no leaching and relatively fast response times, both the PVA and the acrylamide membranes suffered from the same problem, i.e., a strong photo-degradation of the sensing dyes. This characteristic was common to both immobilization methods because it arises from an intrinsic property of the sensing dye. However, the degree of photobleaching in the polyacrylamide membranes was slightly reduced. This resulted from the fact that the sensing molecules of the polyacrylamide were exposed to high levels of blue radiation during the polymerization process. However, this process also resulted in a lower luminescent output from these membranes, thus reducing the signal-to-noise ratio (SNR) of the fiber sensor.

In order to estimate the response time of the sensing membranes they were subjected to alternate cycles between two distinct pH values. With some of the acrylamide membranes response times of approximately $1\,\text{min}$ could be observed. However, these fast membranes suffered from some leaching. By increasing the amount of cross-linking, membranes with no observable leaching were obtained. However, their response time increased dramatically ($> 10\,\text{min}$). Figure 3.12 shows the response of the luminescent output to alternate pH changes (between $pH\,10$ and $pH\,5$) of an external acrylamide membrane with $1\,mm$ thickness. In this particular example, a response time of approximately $15\,\text{min}$ can be estimated for an increase in acidity by 5 pH units. The recovery time measured when the pH was decreased to its original value was approximately $5\,\text{min}$. Both time intervals were measured at 90% of steady response. Different response and recovery times are often observed and are mostly due to diffusion phenomena and non-linear response to pH. In this particular case, the increased thickness of the membrane contributed to increase the time necessary to reach equilibrium.

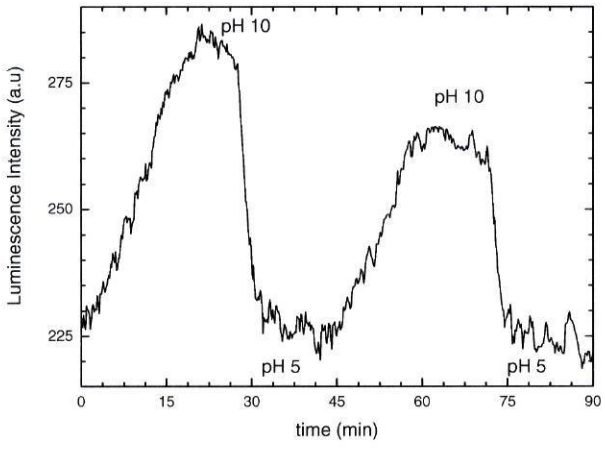


Figure 3.12 Response of acrylamide/CNF membrane to acidic/alkaline cycles with pH changing from $pH = 5$ to $pH = 10$.

From the recorded output it also becomes apparent that, due to a high degree of photobleaching, the sensor response lacks reproducibility. Because this problem arises from an intrinsic property of the sensing dye, the only way to avoid it is to use interrogation techniques which are insensitive to changes in optical power level caused by photobleaching or any other phenomena. Alternatively, photobleaching can be reduced by decreasing the optical power level of the excitation source. However, such action results in an equivalent decrease of the luminescent signal, degrading sensor performance.

Metal ion optical detection

Many types of compounds form colored complexes with metal ions (chelators) [60]. These color changes indicate a modification of the compound absorption spectra due to the binding reaction. An adequate combination of a chelating agent with a luminescent indicator may be used to implement a luminescence based metal ion sensor [66]. Such configuration can be developed as long as the chelator absorption spectrum overlaps either the excitation spectrum (primary filter effect) or the emission of the luminescent dye (secondary filter effect).

The possibility of using CNF as an ion sensor was tested by combining this pH indicator with a chelator agent. A magnesium ion, Mg(II), sensor was tested by co-immobilization in PVA of the CNF indicator with eriochrome black T (EBT) (Sigma-Aldrich, Ref. *E*2377). EBT is dark blue in its free form, therefore it has strong absorption in the red region of the spectrum. However, it acquires a red coloration when bonded to magnesium, which indicates a shift of absorption to lower wavelengths. This way, the absorption spectrum of free EBT overlaps the absorption spectrum of CNF. However, when Mg(II) is present the absorption spectrum of the complex Mg(II)-EBT shifts to shorter wavelengths causing an increase of the CNF fluorescence.

Preliminary tests were performed using the set-up in Figure 3.9. A fiber tip was used to interrogate an external PVA membrane, with CNF and EBT co-immobilized, which was immersed into a $pH\,9$ buffer solution. In parallel, a $0.1\,M$ solution of Mg(II) in a $pH\,9$ buffer was prepared. The response of the probe luminescent signal was then monitored as increasing amounts of the Mg(II) stock solution were added to the main test solution. The spectral response of the modified sensor to an increasing concentration of Mg(II) can be observed in Figure 3.13 (a).

The results obtained show that there is an enhancement of the luminescent response that is proportional to the concentration of Mg(II) in the solution. The enhancement is due to reduction of the interference of the absorption band of free EBT. The plot of the integrated luminescent intensity as a function of the ion concentration is represented in Figure 3.13 (b) and it clearly shows

a linear response to changes in Mg(II) concentration. This shows the feasibility of using modified pH indicators to detect heavy metal ions in aqueous environments.

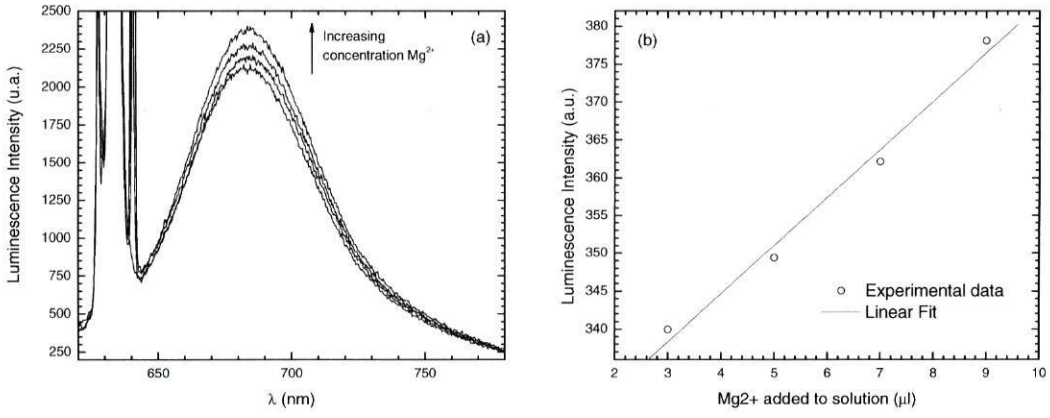


Figure 3.13 Response of the modified PVA/CNF membrane to the presence of increasing concentrations of Magnesium in sample solutions ($3,5,7$ and $9\,\mu L$ of Mg(II) were successively added). (a) Luminescence spectrum; (b) Integrated luminescence intensity.

Work is in progress to improve the sensitivity of the sensing membranes to Mg(II) and to other metal ions. Cross sensitivity of the chelator to pH and other metal ions is a recurrent problem of this type of sensors and it should also be addressed in future work. EBT is not particularly selective to Mg(II) and it will react with other ions, like calcium and potassium. However, other chelating agents are available with increased selectivity. Because CNF is sensitive to acidity level, cross sensitivity to pH is expected to be higher in this particular case. Nevertheless, this dye was used for demonstration purposes only. Because this scheme is based on a filter effect, it will work with a pH insensitive dye, as long as it displays adequate spectral overlap with the absorption of the chelator.

Colorimetric pH indicator combined with luminescent dye

A problem common to all the membranes tested arose from the weak photostability of the luminescent pH indicator. Therefore, the use of more photostable indicator dyes is highly desirable. Recently, in the context of optical oxygen sensing, a family of luminescent sensing dyes has been explored which shows enhanced photostability when compared with more traditional luminescent indicators. These new compounds are metal-organic complexes which show high quantum yields, long lifetimes and increased photostability. In particular, ruthenium based complexes with such properties have been extensively used in oxygen sensing applications.

Although some work has been done in order to render these complexes pH sensitive, this requires the chemical modification of the sensing dye. In a simpler alternative, the sensitivity of

available luminescent dyes to acidity changes can be obtained by combining these luminescent probes with an adequate colorimetric pH indicator [67]. For this scheme to work, however, the absorption spectrum of the colorimetric indicator must overlap the emission spectrum of the luminescent dye (for filter the effect to take place). This way, any change in the absorption spectrum of the colorimetric dye, induced by pH changes, will be reflected in a modification of the luminescent output of the metal-organic complex.

In order to assess the feasibility of this scheme, the ruthenium complex dichlorotris(1,10-phenanthroline)ruthenium(II), $[Ru(phen)_3^{2+}Cl_2]$ (Sigma-Aldrich, ref 343714), with absorption at $470\,nm$ and emission at $610\,nm$, was combined with the colorimetric pH indicator Bromophenol Blue (BPB) (Fluka, ref. 18030), with absorption at $600\,nm$. A combination of both dyes was immobilized in hybrid sol-gel membrane and deposited on the tip of an optical fiber by dip coating. The sensing membranes produced in this way were interrogated using the fiber system of Figure 3.9. A blue laser ($473\,nm$) was used as optical source in order to adequately excite the ruthenium dye. The luminescent output of the membrane containing both dyes was monitored by the CCD spectrometer while the fiber probe was immersed in buffer solutions of extreme pH values ($pH\,1$ and $pH\,10$). The results obtained can be observed in Figure 3.14.

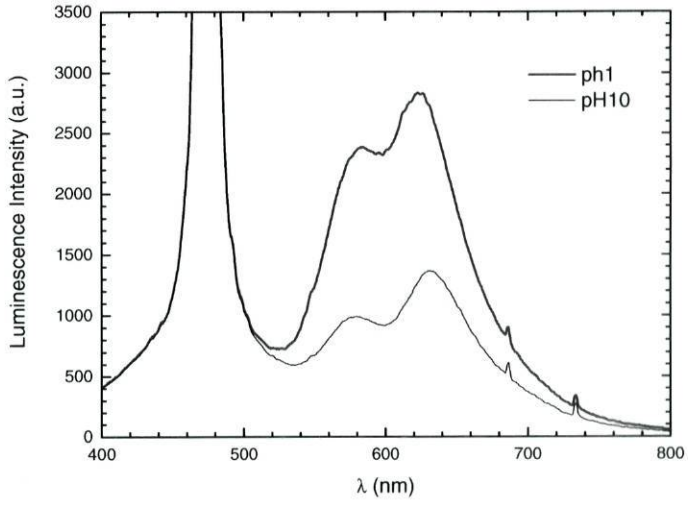


Figure 3.14 Luminescent spectra of Ru(phen) combined with bromophenol blue in acidic ($pH = 1$) and alkaline buffers ($pH = 10$).

The emission spectra obtained show a clear dip at $600\,nm$ which is uncharacteristic of ruthenium dyes and corresponds to the absorption band of the colorimetric indicator. In addition, the overall luminescent intensity is strongly decreased as pH increases. This indicates that resonant energy transfer and the filter effect are probably taking place simultaneously. The presence of

resonant energy transfer is particularly interesting as it typically interferes with the lifetime of the luminophore. This way, there is a chance this dye combination can be used for time resolved measurements of pH. This subject, however, was not addressed and will be the focus of future work.

As a consequence of the superposition of the emission spectrum of Ru(phen) with the absorption spectrum of BPB, the registered luminescent intensity of the sensor is clearly dependent on the acidity of the buffer solutions. A 31% change was estimated for the luminescent intensity measured at the two extreme pH values. Conversely, further tests showed that the luminescence of the ruthenium complex, alone, was approximately constant and independent of the pH of the buffer solutions.

The changes in the luminescent intensity were fast and reversible. This can be confirmed by observing the response of the sensing probe to alternate changes in the sample pH between $pH1$ and $pH10$, which is shown in Figure 3.15. The signal represented in this plot was obtained by monitoring a reduced spectral band around $605 \pm 20\,nm$. The luminescence intensity of this spectral band was decreased by 60% when the pH changed from $pH1$ to $pH10$.

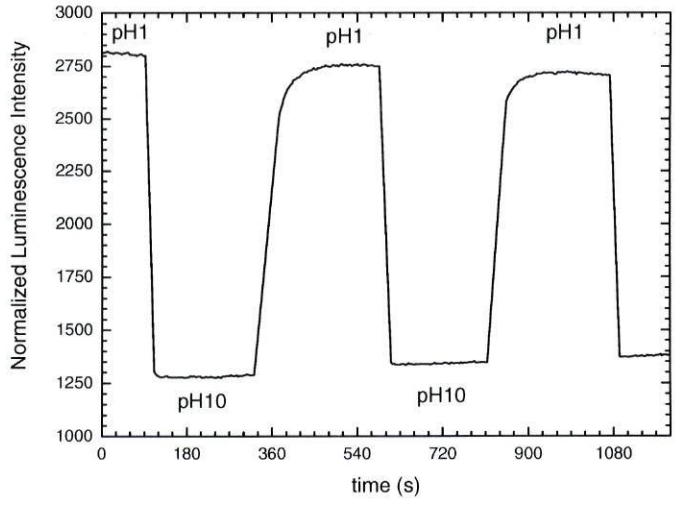


Figure 3.15 Response of a fiber probe coated with Ru+BPB immobilized in a hybrid sol-gel matrix, to acidic/alkaline cycles, with pH changing from $pH1$ to $pH10$.

Response and recovery times of respectively $65s$ and $25s$ were estimated for a change of 9 pH units. In general, much faster responses were obtained with the sol-gel membranes as compared with PVA and acrylamides. The main reason is due to the fact that the sol-gel films were much thinner, allowing equilibrium to be established much faster.

Although the photobleaching effects were not as readily apparent as in the case of CNF, photodegradation was still present in this case. This way, continuous monitoring of the sensor subjected to acid/alkaline cycles resulted in slow degradation of sensor response. By careful observation of the results in Figure 3.15, it can be seen that the degree of quenching, i.e. the relative change in the luminescence intensity of ruthenium for a given pH change, is decreased at each successive cycle (by approximately 2%). This decreased response results from the combined effect of photobleaching of the ruthenium dye with leaching of the colorimetric indicator. Although leaching was not apparent by direct observation of the probed solution, it could be confirmed performing a simple test. The sensing probe was stored in a dark place, immersed in a buffer solution with $pH\,10$ for a period of $48\,h$. Tests performed after this rest period showed a decreased response of the sensor to pH changes. Indeed, when subjected to similar pH changes as in the previous tests, the luminescence output of the probe changed only by 30%. Because the probe was stored in the dark, this clearly indicates leaching of the colorimetric indicator. In addition, observation of the fiber probes under an optical microscope, revealed that the sensing film was slowly degraded by exposure to the alkaline solution.

Further tailoring of the sol-gel membrane is necessary in order to reduce the degree of leaching and increase the chemical resistance of the membrane at high pH. In spite of this, and when compared with the results obtained using CNF, the present scheme showed increased sensitivity and stability. Although some drift was observed, it was small enough to allow sensor calibration to be valid for short utilization periods. Further tailoring of the sol-gel membrane can reduce the leaching problem. In addition, the SNR obtained with ruthenium probes is relatively high; therefore, it is feasible to reduce the excitation intensity without seriously compromising the sensor response, achieving a reduction of the degree of photobleaching.

3.4.3 Ratiometric pH sensor

In spite of its poor photostability, CNF has very appealing characteristics for use in biomedical applications. The pK_a of this indicator lies within the physiological range ($pH\,6$ to $pH\,8$) and is therefore suitable for implementation of biosensors. In addition, CNF has the particularity of being a dual emission pH indicator. This way, in spite of suffering from strong photobleaching, dual wavelength detection and simple signal processing can provide stable pH measurements with this indicator. This is possible because both the acid and the alkaline form of the indicator suffer from similar degrees of photobleaching. This way, ratiometric detection can

eliminate the influence of any signal drift arising from photo-degradation, leaching or any other source of optical power fluctuation.

In order to test the possibility of implementing self-referenced pH measurements using ratiometric detection, an optical fiber coated with a MTEOS based sol-gel membrane doped with CNF was excited by a blue laser and interrogated using the fiber system of Figure 3.9.

Detection was performed using the CCD spectrometer which allowed spectral discrimination. The software of this device also implemented some simple signal processing. The luminescence emission of the CNF/sol-gel membrane was recorded when the fiber probe was immersed in acid ($pH\,3.75$) and alkaline ($pH\,9.36$) buffer solutions. The results obtained can be observed in Figure 3.16.

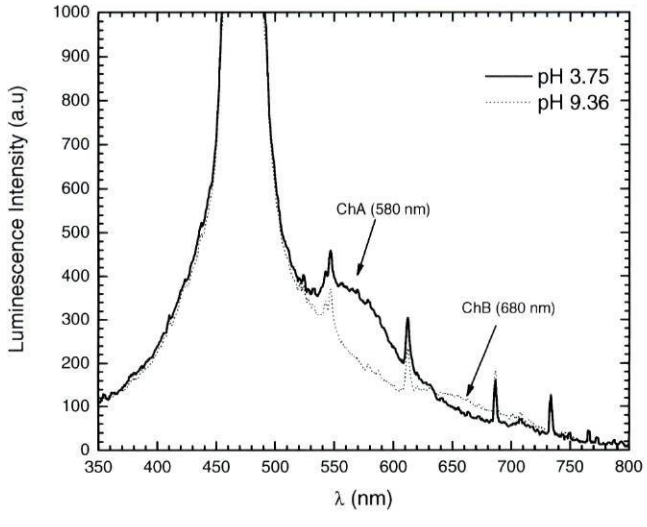


Figure 3.16 Spectral response of CNF, immobilized by a sol-gel membrane on the tip of an optical fiber taper, in acidic ($pH = 3.75$) and alkaline media ($pH = 9.36$).

In spite of poor SNR, which was mainly due to a strong background signal of back reflected laser radiation, the presence of the acidic and alkaline bands of CNF can be clearly identified. In order to apply a ratiometric sensing scheme, the CCD software was used to acquire two signals which were proportional to each of the CNF luminescent bands. This way, a channel A was defined at $580 \pm 5\,nm$, and a channel B at $680 \pm 5\,nm$. The two acquired signals were then processed according to the operation $(ChA - ChB)/(ChA + ChB)$. The luminescent signals A and B respond to pH in a symmetrical manner. On the other hand, their response to any other change in intensity (due to optical source or detector drift, leaching or even photobleaching) will be similar in both channels. Therefore, the processed signal should be independent of any optical power drift, but still responsive to changes of pH level. This can be confirmed by observing the results in Figure 3.17,

where the response of the sensing probe was registered while the sensor was subjected to acid/alkaline solutions with pH of 3.75 and 9.36, respectively.

While the signal corresponding to a single luminescent band (*ChA* or *ChB*) is strongly affected by photobleaching (thin line in Figure 3.17), the processed output is clearly independent of this phenomenon (dark line in the same figure). Because the sol-gel process produced thin films, the response of the sensor was very fast ($\sim 1\,\text{min}$). Thus, a stable, fast and reversible response to pH could be demonstrated using a dual emission indicator dye and a ratiometric detection scheme.

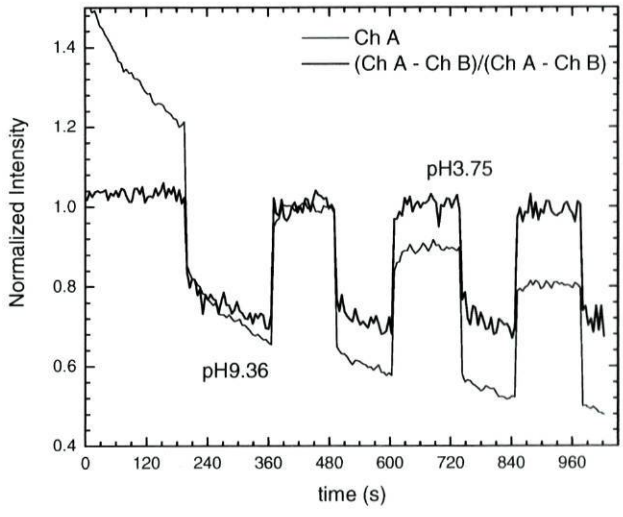


Figure 3.17 Response of CNF in sol-gel fiber probe to a step change of pH (between $pH\,3.75$ and $pH\,9.36$. Thin line – integrated intensity response of acidic band; Dark line – normalized output using ratiometric processing of acidic ($580\,nm$) and alkaline ($680\,nm$) bands.

However, a strong degree of photobleaching was observed, with the luminescence intensity decreasing by approximately $-6\%/\,\text{min}$. This way, although the detected signal was independent of optical power level, when subjected to continuous excitation the sensor SNR rapidly deteriorated as the luminescent output was strongly decreased. Nevertheless, the sensor useful lifetime can be extended by restricting the exposure to the excitation radiation to those periods when measurements are actually being made. Even considering these possibilities, the use of more photostable pH indicators is highly desirable.

3.4.4 Wavelength pH sensor

With an increased research effort being directed towards the synthesis of new luminescent indicators, some interesting results have been reported. The modification of ruthenium dyes with a pH sensitive carboxyl ligand has produced long lived, photostable luminescent indicators suitable to perform acidity measurements [37, 68]. In order to explore the potential of these new compounds,

the complex $[Ru(Ph_2phen)_2DCbpy]^{2+}$, where $Ru(Ph_2phen)_2$ stands for ruthenium-bis(4,7 -diphenyl, 1,10- phenantroline) and DCbpy represents the ligand 4,4-dicarboxy-2,2-bipyridine, was tested. This new compound was synthesized in the Chemistry Department, following a procedure described elsewhere [37]. The suitability of the resulting complex to perform pH measurements was then investigated. For simplicity, the synthesized complex will be referred to as RuDCbpy.

Identical amounts of RuDCbpy were dissolved in buffer solutions of different pH. The spectral response of the obtained solution was then recorded using the fiber system of Figure 3.9. The results obtained can be observed in Figure 3.18, where the luminescence output of RuDCbpy is shown for pH values in the range $2.25 - 9.36$.

In addition to a change of the luminescence intensity as pH is increased, a strong spectral shift is also observed. This spectral shift results from the fact that both the alkaline and acid band of the ruthenium complex are strongly luminescent and are relatively close to each other. While intensity measurements can be used to determine pH, this approach has several associated problems that have already been discussed, photobleaching being the most serious one. Wavelength, on the other hand, is an intrinsic property of the luminescent molecules and is not affected by the number of photobleached molecules, which will only impact the detected intensity. Consequently, the new dye can be used to implement self-referenced, wavelength based pH measurements.

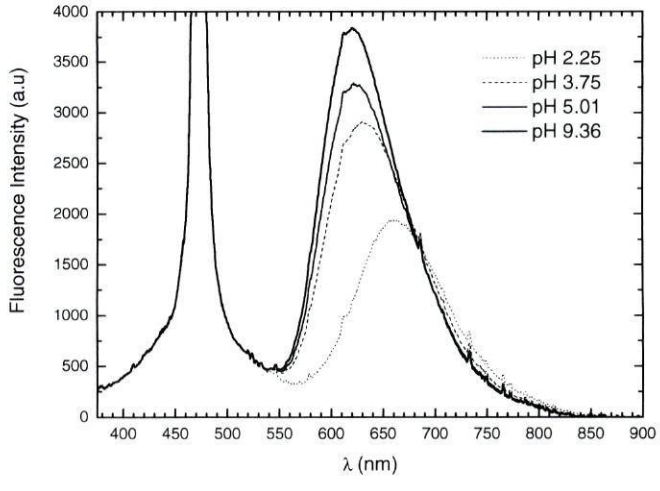


Figure 3.18 Luminescence spectra of Ru(DCbpy) in different buffer solutions.

In order to test this possibility, the luminescence intensity and the spectral emission peak of RuDCbpy were monitored as a function of the pH of sample solutions. The results obtained can be observed in Figure 3.19 (a) and (b), respectively. Both signals clearly follow the expected titration curve described by the Henderson-Hasselbalch equation. The intensity measurements, however, are clearly affected by some intensity fluctuation, probably due to changes in the alignment of the

excitation/interrogation fiber probe. The measurements of the spectral peak of the dye emission, on the other hand, are clearly not affected by these problems.

Therefore, this new ruthenium complex can be used to implement wavelength based pH measurements. But such scheme will require spectral discrimination at the detection stage. Although miniature spectrometers are available at increasingly low cost, this is not a desirable situation. However, because of the presence of a wavelength shift, it is possible to perform the desired measurement based on two simple intensity detections. By performing intensity measurements at two narrow spectral windows ($\sim 5\,nm$), in symmetrical positions of the emission spectrum (relative to the spectral peak), a signal proportional to the wavelength shift, and thus to the pH level, can be obtained. Such detection scheme can be implemented through adequate filtering and two photodetectors, thus avoiding the need for a spectrometer.

In order to demonstrate the feasibility of this scheme, the software of the CCD spectrometer was used to perform the detection of the two spectral signals (A and B) in symmetrical positions of the emission spectrum, and then to implement the operation $(A-B)/(A+B)$.

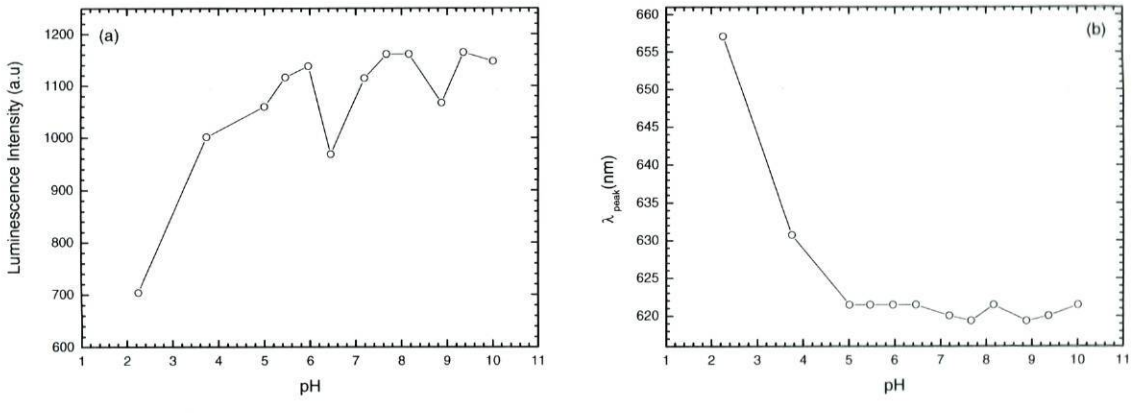


Figure 3.19 Response of RuDCbpy in different buffer solutions. (a) Luminescence intensity as a function of solution pH; (b) peak wavelength as a function of solution pH.

As can be observed in Figure 3.20, the resulting signal is clearly proportional to the wavelength shift and also follows the response to pH predicted by the Henderson-Hasselbalch equation. This clearly demonstrates the feasibility of implementing an intensity based self-referenced pH sensor.

Typically, metal-organic complexes are long lived luminescent indicators. Therefore, the ruthenium complex under study should be suitable to implement a frequency domain pH sensor. For this to be possible, the luminescence lifetimes of both the acidic and alkaline bands of the

indicator should change with pH. In order to confirm this possibility the lifetime of the complex under study was estimated using the experimental fiber system.

By exciting the luminescent indicator with a sinusoidally modulated LED, a luminescent signal with sinusoidal modulation could be detected. However, due to the finite lifetime, τ, of the sensing dye, the luminescent signal was delayed relative to the excitation signal. This time delay can be measured as a phase shift, ϕ, which depends on the modulation frequency, f. As seen before in chapter 2, these parameters are related by

$$\tan\phi = 2\pi f\tau \,. \tag{3.12}$$

This way, plotting $\tan\phi$ as a function of the modulation frequency provides a simple way of estimating the lifetime of the sensing dye. This method was used to estimate the lifetime of RuDCbpy in alkaline ($pH\,9$) and acid buffer solutions ($pH\,2$). To achieve this goal, the modulation frequency of the excitation LED was swept between $1\,kHz$ and $100\,kHz$, while the phase shift was recorded by a lock-in amplifier. In the investigated frequency range the plots obtained were approximately linear and allowed to estimate the lifetime from their slope.

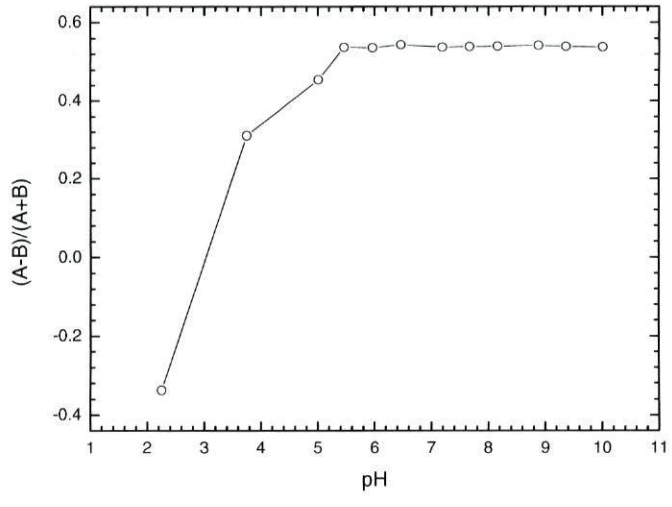


Figure 3.20 The processed signal, based on two intensity measurements, changes with pH proportionally to the wavelength shift and independently of optical power fluctuations.

The resulting data is shown in Figure 3.21. The plots obtained have distinctly different slopes indicating that the dye lifetime is pH dependent. From the experimental data, lifetimes of $334\,ns$ at $pH\,2$, and $541\,ns$ at $pH\,9$ could be estimated. This corresponds to a $200\,ns$ variation induced by a change of 7 pH units. Such a change is adequate to implement a lifetime based pH sensor. In addition, because the average lifetime is in the hundreds of nanoseconds range, frequency domain

interrogation techniques can be implemented with modulation frequencies below $1\,MHz$, which is compatible with low cost optoelectronics.

The new ruthenium complex was shown to be a very versatile pH indicator suitable not only for lifetime based measurements but also capable of providing self-referenced intensity based detection. The immobilization of this complex in a sol-gel matrix was not tested. However, ruthenium based luminescent probes are typically well suited for sol-gel immobilization. This way, this indicator should provide sensing membranes with very interesting properties for optical fiber pH sensing

Due to the relatively simple instrumentation requirements and self-referencing capability, time resolved measurements are very appealing for practical applications. Consequently, additional schemes for frequency domain pH sensing were tested.

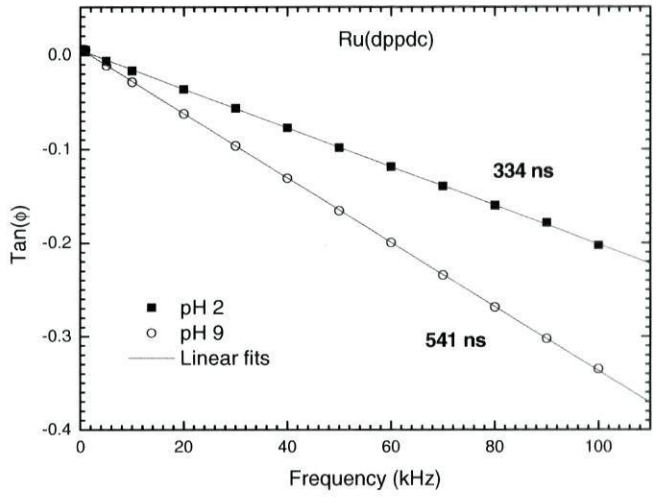


Figure 3.21 Plots used to estimate the lifetime of the RuDCbpy complex in buffer solutions of $pH\,2$ and $pH\,9$.

3.5 Lifetime based pH sensors

In general, lifetime based detection is a powerful technique that can minimize the effect of any optical power change in the fiber system, even those arising from leaching and photobleaching of the indicator dyes. In addition, provided the dye lifetime is sufficiently long, it can be implemented using relatively cheap optoelectronics. Thus, the search for sensing dyes suitable for application of this technique is very strong. Unfortunately, most pH indicator dyes have either very fast lifetimes, which would require high frequency modulation and very expensive electronics, or their lifetime is not pH dependent. Although, as was shown in the previous section, new pH indicator dyes are being produced with very good characteristics for implementation of these techniques, the number

of available dyes with such characteristics is still very limited. On the other hand, the number of short lived pH indicator dyes is relatively high. This way, the search for alternative schemes to render traditional pH indicators suitable for lifetime based techniques is the subject of many researches. One possibility to achieve this purpose is to combine a long lived pH insensitive luminescent dye with a short lived indicator dye. In such cases, the combined response of the two luminophores usually displays a relatively long apparent lifetime, sensitive to the analyte, and suitable for interrogation with much lower modulation frequencies [38, 69].

3.5.1 Combination of indicators with different lifetimes

The possibility of using CNF for frequency-domain lifetime detection was investigated. For this purpose, CNF was combined with $[Ru(phen)_3^{2+}Cl_2]$ resulting in a fluorophore with an apparent lifetime in the hundreds of nanoseconds range. Although the lifetime of the ruthenium dye is not pH dependent, the combined luminescent response should display an apparent lifetime that changes with the medium acidity level.

In order to investigate this possibility, different solutions of Ru(phen) and CNF were prepared. Because the ruthenium dye presents an increased quantum yield, the amount of Ru(phen) had to be diluted several times until the luminescent contribution of both dyes was distinguishable in the detected luminescent signals. The results obtained with the optimized solutions are showed in Figure 3.22 (a) through (c). The emission spectra of the combined dyes was registered in alkaline (pH 9.36) and acid (pH 3.75) buffer solutions. Excitation and detection were performed using the fiber system of Figure 3.9, with the blue laser as excitation source and the CCD spectrometer as detection device.

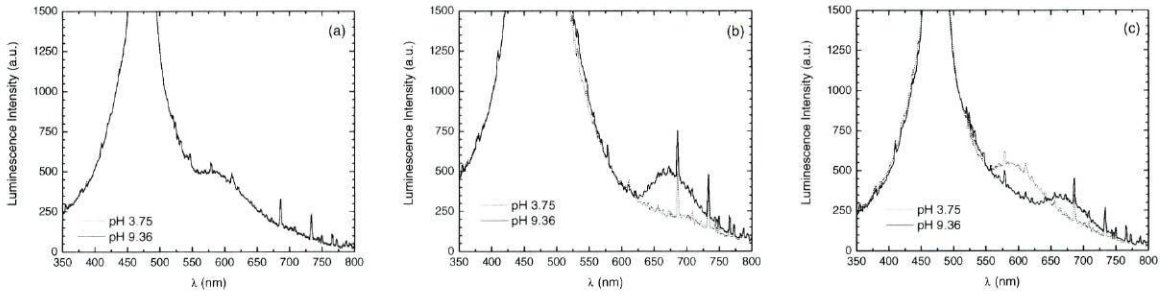


Figure 3.22 Luminescence emission of different pH indicators in acidic (pH 3.75) and alkaline (pH 9.36) media. (a) Ru(phen); (b) CNF; (c) CNF combined with Ru(phen).

In Figure 3.22 (a) it becomes clear that the luminescent emission of the ruthenium dye, alone, does not depend on the pH of the sample solution. CNF, on the other hand, shows its typical alkaline and acid (barely visible) emission bands according to the solution pH (Figure 3.22 (b)).

Finally, the combined luminescent response of both dyes, shown in Figure 3.22 (c), is clearly pH dependent.

In order to verify the influence of the dye combination on the apparent lifetime of their luminescent emission, the lifetimes of the two buffer solutions containing CNF and Ru(phen) were estimated using the frequency domain method described in the previous section.

The results obtained can be observed in Figure 3.23 (b). The plots used to estimate the lifetime of the ruthenium dye, alone, are shown for comparison purposes in Figure 3.23 (a).

The combination of CNF (with lifetimes in the nanosecond range) and Ru(phen) (with $\approx 500\,ns$ lifetime) has suitable characteristics for frequency domain pH measurements. While the ruthenium dye alone is pH insensitive, ($\tau_{pH9.36} \approx \tau_{pH3.75}$), the lifetime of the combination of CNF with Ru(phen) shows increased pH sensitivity ($\tau_{pH3.75} \approx 2.7 \times \tau_{pH9.36}$).

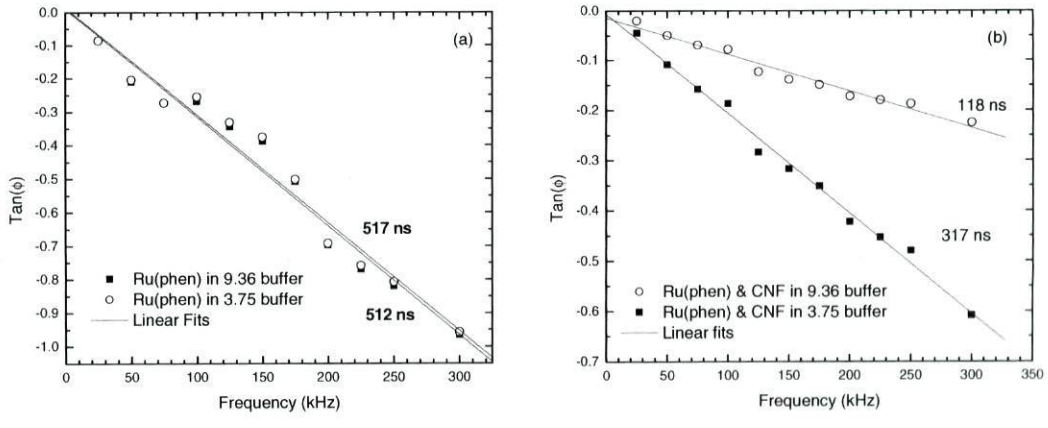


Figure 3.23 Plots used to estimate the lifetime of the luminescent indicators in acidic ($pH\ 3.75$) and alkaline ($pH\ 9.36$) media. (a) Ru(phen); (b) R(phen) combined with CNF.

The results obtained clearly confirm the possibility of using combined luminescent indicators with different lifetimes to obtain luminescent responses suitable for frequency domain pH sensing. The immobilization of these fluorophores in sol-gel matrices is being investigated and should allow the implementation of frequency domain pH optodes using CNF.

3.5.2 Frequency domain interrogation of NIR pH indicators

In the framework of practical applications, the operation of pH sensors in the near infrared region of the spectrum (NIR) is a major step towards low cost instrumentation. Due to the developments in the telecommunications domain, NIR optical fiber and semiconductor components are widely available at low cost. Additionally, excitation and detection in this wavelength range avoids background noise from environmental and biological samples. Several NIR fluorescence indicators for pH determination have already been developed [70]. However, fluorescence indicators

for toxic heavy metal detection and the corresponding optical fiber instrumentation are still in the first stages of development.

Os(II) complexes with α-diimine ligands have been shown to be suitable oxygen luminescent sensors with intense red absorptions [71]. Also, a strategy to make a polypyridyl luminescent complex sensible to pH by using ligands with ionizable functional groups, like carboxylic or hydroxylic functionalities, was demonstrated [68]. In the present work, and in collaboration with the Chemistry Department, several osmium(II) complexes have been synthesized with the different basic ligands, which are represented by their structural formula in Table 3-2. The goal of this effort is to design NIR pH indicators with suitable characteristics to implement pH and heavy ion optical fiber sensors.

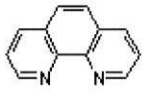
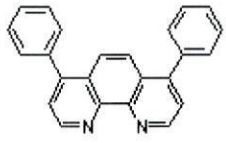
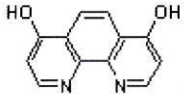
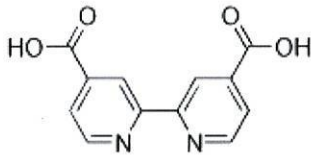
	
1,10-Phenanthroline	4,7-Diphenyl-1,10-phenanthroline
	
4,7-Dihydroxy-1,10-phenanthroline	2,2'-Bipyridine-4,4'-dicarboxylic acid

Table 3-2 α-diimine ligands used in the synthesis of different Os(II) complexes.

From the different complexes synthesized, the ones showing the most favorable characteristics for the intended purpose were selected for further tests. This way, the complexes $[Os(Ph_2Phen)_2(Dcbyp)]PF_6$, $[Os(Phen)_2(Dcbyp)]PF_6$ and $[Os(Ph_2Phen)_2(Phen(OH)_2)]PF_6$ were chosen. For simplicity, in the remaining of the text these compounds will be referred to as Os_1, Os_2 and Os_3 respectively.

In a first stage, the photophysical properties of the luminescent dyes when dissolved in different solvents were characterized. In particular, their absorption and emission spectra were recorded in solutions of methanol and dimethylformamide (DMF).

The absorption spectra obtained for the selected osmium complexes are shown in Figure 3.24 (a) through (c), corresponding, respectively, to the complexes Os_1, Os_2 and Os_3. The corresponding luminescent spectra, on the other hand, can be observed in Figure 3.25 (a) through (c), respectively.

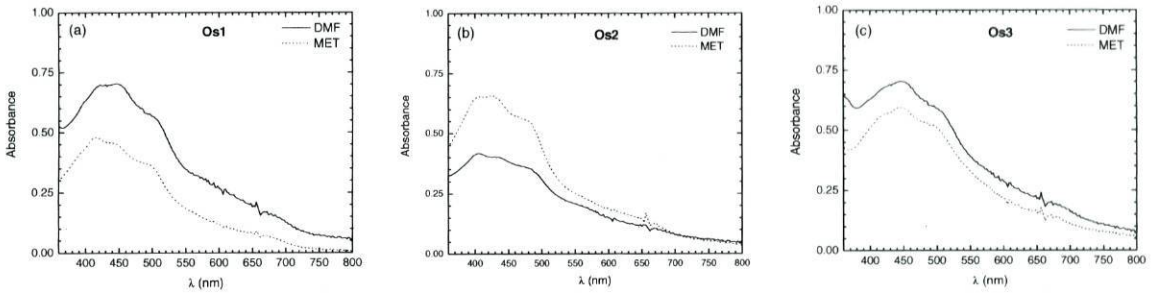


Figure 3.24 Absorption spectra of osmium complexes obtained in solutions of DMF and of Methanol. (a) Os1; (b) Os2; (c) Os3.

The spectra of the osmium(II) complexes showed absorption in the $400\,nm - 700\,nm$ range with a maximum in the $400\,nm - 500\,nm$ interval, either in solution of methanol or of DMF. In spite of this, absorption at $600\,nm$ is still relatively strong, and allows the sensing dyes to be excited by red laser diodes. It was verified that the solvent had some influence on the intensity of the measured absorbance, but not on its spectral distribution.

The emission spectra of all the complexes showed a maximum intensity above $700\,nm$, in the near-infrared spectral region. The luminescence intensity was stronger when the dyes were dissolved in methanol. This is probably due to different degrees of dynamical luminescence quenching by the solvent molecules.

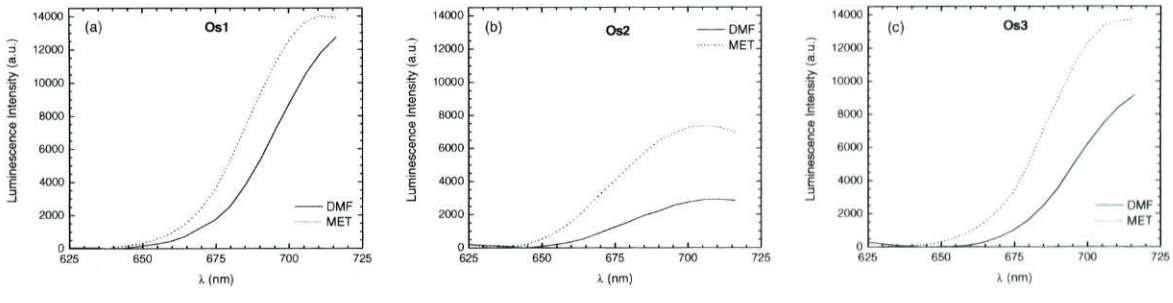


Figure 3.25 Luminescence emission spectra of osmium complexes obtained in solutions of DMF and of Methanol with excitation at $470\,nm$. (a) Os1; (b) Os2; (c) Os3.

Further tests were performed using complexes Os_1 and Os_3. The spectral characteristics of these two indicators in acidic and alkaline solutions were investigated aiming to characterize their sensitivity to changes in the pH level. The obtained absorption spectra, when the dyes were in acid (H_2SO_4, $pH\,1 - pH\,2$) and alkaline (NaOH, $pH\,11 - pH\,12$) solutions are shown in Figure 3.26 (a) and (b). In order to compare their pH response, each pair of absorption spectra was normalized to the highest registered value for that particular dye.

It can be seen that both complexes have a clear response to the medium acidity. However, while Os_1 presents a spectral shift of its absorption peak, in Os_3 the main effect is a decrease in the intensity of the absorption band. Nevertheless, both these changes should translate into variations of the measured luminescence intensities. Indeed, this can be confirmed by observing the emission spectra of Os_1 and Os_3, obtained in alkaline and acid buffers, which are shown in Figure 3.27 (a) and (b).

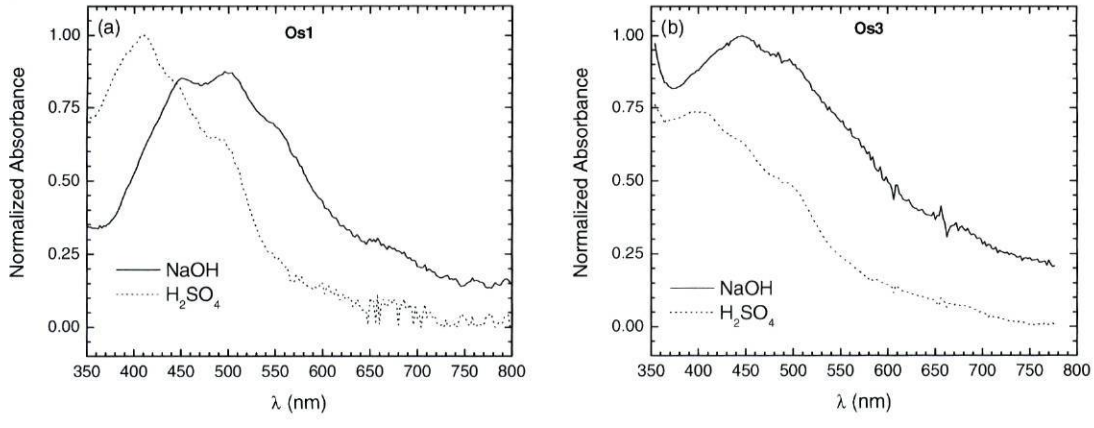


Figure 3.26 Absorption spectra of osmium complexes obtained in acidic (H_2SO_4) and alkaline (NaHO) media . (a) Os1; (b) Os3.

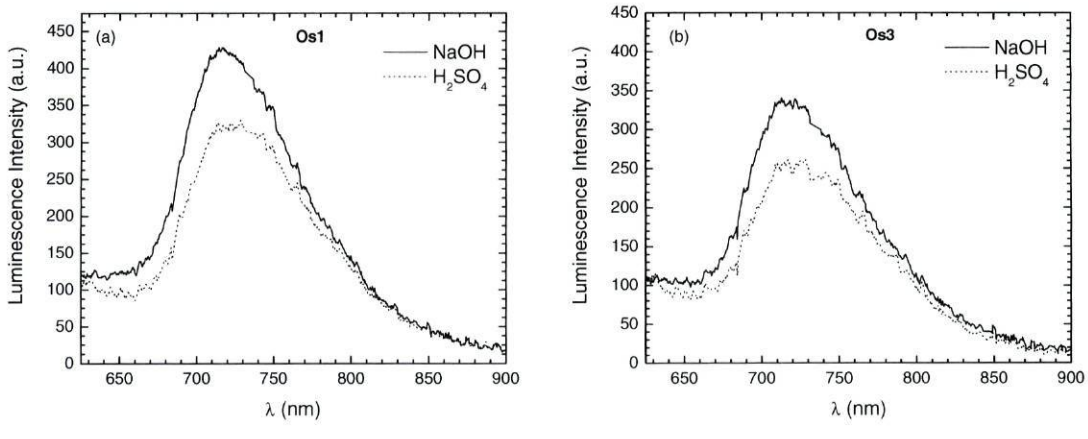


Figure 3.27 Luminescence spectra of the Os(II) complexes in acidic (H_2SO_4) and alkaline (NaOH) media, when excited by a blue laser ($473\,nm$). (a) Os1; (b) Os3.

The complex Os_1 presents a 20% decrease in its luminescence intensity when changing from an alkaline to an acid medium. In an identical situation, Os_3 decreased its luminescence emission by 17%. Therefore, both new dyes present an adequate behavior to be used as intensity based pH sensors with infrared emission.

In order to verify the suitability to use these dyes in frequency domain interrogation schemes, their lifetimes were evaluated while in acid and alkaline buffers. The results obtained are shown in Figure 3.28 (a) and (b).

Although both complexes show some change in their luminescence lifetime according to the solutions pH, this change is very small for OS_3 and much larger for OS_1. From the obtained data it can be estimated that while Os_1 shows a lifetime increase of $\Delta\tau = 50\,ns$ when switching from an alkaline to an acid medium, the lifetime of OS_3 changes only by $\Delta\tau = 8\,ns$ in an identical situation. This way, while both dyes can be used to perform intensity based pH measurements, only OS_1 has suitable characteristics to be used in lifetime based interrogation schemes.

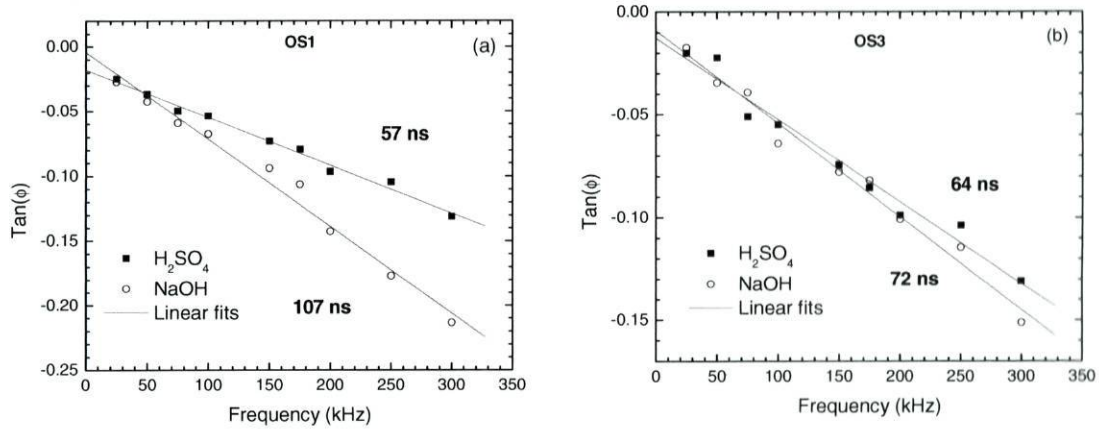


Figure 3.28 Plots used to estimate the lifetime of the Os(II) complexes in acidic (H_2SO_4) and alkaline (NaOH) media. (a) Os1; (b) Os3.

For this reason, this complex was selected for sol-gel immobilization. The immobilization procedure was partially successful. The dye was successfully immobilized in the solid matrix, which showed good adhesion to the optical fiber and no apparent signs of leaching. In addition, the spectral properties of the immobilized dyes were very similar to the ones of the dissolved complex. Only a small blue shift was detected. In solution the spectral emission peak was around $723\,nm$, while after immobilization the luminescence intensity was maximum at $709\,nm$ (see Figure 3.29). This shift was often observed in sol-gel immobilized ruthenium dyes and is usually related to rigidochromism [72].

The lifetime of the immobilized dye also presented an increase relative to the value obtained in solution. While immobilized in a sol-gel matrix, the estimated lifetime of Os_1 was approximately $150\,ns$ (corresponding lifetime data is shown in Figure 3.30 (a)). In acid solution, on the other hand, the measured value was $107\,ns$. This lifetime increase, however, is typically observed in most luminophores, following immobilization in a solid host. In solution, interaction with the solvent

molecules provides the excited dye molecules several non-radiative pathways, which typically reduce their lifetime. After immobilization in the solid host, however, dye molecules are partially protected by the rigid skeleton from interaction with other molecules, thus increasing their excited state lifetime.

On the other hand, physical entrapment is typically non-homogeneous, creating different micro-environments with different apparent lifetimes. As a result, the lifetime of encapsulated dyes results from the combination of several contributions from different dye populations which display different lifetimes. This way, the apparent lifetime of the whole sample typically depends on the observation frequency.

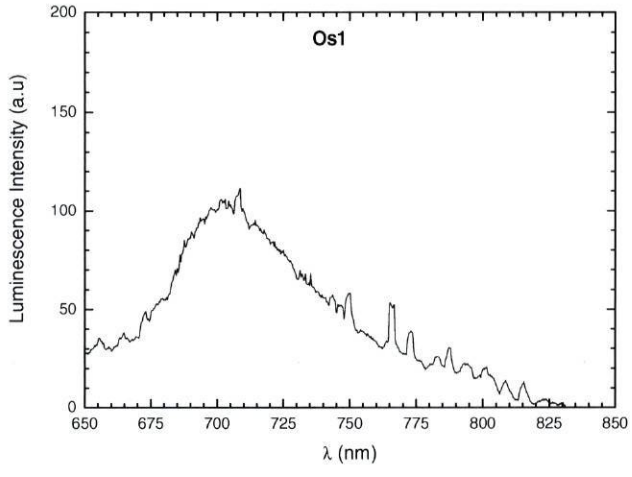


Figure 3.29 Luminescence emission of the Os_1 complex immobilized in a sol-gel membrane. The thin film was deposited on the tip of an optical fiber taper. Excitation ($473\,nm$ laser light) and detection were performed using the fiber system.

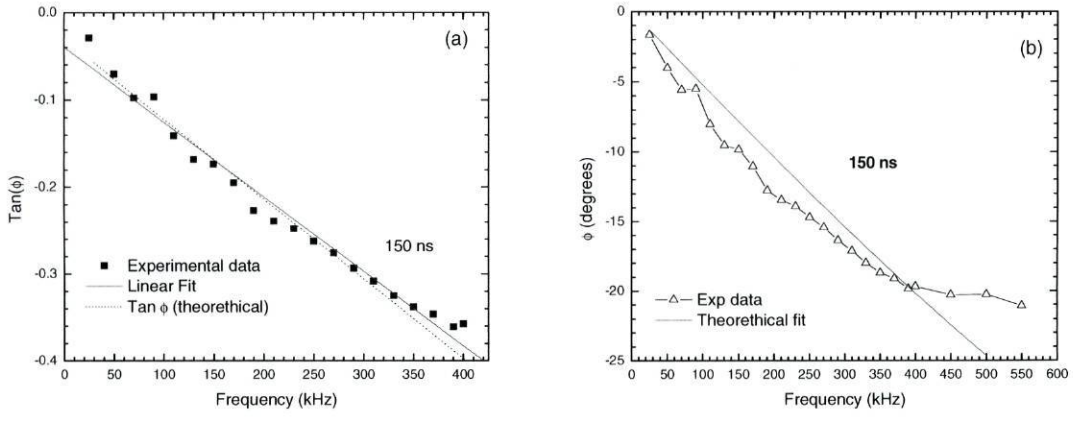


Figure 3.30 Plots used to estimate the lifetime of complex Os1 immobilized in a sol-gel matrix. (a) $\tan\phi[f]$**; (b)** $\phi[f]$.

Indeed, observation of the lifetime data obtained with a sample of Os_1 immobilized in sol-gel allows to identify the presence of matrix heterogeneity. Figure 3.30 (a) shows the plot of $\tan\phi$ as a function of frequency. Deviation from linearity is readily apparent; the change in slope as a function of modulation frequency is due to the fact that the effective lifetime changes as the modulation frequency changes. This fact is more evident in the plot of ϕ as a function of modulation frequency shown in Figure 3.30 (b), where for higher modulation frequencies the phase delay suffers a strong decrease, revealing the presence of some luminescence components with longer lifetimes.

This phenomenon was observed by many authors, particularly in the immobilization of ruthenium dyes in polymeric and sol-gel matrices. Although this causes some non-linearity in the sensor response, it does not impact significantly the sensing properties of the luminescent dyes.

Attempts to observe the response of the luminescence of the encapsulated Os_1 complex to changes in the sample pH were not successful. Although some changes could be observed in the luminescence intensity, variations were very small and not reproducible. This indicates that the produced matrix is not establishing an equilibrium with the aqueous solution. The procedure followed to produce the sol-gel membrane was similar to the one used for the CNF sensors. However, the presence of methanol, which is necessary to dissolve the OS_1 complex, might have interfered with the final characteristics of the resulting membrane. In addition, the solubility of the osmium complexes tested was very small and precipitation was often observed.

Nevertheless, the sol-gel procedure has proven to be a very versatile technique. Tailoring of membrane properties, like porosity and polarity, is possible by changing some of the process parameters. This way, optimization of the immobilization procedures will surely allow to produce a membrane where the complex OS_1 can establish equilibrium with the surrounding media. In this situation, the favorable pH sensing properties, which were observed in solution will also be present in the resulting membrane. This will lead to the implementation of lifetime based pH sensors with excitation/emission in the red/NIR spectral region.

3.6 Conclusions

Several techniques for immobilization of luminescent pH indicators were tested and compared. From the results obtained it was clear that a successful immobilization depends on widely different parameters. From fabrication parameters of the immobilization membrane, to intrinsic properties of the sensing dye and also the characteristics of the sensing media, all should be thoroughly considered.

Many of the materials tested presented properties very well suited for sensing applications; however, several problems were also identified. In the end, no sensing membrane produced ideal results. Nevertheless, it is always possible to establish some compromises between antagonist properties in order to obtain usable sensing membranes.

From all the methods tested, the hybrid sol-gel membranes showed clearly to be the most versatile choice and the most well adapted to be used in optical fiber sensing applications. With adequate tailoring of the process parameters, it was possible to produce good quality thin films on the surface of the optical fiber. Fast response times, reversible response, and minimal leaching were some of the good characteristics achieved. It was found that the properties of the sensing dyes are also fundamental to produce good quality sensing membranes. This way, increased photostability and high quantum yields are desirable properties for any successful application.

In spite of many problems found, some good quality membranes could be produced which allowed to test different interrogation techniques for determination of pH by luminescent methods. This way, although the feasibility of using intensity measurements to determine the acidity level was demonstrated, it was also clear that this method has very little applicability in practical situations. Being very susceptible to optical power fluctuations, problems like photobleaching and leaching of the dyes can introduce serious errors in the measurements performed in this way. Nevertheless, different techniques which can minimize these problems were also tested. This way, the possibility to perform self-referenced pH measurements was shown by using a ratiometric technique. Although this method eliminates the influence of photobleaching in sensor calibration, it can only be implemented with dyes displaying dual emission. In addition, strong photobleaching will eventually reduce the SNR of the sensor response to the point where accurate measurements are no longer possible.

However, it was shown that a new generation of pH indicators is becoming available with increased photostability and with suitability to implement lifetime based techniques. These dyes are metal-organic complexes and their use has been demonstrated in different luminescent sensing applications. A particular case was shown where the pH changes induced a spectral shift of the dye spectral emission. It was then demonstrated that this introduced the possibility of implementing self-referenced intensity based detection scheme, which allowed to perform pH measurements independently from optical power drifts of any origin.

The possibility of using metal organic complexes to implement pH sensors with infrared emission and compatible with frequency domain interrogation was also demonstrated. Although

some difficulties were found in the immobilization of these dyes in a sol-gel membrane, these problems can be solved by adjustment of the fabrication parameters.

Overall, although many typical problems of luminescence based applications were clearly identified, it was also observed that a wide variety of techniques is available which allows to overcome some of the major limitations. Although far from being a straight-forward task, very careful choices of sensing dye, immobilization material and interrogation technique will allow the implementation of high performance sensing systems for pH and other biochemical parameters.

References

[1] Mignani, A.G. and F. Baldini, *Biomedical sensors using optical fibres.* Reports on Progress in Physics, 1996. **59**(1): p. 1-28.

[2] F. Baldini, A. N. Chester, J. Homola, and S. Martellucci, eds. *Optical Chemical Sensors.* NATO Science Series II. Mathematics, Physics and Chemistry. Vol. 224. 2004, Springer.

[3] Aleksandra Lobnik, Ines Oehme, Ivana Murkovic, and O.S. Wolfbeis, *pH optical sensors based on sol-gels: Chemical doping versus covalent immobilization.* Analytica Chimica Acta 1998. **367**: p. 159-165.

[4] Artur Dybko, Wojciech Wroblewski, Ewa Rozniecka, Krzysztof Pozniak, Janusz Maciejewski, Ryszard Romaniuk, and Z. Brzozka, *Assessment of water quality based on multiparameter fiber optic probe.* Sensors and Actuators a-Physical, 1998. **51**: p. 208–213.

[5] Ferguson, J.A., B.G. Healey, K.S. Bronk, S.M. Barnard, and D.R. Walt, *Simultaneous monitoring of pH, CO2 and O-2 using an optical imaging fiber.* Analytica Chimica Acta, 1997. **340**(1-3): p. 123-131.

[6] Swatland, H.J., *Physical Measurements of Meat Quality - Optical Measurements, Pros and Cons.* Meat Science, 1994. **36**(1-2): p. 251-259.

[7] R. Narayanaswamy and O.S. Wolfbeis, eds. *Optical Sensors - Industrial Environmental and diagnostic Applications.* Springer Series on Chemical Sensors and Biosensors, ed. O.S. Wolfbeis. 2004, Springer: Berlin.

[8] Guillermo Orellana and D. Garcia-Fresnadillo, *Environmental and Industrial Optosensing with Tailored Luminescent Ru(II) Polypyridyl Complexes*, in *Optical Sensors - Industrial Environmental and diagnostic Applications*, R. Narayanaswamy and O.S. Wolfbeis, Editors. 2004, Springer: Berlin. p. 309-357.

[9] *PreSens - Precision Sensing GmbH . http://www.presens.de.* [cited 2006].

[10] Amao, Y., *Probes and polymers for optical sensing of oxygen.* Microchimica Acta, 2003. **143**(1): p. 1-12.

[11] Butler, T.M., B.D. MacCraith, and C. McDonagh, *Leaching in sol-gel-derived silica films for optical pH sensing.* Journal of Non-Crystalline Solids, 1998. **224**(3): p. 249-258.

[12] Hartmann, P., M.J.P. Leiner, and P. Kohlbacher, *Photobleaching of a ruthenium complex in polymers used for oxygen optodes and its inhibition by singlet oxygen quenchers.* Sensors and Actuators B-Chemical, 1998. **51**(1-3): p. 196-202.

[13] Lin, J., *Recent development and applications of optical and fiber-optic pH sensors.* Trends in Analytical Chemistry, 2000. **19**(9): p. 541-552.

[14] Browne, C.A., D.H. Tarrant, M.S. Olteanu, J.W. Mullens, and E.L. Chronister, *Intrinsic sol-gel clad fiber-optic sensors with time-resolved detection.* Analytical Chemistry, 1996. **68**(14): p. 2289-2295.

[15] Campbell, M., Y.T. Yang, P.A. Wallace, and A.S. HolmesSmith, *A multipoint quasi-distributed optical fiber pH sensor.* Optical Review, 1997. **4**(1A): p. 111-113.

[16] Wallace, P.A., N. Elliott, M. Uttamlal, A.S. Holmes-Smith, and M. Campbell, *Development of a quasi-distributed optical fibre pH sensor using a covalently bound indicator.* Measurement Science & Technology, 2001. **12**(7): p. 882-886.

[17] de Levie, R., *The Henderson-Hasselbalch equation: Its history and limitations.* Journal of Chemical Education, 2003. **80**(2): p. 146-146.

[18] Debbie Willoughby, Roger C. Thomas, and C.J. Schwiening, *Comparison of simultaneous pH measurements made with 8-hydroxypyrene-1,3,6-trisulphonic acid (HPTS) and pH-sensitive microelectrodes in snail neurones.* Eur J Physiol, 1998. **436**: p. 615-622.

[19] Miao Yuqing, Chen Jianrong, and F. Keming, *New technology for the detection of pH.* J. Biochem. Biophys. Methods, 2005. **63**: p. 1 -9.

[20] David A. Chang-Yen, Yuri Lvov, Michael J. McShane, and B.K. Gale, *Electrostatic self-assembly of a ruthenium-based oxygen sensitive dye using polyion–dye interpolyelectrolyte formation.* Sensors and Actuators B, 2002(87): p. 336-345.

[21] Jason M. Price, Wenying Xu, J. N. Demas, and B.A. DeGraff, *Polymer-Supported pH Sensors Based on Hydrophobically Bound Luminescent Ruthenium(II) Complexes.* Anal. Chem., 1998(70): p. 265-270.

[22] Crisp, M.T. and N.A. Kotov, *Preparation of nanoparticle coatings on surfaces of complex geometry.* Nano Letters, 2003. **3**(2): p. 173-177.

[23] Ignacio Del Villar, Ignacio R. Matías, Francisco J. Arregui, and Richard O. Claus, *Fiber-Optic Hydrogen Peroxide Nanosensor.* IEEE SENSORS JOURNAL, 2005. **5**(3): p. 365-371.

[24] Mohr, G.J., *Polymers for Optical Sensors*, in *Optical Chemical Sensors*, F. Baldini, et al., Editors. 2004, Springer. p. 297-321.

[25] Carofiglio, T., C. Fregonese, G.J. Mohr, F. Rastrelli, and U. Tonellato, *Optical sensor arrays: one-pot, multiparallel synthesis and cellulose immobilization of pH and metal ion sensitive azo-dyes.* Tetrahedron, 2006. **62**(7): p. 1502-1507.

[26] MacCraith, B.D., C. McDonagh, A.K. Mcevoy, T. Butler, G. OKeeffe, and V. Murphy, *Optical chemical sensors based on sol-gel materials: Recent advances and critical issues.* Journal of Sol-Gel Science and Technology, 1997. **8**(1-3): p. 1053-1061.

[27] Podbielska, H., Agnieszka Ulatowska-Jarza, Gerhard Muler, and H.J. Eichler, *Sol-Gels for Optical Sensors*, in *Optical Chemical Sensors*, F. Baldini, et al., Editors. 2004, Springer. p. 353-385.

[28] J. Y. Ding, M.R. Shahriari, and G.H. Sigel, *Fibre Optic pH Sensor Prepared by Sol-gel Immobilisation Technique.* Electron. Lett., 1991. **27**(17).

[29] Colette .M. McDonagh, B.D. MacCraith, and A.K. McEvoy, *Tailoring of sol–gel films for optical sensing of oxygen in gas and aqueous phase.* Anal. Chem., 1998. **70**: p. 45–50.

[30] Ingo Klimant, Falk Ruckruh, Gregor Liebsch, Achim Stangelmayer, and O.S. Wolfbeis, *Fast response oxygen micro-optodes based on novel soluble ormosil glasses.* Mikrochimica Acta, 1999. **131**: p. 35-46.

[31] Makote, R. and M.M. Collinson, *Organically modified silicate films for stable pH sensors.* Analytica Chimica Acta, 1999. **394**(2-3): p. 195-200.

[32] Haley R. Kermis, Yordan Kostov, Peter Harms, and G. Rao, *Dual Excitation Ratiometric Fluorescent pH Sensor for Noninvasive Bioprocess Monitoring: Development and Application.* Biotechnol. Prog., 2002 **18,**: p. 1047-1053.

[33] Barry G. Grossman, Sompoch Boonsopa, and M. Sokol, *Lead-insensitive fiber optic pH sensor and performance under bending.* Optics & Laser Technology, 2005. **37**: p. 199 - 209.

[34] Antonius Song, Stephen Parus, and Raoul Kopelman, *High-Performance Fiber-Optic pH Microsensors for Practical Physiological Measurements Using a Dual-Emission Sensitive Dye.* Anal. Chem., 1997. **69**(5): p. 863-867.

[35] J. N. Demas and B.A. DeGraff, *Applications of luminescent transition metal complexes to sensor technology and molecular probes.* Journal of Chemical Education, 1997. **74**: p. 690-695.

[36] Gerard O'Keeffe, Brian D. MacCraith, Aisling K. McEvoy, Colette M. McDonagh, and J.F. McGilp, *Development of LED-based phase fluorimetric oxygen sensor using evanescent wave excitation of a sol-gel immobilized dye.* Sensors and Actuators B, 1995. **29**: p. 226-230.

[37] Clarke, Y., W.Y. Xu, J.N. Demas, and B.A. DeGraff, *Lifetime-based pH sensor system based on a polymer supported ruthenium(II) complex.* Analytical Chemistry, 2000. **72**(15): p. 3468-3475.

[38] Murtaza, Z., Q. Chang, G.V. Rao, H. Lin, and J.R. Lakowicz, *Long-lifetime metal-ligand pH probe.* Analytical Biochemistry, 1997. **247**(2): p. 216-222.

[39] Koranczi, I., J. Reichert, H.J. Ache, C. Krause, T. Werner, and O.S. Wolfbeis, *Submicron sensors for ion detection based on measurement of luminescence decay time.* Sensors and Actuators B-Chemical, 2001. **74**(1-3): p. 47-53.

[40] Christian Huber, Ingo Klimant, Christian Krause, and O.S. Wolfbeis, *Dual Lifetime Referencing as Applied to a Chloride Optical Sensor.* Anal. Chem., 2001. **73**: p. 2097-2103.

[41] B.D. Gupta and S. Sharma, *A long-range fiber optic pH sensor prepared by dye doped sol-gel immobilization technique.* Optics Communications 1998. **154**: p. 282-284.

[42] Lin, J. and D. Liu, *An optical pH sensor with a linear response over a broad range.* Analytica Chimica Acta, 2000. **408**(1-2): p. 49-55.

[43] C. Malins, H.G. Glever, T.E. Keyes, J.G. Vos, W.J. Dressick, and B.D. MacCraith, *Sol–gel immobilised ruthenium II polypyridyl complexes as chemical transducers for optical pH sensing.* Sensors and Actuators B, 2000. **67**: p. 89–95.

[44] I. Sanchez-Barragan, J.M. Costa-Fernandez, and A. Sanz-Medel, *Tailoring the pH response range of fluorescent-based pH sensing phases by sol–gel surfactants co-immobilization.* Sensors and Actuators B, 2005. **107**: p. 69-76.

[45] Wolfbeis, O.S. and H. Offenbacher, *Fluorescence Sensor for Monitoring Ionic-Strength and Physiological Ph Values.* Sensors and Actuators, 1986. **9**(1): p. 85-91.

[46] N. Opitz and D.W. Luebbers, *New fluorescence photometrical techniques for simultaneous and continuous measurements of ionic strength and hydrogen ion activities.* Sens. Actuat., 1983. **4**(3): p. 473-479.

[47] Weidgans, B.M., *New Fluorescent Optical pH Sensors with Minimal Effects of Ionic Strength*, in *Naturwissenschaftlichen Fakultät IV – Chemie und Pharmazie.* 2004, Universität Regensburg: Regensburg. p. 147.

[48] Noire, M.H., C. Bouzon, L. Couston, J. Gontier, P. Marty, and D. Pouyat, *Optical sensing of high acidity using a sol-gel entrapped indicator.* Sensors and Actuators B-Chemical, 1998. **51**(1-3): p. 214-219.

[49] Tan, W.H., Z.Y. Shi, and R. Kopelman, *Development of Submicron Chemical Fiber Optic Sensors.* Analytical Chemistry, 1992. **64**(23): p. 2985-2990.

[50] Kopelman, R. and W.H. Tan, *Near-Field Optical Microscopy, Spectroscopy, and Chemical Sensors.* Applied Spectroscopy Reviews, 1994. **29**(1): p. 39-66.

[51] Deepak Uttamchandani and S. McCulloch, *Optical nanosensors - towards the development of intracellular monitoring.* Advanced Drug Delivery Reviews, 1996(21): p. 239-247.

[52] J L Gehrich , D W Lubbers, N Opitz, D R Hansmann, W W Miller , K.K. Tusa, and M. Yafuso, *Optical fluorescence and its application to an intravascular blood gas monitoring system.* IEEE Trans. Biomed. Eng. , 1986 **BE-33**: p. 117-32.

[53] Baldini, F., S. Bracci, F. Cosi, P. Bechi, and F. Pucciani, *Controlled-Pore Glasses Embedded in Plastic Optical Fibers for Gastric Ph Sensing Purposes.* Applied Spectroscopy, 1994. **48**(5): p. 549-552.

[54] Antony S. Jeevarajan, Sundeep Vani, T.D. Taylor, and M.M. Anderson, *Continuous pH Monitoring in a Perfused Bioreactor System Using an Optical pH Sensor.* Biotechnol. Bioeng., 2002. **78**(4): p. 467-472.

[55] Jones, T.P., S.J. Coldiron, W.J. Deninger, and M.D. Porter, *A Field-Deployable Dual-Wavelength Fiberoptic Ph Sensor Instrument Based on Solid-State Optical and Electrical Components.* Applied Spectroscopy, 1991. **45**(8): p. 1271-1277.

[56] Maher, M.H. and M.R. Shahriari, *A Fiber Optic Chemical Sensor for Measurement of Groundwater Ph.* Journal of Testing and Evaluation, 1993. **21**(5): p. 448-452.

[57] Ertekin, K., I. Klimant, G. Neurauter, and O.S. Wolfbeis, *Characterization of a reservoir-type capillary optical microsensor for pCO(2) measurements.* Talanta, 2003. **59**(2): p. 261-267.

[58] Mills, A., L. Wild, and Q. Chang, *Plastic colorimetric film sensors for gaseous ammonia.* Mikrochimica Acta, 1995. **121**(1-4): p. 225-236.

[59] Marazuela, M.D. and M.C. Moreno-Bondi, *Fiber-optic biosensors - an overview.* Analytical and Bioanalytical Chemistry, 2002. **372**(5-6): p. 664-682.

[60] Morf, W.E., K. Seiler, B. Rusterholz, and W. Simon, *Design of a Calcium-Selective Optode Membrane Based on Neutral Ionophores.* Analytical Chemistry, 1990. **62**(7): p. 738-742.

[61] Tan, S.S.S., P.C. Hauser, N.A. Chaniotakis, G. Suter, and W. Simon, *Anion-Selective Optical Sensors Based on a Coextraction of Anion-Proton Pairs into a Solvent-Polymeric Membrane.* Chimia, 1989. **43**(9): p. 257-261.

[62] C. Krause, T. Werner, C. Huber, O. S. Wolfbeis, and M.J.P. Leiner, *pH-Insensitive Ion selective optode: A Coextraction Based Sensor for Potassium Ions.* Anal. Chem., 1999. **71**: p. 1544

[63] Cajlakovic, M., A. Lobnik, and T. Werner, *Stability of new optical pH sensing material based on cross-linked poly(vinyl alcohol) copolymer.* Analytica Chimica Acta, 2002. **455**(2): p. 207-213.

[64] Zhujun, Z., Y. Zhang, M. Wangbai, R. Russell, Z.M. Shakhsher, C.L. Grant, W.R. Seitz, and D.C. Sundberg, *Polyvinyl-Alcohol) as a Substrate for Indicator Immobilization for Fiber-Optic Chemical Sensors.* Analytical Chemistry, 1989. **61**(3): p. 202-205.

[65] Odian, G., *Principles of Polymerization.* 2004, New Jersey: John Wiley & Sons.

[66] Kuswandi, B., *Optical Chemical Sensors for the Determination of Heavy Metal Ions: A mini review.* Jurnal ILMU DASAR, 2000. **1**(2): p. 18 - 29.

[67] Jin, W.J., J.M. Costa-Fernandez, and A. Sanz-Medel, *Room temperature phosphorescence pH optosensor based on energy transfer.* Analytica Chimica Acta, 2001. **431**(1): p. 1-9.

[68] Kohle, O., S. Ruile, and M. Gratzel, *Ruthenium(II) charge-transfer sensitizers containing 4,4'-dicarboxy-2,2'-bipyridine. Synthesis, properties, and bonding mode of coordinated thio- and selenocyanates.* Inorganic Chemistry, 1996. **35**(16): p. 4779-4787.

[69] Lakowicz, J.R., F.N. Castellano, J.D. Dattelbaum, L. Tolosa, G. Rao, and I. Gryczynski, *Low frequency modulation sensors using nanosecond fluorophores.* Analytical Chemistry, 1998. **70**(24): p. 5115-5121.

[70] Fabian, J., H. Nakazumi, and M. Matsuoka, *Near-Infrared Absorbing Dyes.* Chemical Reviews, 1992. **92**(6): p. 1197-1226.

[71] Xu, W.Y., K.A. Kneas, J.N. Demas, and B.A. DeGraff, *Oxygen sensors based on luminescence quenching of metal complexes: Osmium complexes suitable for laser diode excitation.* Analytical Chemistry, 1996. **68**(15): p. 2605-2609.

[72] P. Innocenzi, H. Kozuka, and T. Yoko, *Fluorescence properties of the $Ru(bpy)_3^{2+}$ complex incorporated in sol–gel-derived silica coating films.* J. Phys. Chem. B, 1997. **101**(2285–2291).

Chapter 4

Luminescence Based Oxygen Sensors

Summary

The determination of oxygen concentration using luminescence based techniques is a powerful tool for many biomedical and environmental applications. Sensors based on luminescence quenching of transition metal complexes, immobilized in sol-gel based membranes, have been particularly successful in this regard. In this chapter, an overview of the main developments in this research area is presented. In addition, an interrogation system for luminescent measurements in the intensity and phase domain is presented. The system is used to evaluate oxygen sensing fiber probes based on luminescence quenching of ruthenium complexes, immobilized in sol-gel membranes. Several fiber probe geometries are tested and characterized. Experimental results are obtained that provide valuable clues towards the implementation of an ideal sensing system. A scheme for simultaneous determination of temperature and oxygen concentration, with applicability in many luminescence based biochemical sensors, is proposed. Preliminary results are presented which show the viability of an oxygen measurement that is independent of temperature and optical power drifts.

4.1 Introduction

Oxygen is a critical element in an immense range of applications, from life sciences to industry. Being of vital importance to life itself, it is a key parameter in many areas of medicine such as blood gas analyses and monitoring of respiratory cycles. Conversely, its monitoring in the environment, both atmospheric and dissolved oxygen (DO), provides an indication of the ecosystems health. Many biological processes, and their application in industry (fermentation, waste water treatment), depend critically on oxygen concentration. Its strong electron affinity makes it a chemical element with a key role in many industrial processes, from oil industry to nuclear plants. Although an abundant element in the environment, the cost associated with processing, packaging, delivering and using oxygen can be considerable[26]. The accurate on-line knowledge of oxygen

[26] Oxygen is a non-metallic element of atomic number 8. Its symbol is O and its atomic weight is 15.9994. As a free element oxygen makes up to 20.948% of the atmosphere by volume and 45.5% of the lithosphere by weight, where it occurs in the form of various compounds (oxides, silicates, carbonates, phosphates, sulfates, and a variety of more

concentration, both gaseous and dissolved, is highly desirable or even mandatory in many of the applications referred above. Such information will allow improving the systems control and management capability. In this framework, a high performance oxygen sensor is an essential tool in a wide range of applications [1-4]. An outline of the main areas where oxygen measurement plays a critical role is shown in Table 4-1.

Area	Application
Military/government	
Confined space	Shipboard monitoring, cockpit
Nuclear power	Reactor cooling water
Space	Capsule monitoring
Toxic waste	Field monitors
Medical	
Blood gas	Bedside monitors, noninvasive checks
Ventilators	Control respiration cycle
Operating rooms	N2-O2 mixing
Environmental	
Air pollution	Automobile engine management, air quality
Ground/surface water/ocean	BOD determination, pollution monitoring
Municipal water	BOD, water quality, waste treatment plants
Industrial Processes	
Biological	Fermentation, synthesis
Chemical	Petroleum cracking, catalysis
Boiler water	Corrosion control
Nuclear plants	Cooling water monitors
Food/brewing	Carbonation, packaging, process control
Semiconductor	Plating processes
Gas suppliers	O2/CO2 suppliers
Health safety	
Occupational	Mines, silos, tunnels, manhole monitors
Building	Air Conditioner monitors/controls
Inerting	Explosion control
Transportation	
Perishables	Container monitors
Ship safety	Environmental/ explosion control
Auto emissions	Exhaust sensors
Miscellaneous	
Scuba diving	Gas recovery systems
Aquariums	Commercial fish tanks, aquaculture
BOD - biological oxygen demand	

Table 4-1 Sample of the range of applications for oxygen sensors [4].

Historically, oxygen measurements have been performed by gas chromatography, mass spectroscopy, paramagnetic resonance and electrochemical techniques. Many of these methods demand expensive equipment and are not easily applied in a non-laboratorial environment. The

complex compounds). In addition, water contains 88.9% oxygen, by weight. Oxygen can be obtained from decomposition of oxygen-containing compounds, or by the electrolysis of water. These techniques, however, are not adequate for large scale production. The fractional distillation of liquid air is by far the most important method of producing oxygen for commercial purposes.

Clark electrode, based on an electrochemical cell, has been particularly successful in the measurement of dissolved oxygen in life sciences applications. The Clark electrode consists of a sensing platinum electrode (cathode) and a reference silver electrode (anode), immersed in an electrolyte solution and enclosed within an oxygen permeable membrane. The potential of the electrodes is controlled in order to reduce oxygen to hydroxide ions, creating a current that is proportional to the oxygen concentration. The Clark cell is robust and quite reliable. However, it is bulky and its miniaturization can be a complex and expensive process. In addition, because oxygen has to diffuse through the membrane and the electrolyte, response times are usually slow (around a minute). Also, both oxygen and the electrolyte solution are consumed during the measurement process. This requires periodical substitution of the electrolyte. Oxygen consumption, on the other hand, can be critical in some applications where very low volumes and concentrations are typical. Furthermore, there is a tendency of the electrode to drift, besides its inability to endure large pressure differentials. Membrane fouling and degradation can also hinder sensor operation in hazardous environments. Finally, no electrode-based sensor can operate reliably in an hazardous electromagnetic environment.

Consequently, there is substantial interest in the development of more advanced and reliable techniques for oxygen detection. In this context, the determination of gaseous or dissolved oxygen using optical technologies offers several advantages when compared with conventional, electrode-based, techniques. Immunity to electromagnetic interference, fast response times, increased sensitivity and no oxygen consumption are some of the more important features associated with optical oxygen sensing. Dynamic quenching of the luminescence of a molecular indicator by oxygen is the most widely used sensing mechanism for optical detection of this gas. This highly sensitive technique is particularly suited for sensing of biochemical parameters and can be used in combination with optical fiber technologies. The use of optical fiber introduces further advantages, like the possibility of remote detection, multiplexing capability and development of highly compact devices [5-8].

The promise of such highly developed analytical instruments has been the driving force behind strong research efforts applied in this specific field. For this reason, optical oxygen sensing technologies suffered major progresses over the last 20 years. In particular, the introduction of long-lived metal-organic complexes, with high quantum yields and increased photostability, together with developments in immobilization polymer and sol-gel chemistry, and the advent of blue laser diodes and LEDs, allowed the implementation of high performance low-cost instrumentation [9-13]. Presently, optical oxygen sensors based on these technologies are already making their appearance as

commercial products [14, 15]. However, in spite of these great advances, there is still much room for improvement. Leaching and photo-bleaching of the indicators usually degrade the sensor performance and strongly hinder long term applications. Moreover, dependence on temperature and on the level of the excitation optical power must be compensated. Multipoint and distributed sensing of oxygen are also little explored. This way, the scientific community still dedicates a great deal of attention to this particular field [16-18].

In this chapter, an overview of the present state of optical oxygen sensing technology will be given. Both fundamental research aspects and state of the art applications will be addressed. In addition, the implementation of a prototypical optical fiber sensing system for oxygen detection, based on the quenching of luminescence, will be described. The system implemented will be used to identify several critical parameters for sensor performance. Results are presented regarding the optimization of the optical fiber probe geometry, tailoring of the sensing membranes and simultaneous measurement of temperature and oxygen.

4.2 Oxygen sensing by luminescence quenching

Oxygen is a very efficient quencher of almost all luminescent species. In addition, due to its small molecular dimensions, it has high diffusion coefficients in a variety of gaseous and aqueous media. These properties make it a potentially interfering element in many luminescence applications where very often its presence must be avoided; this is usually achieved by degassing solutions with nitrogen. On the other hand, it is not surprising that although several techniques exist for optical detection of oxygen using, for instance, chemiluminescence or reflectometry of hemoglobin, most optical oxygen sensors use dynamic quenching of luminescence as the preferred sensing mechanism [10, 13].

4.2.1 Sensing mechanism

There are several means by which oxygen can quench the luminescence of excited molecular indicators. The dominant mechanism will depend on the interacting molecules and the surrounding environment. Overall, any bimolecular process involving the quencher and the luminescent indicator that deactivates the excited state will result in reduced luminescent intensity and lifetime. Measurement of either of these parameters will provide a way to determine the quencher concentration.

For some organic indicators it is thought that paramagnetic oxygen causes the excited fluorophore to undergo intersystem crossing to a triplet state, by spin-orbit coupling. In fluid

solutions such long-lived triplet states are completely quenched by interaction with solvent molecules and phosphorescence is not observed. Oxidation of the luminescent indicators can also cause quenching by electron transfer where the charged species becomes non-luminescent. In the particular case of long-lived luminescent indicators, energy transfer between oxygen and the luminophore is often the dominant quenching process [9, 19].

The ground state of molecular oxygen is a triplet state, $^3O_2$. Following excitation, oxygen can exist in singlet states generically denoted by $^1O_2$. This way, quenching of excited state luminophores, M^*, usually involves energy transfer from M^* to $^3O_2$ and results in the production of singlet oxygen. The basic steps involved in this process are represented by the following equations:

$$M + h\nu \longrightarrow M^* \qquad excitation\,, \tag{4.1}$$

$$M^* \xrightarrow{k_r + k_{nr}} M + h\nu' or\, \Delta \qquad luminescence\ or\ deactivation\,, \tag{4.2}$$

and

$$M^* + {}^3O_2 \xrightarrow{k_q} M + {}^{*1}O_2 \qquad quenching\,. \tag{4.3}$$

When the ground state luminophore, M, absorbs a photon with adequate energy, $h\nu$, an excited state luminophore, M^*, is obtained. This excited species will eventually return to its ground state. This can happen either by non-radiative processes, where the excess energy, Δ, is thermally dissipated to the surrounding environment, or by emission of a photon with smaller energy, $h\nu'$. The rate at which these radiative and non-radiative events take place is determined by the associated rate constants, given respectively by k_r and k_{nr}, and establishes the excited state lifetime of the luminophore in the absence of the quencher ($\tau_0 = 1/(k_r + k_{nr})$). Depending on the particular luminescent molecule, the excited species can be a short-lived singlet state or a long-lived triplet state; while the former corresponds to fluorescence emission, the later is associated with phosphorescence.

The quenching process introduces an additional deactivation pathway by which the excited luminophores return to their ground state by non-radiative means. The rate of de-excitation will be determined by the quencher concentration, $[O_2]$, and by the apparent rate constant, k_q, of the bimolecular quenching interaction. This way, the presence of the quencher introduces a decay rate given by $k_q[O_2]$. The new deactivation process reduces the number of emission events and, therefore, increasing the quencher concentration will result in a decrease of the luminescence emission. Conversely, the excited state lifetime in the presence of the quencher will be reduced as well (as it is given by $\tau = 1/(k_r + k_{nr} + k_q[O_2])$).

The Stern Volmer equation

Quenching processes are photophysical processes in which there is no chemical interaction between the intervenient molecules. This way, after all the de-excitation steps, the luminophore and the oxygen molecules return unaltered to the ground state and, therefore, oxygen is not consumed. These processes are reversible and, consequently, a reduction in oxygen concentration results in an increase of both the luminescence intensity and the excited state lifetime. All the quenching mechanisms described so far, including energy transfer, are dynamic quenching processes which result from a collisional encounter between the excited luminophore and the quencher molecule. In dynamic or collisional quenching processes the bimolecular interaction is diffusion-limited. This means that the rate constant associated with the intrinsic quenching mechanism is much faster than the diffusion process. Under these conditions, the observed k_q is determined by the diffusion rate. The behavior of the luminescent intensity, I, and the excited state lifetime, τ, of a luminophore subjected to collisional quenching by oxygen can be accurately described by the Stern Volmer (SV) equation:

$$\frac{I_0}{I} = \frac{\tau_0}{\tau} = 1 + K_{SV}[O_2] \tag{4.4}$$

where I_0 and τ_0 are respectively the luminescence intensity and the excited state lifetime in the absence of quencher and $[O_2]$ represents the concentration of oxygen. K_{SV} is the SV constant, and for collisional processes it is given by

$$K_{SV} = k_q \tau_0 . \tag{4.5}$$

Equation (4.4) indicates that both the luminescence intensity and the lifetime will decrease in a hyperbolic fashion with increasing oxygen concentration. Ideally, plots of I_0 / I and τ_0 / τ as a function of $[O_2]$ will be linear with identical slopes of K_{SV}, and provide adequate calibration functions to perform quenching-based oxygen measurements using intensity or lifetime data. The fact that lifetime and intensity present the same behavior, i.e., $I_0 / I = \tau_0 / \tau$, is a signature of pure dynamic quenching [19, 20]. Further details about the SV equation and the different quenching mechanisms are given in chapter two.

Besides being quenched by oxygen, the excited states of most luminescent indicators are usually sensitive to the surrounding environment and will respond to other species like metal ions, oxidants, surfactants, proteins, etc.. This way, in practical systems, the sensing indicator must be isolated from interfering species while still being accessible to oxygen. The most common method to achieve such selectivity is to incorporate the sensing dye in a gas permeable, solvent impermeable

membrane. In addition to selectivity, the membrane provides a solid support for the sensing luminophore, avoiding its loss into the probed medium and permitting the long term use of the sensing device. In the particular case of optical fiber applications, the solid host is used to immobilize the sensing chemistry by depositing a doped thin film on the fiber tip, allowing to obtain very compact sensing probes. Polymers and sol-gel glasses are typically used to immobilize a variety of sensing dyes [21, 22]. Silicone rubbers are widely used in oxygen sensing applications because they are highly permeable to oxygen, yet, being very hydrophobic they are impermeable to most ionic species. In addition, they are biocompatible. The immobilization membrane is essential for practical implementation of a sensing system. Because it will interfere in the way the sensing luminophore interacts with oxygen, its characteristics will be critical for sensor performance [23, 24].

Sensor sensitivity

The main parameters controlling the sensitivity of an oxygen sensing membrane are incorporated in the SV constant, K_{SV}. In general, the greater the value of this constant the greater the sensitivity of the resulting optical oxygen sensor will be. In most luminescence quenching applications, K_{SV} will depend on many factors related with the properties of the sensing luminophore, but also on the characteristics of the immobilization material. For the purpose of identifying and evaluating the influence of such parameters, the SV equation can be rewritten after some simple considerations.

When the sensing film is present in a gaseous environment, for moderate gas pressures the equilibrium oxygen concentration in the polymer film is proportional to the oxygen partial pressure (pO_2) just above the film. This means that, in polymers, oxygen obeys Henry's law which states that

$$[O_2] = K_H \, pO_2, \tag{4.6}$$

where the proportionality constant, K_H, is Henry's constant and determines the oxygen solubility in the host polymer. In addition, for diffusion controlled quenching mechanisms, the bimolecular quenching rate constant, k_q, is related to the diffusion rate constant , k, by

$$k_q = \gamma k \tag{4.7}$$

where γ is the quenching efficiency. For diffusion limited processes involving oxygen usually this parameter is approximately equal to unit, meaning that practically every collisional encounter results in deactivation of the excited luminophore. The actual value of k is dependent on the properties of the medium and on the characteristics of the interacting molecules. In the Smoluchowsky model, k depends on the sum of the diffusion coefficients of the luminophore and the quencher. However,

considering that usually oxygen diffuses much faster than the dye molecule, $D_{O_2} + D_M \approx D_{O_2}$, the diffusion rate constant can then be written as

$$k = \frac{4\pi R_c N}{1000} D_{O_2}, \tag{4.8}$$

where R_c is the collision radius, given by the sum of the molecular radii of the luminophore and oxygen and N is Avogadro's number. Substitution of equations (4.6), (4.7) and (4.8) into equation (4.4) yields

$$\frac{I_0}{I} = \frac{\tau_0}{\tau} = 1 + \frac{4\pi R_c N}{1000} \gamma \tau_0 (D_{O_2} K_H) p O_2 . \tag{4.9}$$

By writing the Stern Volmer equation in this fashion, the parameters influencing the sensitivity of a practical oxygen sensor can be readily identified: the excited state lifetime of the luminescent indicator in the absence of the quencher, τ_0; Henry's constant, K_H, which is a measure of the solubility of oxygen in the host medium; and the diffusion coefficient of oxygen in the sensing membrane, D_{O_2}. The product of D_{O_2} by K_H gives the oxygen permeability of the sensing membrane, P. For sensors of dissolved oxygen, the product $K_H\, p_{O_2}$ has to be replaced by the product of the partition ratio[27] for oxygen times the oxygen concentration in the liquid sampled [25].

In order for the quenching events to take place, the mutual approach of the two molecules involved must occur on timescales smaller than the excited state lifetime of the luminophore. This means that effective quenching by oxygen will only take place when τ_0 exceeds $1/kq[O_2]$. In most polymer matrices, typical values of $kq[O_2]$ are on the order of $10^7 s^{-1}$. This way, short lived luminophores ($< 0.1\,\mu s$) are not suited for oxygen sensing applications. This is in agreement with equation (4.9), which shows that increasing τ_0 will increase the sensor sensitivity to oxygen. A variety of long-lived luminescent indicators is presently available, with lifetimes ranging from a microsecond to several milliseconds, which are commonly used in oxygen sensing applications. Although it is frequent for the lifetime to change after incorporation in a solid membrane, typically increasing, these changes are usually not significant and depend little on the host medium. This way, the order of magnitude of the unquenched lifetime will be determinant for sensor sensitivity and to establish its operating range.

However, a long-lived luminophore does not necessarily result in a very sensitive oxygen sensor. As can be seen in equation (4.9), the nature of the encapsulating medium and its permeability

[27] The partition ratio is the equilibrium distribution of a given analyte between two different phases, e.g. a liquid phase and the polymer. In this particular example, the partition ratio would be given by $K = C_p / C_l$ where C_l is the concentration of analyte in the liquid phase and C_p is the concentration of analyte in the polymer.

to oxygen also play a critical role. This way, a long lived dye enclosed in a membrane with low permeability can result in a sensor of reduced sensitivity. The influence of the host membrane in the sensor response has been widely studied by several authors [23, 25]. It has been found that the solubility of oxygen in most organic polymers does not vary significantly. Therefore, in polymeric media, the key parameter to control oxygen permeability is the diffusion coefficient of oxygen in these materials. The value of D_{O_2} is strongly dependent on the medium viscosity. Mills et al. [26] demonstrated the possibility of obtaining sensing films with widely different sensitivities using the same luminophore encapsulated in a polymer with different fractions of plasticizer. The amount of plasticizer in the polymer encapsulating medium increases the rate of gas diffusion in the medium by increasing the mobility of polymer segments.

In sol-gel thin films, the diffusion coefficient and the solubility of oxygen were also shown to have a strong direct correlation with oxygen detection sensitivity. However, although ormosil films share some polymer characteristics, generally sol–gel films are quite different in structure and properties. It was found that, in general, sol-gel materials present much higher solubility. In addition, the solubility was shown to vary strongly with sol-gel glass composition. Increased solubility was thought to be related with the high porosity characteristic of these materials which translates in large free volumes within the rigid matrix. Diffusion coefficients in sol-gel glasses, on the other hand, are typically much smaller than in most polymers; even so, increased porosity usually translates in higher diffusion coefficients. Nevertheless, the product of these two parameters, usually results in relatively high oxygen permeability for sol-gel materials, comparable with the values observed in silicone rubbers, and higher than in most polymers [27, 28].

In both polymer and sol-gel materials, it was thoroughly demonstrated that the permeability of oxygen sensing films can be tailored in a wide range simply by controlling the properties of the host material. Overall, proper choice of the luminophore lifetime together with control of the properties of the encapsulating medium will result in oxygen sensors suitable for operation in very different ranges of oxygen levels. Typically, these properties should be adjusted in order to provide maximum sensitivity at the average of the operating range for the specific application. If the sensor is too sensitive to oxygen at the average operating pressure, p_{avg}, it might be the case that the luminescent intensity at these oxygen levels, I_{avg}, is strongly reduced to a point where accurate measurements are no longer possible. In order to have an adequate signal-to-noise ratio (SNR) at the average operating oxygen level, the luminophore-polymer combination should be such that $I_{avg} \approx I_0/2$. This way, small changes in pO_2, in the vicinity of p_{avg}, will lie in the range of the maximum sensitivity to quenching.

Deviations from the Stern Volmer equation

The Stern Volmer equation considered previously describes the simplest situation in which a single luminophore, homogeneously distributed, is subjected to pure dynamic quenching and displays a single exponential decay. In practice, however, this ideal situation is seldom observed, and different mechanisms can contribute to deviations from the behavior described by equation (4.4). Although a detailed analysis of deviations from the standard SV equation is given in chapter two, in the following lines the implications of such behaviors are discussed in the specific framework of oxygen sensing.

With some indicators it is possible that static quenching also takes place. In this process oxygen, or other interfering species, is bonded to the ground state luminophore to form a non-luminescent compound. This way, the number of luminophores available for excitation is reduced and luminescent emission is decreased. However, because this process does not interfere with the excited luminophore population, the lifetime remains unchanged. As a consequence, when dynamic and static quenching processes coexist, equation (4.4) is still valid for the lifetime data; however, the luminescence intensity will present a non-linear behavior that can be described by

$$\frac{I_0}{I} = 1 + (K_{SV} + K_S)[O_2] + K_{SV}K_S[O_2]^2, \tag{4.10}$$

in which K_S is the binding constant associated with the static quenching process. Simultaneous static and dynamic quenching usually translates into an upward curvature of the Stern Volmer plot. Fitting of the experimental data to equation (4.10) can then be used to obtain K_{SV} and K_S. Alternatively, these constants can be obtained graphically from the plot of $(I_0 / I - 1)/[O_2]$ versus $[O_2]$, which should be linear. In addition, the lifetime data provides a way to evaluate the dynamic component alone. Although static quenching can be observed in solutions, mainly when some interfering ionic species is present, it is not frequently observed when the luminophore is immobilized in a solid host.

In practice, immobilization of the sensing dye in a solid host often results in a heterogeneous system which can display even more complex quenching behaviors [29, 30]. Typically, micro-heterogeneities in the sensing membrane arise from the existence of different sites in the solid support having different degrees of oxygen accessibility to the immobilized luminophores, and/or incomplete solubilization of the dye in the polymer matrix. Thus, different populations of the same dye can coexist in different microenvironments in the host matrix, exhibiting different quenching behaviors. In these situations, the SV plot will display a non-linear behavior, usually presenting a downward curvature, which is better described by a modified multi-site SV equation

$$\frac{I_0}{I} = \left[\sum_{i=1}^{m} \frac{f_i}{1 + K_{SV_i} pO_2}\right]^{-1}, \tag{4.11}$$

where f_i is the fractional contribution of the i^{th} luminophore population to the luminescence intensity, and K_{SV_i} are the corresponding Stern Volmer constants. The decay kinetics of such a multi-site model corresponds to the combination of multiple single exponential decays arising from the individual populations. The luminescence intensity decay, $I(t)$, of an heterogeneous system with m different components, following a δ-like pulsed excitation is given by

$$I(t) = \sum_{i=1}^{m} \alpha_i e^{-t/\tau_i} \tag{4.12}$$

where α_i are the pre-exponential weighting factors associated with the i^{th} component and τ_i are their corresponding excited state lifetimes. The fractional contribution to the total emission for each component, f_i, either under pulsed or steady-state excitation, is related to the pre-exponential factors and corresponding lifetimes by

$$f_i = \frac{\alpha_i}{\sum_{i=1}^{m} \alpha_i \tau_i} \tag{4.13}$$

Because the sample displays a multiple exponential decay, it is not possible to directly compare the intensity data with the lifetime data for each component. However, a pre-exponential weighted mean lifetime, τ_M can be defined as

$$\tau_M = \frac{\sum_{i=1}^{m} \alpha_i \tau_i}{\sum_{i=1}^{m} \alpha_i}. \tag{4.14}$$

In the absence of static quenching the α's are the same for the quenched and the unquenched sample; therefore, in the absence of quencher the weighted mean lifetime, denoted by τ_{M0}, is given by

$$\tau_{M0} = \frac{\sum_{i=1}^{m} \alpha_i \tau_{0i}}{\sum_{i=1}^{m} \alpha_i}. \tag{4.15}$$

Assuming that each individual component obeys a linear Stern Volmer equation, it is possible to show that

$$\frac{\tau_{M0}}{\tau_M} = \frac{I_0}{I}, \tag{4.16}$$

and, therefore, equation (4.11) can still be applied to lifetime data, as long as the weighted mean lifetimes, τ_M and τ_{M0}, are used. Whenever the SV plot obtained for the intensity data differs from

the SV plot given by the mean lifetime data, there is an indication that static quenching is taking place within the heterogeneous system.

It was already demonstrated by several authors that, considering two distinct sites, it is usually sufficient to obtain an adequate fit to the quenching data [31]. Such model provides a calibration function that depends only on three parameters, K_{SV_1}, K_{SV_2} and f_1,

$$\frac{I_0}{I} = \frac{1}{f_1/(1+K_{SV_1}\cdot pO_2)+(1-f_1)/(1+K_{SV_2}\cdot pO_2)}. \tag{4.17}$$

However, while an adequate fit is provided, care has to be taken in assigning physical significance to this model. Typically, evaluation of lifetime data in a wide range of oxygen partial pressures indicates that the real situation is often more complex. Although two distinct lifetime components can be identified, it is often the case that the contribution of each component varies with oxygen concentration, and can deviate appreciably from the ratios derived from intensity data. Such behavior is not expected for a simple two site model indicating the lack of physical validity. Many other attempts have been made to accurately describe the quenching dynamics using more complex models. These include consideration of multi-exponential decays, Gaussian or log-Gaussian distributions of luminophore natural lifetimes, or even non-linear gas solubility models [32, 33]. Although all these models allow obtaining adequate fits to the experimental data, most of them fail to provide an adequate physical explanation of the origin of the micro-heterogeneities. Transient effects due to diffusion dependency and apparent static quenching are also phenomena that can further complicate the interpretation of the experimental data. Some models exist that allow incorporating these effects as well. Adequate interpretation of the quenching processes kinetics can be critical when studying the properties of complex systems; for this reason, the search for physically accurate models continues [10, 34]. However, the validity of the physical model is not imperative for sensing applications where only a suitable calibration function is needed. This way, in practical sensing systems, usually the simplest model is used provided it gives an adequate fit to the experimental data.

Leaching and photobleaching

Although apparently simple, the detection of the luminescence intensity to obtain an oxygen measurement has a variety of associated problems. The luminescence intensity is not an intrinsic parameter and depends on a great deal of experimental factors. This way, the long term drift of the optical source and detector can introduce serious measurement errors. In the particular case of optical fiber sensors, variable losses induced by vibrations, bending and changes in the coupling

conditions introduce additional sources of error. Consequently, any sensor based on intensity measurements requires some sort of reference channel, in order to remove the deleterious effect of optical power fluctuations. Several schemes are available to provide sensors with an intensity reference. The most common ones include the use of two different detectors used in combination with two optical sources, or detection of back reflected excitation radiation. The use of a second oxygen insensitive dye, in combination with the sensing luminophore, is also an alternative. In any of these cases, the ratio of the sensing signal to the reference signal provides a measurement free of interference from intensity fluctuations. None of these schemes, however, can compensate for the loss of luminescent molecules. Indeed, in addition to the reversible quenching mechanisms described previously, some processes may affect the sensor response in an irreversible way. Leaching and photobleaching of the sensing dye are two critical phenomena that can seriously compromise the long-term response of luminescence based sensors [16, 35].

When operating in aqueous media, the luminescent indicator may be washed out of the solid membrane. This will result in a decrease of the luminescent intensity which can be mistaken for an increase in oxygen concentration. In order to avoid leaching into aqueous media the dye should be preferably immobilized in hydrophobic membranes. However, some dyes are only soluble in hydrophilic media. In order to render them lipophilic they must be conjugated with adequate chemical ligands. Covalent immobilization is also possible, and results in sensors with very long term stability; the chemical processes involved, however, can be very complex. In addition, both these processes can lead to modification of the dye luminescent properties and response to the analyte. In sol-gel glasses, leaching can be minimized by tailoring the size of the pores. Due to the very small size of oxygen molecules, in comparison with the size of typical luminophores, it is relatively simple to ensure efficient encapsulation of the dye while still keeping it accessible to oxygen. However, the porosity of the sol-gel membrane will impact directly its oxygen permeability, and thus the measurement sensitivity. The use of hybrid sol-gel precursors, or ormosils, allows the implementation of hydrophobic membranes in which leaching can be minimized.

Even when the dye is adequately immobilized, excitation with energetic radiation may lead to irreversible photochemical decomposition of the luminophore molecules. Photochemical processes usually involve breaking of chemical bonds or creation of new bonds. The resulting molecule is usually not luminescent and, therefore, the ground state luminophores are not recovered. This process leads to progressive loss of the luminescent intensity, also called photobleaching, and is one of the major obstacles to the long term use of luminescence based sensors. This is a difficult problem to avoid, particularly in oxygen sensors. Singlet oxygen is a major product of the quenching

process used for oxygen sensing. This is a highly reactive species which can attack and destroy the luminescent complexes through oxidation. One way to reduce this problem is to introduce singlet oxygen quenchers or chemical inhibitors into the sensing matrix. Although these schemes can significantly reduce photobleaching, most frequently the chemicals introduced also quench the dye luminescence, thus resulting in decreased sensitivity. In addition, a variety of other processes can be responsible for photobleaching: interaction with the polymer matrix; some luminescent molecules can undergo thermal activation of anti-bonding states which facilitate molecular decomposition; for high luminophore concentrations, the interaction of two excited luminophore molecules can yield stable reduced products which are not luminescent, resulting in permanent deactivation; etc..

Leaching and photobleaching cause the slow decrease in luminophore population, and therefore in luminescent intensity. Because the number of luminescent molecules is reduced, the decrease of luminescence output cannot be compensated by any of the above mentioned reference schemes. This way, a slow drift will be introduced in sensor response which will demand constant recalibration, strongly hindering the long term operation of the sensing system.

Dual emission luminophores, which present two emission bands with different responses to the analyte, can be used to perform ratiometric detection. In this particular case, because both signal and reference wavelengths originate from the same molecular dye, the effect of leaching and photobleaching is compensated. Although this behavior is often found in some pH indicators, it is relatively rare otherwise [36, 37]. Nevertheless, an oxygen sensitive dye displaying dual emission was recently reported [38]. The proposed scheme is based on ratiometric detection of a short lived fluorescence emission, not affected by the presence of oxygen, and a long lived phosphorescence emission which is quenched by oxygen. Because both emissions are originated by the same molecules, this scheme can compensate for photobleaching, as well as for any other optical power fluctuation. Although this scheme was demonstrated to be suitable for long term applications, luminescent indicators with such characteristics are extremely rare.

The preferred method to avoid intensity drift problems is to perform time resolved measurements of the luminescent decay.

4.2.2 Frequency domain interrogation

The excited state lifetime of the sensing luminophores is an intrinsic parameter which is independent of the level of optical excitation power. In addition, provided the products resulting from photobleaching are non-emissive and that there are no photo-induced changes of the dye's microenvironment, the decay parameters of the luminescent indicators will not be affected by the

photodegradation process. Furthermore, as long as a minimum amount of sensing dye subsists, leaching will not impact lifetime measurements. This way, lifetime-based systems will not suffer from any of the problems that plague intensity-based measurements. However, direct measurements of the lifetime require the analysis of the intensity decay that follows a pulsed excitation. Ideally, the excitation impulse, and the impulse response of the detection system should be shorter than the lifetime to be measured, otherwise complex deconvolution procedures must be applied to the experimental data. Therefore, lifetime measurements typically demand expensive instrumentation, like high-speed electronics and fast pulsed optical sources [39, 40].

Alternatively, lifetime measurements can be performed using frequency domain techniques which are usually associated with simpler and cheaper electronics. Additional advantages of frequency domain detection when compared to direct lifetime measurements include: lower noise of the signal waveforms; need for fewer samples, making measurements much faster; and no need for complex deconvolution procedures which add computation time and hinder real time applications. For these reasons frequency domain based detection is becoming increasingly popular for use in luminescence sensing applications [41-45].

The basic principles of this technique were already thoroughly described in chapter 2. In order to implement frequency domain detection, the amplitude of the excitation optical source must be sinusoidally modulated at an adequate frequency. In this situation, the luminescent emission is given by the convolution of the sinusoidal excitation with the luminescence impulse response. This way, the luminescence output is also modulated in amplitude at the same frequency, but presents a phase delay relative to the excitation waveform. It can be shown that, for a single exponential decay, the phase delay, ϕ, can be related to the lifetime by

$$\tan\phi = 2\pi \cdot f \cdot \tau \tag{4.18}$$

where f is the linear modulation frequency. Changes in oxygen concentration will impact the excited state lifetime and, therefore, will change the measured phase. Combining this expression with the Stern Volmer equation allows to establish a relation between the phase delay and the oxygen concentration

$$\frac{\tan\phi_0}{\tan\phi} = \frac{\tau_0}{\tau} = 1 + K_{SV}[O_2], \tag{4.19}$$

where ϕ_0 is the phase measured in the absence of oxygen. In addition to the phase delay, the luminescent signal will also present a decreased modulation depth. This demodulation can be

evaluated by calculating the ratio between the modulation depths[28] of the excitation and the emission signals, and is related to the lifetime and to the modulation frequency by

$$M = \frac{1}{\sqrt{1 + \left(2\pi f \tau\right)^2}}. \tag{4.20}$$

The changes in oxygen concentration will also impact the modulated luminescence intensity, I_f, which is given by

$$I_f = I_0 \frac{\tau}{\tau_0} M = I_0 \frac{\tau}{\tau_0} \frac{1}{\sqrt{1 + \left(2\pi f \tau\right)^2}}, \tag{4.21}$$

where I_0 is the unquenched steady-state luminescence intensity. For a fixed modulation frequency, I_f obeys the Stern Volmer equation and can also be used to determine the oxygen concentration.

The lifetime, and thus the oxygen concentration, can be estimated either by measuring the phase delay, or by evaluating the modulation ratio. In the presence of a single exponential decay, both measurements will yield the same calculated lifetime. However, it was already discussed that after immobilization in a solid membrane, the luminescent emission is usually characterized by a multiple exponential decay. In these situations, the calculated lifetimes are only apparent values resulting from complex weighting of the various decay parameters, and usually the two independent measurements of the lifetime will yield different values. In typical frequency domain applications, the decay parameters can be retrieved by evaluating ϕ and M in a range of frequencies, followed by fitting of the experimental data with adequate theoretical models. This is a very powerful technique often used to obtain information about complex molecular structures using luminescent probes [45].

For sensing applications, however, the goal is to retrieve the information about the quencher concentration based on the lifetime information. In these situations, it is usually sufficient to evaluate the apparent lifetime at a single modulation frequency. This technique allows for very fast measurements and is therefore suited for real time sensing applications. As a consequence of the multiple exponential decay, the relationship between the measured phase and the modulation frequency is given instead by

---

[28] The modulation depth of the excitation signal can be calculated by the ratio of its alternate and continuous components $m_0 = ac/dc$. Because the luminescence signal is given by the convolution of the luminescence impulse response with the excitation signal, the luminescence output will present a reduced modulation depth $m = AC/DC$. The degree of demodulation can be evaluated by calculation of the ratio $M = m/m_0$, and its dependence on the lifetime and modulation frequency is given by equation (4.20). For further details see chapter 2.

$$\tan\phi = \frac{\sum_{i=1}^{m} f_i \sin\phi_i \cos\phi_i}{\sum_{i=1}^{m} f_i \cos^2\phi_i} \tag{4.22}$$

where ϕ_i are the phase angles associated to each of the decay components, characterized by τ_i and f_i. In this situation the evolution of the measured phase delay as a function of oxygen concentration can no longer be described by a simple SV equation, and the non-linear sensor calibration function must be fit by a multi-site quenching model (equation (4.11)).

Modulation frequency and sensitivity

In practical sensing systems, the phase measurement is usually performed using a lock-in amplifier. Given the signal of the photodetector used to measure the luminescent response and a reference signal, the lock-in yields a phase signal and an intensity signal which are proportional to equations (4.18) and (4.21), respectively [46]. Both ϕ and I_f depend simultaneously on the modulation frequency and on the excited state lifetime. This behavior can be observed in Figure 4.1 where the normalized luminescence intensity, I_f / I_0 (figure (a)), and the phase delay (figure (b)), are represented as a function of modulation frequency, for different values of oxygen partial pressure. The data represented in these figures was calculated using equations (4.18), (4.19), and (4.21), considering a luminophore with an unquenched lifetime of $\tau_0 = 5\,\mu s$ and a SV constant $K_{SV} = 5 \cdot 10^{-5}\,Pa^{-1}$. Different oxygen partial pressures were considered, 0, 10, 30, 50 and $101\,kPa$, corresponding respectively to quenched lifetimes of 5.0, 3.3, 2.0, 1.4 and $0.8\,\mu s$.

It can be clearly observed that increasing the modulation frequency will result in an increase of the sensitivity of the phase delay to changes in the oxygen partial pressure. As the modulation frequency is increased, sensitivity reaches a maximum value after which it decreases steadily. From equation (4.18) it is easy to show that the modulation frequency at which the sensitivity is maximal is given[29] by

$$\omega_{opt} = \frac{1}{\tau} \qquad or \qquad f_{opt} = \frac{1}{2\pi\tau}. \tag{4.23}$$

This relationship indicates that, in order to obtain maximum sensitivity for phase measurements using a luminophore of lifetime τ, the excitation source should be modulated at a frequency which is given by the reciprocal of the lifetime [47].

---

[29] From equation (4.18) it can be written $\phi = \arctan\langle\omega\tau\rangle$. Therefore, the sensitivity of the phase angle to changes in the luminophore lifetime is given by $\partial\phi/\partial\tau = \omega/(1+\langle\omega\tau\rangle^2)$. The frequency at which the sensitivity is maximum can then be obtained from $\partial(\partial\phi/\partial\tau)/\partial\omega = 0$, which results in equation (4.23).

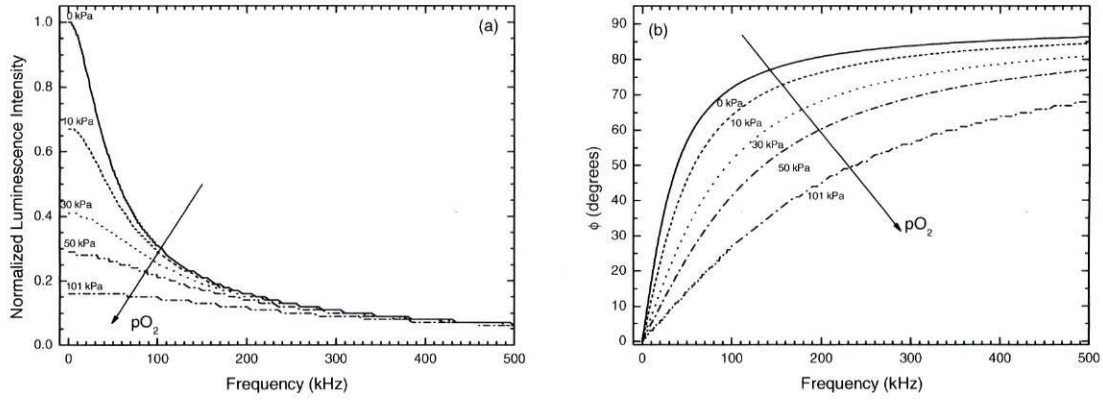


Figure 4.1 Dependence of the normalized luminescence intensity (a) and corresponding phase shift (b) on the modulation frequency of the excitation, f, at different oxygen concentrations, pO_2: 0, 10, 30, 50 and $101\,kPa$.

When the luminophore is modulated at such frequency, the sensitivity is

$$\frac{\partial \phi}{\partial \tau} = \frac{1}{2\tau}, \tag{4.24}$$

and the phase shift is equal to $45°$. In the particular case of the calculated results, the optimum modulation frequency, considering the unquenched lifetime of $5\,\mu s$, is approximately $32\,kHz$.

The optimum frequency given by equation (4.23) is valid whenever the phase noise $\Delta\phi$ is independent of the modulation frequency. However, in a practical oxygen sensing system, this is hardly verified. As the modulation frequency is increased, the modulation ratio is decreased which reduces the measured luminescence intensity. This way, the system signal-to-noise ratio starts to decrease and the phase-noise level becomes frequency dependent. Therefore, a compromise must be established between increasing phase sensitivity and decreasing SNR. It can be demonstrated that, in this situation, the modulation frequency yielding best sensitivity is given instead by [47]

$$f'_{opt} = \frac{1}{\sqrt{2}\,(2\pi\tau)} = \frac{f_{opt}}{\sqrt{2}}. \tag{4.25}$$

On account of the increasing noise, the modulation frequency must be smaller than the ideal value by a factor of $\sqrt{2}$. This way, in the example considered previously, the modulation frequency should be reduced to $22.5\,kHz$.

In addition to this correction, it should be taken into account that the frequency value determined is valid for a specified lifetime value, corresponding to a given oxygen concentration. If the sensor is to operate over a large range of oxygen concentrations, however, the lifetime can change significantly, changing the condition of maximum sensitivity. For this particular situation, the

modulation frequency must be chosen aiming to maximize the phase difference between the two boundary values of oxygen concentration [48]. In this case the optimum modulation frequency is given instead by

$$f''_{opt} = \frac{1}{2\pi\sqrt{\tau_{Q_1}\tau_{Q_2}}}, \tag{4.26}$$

where τ_{Q_1} and τ_{Q_2} are the lifetimes at the limits of the specified oxygen concentrations, Q_1 and Q_2. In the example of Figure 4.1, the maximum interval of $0\% - 100\%$ oxygen concentration is considered. In this range the lifetime changes from $\tau_0 = 5\,\mu s$ in the absence of oxygen to $\tau = 0.8\,\mu s$ at 100% oxygen. If the sensor is intended to operate in this full range, to achieve the best compromise between sensitivity and SNR the optical source should then be modulated at approximately $80\,kHz$. Obviously, this is a compromise situation and, in order to obtain increased sensitivity, limited measurement ranges should be considered.

From this discussion it becomes clear that the unquenched lifetime of the luminophore, along with the oxygen detection range, will determine the magnitude of the modulation frequency. From a practical point of view, it is desirable that the modulation frequency can be kept in the kHz range. Avoiding higher modulation frequencies introduces the possibility of using much cheaper and simpler optoelectronic instrumentation. Operation in this range of frequencies with maximum sensitivity requires that the luminescent indicator should have a lifetime in the microsecond range. Fortunately, as shown in the previous section, luminescent indicators become more sensitive to oxygen has their excited state lifetime increases. In addition, a variety of luminescent indicators is available with lifetimes ranging from microsecond to millisecond. However, to be used successfully in a sensing application, besides having an adequate lifetime, the luminophore properties should fulfill a long list of other requirements. This way, the list of suitable luminophores for oxygen sensing is shorter than expected. Nevertheless, several successful oxygen sensing applications using long-lived dyes, compatible with LED excitation and frequency domain detection, can be found presently in the scientific literature and even in some commercial applications. However, because each application has its specific requirements, particularly in the demanding biomedical and environmental fields, strong research efforts are being dedicated to the search for new indicator dyes and immobilization membranes.

4.2.3 Luminescent indicators and polymers for oxygen sensing

The suitability of a membrane to be applied in an oxygen sensing application depends on a number of properties of both the luminophore and the host material. Particular requirements for the

dye include photostability, high luminescence quantum yields, long lifetime, high molar absorbance, spectral compatibility with available excitation sources and detectors, and good solubility in the polymer host. The immobilization material, on the other hand, should display good permeability to oxygen, impermeability to interfering ions, mechanical and chemical robustness, allow thin film deposition with good adhesion to optical fibers, present adequate optical properties, etc.. Because the properties of dye and solid matrix usually interfere with each other, the characteristics of the final sensing membrane will depend on the particular dye-host combination. Obviously, no perfect dye-host combination can simultaneous fulfill all these requirements, so most frequently compromises must be established which depend on the particular application.

Luminescent indicators for oxygen sensing

A number of different luminescent indicators have been explored as oxygen sensing probes. The most frequently used ones include organic dyes like polyaromatic hydrocarbons and, more recently, organometallic compounds [13, 49, 50].

Most purely organic dyes have short lifetimes, in the nanoseconds range, and are not suitable for quenching-based oxygen sensing applications. Nevertheless, polycyclic aromatic hydrocarbons (PAHs), like pyrene, pyrenebutyric acid, quinoline, and phenanthrene, were initially used as oxygen probes due to their relatively long life times (around $400\,ns$). However, their absorbance maxima are in the ultraviolet or blue range of the spectrum. In addition, due to relatively small Stokes shift, their emission is usually at blue or mid-visible wavelengths. For these reasons, using these dyes typically requires UV excitation, detectors with sensitivity in the blue range of the spectrum and complex filtering systems to avoid overlap of excitation and emission radiation at the detection stage. On top of this, like most organic luminescent probes, PAHs usually suffer from strong photobleaching. The use of PAHs as oxygen sensors, immobilized in different glass or polymer supports, was demonstrated in several applications. Measurements of dissolved oxygen were demonstrated in many biological applications, including *in vivo* monitoring in blood vessels. Nevertheless, the requirement for more complex instrumentation, and the susceptibility to photo-degradation, make PAHs unsuitable for most long term applications. Despite these limitations, PAH are still used in some special applications, like in oxygen sensitive coating used for surface pressure measurement, also known as pressure sensitive paints [51].

Unlike purely organic dyes, organomettalic complexes usually display strong luminescence with long-lived excited states. For these reasons they are specially suited for oxygen sensing applications. Organometallic complexes are typically characterized by a central metallic atom

surrounded by one or several organic ligands. Two major groups can be identified which are being intensively used for oxygen sensing purposes: transition-metal-ligand complexes (TMC), and metalloporphyrins. In Table 4-2 the photophysical properties of some of the most representative oxygen sensing organomettalic indicators can be observed.

TMCs are characterized by a transition-metal, usually ruthenium, osmium or iridium, containing one or more organic ligands (typically α-diimines). In particular, ruthenium complexes have very desirable features for sensing applications. Their metal-to-ligand charge transfer triplet electronic states present long-lived, high-quantum-yield luminescence. Typical lifetimes range from $100\,ns$ to $6\,\mu s$, while emission quantum yields can go up to 0.5. Most ruthenium complexes display strong absorption bands in the visible range ($470\,nm$). Having large Stokes' shifts, their luminescence emission usually takes place around $600\,nm$. Because the absorption of ruthenium dyes overlaps perfectly with the emission of low cost blue LEDs, and their lifetimes lie in the microsecond range, these luminophores are particularly suited for low cost, frequency domain oxygen sensing applications[43]. Presently this family of dyes is probably the most extensively used in oxygen sensing applications. For these reasons their photophysical and photochemical properties have been tested in a very broad range of immobilization materials[9, 24, 33, 52].

A wide variety of organic ligands allows the synthesis of ruthenium dyes with different sensitivities to oxygen or other analytes, and also the adjustment of some of their chemical properties like solubility. The most extensively used oxygen indicators are of the general form RuL_3^{2+}, where L stands for the ligands. The more popular examples are the complexes tris(4,7-diphenyl-1,10-phenanthroline) ruthenium(II), tris(1,10-phenanthroline) ruthenium(II) and tris(2,2'bipyridil) ruthenium(II) which are usually abbreviated as $[Ru(dpp)_3]^{2+}$, $[Ru(phen)_3]^{2+}$, and $[Ru(bpy)_3]^{2+}$, respectively. These compounds are commonly stabilized by forming salts with chloride or perchlorate anions, which renders them hydrophilic. When in solution their unquenched lifetimes are approximately $5\,\mu s$, $0.9\,\mu s$ and $0.6\,\mu s$. This reflects on their oxygen sensitivity, and Ru(dpp) having the longest lifetime is also the most sensitive and widely used ruthenium complex for oxygen sensing applications [26, 53].

Although blue emitting LED and laser diode sources are presently becoming widely available, shifting both the excitation and the emission towards the near infrared is a desirable feature. This aspect is associated with low cost optoelectronics, more sensitive photodetectors, and increased compatibility with biological applications. Osmium complexes with red absorption and emission in the near infrared ($\sim 720\,nm$) were reported to be suitable oxygen sensors. Os^{2+} complexes are more photostable than the analogous ruthenium dyes due to an increased energy gap between the

luminescent state and photochemical unstable d-d states. However, the excited states of Os^{2+} complexes are usually much shorter lived than their ruthenium analogs. For instance, $[Os(dpp)_3]^{2+}$ and $[Os(phen)_3]^{2+}$ have lifetimes of $290\,ns$ and $367\,ns$, respectively. Although phase sensitive detection is still possible using relatively low modulation frequencies, which are easily achievable with low cost red laser diodes, the reduced lifetimes translate into lower sensitivities to oxygen. Nevertheless, reasonable sensitivities over the physiologically and industrially interesting range of 0 to $>1\,atm$ oxygen can be achieved. In addition, the versatility of TMCs, where combinations with a variety of different ligands is possible, may allow the implementation of different Os^{2+} complexes which may have enhanced properties [54].

Like their ruthenium counterparts, osmium dyes are hydrophilic, which makes them insoluble in organic polymers. Recently Iridium, Ir^{3+}, based TMCs were reported possessing high solubility in polymer supports. These dyes display strong green luminescence ($512\,nm$) with absorption at $376\,nm$. Although UV excitation is not an attractive feature, their high quantum yields and relatively long lifetimes ($< 2.0\,\mu s$) make them suitable oxygen indicators.

Probe	Absorption peaks (nm)	Emission peaks (nm)	Lifetime
$[Ru(dpp)_3]^{2+}$	337 , 457	610	$5.0\,\mu s$
$[Ru(bpy)_3]^{2+}$	470	600	$600\,ns$
$[Os(dpp)_3]^{2+}$	454 , 500 , 580 , 650	729	$290\,ns$
$[Os(phen)_3]^{2+}$	432 , 478 , 660	720	$367\,ns$
$Ir(ppy)_3$	376	512	$2.0\,\mu s$
PtOEP	381 , 535	646	$100\,\mu s$
PtTFPP	395 , 541	648	$80\,\mu s$
PdOEPK	410 , 603	790	$460\,\mu s$

Table 4-2 Properties of some organomettalic luminescent probes for oxygen sensing [13].

Platinum and Palladium based porphyrins display strong phosphorescence with very long lifetimes and are, therefore, very sensitive to the presence of oxygen [55]. Platinum octaethyl-porphyrin (PtOEP), for instance, has a relatively high quantum yield (< 0.5) and a lifetime of approximately $100\,\mu s$. The lifetime of palladium octaethyl-porphyrin (PdOEP), on the other hand, is around $770\,\mu s$. Being soluble in organic polymers, their application as oxygen sensors has been reported in different polymeric matrices. PtOEP, probably the most widely used oxygen sensitive porphyrin, has two absorption maxima at $381\,nm$ and $535\,nm$, and peak emission around $646\,nm$.

Although much more sensitive to oxygen as compared to ruthenium dyes, porphyrins usually display more moderate luminescent intensities and lower photostability. The reduced photostability strongly hinders long term operation and is thought to be due to photobleaching of the dye and photodegradation of the polymeric host. Some attempts have been made trying to enhance the sensor resistance to long term excitation by modification of existing dyes and host matrices. Pt^{2+} fluorinated phorphyrins like tetrakis (pentafluorophenyl) porphyrins (PtTFPP), have lower electron density in the phorphyrin rings and also higher redox potentials resulting in increased resistance to photo-oxidation and photo-reduction [56]. The development of Pt^{2+} and Pd^{2+} octaethyl-porphyrin ketones(OEPK) with ten times more photostability than PtOEP has been reported [57, 58]. Although they have slightly lower quantum yields, < 0.1, they have long lifetimes ($61\,\mu s$ and $460\,\mu s$) and their emission and absorption bands are both strongly red-shifted. This way, highly sensitive and photostable oxygen sensors with red absorption and emission in the infrared can be implemented.

Immobilization membranes for oxygen sensing

Presently, a wealth of oxygen sensing indicators is available with good characteristics for practical applications. However, for their successful application, the challenge of adequate immobilization in a solid host, without compromising the dye favorable properties, must be overcome. Depending on the particular immobilization technique, the same dye can display widely different oxygen quenching behaviors. Table 4-3 shows some examples of oxygen sensing membranes with different characteristics obtained with the same sensing dye [27].

The primary requirement that must be fulfilled by a given material in order to provide a suitable oxygen sensing membrane, is to have high permeability to this gas. Silicone rubbers are the material of choice for this purpose, presenting outstanding oxygen permeability (two orders of magnitude greater than most organic polymers); they also provide good chemical and mechanical stability. In addition, being non-polar they are impermeable to interfering ionic species. Unfortunately, most luminescent indicators display poor solubility in silicone matrices.

Some PAHs have been made silicone soluble by chemical modification of the dyes with inclusion of organic chains. More commonly used oxygen indicators, like ruthenium complexes, are usually ionic and have poor solubility in silicone and other hydrophobic polymers. The incorporation of ionic dyes in hydrophilic polymers is possible; however, the resulting membranes are not suitable for operation in aqueous media due to leaching problems and permeability to interfering ions. Incorporation of ruthenium dyes in non-polar polymers, on the other hand, often results in uneven distribution of the dye within the polymer matrix, with formation of aggregated

ion pairs leading to a large portion of the dye molecules not being quenched by oxygen. Several attempts have been made to solve this problem. Soaking silicone membranes in a dichloromethane solution (which causes silicone to swell) doped with Ru(bpy), and subsequent drying, can load the matrix with the sensing dye [59]. The conjugation of ionic sensors with suitable organic anions, or the introduction of co-polymer cross linkers or plasticizers in the polymer, also facilitates dye incorporation in non-polar hosts. In either case, however, aggregate formation can lead to highly non-linear SV responses. Nevertheless, control of membrane sensitivity over a wide range, using the same indicator dye but changing the polymer plasticizer content, was successfully demonstrated [26]. More recently, a method was reported to incorporate ruthenium dyes in silicone rubber by dispersing fumed silica particles doped with an indicator in the polymer matrix. Although the luminescence intensity and the quenching ratio of the new sensing films were much improved, the response and recovery times of the sensors were increased and some non linearity was observed at low concentrations[26, 59, 60].

Film	$K_{SV}\left(Pa^{-1}\right)$	$\tau_0\left(\mu s\right)$	$D\left(cm^2/s\right)$	$K_H\left(Pa^{-1}\right)$
TEOS $R=4$	3.50×10^{-5}	5.1	3.5×10^{-9}	5.8×10^{-4}
MTEOS $R=2$	3.24×10^{-5}	4.9	7.8×10^{-8}	2.5×10^{-5}
Silicone RTV 118	2.5×10^{-4}	5.3	12×10^{-6}	1.2×10^{-6}
Polystyrene	7.0×10^{-6}	5.3	1.87×10^{-7}	2×10^{-6}

Table 4-3 Quenching parameters of Ru(dpp) in different immobilization materials [27].

Metalloporphyrins, being non-polar, are quite soluble in most organic polymers. However, interactions of the organic polymer matrix with the sensing dye usually result in poor photostability. Polymers containing fluorine groups have shown to be stable against photo-oxidation. The presence of C-F groups with higher binding energy than the C-H bond, together with the increased electro-negativity of fluorine, give fluoropolymers high oxygen permeability and increased resistance to photochemical degradation. The combination of Pt or Pd porphyrins with several fluoropolymers has been shown to result in very sensitive and relatively photostable oxygen sensing membranes [56].

In spite of many problems and some limitations, several successful applications with polymeric oxygen sensing membranes were reported with effective practical applicability. The organic nature of most polymers, together with the need to introduce interface chemical species, often make the result of a dye-polymer combination unpredictable with both dye and host matrix properties being changed after combination. This way, besides complex chemical procedures,

polymer based sensing membranes often require thorough characterization. Nevertheless, this variability is what makes polymers one of the most versatile class of materials with new solutions constantly being proposed.

Sol-gel based glasses are a particularly successful example of new polymer-like materials which have extremely attractive features for immobilization of indicator dyes [22]. The sol-gel process is a method of material preparation at room temperature involving the combination of a metal alkoxide precursor, water and a solvent. By this process, materials like tetramethoxysilane (TMOS) or tetraethoxysilane (TEOS) undergo hydrolysis and polycondensation leading to a formation of a gel-like three dimensional silica network [61]. The oxygen sensitive dye can be incorporated in the resulting material by doping of the initial solution. By polymerization and cross linking, the dye will be immobilized in a cage-like microporous structure. Drying and heat treatment can then be applied to densify the gel and eliminate water and solvent, resulting in a doped porous glass material. Therefore, the nature of the sol-gel process allows physical entrapment of water-soluble indicators within the porous rigid structure [35]. Control of porosity allows the elimination of leaching problems, while still permitting access by the analyte, without the need for previous chemical modification of the dye with lipophilic or reactive groups. This way, the dye photophysical properties can remain practically unaltered. The relevant membrane properties, like pore size distribution, refractive index and analyte permeability can be tailored by proper adjustment of the processing parameters. The most important ones are the solution pH, the water precursor ratio (R), the aging time (time between the mixing of initial solution and the coating stage) and the drying conditions[31].

During the solution stage, and prior to solidification, these materials are suitable for deposition of thin films on various substrates by dip coating or spin coating. Other outstanding features of sol-gel glasses are their excellent adhesion to glass and other silica substrates, and good mechanical and optical properties of the coatings. The list of favorable characteristics, together with the high versatility in controlling the final membrane properties, has made sol-gel glasses a material of choice for optical fiber luminescence based sensing applications. A long list of successful optical fiber sensors used for a diversity of analytes has been reported. Measurement of pH, ionic species, certain biomolecules and, of course, oxygen, using doped sol-gel membranes, have been successfully demonstrated [62].

The oxygen sensing properties of sol-gel based membranes were shown to depend strongly on the metal precursor type and other fabrication parameters. The solubility of oxygen in sol-gel glasses is extremely high, due to the presence of a large free volume within the porous structure. Diffusion

coefficients, on the other hand, are smaller than in polymers and can vary widely according to sol-gel type. Tailoring of these properties allows control over the quenching properties of the encapsulated dyes. For gas phase sensing, TEOS based films doped with ruthenium dyes show high sensitivity to oxygen at low concentrations and fast response times. SV responses, however, are highly non-linear, probably due to micro-heterogeneities of the host material. Studies were performed showing the possibility of fine tuning the porosity of TEOS based films within a wide range. Solution aging time and water precursor ratio were shown to be the most determinant parameters [27].

In aqueous environments the quenching response of films is generally lower than in gas phase. The polarity of the sol-gel glass surface is of primary importance for sensor operation in aqueous phase. TEOS based films are hydrophilic, so when in aqueous media its pores get filled with water greatly reducing oxygen solubility and diffusion coefficient within the film. As a consequence oxygen permeability can be extremely low and even very sensitive indicators will perform poorly in such membranes. Furthermore, sensors based on purely inorganic precursors are frequently not stable over time. Drifts of the sensor calibration curves have been observed, caused by aging of the sol-gel matrix. This is thought to be due to continuous condensation of free silanol groups over time and consequently a progressive densification of the matrix. This also makes inorganic sol-gel material more brittle, and films have a tendency to crack if they are made too thick or the drying process is too fast.

Enhancement of the surface hydrophobicity can result in increased sensitivity to oxygen in liquid phase. Because water is kept outside the membrane, oxygen in the liquid phase establishes an equilibrium with the gas phase inside the porous structure, in accordance to Henry's law. This way, the quenching interaction takes place in a gas phase and is therefore more efficient. Sol-gel glasses with increased hydrophobic nature can be produced by using organically modified precursors (ORMOSILs). Ormosil glasses are not as hydrophilic and brittle as glasses made from purely inorganic precursors. As the organic component increases, the material will turn hydrophobic and ion-impermeable, greatly increasing its oxygen sensitivity. In addition, the material becomes more elastic and thicker films can be made without danger of cracking. The vast majority of oxygen sensing applications using sol-gel material uses ruthenium dyes as the preferred indicator. However, the incorporation of mettaloporphirins in ormosil glasses was also demonstrated, with results indicating an increased photostability [28, 63].

In spite of all the favorable characteristics, reproducible fabrication of stable sensor matrices by the sol-gel process is not as simple as often described. All parameters have to be kept constant during the manufacturing process. In this regard, the versatility of a membrane that may be tailored

by slight variations of the processing parameters turns out to be a disadvantage with respect to obtaining materials with identical sensing properties.

Although many successful dye-matrix combinations have been reported, each application has its specificity and there is no universal ideal solution. This way, substantial research efforts continue both in the synthesis of new sensing dyes as well as in the search for new immobilization materials.

4.2.4 Optical fiber oxygen sensors

Optical fiber oxygen sensors based on dynamic quenching of luminescence have been demonstrated with particular success in the last decade. For this contributed a systematic effort of the scientific community, motivated by the great potential of this technology for practical applications, which resulted in the availability of many suitable luminescent indicators and the development of new immobilization materials. The increased availability of semiconductor sources in the UV-blue range of the spectrum provided the missing link for the possibility of low cost applications. Presently, optical fiber oxygen sensors have reached a relative maturity and are already commercially available. In addition, research efforts continue (now with the added contribution from industry) to constantly improve the existing configurations and to further expand the span of possible applications. Therefore, nowadays, a considerable amount of oxygen sensing configurations and their applications can be found in the scientific literature. Although it is not possible to provide the full picture, a few representative examples can be shown, from fundamental sensing configurations to key applications, that allow to understand the present state-of-the-art in the field.

Optical fiber oxygen sensing configurations

Although fiber optics has been used in very early luminescent oxygen sensing applications, the fiber was typically used simply as a light guiding device through which excitation and detection of radiation were performed. Only after the development of polymer and sol-gel immobilization membranes could the first true optical fiber sensing probes be developed. An intrinsic configuration, where the fiber itself becomes the sensor, can be implemented by depositing the oxygen sensitive membrane on the surface of the fiber tip. Although intrinsic probes provide the most compact solutions, the use of an external sensing membrane, physically attached to the fiber tip, is also a possibility. The external configuration introduces some additional engineering problems but has some advantages, like easy substitution of the membrane.

One of the first reports of a truly intrinsic oxygen fiber probe was made by MacCraith et al. [12]. The authors used an evanescent wave configuration, where a sol-gel thin film, doped with

Ru(dpp), was deposited over a $4\,cm$ fiber section with previously removed cladding. In this way, the sensing film could be excited by the evanescent field of the excitation radiation; the emitted luminescence could then be collected by the same fiber. Some advantages of the evanescent configuration, as opposed to coating the fiber tip, include increased flexibility in adjusting sensitivity determining parameters like film length, thickness, porosity and refractive index. In addition, due to an increased sensing area, films can be made very thin, thus decreasing the response time. The sensor response was faster than the gas control system used, which took about $5\,s$ to set the desired O_2 concentration. The enlarged sensing area also results in decreased photobleaching (tip configurations typically imply much higher excitation power densities). The sensor used a blue LED as excitation source and a photodetector to measure the luminescent intensity in a transmission configuration. The utilization of low cost detection and a broad-band source, however, was only possible by using a large core silica fiber $(600\,\mu m)$. Good reproducibility was observed in the quenching measurements over the full $0\% - 100\%$ oxygen concentration range. In a later work, the same authors demonstrated the feasibility of LED based frequency domain detection using a similar fiber probe [64], setting the basis for low cost oxygen sensing instruments.

Although a transmission configuration can be advantageous for some applications, for single point measurements a reflection configuration provides a more practical and compact design. Highly sensitive oxygen detection using a reflection configuration was reported [11]. The sensing tip was a $1\,cm$ long sol-gel porous-core fiber, doped with Ru(dpp), interrogated by a bifurcated fiber with a $250\,\mu m$ diameter core. In this configuration, direct excitation of a much larger dye sample was possible, allowing for very sensitive detection. This way, changes in oxygen concentration below $1\,ppm$ could be detected. For this to be achieved the LED output was modulated by a chopper, and detection of the luminescence intensity was performed using a lock-in amplifier. By this method low frequency noise and background signals could be eliminated. Due to the bulky nature of the sensing membrane, the response time was increased, but a fast response was still recorded $(10\,s - 15\,s)$.The same authors also performed one of the first fiber optic dissolved oxygen measurements, using the phase modulation technique, a fiber tip with partially removed cladding and doped sol-gel coating. Tests performed over months demonstrated long term stability of the phase response which was independent of detector drift and photobleaching [41]. Seeking for low cost materials and improved characteristics, similar configurations were used to test different polymer immobilization matrices, sensing dyes and fiber types [65].

Although TEOS based films demonstrated high sensitivity in the gas phase, the SV plot is typically highly non-linear at higher concentrations. Also, the calibration parameters have a tendency

to drift over time due to very slow aging of the sol-gel matrix. In addition, due to their hydrophilic nature, their response in aqueous environments is greatly reduced. In the quest for better quality, Colette et al. demonstrated high sensitivity dissolved oxygen measurements using organically modified hydrophobic sol-gel membranes [28]. A similar approach was used by Klimant et al., where the new ormosils displayed combined features of classical polymers, such as solubility in organic solvents, and those of sol-gel glasses, such as mechanical stability and a porous structure. Successful immobilization of both ruthenium dyes and platinum porphyrins was reported. Oxygen sensitive membranes based on the new sensing materials were fast responsive, photostable and could be produced with sufficient batch to batch reproducibility. Ormosils also provided more homogeneous and stable membranes which resulted in increased linearity and long term stability of the sensors calibration functions. The new materials were used to implement optical fiber micro-optodes [63]. The tip of multimode fibers ($100\,\mu m / 140\,\mu m$ - core/cladding) was tapered using a heating and pulling method. Optical fiber probes with tip diameters ranging from $50\,\mu m - 10\,\mu m$ were dip coated in sol-gel solutions doped with different sensitive dyes, and after evaporation of the solvents submitted to $190\,^{\circ}C$ during $10\,\mathrm{min}$. The small dimensions of the sensing tip allowed measurements with very high spatial resolution and very fast response times ($250\,ms$). Oxygen gradients with a spatial resolution of up to $20\,\mu m$ were measured in freshwater sediments covered with a $2\,mm$ layer of green algae. Due to the still relatively large core of the optical fibers used, the excitation could be performed by a blue LED and frequency domain interrogation was applied using standard photodetectors. The described oxygen microoptodes demonstrated outstanding features such as high sensitivity, very fast response, excellent photostability and sufficient mechanical stability and, in addition, could be sterilized. This set of properties is highly desirable in a range of biochemical applications where micro-electrodes are traditionally used. In addition, their production cost was shown to rival that of micro-electrodes with comparable properties. Presently, such micro-optodes are commercially available in a variety of configurations and for different analytes (pH and oxygen) [14].

Most optical fiber luminescence sensing applications, including oxygen sensing, are based on large core multimode fibers. This is mainly due to the need for large numerical apertures and coupling efficiencies when broad band LED sources are used. However, single mode fibers can also be used. Nevertheless, they require laser excitation and very sensitive photomultiplier tube (PMT) based detection. Very small fiber optic sub-micron optodes with fiber tips ranging from $0.1\,\mu m - 1\,\mu m$ were produced from standard single mode fibers ($8\,\mu m / 125\,\mu m$). The tapered fibers were coated with aluminum along the longitudinal axis and a small aperture was left at the apex of

the probe tip. The tip end was then coated with a ruthenium doped sol-gel membrane. This way, scattering at the taper interface was avoided allowing much higher spatial resolution. The sensing tips were excited using an argon laser, and collection of the luminescence was performed through a 2×2 fiber coupler which was connected to a cooled PMT. The fiber tip was held by a XY translation stage and its position in the sample was controlled by observation though an inverted microscope set-up. With this scheme the measurement of different levels of dissolved oxygen within a porous polymeric structure ($< 10\,\mu m$ pore size) was performed with good reproducibility and adequate sensitivity. These tests demonstrated the sensors ability to perform intracellular measurements in life sciences applications [66, 67].

Multiplexed oxygen sensing

One of the attractive features of optical fibers is their potential multiplexing capability. This property is also highly desirable in many biomedical and environmental applications where, very often, simultaneous knowledge of multiple analytes is needed, or it is necessary to monitor a single analyte at multiple points. However, the use of traditional multiplexing techniques in luminescence based applications is not straightforward. The broad emission and absorption spectra of most dyes makes wavelength multiplexing a very limited option. In addition, the luminescence decay times of the luminophores severely limit the spatial resolution that can be achieved using time domain discrimination. Consequently, most multipoint luminescence sensing applications usually rely on a different fiber for each sensing point/parameter. These configurations often demand multiple detectors and/or excitation optical sources, or require the use of electronic or mechanical switches [68]. This way, very few multiplexed luminescence based oxygen sensors have been reported so far.

Recently, simultaneous analyses of dissolved oxygen level in four different water streams was demonstrated using four bifurcated optical fibers [69]. In this scheme an intensified CCD array detector was used for detection. This allowed to simultaneously monitor several signals from different optical fibers placed at different positions of the CCD array. Real-time, simultaneous monitoring of four different sensors could be performed by measurement of their respective luminescence intensities. In addition, by using gated detection with different delays, the decay curves of the different luminescent indicators could be obtained. From this data the lifetime was then estimated. Although the acquisition of the full decay curve took several minutes, this could provide an interesting technique for long term monitoring, where stability is more important than sampling rate. Similar detection approaches were applied with multi-analyte sensors using imaging fiber

bundles. The fiber bundle distal end was provided with multiple sensing regions (oxygen, pH, CO_2) with known locations, which could then be monitored on the proximal end by CCD detection [70].

The luminescence emission of most sensing dyes is generally temperature dependent. This way, most optical oxygen sensors need to be provided with a temperature reference. Most commercially available oxygen sensors use conventional technology to measure temperature. In one of the few all-optical approaches adopted to solve this problem, an oxygen sensitive dye was used in combination with an alexandrite crystal on the same fiber tip. The phosphorescence of the crystal was independent of oxygen level and provided the necessary temperature measurement. A frequency domain interrogation scheme allowed simultaneous detection of the two luminescent signals. Simultaneous measurements of oxygen and temperature could be performed with a drift of less than $0.24°C$ in temperature and 0.59% in oxygen concentration, along a continuous operation of $30h$ [17].

Optical fiber oxygen sensors applications

Many variations can be found on the basic schemes just described, where different materials are tested and techniques are adapted to the requirements of each application. Currently, a great variety of biomedical and environmental applications of optical fiber oxygen sensing technology have already been demonstrated. Different sensors have been developed for monitoring dissolved and gaseous oxygen in different environments.

A prototype of a multiparameter sensing probe (pH, CO_2 and O_2) using a different fiber for each indicator dye and employed in intravascular monitoring, was described [71]. The three fibers were encapsulated in a polymer enclosure, which also contained an embedded thermocouple for temperature monitoring, and was protected by a cellulose catheter tubing. The probe described ($\varnothing = 0.6mm$) has been tested *in vivo* on animals, exhibiting satisfactory correlation with data obtained *ex vivo* from electrochemical blood gas analyzers. In clinical trials on volunteers in intensive care and on surgical patients, one of the main problems encountered was the formation of a thrombus around the sensor tip, which altered the value of all the analytes. Fouling of the membrane in biological samples is a common problem affecting conventional sensors and optical sensors alike. More recently, a new non-toxic, bio-compatible polymer coating has demonstrated to be suitable to provide highly effective anti-biofouling properties to luminescence oxygen optodes [72]. Nanometer thick coatings of such materials were shown to significantly reduce the adhesion of thrombocytes to the surface of Ru(dpp) doped silicone layers. The same material was shown to be

effective in protecting sensing membranes from adhesion of bacteria in sensors used for sea water monitoring.

A high performance dissolved oxygen optical sensor based on phase detection using an external membrane configuration was developed for application in waste-water monitoring. A dual LED reference scheme was used to reduce electronic phase drift. Two fibers were used to separately deliver the blue excitation radiation and a red reference signal to the sensing membrane. The sensing layer, a Ru(dpp) doped hydrophobic sol-gel membrane, was deposited on a PMMA (poly(methyl methacrylate)) disc which was designed to maximize the efficiency of excitation. The photodetector was placed in the sensing head for minimization of electronic noise. A thermocouple was used to obtain temperature information and a calibration function correction was incorporated in the signal processing scheme. This way, temperature-independent oxygen measurements could be performed. A detection limit of $< 10ppb$ was achieved and the long term stability reached several months. In addition, the disposable sensing membrane could be easily substituted [42].

Many other similar applications were described with sensing optodes being developed for special conditions. Oxygen measurements could be performed at high temperature; in hyperbaric chambers; sensing heads withstanding sterilization were developed; measurements could be performed in high pressure fermentation reactors; and several *in vitro* and *in vivo* tests were demonstrated successfully [6, 73-75].

Commercial products

Many of the sensing devices described are now being used as tools by many researchers in a laboratory environment. However, only a few of them have developed into commercial products. Several factors contributed to slow down the development of optical fiber luminescence based instrumentation. Most chemical sensors suffer from poor stability, both operational and storage. In addition, many of the chemical processes associated with sensing probe preparation lack the necessary reproducibility and ease of batch preparation. Also the interference of other chemical species is often a problem. Due to the very early stage of industrial development, most of the sensors are still too expensive and are only used where no alternative exists; this way, the market is still too small for some analytes. Even so, optical oxygen sensors are probably the first among the few successful examples breaking through into real commercial products.

Presently, a few companies offer a diversity of oxygen sensing probes. *Ocean Optics* [15] offers a modular system where different kinds of fiber probes, a pulsed blue LED optical source and a preconfigured CCD spectrometer with dedicated software can be acquired separately. The sensing

membranes are based on hydrophobic sol-gel material doped with a ruthenium dye and are deposited on an angle cut fiber tip. Measurements are based on the intensity SV equation. A two point linear calibration can be used but a multiple point polynomial fit is recommended for increased accuracy. All probes can operate in both gaseous ($0\% - 100\%$ $[O_2]$) or aqueous ($0\,ppm - 40.7\,ppm$) environments with a maximum resolution of 0.01% $[O_2]$ or $0.003\,ppm$, respectively. Probes are offered in different kinds of assemblies optimized for specific applications. Using a silica fiber with diameter varying from $200\,\mu m$ to $1000\,\mu m$, the sensing probes can be supplied with a stainless steel protective ferrule for general purpose applications, with an aluminum jacket for tissue monitoring, within a needle tip to be inserted in sample packaging, with non-metallic coating , etc.. Probe lifetime is expected to exceed one year. In spite of their success, these sensors still present some limitations. The sensing membrane performance can be seriously affected by a series of common solvents like acetone and toluene. Autoclavation strongly reduces the probe lifetime and exposure to methanol or hydrogen peroxide can completely destroy it in a prolonged exposure.

PreSense [14] is a German company offering similar oxygen sensing probes where time resolved measurements are used instead. In addition to standard probes, microoptodes with $30\,\mu m$ fiber tips are also available, which are suitable for performing high spatial resolution measurements of biological samples. A support unit capable of simultaneous interrogation of several sensors allows multipoint measurements to be implemented.

Other companies can be found which offer probes optimized for applications in waste-water treatment, or oceanographic applications. Although not advertised, several companies selling oxygen sensors based on conventional technologies are making strong efforts to introduce optical technologies in their products, and maintain close contact with the scientific community. This fact alone is a clear sign of what should be expected in the future about optical oxygen sensing technologies.

4.3 Implementation of an optical fiber oxygen sensor

Some examples of the immense range of potential applications of all-optical oxygen sensors have been shown in the previous sections. While in some instances optical sensors still cannot compete, at least in price, with conventional electrode based sensors, there are clearly situations in which conventional technology simply cannot be applied. Such is the case of oxygen measurement under hazardous electromagnetic conditions. One particular important example of operation in these conditions is monitoring of dissolved oxygen level in *in vivo* Nuclear Magnetic Resonance

(NMR). This is a very attractive technique to investigate cell metabolism due to its non-invasive characteristics. In NMR measurements, the quantity of oxygen available to the cell is one of the most important parameters to monitor during *in-vivo* testing, since cellular metabolism varies as a function of the oxygen concentration of the medium. At present, the measurement of dissolved oxygen level is performed externally to the NMR probe by conventional procedures, namely perfusion and an oxygen electrode. The strong electromagnetic fields surrounding the NMR equipment forbid the use of oxygen electrodes in the measuring probe. The perfusion system used for transport of the cell media outside the probe, towards the oxygen electrode, induces errors due to changes in the sample environment (tubing transport, temperature). Therefore, the development of an optoelectronic sensor prototype for measurement of dissolved oxygen will be a very useful tool for metabolism studies of cell growth in *in-vivo* NMR.

The work presented in the remaining sections of this chapter was part of a project aiming at the implementation of an optical fiber oxygen sensing system with suitable characteristics to be used in a NMR set-up. The primary task was to establish and test a suitable configuration which could, at a latter stage, be implemented at relatively low cost. With this purpose, a prototypical interrogation system was assembled in which different sensing fiber probes could be tested. Preliminary tests were performed which allowed to identify the critical points where optimization was most needed. Several steps were taken towards system optimization. Some results are shown which allow to establish the influence of the geometrical shape of the fiber probe on the performance of the sensing system, and indicate some possibilities of improvement. In addition, a reference scheme is presented, showing the viability to implement simultaneous measurements of oxygen and temperature.

4.3.1 Interrogation system

In order to put into operation a suitable optical oxygen sensing system, some options had to be made. From the previous study performed on the state-of-the-art of this technology, it became clear that the obvious choice was to implement a system based on dynamic quenching of the luminescence of an indicator dye.

Choice of sensing membrane

Ruthenium complexes were chosen as luminescent indicators for several reasons: they have been used with great success in many oxygen sensing applications; their photochemical and photophysical properties in a diversity of immobilization materials are well studied and documented; they are compatible with blue LED excitation; their large Stokes shift facilitates separation of

excitation and emission at the detection stage; their lifetimes are suitable to implement frequency domain interrogation at relatively low modulation frequencies; they have relatively high thermal stability and photostability; their moderate to high sensitivity to oxygen makes them adequate to operate in a broad range of oxygen concentrations; and they are readily available commercially at relatively low price.

For this particular application, Ru(dpp) would probably be the most adequate choice. Its increased lifetime makes it suitable to implement frequency domain interrogation below $100\,kHz$, and provides the highest sensitivity to oxygen. However, among the complexes available, Ru(dpp) is also the most expensive[30], this way, Ru(bpy) was chosen instead. Being 1000 times less expensive than Ru(dpp), this complex still has adequate characteristics for the intended purpose. Ru(bpy) has a much shorter lifetime than Ru(dpp) and, therefore, it is less sensitive to oxygen and requires much higher frequencies for ideal operation. Nevertheless, its spectral properties are very similar and its response to oxygen is still adequate to assess the performance of the sensing system. This way, initial tests of the immobilization procedures requiring a significant amount of indicator dye being used in batch tests could be done at lower cost. Eventually, due to their similar properties, Ru(dpp) can be used at a later stage, to improve system performance, with just minor adjustments required.

The use of ruthenium dyes has been demonstrated in a diversity of host materials. Nevertheless, their solubility in hydrophobic polymers is poor and often requires chemical manipulation of both dye and membrane. Sol-gel materials, on the other hand, allow to encapsulate any dye within their porous structure without the need for chemical modification. In addition, sol-gel glasses are very well adapted to be used with fiber optics. They provide good adhesion to glass surfaces, have favorable optical properties and allow the deposition of very thin films. TEOS based films doped with different ruthenium complexes have demonstrated the highest sensitivity to oxygen in gaseous phase. The dependence of their sensing properties on the processing parameters is also very well documented. The very slow gelation times allow storage of solutions for a long time, minimizing waste of material. This way, although TEOS based sensors provide low sensitivity in aqueous media, they were used in the preliminary tests were the primary goal was to identify optimization opportunities. The fabrication procedure of the sensing membranes will be described in the next section.

---

[30] Presently, the commercial price of Ru(dpp) is approximately 35 USD per mg. Ru(bpy), on the other hand, is available at 35 USD per g.

Instrumentation

The emission spectrum of blue LEDs overlaps almost perfectly with the visible absorption bands of most ruthenium complexes. In addition, LEDs can be easily modulated up to the MHz range. Their robustness and their very low price makes them perfect for low cost applications. In this work a blue LED (NSPB500S) from Nichia Corporation was used as the excitation source. At the recommended nominal driving current ($20\,mA$) its output power was approximately $5\,mW$, while the emission peaked around $470\,nm$. The LEDs used were encapsulated in a traditional lens-shaped transparent acrylic housing which was available in two standard diameters, $5\,mm$ and $3\,mm$. Both models presented a half angle divergence of approximately $15°$. The LEDs were driven in a constant current mode using a Melles Griott laser driver.

For detection of luminescence, a high-gain silicon photodetector from Thor Labs (PDA55) was used. The gain could be adjusted from $0\,dB$ to $40\,dB$, with corresponding bandwidths of $10\,MHz$ to $60\,kHz$. The responsivity at $600\,nm$, the peak of Ru(bpy) emission, was $0.41\,V/A$, approximately two times higher than the corresponding value at $470\,nm$.

For implementation of the frequency domain detection technique, the LED was externally modulated using a Stanford Research Systems (SRS) function generator. Both the output signal of the photodetector and the synchronization signal of the modulation were fed into a lock-in amplifier (SRS 850 - $100\,kHz$). Whenever necessary a pre-amplifier from SRS could be used to provide further electronic filtering and amplification. The phase and rms amplitude value of the luminescence response could be read at the lock-in output or stored in text files for further processing.

Broad band optical sources like LEDs have a very small coupling efficiency when used in combination with standard fibers. This way, in order to achieve proper excitation of the sensing dye, large core multimode fibers must be used instead. The increased numerical aperture of these fibers also improves significantly the collection of the luminescent emission. In this application, a multimode silica/silica fiber from Thor Labs, with core/cladding diameters of $550\,\mu m/600\,\mu m$ and a numerical aperture of 0.22 was used (see section 2.5.3 for details on the transmission spectrum).

Sensing configuration

A 2×2 optical fiber coupler, with $50/50$ coupling ratio, was used to implement the reflection-type sensing configuration represented in the scheme of Figure 4.2. The coupler was made from the same multimode $550\,\mu m/600\,\mu m$ silica fiber used to fabricate the fiber probes. It was purchased from ATI Electronic having a specified maximum insertion loss of $-4.4\,dB$ at $850\,nm$. With this set-up different sensing probes could be tested.

The modulated LED radiation was coupled into one of the arms of the fiber coupler. The sensing probes were connected to one of the output fibers by a modified FC/PC connector; the other coupler output was immersed in index-matching liquid in order to eliminate any Fresnel back reflections. The luminescence signal emitted by the excited sensing tip was guided back to detection through the same fiber. Two consecutive colored glass filters (OGG550 from Schott, $\lambda_{cutoff} = 550\,nm$) were placed before the photodetector to eliminate any remaining blue radiation. The synchronization signal from the LED modulation, and the output of the photodetector, were fed into the lock-in amplifier. In these conditions, the lock-in output was a phase signal proportional to the oxygen concentration. In order to test their response to oxygen, the sensing probes were placed in a small acrylic chamber connected to O_2 and N_2 supplies. A standard O_2 meter (Sper Scientific 840046) was used to monitor the oxygen level inside the chamber. Control of the flux of each gas submitted the sensors to different levels of oxygen.

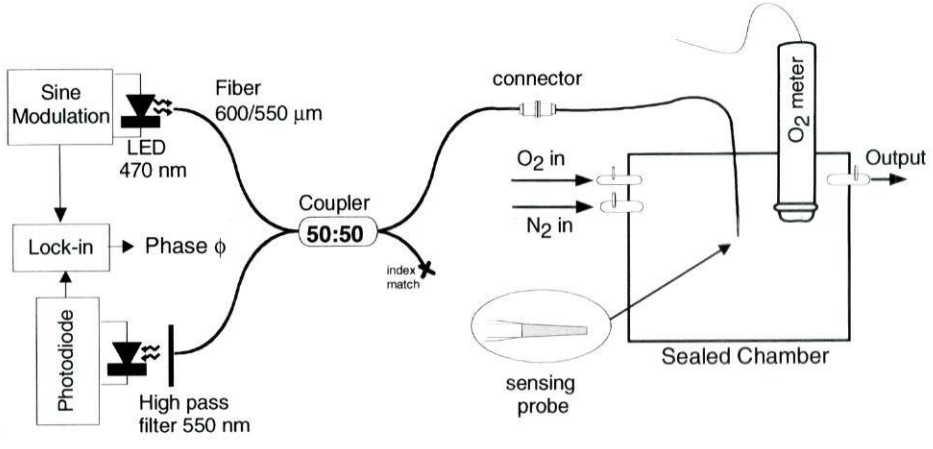


Figure 4.2 Experimental set-up used to test several oxygen sensing probe configurations.

In order to maximize the coupling of the LED radiation into the fiber system three different techniques were tested: a standard microscope objective system; a small diameter ball lens; and direct butt coupling of the fiber to an LED whose encapsulation was partially removed and polished. The detailed results and analysis of these tests are shown in chapter 2. It was demonstrated that the best coupling efficiency using a standard LED could be obtained by using a $10\,mm$ ball lens. An 8% efficiency was obtained with this scheme[31]. However, if the LED encapsulation was removed by polishing, similar results could be obtained by direct butt coupling of the fiber to the emitting surface. Such system can provide the most robust solution in a practical application where

[31] Coupling efficiency, η, can be defined as the ratio of the optical power effectively guided by the optical fiber, P_f, to the total power emitted by the optical source, P_s: $\eta = P_f / P_s$.

the fiber can be optically glued to the LED surface, thus providing maximum coupling efficiency with minimum alignment requirements. Nevertheless, in the laboratory, the use of the ball lens was more convenient because it allowed employment of different LEDs without the need for removing their encapsulation.

In the experimental set-up of Figure 4.2, a ball lens coupling configuration was used. With this system, an optical power of approximately $70\,\mu W$ was available at each output of the fiber coupler. After accounting for a $-4.4\,dB$ insertion loss, this corresponds to only 3.5% of the total optical power emitted by the LED. In chapter 2, an 8% coupling efficiency was measured using a $2\,m$ optical fiber. However, it was shown that this value was in excess of the theoretically achievable maximum due to guiding by the cladding modes. This enhanced the apparent numerical aperture (NA) of the fiber to approximately 0.40. Conversely, in the fiber coupler the cladding modes suffer increased loss and the numerical aperture of the fiber is thus reduced towards its true value of 0.22. In this situation, the maximum coupling efficiency achievable, which is approximately given by NA^2, is reduced to 4.8%. Still this value is higher than the one measured. Nevertheless, it should be taken into consideration that the insertion loss was specified by the manufacturers at $850\,nm$. At $470\,nm$ both the insertion loss and the transmission loss are higher and are probably responsible for the reduced efficiency observed.

The difficulty in coupling suitable levels of radiation into optical fibers when using LED excitation is certainly a critical problem for the successful implementation of a practical system. A more detailed discussion of this subject is given in chapter 2.

Evaluation parameters

The system just described was used to evaluate a variety of different sensing probes. In order to assess and compare their sensitivity and their overall performance, several parameters were evaluated. The standard parameter to assess the sensitivity of the luminescence output to oxygen is the quenching efficiency, which is usually defined by

$$Q = \frac{I_{N_2} - I_{O_2}}{I_{N_2}}, \tag{4.27}$$

where I_{N_2} and I_{O_2} are the luminescence intensities in O_2 and N_2 saturated atmospheres, respectively. The sensitivity of the measured phase delay to changes in oxygen concentration depends not only on the membrane properties, but also on the modulation frequency. Nevertheless, it is possible to estimate the phase sensitivity, independently of the modulation frequency, by calculating the lifetime difference given by:

$$\Delta\tau = \tau_{N_2} - \tau_{O_2} \tag{4.28}$$

where τ_{N_2} and τ_{O_2} are the excited state lifetimes in saturated atmospheres of N_2 and O_2, respectively. The lifetime of the different samples was estimated from the plot of $\tan[\phi]$ as a function of modulation frequency, according to equation (4.18).

For most applications it is desirable for the sensor to present a fast response to changes in analyte concentration. This way, the response time is also an important parameter in sensor design and characterization. Because the luminescence intensity has an hyperbolic dependence on oxygen concentration, in quenching based sensors the recovery times (response to decreasing O_2) are always greater than response times (response to increasing O_2) [76, 77]. Therefore, in order to fully characterize the dynamic behavior of the sensors developed, both response time and recovery time were measured. Typically, both these parameters are defined as the time it takes for the measured signal to achieve 90% of its steady state value. This way, the response time will be denoted as $t_{90}^{\downarrow}$ and the recovery time by $t_{90}^{\uparrow}$.

Measurement of the lock-in output at different oxygen concentrations in the $0\% - 100\%$ range was performed, allowing to obtain intensity or phase SV plots. Assessment of the degree of linearity of the sensor response was performed by evaluation of the parameters from the linear fit. From the slope of the linear fits a rough estimate of the SV constants could be made, providing an additional evaluation of the sensing film sensitivity. A two-site SV model was used for fitting whenever the linear fit showed poor correlation parameters.

When evaluating the phase delay between the excitation and the luminescence emission it should be taken into consideration that the measured signal can have several components arising from different contributions. Assuming that no trace of excitation radiation reaches the detector, the measured phase delay, ϕ_D, would be given by

$$\phi_D = \phi_R + \phi_E \tag{4.29}$$

where ϕ_R is the phase delay due to the limited lifetime of the luminophore and ϕ_E is a phase term introduced by the detection electronics. For a fixed modulation frequency, ϕ_E is constant and its contribution to the measured signal is simply a phase offset. In the experimental set-up, the value of ϕ_E could be obtained by removing the sensing probes and the long-pass filter from the fiber system and measuring the phase delay of the back-reflected excitation radiation. ϕ_E was evaluated for a range of modulation frequencies. This way, in the experiments performed, the true value of ϕ_R at a given modulation frequency could be obtained by subtracting the corresponding phase offset from the lock-in output.

In the detection of the luminescent signals, particular care was taken in order to effectively eliminate any backscattered blue radiation, ensuring that equation (4.29) was approximately true. Two consecutive long-pass colored glass filters were used for this purpose, each having an internal transmittance of less than 0.001% for wavelengths shorter than $510\,nm$. This was done after realizing that even a very small contribution of blue radiation in the detected signal can result in an appreciable error in the phase read by the lock-in. If the optical signal reaching the detector has a red luminescence signal and a residual blue contribution from the excitation, the resulting sinusoidal signal at the photodetector will have a power amplitude P_D and a phase ϕ_D that relate to the excitation and luminescence signals by

$$P_D \sin(\omega t + \phi_D) = P_B \sin(\omega t + \phi_B) + P_R \sin(\omega t + \phi_R), \tag{4.30}$$

where P_B and P_R are the blue and red power amplitudes, respectively, ϕ_B and ϕ_R their respective phase delays, and ω is the angular modulation frequency. In practice, it turns out that $\phi_B \approx \phi_E$. From well known trigonometric relations, it can be written that

$$P_D^2 = P_B^2 + P_R^2 \cos(\phi_R - \phi_B) \tag{4.31}$$

and

$$\tan\phi_D = \frac{P_B \sin\phi_B + P_R \sin\phi_R}{P_B \cos\phi_B + P_R \cos\phi_R}. \tag{4.32}$$

The information regarding the oxygen concentration is in ϕ_R. This way, due to the fact that the lock-in delivers ϕ_D instead of ϕ_R, a phase measurement error is introduced. A similar error occurs with the amplitude measurements. In order to evaluate the susceptibility of the assembled system to phase noise, the values of P_D, P_B, ϕ_D and ϕ_B corresponding to 100% of N_2 were measured experimentally for the different sensing probes. The phase ϕ_R was then numerically calculated with equations (4.31) and (4.32), and the respective relative phase error was evaluated for each sensing probe geometry. This was done using first one and then two long-pass filters at the detector.

4.3.2 Sensing films

The sensing membranes were fabricated by doping a TEOS based sol-gel solution with a ruthenium dye. The deposition of the thin films on the sensing probes was performed by dip-coating the sol-gel solution at controlled speed. In a first stage, an evaluation of the influence of the sol-gel processing parameters on the sensing film properties was performed. For this purpose, the sensing films were deposited on planar substrates (glass slides). This made easier the evaluation of

the film properties and allowed to perfect the fabrication technique. At a later stage, the films with best characteristics were deposited on optical fiber probes.

Sensing membrane fabrication

Optimization of the sensing membranes was not a priority, at least in an initial stage. A membrane that performed reasonably well was needed in order to allow testing the influence of other parameters of the sensing system, like the influence of sensing head geometry, degree of optical filtering, etc.. In this context, after some preliminary tests in which some variations were made on important parameters like the solution pH and the water-precursor ratio, a procedure which yielded homogeneous thin films with no crack formation was chosen.

The sensing films were then fabricated applying the following sol-gel procedure: the precursor, tetraethoxysilane (TEOS), was mixed with the solvent (ethanol) in a volume ratio of $1:1$ and with water in a molar ratio of $R = 4$. The water which was added to the solution had a $0.01\,M$ HCl content, setting the sol-gel pH to approximately 2. Water was added drop wise to the ethanol-precursor mix, while magnetic stirring was applied, promoting homogenization. These steps provided a solution that would eventually become a porous silica glass after drying. At this stage only half of the necessary ethanol content was used. In order to obtain an oxygen sensitive thin film, the remaining ethanol volume was doped with the complex Tris(2,2'-bipyridine) ruthenium (II) chloride hexahydrate $[Ru(bpy)_3]^{2+}$ and added to the sol-gel solution. The ruthenium powder was added in a $0.01\,M$ concentration relative to the total solution volume. Further stirring was applied for 2 hours. The solution was then left to age at ambient temperature. All films were produced by dip-coating, using a dip and drawing speed of $3\,mm/s$. One of the sides of the glass slides was protected in order to prevent coating. This way, the substrates were coated on a single side. Drying of the films was performed at $20°C$ for $24\,h$. Several sensing films were produced using planar glass substrates which were previously cleaned using standard procedures. Several samples were produced using different solution aging times that varied from $2\,h$ to more than $24\,h$. All the steps described were performed in a clean room environment.

Characterization of the sensing films

The films obtained were submitted to different tests in order to assess their suitability to be used in the fabrication of optical fiber oxygen sensing probes. Visual inspection was performed, using an optical microscope, in order to evaluate the film homogeneity. Also, the thickness of the different samples was measured using a diamond tipped stylus profilometer (Sloan, Dektak IIA). In

addition, the oxygen sensing properties of the thin films were tested in the experimental system represented in Figure 4.2. using the evaluation parameters described in the previous section.

Excitation and detection of the luminescence emission were performed using a single fiber which was connected to the sensing system. For that purpose, the fiber tip was carefully polished and placed in contact with the sensing film surface. A picture is shown in Figure 4.3 where both the blue excitation and the orange luminescence emission can be clearly observed. Some luminescence radiation can be seen at the fiber surface. This corresponds to light traveling in cladding modes being gradually lost to the external medium. It is also evident that a major part of the luminescence is emitted towards the substrate. Most of this radiation is guided by the substrate and can be seen emerging at the edges of the glass slide. The collection efficiency of the luminescent signal using this system was very small. It was verified that the level of backscattered blue radiation reaching the detector was much higher than the luminescent signal. This problem was solved by application of the two consecutive long-pass optical filters. The luminescent signals detected in this way were very weak but nevertheless adequate to perform most of the tests.

Overall, very homogeneous thin films could be obtained. The samples were observed using an optical microscope with a magnification of $50\times$, and showed no apparent signs of cracking. The only exception was observed near the borders of the glass slides, where some regions of increased thickness were fractured. This is a typical behavior of TEOS based films, where above a certain critical thickness the stress introduced by the drying process can cause the film to crack and even detach from the substrate surface. All the films produced at coating speeds of $2\,mm/s$ to $3\,mm/s$ presented thicknesses in the $600\,nm - 800\,nm$ range. In this thickness range no cracking problems were observed.

A picture of one of the samples, acquired by optical microscopy with $50\times$ magnification, is shown in Figure 4.4. It can be observed that the doped film presents the strong orange color characteristic of ruthenium dyes. The luminophores were homogeneously dispersed in the sensing matrix and no sign of dye aggregates was seen even at higher magnifications. When excited with light from the blue LED, the films emitted a strong red-orange luminescent signal typical of ruthenium dyes. However, a significant blue shift was observed between the spectra obtained from the sol-gel solution and from the solid matrix. The emission spectrum of the encapsulated dye has a peak emission at $603\,nm$ while in solution the highest luminescence intensity was observed at approximately $616\,nm$. This behavior was observed by other authors and is often called "rigidochromism" [78, 79]. In solution, Franck-Condon relaxation is facilitated by interaction with the solvent molecules and causes the excited luminophore to emit preferably from the lowest excited

states. After immobilization, however, this process is hindered and, therefore, emission takes place from higher energy states, originating the observed blue shift.

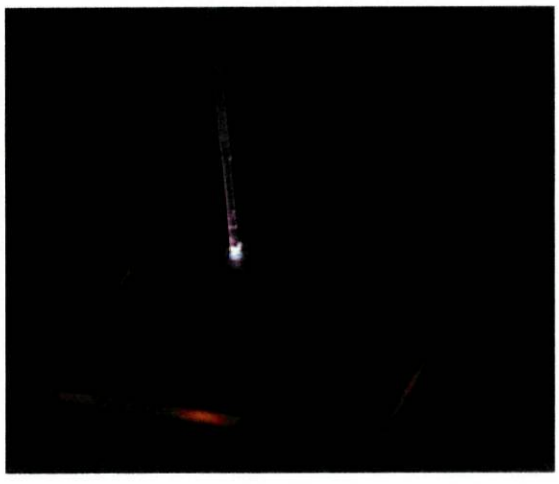


Figure 4.3 Excitation of the sensing film and collection of the emitted luminescence using the same fiber, which was connected to the interrogation system. Most of the luminescence emitted towards the substrate is guided by it and can be seen emerging at the glass slide edges.

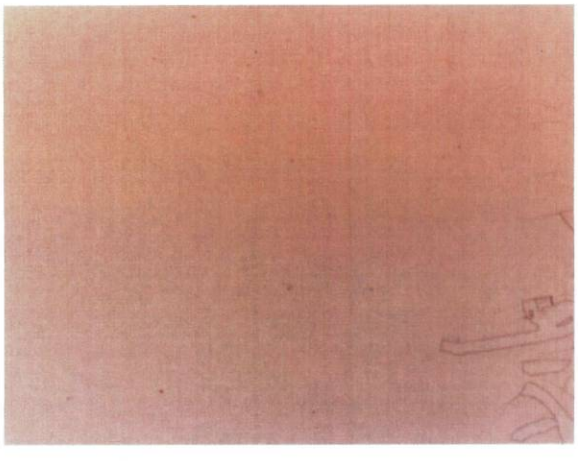


Figure 4.4 Picture obtained by optical microscopy, with a magnification of $50\times$, showing the homogeneous surface of a thin film doped with Ru(bpy). Scratches deliberately made to measure the film thickness using a stylus profilometer can be seen in the lower right corner.

Some of the samples were tested in a controlled gaseous environment in order to assess their oxygen sensing properties. The parameters Q and $\Delta\tau$, defined by equations (4.27) and (4.28) respectively, were evaluated for films with solution aging times varying from $2h$ to more than $24h$. All these samples were dried at $20°C$ for at least $24h$.

In order to obtain $\Delta\tau$ the excited state lifetime of each sample was measured in saturated atmospheres of oxygen and nitrogen. The phase delay ϕ was measured for modulation frequencies

ranging from $10\,KHz - 100\,KHz$. The lifetime could then be estimated by plotting $\tan\phi$ as a function of the modulation frequency. This was done by performing a linear fit to the experimental data and using the slope obtained to calculate the lifetime (equation (4.18)). Ideally, for better results, the measurements should be made in the widest possible frequency range around the optimum modulation frequency of the particular dye. However, in this case the frequency span was determined by the lock-in bandwidth. In Figure 4.5 (a) and (b) the results obtained for two different samples can be observed.

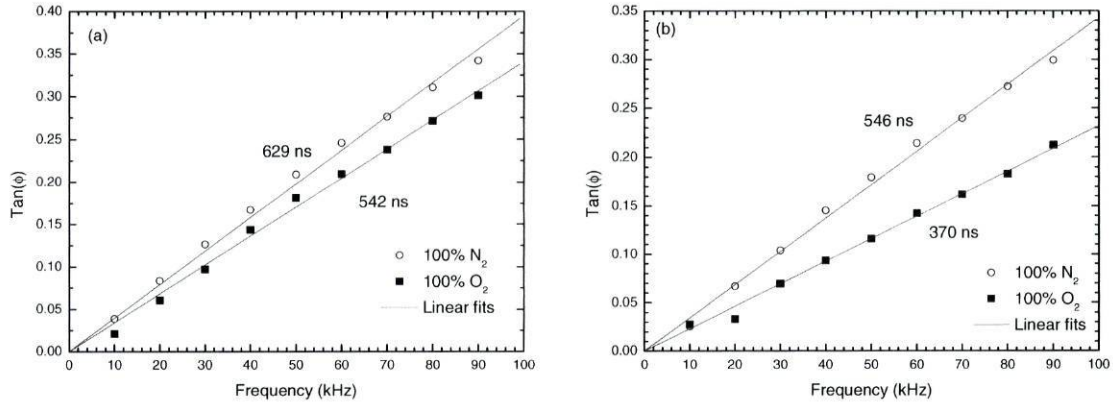


Figure 4.5 Frequency plots used to calculate the excited state lifetime in saturated atmospheres of O_2 and N_2. (a) Results obtained for a film with $3\,h$ aging time. (b) Results obtained for a film with $23\,h$ aging time.

The data displayed in Figure 4.5 (a) was obtained from a sample with a solution aging time of $3\,h$. From these curves a value of $\Delta\tau = 87\,ns$ can be estimated. Using a sample with a solution aging time of $23\,h$, on the other hand, the lifetime difference could be increased to $\Delta\tau = 176\,ns$ (Figure 4.5 (b)). This parameter was evaluated in other samples, and a consistent increase of the lifetime sensitivity with increasing solution aging time could be observed (Table 4-4). According to the literature, an increased solution aging time yields a more porous structure, resulting in sensing membranes with improved permeability to oxygen [27]. In practice, a higher $\Delta\tau$ results from improved quenching efficiency and, therefore, increased sensitivity to oxygen. Therefore, the results observed confirm the enhanced porosity of the films obtained from older solutions.

From Table 4-4 it can also be seen that the unquenched lifetime τ_0 is reduced as the drying time increases. This is a relatively small change, indicating that there is no significant interaction of the dye with the host matrices. Although a reduced τ_0 could have a negative impact on the oxygen sensitivity, the increase in permeability greatly overcomes this effect.

The enhancement of sensitivity with solution aging time was confirmed by the evolution of the quenching efficiencies, Q, of the samples tested. In order to calculate this parameter, the

different samples were submitted to saturation cycles of oxygen/nitrogen. The response of the luminescence intensity to these changes was recorded by the lock-in and allowed calculation of the value of the quenching efficiencies. The results obtained can be observed in Table 4-4 and show that, overall, the values of Q also increase with aging time. This is in agreement with the lifetime data. However, although the trend is the same, the increases observed are smaller and there is even a decrease of Q in sample ii in spite of its higher aging time. This discrepancy is probably due to the fact that the measurement of the quenching efficiency was based on simple intensity measurements. Therefore, the measured values can be affected by optical power drifts, photobleaching and poor SNR (with an higher noise baseline, the relative changes in luminescence intensity will appear smaller).

Indeed, in the configuration used to interrogate the sensing films, the coupling efficiencies of the luminescence into the fiber system were very small. From the signals detected it was estimated that, on the average, the luminescent optical power reaching the photodetector was below one nanowatt. Nevertheless, due to the extreme noise rejection capability of the lock-in, both parameters could be measured. However, the SNR was typically very low and both intensity and phase signals were very unstable. This way, in most of the tests performed, the noise level was high. As a consequence, the uncertainty associated with the values obtained for Q is also higher than the one associated with lifetime data.

In Figure 4.6 (a), the response of the luminescence intensity of sample i to O_2 / N_2 saturation cycles can be observed. Conversely, Figure 4.6 (b) shows the response of the phase delay to the same oxygen concentration changes. The intensity data was used to calculate the value of the quenching efficiency which, in this case, was approximately 40%. However, this data also shows that under constant oxygen concentration, the measured intensity was very unstable. Because the SNR was so small the phase measurements also suffered from major fluctuations. In addition, it can also be seen that after each cycle the sensor response is never fully recovered. This effect is clearly visible in the intensity data and to a less extent in the phase data, and it indicates the presence of irreversible photochemical processes.

These curves can also be used to evaluate the response, $t_{90}^{\downarrow}$, and recovery, $t_{90}^{\uparrow}$, times of the sensors. This was done by calculating the time needed for the sensor to achieve 90% of its equilibrium value. This method is illustrated in Figure 4.7 (a) and (b).

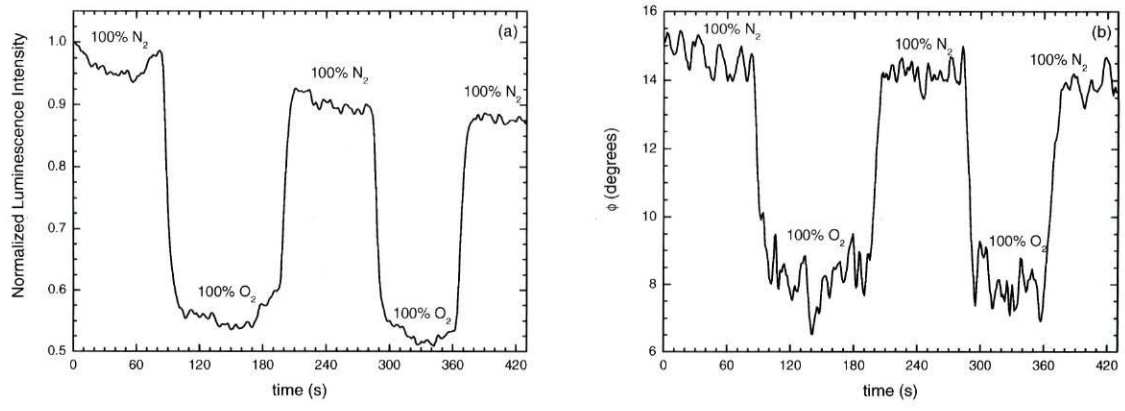


Figure 4.6 Response of a sensing film with short aging time to saturation cycles of O_2/N_2. (a) Luminescence intensity response; (b) Phase response.

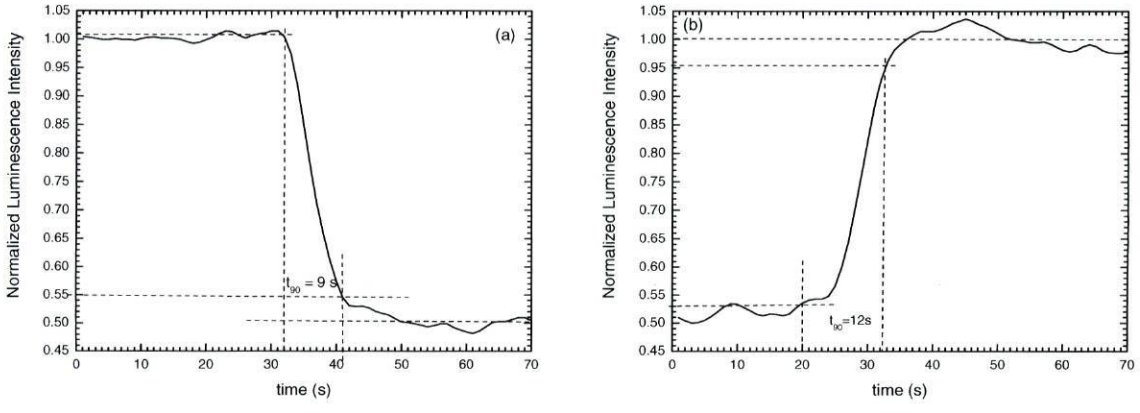


Figure 4.7 Plots used to calculate the response (a) and recovery (b) times of the sensing film when submitted to saturated atmospheres of nitrogen and oxygen.

From these plots it can be estimated that $t_{90}^{\downarrow} \approx 9s$ and $t_{90}^{\uparrow} \approx 12s$. In dynamic quenching processes, the response time is usually determined by the diffusion coefficients. In addition, the hyperbolic dependence of the luminescence intensity on oxygen concentration usually results in recovery times being larger than response times. The fact that in this test both time parameters are nearly identical suggests that the true response times may being masked by the filling time of the oxygen chamber. Nevertheless, in all tests performed the recovery time was always greater than the response time. As can been seen in Table 4-4, both the response and recovery times of all samples were very similar. Even so, a tendency for faster responses as the aging time increases can be observed. This is consistent with an increase in porosity, enhancing the diffusion coefficient which results in faster responses.

Sample *iii* has slightly slower response times. This particular sample was coated at lower dipping speed ($2mm/s$) and, as a consequence, it should present decreased thickness and faster

response times. The fact that this is not observed in practice, resulted from a decreased luminescent signal reducing the signal-to-noise ratio. Higher noise levels resulted in lower Q values and in a greater uncertainty in determining the response time. In fact, obtaining very thin films is usually a good strategy to increase sensor response times. Nevertheless, this will result in decreased luminescence intensity and, therefore, a compromise must usually be established.

In order to obtain the SV plots of the different samples, the sensing films were submitted to several step changes of oxygen concentration, evenly spaced in the $0\% - 100\%$ concentration range. In order to avoid the effect of photobleaching, the SV plots were calculated from the phase responses. The results obtained with sample iv can be observed in Figure 4.8 (a).

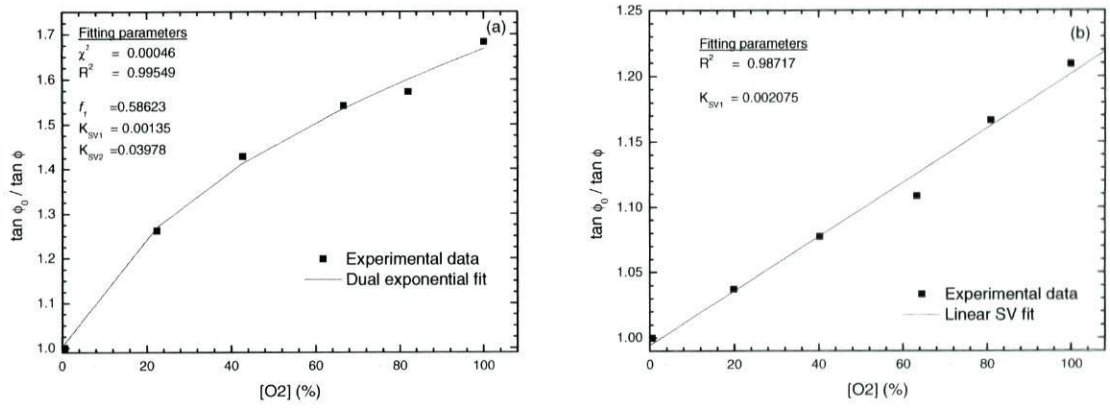


Figure 4.8 Stern-Volmer plots obtained using a sensing film with $\sim 23\,h$ solution aging time. (a) The film dried at ambient temperature; (b) The same film after curing at $80\,^{\circ}C$ for $3\,h$.

The response of the sensor to changes in the oxygen concentration presents a strong non-linearity (linear fit with $R^2 \approx 0.95$) at higher O_2 levels. Similar SV plots were obtained with other samples, indicating that the sensing complex had a heterogeneous distribution inside the porous silica matrix. It has been already demonstrated by different authors that, even when the sensor is homogeneously dispersed, micro-heterogeneities of the matrix itself can cause such behaviors. Figure 4.8 (a) shows that a two site model (equation (4.11)) yields satisfactory fitting to the experimental data ($R^2 = 0.995$ and $\chi^2 = 0.00046$). The primary and secondary Stern-Volmer constants, K_{SV_1} and K_{SV_2}, obtained for the different samples, are also shown in Table 4-4. The constants obtained indicate an increased sensitivity for longer aging times, correlating well with the increased porosity and permeability. However, an exception can be observed in sample iv. Nevertheless, this particular film presented the strongest non-linearity of all samples, with the two fractional contributions, f_1 and f_2 being very similar. This way, the comparison of the samples sensitivity from their SV constants is not straight-forward.

TEOS based films tend to have very slow drying processes. Due to their hydrophilic nature, water and solvent molecules usually remain adsorbed on the pore surface. Therefore, hydrolysis and condensation can still take place for long periods. This can slowly change the film structure and, as a result, the membrane sensing properties can change slightly over time. In order to remove water and solvent from the porous structure, in an attempt to stabilize the sol-gel structure, thermal curing can usually be applied. It has been shown that these treatments can impact the sensor characteristics, causing spectral shifts or decreased quantum yields, but can generally improve the matrix stability.

Sample	Aging time ($h:min$)	Q (%)	τ_0 (ns)	$\Delta\tau$ (ns)	K_{SV_1} ($\%^{-1}$)	K_{SV_2} ($\%^{-1}$)	f_1	$t_{90}^{\downarrow}$ (s)	$t_{90}^{\uparrow}$ (s)	Dip speed (mm/s)
i	2 : 40	40	629	87	1.6×10^{-3}	1.7×10^{-1}	0.98	11	13	3
ii	5 : 30	33	603	92	2.5×10^{-3}	0.9×10^{-1}	0.79	10	13	3
iii	22 : 45	45	593	139	2.5×10^{-3}	8.6×10^{-1}	0.95	14	19	2
iv	22 : 45	50	546	176	1.4×10^{-3}	0.4×10^{-1}	0.59	9	12	3

Table 4-4 Oxygen sensing parameters of the thin films tested

Sample *iv* was submitted to thermal treatment in which it was cured at $80°C$ for $3h$. After the curing process, some of the characterization tests were repeated. Figure 4.8 (b) shows the SV plot obtained for this sample after the thermal treatment. It can be observed that the linearity of the sensor response to oxygen was greatly increased ($R^2 \approx 0.99$). Submission of the sample to high temperatures may have caused the adsorbed water and solvent within the pores to evaporate. In addition, it could have also originated some densification of the solid matrix. These two effects can promote the homogenization of the sensing matrix, resulting in increased linearity.

In Table 4-5 the oxygen sensing characteristics of the film before and after the curing process can be compared. It can be seen that, in spite of the increased linearity, the quenching efficiency after curing is decreased. In addition, the response times become longer. Both these facts agree with a more dense matrix with decreased porous size. Nevertheless, the changes observed are relatively small when compared with the benefit of linear response. This fact is particularly important in a practical application where the system has to be calibrated. While in the case of linear response it is usually sufficient to perform a two point calibration, with non-linear behavior more measurements at known concentrations are needed in order to obtain a suitable calibration function.

Observation of the cured film under the microscope revealed the presence of several cracks that could compromise the long term stability of the sensing membrane. This indicates that the heating and cooling process may have been too fast. Although the results obtained show that

thermal treatments can be advantageous, a more careful investigation is needed in order to obtain the optimal curing parameters.

Drying	Q (%)	K_{SV_1} ($\%^{-1}$)	K_{SV_2} ($\%^{-1}$)	f_1	$t_{90}^{\downarrow}$ (s)	$t_{90}^{\uparrow}$ (s)
$20°C$	50	1.4×10^{-3}	0.4×10^{-1}	0.59	9	12
$80°C$	38	2.1×10^{-3}	-	1.00	10	15

Table 4-5 Comparison of the oxygen sensing parameters of a sample before and after thermal curing

Some studies were performed in order to assess the degree of photobleaching affecting the sensing samples. It was verified that most of the samples, when illuminated for the first time, presented a strong degree of photobleaching. Being illuminated through the optical fiber, the films were submitted to an excitation power density of approximately $44\,mW/cm^2$. In this situation, the observed luminescence output was usually decreased by 25% after one hour of continuous irradiation. This is a high degree of photobleaching which can seriously compromise the long term use of the sensor. Nevertheless, the decrease observed was well fitted by a simple exponential decay. This way, the degree of photobleaching was reduced over time. When monitoring a sample which had been extensively used in other tests, a much slower rate of photobleaching was observed, with the luminescent output being reduced by only 5% after being excited during an hour. Thus, previous irradiation of the samples prior to use can reduce this problem. However, the films treated in this way will present a reduced luminescent output which can compromise the sensor performance.

Due to the presence of photobleaching, the SV plots obtained using intensity measurements can be distorted. A sensor calibration function obtained in this way has very limited validity. To assess the influence of this phenomenon on the samples tested, the SV curve obtained by intensity and phase measurements were compared. A typical result is shown in Figure 4.9 (a). It can be seen that the intensity plot presents a higher slope than that of the corresponding curve obtained from the phase measurements. Therefore, these two plots yield different SV constants for the same sensing film. A possible cause for this discrepancy could be the presence of static quenching. While the intensity plot responds both to static and dynamic quenching, lifetime based measurements are only sensitive to dynamic processes. However, static quenching has never been observed in ruthenium doped sol-gel membranes. In order to exclude this possibility, an attempt was made to correct the intensity SV curve for the effect of photobleaching.

The SV plots were obtained by consecutively increasing the oxygen concentration. During this process, both the intensity and the phase outputs were recorded by the lock-in to a text file. The result of these tests was a time scope of the intensity and phase showing a series of consecutive steps corresponding to each oxygen concentration. Calculation of the average value in these steps yields a series of intensity/phase points that correspond to the Stern-Volmer plots. If photobleaching occurs during acquisition of this data, however, the measured values of the luminescence intensity are smaller than they should be if only quenching was present. This way, the degree of quenching seems higher than it really is. By dividing the intensity time scope by an adequate exponential decay function the effect of photobleaching can be removed from the acquired SV plot. Using a small software routine (Solver from Excel), the parameters of the exponential decay that caused the distortion observed could be calculated. The function yielded by the program to correct the intensity plot of Figure 4.9 (a) can be observed in Figure 4.9 (b). The decay function obtained was then compared to real photobleaching data. A very good correlation was observed between the experimental data (black dots in Figure 4.9) (b) and the calculated decay function. This fact, and the good agreement between the lifetime SV plot and the corrected intensity SV curve (also shown in Figure 4.9 (a)) indicate the distortion observed should be due to photobleaching alone.

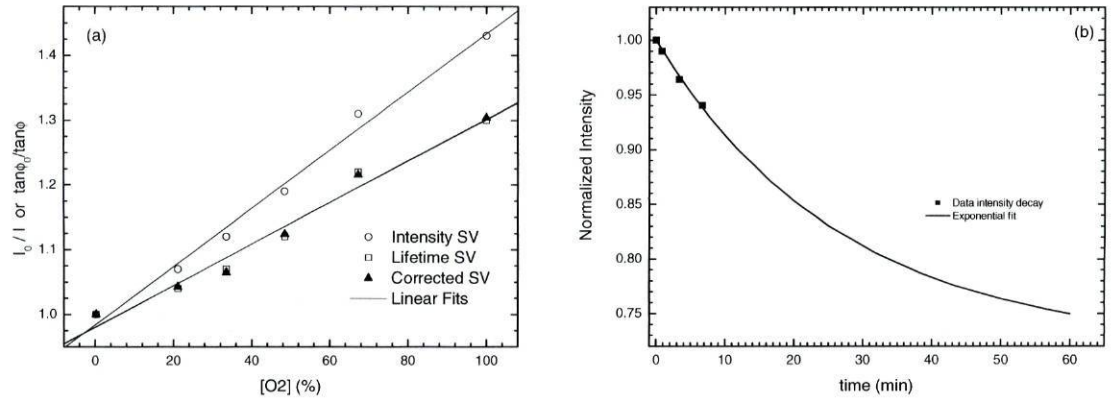


Figure 4.9 (a) Comparison of the SV plots obtained with intensity and lifetime measurements. The two plots are coincident if photobleaching is accounted for. (b) Exponential decay of luminescence intensity due to photobleaching. The black dots correspond to experimental data. The dark line was estimated from the fitting of the lifetime and the intensity SV data.

Photobleaching and low SNR were the main problems observed with the sensing films produced. Effectively solving the photobleaching problem requires sophisticated approaches like introducing singlet oxygen scavengers in the sensing film, or chemically modifying the dye or even the host material. A simpler alternative is to reduce the excitation optical power density. This can be done either by reducing the excitation optical power injected into the fiber system or by enlarging

the excited sensing area. The first choice is not a viable option since it would further reduce the SNR. An enlarged sensing area, however, could simultaneously reduce photodegration and increase the collection of the luminescence signal. Both effects would contribute to higher SNR and, therefore, to enhanced sensor response. Fiber probes with different geometries were designed taking these facts into consideration.

4.3.3 Fabrication and testing of different fiber probe geometries

The geometric arrangement used to test the sensing films, where the fiber tip was simply put in contact with the external membrane, showed a poor collection efficiency of the luminescence emission. Thus, the signals detected were very faint and, due to low SNR, measurements were affected by large fluctuations. Furthermore, photobleaching was shown to affect the sensor performance. But it is to be expected that the implementation of intrinsic fiber probes will result in some improvements in the performance of the sensing system. In order to asses the influence of the fiber probe geometry on the luminescence collection efficiency and overall system performance, different configurations were tested.

Fabrication of the optical fiber sensing probes

Four different sensing probe geometries were fabricated and coated with an oxygen sensing film. The different configurations tested are represented schematically in Figure 4.10. In all cases the same optical fiber lead was used to guide the excitation radiation to the sensing region and to capture the emitted luminescence signal, guiding it back to detection.

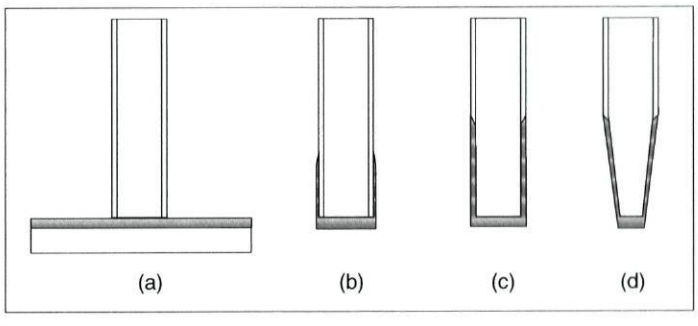


Figure 4.10 Different fiber probe geometries fabricated using multimode silica fiber: (a) glass slide; (b) fiber tip; (c) unclad fiber tip; (d) fiber taper.

Configuration (a) is an extrinsic configuration, and the sensing probe is a glass slide coated with the sensing thin film that is in contact with the polished fiber tip. This configuration was used to perform the characterization of the thin film presented in the previous section. Configurations (b), (c) and (d) are intrinsic configurations where the sensing film is deposited directly onto the fiber tip.

Configuration (b) is the most typical configuration where only the fiber tip is coated. Although the sensing area is the same as in the glass slide configuration, the coupling efficiency is expected to improve due to elimination of the fiber/glass-slide interface.

In configuration (c), the cladding of a $2\,cm$ length section at the fiber tip was removed and then the fiber tip was coated. By removing the fiber cladding, the film on the lateral surface of the fiber can also be excited by the evanescent field. The emitted luminescence, on the other hand, is coupled into the fiber by the inverse process. This way, the size of the sensing surface is enlarged and, most importantly, a higher luminescence signal will be collected and photobleaching will be reduced. This configuration was used by many authors to perform evanescent excitation of sensing films, particularly in bio-sensing applications. In such cases, however, the sensing layer is typically applied only on the lateral surface of the fiber, and the fiber end-face is coated with an absorbing layer [80]. This is done to take advantage of the low penetration depth of the evanescent field and to avoid the excitation radiation from reaching the solution where it could excite other luminescent species or be scattered, thus creating background noise. In the particular case of an oxygen sensing application, however, this is usually not a critical problem. This way, since the goal is to maximize the sensing area and the collected luminescent signal, the whole fiber tip was coated with the sol-gel film.

Also in the context of bio-sensors applications, it was demonstrated by several authors that tapering the fiber probe can improve the light collection efficiency [81, 82]. This happens because the fiber taper acts as a mode transformer. The high order modes typically excited by the luminescence emission, are gradually transformed in lower order modes as they approach the base of the tapered fiber and can then be guided in the cladded section of the fiber. The number of modes which can be supported by a multimode optical fiber with core radius r_{co} can be estimated from $V^2/2$, where the V-number is given by

$$V = \frac{2\pi r_{co}}{\lambda}\sqrt{n_{co}^2 - n_{cl}^2} \tag{4.33}$$

and n_{co} and n_{cl} are, respectively, the core and the cladding refractive indices, and λ is the wavelength of the guided radiation. From this relation it can be seen that, by changing the cladding refractive index or the fiber radius, the number of supported modes is changed. In particular, when the fiber cladding is removed and substituted by a sol-gel film, or immersed in an aqueous solution, the external refractive index is lowered, increasing the number of propagating modes. This way, there will be a mode mismatch between the fiber probe and the guiding fiber which will result in decreased luminescence collection. However, the reduction of the fiber tip radius can be used to

match the guiding capacity of the two fiber sections, thus improving luminescence detection. From equation (4.33) it is easy to show that the mode matching condition is obtained when the tip radius, r_{tip}, obeys the relation

$$r_{tip} = r_{co}\sqrt{\frac{(n_{co}^2 - n_{cl}^2)}{(n_{co}^2 - n_{tip}^2)}} \tag{4.34}$$

where n_{tip} is the refractive index of the sensing film. While reducing the radius of the whole sensing tip in a step fashion would satisfy the mode matching requirements, usually high scattering losses take place at the interface between the different diameter regions. Nevertheless, this scattering loss can be eliminated by increasing the fiber radius in a tapered fashion from r_{tip} to r_{co}.

In the present work, a tapered fiber configuration was also tested. In this particular case, the core and cladding refractive indices were, respectively, $n_{co} = 1.458$ and $n_{cl} = 1.441$. In addition, it is known from the literature that TEOS based films usually have a refractive index around $1.40 - 1.43$, depending on porosity (this results from the air filled pores lowering the effective refractive index; the refractive index of bulk silica is ~ 1.46). This way, in order to obtain mode matching between the sensing tip and the guiding fiber, r_{tip} should be in the range $150\,\mu m - 214\,\mu m$. Taking this into consideration, in configuration (d), the uncladded fiber tip ($2\,cm$) was tapered, acquiring a conical shape (with $550\,\mu m$ at the base and $300\,\mu m$ at the tip), and then coated with the sensing film.

In order to achieve a successful fabrication of sensing probes, the fiber tips were carefully prepared prior to coating. All fibers were cut using an appropriate fiber cleaver in order to obtain an end-face which was perpendicular to the fiber axis. In order to ensure optical quality of the surface in the fiber end-face, an adequate polishing procedure was applied. The optical fiber presented a secondary protective hard cladding which had to be removed prior to the etching process. After soaking the fiber tip with acetone, the hard cladding could be removed with a cutting tool. After this step, the fiber tips were cleaned in an ultrasonic bath of ethanol and then rinsed with pure water and dried.

The fiber silica cladding was removed by chemical etching with a 40% solution of hydrofluoric acid (HF). The same process was used to fabricate the fiber tapers. In this particular case, the $2\,cm$ fiber segment was immersed in the acid solution at controlled speed. This way, at the end of the dipping process, the etching time is longer at the fiber tip and gradually smaller along the fiber segment. If the etching rate of the acid is known, and the dipping speed is controlled accordingly, the fiber can acquire the desired conical shape.

In order to determine the etching rate, a fiber was immersed in the acid solution. The fiber tip was removed every $5\,min$ for measurement using an optical microscope. The results obtained are

shown in Figure 4.11. In this plot it can be clearly seen that the cladding and the core present distinct etching rates. This is due to the different compositions of the glasses in these two regions. Nevertheless, within each region the fiber diameter decreases in a linear fashion. The etching rates can then be easily obtained from the slopes of the linear fits represented in Figure 4.11.

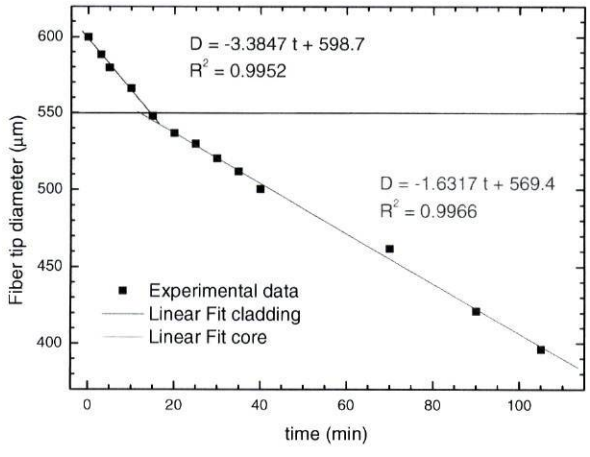


Figure 4.11 Evolution of the fiber diameter during immersion in HF. The etching rate in the cladding is higher than the etching rate in the core due to different glass compositions.

While in the cladding the fiber diameter decreases at $3.4\,\mu m/min$, in the core the etching rate is reduced to $1.6\,\mu m/min$. With this data the etching times and dipping speeds necessary to obtain a particular fiber shape could be calculated. It can be easily seen, for instance, that the removal of the fiber cladding will be complete after approximately $15\,min$.

All the fabrication procedures were undertaken in a dust free clean room environment. Prior to coating, the fibers were submitted to an ultrasonic bath for cleaning. It was verified that some of the etched fibers presented some irregularities at the surface. It was later confirmed that this was due to incomplete removal of the secondary hard cladding at some points. This demonstrated the need for a carefully cleaned fiber if a smoothly etched surface is to be obtained. Some of the fiber probes were discarded and the fabrication procedure was repeated with extra care in the cleaning steps. All the fiber tips were then coated using a sol-gel solution prepared according to the procedure described in the previous section. In all cases the solution aging times were greater than $48\,h$ and drying was performed at ambient temperature for at least $24\,h$.

Characterization of the optical fiber probes

The different fiber probes obtained were tested and compared using the interrogation system of Figure 4.2. All the sensing geometries were compared in terms of their oxygen sensing parameters. In addition, the excitation and collection efficiency of each configuration were also

evaluated. This was done by measuring the level of luminescent optical power reaching the photodetector after passing through the optical filters (P_d). By removing the filters, on the other hand, the back reflected blue radiation could be measured. In the absence of the filters the magnitude of the detected blue signal was much higher than the luminescence level. This way, it was assumed that the total power detected in this situation corresponded approximately to the level of back reflected excitation light (P_b). By placing a single long pass filter, the detected blue radiation was greatly decreased but its contribution to the total power detected was still not negligible. This particular situation was used to assess the influence of the background noise on the phase signal. A summary of the main results obtained is shown in Table 4-6.

Geometry	$Q\,(\%)$	$\Delta\tau\,(ns)$	Response time (s)	$P_d\,(nW)$	$P_b\,(nW)$
(a) Slide	30 – 50	72 – 176	9 – 11	0.36 (1)	-
(b) Tip	34 – 44	246	20 – 60	0.65 (1.81)	118 (1)
(c) Uncladded	55	250	20	0.72 (2.0)	19 (0.16)
(d) Taper	65	350	11 – 13	1.29 (3.58)	18 (0.18)

Table 4-6 Comparative results for the tested fiber probe configurations.

With configuration (b) no uniform thin films could be obtained. The films were thicker at the tip than at the lateral surface. This is a consequence of the dip coating fabrication technique. When drawing the fiber out of the sol-gel solution, there was the tendency for a drop to be formed at the fiber end surface due to surface tension. This way, the films deposited were much thicker than expected. This can be seen in Figure 4.12 (a), where a microscope photograph of a coated tip can be observed. The film deposited at the fiber tip is clearly much thicker than the one obtained on the lateral surface of the fiber. In some fibers this lead to film cracking and detachment of the coating from the fiber probe (Figure 4.12 (b)). The response times of several fiber tips employing this geometry and with the same sol-gel parameters, varied from $20s$ to $60s$. The different values obtained are probably due to different film thicknesses. This shows that, with dip coating, it is not possible to obtain repeatable films, with uniform thickness, on the fiber tip.

In spite of these problems, due to the increased thickness and to the more efficient fluorescence coupling, a significant increase in SNR was observed. In comparison with configuration (a), the value of the detected luminescent power, P_d, increased by a factor of 1.8. Although the coating parameters were similar in all geometries, smaller values of Q were obtained with this configuration, but the differences, nevertheless, were relatively small. The increased film

thickness can lead to the existence of some dye molecules being completely inaccessible to oxygen and, therefore, not being quenched. This can introduce a background luminescence which reduces the relative intensity changes used to calculate Q. Indeed, the values of $\Delta\tau$ show an increase relative to the glass slides values indicating that the oxygen sensitivities should be higher. This is consistent with the higher aging times of the solution used to coat the fibers ($> 48\,h$) and with the fact that the lifetime measurements are not affected by an eventual background signal.

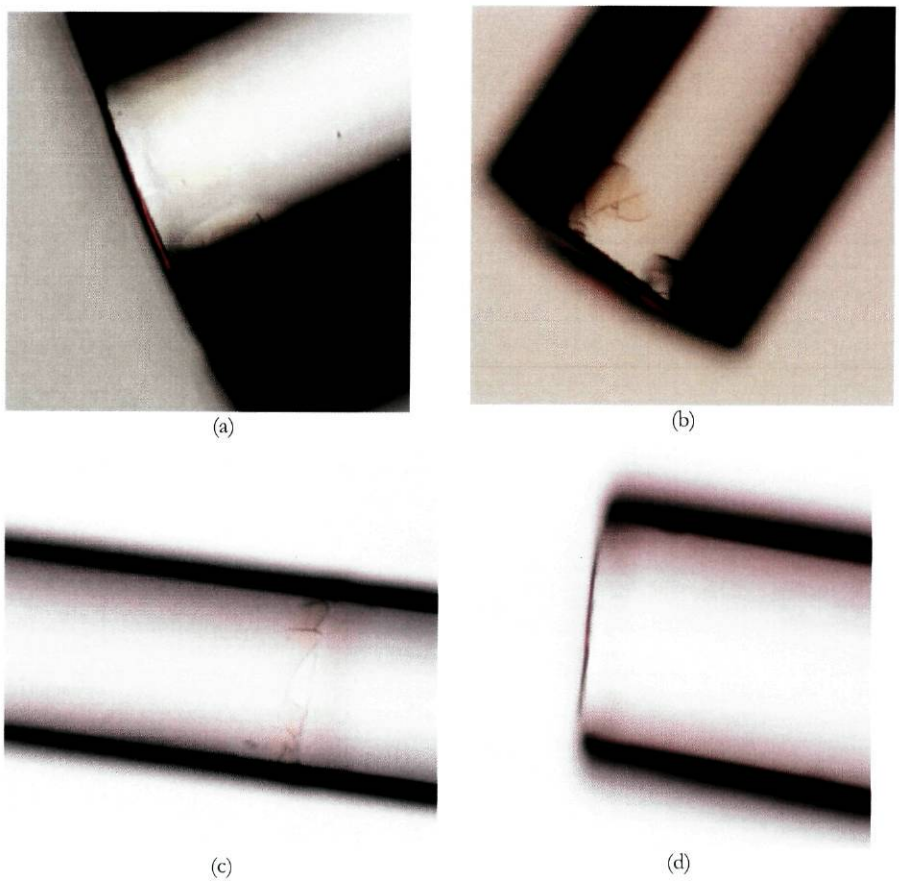


Figure 4.12 (a) Microscope photographs of some fiber probes; (a) Tip probe showing the formation of a much thicker film at the fiber end-face ($\times 50$). (b) Tip probe showing detachment of the thin film due to increased thickness($\times 50$). (c) Base of the fiber taper showing the border of the sensing coating ($\times 50$). (d) Tip of the fiber taper showing very uniform coating both on the lateral surface and on the end-face of the fiber tip ($\times 100$).

With configuration (c), uniform thin films were obtained on the uncladded surface of the fiber. However, due to the 'drop' effect of dip coating, on the tip of the fiber the resulting films were non-uniform and too thick. Response times of approximately $20\,s$ were obtained. This probably results from averaging of the faster response from the side of the fiber, where the film is thinner, with the much slower response from the top. Also some improvement in Q and $\Delta\tau$ parameters can be observed. However, no significant changes in the luminescence coupling

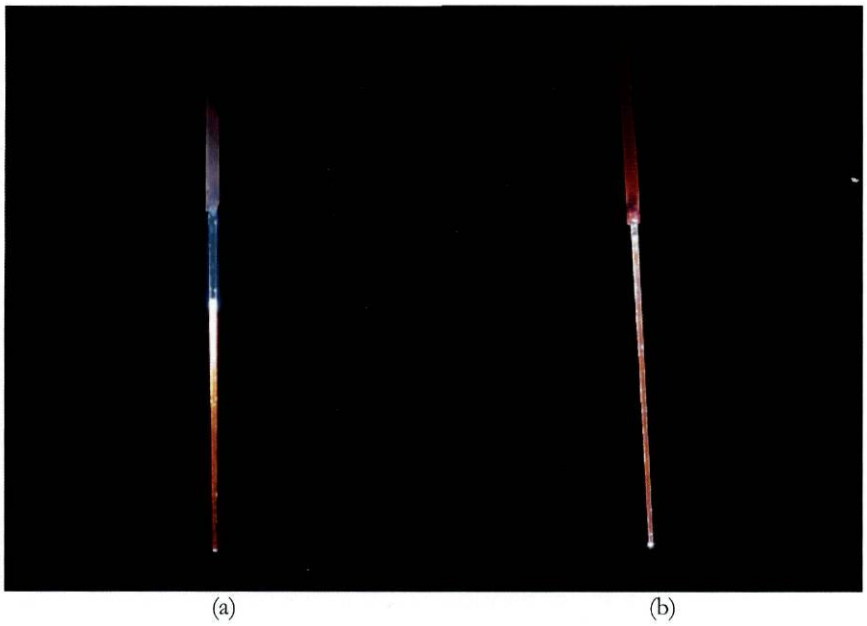
efficiency were observed in comparison to the results of configuration (b). This may indicate that, in spite of the much larger emission area, the contribution from the film on the fiber lateral surface to the fluorescence signal is comparatively small due to poor guiding from this region. In fact, luminescence emission originating from the fiber lateral surface excite preferably higher order modes, which are not guided by the cladded fiber.

With configuration (d), due to the fiber geometry, uniform thin films resulted both on the side and on the tip of the fiber. The smaller tip area contributed to a reduced 'drop' effect. Shorter response times clearly indicated that the overall film thickness is similar to the one obtained with the glass slides. In fact, the pictures in Figure 4.12 (c) and (d), showing respectively the base and the tip of the fiber taper, allow to confirm very uniform coating of the fiber. This is also shown by the increase in Q and $\Delta\tau$, which also denote better quenching efficiency and sensitivity. With this configuration, several sensing probes with very similar parameters were obtained showing good reproducibility. A great improvement in the SNR was registered in the tests performed with this configuration, as P_d increased by a factor of 3.5 relative to the glass slide design. In Figure 4.13, pictures obtained when two similar fiber tapers were excited with blue radiation can be observed. The picture on the left (a) shows significant loss of blue radiation at the base of the fiber taper. This was due to the fact that, in this particular case, the sol-gel coating was not applied over the full length of the taper, thus causing loss of blue radiation in the unclad segment of the fiber. This situation was completely avoided in the taper shown in picture (b), where the coating was applied over the full length of the fiber probe.

In the last column of Table 4-6 the degree of detected backscattered blue radiation in each configuration (P_b) can also be seen. In configuration (b), the level of backscattered radiation is six times higher when compared with configurations (c) and (d). Considering the respective levels of detected radiation (P_d) this means that, even after attenuation by a factor of 1000 (obtained with a single filter)[32], a significant amount of blue light is still mixed with the luminescence signal. The attenuated blue power amplitude is still 18% of P_d in configuration (b), 2.6% of P_d in configuration (c) and 1.4% of P_d in configuration (d). According to numerical calculations using equations (4.31) and (4.32), this will introduce phase errors of respectively 5.5%, 0.7% and 0.4%. In the implemented experimental set-up this problem was avoided by using two cascaded long-pass filters

[32] At the LED peak emission of $470\,nm$, the internal transmission of the filter is actually much lower (0.001%); however, it was verified experimentally that due to the long tail of the LED emission into higher wavelengths, the average attenuation achieved was approximately a factor of 1000.

corresponding to an attenuation factor of approximately 10^6. In this case the error dropped below a negligible 0.005% in all configurations.



(a) (b)

Figure 4.13 Picture of fiber tapers excited by a blue LED in a 21% oxygen atmosphere.

This clearly shows the need to use sensing schemes which minimize the level of backscattered radiation. In this context, the large Stokes shift of ruthenium dyes, $\sim 140\,nm$, is a favorable characteristic of this system. The use of sensing dyes with smaller Stokes shifts can seriously worsen the situation. In general, double filtering is not a desirable situation from a practical point of view, but it can be bypassed by using filters with higher performance. In this particular scheme, a short pass filter at the LED output would allow to eliminate the red tail of the LED, greatly reducing the filtering needs at the detection stage. However, it was verified that placing a standard filter, with a thickness of $3\,mm$, between the optical source and the input fiber reduced significantly the coupling efficiency. In a practical system, however, a thinner filter could be used. Narrow band laser excitation would also favor the excitation/emission discrimination. In any case, it was shown that the geometry of the sensing probe also plays a very important role in reducing the background noise. The reduced values of returning blue radiation also indicate that the excitation radiation is being absorbed more efficiently by the larger sensing area. This translates in increased luminescent emission, higher SNR and improved system performance.

Results obtained with the fiber taper

From the analysis of the results obtained it becomes clear that fiber tapering is a right step towards the sensing probe optimal configuration. Its particular geometrical shape allows a more

efficient collection of the luminescent emission, enhancing the system performance. This way, in order to better evaluate the improvements, the full characterization of the sensing system was performed using a tapered sensing probe. In Figure 4.14 the plot of $\tan\phi$ as a function of modulation frequency obtained with a fiber taper can be observed. Besides allowing to calculate a $\Delta\tau = 350\,ns$, it also shows a great increase in the difference between phase measurements obtained in N_2 and O_2 saturated atmospheres as the modulation frequency increases from $10\,kHz$ to $90\,kHz$. In the present set-up, a modulation frequency of $75\,kHz$ was used due to bandwidth limitations of the overall system. For a luminescence lifetime of approximately $600\,ns$, the phase difference is expected to be maximum around $188\,kHz$, which is the ideal modulation frequency as given by equation (4.25). If operation over the full range of oxygen concentrations is intended, equation (4.26) must be used instead, yielding an ideal modulation frequency of $374\,kHz$ This way, an increase in modulation frequency is expected to improve sensor performance.

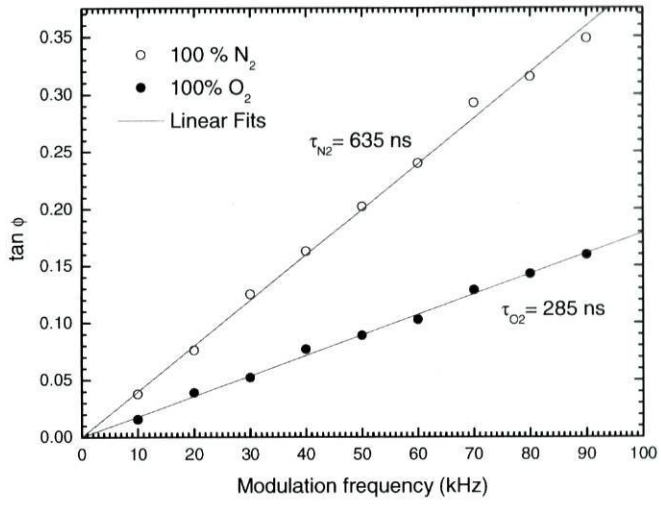


Figure 4.14 Plot of $\tan\phi$ as a function of modulation frequency for the fiber taper in 100% O_2 and 100% N_2.

In this particular case, some tests were performed using a $90\,kHz$ sinusoidal modulation. Although a slight enhancement was observed in the phase sensitivity, due to diminished modulation depth the system noise level was slightly increased and the overall performance was actually deteriorated. The decreased modulation depth was much higher than the theoretically predicted for the luminescence response. This was due to the fact that, in this particular case, an additional demodulation was being introduced by the detection electronics which was operating in the limit of the lock-in bandwidth. Using an improved bandwidth, however, it is expected that the system will present superior performance at higher modulation frequencies.

In figures Figure 4.15 (a) and (b) the phase and the fluorescence intensity response of the sensing system to O_2/N_2 saturation cycles can be observed. The phase signal still shows some instability indicating the need for further SNR improvement. Nevertheless, signal stability is greatly enhanced when compared with the results obtained with other probe configurations. It can also be observed that photobleaching is still present. It was verified that the degree of photobleaching was very similar in all configurations.

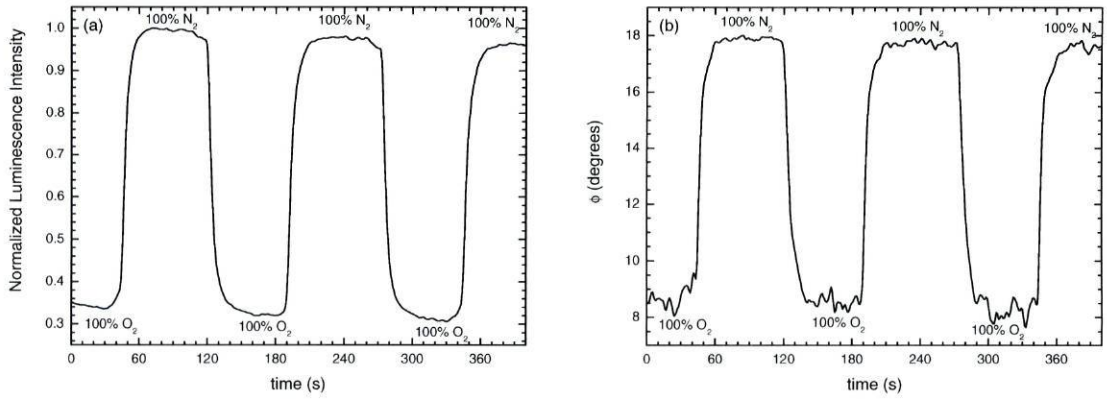


Figure 4.15 Response of fiber taper to O_2/N_2 saturation cycles: a) Normalized luminescence intensity response; b) phase response.

However, because the SNR is much improved using the taper configuration, the excitation optical power can be reduced, aiming to minimize photobleaching effects. To investigate this possibility, the fiber probe was submitted to saturation cycles using three different levels of excitation optical power. This way, the same test was performed using 100%, 50% and 25% of the available excitation optical power. This was achieved by reducing the LED drive current. In Figure 4.16 the results obtained for the phase and intensity responses can be compared. In the case of the intensity results all the curves are normalized to the maximum output value obtained with 100% LED excitation. As expected, the results show that photobleaching is higher when increased excitation optical powers are used. In Figure 4.16 (a) it can also be observed that for 50% and 25% excitation, the intensity output still allows to perform adequate measurements, with minimum effects of photobleaching.

In the phase responses it can be seen that the amplitude of the phase changes is identical in all cases (except for an offset in the 100% signal) showing a relative insensitivity to the optical power level. However, due to the reduced levels of luminescence intensity, the SNR is greatly reduced and the phase measurements show increased instability with reduced excitation power. Therefore, a compromise must be established between the degree of photo-degradation and the achievable

resolution. It can also be observed that the phase response of the signal suffering from higher degree of photobleaching seems to be affected by this process.

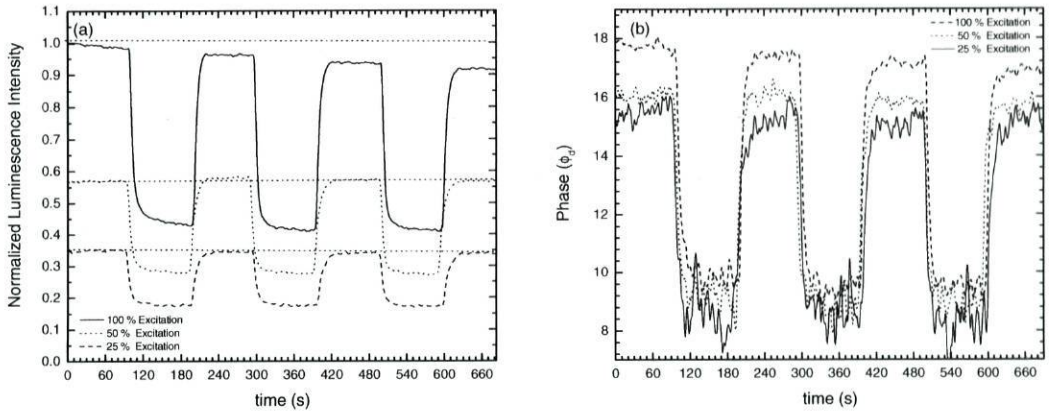


Figure 4.16 Comparison of the intensity (a) and phase (b) responses to saturation cycles of O_2 / N_2, with different levels of excitation optical power.

In order to better evaluate the susceptibility of the phase signal to luminescence intensity, an additional test was performed at constant oxygen level. With the sensing probe in a 21% O_2 atmosphere, the optical power injected into the fiber system was changed by up to 25%. Figure 4.17 shows the consequence of this variation in the intensity and phase of the fluorescence signal. Although a significant change in the intensity response occurs, the phase response remains essentially unchanged. Closer inspection of the results shows that the intensity change introduced would correspond to a variation of approximately 20% in the oxygen level. On the other hand, the maximum phase variation detected in this test was approximately $0.4°$. This corresponds to an oxygen change of approximately 1%, which as will be shown in the next pages, is in the limit of detection of the system tested. This confirms the ability of the phase detection scheme to avoid power fluctuations induced errors. However, it also indicates that the phase drifts observed in Figure 4.16 (b), may have been due to the effect of photobleaching. In principle, lifetime based techniques should not be affected by photodegradation of the sensing dye. However, it has been shown that this is not always the case. Whenever the products of photodecomposition are luminescent or when the host matrix is chemically altered, the measured lifetime can suffer slight changes which affect the phase measurements. In the present system it is unlikely that the bleached ruthenium products are luminescent. Therefore, it is more likely that these changes can be due to slow modifications of the sol-gel matrix. In fact, TEOS based films were reported to need several weeks or even months to achieve a completely stable configuration.

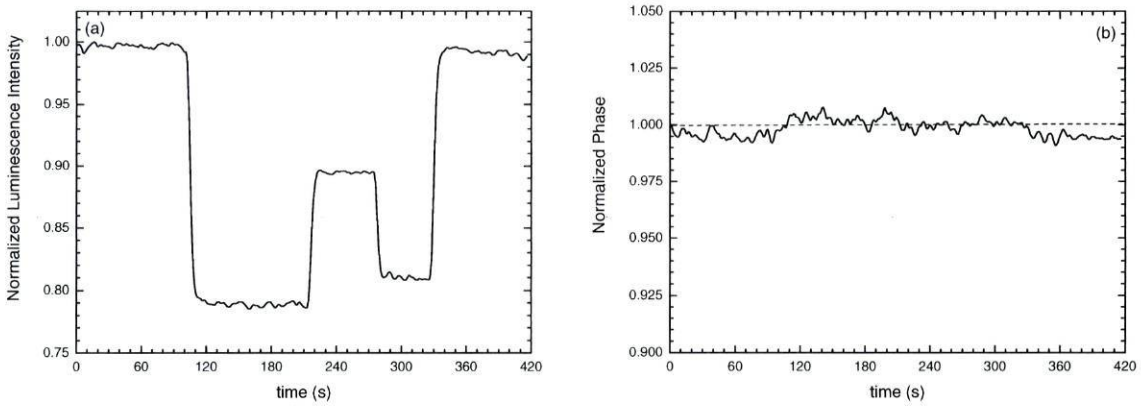


Figure 4.17 Response of the sensor to variations in the optical power level injected into the fiber system, in an atmosphere of 21% O_2: a) Normalized luminescence intensity response; b) Normalized phase response.

The Stern-Volmer plots obtained from phase measurements using all configurations are clearly non-linear, indicating micro-heterogeneities of the sensing membrane. The two site model was used to perform fitting of the data obtained with the fiber taper. The following fitting parameters were obtained: $f_1 = 0.917$, $K_{SV_1} = 9.2 \times 10^{-3}\,\%^{-1}$ and $K_{SV_1} = 1{,}6\%^{-1}$. The fact that f_1 is much larger than f_2 indicates a clear predominance of one of the environments. The small heterogeneities existent are related with the sol-gel film formation process. This way, it is likely that the sensor transfer function can change over time. Nevertheless, as shown with the glass slides, linearity can be improved with an adequate thermal treatment which promotes homogenization. The curing treatment may also speed up the stabilization of the sol-gel matrix and, therefore, contribute to minimize some of the problems just described. This point deserves further investigation and will be the object of future work.

In order to estimate the sensor resolution, a simple approach was used. Figure 4.18 shows a Stern-Volmer plot obtained with the fiber taper in which two distinct oxygen concentration ranges with different sensitivities can be identified. Sensitivity is higher in the $0\% - 20\%$ concentration interval and lower in the $20\% - 100\%$ range. Reasonably good linear fits can be adjusted to each one of these ranges. For most biological applications, only the first interval is relevant. This way, a linear fit ($R > 0.99$) was applied to the first interval:

$$\frac{\tan\phi_0}{\tan\phi} = 1 + 1.7 \times 10^{-2}[O_2] \tag{4.35}$$

Under these conditions, equation (4.35) is an approximate transfer function of the sensing system which was used to estimate system resolution. For this purpose the system phase response

was recorded while steps of O_2 concentration were applied to the sensing probe. The results obtained can be observed in Figure 4.19 (a). Analysis of this data indicates a *rms* phase fluctuation, $\Delta\phi$, of 0.06° with a detection bandwidth of $78\,mHz$. Assuming that the system resolution is given by

$$\phi_{min} = \frac{2\Delta\phi}{\sqrt{\Delta B}} \tag{4.36}$$

where ΔB is the system bandwidth, this translates in a minimum detectable phase change of $0.4^\circ / \sqrt{Hz}$. According to the system transfer function this corresponds to a minimum detectable oxygen variation of approximately 1%.

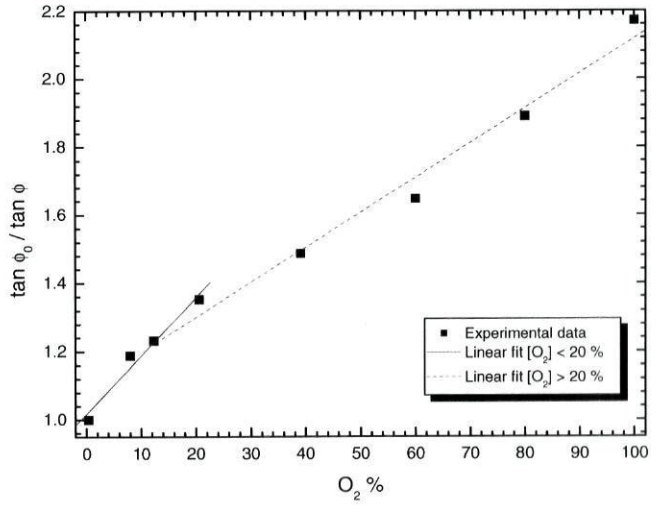


Figure 4.18– Stern-Volmer plot obtained from the phase response of the fiber taper with a linear fit for the $0\% - 20\%$ O_2 concentration range and a second fit for the range $20\% - 100\%$.

A similar analysis can be performed for the case of the fluorescence intensity response and the results are shown in Figure 4.19 (b). A more stable behavior is clear when compared with the phase steps, which turns out a better value for the minimum detectable oxygen concentration (0.1%) using the intensity detection method. This result is a consequence of the fact that the processing required to extract the phase information from the detected signal is more complex when compared with the one needed to recover the intensity and, therefore, more prone to error when the level of optical power detected is very low.

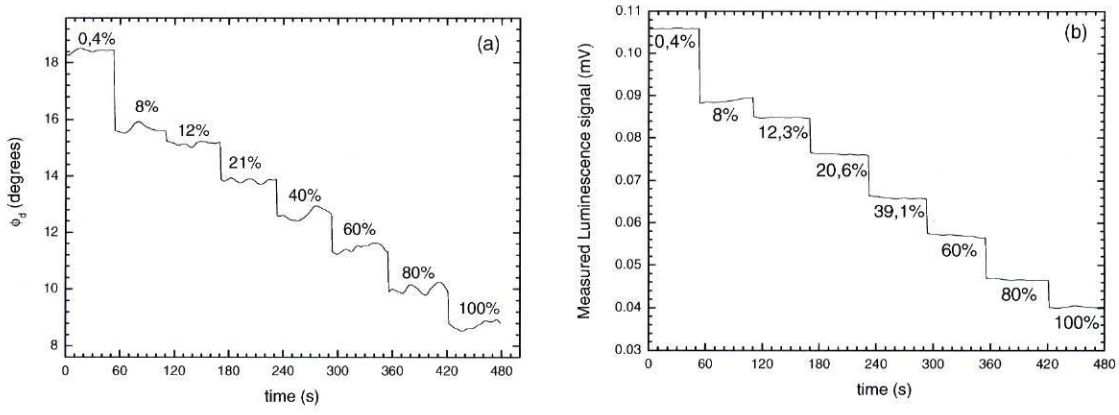


Figure 4.19 System response to step variations of oxygen concentration: (a) phase response; (b) luminescence intensity response.

To obtain full advantage of the intrinsically favorable characteristics of the phase fluorometry technique, the optimization of signal processing and power levels in the system is needed. In this context, the importance of sensing head design and efficient coupling of the excitation radiation into the fiber system is clear; topics that were in the mainstream of the present work. Therefore, a more detailed investigation of the optimal sensing head design is a subject that should be addressed in a future work. In particular a theoretical model able to evaluate the sensing head performance would be of great value.

With this in mind, some preliminary calculations were performed in order to compare the efficiency of configurations (c) and (d). A simple approach based on geometrical optics was used. In addition, it was considered that each point of the sensing film was a lambertian emitter (see chapter 2). The results obtained did indicate that the fiber taper configuration has an higher collecting efficiency. However, this was only true for very small taper lengths ($< 5\,mm$). For longer tapers, the simplified model yielded a higher efficiency for configuration (c). This way, the obtained results did not correlate well with the experimental observations, indicating that a more fundamental approach is needed. Recently, MacCraith et al. [83] presented a study on luminescence emission from dielectric interfaces. The authors showed that, under certain conditions, the emission of luminescence from a thin film into the substrate can present strong anisotropy. This way, coated fiber tapers can achieve coupling improvements that exceed what would be expected from a strictly ray optics calculation. If these radiation distributions are taken into consideration when designing the fiber profile, increased performance can be obtained. Therefore, a more complete model able to take these effects into consideration will be a valuable tool for designing improved sensing heads.

The final goal of the present work is to develop an oxygen fiber sensor for DO measurements. For that reason, some tests were carried out trying to assess the suitability of the sensing probes developed to perform DO measurements. However, due to the reduced SNR associated with the very poor response to oxygen of TEOS encapsulated dyes, no changes could be observed in the luminescence intensity. TEOS based glasses are hydrophilic, so when immersed in aqueous media the pores of the sensing membrane are filled with water. This greatly reduces the oxygen solubility of the sensing membrane. In addition, because oxygen has to repeatedly partition between the gas phase and the liquid phase when traveling in the partially filled pores, the diffusion coefficient is also greatly reduced. As a consequence, the permeability of the sensing films fabricated to oxygen in aqueous media is probably very small. For the purpose of DO measurements, hybrid precursors with substantially higher oxygen permeability should be used. The use of such materials in combination with ruthenium dyes with higher sensitivity to oxygen, like Ru(dpp), will result in a sensing membrane suitable to be used in aqueous environments. The combination of these materials with optical fiber using optimized geometries will surely allow to implement a sensing system with enhanced performance, suitable to be used in *in vivo* NMR applications.

4.4 Temperature reference scheme for Optical O_2 sensors.

Temperature is also an important environmental and physiological parameter that can influence the rates of many biological and chemical processes. Consequently, its knowledge is often necessary in a wide range of applications. For this reason alone, an optical temperature sensor can be a very useful tool in many applications where standard technology cannot be applied. In the particular case of optical oxygen sensing, or any other luminescence based sensor, however, the determination of temperature is mandatory as it can greatly influence the measurement accuracy.

The increase of temperature enhances the probability of non-radiative transitions. This way, both the quantum yield and the lifetime of molecular luminophores are reduced as temperature increases. The extent of these effects will depend on the magnitudes of the dye lifetime and its emission energy. Generally, quenching by temperature is more pronounced in dyes with longer lifetimes and larger emission wavelengths. This way, all ruthenium dyes are particularly sensitive to temperature. The phase delay being directly proportional to the excited state lifetime also depends on the temperature. This way, any change in temperature will introduce changes in both intensity and phase values that could be mistaken for a change in oxygen concentration, causing serious measurement errors. In the particular case of sensors based on dynamic quenching processes, the temperature influences the response of the sensor in an additional way. It was already shown that

the quenching rate constant k_q is directly proportional to the quenching efficiency, γ, and to the diffusion coefficient. The diffusion coefficient, D, in turn is related to temperature through the Stokes-Einstein equation, where

$$D = \frac{k_B T}{6\pi R\eta}. \tag{4.37}$$

In this expression k_B is the Boltzmann's constant, T is the absolute temperature, R is the molecular radius and η is the solvent's viscosity. This shows that the SV constant depends directly on the temperature. This way, the sensor calibration function is temperature dependent. From this discussion it becomes clear that, in order to determine accurately the level of oxygen using a quenching based sensor, simultaneous knowledge of temperature is necessary.

Some optical temperature sensors which measure the luminescence decay lifetime of certain phosphorescence materials are already commercially available. These could be used in combination with an oxygen sensing dye to provide temperature information in an all-optical sensing approach. However, these sensors usually present some cross-sensitivity to oxygen and demand immobilization in oxygen impermeable materials. This way, very few reports have been made on simultaneous measurement of oxygen and temperature using optical techniques. Liao et al. [17] for instance, used an oxygen sensitive dye and a ruby crystal immobilized in the same optical fiber and performed simultaneous measurement using frequency multiplexing techniques. Klimant et al. [84], on the other hand, developed ruthenium based micro-optode thermometers which were suitable for micro scale temperature measurements. The sensor had minimum cross-sensitivity to oxygen and could be used in combination with oxygen micro-optodes using the same interrogation system. However, sensing was performed using distinct fiber probes and each sensor used a separate optical source. This way, although some optical temperature reference schemes have been proposed, commercially available luminescent sensors still rely on conventional technology for simultaneous determination of temperature. Because this solution is incompatible with certain applications where an all optical fiber probe must be used, the development of further alternatives is highly desirable.

In the following pages, results are presented which show the feasibility of using part of the back reflected excitation radiation and a colored glass optical filter to perform simultaneous measurements of oxygen and temperature. Results are presented indicating that the scheme proposed allows to perform temperature measurements which are independent of the optical power level.

4.4.1 Proposed configuration

In order to obtain a temperature measurement that is independent of the oxygen concentration, part of the excitation radiation (which is back reflected from the sensing probe) can be used. The spectral characteristics of this radiation are independent of the oxygen concentration and are independent of the fiber probe temperature, provided the LED is thermally stabilized. However, the back reflected blue radiation can be made temperature dependent when propagating through a colored glass long pass filter placed at the distal end of the sensing probe.

Colored glass filters are usually doped with absorbing semiconductor material. It is the energy band configuration of this material that determines the absorption characteristics of the filter. In particular, the band gap energy establishes the onset of absorption and the wavelength of the filter cut-off. In the ambient temperature range, the band gap energy of semiconductors has a well-known linear temperature dependence [85]. This way, the cut-off wavelength of colored glass long-pass filters has a linear dependence on temperature. If the edge of the filter is made to coincide with the spectral peak of the excitation optical source, the back reflected blue radiation becomes temperature dependent and can be used to determine the temperature of the sensing probe.

In order to implement the proposed scheme, the experimental system previously used to test the fiber probes was modified in some ways. The modified set-up is represented in Figure 4.20. The same excitation source and modulation system were used. In a first approach, the oxygen sensing fiber probes and the temperature sensing probe were implemented using different fibers which were connected to different outputs of the fiber coupler and placed close together in an oxygen/temperature controlled environment. For the oxygen probe, an optical fiber taper coated with doped sol-gel glass was used.

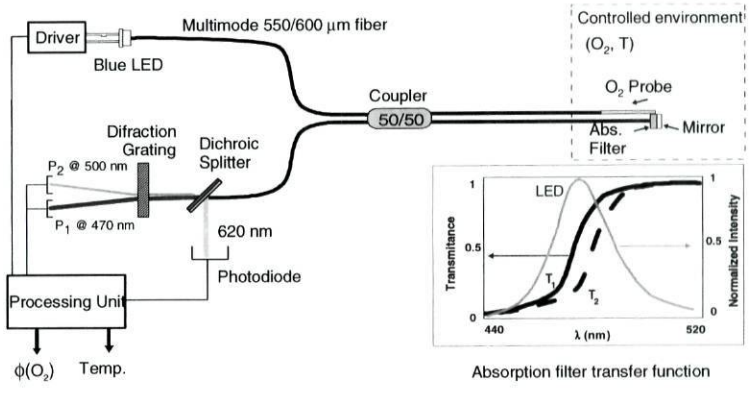


Figure 4.20– Experimental set-up for simultaneous measurement of oxygen and temperature. Insert: the transmittance of low pass filter for two different temperatures and the LED emission spectrum.

For the temperature probe a mirror and a long-pass absorption filter with cut-off wavelength of $455\,nm$ (GG455 –Schott glass) were placed on the tip of the fiber. The cut-off wavelength of this filter is shifted to higher wavelengths with increasing temperature by $0.08\,nm/^{\circ}C$. The choice of this filter was made in order to maximize sensitivity by coinciding the cut-off wavelength with the spectral emission peak of the LED. The inset in Figure 4.20 illustrates the sensing principle by showing a scheme of the relative position of the filter transfer function and the LED spectrum for two distinct temperatures.

The luminescent signal ($620\,nm$) from the ruthenium complex carrying the oxygen information, and the blue signal ($470\,nm$) with the temperature information, were guided back to detection by the fiber coupler. These signals were separated, at the fiber output, by a dichroic beam splitter. The luminescent signal was fed into a lock-in amplifier where it was compared with a reference signal from the LED modulation. In these conditions the lock-in output was an amplitude/phase signal proportional to the oxygen concentration. Conversely, the spectrum of the blue signal was spatially distributed by a diffraction grating. Two photodiodes were then used to obtain two signals, centered at $470\,nm$ (P_1) and at $500\,nm$ (P_2), with a bandwidth of $\approx 3\,nm$. While signal P_1 overlapped with the edge of the filter and became strongly temperature dependent, signal P_2 overlapped with a transmission maximum of the filter and remained independent of temperature. Using this detection scheme, the ratio P_1/P_2 provided a signal that was independent of optical power drifts and contained information on the sensing head temperature.

Because the optical filter used had standard diameter of $25\,mm$, at this stage the temperature probe was bulky. This way, in order to change the temperature of both fiber probes simultaneously a small oven was constructed. Heating was achieved by placing inside the compartment a $1\,W$ ceramic resistor. Control of the current passing trough the resistor allowed control of the temperature inside the oven. This scheme, however, could not be used inside the gas chamber used in previous tests because the oxygen chamber was made in acrylic. This way, oxygen and temperature measurements had to be taken alternatively. In spite of this obstacle, some tests were performed in order to evaluate the viability of temperature and oxygen measurements with the proposed scheme.

4.4.2 Self referenced temperature measurements

In a practical sensing system, the temperature information is used to compensate for temperature induced drifts. In order for this correction to be possible, however, the temperature behavior of the oxygen sensing probes must be accurately known. This information is usually stored

in the processing system, and allows to retrieve the true values of oxygen concentration. In this context, prior to test the feasibility of measuring the temperature based on the shift of the filter cut-off, the degree of influence of temperature on the response of the oxygen sensing probe was investigated.

Effect of temperature on the oxygen sensor

The effect of temperature on the output of the oxygen sensing probe was evaluated using the set-up of Figure 4.20. For this purpose, the output signal phase and the luminescent intensity were measured while the fiber probe was submitted to different temperatures in the range $15\,°C - 60\,°C$. All tests were performed using an ambient atmosphere with constant 21% oxygen concentration. The results obtained in these tests can be observed in the plots of Figure 4.21.

The curves obtained clearly show that both the lifetime and the luminescence intensity of the sensing dye depend strongly on the temperature. Fortunately, the variation of both parameters with temperature is linear and reversible. This feature reduces significantly the complexity of the processing scheme that should be used in a practical system.

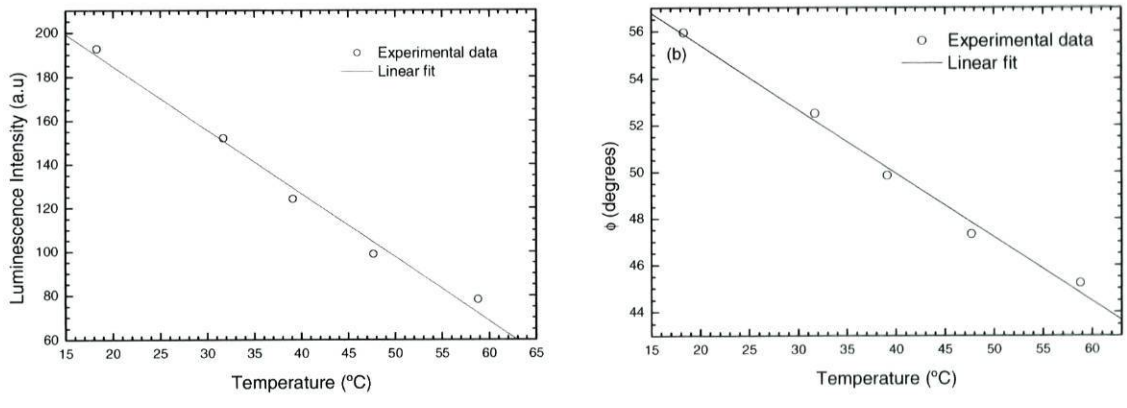


Figure 4.21 Effect of temperature on the output of the oxygen sensing probe: (a) luminescence intensity response; (b) phase response.

Characterization of the implemented temperature sensor.

The configuration of Figure 4.20 was also used to measure the temperature using the spectral information of the blue radiation reflected by the temperature probe. The measurements were performed under a constant oxygen concentration of 21%. In a preliminary stage, the temperature dependence of the reflected LED spectrum was investigated using an optical spectrum analyzer.

The result of this test is shown in Figure 4.22 and allows to confirm that the spectral characteristic of the reflected excitation radiation is rendered temperature dependent by the presence of the long pass filter. The temperature dependence is maximum around $465\,nm$, in the vicinity of the LED spectral peak and coinciding with the filter cut-off. This dependence vanishes for longer wavelengths ($> 480\,nm$), where the filter transmittance is maximum (see insert in Figure 4.20). As the temperature increases, the band edge of the filter material shifts towards the red, and less radiation is transmitted. In Figure 4.22 (b) it can be seen that the detected optical power at $465\,nm$ decreases linearly as the temperature increases. Therefore, it is confirmed that the backscattered radiation can be used to implement a temperature measurement. The results of this test also allowed to determine the optimal operation wavelengths. Although the maximum sensitivity to temperature changes was observed at $465\,nm$, the optical power detected at $470\,nm$ was higher. Because sensitivity at this wavelength was only slightly below the maximum, in the tests detection was performed at this wavelength in order to improve the SNR. This way, the detection system was adjusted to acquire the measurement signal at $470\,nm$ (P_1) and a reference signal at $500\,nm$ (P_2).

In order to evaluate the influence of the optical power level on the temperature measurement, the outputs P_1 and P_2 were measured for two different radiation coupling conditions, identified by High and Low. In the Low condition the optical power reaching the detector was 20% less than in the High condition. In Figure 4.23 the temperature dependency of signal P_1 at the two different levels of optical power can be observed.

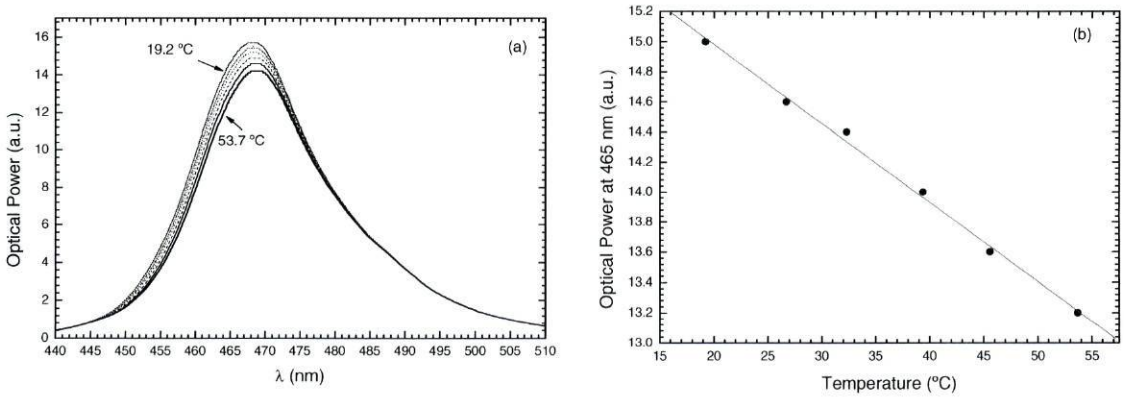


Figure 4.22 Response of sensing configuration to temperature changes in the range $19\,°C - 54\,°C$. (b) Spectral behavior of the back reflected excitation radiation. (b) Temperature dependence of the return optical power at $465\,nm$.

The results show that the optical power (P_1) of the LED at the central wavelength is a linear function of temperature. However, it is also clear that this measurement is not independent of the optical power level. The 20% decrease in optical power can clearly be observed in the resulting

plots, indicating that the temperature measurements will be affected by any drift of optical power arising from detector drift, change in coupling condition, etc.. In this context, the implementation of a reference scheme providing immunity to these phenomena is highly desirable.

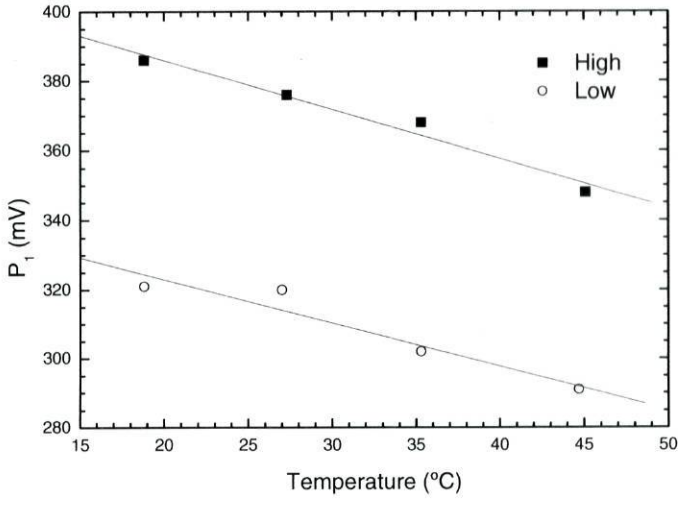


Figure 4.23 Temperature response of P_1, detected at $470\,nm$ nm, for 100% optical power (High) and 80% optical power (Low). Temperature range $19\,^{\circ}C - 45\,^{\circ}C$.

To achieve immunity to optical power fluctuations, the curves in Figure 4.23 were divided by the reference signal, P_2, which has negligible temperature dependence. Aiming to optimize the processing scheme, the ratio P_1 / P_2 was performed at two different reference wavelengths. P_2 was detected at $496\,nm$ (Ratio A) and at $500\,nm$ (Ratio B). The results corresponding to each of these processing operations are shown in Figure 4.24 (a) and (b).

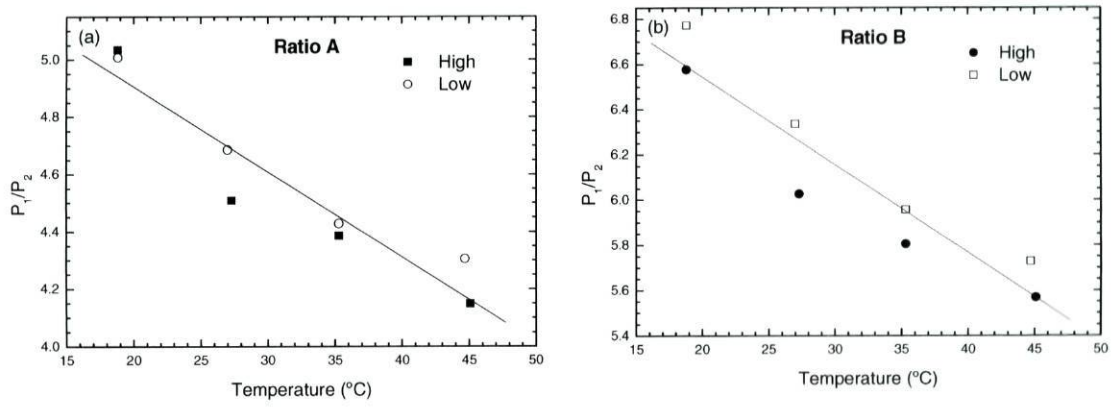


Figure 4.24 Temperature dependence of P_1 / P_2, for 100% optical power (High) and 80% optical power (Low). (a) Ratio A, detection of P_2 at $496\,nm$; (b) Ratio B, detection of P_2 at $500\,nm$.

Comparing the processed signal with the original data it can be observed that an optical power drift of approximately 20% in P_1 is reduced to a 4% variation when Ratio B is performed (Figure

4.24 (b)), and to a 1% variation in Ratio A (Figure 4.24(a)). Both the $496\,nm$ and the $500\,nm$ optical power signals have negligible temperature dependence. However, for longer wavelengths the optical power available decreases very fast and noise is introduced in the ratio operation. At shorter wavelengths, on the other hand, the temperature dependence starts to arise, thus compromising the reference scheme. Nevertheless, the results can be slightly improved with signal processing. If the operation $(P_1 - P_2)/(P_1 + P_2)$ is performed instead, the noise is slightly decreased and the 20% change in P_1 induces a 0.7% change in Ratio A and 1.1% in Ratio B. This shows that the data dispersion comes from a low SNR and an increase in the LED output power will benefit the sensor performance. The relatively high dispersion verified is partially due to poor control of the oven temperature. It was not easy to stabilize the temperature with the improvised system, and there was no guarantee that the temperature was uniform inside the test compartment. This way, the system performance may be better than what is apparent from these experiments.

In order to fully optimize this sensing system, a more detailed study is necessary on the possible P_1 and P_2 wavelength combinations. The relative position of the filter and LED spectra can be tuned within a few nanometers, by controlling the temperature of the LED emission junction. This control and an optimized signal/reference combination will surely allow to improve the performance of the system.

Not withstanding these aspects, the results obtained demonstrate the viability of performing temperature measurements using the proposed configuration. Because the sensing scheme depends only on the excitation source–filter combination, this scheme can be used, in principle, with any luminescence based sensor. For practical applications, however, further miniaturization must be achieved. A miniaturized temperature sensing head can be implemented simply by using a smaller filter and mirror combination. In principle, it is possible to introduce the filter and mirror in the oxygen sensing probe, so a single fiber could be used. This approach, however, requires careful design in order to avoid deterioration of the oxygen sensor performance. Also the detection system could be greatly improved. In the present system, the presence of many bulk optical elements between the fiber and the detectors caused serious loss of optical signal, reducing the SNR and the overall sensor performance. Presently, miniature CCD spectrometers are available that could be used to perform the spectral discrimination of the optical signals. With this scheme, signal loss would be greatly reduced and the bandwidth and spectral position of the measurement and reference signals could be fully optimized.

4.5 Conclusion

Several technological challenges to the optimization of luminescence based optical fiber oxygen sensors were addressed. An optical fiber system, capable of interrogating luminescence based sensing probes, was implemented. The performance of the different probes was assessed using both phase and intensity measurements. In particular, four sensing head geometries were tested and compared. A tapered fiber tip structure showed the best performance and, in particular, the results obtained from this design were very reproducible. This sensor configuration provides a higher excitation efficiency and reduced level of backscattered excitation radiation. These results indicate that a more detailed study of the sensing probe geometry can be very fruitful. Preliminary calculations showed that the benefits of fiber tapering exceed what is expected from a geometrical optics interpretation. Therefore, a more fundamental theoretical model can be of great help in the search for the ideal configuration. The use of non-imaging optics concepts can also be of great help in this regard.

An all optical configuration for simultaneous measurement of oxygen concentration and temperature was also demonstrated. Encouraging preliminary results were obtained. Further integration of the sensing head can be achieved if the mirror and the absorption filter are placed on the tip of the oxygen fiber probe. A single fiber will provide a much more compact solution. In addition, and due to the presence of the mirror, part of the luminescence radiation which is lost in the standard configuration could then be detected. The implementation of such probe demands a careful design. By controlling the LED operating temperature, its central wavelength can be tuned within a few nanometers. This can be used to optimize the overlap of the filter transfer function with the LED spectrum, thus increasing the efficiency of the optical power reference scheme. The principle of operation of this configuration can easily be extended to other optical fiber sensors that are based on quenching of the fluorescence

Overall, the results obtained during this research clearly show that luminescence techniques offer a practical path with a great potential to develop many novel fiber optic sensing systems for environmental and biomedical applications.

4.6 References

[1] R. Ramamoorthy, P. K. Dutta, and S.A. Akbar, *Oxygen sensors: Materials, methods, designs and applications.* Journal of Materials Science, 2003. **38**: p. 4271 - 4282.

[2] Rachel A. Yotter and D.M. Wilson, *Sensor Technologies for Monitoring Metabolic Activity in Single Cells—Part I: Optical Methods.* IEEE Sensors Journal, 2004. **4**(4): p. 395-411.

[3] Rachel A. Yotter and D.M. Wilson, *Sensor Technologies for Monitoring Metabolic Activity in Single Cells—Part II: Nonoptical Methods and Applications.* IEEE Sensors Journal, 2004. **4**(4): p. 412-429.

[4] Arthur E. Colvin JR., Terry E. Phillips, Joseph A. Miragliotta, R. Ben Givens, and C.B. Bargeron, *A novel solid-state oxygen sensor.* Johns Hopkins APL Technical Digest, 1996. **17**: p. 377-385.

[5] Orellana, G., *Luminescent optical sensors.* Anal Bioanal Chem, 2004. **379**: p. 344–346.

[6] R. Narayanaswamy and O.S. Wolfbeis, eds. *Optical Sensors - Industrial Environmental and diagnostic Applications.* Springer Series on Chemical Sensors and Biosensors, ed. O.S. Wolfbeis. 2004, Springer: Berlin.

[7] Otto S. Wolfbeis, *Fiber Optic Chemical Sensors and Biosensors.* Anal. Chem., 2002. **72**: p. 81R-89R.

[8] Otto S. Wolfbeis, *Fiber Optic Chemical Sensors and Biosensors.* Anal. Chem., 2004. **76**: p. 3269-3284.

[9] E. R Carraway, J. N. Demas, B. A. DeGraff, and J.R. Bacon, *Photophysics and photochemistry of oxygen sensors based on luminescent transition-metal complexes.* Analytical Chemistry, 1991. **63**: p. 337-342.

[10] Guillermo Orellana and D. Garcia-Fresnadillo, *Environmental and Industrial Optosensing with Tailored Luminescent Ru(II) Polypyridyl Complexes*, in *Optical Sensors - Industrial Environmental and diagnostic Applications*, R. Narayanaswamy and O.S. Wolfbeis, Editors. 2004, Springer: Berlin. p. 309-357.

[11] M. K. Krihak and M.R. Shahariari, *Highly sensitive, all solid state fibre optic oxygen sensor based on the sol-gel coating technique.* Electronics Letters, 1996. **32**: p. 240-242.

[12] Brian. D. MacCraith, Gerard O'Keeffe, C.M. McDonagh, and A.K. McEvoy, *LED-based fibre optic oxygen sensor using sol-gel coating.* Electronics Letters, 1994. **30**: p. 888-889.

[13] Amao, Y., *Probes and polymers for optical sensing of oxygen.* Microchimica Acta, 2003. **143**(1): p. 1-12.

[14] *PreSens - Precision Sensing GmbH . http://www.presens.de.* [cited 2006].

[15] *Ocean Optics, Inc. www.oceanoptics.com.* [cited 2006].

[16] Paul Hartmann, Marc J. P. Leiner, and P. Kohlbacher, *Photobleaching of ruthenium complex in polymers used for oxygen optodes and its inhibition by singlet oxygen quenchers.* Sensors and Actuators B, 1998. **51**: p. 196-202.

[17] Shih-Chu Liao, Zhong Xu, Joseph A. Izatt, and J.R. Alcala, *Real-time frequency domain temperature and oxygen sensor with a single optical fiber.* IEEE Transact. on Biomedical Eng., 1997. **44**(11).

[18] Barry J. Prince, Alan W. Schwabacher, and P. Geissinger, *A Readout Scheme Providing High Spatial Resolution for Distributed Fluorescent Sensors on Optical Fibers.* Anal. Chem., 2001. **73**: p. 1007-1015.

[19] Valeur, B., *Effects of intermolecular photophysical processes on fluorescence emission*, in *Molecular Fluorescence: principles and applications.* 2002, Wiley VCH: Weinheim. p. 72-124.

[20] Joseph R. Lakowicz, *Quenching of fluorescence*, in *Principles of Fluorescence Spectroscopy*. 1999, Kluwer-Plenum: New York. p. 237-265.

[21] Mohr, G.J., *Polymers for Optical Sensors*, in *Optical Chemical Sensors*, F. Baldini, et al., Editors. 2004, Springer. p. 297-321.

[22] Podbielska, H., Agnieszka Ulatowska-Jarza, Gerhard Muler, and H.J. Eichler, *Sol-Gels for Optical Sensors*, in *Optical Chemical Sensors*, F. Baldini, et al., Editors. 2004, Springer. p. 353-385.

[23] Wenying Xu, Robert Clayton McDonough III, Brandi Langsdorf, J. N. Demas, and B.A. DeGraff, *Oxygen sensors based on luminescence quenching: Interactions of metal Complexes with the polymer supports.* Analytical Chemistry, 1994. **66**: p. 4133-4141.

[24] Heather M. Rowe, Wenying Xu, J. N. Demas, and B.A. DeGraff, *Metal ion sensors based on a luminescent ruthenium(II) complex: the role of polymer support in sensing properties.* Applied Spectroscopy, 2002. **56**: p. 167-173.

[25] Xin Lu and M.A. Winnik, *Luminescence Quenching in Polymer/Filler Nanocomposite Films Used in Oxygen Sensors.* Chem. Mater., 2001. **13**: p. 3449-3463.

[26] Andrew Mills, *Controlling the sensitivity of optical oxygen sensors.* Sensors and Actuators B, 1998. **51**: p. 60-68.

[27] Colette M. McDonagh, P. Bowe, K. Mongey, and B.D. MacCraith, *Characterisation of porosity and sensor response times of sol-gel-derived thin films for oxygen sensor applications.* Journal of Non-Crystalline Solids, 2002. **306**: p. 138-148.

[28] Colette .M. McDonagh, B.D. MacCraith, and A.K. McEvoy, *Tailoring of sol–gel films for optical sensing of oxygen in gas and aqueous phase.* Anal. Chem., 1998. **70**: p. 45–50.

[29] E. R Carraway, J. N. Demas, and B.A. DeGraff, *Luminescence quenching mechanism for microheterogeneous systems.* Analytical Chemistry, 1991. **63**: p. 332-336.

[30] Geddes, C.D., *Optical halide sensing using fluorescence quenching: theory, simulations and applications-a review.* Measurement Science and Technology, 2001. **12**: p. R33-R88.

[31] Baker, G.A., B.R. Wenner, A.N. Watkins, and F.V. Bright, *Effects of processing temperature on the oxygen quenching behavior of tris(4,7 '-diphenyl-1,10 '-phenanthroline) ruthenium (II) sequestered within sol-gel-derived xerogel films.* Journal of Sol-Gel Science and Technology, 2000. **17**(1): p. 71-82.

[32] Mills, A., *Optical sensors for oxygen: a log-gaussian multisite-quenching model.* Sensors and Actuators B-Chemical, 1998. **51**(1-3): p. 69-76.

[33] J. N. Demas, B. A. DeGraff, and W. Xu, *Modeling of luminescence quenching-based sensors: comparison of multisite and nonlinear gas solubility models.* Analytical Chemistry, 1995. **67**: p. 1377-1380.

[34] Vladimir I. Ogurtsov, Dmitri B. Papkovsky, and N.Y. Papkovskaia, *Approximation of calibration of phase-fluometric oxygen sensor on the basis of physical models.* Sensors and Actuators B, 2001. **81**: p. 17-24.

[35] T.M. Butler, B.D. MacCraith, and C. McDonagh, *Leaching in sol–gel-derived silica films for optical pH sensing.* Journal of Non-Crystalline Solids, 1998. **224**: p. 249-258.

[36] Antonius Song, Stephen Parus, and Raoul Kopelman, *High-Performance Fiber-Optic pH Microsensors for Practical Physiological Measurements Using a Dual-Emission Sensitive Dye.* Anal. Chem., 1997. **69**(5): p. 863-867.

[37] Haley R. Kermis, Yordan Kostov, Peter Harms, and G. Rao, *Dual Excitation Ratiometric Fluorescent pH Sensor for Noninvasive Bioprocess Monitoring: Development and Application.* Biotechnol. Prog., 2002. **18**: p. 1047-1053.

[38] Yordan Kostov, Kelly A. Van Houten, Peter Harms, Robert S. Pilato, and G. Rao, *Unique Oxygen Analyzer Combining a Dual Emission Probe and a Low-Cost Solid-State Ratiometric Fluorometer.* Applied Spectroscopy, 2000 **54**(6): p. 864-868.

[39] Valeur, B., *Principles of steady-state and time-resolved fluorometric techniques*, in *Molecular Fluorescence: principles and applications*. 2002, Wiley VCH: Weinheim. p. 155-199.

[40] Joseph R. Lakowicz, *Time-Domain Lifetime Measurements* in *Principles of Fluorescence Spectroscopy*. 1999, Kluwer-Plenum: New York. p. 95-141.

[41] M. T.Murtagh, D. E. Ackley, and M.R. Shahriari, *Development of a highly sensitive fibre optic O_2/DO sensor based on a phase modulation technique*. Electronics Letters, 1996. **32**: p. 477-479.

[42] Colette McDonagh, C. Kolle, Aisling K. McEvoy, D. L. Dowling, A. A. Cafolla, S. J. Cullen, and B.D. MacCraith, *Phase fluorometric dissolved oxygen sensor*. Sensors and Actuators B, 2001. **74**: p. 124-130.

[43] Gerard O'Keeffe, Brian D. MacCraith, Aisling K. McEvoy, Colette M. McDonagh, and J.F. McGilp, *Development of LED-based phase fluorimetric oxygen sensor using evanescent wave excitation of a sol-gel immobilized dye*. Sensors and Actuators B, 1995. **29**: p. 226-230.

[44] Otto S. Wolfbeis, Ingo Klimant, Tobias Werner, Christian Huber, Ute Kosch, Christian Krause, Gerhard Neurauter, and A. Durkop, *Set of luminescence decay time based chemical sensors for clinical applications*. Sensors and Actuators B, 1998. **51**: p. 17-24.

[45] Joseph R. Lakowicz and I. Gryczynski, *Frequency-domain fluorescence spectroscopy*, in *Topics in Fluorescence Spectroscopy*. 1991, Plenum: New York. p. 293-335.

[46] Zhiyi Zhang, K. T. V. Grattan, and A.W. Palmer, *Phase-locked detection of fluorescence lifetime*. Review of Scientific Instruments, 1993. **64**: p. 2531-2540.

[47] Vladimir I. Ogurtsov and D.B. Papkovsky, *Selection of modulation frequency of excitation for luminescence lifetime-based oxygen sensors*. Sensors and Actuators B, 1998. **51**: p. 377-381.

[48] Ogurtsov, V.I. and D.B. Papkovsky, *Application of frequency spectroscopy to fluorescence-based oxygen sensors*. Sensors and Actuators B-Chemical, 2006. **113**(2): p. 608-616.

[49] J. N. Demas and B.A. DeGraff, *Applications of luminescent transition metal complexes to sensor technology and molecular probes*. Journal of Chemical Education, 1997. **74**: p. 690-695.

[50] Sang-Kyung Lee and I. Okura, *Porphyrin-doped sol-gel glass as a probe for oxygen sensing*. Analytica Chimica Acta, 1997. **342**: p. 181-188.

[51] Bharathibai J. Basu and K.S. Rajam, *Comparison of the oxygen sensor performance of some pyrene derivatives in silicone polymer matrix*. Sensors and Actuators B, 2004. **99**: p. 459-467.

[52] J. N. Demas and B.A. DeGraff, *Design and applications of highly luminescent transition metal complexes*. Analytical Chemistry, 1991. **63**: p. 829A-837A.

[53] Andrew Mills and F.C. Williams, *Chemical influences on the luminescence of ruthenium diimine complexes and its response to oxygen*. Thin Solid Films, 1997. **306**: p. 163-170.

[54] Xu, W.Y., K.A. Kneas, J.N. Demas, and B.A. DeGraff, *Oxygen sensors based on luminescence quenching of metal complexes: Osmium complexes suitable for laser diode excitation*. Analytical Chemistry, 1996. **68**(15): p. 2605-2609.

[55] Sang-Kyung Lee and I. Okura, *Photoluminescent determination of oxygen using metalloporphyrin-polymer sensing systems*. Spectrochimica Acta Part A, 1998. **54**: p. 91-100.

[56] Sang-Kyung Lee and I. Okura, *Photostable Optical Oxygen Sensing Material: Platinum Tetrakis(pentafluorophenyl)porphyrin Immobilized in Polystyrene*. Analytical Communications, 1997. **34**: p. 185-188.

[57] Papkovsky, D.B., G.V. Ponomarev, W. Trettnak, and P. Oleary, *Phosphorescent Complexes of Porphyrin Ketones - Optical-Properties and Application to Oxygen Sensing*. Analytical Chemistry, 1995. **67**(22): p. 4112-4117.

[58] Hartmann, P. and W. Trettnak, *Effects of polymer matrices on calibration functions of luminescent oxygen sensors based on porphyrin ketone complexes*. Analytical Chemistry, 1996. **68**(15): p. 2615-2620.

[59] Ingo Klimant and O.S. Wolfbeis, *Oxygen-sensitive Luminescent materials basead on silicone-soluble ruthenium diimine complexes.* Analytical Chemistry, 1995. **67**: p. 3160-3166.

[60] Chun-Man Chan, Mee-Yee Chan, Minquan Zhang, W. Lo, and K.-Y. Wong*, *The performance of oxygen sensing films with ruthenium-adsorbed fumed silica dispersed in silicone rubber.* Analyst, 1999. **124**: p. 691-694.

[61] Larry L. Hench and J.K. West, *The sol-gel process.* Chemical Reviews, 1990. **90**: p. 33-72.

[62] Brian D. MacCraith, Colette M. McDonagh, Gerard O'Keeffe, Aisling K. McEvoy, T. Butler, and F.R. Sheridan, *Sol-gel coatings for optical chemical sensors and biosensors.* Sensors and Actuators B, 1995. **29**: p. 51-57.

[63] Ingo Klimant, Falk Ruckruh, Gregor Liebsch, Achim Stangelmayer, and O.S. Wolfbeis, *Fast response oxygen micro-optodes based on novel soluble ormosil glasses.* Mikrochimica Acta, 1999. **131**: p. 35-46.

[64] Brian D. MacCraith, Gerard O'Keeffe, Aisling K. McEvoy, Colette M. McDonagh, John F. McGilp, Brendan O'Kelly, J. Des O'Mahony, and M. Cavanagh, *Light-emitting-diode-based oxygen sensing using evanescent wave excitation of a dye-doped sol-gel coating.* Optical Engineering, 1994. **33**: p. 3861-3866.

[65] Gargi Vishnoi, Masayuki Morisawa, Tatsuya Mizukami, Koji Uchiyama, and S. Muto. *Studies on the improvement of sensitivity and stability of fiber optic oxygen sensing based on cladding fluorescence.* in *Proccedings SPIE.* 1997 Vol. 3105, p. 114-121.

[66] Uttamchandani, D. and S. McCulloch, *Optical nanosensors - towards the development of intracellular monitoring.* Advanced drug Delivery Reviews, 1996. **21**: p. 239-247.

[67] S. McCulloch and D. Uttamchandani. *Fibre optic micro-optrode for dissolved oxygen measurements.* in *Science, Measurements and Technology, IEE Proceeding.* 1999: IEEE. Vol. 146, p. 123-127.

[68] Holst, G., R.N. Glud, M. Kuhl, and I. Klimant, *A microoptode array for fine-scale measurement of oxygen distribution.* Sensors & Actuators B, 1997. **38-39**: p. 122-129.

[69] Juan Dıaz-Garcıa, José M. Costa-Fernández, Nerea Bordel-Garcıa, and A. Sanz-Medel, *Room-temperature phosphorescence fiber-optic instrumentation for simultaneous multiposition analysis of dissolved oxygen.* Analytica Chimica Acta, 2001. **429**: p. 55–64.

[70] Ferguson, J.A., B.G. Healey, K.S. Bronk, S.M. Barnard, and D.R. Walt, *Simultaneous monitoring of pH, CO2 and O-2 using an optical imaging fiber.* Analytica Chimica Acta, 1997. **340**(1-3): p. 123-131.

[71] Mignani, A.G. and F. Baldini, *Biomedical sensors using optical fibres.* Rep. Prog. Phys., 1996. **59**: p. 1-28.

[72] Navarro-Villoslada, F., G. Orellana, M.C. Moreno-Bondi, T. Vick, M. Driver, G. Hildebrand, and K. Liefeith, *Fiber-optic luminescent sensors with composite oxygen-sensitive layers and anti-biofouling coatings.* Analytical Chemistry, 2001. **73**(21): p. 5150-5156.

[73] Zhao, Y.D., A. Richman, C. Storey, N.B. Radford, and P. Pantano, *In situ fiber-optic oxygen consumption measurements from a working mouse heart.* Analytical Chemistry, 1999. **71**(17): p. 3887-3893.

[74] M. D. Stokes and G.N. Somero, *An optical oxygen sensor and reaction vessel for high-pressure applications.* Limnol. Oceanogr., 1999. **44**(1): p. 189-195.

[75] Jeffrey T. Remillard, Jeffrey R. Jones, Ben D. Poindexter, Chaitanya K. Narula, and W.H. Weber, *Demonstration of a high-temperature fiber-optic gas sensor made with a sol-gel process to incorporate a fluorescent indicator.* Applied Optics, 1999. **38**(25): p. 5306-5309.

[76] Andrew Mills and Q. Chang, *Modelled Diffusion-controlled Response ans Recovery Behavior of a Naked Optical Film Sensor With a Hyperbolic-type Response to Analyte Concentration.* Analyst, 1992. **117**: p. 1461-1466.

[77] R. Herne, J. Brocas, and E.V. Donckt, *The response time of optical sensors based on luminescence quenching.* Analytica Chimica Acta, 1998. **364**: p. 131-141.

[78] P. Innocenzi, H. Kozuka, and T. Yoko, *Fluorescence properties of the $Ru(bpy)_3^{2+}$ complex incorporated in sol–gel-derived silica coating films.* J. Phys. Chem. B, 1997. **101**(2285–2291).

[79] K. Maruszweski et al., *Physicochemical properties of $Ru(bpy)_3^{2+}$ entrapped in silicate bulks and fiber thin films prepared by the sol–gel method.* Chem. Phys. Lett., 1999. **314**: p. 83–90.

[80] Anderson, G.P., J.P. Golden, and F.S. Ligler, *An evanescent wave biosensor - Part I: Fluorescent signal acquisition from step etched fiber optic probes.* IEEE Transact. on Biomedical Eng., 1994. **41**(6): p. 578-583.

[81] L.C. Shriver-Lake et al, *The effect of tapering the optical fiber on evanescent wave measurements.* Anal. Lett., 1992. **25**: p. 1183–1199.

[82] Anderson, G.P., J.P. Golden, L.K. Cao, D. Wijesuriya, L.C. Shriverlake, and F.S. Ligler, *Development of an Evanescent-Wave Fiber Optic Biosensor.* Ieee Engineering in Medicine and Biology Magazine, 1994. **13**(3): p. 358-368.

[83] Blue, R., N. Kent, L. Polerecky, H. McEvoy, D. Gray, and B.D. MacCraith, *Platform for enhanced detection efficiency in luminescence-based sensors.* Electronics Letters, 2005. **41**(12): p. 682-684.

[84] I. Klimant, M. Kuhl, R. N. Glud, and G. Holst, *Optical measurement of oxygen and temperature in microscale: strategies and biological applications.* Sensors and Actuators B, 1997. **38-39**: p. 29-37.

[85] Michael Bass, *Handbook of Optics.* Vol. I. 1995: MacGraw-Hill.

Chapter 5

Application of Quantum Dots to Optical Oxygen Sensing

Summary

Semiconductor nanoparticles, or quantum dots, with their relatively high quantum yield, narrow luminescence spectrum, outstanding photostability and the ability to tune their optical properties, are ideal for biological tagging and a very powerful tool for chemical sensing applications. In this chapter, an overview of this rapidly expanding area of research is presented. Additionally, results are shown, with emphasis on their application in optical oxygen sensing, which establish quantum dots as suitable temperature and intensity references for incorporation in luminescence based chemical sensors. The possibility of wavelength multiplexing applications using luminescent nanocrystals is also explored. This concept is demonstrated in a system for multipoint measurement of oxygen and temperature.

5.1 Introduction

The advent of nanotechnology, introducing human control over matter at the nanometer scale, has produced a new class of materials with exciting properties. New sets of tools can be created in a diversity of domains. In particular, biochemical applications are already benefiting from the versatility of nanoparticles with a variety of sizes, shapes and compositions (metal, polymer, semiconductor,...)[1, 2]. The reduced dimension is the key factor leading to the possibility of enhancement and tailoring of many of the material properties (electrical, optical,...), which become size and/or shape dependent at such scale. Enhanced mechanical properties, very strong scattering or unique luminescent properties are examples of some of the features that can be readily controlled. In addition, the small scale facilitates bioconjugation (i.e., combination of the nanoparticle with biomolecules like antibodies) allowing such properties to be integrated in biological systems. This way, the performance of conventional techniques can be greatly improved and an entirely new set of exciting applications becomes available[3, 4].

In particular, fluorescent semiconductor nanocrystals, or quantum dots (QDs), are especially attractive for biochemical sensing and imaging applications. Fluorescence is the basis of a large

number of bioassays and chemical sensing techniques. In this field, the unique optical properties of nanometer scale QDs are highly favorable when compared to those of traditional molecular fluorophores. The ability to tune their luminescence characteristics by simple control of the particles size, combined with relatively high quantum yields, narrow fluorescence emission, very broad absorption spectrum and an outstanding photo-stability provide the solution to many of the problems associated with traditional luminescence sensors and are the promise for a completely new set of applications[5, 6].

In this chapter, an overview will be given covering the main applications of semiconductor nanocrystals in the field of optical sensing. In addition, experimental results will be presented, in the context of luminescent oxygen sensors, which establish QDs as excellent tools with capability to improve the performance of luminescent sensing systems. For a better understanding of the optical properties of semiconductor nanocrystals, a brief overview of semiconductor physics and semiconductor quantum structures will be given first. For further details on these matters, extensive literature is available [7-9].

5.2 Semiconductors

When a large number of single atoms come together to form a crystalline solid their discrete electronic wave functions start to overlap and eventually generate quasi-continuous bands of allowed electronic states. Different bands are usually separated by a gap of forbidden energies (Figure 5.1(a)). The magnitudes of these gaps, and the energy range of the bands, depend on crystal symmetry and on inter-atomic spacing. The distribution of electrons in the highest occupied band, the valence band, along with the magnitude of the energy gap, E_g, that separates it from the next allowed energy band (the conduction band), determines the materials electrical, optical, and chemical properties. Three illustrative situations are depicted in Figure 5.1(b).

When the highest occupied band is partially filled, electrons are free to move under the influence of a small external field and the material is a good conductor. This is the characteristic that gives metals their high conductivity, high reflectivity and opacity to visible radiation. On the other hand, when the valence band is completely filled, in order to obey Pauli's exclusion principle, electrons are not allowed to move freely. In such situation, the conductivity of the material will depend on the magnitude of the band gap. If E_g is large compared to the energy the electron can pick up from an external field, electrons will remain in the valence band, there will be no net charge movement, and the material is called an insulator (e.g. in diamond $E_g = 7eV$). When E_g is not so large ($< 3eV$) the material is called a semiconductor. At absolute zero, the valence band of an ideal

semiconductor is completely filled and the conduction band is empty[33]. As temperature rises, however, electrons in the valence band may acquire enough thermal energy to cross the narrow energy gap and be promoted to the conduction band, where they can easily move. In addition, each electron crossing the gap leaves a vacancy, or a 'hole', in the valence band, which will allow charge movement to occur in this band as well. This way, semiconductors behave like insulators at $0\,K$, and as progressively better conductors as temperature rises.

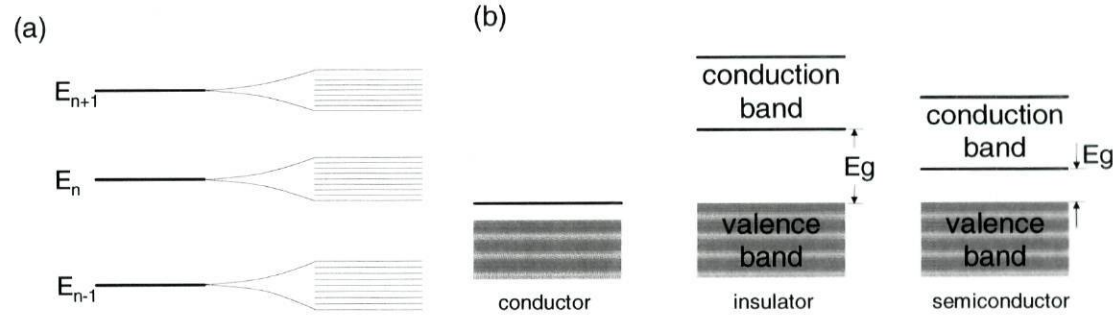


Figure 5.1 (a) In a crystalline solid the energy levels of isolated atoms originate quasi-continuous energy bands separated by forbidden energy gaps. (b) The distribution of electrons in the valence band, and the magnitude of the energy gap, E_g, between the conduction and the valence band, determine the properties of the material. Adapted from [10].

Silicon (Si) and germanium (Ge), elements from periodic table group B-IV, are two important examples of intrinsic semiconductors. The atoms of these materials arrange themselves in a diamond like crystalline structure, sharing their four valence electrons with four other neighboring atoms in a tetrahedral arrangement. Their ambient temperature band gaps are respectively $1.12\,eV$ and $0.67\,eV$. At $300\,K$, the conductivity of such semiconductors is still poor (few electrons are thermally excited over a band gap of $1.12\,eV$). However, their charge carrier density can be greatly enhanced by introducing impurities with excess (donor) or shortage (acceptor) of electrons into the crystal lattice[34]. These donor/acceptor impurities introduce electrons/holes that are weekly bonded to the crystal lattice, they are thus easily excited, dramatically improving conductivity at ambient temperature. Typically, very small doping concentrations (one part in 10^7) are enough to increase the conductivity of the material dramatically. Doped semiconductors are called extrinsic, as opposed to pure or intrinsic semiconductors. In addition to such elemental semiconductors, important binary

[33] At absolute zero the chemical potential equals the Fermi energy which is the energy of the uppermost level filled with carriers. At $T = 0\,K$ the Fermi energy lies within the band gap, the valence band is thus completely filled and the conduction band is empty.

[34] Phosphor (P), with five valence electrons, will behave like a donor in a Si matrix; Boron (B), on the other hand, with only three valence electrons, would be an acceptor.

semiconductors combine elements from groups III-V (eg. gallium arsenide - GaAs) or II-VI (eg. cadmium selenide - CdSe). More complex ternary and quaternary semiconductor alloys are also possible. This allows a tremendous versatility in tailoring conductivity and band gap magnitude, providing ways to engineer materials with widely different electrical, optical and chemical properties. Such materials are responsible for a 'revolution' in electronics and optoelectronics, and represent one of the foundations of today's technological development.

5.2.1 Interband absorption

The optical properties of semiconductor materials are of particular interest for sensing applications. Semiconductors interact with light over a wide spectral range ($0.1\,\mu m - 1000\,\mu m$). In the near-UV to the near-infrared region of the spectrum, the dominant effect is absorption at the band edge and by impurities [11]. This way, both the absorption and the luminescence emission spectra of a semiconductor material are determined by its energy band structure. Only with quantum calculations the complex configuration of the valence and conduction bands can be fully determined. This structure is usually represented in the form of dispersion diagrams plotting energy, E, as a function of the electron momentum, p, or electron wavevector[35], k. The simplest case arises for free electrons in vacuum. In this situation, in the absence of a potential ($U(r) = 0$ everywhere) and with no boundary conditions, the electron has only kinetic energy and the solutions of the Schrödinger equation[36] are plane waves obeying the following dispersion relation:

$$E = \frac{p^2}{2m_0} = \frac{\hbar^2 k^2}{2m_0}, \tag{5.1}$$

where m_0 is the electronic mass and $\hbar$ is the reduced Planck constant. This function corresponds to the parabolic curve represented by the thin line in Figure 5.2. In a semiconductor, considering a very simplified model, it is assumed that the electrons reaching the conduction band travel through the material with very little interaction with the positively ionic cores and can thus be considered nearly free. It is, however, the periodic nature of this weak interaction with the lattice that influences the

---

[35] The electron wavevector is defined by the *de Broglie* relation ($p = \hbar k$).

[36] In quantum mechanics, the information about particle position and momentum can be deduced from its associated wave function $\psi(x,t)$. The evolution of the wave function is governed by the Schrödinger equation, which in one dimension takes the form: $-\frac{\hbar}{2m}\frac{\partial^2}{\partial x^2}\psi(x,t) + U(x)\psi(x,t) = i\hbar\frac{\partial}{\partial t}\psi(x,t)$. It is usually simplified by considering time and space dependence separately. The energy eigenstates of the system can be determined by solving the time-independent Schrödinger equation: $-\frac{\hbar}{2m}\frac{\partial^2}{\partial x^2}\psi(x) + U(x)\psi(x) = E\psi(x)$. For a free particle, $U(x) = 0$, and the solutions of the Schrödinger equation are plane waves of the form $\psi(x) = Ae^{ikx}e^{-iEt/\hbar}$, where A is a normalization constant.

motion of electrons altering the dispersion relation of semiconductors. The periodic arrangement of the crystal subjects the electrons to a potential with the same periodicity as the lattice. This means that, considering a certain direction x along the crystal, the potential repeats itself after a distance equal to the lattice spacing, $a_L = a$, along the same direction:

$$U(x) = U(x + a) = U(x + 2a) = ... \tag{5.2}$$

According to Bloch's theorem, this periodicity is imposed on the electronic wave function and, therefore, the time-independent Schrödinger equation, with a periodic potential, should be satisfied by solutions of the type:

$$\psi(x) = e^{ikx} u_k(x), \qquad u_k(x) = u_k(x + a), \tag{5.3}$$

which leads to

$$\psi(x + na) = e^{ikna} \psi(x). \tag{5.4}$$

This way, due to the periodicity imposed by the potential on the wavefunction, k values differing by a factor of $2\pi n/a$ appear to be equivalent. This is a direct consequence of the translational symmetry of space, reflecting the periodic nature of the lattice. Each of the equivalent intervals

$$\frac{-\pi}{a} < k < \frac{\pi}{a}; \quad \frac{\pi}{a} < k < \frac{3\pi}{a}; \quad \frac{3\pi}{a} < k < \frac{5\pi}{a}; ..., \tag{5.5}$$

of width $2\pi/a$, contains the full set of possible nonequivalent k values and is called a Brillouin zone[37]. The corresponding dispersion diagram is represented by the thick lines shown in Figure 5.2. It can be seen that, within each Brillouin zone, the dispersion relation is almost the same as for a free particle. However, the dispersion curve has discontinuities at the points

$$k = \frac{\pi}{a} n; \qquad n = \pm 1, \pm 2, \pm 3, ... \tag{5.6}$$

These k values correspond to wavelengths that fulfill the Bragg condition of the crystal lattice, originating strong reflections of the electronic wave function. This way the electron is unable to propagate through the crystal and is associated with a standing wave. The discontinuities that thus arise in the $E - k$ diagram correspond to the gaps of forbidden energies of the semiconductor. In a general three-dimensional semiconductor, the band structure can be quite more complicated, with numerous bands, sometimes with several energy maxima and minima, and having different configurations for different crystallographic directions. Moreover, energy levels within the band gap,

[37] Typically, it is sufficient to consider only the first Brillouin zone to fully describe the semiconductor band structure.

often called traps, can arise from impurities, donors/acceptors, and even defects. A more realistic band diagram for GaAs can be observed in Figure 5.3.

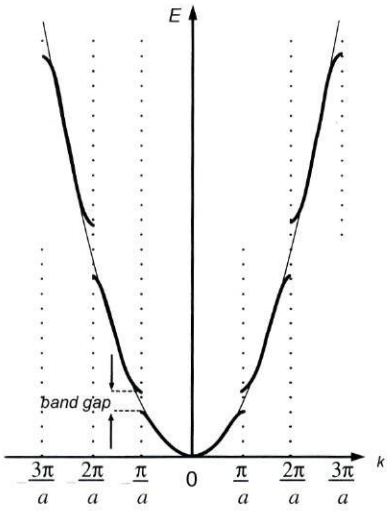


Figure 5.2 Dispersion relation of a particle in a one-dimensional periodic potential (the thin line describes the kinetic energy of a free particle). The discontinuities at $k = \pi n / a$, correspond to standing waves that cannot propagate due to multiple reflections from the periodic boundaries originating the forbidden energy gaps. Adapted from [9].

Four energy bands are represented, one electronic band originated from atomic s orbitals (top line), and three hole bands, originated from atomic p orbitals (bottom lines)[38]. GaAs is an example of a direct gap semiconductor, meaning that the valence and conduction band energy extremes correspond to the same momentum. If, however, the conduction band minimum and the valence band maximum occur at different momentum values, the semiconductor is said to have an indirect band-gap (eg. Si and Ge). The nature of the band gap has important consequences for the optical properties of the material.

In order for interband transitions to occur, like processes of absorption or emission of a photon, the conservation of energy and momentum must be observed. In direct band gap semiconductors, the electron momentum does not change significantly during photon absorption ($\Delta k_e \approx 0$). Since the momentum of the incoming photon is small in comparison, the electron wavevector is automatically conserved. On the other hand, in an indirect band gap material, the electron momentum must change significantly for the transition to occur ($\Delta k_e \neq 0$). This is only

[38] The three valence bands originate from *p*-orbitals and are usually referred to as 'light-hole band', 'heavy-hole band' and 'split-off hole band'. The names come, respectively, from the different effective masses, and from the lower energy offset. The single conduction band is originated from *s*-orbitals and is also called electron band.

possible if a lattice phonon[39] with adequate momentum is involved in the process. Either emission or absorption of phonons is possible. The two types of band gap just described are represented in Figure 5.4.

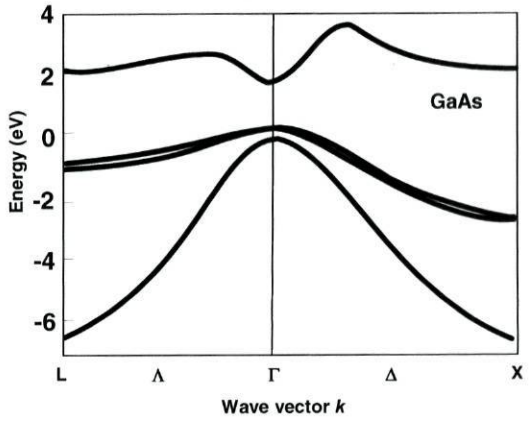


Figure 5.3 Band structure of GaAs. Dispersion curves are shown for two different crystallographic directions, Γ →X and Γ→ L. Adapted from [7].

Since indirect absorption is a second order process, it is much less probable than a direct transition. Direct band gap semiconductors are, therefore, expected to be much better absorbers and emitters of radiation. For study of the optical properties of such materials, it is often sufficient to consider only the small portion of the band structures near $k = 0$. In this region, the conduction and valence bands are approximately parabolic, and their dispersion relations are given respectively by $E_c(k)$ and $E_v(k)$, where

$$E_c(k) = E_g + \frac{\hbar^2 k^2}{2m_e^*}$$
$$E_v(k) = -\frac{\hbar^2 k^2}{2m_h^*} \tag{5.7}$$

and m_h^* and m_e^* are the effective masses[40] of electrons and holes in their respective bands. $E = 0$ corresponds to the top of the valence band. From these relations it is evident that conservation of energy during a transition between the two bands requires that

$$\hbar\omega = E_g + \frac{\hbar^2 k^2}{2m_e^*} + \frac{\hbar^2 k^2}{2m_h^*}, \tag{5.8}$$

---

[39] Lattice vibrations are quantized in discrete energies, the phonon is the lattice vibration quantum.

[40] The effective mass m^* is generally different from the free electron mass m_0 and accounts for the effect of the lattice potential on the charge carriers. Under the influence of an external force the electron behaves as if its mass was m^*. Generically, m^* is not constant and is defined by the curvature of the $E - k$ diagram: $m^* = \hbar^2 (d^2E/dk^2)^{-1}$. In the region near $k = 0$, however, it can be considered approximately constant. This is called the constant effective mass approximation or parabolic approximation.

which will happen whenever the photon energy ($\hbar\omega$) exceeds that of the band gap, E_g. Since there is a continuous range of energy states within the valence and conduction bands, this condition, establishes a threshold behavior for interband absorption. Photons with energies lower than E_g will not be absorbed; any photon with energy higher than E_g will be absorbed (the upper limit will be established by the extreme limits of the participating bands).

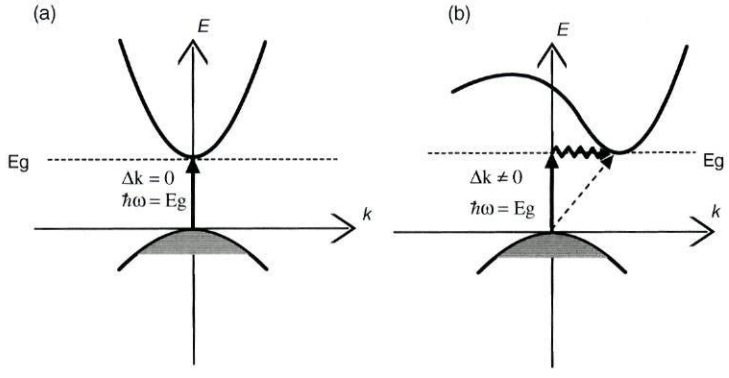


Figure 5.4 Excitation across the band gap by photon absorption with $E_g = \hbar\omega$: (a) direct gap semiconductor, no change in the electron momentum ($\Delta k = 0$); (b) indirect gap semiconductor, electron momentum must change by phonon absorption or emission ($\Delta k \neq 0$). Adapted from [7].

The absorption coefficient, α, for photons of a given energy is proportional to the probability of the transition P_{if}, the density of electrons in the initial state n_i, the density of available final states n_f, and results from summation over all possible transitions separated by the photon energy $\hbar\omega$. It can be calculated by

$$\alpha(\hbar\omega) = C\sum P_{if} n_i n_f , \tag{5.9}$$

where C is a constant. For a direct band gap semiconductor this relation results in an absorption coefficient with the following behavior:

$$\alpha(\hbar\omega) = \begin{cases} 0 & for \quad \hbar\omega < E_g \\ A(\hbar\omega - E_g)^{1/2} & for \quad \hbar\omega \geq E_g \end{cases}, \tag{5.10}$$

where A is a constant independent of the radiation frequency, ω. A plot of the optical absorption for a direct band gap semiconductor calculated using these expressions can be seen in Figure 5.6, represented by the dashed line. It shows that, near the band edge, the absorption coefficient presents a sharp transition at photon energies equal to E_g confirming the expected threshold behavior. This prediction showed to be in good agreement when compared with experimental data obtained at room temperature from a variety of semiconductors materials [12]. In fact, the onset of absorption is one of the methods to determine the magnitude of the band gap experimentally. In

Table 5-1 the photon wavelength for band edge absorption can be seen for some common semiconductors.

For many semiconductors, however, it is found that the frequency dependence of absorption predicted by equations (5.10) is only approximately obeyed. This happens for a variety of reasons. Real semiconductors contain trap states due to impurities and defect whose energies may lay within the band gap; therefore, absorption for photon energies less than E_g may become possible. In addition, the calculations presented are only valid for the parabolic approximation, where $k \approx 0$. For higher energies the joint density of states will have a different frequency dependence. In these cases the full complex band structure must be considered.

Semiconductor Type	Composition	Gap type	Eg (eV)	λg (nm)
elemental	Si	i	1.11	1100
elemental	Ge	i	0.66	1900
III-V	GaAs	d	1.43	870
III-V	AlAs	i	2.15	580
III-V	$Al_{03}Ga_{0.7}As$	d	1.80	690
II-VI	CdTe	d	1.44	860
II-VI	CdS	d	2.42	510
IV-VI	PbTe	i	0.29	4300

Table 5-1 Properties of some common semiconductors. Gap type, direct (d) or indirect (i); Band gap energy E_g; and equivalent photon wavelength, λ_g. Data obtained from [11].

Finally, Coulomb interaction between the electron and the hole where neglected. This interaction can strongly enhance the absorption near the band edge through the formation of excitons, a bonded electron-hole pair. This effect is stronger for larger band gaps and it is better observed at lower temperatures. However, for certain important materials like GaAs, it can be significant even at ambient temperatures. In addition, exciton effects can be enhanced in lower dimensional semiconductor structures like quantum wells and quantum dots. For this reason they will be further discussed.

Excitons

Upon photon absorption in a crystal, the excited electron crosses the gap to the conduction band leaving behind a hole in the valence band. Under certain conditions, the Coulomb interaction

between these two charges with opposite signs, coexisting in the same spatial region, is strong enough to create a bound electron-hole pair. This neutral pair is called an exciton and can move as a whole through the crystal. Typically, in most semiconductors the exciton radius is large, encompassing many lattice spacings. This results in weakly bound excitons, also called 'Free excitons'[41].

Free excitons support a set of energy levels like those in a hydrogen atom that can be adequately explained using the Bohr model. This way, in order to describe the interacting electron and hole, the three-dimensional, time-independent Schrödinger equation takes the form:

$$-\left[\frac{\hbar^2}{2m_e^*}\nabla_e^2\psi + \frac{\hbar^2}{2m_h^*}\nabla_h^2\psi\right] - \frac{e^2}{\varepsilon|\mathbf{r}_e - \mathbf{r}_h|}\psi = E\psi \tag{5.11}$$

where ∇^2 is the Laplacian operator[42], e is the electronic charge and $\mathbf{r}_e$ and $\mathbf{r}_h$ are the position vectors of electron and hole, respectively. While the first two terms correspond to the electron and hole kinetic energies, the third term accounts for their columbic interaction. This equation is the same one used for the Hydrogen atom, except that it is taken into consideration that the electron and hole are moving through a medium with a high dielectric constant ε. In addition, the electron-hole effective masses are used instead of the electron and proton masses. Applying these specifications to the standard Bohr model, it is possible to obtain the energies of the exciton bound states. These are given by

$$E(n) = -\frac{\mu e^4}{2\hbar^2\varepsilon_r^2}\frac{1}{n^2} = -\frac{R_H\mu}{\varepsilon_r^2 n^2} = \frac{R_X}{n^2}, \tag{5.12}$$

where n is the principal quantum number and R_H is the Rydberg energy of the Hydrogen atom ($13.6eV$). R_X is introduced here as the exciton Rydberg energy. The parameter μ is the electron-hole reduced mass defined by

$$\frac{1}{\mu} = \frac{1}{m_e^*} + \frac{1}{m_h^*}. \tag{5.13}$$

The radius of the electron-hole orbit, r_n, also called the Bohr radius of the exciton, which is associated with the energies given in (5.12), can be calculated from:

$$r_n = \frac{\varepsilon_r\hbar^2}{\mu e^2}n^2 = \frac{\varepsilon_r a_H}{\mu}n^2 = n^2 a_X. \tag{5.14}$$

---

[41] Tightly bonded excitons localized on individual atom sites are also possible. They are called Frenkel excitons, and occur more often in insulator crystals.

[42] The Laplacian operator is defined by $\nabla^2 = \partial^2/\partial x^2 + \partial^2/\partial y^2 + \partial^2/\partial z^2$.

Here a_H is the Bohr radius of the hydrogen atom ($5.29 \times 10^{-11} m$). These equations show that the exciton ground state ($n = 1$) has the largest binding energy ($E_1 = R_X$) and the smallest radius ($r_1 = a_X$). The ground state binding energy and the exciton Bohr radius depend upon the effective masses of the electron and hole and vary with semiconductor composition. This is shown in Table 5-2 for several direct gap semiconductors. It can be observed that, as the band gap energy increases, R_X increases and, as a consequence, the exciton Bohr radius is reduced. This is explained by the fact that ε_r tends to decrease and μ to increase as E_g becomes larger.

In order for the electron and hole to move together as a bonded pair their group velocity should be the same. This way, the formation of excitons is most probable near the band edge ($k = 0$) where the bands gradients are the same[43]. The energy of an exciton created during a direct transition is equal to the energy required to create the electron-hole pair, i.e. E_g, less the binding energy due to the Coulomb interaction, given by (5.12). This way, the energy of the exciton levels will be given by

$$E_n = E_g - \frac{R_x}{n^2} + \frac{\hbar^2 k^2}{2\left(m_e^* + m_h^*\right)}. \tag{5.15}$$

The last term on the right represents the kinetic energy of the exciton. This means that an exciton can be formed whenever the photon energy equals E_n. Because this is an energetically favorable situation, compared to free electron-hole formation, the probability of exciton formation is expected to be high. In such case, strong absorption lines with energies just below E_g should be observed. The schematic representation of the energy levels corresponding to E_n can be seen in Figure 5.5.

Crystal	E_g (eV)	R_x (meV)	a_x (nm)
GaN	3.5	23	3.1
ZnSe	2.8	20	4.5
CdS	2.6	28	2.7
CdSe	1.8	15	5.4
CdTe	1.6	12	6.7
GaAs	1.5	4.2	13
InP	1.4	4.8	12
GaSb	0.8	2.0	23

Table 5-2 Calculated Rydberg constant and Bohr radius of free excitons in several direct band gap compound semiconductors. Data obtained from [7].

[43] The group velocity of an electron in a band is given by the gradient of the dispersion diagram: $v_g = \left(1/\hbar\right)\partial E/\partial k$

The manifestation of exciton lines in the absorption spectrum, however, is best observed in very pure intrinsic semiconductor samples and at very low temperatures. This happens because free electrons have a shielding effect over the coulomb interaction of the electron-hole pair, weakening their binding energy. In addition, exciton peaks are hardly observable at room temperature because the binding energy is readily supplied by phonons ($k_B T \gg R_X$); hence, these excitons become very short lived states.

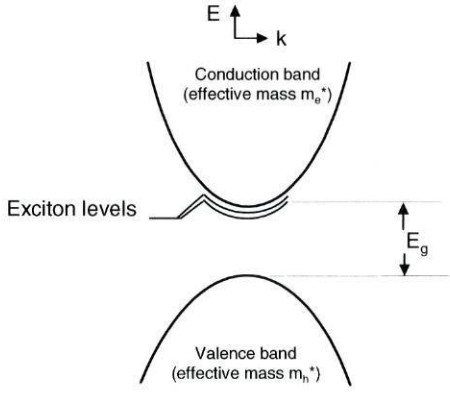


Figure 5.5 Exciton levels relative to the conduction band edge, for a simple parabolic band structure. Adapted from [12].

In many semiconductors, like GaAs, only a single line is observed, nevertheless still making a sizeable contribution, even at room temperature, to the magnitude of the absorption above and below the band edge. Binding of electrons and holes increases both the density of states and the probability of transition. In this context, the magnitude of the absorption coefficient can be greatly enhanced. In Figure 5.6, the calculated optical absorption coefficients for direct transitions in the simple band model, neglecting and including the $n = 1$ exciton peak below the band edge, are shown.

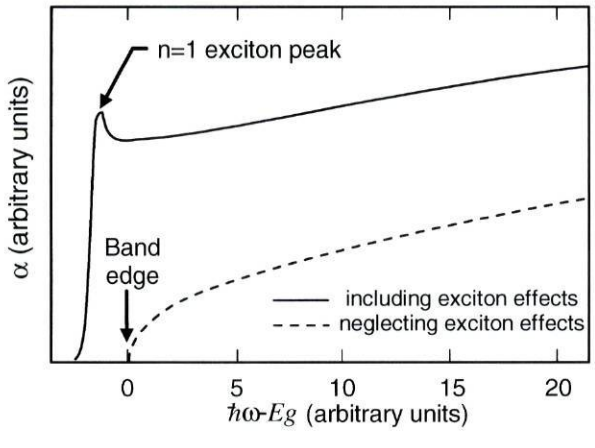


Figure 5.6 Calculated optical absorption coefficient for direct transitions neglecting (dashed line) and including (dark line) the n=1 exciton peak below the band edge. Adapted from [12].

The comparison of the two situations shows that, as a result of the creation of excitons, a strong resonance is observed just below the band edge. In addition, the overall absorption coefficient is enhanced for higher energies. Such strong contributions have been observed experimentally in several semiconductor samples and cannot be neglected in the characterization of these materials [11, 12]. Moreover, excitons play an important role in state of the art semiconductor applications where nanometer size structures, like quantum wells, are used and non-linear effects are explored.

5.2.2 Interband luminescence

Once a given absorption event separates an electron and a hole, they eventually recombine after a finite time interval. This recombination process can happen either by emission of a photon or by non-radiative mechanisms. The former is called luminescence and, like absorption, it will only happen if conservation of energy and momentum are simultaneously observed. In a direct band gap semiconductor an electron recombines with a hole having the same momentum; this is called a vertical transition and is represented in the diagram of Figure 5.7. In such case, the energy of the emitted photon is given by equation (5.8). Indirect transitions, on the other hand, demand the interaction with lattice phonons. This reduces the probability of occurrence, making indirect gap materials poor emitters.

The emission rate depends on the same factors that regulate absorption. The recombination rate, R, of a given semiconductor can be represented by

$$R = n_i n_f P, \tag{5.16}$$

where n_i and n_f are the densities of the initial and final states, respectively, and P is the probability that an electron per given volume of the conduction band will recombine with a hole per given volume of the valence band. This probability is proportional to the absorption coefficient. Although emission is, in many ways, the inverse process of absorption, a fundamental aspect differentiates the two mechanisms. Emission is a non-equilibrium process, and is dependent on the population of the higher energy levels by excited charge carriers. A transition having a high probability is a necessary condition for high emission intensity but, ultimately, the later will be determined by the degree of occupancy of excited states. For excited levels to be populated, energy must be supplied to the charge carriers in the fundamental state. The means by which the excitation of carriers is attained establishes the name of the process of emission that follows. This way, in electroluminescence, excitation is performed by an electrical current, which injects electrons in the conduction band and

holes in the valence band. Conversely, in photoluminescence the energy of the carriers is supplied by high frequency photons, with energy higher than E_g (usually provided by blue or UV radiation).

The mechanisms involved in photoluminescence are represented in Figure 5.7(a). After absorption of high energy photons ($\hbar\omega_L$), electrons that are initially injected into higher levels of the conduction band tend to rapidly relax towards the band edge. This is achieved by emission of phonons on very short timescales ($\sim 100fs$), much faster than radiative lifetimes which are in the nanoseconds range. Similar conditions apply to the relaxation of holes taking place in the valence band. As a result, electrons and holes accumulate in the bottom of their respective bands prior to recombination, which can happen by emission of photons with energies very close to E_g, or by non-radiative pathways. In the meantime, thermal distributions of the levels occupancy at the band edge are formed. These occupancy factors can be determined by applying Statistical Physics to the electrons and holes distributions. For low carrier densities the approximate distribution is given by Boltzmann statistics. This results in temperature dependent linewidths approximately given by k_BT, where k_B is Boltzmann's constant. This particular case is represented by the shading in the diagram of Figure 5.7 (b). For higher densities, Fermi-Dirac statistics must be used. These distributions will determine the shape of the emission spectrum of the semiconductor which, in either case, will be a relatively sharp peak around the band gap energy. No matter how the electrons are excited in the first place, the emission will always happen near the band edge.

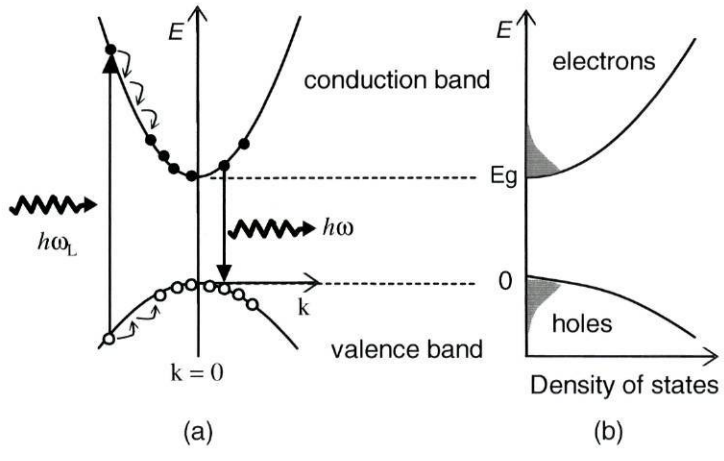


Figure 5.7 (a) Photoluminescence in a direct gap semiconductor: after photo excitation ($\hbar\omega_L$) both electrons and holes rapidly relax to the bottom of the respective bands before recombination and photon emission ($\hbar\omega$). (b) Density of states and level occupancies after optical excitation. Shadings show the distribution function described by Boltzmann statistics. Adapted from [7].

The luminescence and absorption spectra of a thin film of Gallium Nitride (GaN) are shown in Figure 5.8, represented respectively by thick and thin lines. The data was acquired at $4K$. It

shows that the emission spectrum is a relatively narrow emission line close to the band gap energy, which at this temperature is $3.5eV$, while absorption shows the typical threshold behavior with onset at E_g and continuous absorption for higher energies.

The results shown here were obtained from a very high quality sample, at very low temperature[7]. Commonly, more complex spectra can be obtained. In alternative to interband transitions, radiative emission may occur through intermediate states. For instance, an electron may drop from the conduction band to donor states by a non-radiative process and perform a radiative transition to a valence or acceptor level. This would result in an emission peak with energies below E_g. Surface states may also play an important role in luminescence. They have well defined defect states that can trap carriers and can be a source of strong luminescence. Materials with high surface areas usually show enhanced luminescence.

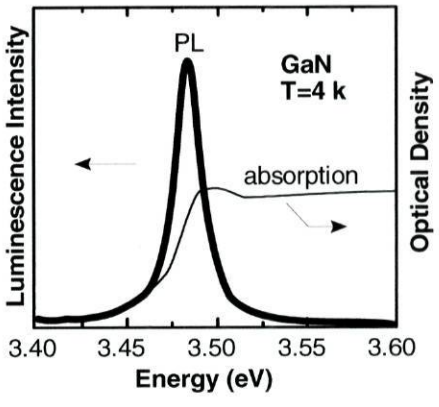


Figure 5.8 Luminescence (thick line) and absorption (thin line) spectra of a GaN layer of thickness $0.5\,mm$, at $4\,K$. Obtained from [7].

On the other and, all radiative processes compete with similar non-radiative recombination pathways. These can arise from multiphonon emission, Auger processes and non-radiative surface states or defect states. If these non-radiative relaxation processes occur in a faster time scale than the radiative transitions, the emission efficiency will be very low, i.e., for efficient luminescence the radiative lifetime must be much shorter than the non-radiative lifetime. This is why direct band gap semiconductors are much better emitters than the long-lived indirect gap materials. Finally, the annihilation of a coupled electron-hole pair, i.e. an exciton, may originate the presence of very sharp peaks at energies below the band edge.

A given combination of any of these mechanisms may result in a complex emission spectrum, very rich in information about the sample band structure. For this reason photoluminescence is a powerful tool for characterization of materials in general and semiconductors in particular.

Knowledge of the properties of absorption and emission of radiation by semiconductors is of fundamental importance to the design of many optoelectronic devices like diode lasers and photodetectors. By controlling the semiconductor composition it is possible to engineer a diversity of materials with different optical and electrical properties. However, present technologies are already a step forward, and a higher degree of control in semiconductor properties can be achieved by implementation of nanometer sized structures with different semiconductor materials, taking advantage of quantum confinement effects.

5.3 Quantum confined semiconductor structures

The optical properties of solids are not usually size dependent. A piece of Ruby crystal, for instance, will have its characteristic red color, independent of its size. However, this is true only if the sample is large. If the size of the crystal is made sufficiently small, its optical properties will depend on its dimensions. This size dependence is a consequence of the quantum confinement effect. According to Heisenberg, if a particle is confined to a region Δx, along the x direction, then an uncertainty given by

$$\Delta p_x \sim \frac{\hbar}{\Delta x} \tag{5.17}$$

will be introduced in its momentum. If this particle, of mass m, is otherwise free, confinement along x will increase its kinetic energy by

$$\Delta E = \frac{(\Delta p_x)^2}{2m} \sim \frac{\hbar^2}{2m(\Delta x)^2}. \tag{5.18}$$

This contribution will only be significant if it is of the same magnitude or greater than the particles' kinetic energy due to thermal motion along the x direction[44], i.e., if

$$\frac{\hbar^2}{2m(\Delta x)^2} > \frac{1}{2}k_B T. \tag{5.19}$$

Such condition determines that the quantum size effects will be important when

$$\Delta x \sim \sqrt{\frac{\hbar^2}{mk_B T}}. \tag{5.20}$$

This will happen whenever Δx is of the same order of magnitude as the de Broglie wavelength for thermal motion[45], typically tenths of nanometers. The lattice spacing in semiconductors is still

[44] Each degree of freedom of the motion has a thermal energy of $k_B T/2$.

considerably smaller than the de Broglie wavelengths associated with electrons and holes, $\lambda_{e,h}$, or than the Bohr radius associated with excitons (see Table 5-3).

	Range (nm)
a_L	0.1–0.6
$\lambda_{e,h}$	1-100
a_X	1 – 30

Table 5-3 Typical values of lattice spacing, a_L, electron/hole de Broglie wavelength, $\lambda_{e,h}$, and fundamental exciton Bohr radius, a_X, for common semiconductor materials. Data collected from [7, 9].

In this context, it is possible to implement artificial semiconductor structures which in one, two or three dimensions are smaller than $\lambda_{e/h}$ or a_X, but still larger than a_L. In such arrangements, elementary excitations will experience quantum confinement, or finite motion, along the confinement axis, and infinite motion in the remaining directions. In addition, because the structure includes several lattice spacings, many of the approximations used to study bulk semiconductors (like the constant effective mass approximation and the bulk dielectric constant) can still be used for quantum structures.

Depending on the electrons being confined in one, two or three dimensions, the resulting structures can be classified respectively as quantum wells (1D confinement), quantum wires(2D confinement) and quantum dots (3D confinement).

A direct consequence of the physical confinement is that the energy levels of the excited carriers will become quantized. This way, along the confinement direction, electron and hole states will be discrete rather than continuous. The wave functions and energies of the quantized states in the conduction and valence band can be calculated by using the Schrödinger equation and the effective mass approximation.

5.3.1 Infinite square potential well

The easiest case to consider is the one dimensional quantum well, which in the simplest approximation can be treated as an infinitely deep square well. In this particular case the Schrödinger equation does not have to be solved in three dimensions. Instead, the free motion in the x, y plane

[45] The de Broglie wavelength is defined by $\lambda_B = h/p$. Considering that the electron kinetic energy associated with thermal motion is given by $3kT/2$, the resulting associated wavelength would be $\lambda_e = h/\sqrt{3kTm_e^*}$. If only one dimension is considered the resulting wavelength would be instead $\lambda_e = h/\sqrt{kTm_e^*}$.

can be separated from the quantized motion in the z direction. This can be done by separation of variables, writing the wave equation in the form:

$$\psi(x,y,z) = \psi(x,y)\varphi(z), \tag{5.21}$$

and then solving separately for $\psi(x,y)$ and $\varphi(z)$.

In the xy plane, the motion is free and the electron/hole wave functions are described by plane waves[46]. Considering the effective mass approximation, the energy corresponding to this motion is just kinetic and is determined by

$$E(\mathbf{k}) = \frac{\hbar^2\mathbf{k}^2}{2m^*_{e,h}}, \tag{5.22}$$

where $\mathbf{k}$ is the wavevector in the xy plane. Along the z direction, however, the charge carriers are confined, being subjected to a potential described by

$$U(z) = \begin{cases} 0 & for \quad 0 \le z \le d \\ \infty & otherwise \end{cases}, \tag{5.23}$$

where d is the width of the well. Inside the well the potential is zero and the solutions of the Schrödinger equation are similar to those given for a free particle. However, outside the well the potential goes to infinity, forcing the wave-functions to become zero at the boundaries. The boundary conditions are, therefore, $\varphi(0) = 0$ and $\varphi(d) = 0$. By application of these settings to the general solutions it turns out that k can only take the values

$$k = \frac{n\pi}{d}, \text{ with} \quad n = 1,2,3,... \tag{5.24}$$

This establishes a discrete set of states defined by the quantum number n, corresponding to wave functions of the form

$$\varphi(z) = A_n \sin\left(\frac{n\pi z}{d}\right), \tag{5.25}$$

where A_n are normalization constants, and with definite energy values given by

$$E_n = \frac{\hbar^2 k_n^2}{2m^*_{e,h}} = \frac{\hbar^2 n^2\pi^2}{2m^*_{e,h}d^2}. \tag{5.26}$$

---

[46] For 2-dimensional free motion, the Schrödinger equation takes as solutions plane waves of the form: $\psi(x,y) = 1/\sqrt{A}e^{i\mathbf{k}\cdot\mathbf{r}}$, where A is the normalization area, and $\mathbf{k}$ and $\mathbf{r}$ are limited to the xy plane.

This kind of wave-functions corresponds to standing waves inside the well with nodes at the boundaries. The first three energy levels, and the corresponding wave functions, $\varphi(z)$, calculated for an infinitely deep GaAs square well of width $d = 10\,nm$, can be seen in Figure 5.9.

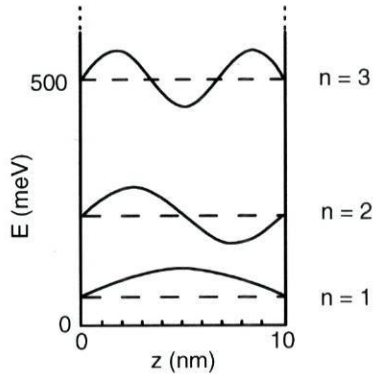


Figure 5.9 First three energy levels, and respective wave functions, for an infinitely deep square well in GaAs of width $d = 10\,nm$. Adapted from [9].

In contrast with Classical Mechanics, where the minimum energy can be zero, the lowest level has energy $E_1 > 0$. This is called the zero point energy, which is a direct consequence of the particle confinement, and can be derived from the Heisenberg uncertainty principle. Equation (5.26) shows that the confinement energy is higher for strongly confined particles (smaller d). In addition, it can be seen that the energy difference between neighboring levels grows monotonically with increasing n. In this particular case, considering an electron with $m_e^* = 0.1 m_0$, the energies of the two first levels are respectively $38\,meV$ and $150\,meV$. Taking into consideration that at $300\,K$ the thermal energy is $k_B T \sim 25\,meV$, quantum size effects in quantum wells are expected to be observed even at room temperature.

In practice, a quantum well can be produced by sandwiching a thin layer of semiconductor material, like GaAs, between two thick layers of an insulator or a semiconductor material with higher band gap energy, for example AlGaAs (aluminum gallium arsenide). The potential barrier is provided by the difference in their respective band edge energies. This way, in real quantum wells the potential barriers are of finite height. This allows the particles to tunnel into the barriers, resulting in spreading of the wave functions and lowering the effective confinement energies. In addition, while infinite wells support an infinite number of energy states, in real wells the total number of confined states is determined by the well width and height. Nevertheless, the infinite square well model gives a good insight of real quantum well properties and is used in practice due to its extreme simplicity.

Therefore, the total energy of an electron or hole in the n^{th} level of a quantum well will be given approximately by the sum of the free motion energy in the xy plane (equation (5.22)) with the confinement energy along z (equation (5.26)), i.e.:

$$E^{total}(\mathbf{k},n) = E(\mathbf{k}) + E_n^{e,h}. \tag{5.27}$$

This equation shows that the total energy of charge carriers, in a semiconductor quantum well, is dependent on the dimensions of the physical structure, and can thus be easily controlled. The smaller the width of the well, d, the higher the total energy. This has direct consequences in the absorption and emission properties of quantum well based devices and is used in practice to control the characteristics of many commercial products.

5.3.2 Infinite potential well with spherical symmetry

A very simple model can also be used to assess the consequences of charge carrier confinement in all three dimensions. A $3D$ confined structure is called a quantum dot. In the simplest approach, an electron in an ideal quantum dot can be seen as a particle in a spherically-symmetric infinite potential well defined by:

$$U(r) = \begin{cases} 0 & for \quad a \le r \\ \infty & for \quad a > r \end{cases} \tag{5.28}$$

Since the potential is dependent only on the radial distance, the problem is best solved in spherical coordinates. In this case the wave function should be separable into functions of r, θ and ϕ [13]:

$$\psi = R(r)Y(\theta,\phi), \tag{5.29}$$

and can be written in the form

$$\psi_{n,l,m}(r,\theta,\varphi) = \frac{u_{n,l}(r)}{r} Y_{lm}(\theta,\varphi), \tag{5.30}$$

where n is the principal quantum number, l is the orbital quantum number and m is the magnetic quantum number. The functions $Y_{lm}(\theta,\varphi)$ are called the spherical harmonics and are the same for any spherical symmetric potential. The actual shape of the potential affects only the radial part of the wave function, $u_{n,l}(r)$, which is determined by the equation:

$$-\frac{\hbar^2}{2m}\frac{d^2u}{dr^2} + \left[U(r) + \frac{\hbar^2}{2mr^2}l(l+1)\right]u = Eu. \tag{5.31}$$

To obtain the allowed energy values in a quantum dot, this equation must be solved considering the boundary conditions imposed by the potential in equation (5.28). In such case, the allowed energy values are expressed as follows [13]:

$$E_{nl} = \frac{\hbar^2 \chi_{nl}^2}{2ma^2}, \tag{5.32}$$

where χ_{nl} is the n^{th} root of the l^{th} order spherical Bessel function. Bessel roots must be determined numerically. For $l = 0$, however, their values are given by $n\pi$ and the corresponding energy values coincide with those obtained for a particle in a rectangular well (equation (5.26)).

5.3.3 Confinement in real quantum dots

Although a three dimensional quantum box, with spherical or cubic shape, corresponds to an idealization that cannot be found in nature, these simplified quantum dot models can be used to understand the basic properties that arise from three dimensional spatial confinement. In real quantum dots, however, electron and hole are forced to be closer together and their interaction plays a major role that cannot be neglected. More realistic models can be used that take into consideration the properties of excitons when confined in three dimensions. Different approaches are used, according to the degree of confinement [14]. Two limiting cases, which provide clear physical results described by analytical expressions, are usually studied: the weak confinement regime where the dot radius is larger than the exciton Bohr radius; and the strong confinement limit in which the dot is smaller than the Bohr radius.

Weak confinement

The weak confinement model describes the situation where the dot radius, a, is small but still a few times larger than the exciton Bohr radius, a_X. Under these circumstances, the interacting electron and hole can still be described by the Hydrogen-like Schrödinger equation (equation (5.11)), which is written in terms of spatial coordinates for the electron and hole, separately.

This equation can be solved by separating variables into center of mass coordinates and relative coordinates. The resulting equations are still subjected to the condition that $\psi(a) = 0$, imposed by the boundaries of the dot. However, under the assumption that $a \gg a_X$, an approximate solution can be obtained supposing that the electron and hole remain correlated and that the confinement imposed by the dot boundaries acts only on the center of mass translational motion of the exciton. This way, the dispersion relation of the confined exciton can be obtained by substituting the kinetic energy term in the dispersion relation of the free exciton (equation (5.15)) by

a spherical confinement energy term (equation (5.32)). The energy of a weakly confined exciton can then be expressed by

$$E_{nml} = E_g - \frac{R_X}{n^2} + \frac{\hbar^2 \chi_{ml}^2}{2Ma^2}, \tag{5.33}$$

where M stands for the exciton effective mass, which is given by

$$M = m_e^* + m_h^*. \tag{5.34}$$

The energy states of an exciton in a quantum dot can thus be characterized by three quantum numbers. The quantum number n describes the exciton internal states that arise from the electron-hole Coulomb interaction. Increasing n corresponds to states labeled $1S;2S,2P;3S,3P,3D;...$ The two additional quantum numbers, l and m, describe the center of mass motion confined by an external potential. Increasing m and l correspond to states labeled $1s,1p,1d...,2s,2p,2d...$, etc..

In comparison with the free exciton, the confined exciton has its energy shifted to higher energies by the spherical confinement term. For the lowest state, with quantum numbers $n = 1$, $m = 1$ and $l = 0$, the resulting energy is

$$E_{1S1s} = E_g - R_X + \frac{\pi^2 \hbar^2}{2Ma^2} \tag{5.35}$$

In this particular case, for evaluation purposes, the energy shift imposed to the exciton by the confinement term can be written as

$$\Delta E_{1S1s} = \frac{\mu}{M}\left(\frac{\pi a_X}{a}\right)^2 R_X. \tag{5.36}$$

In this form it is easily confirmed that, as long as $a \gg a_X$, ΔE_{1S1s} is smaller than R_X. This result shows that the confinement energy is small compared with the exciton binding energy and justifies the terminology 'weak confinement'.

The blue shift of the band gap, which results from confinement, was observed experimentally in many confined semiconductor structures [8, 14]. For the range $10a_X \geq a \geq 3a_X$, this shift was accurately described by equation (5.35).

Strong confinement

In the strong confinement limit, the quantum dot radius is much smaller than the exciton Bohr radius. In this situation, the individual kinetic energies of the electron and hole due to the spherical spatial confinement grow very fast as size decreases and the exciton binding energy becomes negligible in comparison. These confinement energies are given, respectively, by

$$E_{ml}^{e} = E_g + \frac{\hbar^2 \chi_{ml}}{2m_e a^2}$$
$$E_{ml}^{h} = \frac{\hbar^2 \chi_{ml}}{2m_h a^2} \qquad (5.37)$$

The total excess energy, due to confinement, for the lowest electron and hole $1S1s$ states is thus

$$\Delta E_{1S1s} = E_{1s}^{e} + E_{1s}^{h} - E_g = \frac{\hbar^2 \pi^2}{2\mu a^2}, \qquad (5.38)$$

and can be written in the form

$$\Delta E_{1S1s} = \left(\frac{\pi a_X}{a}\right)^2 R_X . \qquad (5.39)$$

It is easily seen that, while this term is small in the weak confinement regime, it becomes much larger than R_X in the limit where $a \ll a_X$. This way, in first approximation, the electron and hole movements within the dot can be considered totally uncorrelated, i.e., the Coulomb interaction can be ignored. Therefore, the individual charge carriers have the discrete energy spectra given by equations (5.37). In these circumstances, it can be shown, by considerations of energy and momentum conservation, that optical transitions between electron and hole states with the same principal and orbital quantum numbers are allowed. These transitions correspond to absorption lines at energies:

$$E_{nl} = E_g + \frac{\hbar^2}{2\mu a^2} \chi_{nl}^2, \qquad (5.40)$$

and give quantum dots in the strong confinement regime an atomic like spectrum. For this reason, quantum dots are often referred to as "artificial" atoms, having a discrete spectrum that is controlled according to their size.

However, taking into consideration that both electron and hole are confined into a space smaller than the Bohr radius of the exciton, they should not be considered as mutually independent. Therefore, in a more realistic approach, the Schrödinger equation should include the individual kinetic energy terms, the Coulomb potential and the confinement potential as well. Such equation would read:

$$\left[-\frac{\hbar^2}{2m_e}\nabla_e^2 - \frac{\hbar^2}{2m_h}\nabla_h^2 - \frac{e^2}{|\mathbf{r}_e - \mathbf{r}_h|} + U(r)\right]\psi = \psi E . \qquad (5.41)$$

In this case, since the confinement potential $U(r)$ affects both the individual particles and their bound state, it is not possible to separate center of mass motion from relative particle movement and the equation is not easily solved. Many authors suggested different approaches to this problem

from which resulted some approximate analytical expressions or even numerical solutions that are in good agreement with experimental data. Brus et. al [15] showed that, for cadmium sulfide (CdS) and CdSe nanocrystals, the size dependence of the fundamental electron-hole state can be accurately described by

$$E_{1S1s} = E_g + \frac{\pi^2\hbar^2}{2a^2\mu} - 1.786\frac{e^2}{\varepsilon a}. \tag{5.42}$$

The last term to the right expresses the electron-hole Coulomb interaction and it should be compared with the exciton Rydberg energy ($R_X = e^2/2\varepsilon a$). The comparison shows that, considering the strong confinement limit in small quantum dots, the Coulomb term is in fact stronger than the corresponding exciton energy in the bulk semiconductor. This is a feature unique to quantum dots and establishes the strongly confined exciton, which is no longer the Hydrogen like exciton, as their elementary excitation. Equation (5.42) also shows that, as the dot size decreases, the Coulomb term shifts the total energy to lower energies with a a^{-1} dependence. Conversely, the confinement term adds to the total energy with a a^{-2} dependence. This way, for smaller dot sizes the confinement term becomes dominant and the global effect of decreasing the nanocrystal size is a blue shift in the band edge energy.

In spite of considering only the limiting cases of either weak or strong confinement, no fundamental discontinuity arises when $a \approx a_X$. Numerical calculations have provided evidence that there is a smooth transition between the two regimes. Moreover, the models developed allowed analysis of the problem using elementary quantum mechanics and bulk semiconductor concepts and still extract intuitive conclusions and identify trends. Validation of such models has been obtained by several authors, either by experimental data or by numerical solution of equation (5.41).

5.3.4 Interband transitions in quantum structures

Like bulk semiconductors, semiconductor quantum structures interact with optical photons by way of interband transitions. Since confinement modifies the energy states distribution and the total energy of the charge carriers, it is expected that these changes will reflect upon the emission and absorption properties of these devices. Indeed, taking as example a one dimensional quantum well, the electron and hole energies in their respective bands are given by:

$$\begin{aligned} E_c(k) &= E_g + \frac{\hbar^2 k_{xy}^2}{2m_e^*} + E_n^e \\ E_v(k) &= -\frac{\hbar^2 k_{xy}^2}{2m_h^*} - E_n^h \end{aligned} \tag{5.43}$$

where E_n^e and E_n^h are, respectively, the electron and hole confinement energies defined in equation (5.26). Comparing these expressions with those obtained for a bulk sample (see equations (5.7)), it is found that, in quantum structures, the confinement energy adds to the band gap energy, shifting E_g to higher energies. In addition, energy levels become quantized. Therefore, instead of the single parabolic band found in bulk materials, a set of sub-bands corresponding to $n = 1,2,3...$ appears in quantum well structures. These energy sub-bands correspond to parabolas, $\hbar^2 k_{xy}^2 / 2m_{e,h}^*$, separated by energies $\hbar^2 \pi^2 / 2m_{e,h}^* d^2$, and are represented in the diagram of Figure 5.10.

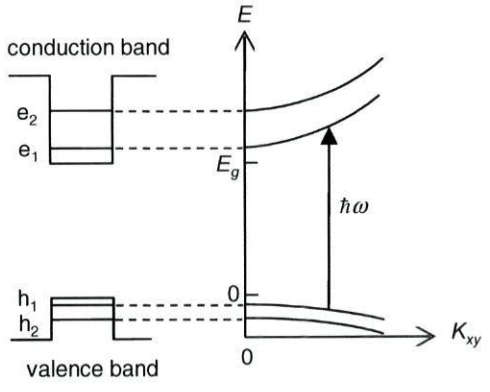


Figure 5.10 The $n = 1$ interband optical transition in a quantum well at finite k_{xy}. Adapted from [7].

Optical transitions can only take place between these sub-bands. Moreover, in the particular case of quantum wells, it can be shown that only transitions between hole and electron states with $\Delta n = 0$ are allowed[47]. This means that the electron and hole states should have the same quantum number n. Transitions between states with different quantum number, $\Delta n \neq 0$, are forbidden. The diagram in Figure 5.10 shows a transition between the $n = 1$ levels (from $n_h = 1$ hole level to $n_e = 1$ electron level), at some finite k_{xy} value. This could happen by absorption of a photon with energy

$$\hbar\omega = E_g + E_1^h + E_1^e + \frac{\hbar^2 k_{xy}^2}{2\mu}. \tag{5.44}$$

This way, the threshold of absorption for $n = 1$ transitions arises at photon energies $\hbar\omega = E_g + E_1^h + E_1^e$, which take place at $k_{xy} = 0$. Transitions occurring between excited states ($n > 1$) establish further absorption thresholds, coinciding with the edge of each sub-band. This should be compared with equation (5.8) for bulk semiconductors.

[47] In infinite quantum wells, wave-functions with different quantum number are mutually orthogonal. This is not necessarily true for finite wells. Nevertheless, $\Delta n \neq 0$ transitions are usually very weak in these cases.

In the higher energy limit, when photon energies are higher than the gap energy of the well walls, absorption will have the typical behavior observed in bulk samples.

Generally, besides shifting the onset of absorption to higher energies, confinement limits the wave-vector dimensional span. This has strong effects in the resulting density of energy states, and consequently in the absorption and emission properties of quantum semiconductor devices. The density of electron and hole states can be generically expressed by

$$\rho(E) \propto E^{D/2-1} \qquad D = 1,2,3 \tag{5.45}$$

where D is the number of degrees of freedom for the charge carriers and the energy is measured relative to the edge of the respective band. The resulting distributions can be seen in the schematics of Figure 5.11.

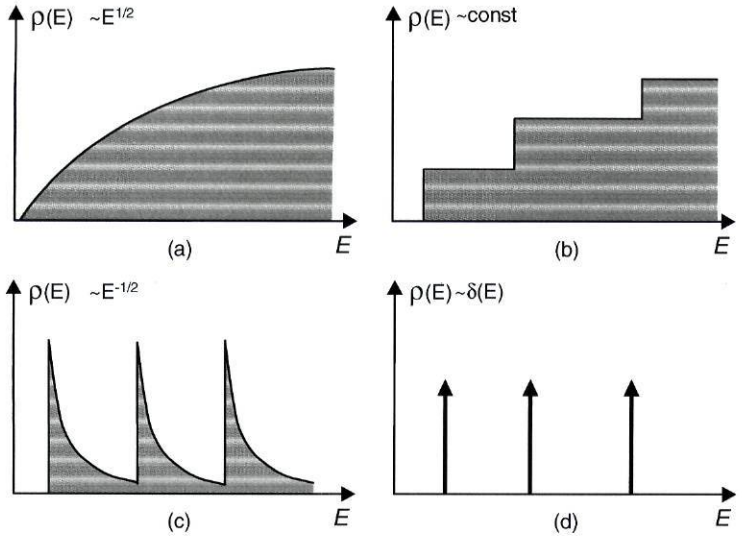


Figure 5.11 Distribution of the density of electron/hole states for (a) bulk semiconductor – no confinement; (b) quantum well – 1D confinement; (c) quantum wire – 2D confinement; (d) quantum dot – 3D confinement. Adapted from [14].

For $D = 3$ there is no charge confinement and $\rho(E)$ has the typical square root dependence observed in bulk semiconductors, which results in the absorption coefficient described by equation (5.10). For $D = 2$ and $D = 1$, a number of discrete sub-bands appear as a result of spatial confinement. Within each sub-band $\rho(E)$ obeys equation (5.45), the density of states is thus constant within each quantum well sub-band,($\rho(E) = \mu / \pi\hbar^2$), and has a $1/\sqrt{E}$ behavior in quantum wire sub-bands. The steps seen in quantum well absorption coincide with the threshold established by the transitions between excited states (from $n_h = 2$ to $n_e = 2$, from $n_h = 3$ to $n_e = 3$, and so on). Finally, for $D = 0$, a zero-dimensional structure is obtained, the charge carriers are confined in all three dimensions, and therefore have total quantization of their energy states. These structures

correspond to quantum dots and have a δ-function-like density of states, which results in an atomic- like discrete absorption spectrum.

Excitons and absorption in quantum structures

It was already discussed how the Coulomb attraction between the electron-hole pair formed upon absorption can enhance both emission and absorption spectra of bulk semiconductors by formation of excitons. The attraction between electron and hole increases the probability of transitions that occur at energies given by the free particles energy less the binding energy of the exciton (equation (5.15)). Experimental observations in quantum well structures have shown an enhancement in exciton binding energies by a factor of ~ 2.5. This is a direct consequence of the confinement imposed to the charge carriers [7]. Electrons and holes are forced to be closer together than they would be in a bulk semiconductor, increasing their attractive potential. This way, with quantum confinement, stable excitons can be formed even at ambient temperatures.

This can be observed in Figure 5.12, where the room temperature absorption spectrum of a multiple quantum well structure (MQW) of GaAs/AlGaAs can be compared with the bulk absorption spectrum of GaAs at the same temperature. The structure consisted of 70 wells of width $10\,nm$.

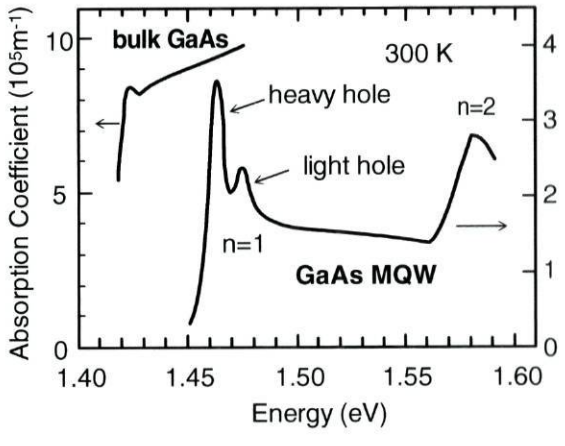


Figure 5.12 Room temperature absorption of GaAs/$AlGa_{0.28}As_{0.72}$ multiple quantum well structure (MQW) containing 77 GaAs wells of width 10 nm. The bulk GaAs absorption spectrum at room temperature is shown for comparison. Obtained from [7].

Although exciton effects have a non-negligible contribution in the bulk sample, exciton peaks are hardly noticed. Conversely, in the MQW structure, both the heavy hole and light hole exciton peaks are clearly distinguished and appear superimposed on the ladder-shaped absorption coefficient

characteristic of these structures. Exciton enhancement is expected to increase for lower dimensional structures like quantum dots.

Luminescence in quantum structures

Luminescence processes in quantum structures obey the same general principles observed in bulk semiconductors. Excited levels must first be populated by electrical or optical processes. Light generation by electron-hole recombination usually follows. Emission results from band edges transitions, after some non-radiative relaxation processes depopulate the higher energy levels, thus resulting in relatively narrow[48] emission peaks.

In the particular case of quantum wells, however, the lowest available electron/hole levels correspond to $n = 1$ confined states. Therefore, at low intensities[49], the luminescence spectrum of such structure would be a narrow peak, of width $\sim k_B T$, at energies given by equation (5.44) with $k_{xy} \approx 0$. Due to thermal broadening, usually light-hole and heavy-hole exciton peaks are not resolved and a single emission peak is observed.

In summary, it is observed that, in general, the most direct consequence of confinement is the quantization of energy levels. In addition, the band gap energy of semiconductor quantum structures is shifted to higher energies, in relation to E_g, by the confinement energy. Since the latter is size dependent, this means that it becomes possible to control the position of the band edge by simple structural manipulation. Ultimately this results in the possibility of tuning the emission wavelength of the luminescent devices. Furthermore, the stronger overlap of the confined carriers' wave functions increases the density of states and the probability of exciton formation (which become visible even at ambient temperatures). This greatly improves the radiative transition probability which results in shorter lifetimes. As a consequence, radiative transitions prevail over competing non-radiative processes increasing the overall luminescence output.

In practice, quantum confinement results in devices with greatly enhanced luminescence properties readily controlled by their physical structure layout. In the particular case of laser devices, for instance, this translates into lower lasing thresholds and enhanced thermal stability. A higher degree of confinement is expected to improve even further these properties. Indeed, QD lasers have been demonstrated showing enhanced features relative to their quantum well counterparts[16-18].

---

[48] The width of the emission peak is determined by temperature and carrier density.

[49] At high enough intensities, higher levels can be excited and secondary peaks can be observed.

5.3.5 Technology

Nanometer sized quantum well structures can be made using techniques of advanced epitaxial[50] crystal growth, like molecular beam epitaxy (MBE) and metal-organic chemical vapor phase deposition (MOCVD)[19]. The layers thicknesses can be controlled with atomic precision using these techniques. Presently, this is a mature technology used to fabricate high performance quantum well based devices, like laser diodes and photo detectors, which are commercially available. For example, GaAs quantum well devices emitting around $800\,nm$ are widely used in compact disc players and printers. Using GaAs or InP (indium phosphide) based alloys, on the other hand, the emission can be shifted either towards the red or towards the infrared, to be used in optical telecommunication systems (from $1.3\,\mu m$ to $1.55\,\mu m$).

Quantum wires can be made by lithographic patterning of quantum well structures or by epitaxial growth over patterned substrates. Their properties are being widely explored in research laboratories all over the world [20].

The main procedures by which quantum dots can be fabricated include diffusion controlled growth, lithography, epitaxy and colloidal chemistry [21-24]. Empirical methods of diffusion controlled growth of nanocrystals in a glass matrix have been known for decades, and even for centuries (stained glass windows). Color glass filters, made by Schott and Corning, are made from semiconductor nanocrystals embedded in a glass matrix; their cut-off wavelength depends on the size of the nanoparticles. They are made using commercial techniques of diffusion controlled growth from a supersaturated solution. Nanocrystal formation results from a phase transition in the viscous solution. The process is controlled by diffusion of ions dissolved in the glass matrix, at temperatures between that of the glass transition and that of melting. The high temperatures involved, however, typically in the range between $550\,^{\circ}C$ and $700\,^{\circ}C$, are responsible for increasing defects concentration [23].

In the mid eighties, many attempts were made to use e-beam and ion-beam techniques to fabricate QDs for optoelectronic applications. Lithographic patterning was used for obtaining 1-D confined quantum wells; confinement in the two remaining dimensions could be achieved by subsequent etching of pillars over the resulting quantum well structures [25]. This process scheme, however, introduced defects into the structure; it was slow and produced only low densities of QD. Epitaxial growth over pre-patterned substrates can also be used [26]. Patterning of pyramidal shaped

---

[50] Epitaxy is the name given to any technique of crystal growth aiming at he formation of a very high quality crystalline thin layer on top of a thicker, lower quality, substrate crystal.

recesses on a substrate can be obtained by selective ion-etching. QDs can then be grown into these recesses by epitaxial growth techniques. In this case the density of the QDs is limited by the mask pattern. More recently, techniques exploring self-assembly mechanisms are being successfully explored. Quantum Dots are grown, by MBE or MOCVD, over a substrate with a different lattice constant. In strongly lattice mismatched systems three-dimensional islands form spontaneously, above a certain critical thickness, to reduce strain. This is also called the Stranski-Krastanov growth mode [24, 27]. Although some problems persist concerning dot size dispersion, random island distribution and high sensitivity to growth parameters, this technique is better developed and controlled than the previous ones, and important advances have been made. Moreover, in all the previous techniques, the resulting quantum dots are obtained in a solid matrix, and further processing of their properties is therefore hindered.

In an alternative approach, quantum dots can be obtained in a solution using chemical processes [22]. Methods of colloidal chemistry where semiconductor nanoparticles are formed in a liquid suspension have been particularly successful [17]. Quantum dots produced in this way are also known as semiconductor nanocrystals. These types of QDs are suitable for further chemical processing (for instance, they can be made water soluble) and, therefore, specially suited for biochemical and sensing applications involving luminescence. For this reason, further details about these techniques will be discussed in the next section.

The existence of a wide variety of fabrication techniques, some being relatively simple, along with the advantages expected from a higher degree of confinement, have made quantum dots extremely attractive and turned them into one of the main topics of present day research in nanotechnology. Their amazing optical, electrical and chemical properties have long exceeded their initial range of applications in optoelectronic devices. New interesting applications are being explored every day. The remaining of this chapter is dedicated to luminescent semiconductor nanocrystals and their applications in the field of optical sensing.

5.4 Semiconductor nanocrystals

Quantum Dots are extremely small particles of semiconductor material, consisting of a few hundreds to a few thousands of atoms. Their small size, ranging from $1\,nm$ to $20\,nm$, is mostly responsible for their unique optical, electrical and chemical properties. The main differences between the macrocrystalline material and the corresponding nanocrystal arise from two fundamental factors that are size related. The first one is associated with the large surface to volume

ratio of nanoparticles and the second one is related to the three-dimensional quantum confinement of their charge carriers.

The mechanism by which quantum confinement provides quantum dots with greatly enhanced luminescence properties has already been discussed. Bright and relatively narrow luminescence spectrum, wide range absorption and tunability of the emission peak are some of the features that can be readily controlled by just changing the size of the nanoparticles.

On the other hand, both the physical and chemical properties of the semiconductor are particularly sensitive to the surface structure. The large relative surface areas of quantum dots (up to 95% of its atoms can be in the surface) are well-suited to be functionalized with organic or inorganic molecules. The resulting molecular coating will define the way QDs interact with the external medium and how sensitive/insensitive their luminescence will be to a particular environmental factor.

5.4.1 Colloidal chemistry

The growth of semiconductor nanoparticles can be initiated in a solution by chemical methods. The use of colloidally dispersed pigments is so old that its use can be traced back to pre-historic paintings. Ancient Egyptians prepared colloidal[51] dispersions as inks. Throughout history these technologies have been widely used but not fully understood. Only in the XIXth century visionaries like Michael Faraday started to unveil the mysteries behind the extraordinary properties of nanocrystalline systems. In the modern age, first experiments with semiconductor nanocrystals were made in the early eighties at the Bell Labs, by Louis Brus[21], and in the Yoffe Institute in S. Petersburg by Alexander Efros and A.I. Ekimov[28].

The nanocrystals made by colloidal chemistry methods are usually obtained in a liquid suspension, at moderate temperatures. Lower temperatures (typically below $300\ ^{\circ}C$) are favorable to minimize the number of lattice defects. These methods are amenable to further chemical processing by which the dot surface can be coated with organic or inorganic layers that, besides providing a way to control surface states, will define their affinities. After the chemical processing is complete immobilization in sol-gel or polymer matrices is also possible. For these reasons this is the preferred method to produce QDs for chemical sensing and biochemical applications.

---

[51] When two or more states of matter coexist in a uniform way a colloidal combination is obtained. For example: a solid suspended in a liquid (fat in milk) , a liquid suspended in a gas (fog), etc.. A colloid is distinguished from a regular suspension by the fact that the suspended particles do not aggregate when the suspension is left still.

Through a series of engineered reactions, using adequate precursors, the semiconductor material is made to precipitate from a solution. The process is controlled, with the presence of stabilizing agents, in such a way that the aggregation of particles is arrested before they reach a certain critical size, while still within the quantum confinement regime. The size of the crystallites obtained is controlled by temperature, mixing rate of reagents, and by the concentration of the stabilizer. The final result is a colloidal dispersion, in which very small fluorescent semiconductor solid particles are suspended in the liquid solvent.

However, these nanocrystalline QDs are very reactive and become easily polluted by solvent molecules or impurities. Oxidation, impurities and surface defects provide quenching mechanisms that compromise the photoluminescence efficiency of the nanocrystals. In order to obtain chemical stability and high quantum yields, some stabilization strategies have to be followed. The most successful one consists of coating the surface of the semiconductor core with a protective shell of non-reactive, transparent and structurally related material. Cadmium-Selenide QDs are usually coated with some layers of zinc sulfide (ZnS) [29, 30], a semiconductor material with a higher band gap energy. This prevents oxidation and provides passivation of trap states and surface defects resulting in photoluminescence that is essentially due to band edge recombination. The quantum yields of bare CdSe quantum dots, originally $5\% - 15\%$, were reported to increase to $30\% - 50\%$ when coated with 1.3 monolayers of ZnS. Increasing the thickness of the outer shell further than this optimal value resulted in decreased yields, probably due to the creation of defects in the ZnS surface as surface tension rises. The temperature of the coating process is critical and can greatly influence the size dispersion of the resulting nanoparticles. Presently, core-shell quantum dots with narrow size distributions, with a dispersion as low as 5%, can be obtained by size selective precipitation methods. When provided with the passivating shell, semiconductor nanocrystals have very bright and stable emission. Depending on the excitation optical power, photobleaching, a major problem with traditional dyes, is extremely small or non-existing.

Further capping layers are usually added on top of this inorganic shell that provide increased stability and can define the nanoparticle functionality. Biocompatible organic interfaces can help to make QDs water soluble and stabilized in biological buffers [31, 32]. Reactive groups can be added to their surface for subsequent conjugation with biomolecules. All this can be achieved while maintaining their photophysical properties virtually intact.

5.4.2 Optical properties

Luminescence

The luminescence emission of quantum dots, like that of bulk semiconductors, is essentially due to electron-hole recombination at the band-edge. In nanocrystals, however, the band edge energy is shifted to higher energies due to confinement. This way, QDs have their emission peak shifted towards the blue relative to the bulk band gap wavelength. These transitions have an associated lifetime that is in the $10\,ns - 20\,ns$ range. Because of thermal broadening, though, the resulting photoluminescence spectra have line-widths given approximately by $k_B T$. This way, the emission spectrum of a single QD, at ambient temperatures, can have full widths at half maximum (FWHM) of a few nanometers.

The major source of emission broadening in QDs, however, comes from their size distribution. In a colloidal dispersion the solid particles have approximately, but not exactly, the same size. Because the emission of a QD is related to its size, the slight differences in size result in slight variations in the emission wavelength. As a consequence, the emission spectrum of a certain ensemble of nanocrystals will be much broader than the individual QDs spectra. Presently, size distributions with less than 5% variation are achievable. This translates into a FWHM of approximately $25\,nm - 30\,nm$, which is quite narrow in comparison to the spectral response of many luminescent dyes. This way, in contrast with traditional dyes, which have broad emission spectra with a characteristic long red tail, nanocrystals present a symmetrical (approximately Gaussian) and relatively narrow emission spectrum. Several examples of emission spectra of CdSe-ZnS core quantum dots can be observed in Figure 5.13(b).

While most dyes present severe photodegradation when illuminated by energetic radiation, quantum dots have demonstrated to be extremely photostable in most situations. Although photobleaching has been reported in bare dots, nanocrystals with an adequate protective shell are known to remain extremely bright even after several hours of moderate to high levels of UV radiation exposure. On the other hand, the luminescence emission of common dyes can vanish completely after a few minutes.

In practice, the photostability of nanocrystals depends on their surface coatings (bare dots or core shell), and on the surrounding environment (solution or solid matrix). Depending on these circumstances, different behaviors have been observed. Some authors reported photo-enhancement, i.e., a gradual increase of the luminescence intensity, under UV irradiation, both in solution and in solid hosts [33, 34]. Both reversible and non-reversible photo-enhancements were observed and,

usually, both components coexist. The increase in luminescence is explained by a light-induced rise of the dots potential barrier, preventing excited carriers form escaping the QD and favoring radiative recombination. Photo-induced passivation of surface defects is another possible mechanism involved. After enhancement, slow photo-degradation usually follows. The time scales of these behaviors depend strongly on the power densities to which the samples are submitted.

For CdSe nanocrystals, encapsulated in a glass matrix, the photoluminescence intensity shows a linear dependence with the excitation optical power up to moderately high power densities ($\sim 400 W/cm^2$). For higher excitation powers, excited carrier densities dramatically increase and the dependence is no longer linear. In addition, shifts in the band-edge luminescence can be observed either due to 'band-filling' processes[52] (blue shift) or to photo-induced heating of the sample [35].

A lot of research has been done regarding the photostability of QDs; but results that sound contradictory are often reported. These apparent contradictions, however, are often due to differences in host environments or nanocrystal chemistry. A deeper understanding of the mechanisms underlying these behaviors is needed. Due to the strong research effort concerning the subject, however, progress is being constantly achieved, providing tools to control the already outstanding photostability of semiconductor nanocrystals.

Absorption

Due to three-dimensional quantum confinement, an ideal QD has a discrete density of states and an atomic-like absorption spectrum. In a real QD ensemble, however, size dispersion along with thermal broadening results in a clustered absorption spectrum spanning a continuous range of energies and featuring some peaks at relevant energies (given approximately by equation (5.40)). This way, like bulk semiconductor materials, nanocrystal QDs will absorb any wavelength to the blue of their emission peak, i.e., any photon with energy higher than that of the lowest transition is absorbed. Moreover, the probability of absorption grows with increasing photon energy, as more and more higher energy transitions become possible. The absorption spectra of several CdSe-ZnS bare core nanocrystals are shown in Figure 5.13(a). The very broad absorption spectrum observed in real QDs is a major feature when compared with organic dyes whose absorptions are relatively narrow, and in the vicinity of their emission (small Stokes shift). This means that QDs can be excited by any wavelength lower than its emission peak. The excitation wavelength impacts the

[52] At low laser power densities, where only a few electron–hole pairs are created, the bands are filled up to energy E_1; as further pairs are created at increased power density, the new pairs occupy the next possible position in the bands and the bands are filled up to E_2. Therefore, the energy of the transition is blue shifted.

intensity of the resulting fluorescence, but not the emission wavelength. Therefore, QDs will greatly benefit from broadband excitation and, unlike dyes, several QDs can be simultaneously excited by the same optical source.

Tunability

Since both the emission peak and the absorption onset are determined ultimately by the confinement energy, both these parameters become size dependent in nanocrystals. This way, tunability of emission and absorption spectra can be achieved by simple control of the nanoparticles size. Currently, nanocrystalline QDs are available in a wide variety of emission wavelengths. Depending on the particles size, the emission of CdSe quantum dots can be continuously tuned from $465\,nm$ to $640\,nm$, corresponding to a size range from $1.9\,nm$ to $6.7\,nm$, respectively. Figure 5.13 shows the absorption and emission spectra of CdSe-ZnS nanoparticles with different sizes. This data shows that virtually any wavelength in the visible range can be achieved. In addition, because only the nanocrystals size changes, all of these particles are still CdSe; hence, each can be prepared with the same quantum yield, surface chemistry and set of environmental sensitivities. Conversely, when using traditional dyes, different emission wavelengths are provided by completely different chemical species, sometimes presenting dramatically different quantum yields and chemical properties.

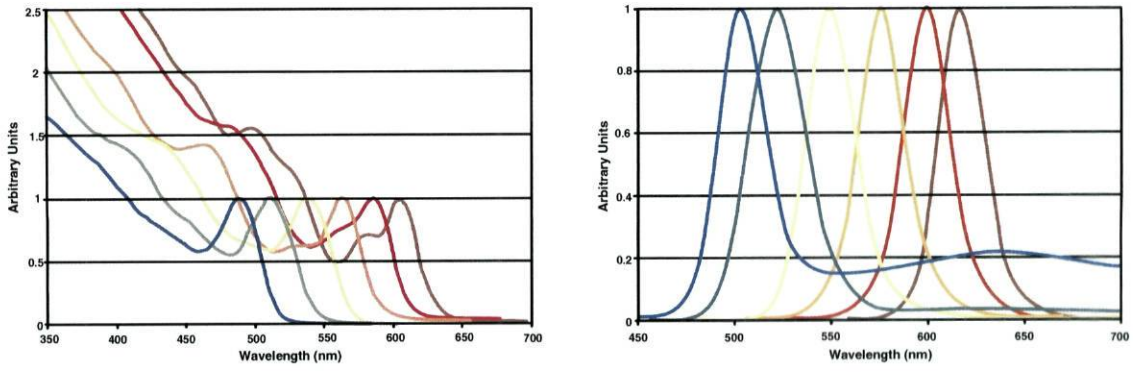


Figure 5.13 Typical absorption, (a), and emission spectra, (b), of CdSe-ZnS core nanocrystals. Available at Evident Technologies Inc. [36].

Two of the emission spectra in Figure 5.13 (b) present a broad peak at longer wavelengths. These lower energy emissions result from recombination of surface states. The effect is stronger in smaller dots due to their increased surface area. The application of a ZnS shell passivates the surface states, completely eliminating lower energy emissions in core-shell quantum dots.

There are practical limitations to the size of the particles that can be achieved with a certain material. When the nanocrystals are made progressively bigger, the quantum confinement is eventually lost. On the other hand, they cannot be made infinitely small. This way, any given material provides tunability over a limited wavelength range. In order to cover a wider range of wavelengths a variety of materials should be used. For example, cadmium-tellurium (CdTe) quantum dots emit further into the red (600nm-725nm) while high-energy emission is possible with CdS (350nm-470nm). Infrared emission has also been reported (800nm-2000nm) using lead selenide/sulfide (PbSe/S) nanoparticles. Table 5-4 shows the semiconductor materials most commonly used to fabricate nanocrystals by chemical methods. The wavelength range and the corresponding particle size covered by each material are also shown. Roughly, a wavelength range of $2000\,nm$ is covered with four different materials.

Semiconductor Material	Emission Range (nm)	QD size range (nm)	QD type
CdSe	465 – 640	1.9 – 6.7	Core
CdSe/ZnS	490 – 620	2.9 – 6.1	Core-Shell
CdTe/CdS	620 – 680	3.7 – 4.8	Core-Shell
PbS	850 – 950	2.3 – 2.9	Core
PbSe	1200 – 2340	4.5 – 9	Core

Table 5-4 Luminescence emission range of quantum dots made of different semiconductor materials and of different sizes. Available at Evident Technologies Inc. [36].

Advantages

In comparison with traditional molecular dyes, QDs have bright, narrow and stable photoluminescence. Furthermore, they possess a larger Stokes shift, and it is also possible to tune their properties. This set of characteristics gives nanocrystals a great advantage in many traditional luminescence applications. In particular, multiplexing applications can be greatly simplified. The reduced spectral overlap of emission along with broad absorption spectra allows the system complexity to be reduced by decreasing the need for filtering and multiple excitation sources. Reduced overlap also means that the whole emission spectrum can be collected, resulting in increased signal to noise ratio and therefore greater sensitivity.

In addition to superior performance in traditional applications, QDs allow new exciting applications. Their exceptional photostability, along with the ability of providing nanocrystals with biocompatible coatings, resistant to metabolic degradation, allow for unprecedented long term *in-*

vitro and *in-vivo* imaging applications. The relatively large surface area of QDs is adequate to be coated with multiple antibodies or receptors allowing specific and controlled response either to one or to multiple analytes, simultaneously.

Potential problems

Uncoated quantum dots become very sensitive to the external environment. Impurities, oxidation, activation of surface defects, are some of the mechanisms that can easily degrade the nanocrystals luminescence properties. Although passivation with organic and inorganic layers has shown to provide QDs with outstanding photostability, this can be a problem when the external medium is hazardous. Nevertheless, careful choice of the QDs coating can turn this problem into an advantage as it can provide very specific and sensitive luminescent sensors.

The relatively large size of QDs, along with their chemical nature, does not allow these particles to diffuse through cellular membranes easily. This implies that invasive approaches must be used for intracellular assays to be performed. Alternatively, QDs must be conjugated with membrane permeable peptides. This approach, however, further increases their size and can interfere with physiologic behavior.

In biological applications very often single molecule spectroscopy is performed. One of the mechanisms to identify single molecule emission is by observing fluorescence blinking, i.e., under continuous photo-excitation their luminescent emission is interrupted by random off-periods. With QDs such assays can be compromised by the tendency of single QDs to blink for long periods. These periods can be as long as several seconds. Although this occurrence is also known to happen with molecular fluorophores, their blinking intervals are in the sub-millisecond range. Moreover, QDs blinking is known to be dependent on excitation optical power, temperature and surrounding environment. When QD ensembles are used, however, the blinking is averaged and stable photoemission is observed.

Although functionalization of the nanoparticles surface can improve their biocompatibility, the composition of some semiconductor nanoparticles, which can include cadmium or lead, can pose serious toxicity problems in long term applications. Nevertheless, less toxic materials from which quantum dots can be obtained are presently being investigated by different companies.

5.4.3 Commercial products

Presently, several companies offer a variety of products based on luminescent semiconductor nanocrystals. Quantum Dot Corporation [37] and Evident Technologies [36], two U.S. companies, are the major players operating in this particular field. The former offers exclusively bioconjugated QDs while the later provides a wider variety of products. The focus of Quantum Dot Corporation products is the application of QDs in life sciences, mainly for bio-labeling and bio-imaging applications. This company offers a wide range of conjugated nanocrystals (coated with proteins, anti-bodies, etc) dedicated to different purposes (protein analysis, DNA, labeling, imaging, etc). Its technology is mainly based on cadmium selenide, and their products are usually provided in solution form.

Although more recently, Evident is also producing bioconjugated QDs. This company offers a wider range of products aiming at different applications, like optoelectronics, sensing, solar cells, etc. Evident can provide nanocrystals either as bare or as core-shell QDs (the core-shell configuration is only available for certain materials). Using different semiconductor materials, it offers products emitting from $465\,nm$ to $2340\,nm$ (see Table 5-4). The nanocrystals are usually provided in liquid suspension, dissolved in toluene and stabilized with surfactants.

More recently, however, Evident is also offering nanocrystals incorporated in a variety of composite materials. QDs incorporated in sol-gel materials, polymers, particles and powders, U.V. and thermally curable resins, can be acquired. This will allow users not to worry about the immobilization procedure, which can be very tricky, and focus on the intended applications. Showing some concern about the environmental and health impact of these nanoparticles, Evident is now offering bio-conjugated nanocrystals in which the core material is heavy-metal free. These quantum dots are based on the ternary compound InGaP.

Nanoco [38] is another company, situated in the U.K., that makes quantum dots its business since 2001. Initially with a limited set of products (basically CdSe and CdTe core shell nanocrystals provided in powder form), it has recently expanded the offer. Presently, Nanoco offers QDs based on a variety of materials (new materials include gallium and indium). It offers a long list of options for the external coating of the nanocrystals that will suit them for diverse applications.

These three examples are representative of a whole universe of new companies investing in nano-materials technologies. Their recent history clearly indicates a rapidly expanding market and an effort to provide more application oriented products. This in turn will contribute to further expand the range of applications. The widespread application of nanotechnologies, however, is raising concerns about the environmental and health impact of a growing variety of nanomaterials,

especially when they are ready to be incorporated into consumer products. Nowadays, the scientific community is engaged in a great controversy regarding these matters [39, 40]. The few toxicity studies available are often inconclusive. Since a great variety of materials and situations is involved this calls for a concerted effort of both scientists and public authorities to support fundamental research aiming at the definition of scientifically valid, low-cost, fast throughput toxicity tests to assess potential environmental and health risks. Taking into consideration the potential benefits of these technologies it is certainly worth the effort.

5.5 Optical sensing applications of quantum dots

The combination of appealing optical properties with biochemical versatility make QD nanocrystals an attractive tool in a growing range of applications. From biochemical sensing [41] and imaging, to telecommunications [16], and even quantum mechanics [42], new applications are being reported everyday. In the field of optical sensors, the ability to tune the quantum dots unique optical properties and tailor their chemical and biological characteristics are particularly appealing for biochemical applications. The use of nanocrystalline QDs in different fields of optical sensing will be addressed in the following sections

5.5.1 Physical sensors

Nanocrystalline QDs are most widely used in chemical and biological sensors; however, the behavior of their optical properties with temperature makes them excellent temperature probes with a wide range of applications [43-46].

CdSe nanocrystals coated with a passivating layer of ZnS and entrapped in a polymer matrix (poly(lauryl methacrylate)-PLMA) were reported to have attractive properties for optical thermometry applications [47]. The $600\,nm$ emitting nanocrystals, entrapped in a $5\,mm$ thick PLMA disk, were subjected to temperature changes in a range of $200\,^{\circ}C$, while excited with a $488\,nm$ laser line. Monitoring of the resulting photoluminescence revealed that the wavelength maximum (λ_{max}), the linewidth, and the intensity of this emission were all strongly temperature dependent. A blue shift in λ_{max} of $20\,nm$ was observed, while the temperature decreased from $42\,^{\circ}C$ to $-173\,^{\circ}C$. In the same range, the FWHM decreased from $26\,nm$ at higher temperatures to $22\,nm$ at lower temperatures. The strongest effect was, however, observed in the photoluminescence intensity which increased by a factor of five as temperature decreased. In particular, for the near ambient temperature range ($5\,^{\circ}C$ to $40\,^{\circ}C$), the photoluminescence intensity change was linear and on the order of -1.3% per $^{\circ}C$. It was shown that, in this particular range, the wavelength shift was small

($\approx 2\,nm$) and the FWHM variation was negligible ($< 1\,nm$). All the changes were reversible with temperature. Good reproducibility was observed even after 3 hours of continuous irradiation, demonstrating the good photostability of QDs. This temperature behavior was essentially identical for QDs excited at different wavelengths (460, 530, and $580\,nm$) and in different matrices (polymer and sol-gel).

This data establishes the suitability of QDs as good temperature indicators for sensing applications. The authors suggested the use of CdSe-ZnS nanocrystals as an internal temperature reference in pressure sensitive paints. This type of paint is used in stationary wind tunnel tests. The surface under study is painted with an oxygen sensitive dye that under proper illumination provides a luminescent mapping of pressure distribution. The dyes luminescence, however, is invariantly temperature dependent and some temperature reference is needed. The fact that the fundamental emission mechanism of QDs is not sensitive to collisional quenching by oxygen makes them suitable for use as reference in this kind of application.

5.5.2 Chemical sensors

In contrast to the widespread use of QDs in biological applications, the use of semiconductor nanoparticles as chemical sensing probes is just starting to develop [48]. Few reports have been published concerning the application of semiconductor nanocrystals as luminescent indicators for detection of chemical species. However, without the passivating shell and protective capping, the luminescence of core QDs can be very sensitive to the surrounding chemical environment. This can be the path for using nanocrystals as chemical sensors, provided some selectivity can be achieved. The desired selectivity can be controlled by chemically tailoring the outer surface of the semiconductor nanoparticles.

Coating the QD surface with suitable ligands can have a strong effect on its luminescent response to specific chemical species [29]. Chen and Rosenzweig [49] were able to alter the selectivity of CdS nanoparticles to respond either to zinc or copper ions, simply by changing their capping layer. They showed that, while polyphosphate-capped CdS quantum dots responded to almost all mono and divalent metal cations (showing no ion selectivity), thioglycerol-capped CdS nanocrystals were sensitive only to copper and iron ions. The QDs luminescence was quenched by iron and copper, but was not affected by other ions occurring at similar concentrations. On the other hand, the luminescence emission of L-cysteine[53]-capped CdS quantum dots was enhanced in

[53] Cysteine is a naturally occurring hydrophobic amino acid which is found in most proteins.

the presence of zinc ions but was not affected by other cations like copper, calcium and magnesium. Some quenching by iron was observed, however. The quenching by iron, which interfered with the detection of copper and zinc, was attributed to an inner filter effect, and could be eliminated by adding fluoride ions to the solutions in order to form a colorless complex. Using this set of QD probes, the authors established the selective detection of zinc and copper in physiological buffer samples, where several other metal ions were present. Quantitative measurements were performed where detection limits of $0.8\,\mu M$ and $0.1\,\mu M$ were achieved for zinc(II) and copper(II), respectively. This was claimed to be the first use of semiconductor nanoparticles as selective ion probes in aqueous samples. More recently, the detection of copper in physiological buffer solutions, with a detection limit of $0.1\,nM$, was achieved by using CdSe-ZnS nanocrystals modified with bovine serum albumin[54][50].

The same principle can be applied for the detection of inorganic anions. The use of surface modified CdSe quantum dots functionalized with *tert*-butyl-*N*-(2-mercaptoethyl)-carbamate (BMC) groups for the determination of cyanide was demonstrated by W.J. Jin et al.[51]. The luminescent emission of the modified QDs was found to be strongly quenched in the presence of cyanide ions (CN^-). The presence of both static and dynamic quenching was revealed by a non-linear Stern-Volmer plot [52]. In spite of this, an empirical fit to the quenching data allowed the determination of cyanide with a detection limit of $1.1\times10^{-7}\,M$. The presence of other ionic species like NO^{3-}, Cl^-, SCN^- did not exhibit any significant effect on the luminescence emission of the modified QDs, demonstrating selectivity. However, some luminescence quenching was observed in the presence of the anions I^-, NO_2^- and Br^-. Nevertheless, quenching by cyanide was much stronger and a very small concentration of these interfering ions (typical in environmental studies) should present no problem. In addition, further surface modification can be applied in order to eliminate these cross sensitivities. Alternatively, surface modification can promote sensitivity to other ionic species. Overall, these results indicate the feasibility of using surface modified QDs as analytical probes for the determination of chemical species.

In a different approach, molecular imprinting technology was used to render the photoluminescence of semiconductor nanocrystals sensitive to specific molecules[53]. If the synthesis of a polymer is made in the presence of an imprint or template molecule, cavities will be produced in the polymer, which are highly selective for the imprint. C.I. Lin et al. prepared molecular imprinted polymers (MIP) with photoluminescence property using CdSe nanoparticles

---

[54] Bovine serum albumin (BSA) can be used as a diluent or a blocking agent in numerous applications including immunoassays. BSA is used to stabilize some enzymes during digestion of DNA. This protein does not affect other enzymes that do not need it for stabilization.

functionalized with 4-vinylpyridine. Several polymers containing the QDs were imprinted with different template molecules (caffeine, uric acid, L-cysteine). The resulting solid polymers were ground to a fine powder and sieved. The template molecules were then extracted from the obtained powder. A schematic representation of the preparation procedure can be observed in Figure 5.14(a).

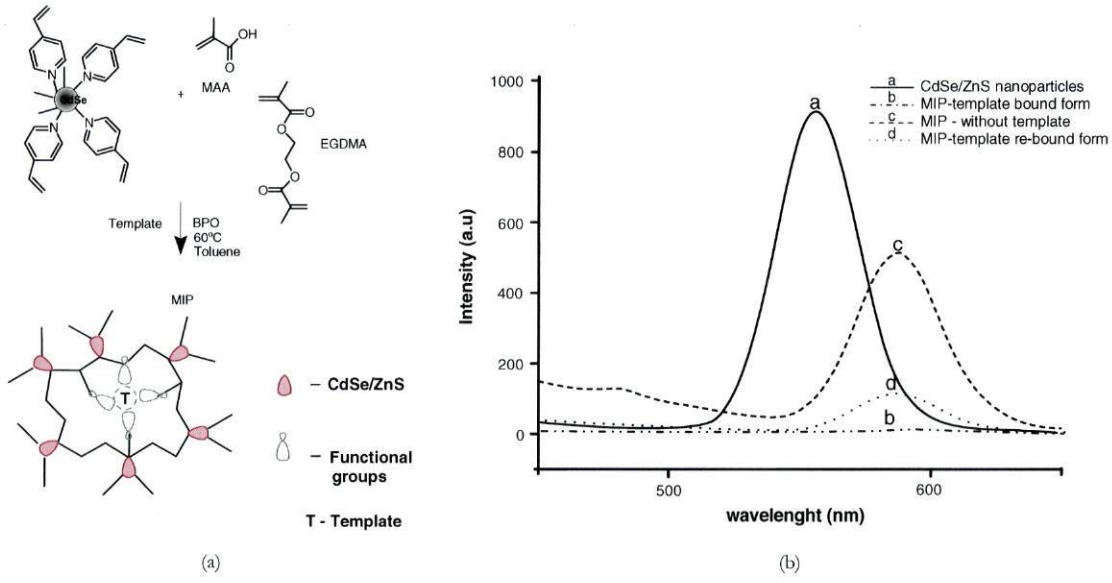


Figure 5.14 (a) Scheme for the preparation of the CdSe/ZnS incorporated MIP. (b) Comparison of luminescence emission spectrum of CdSe/ZnS with spectra of caffeine imprinted MIP in the template bound, free and re-bound forms. Data taken from [53].

Detection of the analytes was performed by incubation of the MIPs with the corresponding template molecules in aqueous solutions. It was observed that the photoluminescence emission of the MIPs was strongly quenched in the presence of the respective templates; however, no quenching occurred in the presence of other molecules. Strong quenching was observed for the caffeine imprinted polymer in the presence of caffeine, but the presence of analogous molecular structures like theophylline[55] and theobromine[56] had no effect on the photoluminescent emission. Also, a control polymer, with no imprint, showed no change in the QDs photoluminescence. These results demonstrate that it is possible to couple nanocrystals with the selective recognition capability of MIPs, opening several possibilities for the application of semiconductor nanoparticles in optical chemical sensing.

[55] Theophylline is a member of the xanthine family, and it bears structural and pharmacological similarity to caffeine. It is naturally found in black tea and green tea.

[56] Theobromine is a bitter alkaloid of the methylxanthine family, which also includes the similar compounds theophylline and caffeine. It is the primary alkaloid found in cocoa and chocolate, and is one of the causes for chocolate's mood-elevating effects.

5.5.3 Biosensors

The unique optical properties of QDs establish them as appealing alternatives to traditional organic dyes in the context of biotechnology, offering potentially greater performance in fluorescence based immunoassays and bio-imaging applications [32, 41, 54]. The introduction of QD technology in the biological domain involves its chemical stabilization, the control of its hydrophobic/hydrophilic properties and, finally, its conjugation with a biomolecule of interest, which will define its functionality. All these processes will strongly impact the luminescence properties of the nanoparticle. Nevertheless, several successful strategies have been developed to covalently or non-covalently bind biomolecules to surface modified nanocrystals, and some of these bioconjugated QDs are already commercially available [37]. The size of QDs, which is much larger than that of single dye molecules, will allow their simultaneous conjugation with more than one biomolecule. This provides QDs with the potential for increased sensitivity, multi-analyte detection with a single QD, and other new functionalities. On the other hand, the increased size also raises some concerns about interference with the biomolecules mobility and functionality.

In one of the first reported applications of semiconductor nanoparticles in a bio-assay, CdSe-ZnS quantum dots, covalently coupled to a protein, presented 20 times more luminescence intensity in comparison to Rhodamine. Additionally, the QDs were reported to be 100 times more resistant against photobleaching. This allowed the authors to perform ultrasensitive detection at the single-dot level. However, an on/off behavior of single dot emission was observed. This fluorescence 'blinking', also observable in some dye molecules, can have off-periods of several seconds in QDs which can compromise measurements. While preserving the optical properties of the nanoparticles, the authors also demonstrated that the attached biomolecules were still active and able to recognize specific analytes. The first example of a nanocrystal *in-vitro* immuno-assay was the case of quantum dots labeled with IgG antibodies[57], which were recognized and agglutinated by polyclonal anti-igG[58]. The authors also demonstrated cell labeling by transporting QD-transferrin[59] bioconjugates into cultured HeLa[60] cells via receptor-mediated endocytosis[61][55].

---

[57] An antibody is a protein used by the immune system to identify and neutralize foreign objects like bacteria and viruses. Each antibody recognizes a specific antigen unique to its target. IgG is a specific type of antibody, it is a monomeric immunoglobulin and is approximately equally distributed in blood and in tissue liquids.

[58] Anti-igG are the specific antigens for igG antibodies. An antigen is a substance that stimulates an immune response, especially the production of specific antibodies. Antigens are usually proteins or polysaccharides.

[59] Transferrin is a protein for iron ion delivery. When transferrin loaded with iron encounters a transferrin receptor on the surface of a cell, it binds to it and is consequently transported into the cell in a vesicle.

[60] In biological and medical research, a HeLa cell is a cell which is derived from cervical cancer cells taken from a woman named Henrietta Lacks, who died from the cancer in 1951, and circulated (without Lacks' knowledge or permission) by

The potential of QDs for multicolor assays was first demonstrated by Bruchez et. al. when two different sized CdSe-CdS nanocrystals, emitting green and red luminescence, were specifically bound to different parts of 3T3 mouse fibroblast cells[62], and were excited by a single optical source[5]. In this pioneer experiment some nonspecific binding was observed. Higher degrees of specificity are required in *in-vivo* applications where background biomolecules can generate false positives. Stabilization and conjugation techniques are rapidly evolving and higher levels of specificity have been achieved by different authors [56-58]. Recently, Mattoussi et al. [58] prepared CdSe-Zn QDs with mixed protein adaptors to provide recognition of antibodies. The QD complexes prepared can be conjugated to a wide range of antibodies, thus providing a whole new set of highly specific probes. A representative example is illustrated in Figure 5.15. The obtained QD-antibody conjugates were used in several direct, sandwich and competition fluorescence based immunoassays, to detect different toxins (staphylococcal enteroxin B, cholera toxin) and small molecule explosives. In the several assays performed, limits of detection were achieved that were, at least, as low as the ones obtained with dye-based assays [6].

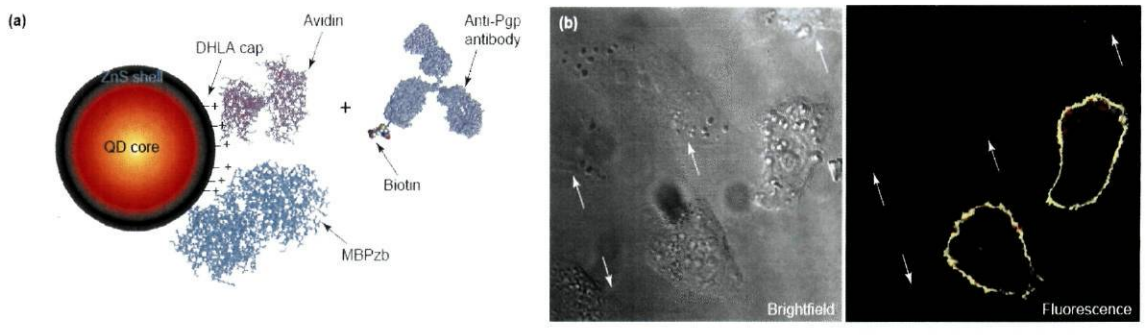


Figure 5.15 Specific labeling of live cells with QDs. (a) Positively charged avidin and maltose-binding protein, with a positively charged tail (MBPzb) self assembled on the negatively charged surface of QDs capped with dihydrolipoic acid (DHLA), can bind to biotinylated molecules such as antibodies specific for Pgp. (b) Labeling of the cell membrane with the QD bioconjugates: only cells that express detectable levels of Pgp–GFP, and not those that do not express Pgp–GFP (marked with arrows), are labeled. Yellow coloring in the fluorescence image indicates an overlap of green (Pgp–GFP) and red (QDs bioconjugate) fluorescence emission. (See Ref. [58, 59]for further details)

George Gey. Initially, the cell line was said to be named after a "Helen Lane", in order to preserve Lacks' anonymity. HeLa are considered "immortal". They do not die of old age and can divide an unlimited number of times as long as basic cell survival conditions are met. They are used as model cancer cells and for studying cellular signal transduction. It has been estimated that the total mass of HeLa cells today far exceeds that of the rest of Henrietta Lacks' body.

[61] Endocytosis is a process whereby cells absorb material (molecules or other cells) from outside by engulfing it with their cell membranes.

[62] The 3T3 cell line is an important fibroblast culture, widely utilized in laboratory research, which was established from disaggregated tissue of an albino Swiss mouse.

The same authors performed the first study about fluorescence resonance energy transfer (FRET) in QD-protein conjugates. Nanocrystals were used as energy donors to acceptor dye molecules that were attached to the conjugated proteins. This configuration allowed the exploration of the influence of parameters such as donor-acceptor spectral overlap and donor-acceptor ratio on the FRET efficiency [60]. The resultant FRET enhancement will contribute for increased assay sensitivity. These studies are intended to evaluate the possibility of quantifying analyte concentrations by fluorescence quenching. In sequence of the results obtained, a prototype of a QD FRET sensor for sugar detection was presented. Each QD was conjugated, via His-Zn coordination, with 15 to 20 maltose binding proteins (MBP) and with further processing a QSY-9[63] quencher was bonded to each MBP. For two reasons the concentration dependent quenching of the QD emission was obtained; (1) the QSY-9 absorption overlapped perfectly with the emission of the $555\,nm$ emitting QDs, and (2) its separation distance from the QD center was within the range of FRET critical radius. When maltose was added to the solution, the quencher was displaced and FRET was interrupted. An apparent binding constant of $7.0\,\mu M$ was found from the titration[64] curve with maltose. A response was obtained only with certain sugars, showing that the QD-MBP conjugate kept its specificity. These results confirmed QDs as excellent FRET donors, establishing a new tool for sensitive and specific biosensing [6].

Besides outperforming dyes in traditional bioassay applications, QDs also introduced new possibilities. Their unique photostability and potentially low cytotoxicity allow long term *in vivo* imaging [31, 57, 61] and monitoring of dynamic cell processes. Although cadmium ions alone can be highly toxic to cells, coating the core-shell dots with lipid layers minimizes the risk of contamination. In addition, non-heavy-metal semiconductors nanocrystals are becoming available. With QDs, wavelength multiplexing for simultaneous multianalyte determination becomes facilitated. Recently the incorporation of different sized QDs into polymeric microbeads with precisely controlled ratios has been reported. Controlling the types of nanocrystals and their relative ratio inside the bead makes it possible to create optically encoded microbeads which are highly suitable for multiplexing applications. This concept was demonstrated by performing a multiplexed DNA hybridization assay using triple-colored beads [62].

The successful realization of several fundamental bioassays has been demonstrated with bioconjugated nanocrystals. Additionally, new exciting functionalities were explored. In face of these

---

[63] Commercially available standard quencher.

[64] Titration is a standard laboratory method of chemical analysis which can be used to determine the concentration of a known reactant.

developments, bioconjugated QD technology will soon transform semiconductor nanocrystals in a standard tool for biotechnology applications.

5.6 Quantum dots as auxiliary tools in biochemical sensors

In the field of biochemical sensing, QDs can be used not only as sensors, but also as auxiliary tools for improvement of the sensing system performance. In the remaining part of this chapter, work exploring the potential applications of QDs as tools for biochemical sensing will be presented, focused on optical oxygen sensing systems. Due to their high versatility, and depending on the position of their emission peak relative to the oxygen sensing dye, luminescent nanocrystals can fulfill different tasks within the sensing system.

QDs as excitation sources

If the emission spectrum of the nanocrystals is made to coincide with the absorption spectrum of the sensing dye, the nanocrystals could be used as an excitation source. This way, depending on the specific application, the QDs could be placed in a strategic position, or even mixed with the dye within the immobilization matrix, in order to provide more efficient and localized excitation. This could have particular interest in multi-sensing applications, where several dyes must be used, and sometimes more than one excitation source is needed. That is not a desirable situation since system cost and complexity will be greatly increased. However, QDs could be tuned to overlap with the absorption spectrum of each one of the dyes, and, due to their broad absorption spectra, all of the nanoparticles could be excited by a single source. Another possibility is to combine several QDs in order to produce a synthesized source with an emission pattern that exactly matches the absorption of the dye, achieving maximum efficiency.

Presently, several companies advertise CdS nanocrystals with emission ranging from $400\,nm$ to $480\,nm$. This range of energetic radiation overlaps well with the absorption of several sensing dyes, including oxygen-sensing ruthenium complexes. They can be excited by any UV source. These products are offered either as a solid powder, dispersed in solutions, or even in the form of curable polymers and resins. However, they are still very expensive, and are only produced by special order, and for certain minimum quantities. For this reason this particular application was not tested in the present work. Nevertheless, because this is a very fast developing technology, the situation will change as the demand starts to increase. In alternative, these ideas could be tested using NIR sensing dyes with absorption in the visible range where QDs are well established.

QDs as temperature probes

The luminescent emission of CdSe nanocrystals has been reported to change with temperature. The wavelength maximum, the emission width and its intensity are all strongly temperature dependent. As temperature increases, the luminescence intensity decreases, the spectral width increases and the peak wavelength shifts towards the red. All these changes are linear and reversible in a wide range of temperatures. After the passivation process, core-shell quantum dots can be made chemically inert, inclusive to oxygen. This way, QD would be perfect temperature sensing probes to be used in the context of luminescent based biochemical sensors.

A major class of luminescence sensors is based on quenching mechanisms. Because this is a diffusion based process, the luminescent characteristics of the sensing dyes, like oxygen-sensing ruthenium complexes, strongly change with temperature. In order to univocally determine the oxygen level, knowledge of the temperature is also needed. Using QDs with adequate spectral characteristics, in combination with the sensing dye, can provide the sensor with the necessary temperature reference. The excited state lifetime of QDs is very fast (ns range) when compared with those found in ruthenium complexes (μs range). This way, for simultaneous detection of temperature and oxygen, frequency multiplexing might be used as an alternative to the wavelength discrimination scheme.

QDs as intensity reference

In the case of sensors based on the detection of luminescent optical power there is, most frequently, the need for a referencing scheme. Otherwise, it will be impossible to discriminate changes due to the measurand from changes due to optical power drift of the optical source, changes in coupling conditions, etc.. In the particular case of luminescence based optical sensors [63], leaching and photobleaching of the sensing dye are often the main sources of optical power drift. To minimize these problems, frequency domain fluorometry is often used in optical oxygen sensors [64]. With this technique, a phase shift can be measured that depends only on the excited state lifetime, which is proportional to the oxygen concentration and independent of the optical power level. However, it has been reported that photo-bleaching of the dye also changes the excited state lifetime and the phase response [65]. Moreover, sometimes an intensity-based system is often a simpler, less expensive alternative. Most common intensity referencing schemes include the use of a second analyte-insensitive dye and ratiometric detection of two wavelengths [66]. Ratiometric schemes can also be used with detection of back-reflected excitation radiation (corresponding to

Fresnel reflections in the fiber system). However, most available dyes suffer from photo-bleaching and full referencing cannot be achieved with the ratio of luminescence to the excitation radiation.

Nanocrystal QDs can provide excellent intensity references because of their brightness and photo-stability. Their wavelength can be tuned in order to avoid overlap with the emission spectra of the sensing dye and excitation source. Control of the shell chemistry can provide insensitivity to the analyte. However, any nanocrystals whose absorption spectrum overlaps with the emission of the sensing dye cannot be used, otherwise the QDs emission would depend on the analyte as well. If these conditions are fulfilled, the nanoparticles luminescence intensity will depend only on the available excitation optical power. On the other hand, the fluorescence of the sensing dye is sensitive both to the analyte concentration and to the excitation optical power. Therefore, ratiometric processing, which can be achieved with a spectrometer or with an adequate set of filters and photodetectors, will provide an output signal which is independent of the optical power level along the system. Because the QDs can be immobilized in the same location of the sensing dye, all of the losses in the optical path up to detection are compensated as well, providing full intensity referencing. This idea can be applied to multiple sensors in different locations as long as no spectral overlaps of any of the signals occur. Due to the different lifetime magnitudes found in QDs and dyes, a compensation scheme in the frequency domain is also an option to be explored.

QDs as oxygen sensors with unique spectral signatures

In the particular case where the luminescence emission of the nanocrystals has a peak wavelength longer than that of the sensing dye's emission, the QDs themselves can become sensitive to the analyte. This will happen because their absorption spectrum is very broad and includes every wavelength to the blue of the emission peak. This way, the QDs will absorb the sensing dye's luminescence and both emissions will be analyte dependent. In the particular case of ruthenium based oxygen sensors, any quantum dot whose emission peak is higher than $620\,nm$ (the emission peak of most ruthenium complexes) will be a potential oxygen sensor. Several combinations can be used in order to obtain oxygen sensitivity, at multiple wavelengths, in the near infrared (NIR) region of the spectrum. This would provide the basis for wavelength multiplexing of optical oxygen sensors.

Presently, very few core-shell nanocrystals are offered commercially in this wavelength range. The higher emission wavelength of CdSe-ZnS nanocrystals is $680\,nm$. Lead sulfide and lead selenide quantum dots can provide emission from $800\,nm$ to $2200\,nm$; however, they are presently sold without passivation shell, which makes them particularly vulnerable to oxygen or other

contaminants. Also, their spectral width (FWHM) can be as high as $200\,nm$, greatly reducing the number of possible channels.

Despite present limitations, QD technology is developing very fast. Very soon other solutions for narrow emitting NIR core-shell nanocrystals could be available. Also, with the presently available core-shell QDs, the multiplexing capabilities can be used for sensors with emission further into the blue (several fluorescent pH probes emit in the $500\,nm$ region).

Any excitation source used for the ruthenium complex, usually a blue LED or a laser with emission peak near $470\,nm$, will also excite all the QDs. This way, some care has to be taken in sensor design in order to ensure that the main source of optical excitation reaching each sensing QD is the corresponding sensing dye emission.

5.6.1 Samples preparation and characterization

In order to test some of the ideas presented in the previous paragraphs, different semiconductor nanocrystals where acquired and immobilized by the sol-gel process in thin films or bulk glass samples. For sensing of oxygen, different ruthenium dyes were also immobilized in thin films and bulk glass samples using similar methods.

Preparation of QD samples

Different nanocrystals were acquired from *Nanoco* [38] and from *Evident Technologies* [36]. CdSe-ZnS core-shell quantum dots, emitting at $520\,nm$ and $600\,nm$, were available in the form of solid powder. CdTe-ZnS core-shell quantum dots emitting at $680\,nm$ were available in a solution of toluene, stabilized with adequate surfactants. For the sake of simplicity, these nanocrystals will be identified according to their emission peak wavelengths using the following notation: QD_{520}, QD_{600}, QD_{680}[65]. Core shell QDs were chosen because they have a semiconductor material core, CdSe or CdTe, coated with a passivating layer of ZnS, providing higher stability of their luminescent properties. The nanocrystals were used to dope different solutions of a non-hydrolytic[66] sol-gel with a concentration of $5\,mg/ml$. The CdSe powder was incorporated directly into the sol-gel solution. For the CdTe nanocrystals the same was done after evaporating the toluene solvent. The sol-gel procedure is the property of Waveguide Solutions Inc. and is described elsewhere [67]. After stirring for $6-8$ hours, to obtain a homogeneous mixture, the solutions were filtered through a 0.1 micron

[65] These wavelengths correspond to those stated by the manufacturer with a $\pm 10\,nm$ uncertainty, and will be used as reference; the actual emission peak of each sample can differ slightly form these values.

[66] In non-hydrolytic sol-gels water is not added during the fabrication process, unlike what happens in hydrolytic sol-gels.

filter. Thin films and bulk samples with different characteristics were made by spin coating ($1500\,r.p.m.$) or molding in silicone. All the samples were subjected to temperature treatments under a nitrogen flux. The exact baking times and temperatures (ranging from $100\,°C$ to $200\,°C$) depended on the sample thickness. After the thermal treatment, a dense glass material was formed that protected the nanoparticles from oxidation and contact with other impurities. For comparison purposes, the $520\,nm$ emitting QDs were also incorporated into a hydrolytic sol-gel solution[67].

Characterization of QD samples

To assess the impact of the immobilization procedures on the luminescence properties of the nanocrystals, the samples were submitted to some characterization. For this purpose all the samples, both solutions and solid films, where excited using a blue LED (Nichia- $470\,nm$) and their luminescent emission was recorded with a dual-channel CCD spectrometer. The spectrometer was an Ocean Optics $S2000$, with channel 1 ranging from $282\,nm$ to $607\,nm$, with no filter, and channel 2 ranging from $575\,nm$ to $835\,nm$, with a built-in filter having a cut-off wavelength at $550\,nm$.

Preliminary tests showed that, although the thin films ($\sim 5\,\mu m$) were luminescent, the signal-to-noise ratio was very low in most of the samples. This was not the case of thicker samples ($> 0.5\,mm$) which were strongly luminescent. Because not enough material was available to test higher doping concentrations of the thin films, the bulky samples were used in most of the applications tested.

Figure 5.16 shows the recorded luminescence spectra of two different sol-gel solutions doped with QD_{520}. The non-hydrolytic solution is strongly luminescent, peaking at $529\,nm$. In the hydrolytic solution, on the other hand, the QDs luminescence appears strongly reduced. The strong quenching, also present in the films resulting from this solution, can be due to the interaction with the highly reactive OH^- groups. In the non-hydrolytic sol-gel, however, water is not part of the process, thus resulting in a more favorable environment for encapsulation of the nanocrystals. This could be confirmed when it was observed that the luminescent properties of the QDs remained practically intact upon solidification of the sol-gel matrix.

Besides a small blue shift of the peak wavelength ($524\,nm$ in the solid film, $529\,nm$ in the solution), the nanocrystals remained strongly luminescent upon immobilization. In all the other films and bulk samples obtained from non-hydrolytic solutions the different QDs preserved their luminescence properties. This can be observed in Figure 5.17 where the emission spectra of samples

[67] The details of this hydrolytic sol-gel procedure are given in the subsection regarding immobilization of the ruthenium dyes.

doped with QD_{520}, QD_{600} and QD_{680} are shown, together with the emission profile of the blue LED used for excitation. The observed emission peaks ($524\,nm$, $608\,nm$ and $696\,nm$, respectively) and linewidths (FWHM of $\sim 31\,nm$) are within the manufacturers specifications. This demonstrates little interaction between the solid host matrix and the embedded nanocrystals, thus establishing a successful immobilization.

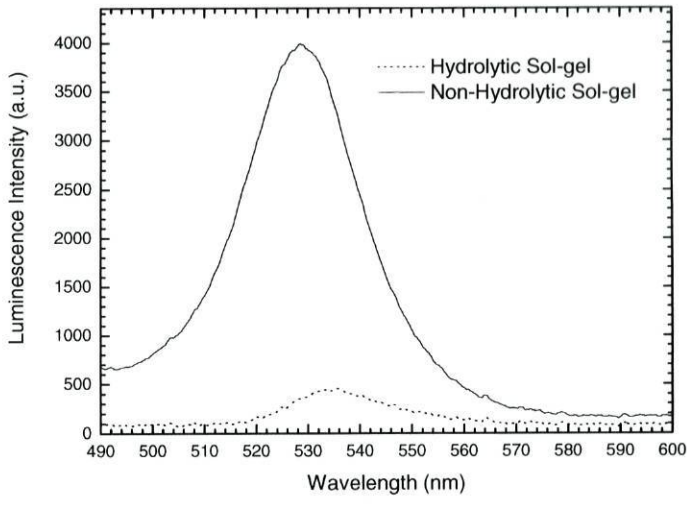


Figure 5.16 Luminescent emission of QD_{520} incorporated into different sol-gel solutions. Hydrolytic sol-gel (dotted line) and non-hydrolytic sol-gel (black line).

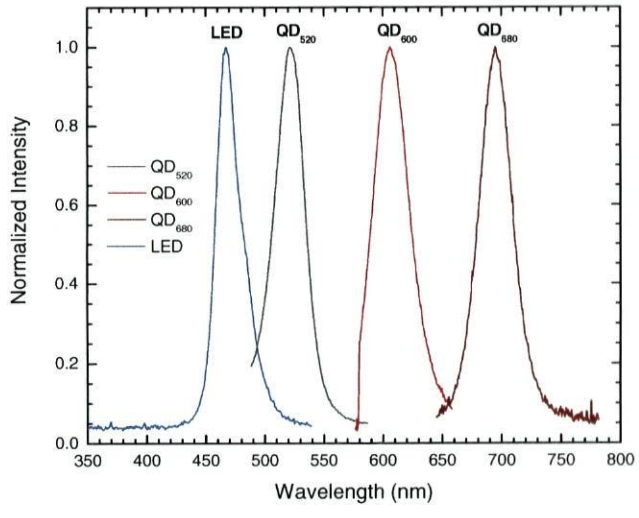


Figure 5.17 Normalized emission spectra of QD samples immobilized in non-hydrolytic sol-gel. Peak emissions from blue to red are $520\,nm$, $610\,nm$ and $680\,nm$. The spectrum of the excitation source, a blue LED ($470\,nm$), is also shown.

In order to evaluate the photostability of the films obtained, a sample doped with QD_{520} was subjected to continuous irradiation. The blue light from the LED was guided to the sample by a

fiber bundle with $4\,mm$ external diameter[68]. The sample was illuminated with a power density of approximately $20\,mW/cm^2$ for a period of $16\,h$. A $400\,\mu m$ core optical fiber was used to carry the photoluminescence signal to the CCD spectrometer. The behavior of the integrated luminescence intensity was then recorded as a function of time. For reference purposes, the power emitted by the LED was also registered. The behavior of the QDs luminescence during the test can be observed in Figure 5.18. The signal shown was first normalized relative to the LED output power and then to the initial luminescence level.

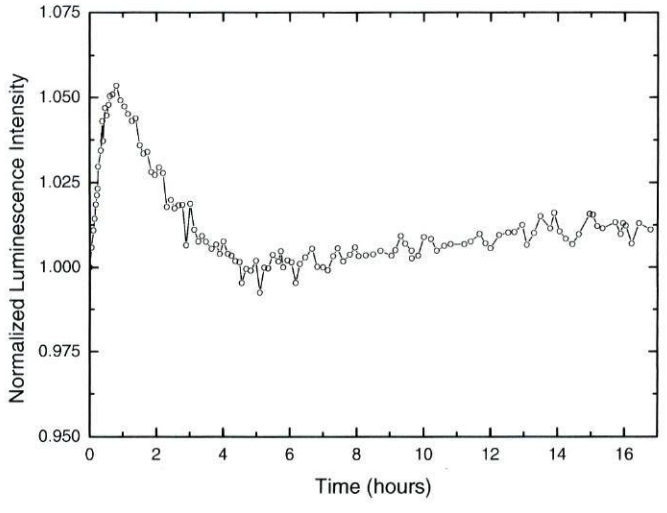


Figure 5.18 Time behavior of the luminescent output of a bulk sample of non-hydrolytic sol-gel, doped with QD_{520}, while irradiated with blue radiation ($\sim 20\,mW/cm^2$).

A luminescence enhancement was observed during the first hour of the test where the detected intensity was increased by 5%. After this period the detected power decreased at a slower rate, and it was back to the initial level after 3 more hours. For the remaining part of the test period the luminescence intensity remained reasonably stable (the variations observed were within 1%).

Enhancement of the luminescence of photo-excited semiconductor nanocrystals entrapped in a solid matrix has already been observed in different materials by several authors [33, 34]. It is a transient effect that can have reversible and non-reversible components. It is attributed to a light-activated increase in the dot potential barrier, preventing the excited carriers from escaping the dot and recombining non-radiatively with defects at the outer surface. These mechanisms are dominant with low to moderate excitation intensities (up to $20\,W/m^2$), and are usually followed by very slow photo-degradation. For very high power densities (hundreds of W/cm^2) photobleaching is the dominant process. For the applications explored in this work the power densities are comparably

[68] The actual light guiding diameter was approximately $3.25\,mm$.

very low and photo-degradation was barely noticed after several hours of continuous illumination. Besides the initial photo-enhancement (which was unnoticeable in samples previously exposed), the luminescence output of the samples doped with CdSe-ZnS nanocrystals could be considered approximately constant during the experiments performed.

This was not the case of the samples doped with CdTe-ZnS. Curing of these samples could not be completed adequately, probably due to some interference of the surfactant used to stabilize the nanocrystals in toluene. This way, slow photo-degradation of the luminescence was observed in most samples doped with QD_{680}.

Preparation of the oxygen sensing samples

Two different ruthenium complexes were used as oxygen sensors in the experiments: $[Ru(bpy)_3]$-Tris (2,2'-bipyridine) ruthenium (II) chloride hexahydrate and [Ru(dpp)]-Tris(4,7-diphenyl-1,10-phenanthrolin) (I)chloride hexahydrate (purchased from Aldrich). Both dyes present strong and broad luminescent emissions centered at $620\,nm$ when excited with blue radiation ($470\,nm$). The intensity and the excited state lifetime of their luminescence are both highly quenched in the presence of oxygen. The lifetimes of Ru(bpy) and Ru(dpp) are approximately $1\,\mu s$ and $5\,\mu s$, respectively. The latter has increased sensitivity to oxygen [68].

Different samples of thin films and bulk glasses, doped with the sensing dyes, were produced using distinct sol-gel protocols. The same process that was used to encapsulate the QDs in a non-hydrolytic sol-gel [67] was used to produce thin films and bulk glass samples doped with Ru(bpy) and Ru(dpp). The samples produced in this way, however, had low oxygen sensitivity, due to the low porosity of the resulting sol-gel matrix. This way, a hydrolytic sol-gel was also used seeking to produce more sensitive samples [69]. Methyltriethoxysilane ($0.252\,mol$), dimethyldimethoxysilane ($0.252\,mol$) and water ($0.389\,mol$) were mixed for 1 hour at room temperature. Dibutoxyaluminoxy-triethoxysilane ($0.107\,mol$) was then added and mixing was continued under nitrogen and at room temperature for 20 hours. Ru(bpy) was used to dope different sol-gel solutions with concentrations of $5\,mM$, $10\,mM$ and $15\,mM$. The solutions obtained were filtered through a 0.1 micron filter and different films were then produced by spin coating ($1500\,r.p.m.$). The films curing process was done at $100\,^{\circ}C$ for 2 hours, followed by $120\,^{\circ}C$ for 6 hours. Thin films with thickness of approximately $6.0\,\mu m - 7.5\,\mu m$ were obtained. The thickness of the thin film samples was measured using a profilometer.

Characterization of the oxygen sensing samples

In order to test the suitability of the ruthenium doped samples to be used as oxygen sensors, their luminescence properties were also evaluated. Their response to oxygen was tested in a sealed chamber where the oxygen/nitrogen content was controlled. The oxygen concentration was measured using a polarographic oxygen sensing probe (Dissolved Oxygen Meter – 840041, from SPER Scientific). The emission spectra and the luminescence intensity were recorded while the samples were submitted to O_2 / N_2 saturation cycles. The data obtained was used to estimate the quenching efficiency, Q, and the response and recovery times (t_{up} and t_{down}, respectively) to changes in oxygen concentration. The quenching efficiency is a measure of oxygen sensitivity, and is defined by

$$Q = 100 \times \frac{I_{N_2} - I_{O_2}}{I_{N_2}}, \tag{5.46}$$

were I_{N_2} and I_{O_2} are the luminescence intensities in saturated atmospheres of nitrogen and oxygen, respectively. Submitting the samples to a range of oxygen concentrations in the 0% to 100% interval, and registering the luminescence intensity, I, the Stern-Volmer plots of the different sensing elements could also be obtained. The Stern-Volmer (SV) equation describes the quenching mechanism and is used to calibrate the sensor response [70]. It is defined by

$$\frac{I_0}{I} = 1 + K_{SV}[O_2], \tag{5.47}$$

where I_0 is the unquenched luminescence intensity, K_{SV} is the Stern-Volmer constant and $[O_2]$ corresponds to the oxygen concentration. The value of K_{SV} is dependent on the diffusion coefficient and on the unquenched luminescence lifetime of the dye, and provides a measure of the sample sensitivity to oxygen.

Although all the samples displayed strong luminescence (see Figure 5.19), the luminescence signals obtained from the samples doped with $5\,mM$ Ru(bpy) were much weaker when compared with the samples doped with higher concentrations (by a factor of 3 to 5). For this reason, no further tests were performed with these particular samples.

Both sol-gel hosts were found to be adequate for encapsulating the ruthenium dyes. The emission spectra obtained were similar to those obtained in solution, indicating a successful immobilization. Figure 5.20 (a) and (b) shows the luminescence spectra of hydrolytic and non-hydrolytic samples, respectively, when submitted to different oxygen concentrations. The hydrolytic sample shows a more pronounced response to oxygen variations, indicating that the encapsulated

dye is more accessible to this gas, probably due to increased porosity. Conversely, the non-hydrolytic sample has a poor response to changes in the oxygen concentration indicating a sol-gel material with higher density. In addition some features appear in the luminescence spectrum indicating some interaction of the dye with the host matrix.



Figure 5.19 Thin film doped with $10\,mM$ Ru(bpy) displaying strong luminescence when excited with a blue LED.

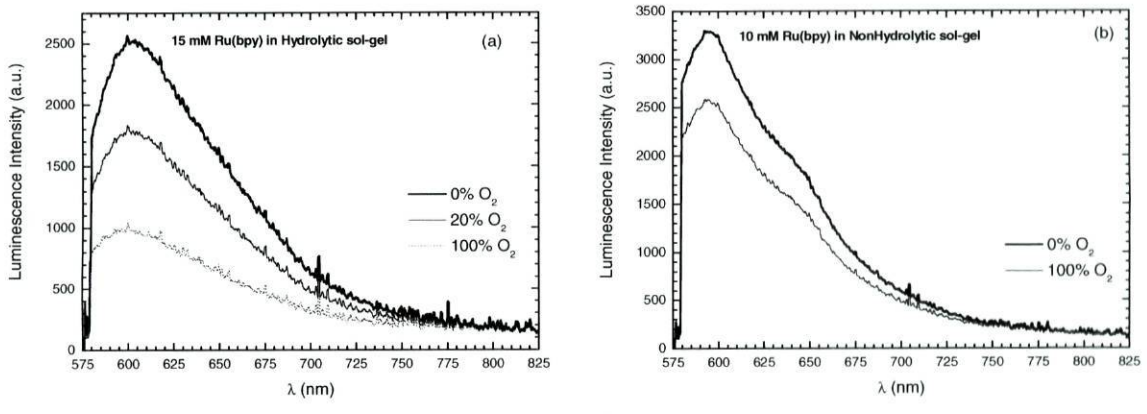


Figure 5.20 Luminescence spectra of sensing samples submitted to different oxygen concentrations. a) Hydrolytic sol-gel doped with 15 mM Ru(bpy). b) Non-hydrolytic sol-gel doped with 10 mM Ru(bpy).

A quantitative evaluation of the oxygen sensitivity of the different samples can be done by comparing the obtained quenching efficiencies, shown in Table 5-5. Higher sensitivities were obtained with the hydrolytic sol-gel. All the hydrolytic samples doped with either $10\,mM$ or $15\,mM$ showed quenching efficiencies in the $65\% - 70\%$ range. The non-hydrolytic samples doped with

Ru(bpy), on the other hand, showed much lower sensitivities, on the 20% range. The reduced oxygen permeability of this sol-gel is thus confirmed. Even when doped with Ru(dpp), a dye with an increased sensitivity to oxygen, the quenching efficiencies obtained were below 50%.

The Stern-Volmer constants of the different samples were roughly estimated from the corresponding plots, assuming a linear response to oxygen. The values obtained, shown in Table 5-5, are reasonably correlated with the quenching efficiencies measured (the hydrolytic samples presented higher values when compared with the non-hydrolytic ones). Observation of the SV plots obtained reveals, however, a non-linear response in all cases. Two representative examples can be observed in Figure 5.21. Plot (a) corresponds to an hydrolytic sample doped with $15\,mM$ Ru(bpy) and plot (b) to a non-hydrolytic sample doped with 0.25% weight Ru(dpp). The non-linearity in the response to oxygen arises from heterogeneities in the encapsulating sol-gel material. It indicates that the dye exists in different environments within the solid matrix, which have different oxygen accessibilities. Taken this fact into consideration, and comparing the results obtained, it can be concluded that the non-hydrolytic samples presented overall an increased homogeneity.

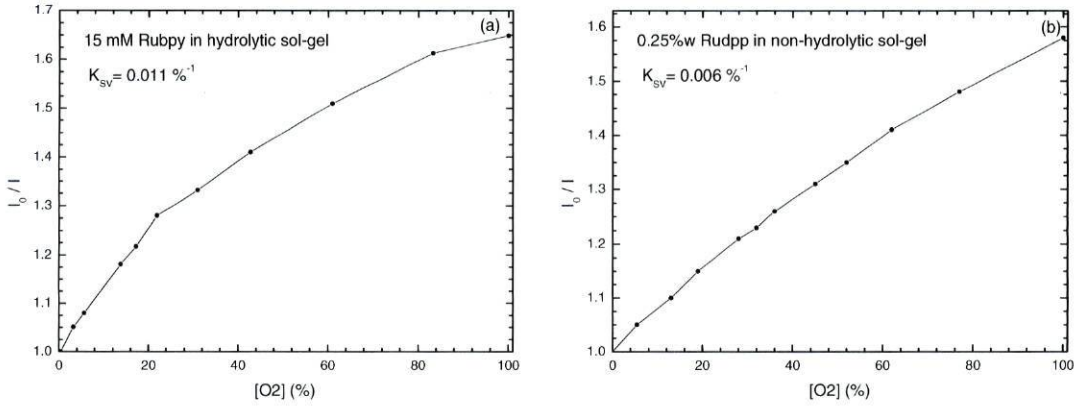


Figure 5.21 Stern Volmer plots of two different oxygen sensing samples: (a) A hydrolytic sample doped with $15\,mM$ Ru(bpy); (b) A non-hydrolytic sample doped with 0.25% weight Ru(dpp).

The dynamic response to changes in the oxygen concentration was also evaluated. The response obtained from a hydrolytic and from a non-hydrolytic sample can be observed in Figure 5.22(a) and (b), respectively. From this data, the response times could be estimated. Using similar plots, response times in the $10\,s - 20\,s$ range were estimated for all samples tested. Detailed values are given in Table 5-5. No substantial differences are observed in this parameter when comparing the responses of hydrolytic and non hydrolytic samples. The higher response time observed in the sample doped with Ru(dpp) is mainly due to its increased thickness ($\sim 50\,\mu m$). Similar response times of the hydrolytic and non-hydrolytic films indicate that the oxygen diffusion coefficients of

both sol-gel matrices should be approximately the same, and that the observed sensitivity differences results from different oxygen solubilities rather than different porosities.

The results in Figure 5.22 reveal another striking difference between the two host matrices. While in the non-hydrolytic film the luminescence intensity is fully recovered after a quenching cycle, the hydrolytic film shows a non-recoverable degradation of its luminescent signal. This behavior is related to photobleaching of the dye, which is stronger in the presence of oxygen.

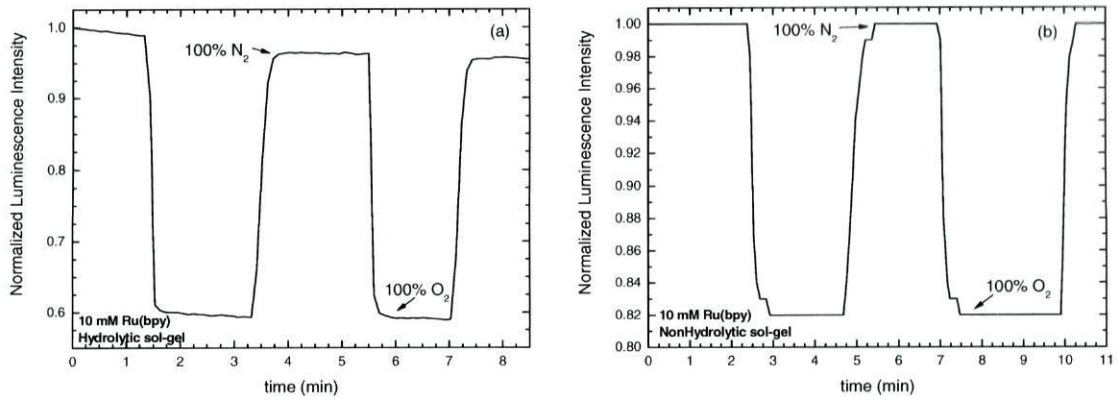


Figure 5.22 Response of sensing samples to O_2 / N_2 saturation cycles. a) Hydrolytic sol-gel doped with 10 mM Ru(bpy); b) Non-hydrolytic sol-gel doped with 10 mM Ru(bpy).

To obtain a more complete characterization of the degree of photostability of the different samples, they were submitted to continuous irradiation by the blue LED, for periods ranging from $10h$ to $24h$. All the tests were performed in a 21% O_2 atmosphere. The power density reaching the sensing films was approximately $20 mW / cm^2$. The degree of photobleaching was evaluated in four different samples: a hydrolytic sol-gel thin film (thickness of $7.5 \mu m$) doped with Ru(bpy) ($15 mM$); a hydrolytic sol-gel thin film ($7.5 \mu m$) doped with Ru(bpy) ($10 mM$); a non-hydrolytic sol-gel thin film ($5 \mu m$) doped with Ru(bpy) ($10 mM$); and a non-hydrolytic sol-gel thin film ($\sim 50 \mu m$) doped with Ru(dpp) (0.25% weight) The behavior of the different samples can be observed in Figure 5.23.

The hydrolytic sol-gel samples showed a higher degree of photo-degradation. The maximum effect was observed for the sample doped with $15 mM$ Ru(bpy) where, after 10 hours of irradiation, the luminescent intensity decreased by approximately 30%. For the sample with $10 mM$ Ru(bpy), the decrease was of 23% after 10 hours and of 32% after 17 hours. On the other hand, the non-hydrolytic samples showed a remarkable photostability and, after 23 hours of continuous irradiation, the luminescence intensity was still above 96% of the initial value. These results are well correlated with the oxygen sensitivity of the different samples. Photo-degradation is an oxygen assisted process and is higher in samples with increased quenching efficiency.

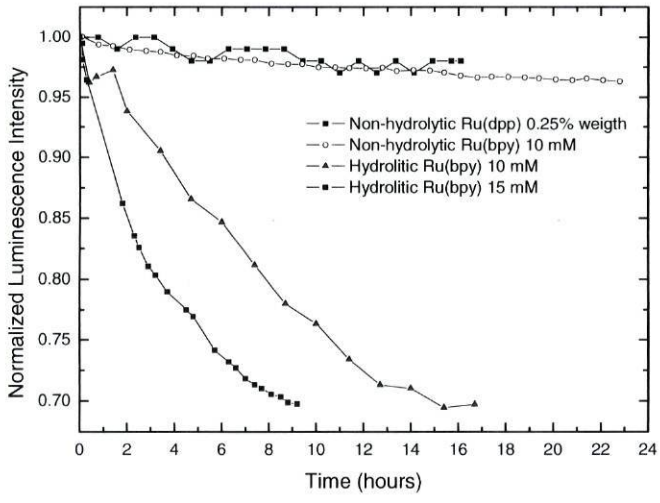


Figure 5.23 Time behavior of the luminescent output of different sol-gel films, doped with Ru(bpy)/Ru(dpp), while the samples were irradiated with blue radiation ($20\,mW/cm^2$).

	Ru(bpy) 10mM Hydrolytic	Ru(bpy) 15mM Hydrolytic	Ru(bpy) 10mM Non-hydrolytic	Ru(dpp) 0.25% Non-hydrolytic
Q (%)	70	66	23	42
K_{SV} $[O_2]\%^{-1}$	0.009	0.011	0.0024	0.006
t_{up} (s)	30	27	18/28	125
t_{down}(s)	15	17	13	73
Thickness (μm)	7.7-6.0	7.7-6.0	5.0	50
I/I_0 after 1 hour	0.97	0.91	0.99	1
I/I_0 after 5 hours	0.86	0.76	0.98	0.99
I/I_0 after 10 hours	0.77	0.70	0.97	0.98
I/I_0 after 20 hours	0.68	-	0.96	-

Table 5-5 Results of the characterization of different oxygen sensing samples showing data regarding quenching efficiency, Stern-Volmer constant, response times and photostability.

In spite of the strong decrease in the luminescence of many of the samples, at the end of the tests all samples still provided a high luminescent intensity and an adequate response to oxygen changes. A 10% decrease in the quenching efficiency was observed in the sample suffering from the higher degree of photobleaching (hydrolytic $15\,mM$ Ru(bpy)). In addition, the rate of photo-degradation was decreasing with time (see Table 5-5 and Figure 5.23). This was probably because the first dye molecules to be bleached were those exposed to a higher energy density and those more accessible to oxygen. This way, the remaining dye molecules are more inaccessible to oxygen, and receive less excitation radiation. This is translated into a decreased sensitivity but also into a

decreased bleaching rate. The non-hydrolytic sol-gel samples have demonstrated a high photostability, and can provide an interesting solution in long term applications where sensitivity is not a priority.

The samples obtained are not optimized in terms of oxygen sensing response; for instance, quenching efficiencies higher that 90% where reported with other sol-gel protocols [69]. Nevertheless, they are perfectly suited for the intended purpose, i.e., to test the potential of application of QDs in the field of oxygen sensing.

5.6.2 Quantum dots as temperature probes

Semiconductor nanocrystals have been reported to have suitable characteristics to be used in luminescence thermometry applications. To explore the potential of QDs to be used as a temperature reference in luminescence based chemical sensors, the luminescent emission of some of the samples doped with nanocrystals was characterized as a function of temperature.

Experimental details

Characterization of the behavior of the luminescent emission of different QD samples was performed using the experimental set-up in Figure 5.24.

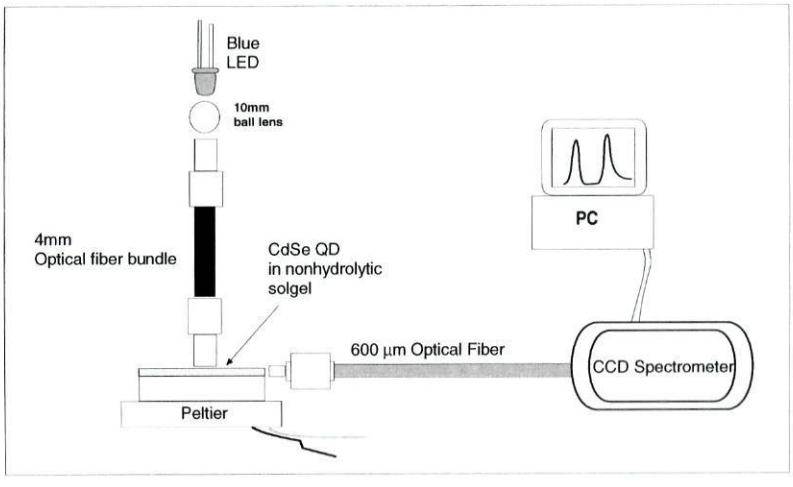


Figure 5.24 Experimental set-up used to characterize the temperature behavior of the luminescent emission of the samples doped with QDs.

The samples were placed in thermal contact (using thermal paste) with a Peltier device that controlled their temperature. Due to their broad absorption spectra, all the nanocrystals could be excited using a single blue LED ($470\,nm$ from Nichia). Optical fiber bundles with $4\,mm$ diameter were used to lead the excitation radiation to the QDs. A $10\,mm$ ball lens was placed between the LED output and the fiber bundle in order to optimize coupling. A $600\,\mu m$ multimode fiber cable,

oriented at 90° relative to the excitation fiber, was used to collect the luminescence signals. The spectral response of the QD doped samples to temperature changes was recorded using a dual channel CCD spectrometer (S2000 Ocean Optics) and a PC with adequate software.

After completing the characterization of several samples, the possibility to perform temperature measurements independently of the optical power level in the system was tested. As the samples temperature was increased, the intensity of their luminescence emission was decreased, the peak wavelength was red-shifted and the linewidth was broadened. Since, in the room temperature range, the red-shift of the central wavelength of the luminescent emission from QDs depends on temperature in a linear fashion, we developed a simple detection scheme in order to obtain self-referenced temperature measurements. Two signals, S_1 and S_2, corresponding to two narrow spectral windows on opposite sides of the peak of the emission spectrum of the QDs were normalized according to $(S_1 - S_2)/(S_1 + S_2)$, and it was realized that the resulting normalized output is proportional to temperature and independent of the optical power level in the system.

Results and discussion

All sensors were made from non-hydrolytic sol-gel doped with QDs and the results of many tests showed that they had similar behavior. All samples were strongly luminescent when excited by the blue radiation, presenting a nearly symmetrical emission spectrum with a FWHM of approximately $30\,nm$. This is in agreement with the 5% variation in the QDs size distribution stated by the manufacturer and demonstrates that the nanocrystals luminescent properties were maintained upon the sol-gel immobilization procedures.

As the temperature of the sensing samples was increased, the luminescence intensity decreased, the peak wavelength shifted towards the red and the spectral width increased. In the temperature range investigated, these changes were linear and reversible. In Figure 5.25(a) the spectral response of a $1cm^2$ ($\approx 1mm$ thick) bulk glass doped with QD_{520} is presented. The temperature of the sample was increased from $14\,°C$ to $43\,°C$. From this data it could be estimated that the luminescence intensity was decreased, as temperature increased, with a rate of -1.6% per $°C$. Figure 5.25(b) shows a similar behavior obtained with a thin film ($\approx 12\,\mu m$) doped with QD_{600}. For this sample an intensity decrease of approximately $-0.7\%/°C$ was estimated as the temperature increased. Rates between $-0.7\%/°C$ and $-1.6\%/°C$ were found in other samples.

Thermal quenching of the luminescence is due to the increased efficiency of non-radiative processes as temperature increases. At room temperature the dominant quenching effect is related to excited carriers escaping the dot by phonon assisted scattering processes. This mechanism is

dependent on the dots size and can partially explain the differences in sensitivity observed with different QDs. In addition, physical differences between samples, like distinct film thickness, presence of heterogeneities and impurities, etc., could further contribute to differences in the observed quenching rates.

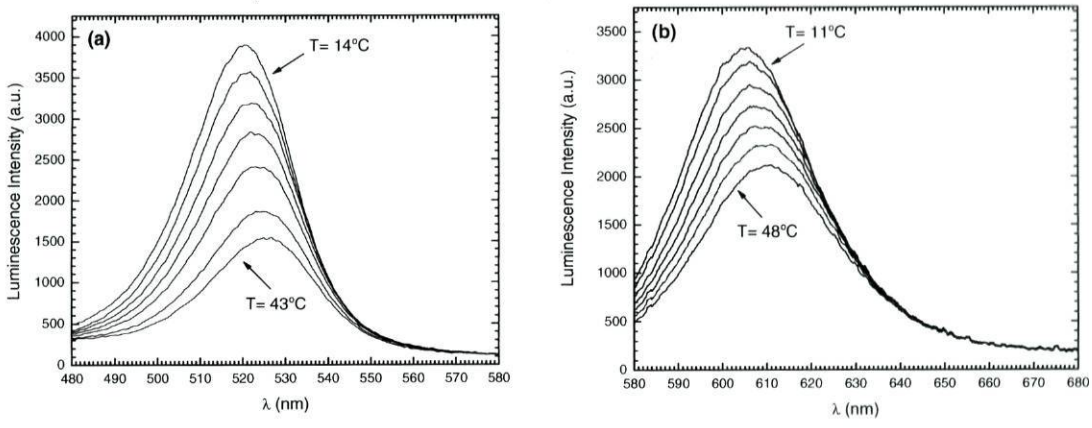


Figure 5.25 Temperature response of the luminescence emission of CdSe-ZnS nanocrystals for a temperature range from $11\,^{\circ}C$ to $48\,^{\circ}C$: a) QD_{520} in bulk sol-gel glass; b) QD_{600} in sol-gel thin film.

It can also be observed, in both samples, that the peak wavelength, λ_{peak}, increased in a linear fashion as the temperature was increased. This can be seen in more detail in Figure 5.26, where the peak wavelength of the luminescent emission of a sample doped with QD_{600} is plotted as a function of temperature. Although a linear behavior is apparent, relatively high data dispersion can be observed. This happened because the emission peak was relatively broad and the determination of λ_{peak} was not straightforward. Nevertheless, the experimental data is well fitted to the Varshni relation which describes the temperature dependence of the band gap energy in the bulk semiconductor [71]. This empirical relation is described by

$$E_g(T) = E_{g_0} - \alpha \frac{T^2}{(T+\beta)}, \tag{5.48}$$

where E_{g_0} is the band gap energy at $0\,K$, α is the temperature coefficient ($\partial E_g / \partial T$), and β is close to the Debye temperature of the material. The best fit to the experimental data was obtained considering $E_{g_0} = 2.16\,eV$, $\alpha = 7 \times 10^{-4} eV/K$ and $\beta = 265\,K$. The value of the band gap was increased, relative to the bulk value, in order to accommodate for the confinement energy. Although these parameters differ from the values known in the literature for bulk CdSe: $(2.8 - 4.1) \times 10^{-4} eV/K$ for α and $(181 - 315)K$ for β, the deviation is not considerable. These results indicate that the dominant process behind the temperature dependence of the luminescence

peak in QDs is the same as in the bulk semiconductor; therefore, it should be independent of the dot's size.

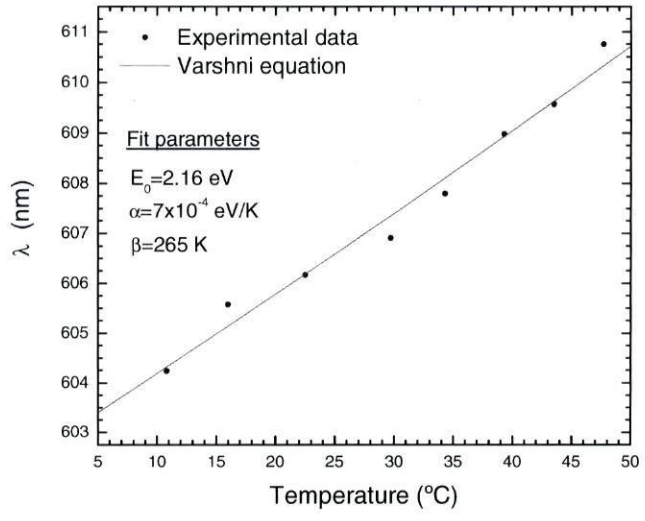


Figure 5.26 Experimental data showing the position of λ_{peak} as a function of temperature, for a QD_{600} thin film (dots), and the fit obtained using Varshni equation (line).

As temperature increases, the band gap energy decreases because the crystals lattice expands and the inter-atomic bonds are weakened. As a consequence, less energy will be necessary to excite a charge carrier. On the other hand, it can be calculated that the change in the dot size due to thermal expansion has a negligible effect in the confinement energy. In addition, because the energy gap of both core and shell material change, although at different rates, the confinement energy change is still small when compared to the observed shift. Comparing the behavior of wavelength shift in different samples it was concluded that the rate of change of λ_{peak}, towards longer wavelengths, as the temperature increased was, in all cases, approximately $0.2\,nm/°C$. The similar wavelength shift responses in all samples further confirms that the intrinsic response to temperature is ruled by the same band gap shift observed in bulk semiconductors.

Either the luminescence intensity variation or the shift in λ_{peak} can be used to obtain temperature information. However, simple intensity measurements are prone to error due to optical power source fluctuations, detector drift, changing in coupling conditions, etc.. In order to evaluate the system susceptibility to optical power changes, the luminescent intensity response of QD_{600} to temperature was recorded for three different levels of LED output power (100%, 90% and 80%). In Figure 5.27(a), it is clearly shown that the luminescence intensity response depends strongly on the LED output. Additionally, in each individual curve, a non-linearity can be observed at lower

temperatures, which was due to condensation of water on the surface of the sample that consequently changed the coupling conditions.

A simple detection scheme can be implemented in order to take self-referenced temperature measurements. If two signals, S_1 and S_2, corresponding to two narrow spectral windows on opposite sides of the spectrum, are normalized according to $(S_1 - S_2)/(S_1 + S_2)$, the resulting output will be proportional to temperature and independent of the optical power level in the system. This procedure was implemented using a QD_{600} thin film. With software controlling the CCD spectrometer it was possible to obtain signals S_1 and S_2 corresponding to the spectral windows $595\,nm - 600\,nm$ and $620\,nm - 625\,nm$, respectively. The normalization scheme was applied to the curves in Figure 5.27(a). The resulting plots, given in Figure 5.27(b), show that the normalized output has a linear dependence with temperature and is independent of changes in the system optical power level (data dispersion was within noise level). An accuracy of approximately $0.3\,°C$ was estimated by linear regression analysis. This demonstrates that, with this detection scheme, QDs can be used as self-referenced temperature probes suitable for chemical sensing applications. The nanocrystals can be used in combination with a sensing dye, allowing to simultaneously obtain information about a chemical parameter and about temperature. Due to the ability to tune their optical properties, QDs with no spectral overlap with a particular sensing dye can easily be chosen.

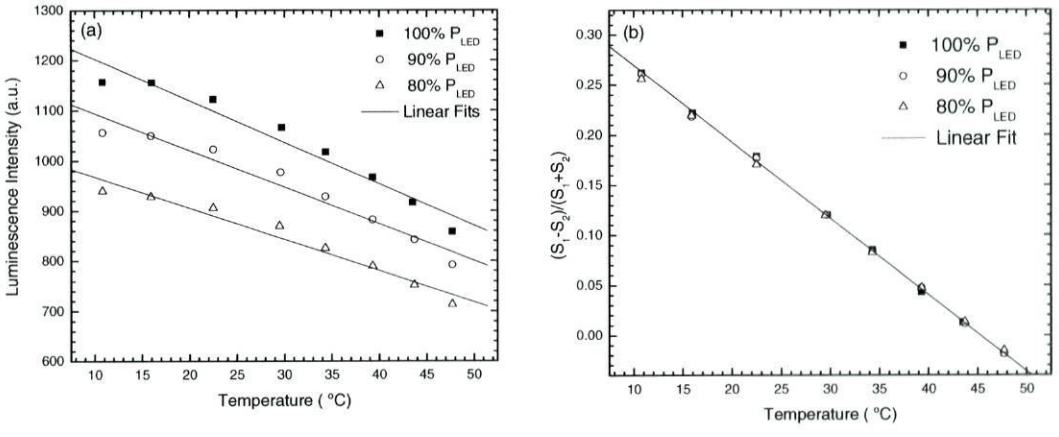


Figure 5.27 a) Luminescent intensity of QD_{600} as a function of temperature for three levels of LED optical power ($100\,\%$, $90\,\%$, and $80\,\%$); b) Corresponding normalized output.

The samples were tested in a temperature range near ambient conditions (approximately $10\,°C$ to $50\,°C$), which is appropriate for most chemical and biochemical sensing applications. However, applications in more extreme situations are also possible. It has been reported in the literature that the temperature response of CdSe nanocrystals is reversible in a temperature range from $100\,K$ to $315\,K$ (although it is not linear over the full range). Also, the solgel samples were

cured at $200\,°C$ without damaging the QDs, indicating that, as long as the emission is not completely quenched, temperature measurements could be made in this range.

Blinking of the luminescence of single quantum dots has been reported [72]. However, when using bulk samples doped with nanocrystals, the average luminescent output observed is stable. Throughout all the tests performed, an outstanding photostability was observed in the majority of the samples. Still, for this to be achieved, core-shell QDs must be used. In addition, curing of the sol-gel material must be performed under nitrogen to prevent oxidation.

All tests were performed using low excitation power densities varying from $2\,mW/cm^2$ to $40\,mW/cm^2$. In this range, the luminescence intensity depends linearly on the excitation optical power. A linear behavior is expected for power densities up to about $400\,W/cm^2$, while saturation behaviors could be observed at higher powers (above $100\,kW/cm^2$). At such levels a blue shift in the emission peak can be observed [35]. In the system presented, where large diameter optical fiber bundles were used, these limits would correspond to very high optical power levels not likely to be reached in a practical situation. However, when using standard single mode optical fibers in combination with laser sources, very high energy densities can be attained. In such hi-power regimes the excitation radiation itself can change the temperature of the sample. Because this can compromise the proposed referencing scheme, it should be taken into consideration when designing a practical system.

5.6.3 Quantum dots as an intensity reference

The enhanced photostability of QDs, together with the ability to tune their emission wavelength, provide the opportunity to implement reliable intensity-reference schemes using their luminescent properties. This possibility was demonstrated in the context of oxygen sensing.

Experimental details

In order to test the possibility of using the luminescence of semiconductor nanocrystals to provide a reference signal in an intensity based optical oxygen sensor, the experimental set-up displayed in Figure 5.28 was implemented. A hydrolytic sol-gel thin film, doped with $10\,mM$ Ru(bpy), was used as the oxygen sensing element. The reference was provided by a bulk glass sample (approximately $1\,mm$ thick) doped with QD_{520}. Both samples were placed in close contact inside a sealed chamber with two valves used to supply nitrogen and oxygen as needed (see picture in Figure 5.29). The flux of each gas was controlled to adjust the level of O_2 inside the chamber. A polarographic probe was used to monitor oxygen concentration. A blue LED ($470\,nm$, Nichia) was

used as the excitation optical source. The LED radiation was guided to the samples by a $4\,mm$ diameter optical fiber bundle. Both luminescent signals were detected using a $4\,mm$ diameter Y splitter optical fiber bundle, which guided the sensor output into the two channels of the CCD spectrometer (S2000 OceanOptics). The detection fiber was oriented at $90°$ to the excitation fiber in order to avoid excessive optical background noise from back reflected excitation radiation.

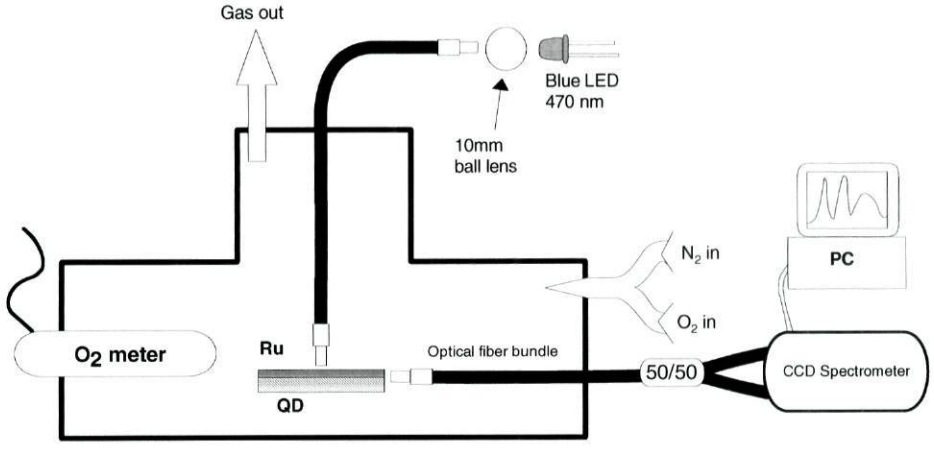


Figure 5.28 Experimental setup used to test CdSe nanocrystals as intensity reference in a luminescent oxygen sensor.



Figure 5.29 Picture showing simultaneous excitation of an oxygen sensing film and a bulk sample doped with QD_{520}. The strong luminescence of both samples can easily be observed.

Some precautions were taken in order to ensure that the QDs luminescence was independent of the oxygen level in the chamber. The non-hydrolytic sol-gel was cured at an elevated temperature to reduce the porosity of the resulting glass and minimize the permeability to oxygen. Additionally, using QDs with a core-shell structure provided further protection of the luminescent core from oxidation and other possible contaminations. Finally, QD_{520} were used in order to avoid spectral overlap with both the excitation source and the sensing dye. Only wavelengths lower than $520\,nm$

are absorbed by these nanocrystals, therefore, its luminescent intensity will be affected by the excitation radiation but not by the emission of Ru(bpy). As a consequence of these actions, oxygen had no effect on the QD's emission, which was proportional only to the exciting optical power. In this situation, the ratio between the emission of Ru(bpy), which depends on oxygen concentration and on the excitation optical power level, and the emission of QD_{520}, should be independent of any optical power drift in the sensing system. Some tests were performed to assess the efficiency of this scheme.

Experimental Results

Two simple experiments were carried out to demonstrate the proposed intensity referencing scheme using the experimental setup shown in Figure 5.28. First, the output optical power of the excitation LED, P_{LED}, was successively set at three different levels: 100%, 82% and 63%. This was achieved by changing the LED's drive current. During this test, the concentration of oxygen remained constant (21%). In the second test, the oxygen level of the chamber was changed in a controlled way, while the drive current of the LED was set to a constant value. The experimental results obtained with these tests can be observed in Figure 5.30(a) and Figure 5.30(b), respectively.

As expected, when the LED output power was decreased, the luminescent emissions of the sensing dye and of the nanocrystals were decreased in the same proportion. However, when the oxygen level was successively set to 0%, 20% and 100%, only the emission of the sensing dye responded to the changes in concentration. The luminescent intensity of the QDs remained constant and proportional to the LED output.

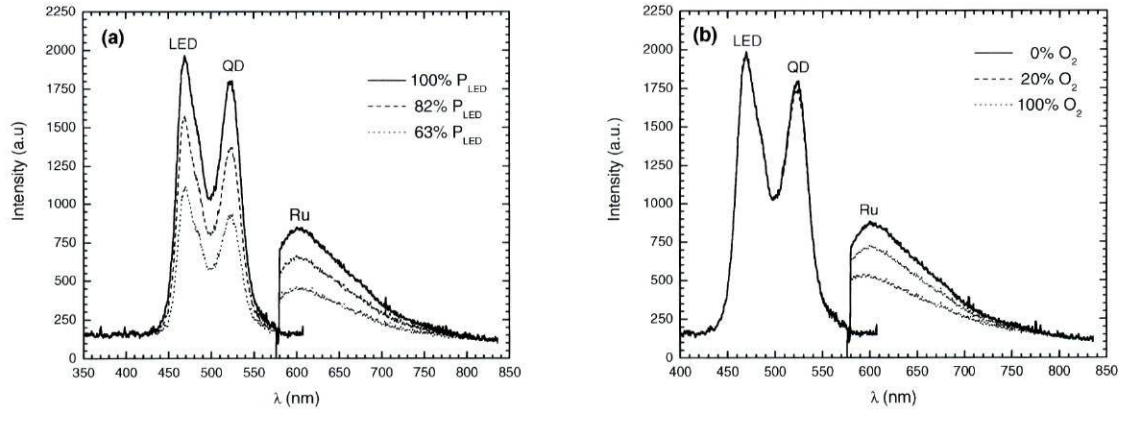


Figure 5.30 Spectral behavior of the LED, the reference signal (QD) and the sensing dye (Ru) when: (a) P_{LED} was decreased from 100% to 82% and 63%, in a 21% O_2 atmosphere; (b) The O_2 level was set to 0%, 20% and 100%, with constant P_{LED}.

Some overlap was observed between the emission of the LED and that of the QDs, but the spectral peaks of the optical source, of the reference signal and of the sensor were easily discriminated by the CCD spectrometer. With adequate software it was straightforward to acquire electrical signals proportional to the optical power of the LED, QD and Ru(bpy). The results shown in Figure 5.30(a) and Figure 5.30(b) indicate that, performing a ratio operation between the signal of the sensing dye, P_{Ru}, and the signal of the nanocrystal, P_{QD}, will yield a normalized output that is independent of the level of excitation optical power in the sensing system. In addition, the ratio P_{Ru} / P_{QD} will be proportional to the concentration of oxygen in the test chamber. To verify the degree of immunity to fluctuations of the excitation optical power obtained with this scheme, the sol-gel samples were submitted to saturation cycles of O_2/N_2, while the drive current of the LED was modulated by a slow varying triangular wave that changed P_{LED} between 100% and 70%.

Preliminary tests showed that the scheme would only work properly if the offset of each signal, corresponding to the dark current of the CCD, was removed prior to normalization. This way the ratio $(P_{Ru} - P_{dark})/(P_{QD} - P'_{dark})$, was performed instead. The correction factors P_{dark} and P'_{dark} are the offsets of the spectral windows associated with the QDs and the dye. Figure 5.31 shows the results of tests performed of the compensation scheme before, plot (a), and after, plot (b), the offset correction.

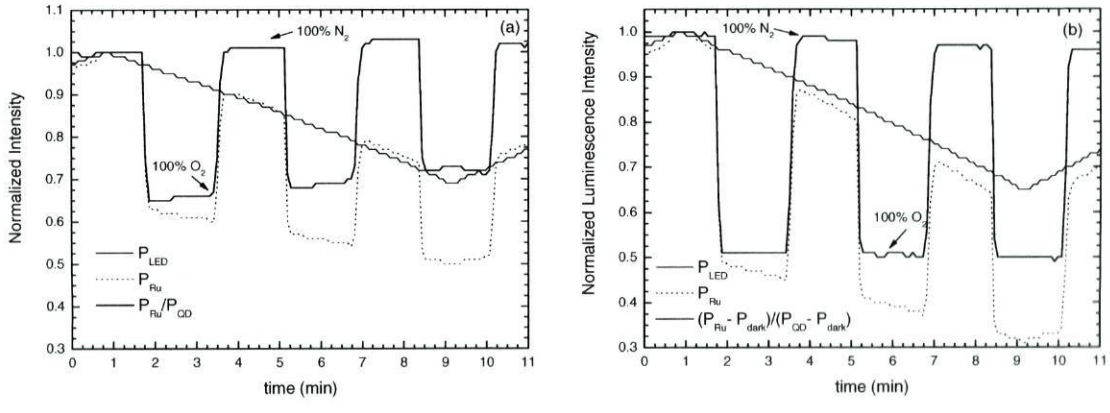


Figure 5.31 Sensor response to O_2/N_2 saturation cycles while P_{LED} changed slowly from 100% to 70%. Both the raw luminescent output, P_{Ru}, and the normalized signal P_{Ru} / P_{QD} are shown. The result of the processing scheme is shown before (a) and after (b) dark offset correction.

It is clearly shown in Figure 5.31 that, while the luminescence output of Ru(bpy) was strongly affected by the oxygen level in the chamber and by changes in excitation optical power, the intensity ratio, $(P_{Ru} - P_{dark})/(P_{QD} - P'_{dark})$, responded only to variations of O_2 concentration. Comparison of Figure 5.31 (a) and (b) demonstrates the strong influence of the dark current offset, that should be removed prior to normalization for effective drift compensation. Further tests demonstrated that a

decrease of 82% in P_{Ru} caused by a decrease in the excitation optical power impacted our measured oxygen concentration by only 4%. The immunity was further improved when the outputs of the sensing dye and of the QDs reference were normalized according to the operation $(P_{Ru} - P_{QD})/(P_{Ru} + P_{QD})$. Before performing this operation the dark current offset was removed from each signal. In this case, the error was reduced to 2.7% after a near 80% decrease in the LED optical power. In this particular configuration, the slight overlap between the spectra of LED and QDs prevented further improvement. Then a smaller detection fiber ($400\mu m$ diameter , Ocean Optics) was used, positioned so that no LED radiation could be collected. In this case the highest variation observed was smaller than 1.5%, which was within the noise level of the system. Figure 5.32 clearly shows that, regardless of intensity fluctuations of the excitation source, the sensor response is directly proportional to the oxygen concentration. The same result can be obtained with more selective filtering or using a quantum dot with a longer wavelength and no overlap with the excitation source spectrum. These results clearly establish semiconductor nanocrystals as suitable intensity references in luminescence based optical sensors.

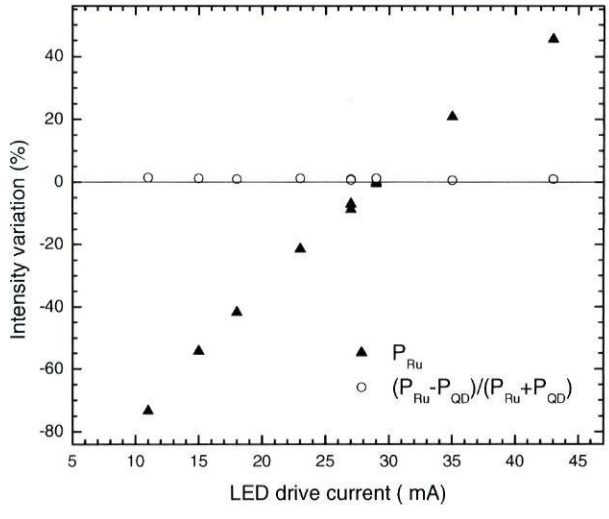


Figure 5.32 Response of P_{Ru} and $(P_{Ru} - P_{QD})/(P_{Ru} + P_{QD})$ to changes in LED optical power.

Although the system presented eliminates the dependence from any drift arising from the excitation source, or from losses induced in the fiber system, the photodegration of the dye cannot be compensated. As the plot in Figure 5.31 (b) shows, after each saturation cycle, the luminescence intensity was not fully recovered due to photobleaching. It was already shown that this effect was much stronger in the hydrolytic samples. On the other hand, for tests with duration of few minutes, the non-hydrolytic samples could be considered extremely photostable. This was also the case of the nanocrystals when immobilized in non-hydrolytic matrices. This means that a combination of QDs

with a Ruthenium dye, both immobilized in a non-hydrolytic sol-gel, would make a very stable self-referenced oxygen sensor, suitable for long term use. The photostability of the Ru(bpy) when immobilized in non-hydrolytic sol-gel, however, results from the low permeability to oxygen of this material. This way, the quenching efficiency, Q, of such sensor, would be very small when compared with the values that can be obtained with porous sol-gel samples (see results in Table 5-5). Nevertheless, for long-term use, where stability is more important than sensitivity, like in some environmental applications, the results obtained can provide an interesting solution.

The excitation power density reaching the sample must be taken into consideration for the referencing scheme to be valid. As discussed in the previous section, for very high power densities the luminescence of the dots will not change linearly with the excitation. Nevertheless, this will not be a problem for a long range of moderate to low excitation powers, adequate for a variety of applications. Additionally, some concern could arise from the temperature dependence of the QDs luminescence. However, it was demonstrated in the previous section that the wavelength shift information of the emission peak can be used to provide a self-referenced measurement of temperature. With knowledge of the sample temperature, it will then be possible to calculate the reduction in the QDs emission due to thermal quenching and still use its luminescence signal as an intensity reference. This way, the schemes explored in the previous sections provide the basis to implement a self-referenced intensity-based oxygen sensor with temperature drift compensation.

5.7 Multiplexing applications of quantum dots

The lack of multiplexing approaches for optical oxygen sensing is another critical problem, especially in environmental applications, where determination of the analyte at multiple points is needed. Presently, the available technologies have usually been developed for single point measurements. Simultaneous measurement of several parameters requires a multiplexing sensing system. At present a few functional luminescence based sensing systems do this. They rely on several optical fibers, each of them leading to a measurement point for a specific parameter [73]. Also, the possibility of distributed chemical sensing with luminescent cladding optical fibers has been addressed, but no further progress has been reported [74]. A more adequate approach would be to incorporate multiple luminescent sensors in a fiber optic distributed sensor network. In the context of optical oxygen sensors, the ideal situation would be to perform multipoint measurement of oxygen and temperature with the same optical fiber system. In the following sections results that represent important steps towards such a system are described.

5.7.1 Multipoint temperature sensing with quantum dots

The possibility to tune the emission peak of the QDs luminescence provides an excellent opportunity to explore their application in multiplexed sensing systems. This possibility was demonstrated by implementing multipoint temperature measurements with different nanocrystals.

Experimental details

In order to demonstrate the possibility of simultaneous interrogation of several QDs with the same fiber system, two different topologies were implemented: a parallel configuration for simultaneous interrogation of two QDs where the system worked in reflection, and a series configuration for interrogation of two different samples where the system worked in transmission. The corresponding experimental set-ups can be seen in Figure 5.33(a) and Figure 5.33(b), respectively. The same excitation source and detection instrumentation that were used in the set-up of Figure 5.24 were also used in both multiplexing configurations. Optical fiber bundles with 4 mm diameter were used both for excitation and detection.

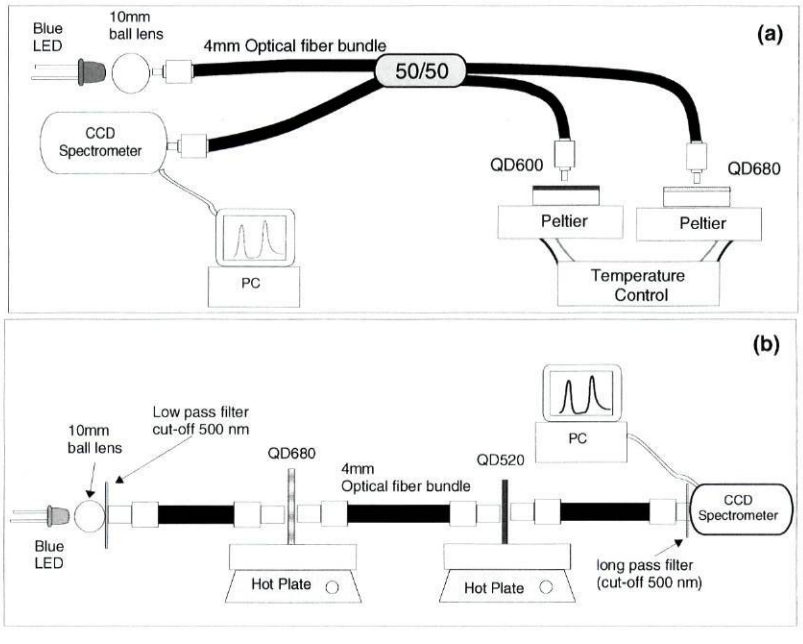


Figure 5.33 Experimental setups for simultaneous interrogation of temperature in two locations using different QD samples: (a) parallel configuration; (b) series configuration.

In the transmission setup, the nanoparticles with longer emission wavelength were placed first in the series. If the sensor with the QDs of shorter wavelength emission was placed first, its luminescence signal would have been absorbed by the nanocrystals of the second sensor. In this particular configuration, the level of excitation optical power reaching the CCD is much higher than

in a reflection configuration. This way, additional optical filtering was necessary to achieve increased noise rejection. A short pass filter (cut-off wavelength at $500\,nm$) was placed at the fiber input and a long pass filter (cut-off wavelength at $500\,nm$) was placed at the fiber output. In addition, in this configuration hot plates were used to control the QDs temperature. In both setups the temperature of each sensor was independently varied and simultaneous interrogation of the two sensors was evaluated.

Results and discussion

The possibility of self-referenced intensity-based multiplexed temperature measurements with QDs was tested in a reflection configuration using the set-up of Figure 5.33(a) to interrogate two samples: a thin film of QD_{600} and a thick film doped with CdTe-ZnS nanocrystals with emission peak at $680\,nm$ (QD_{680}). The temperature of each sample was changed independently. The spectral response of both samples (after subtracting the dark spectrum) can be seen for two different cases. In Figure 5.34(a), the temperature of QD_{600} was changed from $10\,°C$ to $36\,°C$, and the temperature of QD_{680} was kept constant ($21\,°C$). In Figure 5.34(b), the temperature of QD_{680} was changed from $11\,°C$ to $34\,°C$, and the temperature of QD_{600} was kept constant ($21\,°C$). The corresponding normalized outputs are inserted in the respective figures.

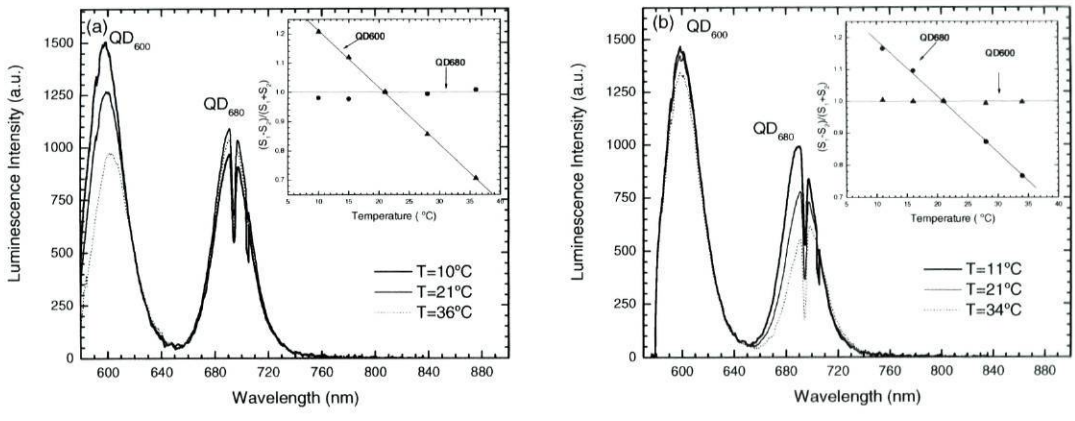


Figure 5.34 Spectral response of two QD samples, in a reflection configuration, to temperature variations (insert: normalized outputs): a) QD600 temperature was changed and QD680 temperature was kept constant; b) QD_{680} temperature was changed and QD_{600} temperature was kept constant.

Clearly, the intensity and the peak wavelength of the QDs luminescent emission change when the sample temperature is changed. Intensity fluctuations are also noticeable in the QDs with constant temperature. However, this was due to a low signal-to-noise ratio and their peak wavelength remains constant. This error is mostly corrected by normalizing the signal as discussed

earlier (see inserts in Figure 5.34) and, as a result, an output signal proportional to the wavelength shift, and independent of power drift, could be obtained.

To assess the validity of this statement the normalized responses of both QDs were recorded in real time as their temperatures were changed alternatively. Figure 5.35 (a) shows the response of the processed outputs obtained from the samples doped with QD_{680} and QD_{600}, to alternate and independent changes in their temperatures. In Figure 5.35(b) signals proportional to the respective luminescence intensities are shown for comparison. The results demonstrate that the processed outputs clearly follow the temperature variations and do not suffer from the effect of intensity fluctuations, which are clearly visible in plot (b). Furthermore, it can be observed that the change in the temperature of one of the samples had no effect on the other sample output.

The data obtained, clearly demonstrates the possibility of implementing self-referenced wavelength multiplexed temperature sensing systems using semiconductor nanocrystals. With this configuration, the number of sensing points could easily be increased using additional QDs, emitting at different wavelengths, together with the necessary fiber couplers. Considering the spectral width of these nanocrystals, however, the number of possible channels is somewhat limited. Nevertheless, at least ten channels per interrogation system should be possible.

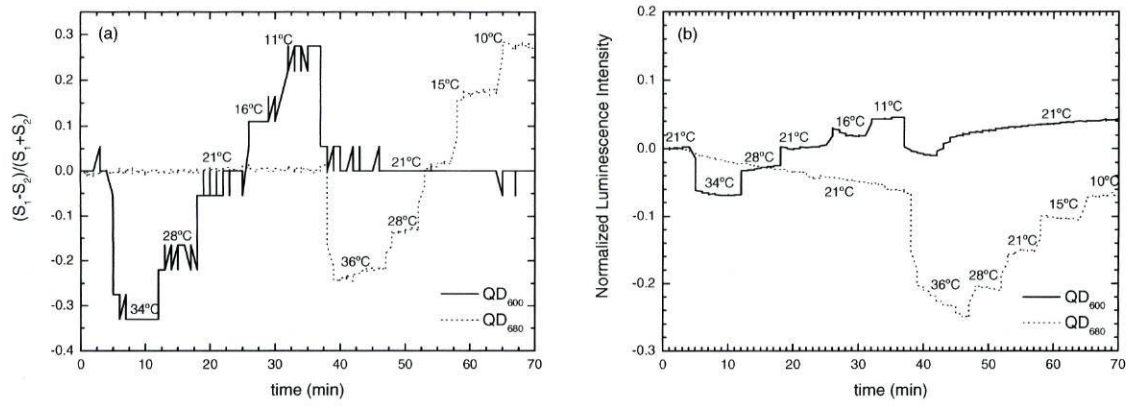


Figure 5.35 Simultaneous temporal responses of both samples submitted to independent temperature changes: a) normalized outputs; b) luminescence intensity responses.

The same principle was tested in a transmission configuration (Figure 5.33(b)) using two thick films doped respectively with QD_{520} and with QD_{680}. Because QDs absorb at any wavelength lower than their emission peak, in a transmission configuration the samples must be placed in an ordered sequence (longer wavelengths first) to avoid mutual absorption. This way, in this particular test, QD_{680} was placed first in the series. The temperature of each sample was changed alternatively, using hotplates, while their spectral response was recorded. The spectra of each sample can be observed in

two different situations. In Figure 5.36(a), the temperature of QD_{520} was changed, while the temperature of QD_{680} was kept constant ($21\,^{\circ}C$). In Figure 5.36(b) the temperature of QD_{680} was changed while the temperature of QD_{520} remained constant ($21\,^{\circ}C$). The normalized output responses are inserted in their respective figures.

This configuration is intrinsically more affected by noise from the excitation source. In spite of double optical filtering and subtraction of dark spectrum, a strong background signal was observed, particularly in the QD_{680} output. The grating in channel 2 of the CCD was optimized for the spectral range $575\,nm$ to $835\,nm$; this way, it was more affected by scattered LED radiation. This fact, together with the different filters used, could be responsible by the peak observed at $625\,nm$. In addition, because the curing process of the samples doped with QD_{680} was not completed, this particular sensor was suffering from photobleaching, which caused a gradual decrease in its luminescent emission. The CdTe nanocrystals were obtained as a suspension in a liquid solvent (toluene) stabilized with surfactants. Consequently, in spite of the solvent being evaporated prior to sol-gel immobilization of QD_{680}, the surfactant may have interfered with the curing process. Nevertheless, the normalized outputs clearly show temperature measurements that are mutually independent and insensitive to intensity changes. This is a clear advantage and it further demonstrates the self-referenced capabilities of the processing scheme proposed.

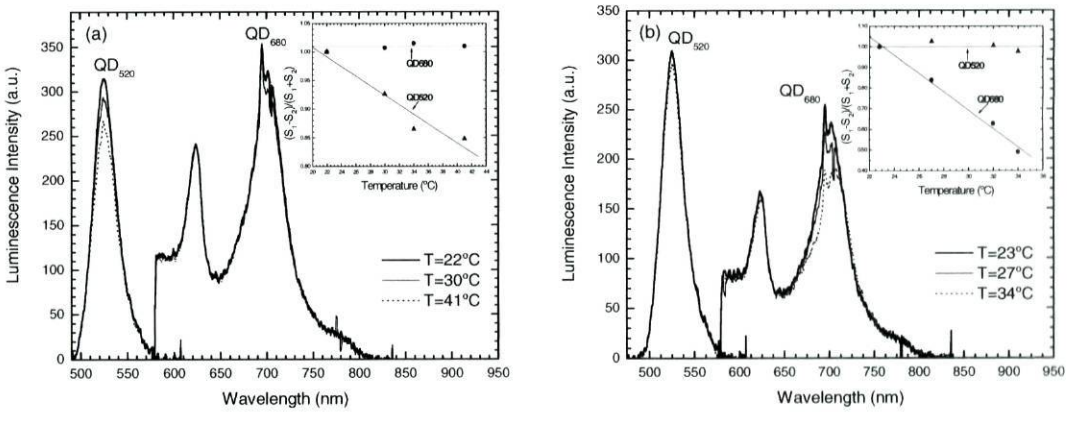


Figure 5.36 Spectral response of two QD samples, in a transmission configuration, to temperature changes (insert: normalized outputs): a) QD_{520} temperature was changed and QD_{680} was kept constant. b) QD_{680} temperature was changed and QD_{520} was kept constant.

Some design considerations should be investigated to improve the performance of this series configuration. In particular, the implementation of evanescent excitation/detection geometries that could allow for increased number of sensing points. The main problem to overcome is to achieve the equalization of the excitation optical power reaching each sensing point.

5.7.2 Quantum dots as oxygen sensors with unique spectral signature

Nanocrystals whose emission wavelengths are higher than $600\,nm$ can absorb the luminescent signal from ruthenium dyes. This way, their emission can be made oxygen dependent. This provides the opportunity for using QDs in combination with ruthenium complexes to implement oxygen sensors with different spectral signatures. A set of oxygen sensors with different emission wavelengths could then be used in multiplexed sensing applications. To test this possibility, the response of combined samples of CdTe nanocrystals with Ru(bpy) to changes in oxygen concentration was characterized.

Experimental details

Core-shell CdTe nanocrystals, with emission centered at $680\,nm$, were used to provide a luminescent oxygen sensor with a different spectral profile. Because these QDs have a protecting shell and were immobilized in a dense glass material, they did not suffer from direct oxidation. In spite of this, because of the spectral position of their emission peak, these particular QDs can absorb the luminescent emission of the ruthenium complexes, hence become sensitive to the oxygen concentration. However, the LED excitation radiation can also be absorbed by these nanocrystals. This way, two contributions for the QDs luminescence can coexist, an oxygen sensitive signal due to excitation by the sensing dye emission and a signal with no sensitivity to oxygen due to direct excitation by the LED. The ideal situation would be to ensure that only the former is present.

In order to test this idea, different sensing configurations were used. A bulk glass sample (thickness of approximately $1\,mm$) doped with QD_{680} was combined with different oxygen sensitive samples (doped with ruthenium dyes) and was tested in the setup of Figure 5.37.

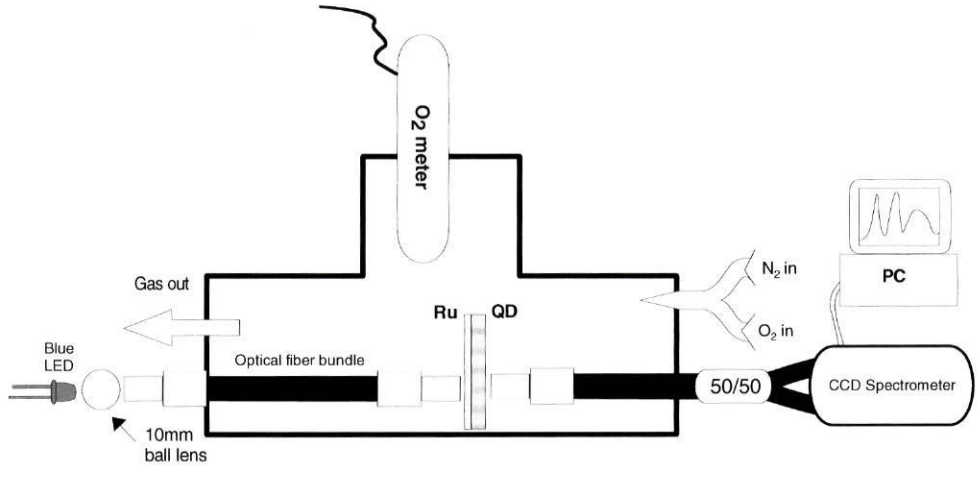


Figure 5.37 Experimental setup used to test the sensitivity of different QDs and sensing dye combinations to changes in oxygen concentration.

The same excitation source and detection instrumentation that were used in the set-up of Figure 5.28 were also used in this system. However, as is shown in Figure 5.37, in this experiment a transmission configuration was used instead. In all tests performed the sample doped with sensing dye was placed facing the incoming LED radiation; the QD_{680} bulk glass was then placed in close contact with the sensing sample. In some of the tests a long-pass filter (with cut-off at $600\,nm$) was placed between the sensing sample and the QD_{680} sample. This way, direct excitation of the QDs by the excitation radiation could be eliminated.

Different test samples were evaluated by submitting the sensors to saturated atmospheres of oxygen and nitrogen. To compare the sensitivity of the different sensors, a spectral quenching coefficient, $\alpha(\lambda)$, was defined as follows:

$$\alpha(\lambda) = \frac{P_{O_2}(\lambda)}{P_{N_2}(\lambda)}, \tag{5.49}$$

where $P_{O_2}(\lambda)$ and $P_{N_2}(\lambda)$ are the optical powers of the luminescent emission at each wavelength in saturated atmospheres of O_2 and N_2, respectively. The parameter α is a measure of oxygen sensitivity at each wavelength. The usual quenching efficiency, Q, defined by equation (5.46) was also evaluated.

Results and discussion

In the first experiment, a bulk glass sample doped with QD_{680} was combined with a thin film of hydrolytic sol-gel doped with $10\,mM$ Ru(bpy), as shown in Figure 5.37. In this situation, the amount of excitation optical power crossing the sensing film without being absorbed and reaching the QDs was still very high. This way, the QDs emission was mainly due to this direct excitation and no response to oxygen was observed. Placing a long-pass filter between the samples (cut-off at $600\,nm$) eliminated the LED radiation reaching the QDs. After this was done, however, the amount of power emitted from the thin Ru(bpy) film and reaching the QDs was not enough to produce any noticeable response from the nanocrystals.

Changing the thin film to a bulk glass sample of non-hydrolytic sol-gel (approximately $1\,mm$ thick), doped with $10\,mM$ Ru(bpy), resulted in an almost complete absorption of the LED radiation by the sensing dye sample. Nevertheless, a long pass filter was placed between the samples. In this situation, the QDs emission was only due to absorption of radiation emitted by the sensing dye and therefore, the dependency on oxygen concentration could be observed. In Figure 5.38 (b), the response of the combined sensing element, when submitted to saturated atmospheres of oxygen and nitrogen, can be observed. In Figure 5.38 (a) the response of the bulk Ru(bpy) sample, obtained in

the same conditions, is shown for comparison purposes. Inserted in each of these figures is a schematic representation of the sensing samples configuration. The emission peak of the nanocrystals is clearly seen in situation (b). In addition, some features appear in the spectral region of $650\,nm - 675\,nm$, looking like a secondary peak or a depression in the dye emission, which could be due to some wavelength dependent absorption of the dye radiation by the QDs. The emission of the nanocrystals is now clearly oxygen dependent. However, due to the increased thickness of the sensing sample and because Ru(bpy) was immobilized in a glass material with low oxygen permeability, the quenching efficiency of this configuration was very small ($Q \approx 10\%$). Even so, an increased sensitivity is apparent in the spectral region corresponding to the QDs emission.

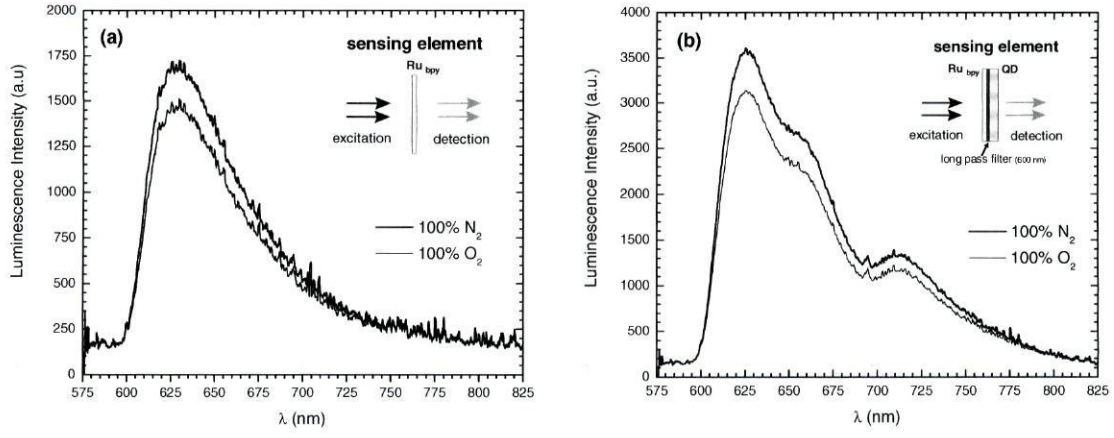


Figure 5.38 Spectral responses in saturated atmospheres of N_2 an O_2 (Inserted: a scheme of the sensing configuration): (a) Ru(bpy); (b) Ru(bpy) + long pass filter ($600\,nm$) + QD_{680}.

To quantify the differences between the two configurations, their respective spectral quenching efficiencies, $\alpha(\lambda)$, were calculated. The resulting plots are presented in Figure 5.39. The comparison between α_1 and α_2, the spectral quenching efficiencies of the Ru(bpy) sample with and without the presence of QDs, respectively, clearly shows an increased sensitivity in the spectral region between $700\,nm - 800\,nm$ (Figure 5.39 (a)). This is even more obvious when the difference between the two coefficients is plotted (Figure 5.39 (b)), showing that the peak enhancement occurs at approximately $760\,nm$. At this particular wavelength, the quenching efficiency is improved by a factor of 2.4. This result demonstrates that the combination of ruthenium dyes with adequate nanocrystals provides a mechanism by which sensitivity to oxygen can be created in different spectral regions.

Further tests were performed searching to obtain higher quenching efficiencies. For this purpose, Ru(dpp) was used as the oxygen sensitive dye instead. A non-hydrolytic sol-gel thin film, with an approximate thickness of $50\,\mu m$ and doped with this dye (0.25% weight), was tested for

three different cases where the sensing element was: (1) a single Ru(dpp) film; (2) a Ru(dpp) film followed by the QD_{680} layer; (3) a Ru(dpp) film followed by a long pass filter (cut-off at $600\,nm$) and the QD_{680} sample. These sensor configurations are depicted in inserts of Figure 5.40(a), Figure 5.40(b) and Figure 5.41, respectively. Configuration (2) was used to assess the influence of direct excitation of the nanocrystal from the LED.

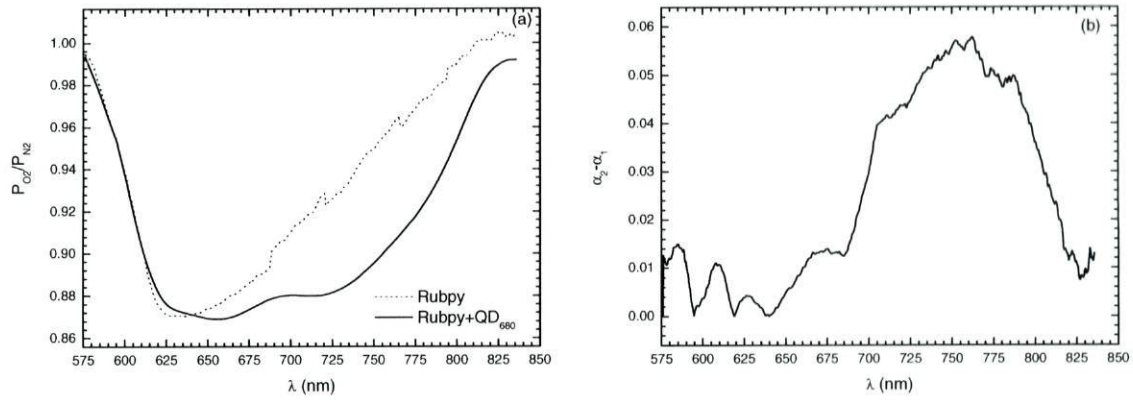


Figure 5.39 (a) Oxygen sensitivity, $\alpha\langle\lambda\rangle$, for a $10\,mM$ Ru(bpy)non-hydrolytic sample with (dark line) and without (doted line) the presence of QD_{680}; (b) Evaluation of the relative sensitivity enhancement between the two configurations.

The spectral response obtained in saturated atmospheres of N_2 and O_2, for each configuration, can also be seen in the corresponding figures. Figure 5.40(a) shows the typical response of Ru(dpp) in the presence of oxygen. A quenching efficiency of 35.8% was measured. This is still a relatively small change, which is a consequence of using a very dense non-hydrolytic sol-gel glass. Very similar values were obtained with the other two sensing configurations. In those two cases the emission peak of the QDs, at approximately $710\,nm$, could be observed. Careful analysis of the experimental results revealed that, when compared with configuration (1), configurations (2) and (3) show enhanced oxygen sensitivity in the spectral region $700\,nm - 800\,nm$ (which corresponds to the QDs emission).

This increase in sensitivity was quantified by plotting the coefficient α as function of wavelength. In Figure 5.42(a) the plots of α_1, α_2 and α_3, corresponding respectively to configurations (1), (2) and (3), can be observed. Figure 5.42(b) shows the differences in sensitivity $\alpha_1 - \alpha_2$ and $\alpha_1 - \alpha_3$. It can be clearly observed that configurations (2) and (3) present increased oxygen sensitivity in the spectral region corresponding to the QDs emission. The enhancement is higher in configuration (3), where the filter was used, indicating that in configuration (2) some of the LED radiation was reaching the QDs. For the implementation of a practical system careful design of the sensing head is needed in order to avoid this problem.

It can be concluded, from Figure 5.42(b), that the improvement in the quenching coefficient α is maximum at approximately $768\,nm$. At this particular wavelength, a comparison of the spectral quenching efficiencies indicates that the sensor design shown in configuration (2) is more sensitive than that of configuration (1) by a factor of 1.8. Configuration (3), on the other hand, shows a two-fold (factor of 2.2) increase. In spite of the enhanced quenching efficiencies, both Q and α, the relative enhancement obtained by introducing the QDs was very similar to that obtained with the Ru(bpy) sample. This is in agreement with the fact that, while the overall sensitivity to oxygen of the sensor depends on the sensing dye sample, the relative increase obtained by introducing the QDs depends only on their absorbance at the spectral region coinciding with the dye emission. The latter is the same in the two experiments performed.

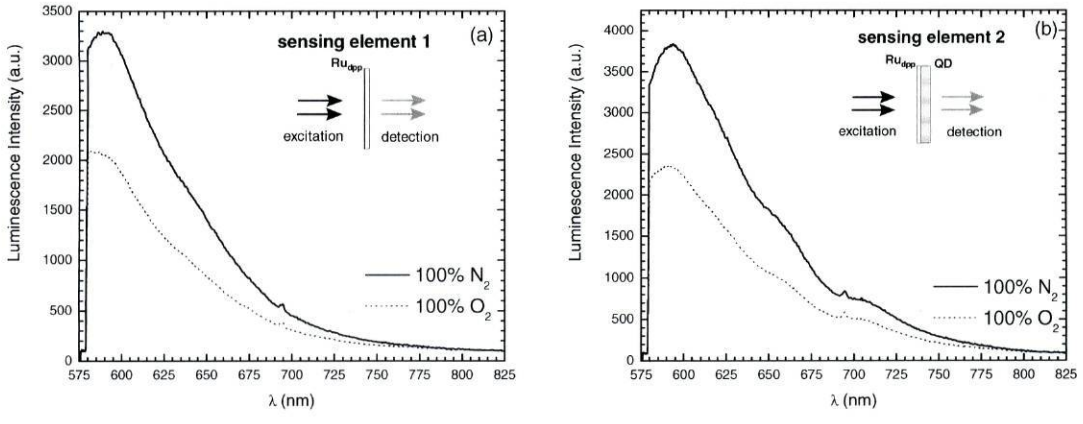


Figure 5.40 Spectral responses in saturated atmospheres of N_2 an O_2 (Insert: scheme of the sensing configuration): (a) Ru(dpp); (b) Ru(dpp) + QD_{680}.

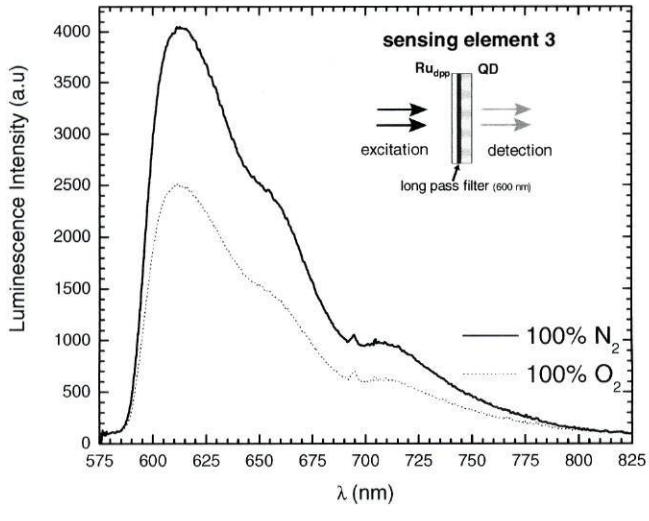


Figure 5.41 Spectral responses in saturated atmospheres of N_2 an O_2 (Insert: scheme of the sensing configuration: Ru(dpp) + long pass filter (600 nm) + QD_{680}).

These results demonstrate that it is possible to obtain oxygen sensitivity in different spectral regions. The ideal situation would be to have nanocrystals emitting in the near infrared with no spectral overlap with the ruthenium dyes. The application of this principle using nanocrystals with different emission peaks, combined with the adequate sensing dye, would allow to obtain a set of oxygen sensors with different spectral signatures, suitable for wavelength multiplexing.

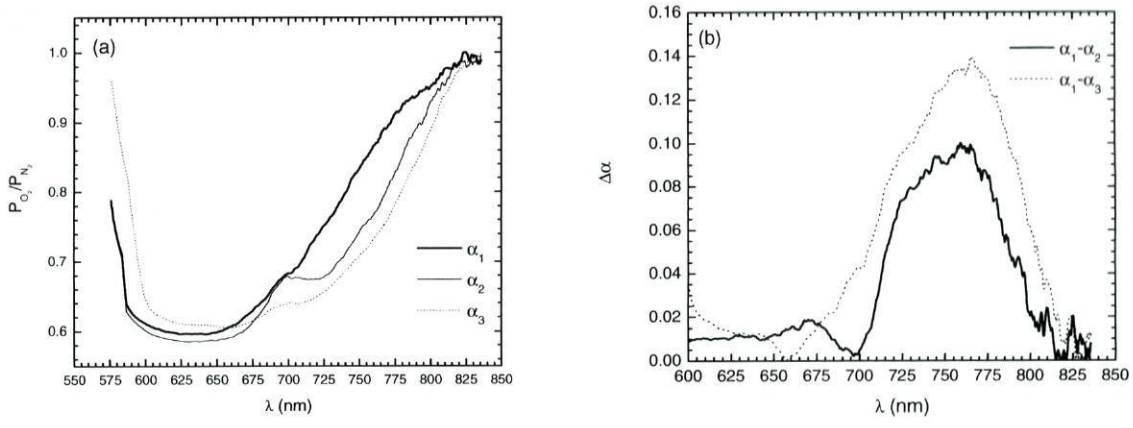


Figure 5.42 (a) Oxygen quenching efficiency, $\alpha(\lambda)$, for configurations 1, 2 and 3; (b) Sensitivity enhancement of configurations (2) and (3) relative to configuration (1).

Nanocrystals with longer emission wavelengths would greatly enhance the performance of sensors based on configurations (2) and (3) since their emission spectra would not overlap with that of sensing dye. However, at the time when these experiments were conducted, CdTe nanocrystals emitting at $680\,nm$ were the only near infrared core-shell QDs available. PbSe nanoparticles with higher emission wavelengths ($1300\,nm - 1500\,nm$) were also tested. But these were not core-shell QDs, and without the protection of the passivating layer their luminescence was strongly quenched upon sol-gel immobilization. Nevertheless, QD technology is rapidly evolving and core-shell nanocrystals with IR emission will soon be available, providing interesting solutions for near infrared wavelength multiplexed chemical sensors.

5.8 Conclusion

The introduction of semiconductor nanocrystals technology in the field of chemical and biological sensors is a relatively new trend. Nevertheless, the application of QDs in many fundamental bio-assays, bio-imaging and chemical sensing techniques has already been successfully demonstrated. In addition to providing several advantages when compared to traditional dyes, nanocrystals have introduced a new set of possibilities, from increased multiplexing capabilities to long term imaging of live cells. The recent progress in the application of QDs in the field of

biochemical sensors, together with a substantial worldwide research effort in the development of the associated technology, will surely establish semiconductor nanocrystals as high performing bioanalytical tools and provide new capabilities for physical, biological and chemical sensors.

In the present work these possibilities have been explored by incorporating quantum dots in an optical oxygen sensing system. It was demonstrated that, due to the intrinsic properties of the QDs luminescence, it is possible to perform temperature measurements independently of any optical power drift. Such capability has great potential to provide a stable temperature reference in many biochemical luminescence-based applications. In the particular case of oxygen sensing, the nanocrystals can provide information about the temperature while the sensing dye measures oxygen. This way the temperature drift of the oxygen sensing dye can be compensated.

The outstanding photostability of QDs was used to provide a stable intensity reference in a luminescence based oxygen sensor. The scheme presented could perform intensity-based oxygen measurements with almost complete immunity to system optical power drift. Although the error introduced by bleaching of the dye could not be corrected, it was shown that the combination of QDs with Ru(dpp), both immobilized in non-hydrolytic sol-gel, could provide a very stable, self-referenced, intensity based oxygen sensor for long term applications where sensitivity is not the most important factor.

The temperature measurements performed with QDs are based on a wavelength shift; their luminescence intensity shows a linear dependence on temperature. For this reason, QDs could potentially be used to provide an intensity-based oxygen sensor with temperature and optical power drift compensation. Considering the possibility of tuning their optical properties, the results obtained show that QDs could be used more generically to implement any self-referenced intensity-based luminescent chemical sensor with temperature compensation.

Due to the fact that the excited state lifetimes of QDs and ruthenium dyes differ by an order of magnitude, the temperature compensation scheme presented here could be implemented using frequency domain spectroscopy. The system would work with a single photodetector and phase sensitive detection. Such a simple scheme would be practically insensitive to photobleaching of the sensing dye, immune to optical power drift, and insensitive to temperature changes. An adequate processing scheme to implement such oxygen sensing system is currently under investigation.

These schemes will work in a broad temperature range and with medium to high levels of excitation optical power. However, for very high power densities (hundreds of kW/cm^2), band-filling effects and self-heating of the sensing samples can compromise measurements. Although such power densities could be reached when using laser sources in combination with optical fibers, these

power levels are usually avoided to prevent bleaching of the sensing dyes. Nevertheless, these limits should be taken into consideration when designing a practical system.

The multiplexing capabilities of QDs were demonstrated by performing multiple-point, self-referenced, temperature measurements, using their luminescent signals, both in transmission and in reflection configurations. Due to the relatively broad FWHM of the nanocrystals, arising from their size dispersion, the number of possible measurement channels in a single interrogation system is somewhat limited (seven to ten channels in the visible range). Nevertheless, the possibility of implementing a system with a few biochemical probes, with temperature and drift compensation, in the same fiber system, using a single excitation source, is very appealing for a wide range of applications.

The possibility of combining QDs with sensitive luminescent dyes to obtain chemical sensing with multiplexing capability was also demonstrated. This was done in the context of an oxygen sensing system by combining ruthenium dyes with QDs with deep red emission. Although the spectra of both materials were slightly overlapped, the oxygen sensitivity of the near-infrared QDs was clearly observed. The results presented indicate that this scheme provides a way to obtain oxygen sensitivity in different regions of the spectrum. With QDs emitting further in the infra-red, a set of oxygen probes with distinct wavelengths could be obtained. Although NIR emitting core-shell nanocrystals are not presently available, at least commercially, the situation will soon change in such a fast developing market. A more sophisticated approach to this subject would be to functionalize the dots surface to become oxygen sensitive. This could be done, for instance, by resonant energy transfer between the dot and an oxygen sensing dye immobilized on its surface.

Overall, the results presented in this chapter establish semiconductor nanocrystals as auxiliary tools with great potential to solve many problems in biochemical sensing systems. In particular, important steps were taken towards the implementation of a multi-parameter distributed sensing network, with temperature and drift compensation, and with great potential for environmental and biomedical applications.

5.9 References

[1] Liang, S., D.T. Pierce, C. Amiot, and X.J. Zhao, *Photoactive nanomaterials for sensing trace analytes in biological samples.* Synthesis and Reactivity in Inorganic Metal-Organic and Nano-Metal Chemistry, 2005. **35**(9): p. 661-668.

[2] Ozkan, M., *Quantum dots and other nanoparticles: what can they offer to drug discovery?* Drug Discovery Today, 2004. **9**(24): p. 1065-1071.

[3] Sharron G. Penn, Lin He, and Michael J. Natan, *Nanoparticles for bioanalysis.* Current Opinion in Chemical Biology, 2003. **7**(5): p. 609-615.

[4] Jens M. Kurner, Ingo Klimant, Christian Krause, Erika Pringsheim, and O.S. Wolfbeis, *A New Type of Phosphorescent Nanospheres for Use in Advanced Time-Resolved Multiplexed Bioassays.* Analytical Biochemistry, 2001. **297**: p. 32–41.

[5] Marcel Bruchez Jr., Mario Moronne, Peter Gin, Shimon Weiss, and A. Paul Alivisatos, *Semiconductor nanocrystals as fluorescent biological labels.* Science, 1998. **281**: p. 2013–2016.

[6] Hedi Mattoussi, Igor L. Medintz, Aaron R. Clapp, Ellen R. Goldman, Jyoti K. Jaiswal, Sanford M. Simon, and J.M. Mauro, *Luminescent quantum dot-bioconjugates in immunoassays, FRET, biosensing, and imaging applications.* JALA, 2004. **9**: p. 28–32.

[7] Fox, A.M., *Optical properties of solids.* Oxford Master Series in Condensed Matter Physics. 2001: Oxford University Press.

[8] Joseph H. Simmons and K.S. Potter, *Optical Materials.* 2000, San Diego: Academic Press.

[9] Davies, J.H., *The Physics of low-dimensional semiconductors: an introduction.* 1998, Cambridge: Cambridge University Press.

[10] Peter W. Miloni and Joseph H.Eberly, *Lasers.* 1988: John Willey & Sons Inc.

[11] Perkowitz, S., *Optical characterization of semiconductors: infrared, raman, and photoluminescence spectroscopy.* Techniques of Physics, ed. N.H. March. Vol. 14. 1993, London: Academic Press.

[12] *Handbook of optics: devices, measurements and properties.* 2nd ed, ed. M. Bass. Vol. II. 1995, New York: McGraw-Hill.

[13] Griffiths, D.J., *Quantum mechanics in three dimensions*, in *Introduction to Quantum Mechanics*, J. Chalice, Editor. 2005, Pearson Prentice Hall: New Jersey. p. 131-200.

[14] S. V. Gaponenko, *Optical properties of semiconductor nanocrystals.* Cambridge Studies in Modern Optics, ed. P. L. Knight and A. Miller. Vol. 23. 1998, Cambridge: Cambridge University Press.

[15] M G Bawendi, M L Steigerwald, and L.E. Brus, *The quantum mechanics of larger semiconductor clusters ("quantum dots").* Annual Review of Physical Chemistry, 1990. **41**: p. 477-496.

[16] Marius Grundmann, *The present status of quantum dot lasers.* Physica E, 2000. **5**: p. 167-184.

[17] Victor I. Klimov, *Nanocrystal quantum dots.* Los Alamos Science, 2003. **28**: p. 214-220.

[18] Ledentsov, N.N., M. Grundmann, F. Heinrichsdorff, D. Bimberg, V.M. Ustinov, A.E. Zhukov, M.V. Maximov, Z.I. Alferov, and J.A. Lott, *Quantum-dot heterostructure lasers.* IEEE Journal of Selected Topics in Quantum Electronics, 2000. **6**(3): p. 439-451.

[19] *Molecular beam epitaxy: applications to key materials.* , ed. R.F.C. Farrow. 1995, Park Ridge NJ, : Noyes Publications.

[20] Xia, Y.N., P.D. Yang, Y.G. Sun, Y.Y. Wu, B. Mayers, B. Gates, Y.D. Yin, F. Kim, and Y.Q. Yan, *One-dimensional nanostructures: synthesis, characterization, and applications.* Advanced Materials, 2003. **15**(5): p. 353-389.

[21] Brus, L., *Chemical approaches to semiconductor nanocrystals.* Journal of Physics and Chemistry of Solids, 1998. **59**(4): p. 459-465.

[22] T. Trindade, P. O'Brien, and N. L. Pickett, *Nanocrystalline semiconductors: synthesis, properties, and perspectives.* Chemistry of Materials, 2001. **13**(11): p. 3843-3858.

[23] Ekimov, A., *Growth and optical properties of semiconductor nanocrystals in a glass matrix.* Journal of Luminescence, 1996. **70**: p. 1-20.

[24] C. P. Collier, T. Vossmeyer, and J.R. Heath, *Nanocrystal superlatices.* Annu. Rev. Phys. Chem., 1998. **49**: p. 371-404.

[25] Scherer, A. and H.G. Craighead, *Fabrication of small laterally patterned multiple quantum-wells.* Applied Physics Letters, 1986. **49**(19): p. 1284-1286.

[26] Fukui, T., S. Ando, Y. Tokura, and T. Toriyama, *Gaas tetrahedral quantum dot structures fabricated using selective area metalorganic chemical vapor-deposition.* Applied Physics Letters, 1991. **58**(18): p. 2018-2020.

[27] Skolnick, M.S. and D.J. Mowbray, *Self-assembled semiconductor quantum dots: Fundamental physics and device a tipplications.* Annual Review of Materials Research, 2004. **34**: p. 181-218.

[28] Ekimov, A.I., *Optical-properties of semiconductor quantum dots in glass matrix.* Physica Scripta, 1991. **T39**: p. 217-222.

[29] Margaret A. Hines and Philippe Guyot-Sionnest, *Synthesis and characterization of strongly luminescing ZnS-capped CdSe nanocrystals.* J. Phys. Chem., 1996. **100**: p. 468-471.

[30] B. O. Dabbousi, J. Rodriguez-Viejo, F. V. Mikulec, J. R. Heine, H. Mattoussi, R. Ober, K. F. Jensen, and M. G. Bawendi, *(CdSe)ZnS Core-shell quantum dots: synthesis and characterization of a size series of highly luminescent nanocrystallites.* J. Phys. Chem. B, 1997. **101**: p. 9463-9475.

[31] Kirchner, C., T. Liedl, S. Kudera, T. Pellegrino, A.M. Javier, H.E. Gaub, S. Stolzle, N. Fertig, and W.J. Parak, *Cytotoxicity of colloidal CdSe and CdSe/ZnS nanoparticles.* Nano Letters, 2005. **5**(2): p. 331-338.

[32] Jurgen Riegler and T. Nann, *Application of luminescent nanocrystals as labels for biological molecules.* Anal Bioanal Chem, 2004. **379**: p. 913–919.

[33] Korsunska, N.E., M. Dybiec, L. Zhukov, S. Ostapenko, and T. Zhukov, *Reversible and non-reversible photo-enhanced luminescence in CdSe/ZnS quantum dots.* Semiconductor Science and Technology, 2005. **20**(8): p. 876-881.

[34] Zhelev, Z., R. Jose, T. Nagase, H. Ohba, R. Bakalova, M. Ishikawa, and Y. Baba, *Enhancement of the photoluminescence of CdSe quantum dots during long-term UV-irradiation: privilege or fault in life science research?* J Photochem Photobiol B, 2004. **75**(1-2): p. 99-105.

[35] P. Verma, G. Irmer, and J. Monecke, *Laser power dependence of the photoluminescence from CdSxSe1-x nanoparticles in glass.* Journal of Physics-Condensed Matter, 2000. **12**(6): p. 1097-1110.

[36] *Evident Technologies.* [cited 2005]. www.evidenttech.com.

[37] *Quantum Dot Corporation.* [cited 2005]. www.qdots.com.

[38] *Nanoco Technologies.* [cited 2005]. www.nanoco.biz.

[39] Hoet, P.H.M., A. Nemmar, and B. Nemery, *Health impact of nanomaterials?* Nature Biotechnology, 2004. **22**(1): p. 19-19.

[40] Colvin, V.L., *The potential environmental impact of engineered nanomaterials.* Nature Biotechnology, 2003. **21**(10): p. 1166-1170.

[41] Alivisatos, P., *The use of nanocrystals in biological detection.* Nat Biotechnol, 2004. **22**(1): p. 47-52.

[42] Ferry, D.K., J.P. Bird, and R. Akis, *Quantum dots: applications in technology and in quantum physics.* Physica E-Low-Dimensional Systems & Nanostructures, 2004. **25**(2-3): p. 298-302.

[43] V. Biju, Y. Makita, A. Sonoda, H. Yokoyama, Y. Baba, and M. Ishikawa, *Temperature-sensitive photoluminescence of CdSe quantum dot clusters.* Journal of Physical Chemistry B, 2005. **109**(29): p. 13899-13905.

[44] O. Labeau, P. Tamarat, and B.Lounis, *Temperature dependence of the luminescence lifetime of single CdSe/ZnS quantum dots.* Physical Review Letters, 2003. **90**(25).

[45] Yi-hong Wu, K. Arai, and Takafumi Yao, *Temperature dependence of the photoluminescence of ZnSe/ZnS quantum-dot structures.* Physical Review B, 1996. **53**(16): p. R 10 485 - R 10 488.

[46] Wang, S.P., S. Westcott, and W. Chen, *Nanoparticle luminescence thermometry.* Journal of Physical Chemistry B, 2002. **106**(43): p. 11203-11209.

[47] Glen W. Walker, Vikram C. Sundar, Christina M. Rudzinski, Aetna W. Wun, Moungi G. Bawendi, and Daniel G. Nocera, *Quantum-dot optical temperature probes.* Appl. Physics Lett., 2003. **83**(17): p. 3555-3557.

[48] Catherine J. Murphy, *Optical sensing with quantum dots.* Analytical Chemistry, 2002. **74**: p. 520A-526A.

[49] Yongfen Chen and Z. Rosenzweig, *Luminescent CdS quantum dots as selective ion probes.* Analytical Chemistry, 2002. **74**(19): p. 5132-5138.

[50] Hai-Yan Xie, Jian-Gong Liang, Zhi-Ling Zhang, Yi Liu, Zhi-Ke He, and D.-W. Pang, *Luminescent CdSe-ZnS quantum dots as selective Cu2+ probe.* Spectrochimica Acta Part A, 2004. **60**: p. 2527–2530.

[51] Wei Jun Jin, Jose M. Costa-Fernandez, Rosario Pereiro, and A. Sanz-Medel, *Surface-modified CdSe quantum dots as luminescent probes for cyanide determination.* Analytica Chimica Acta, 2004. **522**: p. 1–8.

[52] Geddes, C.D., *Optical halide sensing using fluorescence quenching: theory, simulations and applications-a review.* Measurement Science and Technology, 2001. **12**: p. R33-R88.

[53] Chin I. Lin, Abraham K. Joseph, Chao Kang Chang, and Y.D. Lee., *Molecularly imprinted polymeric film on semiconductor nanoparticles: analyte detection by quantum dot photoluminescence.* Journal of Chromatography A, 2004. **1027**: p. 259–262.

[54] Jaiswal, J.K. and S.M. Simon, *Potentials and pitfalls of fluorescent quantum dots for biological imaging.* Trends in Cell Biology, 2004. **14**(9): p. 497-504.

[55] Warren C.W. Chan and Shuming Nie, *Quantum dot bioconjugates for ultrasensitive nonisotopic detection.* Science, 1998. **281**: p. 2016-2018.

[56] Xingyong Wu, Hongjian Liu, Jianquan Liu, Kari N. Haley, Joseph A. Treadway, J. Peter Larson, Niangfeng Ge, Frank Peale, and M.P. Bruchez, *Immonofluorescent labeling of cancer marker Her2 and other cellular targets with semiconductor quantum dots.* Nature Biotechnology, 2002. **21**: p. 41-46.

[57] Benoit Dubertret, Paris Skourides, David J. Norris, Vincent Noireaux, Ali H. Brivanlou, and Albert Libchaber, *In vivo imaging of quantum dots encapsulated in phospholipid micelles.* Science, 2002. **298**: p. 1759–1762.

[58] Jaiswal, J.K., H. Mattoussi, J.M. Mauro, and S.M. Simon, *Long-term multiple color imaging of live cells using quantum dot bioconjugates.* Nature Biotechnology, 2003. **21**(1): p. 47-51.

[59] Mattoussi, H., J.M. Mauro, E.R. Goldman, G.P. Anderson, V.C. Sundar, F.V. Mikulec, and M.G. Bawendi, *Self-assembly of CdSe-ZnS quantum dot bioconjugates using an engineered recombinant protein.* Journal of the American Chemical Society, 2000. **122**(49): p. 12142-12150.

[60] Clapp, A.R., I.L. Medintz, J.M. Mauro, B.R. Fisher, M.G. Bawendi, and H. Mattoussi, *Fluorescence resonance energy transfer between quantum dot donors and dye-labeled protein acceptors.* Journal of the American Chemical Society, 2004. **126**(1): p. 301-310.

[61] Jain, R.K. and M. Stroh, *Zooming in and out with quantum dots.* Nature Biotechnology, 2004. **22**(8): p. 959-960.

[62] Han, M.Y., X.H. Gao, J.Z. Su, and S. Nie, *Quantum-dot-tagged microbeads for multiplexed optical coding of biomolecules.* Nature Biotechnology, 2001. **19**(7): p. 631-635.

[63] Orellana, G., *Luminescent optical sensors.* Anal Bioanal Chem, 2004. **379**: p. 344–346.

[64] C. McDonagh, C. Kolle, A.K. McEvoy, D.L. Dowling, A.A. Cafolla, S.J. Cullen, and B.D. MacCraith, *Phase fluorometric dissolved oxygen sensor.* Sensors and Actuators B, 2001. **74**: p. 124-130.

[65] Paul Hartmann, Marc J.P. Leiner, and Petra Kohlbacher, *Photobleaching of a ruthenium complex in polymers used for oxygen optodes and its inhibition by singlet oxygen quenchers.* Sensors and Actuators B, 1998. **51**: p. 196–202.

[66] Song, A., S. Parus, and R. Kopelman, *High-performance fiber optic pH microsensors for practical physiological measurements using a dual-emission sensitive dye.* Analytical Chemistry, 1997. **69**(5): p. 863-867.

[67] Ramazan Benrashid and P. Velasco, *High performance sol-gel spin-on glass materials.* 2005, Waveguide Solutions: Charlotte, NC. p. 27.

[68] Maccraith, B.D., C.M. Mcdonagh, G. Okeefe, E.T. Keyes, J.G. Vos, B. Okelly, and J.F. Mcgilp, *Fiber optic sensor based on fluorescence quenching of evanescent-wave excited ruthenium complexes in sol-gel derived porous coatings.* Analyst, 1993. **118**(4): p. 385-388.

[69] Colette .M. McDonagh, B.D. MacCraith, and A.K. McEvoy, *Tailoring of sol–gel films for optical sensing of oxygen in gas and aqueous phase.* Anal. Chem., 1998. **70**: p. 45–50.

[70] Joseph R. Lakowicz, *Principles of Fluorescence Spectroscopy.* 2 ed. 1999, New York: Kluwer-Plenum.

[71] Odonnell, K.P. and X. Chen, *Temperature-dependence of semiconductor band-gaps.* Applied Physics Letters, 1991. **58**(25): p. 2924-2926.

[72] Wilfried G. J. H. M. van Sark, Patrick L. T. M. Frederix, Ageeth A. Bol, Hans C. Gerritsen, and Andries Meijerink, *Blueing, bleaching, and blinking of single CdSe/ZnS quantum dots.* Chemphyschem, 2002. **3**(10): p. 871-879.

[73] G.Holst, R. N. Glud, M. Kuhl, and I. Klimant, *A microoptode array for fine-scale measurement of oxygen distribution.* Sensors and Actuators B-Chemical, 1997. **38**(1-3): p. 122-129.

[74] Lieberman, R.A., L.L. Blyler, and L.G. Cohen, *A distributed fiber optic sensor based on cladding fluorescence.* Journal of Lightwave Technology, 1990. **8**(2): p. 212-220.

Chapter 6

Conclusions and Future Perspectives

Summary

In this chapter, some conclusions regarding the work developed are presented. In addition, an outline of the main achievements is provided. Some hints for future work are briefly described, including further developments of the present work and some new directions to explore.

6.1 Introduction

The present work was the first approach of the Optoelectronics Unit of INESC Porto to the area of biochemical optical fiber sensing. This unit has a long research record in optical fiber sensing of physical parameters, but there was no previous experience in this particular area. Consequently, due to the multidisciplinary character of this research field, there was the need to establish several collaborations with partners with experience in Chemistry and Biochemistry. These contacts resulted in joint projects with Departamento de Química at FCUP, with Instituto de Tecnologia Química e Biológica (ITQB) at Oeiras, and with the Department of Physics and Optical Sciences of the University of North Carolina at Charlotte, USA, which established the background for the present work.

6.2 Luminescence based pH sensing - main achievements

This work was developed in collaboration with the Departamento de Química at FCUP with the main goal of exploring the potential of luminescence based techniques for application in optical fiber sensors for pH and heavy metal ions.

In order to evaluate different sensing membranes, an optical fiber system able to perform luminescence measurements using intensity based and frequency domain interrogation was implemented. Most of the work was developed aiming to identify the techniques with most potential and their associated problems. In this context, some interesting results were obtained:

- Several techniques of dye immobilization were tested and compared. The possibility of tuning membrane properties by changing the fabrication parameters was successfully explored. Sol-gel based membranes, using ormosil precursors which have excellent compatibility with optical fiber technology, were developed.
- Different techniques for interrogating pH sensing membranes were demonstrated. Using different dye/host combinations, measurements were performed using simple intensity detection, ratiometric detection, wavelength shift detection and lifetime based detection.
- The feasibility of metal ion detection using pH sensing technology was demonstrated.
- New sensing dyes, with near infrared emission/excitation, were tested, showing adequate characteristics for frequency domain interrogation using low cost optoelectronics.

6.3 Luminescence based oxygen sensors - main achievements

This work was developed in a collaboration with ITQB, where the main goal was the development of an all optical sensing system, using optical fibers, for dissolved oxygen measurements in the study of cell metabolism in a nuclear magnetic resonance device.

An optical fiber system was implemented suitable for interrogation of luminescence based biochemical sensors by intensity and frequency domain spectroscopy. Oxygen sensitive films were obtained by immobilization of a ruthenium complex in a porous glass sol-gel matrix. The resulting solutions were used to coat different fiber sensing probes. The test system implemented allowed to identify a number of problems associated with luminescence based sensing systems. Optimization was achieved in some cases.

- Different techniques for coupling light into the optical fiber system using broad band sources were compared. The advantages and drawbacks of different coupling methods were clearly identified.
- Four different optical fiber sensing configurations were implemented and compared. The results obtained provided valuable information on the influence of the sensing probe geometry on the system performance. Several clues for optimization of the sensing system based on tailored fiber probe geometries were obtained.
- A new scheme for simultaneous detection of a chemical parameter and temperature was successfully demonstrated. Temperature measurements were performed independently of optical power drifts. The system proposed used part of the excitation radiation, and can therefore be applied to virtually any luminescence based sensor.

6.4 Application of semiconductor nanoparticles - main achievements

In collaboration with the University of North Carolina at Charlotte, USA, the potential applications of semiconductor nanocrystals (or quantum dots - QDs) to optical oxygen sensing were investigated. Several opportunities for the application of luminescent nanocrystals in optical fiber sensing systems were identified. Some of these schemes were actually demonstrated in the context of an optical fiber luminescence based oxygen sensing system. These new applications of quantum dots are the most innovative aspect of the work developed.

- The possibility of implementing an intensity based luminescence sensor with immunity to optical power drift was demonstrated using an oxygen sensitive dye in combination with reference luminescent semiconductor nanocrystals.
- The use of quantum dots as self-referenced, intensity based, temperature probes was successfully demonstrated. The properties of the sensing probes developed were shown to be very well adapted for use as temperature references in luminescence based biochemical sensors.

The multiplexing potential of quantum dots was also evaluated in the following applications:

- Multipoint self-referenced temperature measurements by wavelength multiplexing using quantum dots was demonstrated, in reflection and transmission fiber sensing configurations.
- The possibility of obtaining oxygen sensors with different spectral signatures for multiplexing applications, using quantum dots in combination with ruthenium dyes, was successfully demonstrated.

6.5 Conclusions and future perspectives

Work developed

Due to the lack of previous experience in the field of luminescence based sensing, in an initial stage, a great deal of the work had to be performed based on previous research by other authors, with the goal to obtain the basic skills necessary for implementation of luminescence based sensors, to identify the main difficulties and to search for possible innovation opportunities.

In this context, several exploratory tests were performed using different luminescent pH indicators and immobilization materials. Different polymer based sensing membranes were tested and compared. In all the materials explored a physical entrapment method, where the sensing dye is encapsulated in the polymeric network, was chosen by its simplicity and versatility. The main

problems encountered in all methods were due to leaching and photobleaching of the sensing dyes. In all cases, the degree of leaching could be reduced by increasing the degree of cross-linking, which, however, also increased the response time of the sensor. Nevertheless, in most cases reasonable compromises between the two parameters could be established. This way, membranes with suitable characteristics for luminescence sensing in aqueous environments could be produced with acrylamides (by photo-induced polymerization), PVA (Poly vinyl alcohol) and hybrid sol-gel materials. Although both PVA and acrylamides presented some problems regarding immobilization on the surface of optical fibers, the properties of these membranes were otherwise very favorable and should be further explored, either as external membranes or in combination with plastic fibers (where adhesion to the fiber surface might be increased). Sol-gel based membranes demonstrated to be the most adequate ones for immobilization on the fiber tip. These materials showed a versatile control of their properties by changing the process parameters. While this characteristic is appealing when seeking for optimization, it also introduces difficulties. In order to obtain reproducible results, the fabrication parameters should be strictly observed.

With some of the membranes fabricated different interrogation techniques, using pH indicators, could be tested. From the results obtained it became clear that while intensity based detection is appealing by its simplicity, it does not provide the necessary stability and reproducibility. Nevertheless, several very interesting referencing techniques could be identified. While ratiometric measurements are very effective in eliminating the effects of photobleaching, leaching, and other signal drift, they require spectral discrimination and, obviously, a dye displaying dual emission. A similar alternative was demonstrated with a pH sensitive ruthenium dye displaying a pH dependent wavelength shift. It was shown that, in this case, two simple intensity measurements in symmetrical spectral positions (relative to peak emission) could be used to implement self-referenced intensity based pH measurements. This dye has the added advantage of increased photostability and the possibility of lifetime based sensing. Indeed, the most appealing referencing technique is based on frequency domain interrogation. With this method, self-referenced lifetime based sensing can be implemented using relatively simple and low cost instrumentation. However, this is only possible if the dye presents relativity long lifetimes (hundreds of nanoseconds or higher) which, in addition, should display adequate sensitivity towards the analyte. In this context, new osmium based complexes were developed and tested, which showed near infrared emission and adequate characteristics for frequency domain pH sensing. In a future approach the properties of these dyes should be further improved and explored, and used to implement metal ion sensors.

At a more advanced stage of this work, a prototypical fiber system for interrogation of luminescence based fiber sensing probes was implemented. This system allowed intensity or frequency domain interrogation of the sensing membranes. From very early experiments the primary difficulty identified was the very low level of the detected luminescence emission. Although the use of laser excitation can partially solve this problem, broad band sources like LEDs are highly convenient for low cost applications. Therefore, optimization of the injection of radiation into the fiber system and improvement of the collection of the luminescence signal were two problems worth investigation, particularly if the use of expensive photomultiplier tubes is to be avoided.

Therefore, different coupling systems were experimented using a LED and a large core multimode optical fiber. It was verified that whenever the emission area of the optical source exceeds that of the fiber core, best results are obtained by direct butt-coupling of the fiber onto the emission surface. In a practical application this means that an optimized pigtailed source is the best solution. In addition, sources with increased radiance and fibers with high numerical aperture should be used. If a versatile system is needed instead, the use of ball lenses was shown to outperform traditional coupling techniques. Theoretically, the best result that can be achieved with this system, when large area sources are used, is to retrieve the efficiency that would be obtained with butt coupling. The overall quality, and the level of optical output in particular, of LEDs is presently increasing very fast. In addition, a wide variety of optical fibers with large cores and numerical apertures is becoming available. While their price is somewhat high, the situation is bound to change with an increasing market. Plastic fibers, by their reduced cost, can be an excellent alternative in short distance applications. With such fibers, very large cores and numerical apertures are possible. With the fiber core exceeding the emission area, the use of a ball lens can introduce significant improvements. Alternatively, the use of non-imaging concepts can be applied in designing special shaped fiber tips which can achieve very high coupling efficiencies.

In this work it was verified that the geometrical shape of the fiber sensing tip can have a strong influence on the system performance. The efficiency of excitation, the efficiency of luminescent emission collection and the level of backscattered excitation radiation are all strongly dependent on the particular shape of the sensing tip. The results obtained demonstrated that fiber tapering is clearly a right step towards the optimization of sensing systems. A theoretical model of the fiber sensing tip can be a valuable tool in designing optimized sensing heads, particularly if the anisotropy that seems to be associated to the luminescence emission of thin films into the substrate is accounted for. Non-imaging optics concepts have also a tremendous potential for optimization of the shape of the optical fiber probe, and this is a subject worth investigating.

The final application of the system developed was the determination of dissolved oxygen (DO). In this context, it was confirmed that TEOS based films, being hydrophilic, have poor performance in aqueous media. Nevertheless, the use of hydrophobic sol-gel membranes was demonstrated by several authors as being suitable for DO sensing. Indeed, this was observed in the present work when pH sensing membranes using such materials were successfully demonstrated. As sol-gel materials are very versatile, further optimization of DO sensors is possible, which will allow to use the developed sensing heads for application in aqueous environments.

In a later stage of the work, the potential of semiconductor nanoparticles in the field of luminescence sensing was addressed. These materials were confirmed to be very versatile and several possible applications were identified, some of which were successfully demonstrated in the context of an optical oxygen sensor. Due to their extraordinary photostability, quantum dots were established to be very suitable for use as intensity references. Although the scheme implemented was shown to be very effective in eliminating the influence of any optical power drift, it did not solve the problem of photo-degradation of the sensing dye. Nevertheless, it was demonstrated that the use of non-hydrolytic sol-gel materials allowed to significantly improve the stability of ruthenium dyes. However, this was achieved at the cost of a decreased sensitivity. In spite of these limitations, the combination of quantum dots and sensing dye immobilized in non-hydrolytic sol-gel could be used in long term applications where stability is more important than sensitivity.

Quantum dots were also shown to allow the implementation of oxygen sensors with different spectral signatures. This was done by using red absorbing quantum dots, with emission in the near infrared, which absorbed the emission of the ruthenium dye and became, in this way, sensitive to oxygen changes. Although the work presented allowed a proof of principle demonstration, the results obtained can be greatly improved in several ways. The use of different quantum dots with no overlap of their emission with the ruthenium emission could significantly improve spectral discrimination of different oxygen sensors. In particular, the use of several different combinations can be used to implement multipoint oxygen sensors. The fast evolution of quantum dot materials will surely contribute for their availability at the desired wavelengths in a near future. The proposed system could also benefit from a more elegant approach at the chemical level. The immobilization of the ruthenium molecules on the surface of the nanocrystals can provide a much more efficient way to implement a new oxygen sensor, namely by introducing resonant energy transfer, by allowing to use a single sensing film, and by eliminating the need for filtering.

Most of the configurations proposed in this work with quantum dots could, in principle, be implemented with time resolved measurements, namely using frequency domain interrogation. The

fact that semiconductor nanocrystals have lifetimes in the nanosecond range, two orders of magnitude lower than those of the ruthenium dyes, would be suitable to implement different schemes to discriminate the two signals or to create combined responses of nanocrystal-dye pairs suitable for multiplexed measurements.

Future perspectives

The work developed allowed the acquisition of some of the necessary skills to approach biochemical fiber sensing and provided the opportunity to identify a number of problems still affecting luminescence based sensors. Some of these problems could be addressed and optimization schemes were proposed and demonstrated. Nevertheless, many of the solutions presented could be further improved in future developments of the present work:

- Improvement of the properties of the synthesized osmium complexes and their application in metal ion sensing by combination of the luminescent dyes with adequate chelating agents and host materials.
- A more systematic study of the influence of the fiber probe geometry on the system performance, namely by investigating an increased number of geometries. For this experimental study the development of a theoretical model capable of predicting the sensing head performance would be of great value. Also, improvement of the taper fabrication processes would be an added value. Electric arc and heating should be explored.
- Optimization of the oxygen sensing membranes. The exploration of hybrid sol-gel membranes together with the use of dyes with increased sensitivity, like porphyrins, is a necessary step towards the implementation of dissolved oxygen sensor to operate in near anaerobic conditions.
- The development of an all-optical sensing head for simultaneous determination of oxygen and temperature. This includes improvement of the sensing head design in the filter/mirror approach. In the case of using quantum dots as temperature probes, the implementation of such multiparameter sensing heads includes investigation of the best configuration for co-immobilization of quantum dots and oxygen sensitive dyes, and suitable interrogation schemes for the dual parameters.
- Improvement of the multiplexing configurations using QDs. Development of this solution includes study of other quantum dot/sensing dye combinations, and the investigation of the possibility of synthesizing oxygen sensitive QDs eliminating the need

for ruthenium dyes. Exploring the application of this scheme for sensing of other parameters is also an interesting possibility.

In addition to improvements of the work developed, several opportunities for additional research guidelines were identified:

- Use of standard fiber technology. The application of oxygen sensing technology in environmental applications has a great potential. However, the use of expensive and bulky large core fibers can be a serious obstacle to this purpose. In this context, the use of standard fiber technology is highly desirable. Although blue lasers are still expensive, they will allow the use of standard multimode or even single mode fibers in luminescence based applications. In addition, the application of standard fiber technology in biochemical sensing would then allow to explore a diversity of standard processing techniques and fiber devices, where INESC Porto has a considerable know how. The use of fiber Bragg gratings and long period fiber gratings, in particular, may allow to implement very interesting configurations. This way, many opportunities arise provided laser sources are used.
- Application of other optical mechanisms for biochemical sensing. Besides luminescence, other optical phenomena are commonly used in biochemical sensing, like absorption spectroscopy and refractive index measurements. Also in these fields, many different configurations can be implemented using standard fibers and compatible devices and techniques, which would once more take advantage of INESC Porto expertise in fiber sensing and integrated optics.
- A diversity of nanomaterials, other than quantum dots, is presently being used in very exciting sensing applications. Metallic nanoparticles and carbon nanotubes are just two representative examples. These types of materials usually allow their properties to be tailored according to their size or geometry. This way, electrical, optical or mechanical properties can be adjusted to suite different applications. The use of such materials can allow to implement innovative sensing configurations with enhanced performance.

From the work developed some opportunities for new research projects were identified where the knowledge obtained could offer a fruitful contribution. These projects also provide a framework for the guidelines described above to be explored. Therefore, the following projects are presently under evaluation:

- Development of an oxygen sensor for monitoring waste water treatment plants. In this specific application, in waters with high hydrocarbon residues content, membrane fouling is often a major impediment for traditional oxygen sensors to function adequately. This way, the investigation of sol-gel membranes suitable for such environments is a problem to be addressed, aiming to organize a project which includes the interest and collaboration of a major oil processing company.
- Development of catheter-type sensing probe for intra vascular oxygen monitoring in living animals. This application requires miniaturization of the oxygen sensing probe, the study of its biocompatibility and the development of an autonomous interrogation unit which will allow to perform tests in the field. This project was established with a pharmacology research laboratory which routinely uses live animals in its assays.
- Development of optical sensors for monitoring oxidative stress in living cells. For this application several parameters must be monitored, like nitrous oxide or superoxide ion. This will demand an investigation of the available sensing mechanisms and the development of multiparameter sensing strategies. This project was established with the Chemistry Department at FCUP and the Pharmacy Faculty at University of Coimbra.
- Development of multiparameter sensing chips. This application requires the development of integrated optics sensing platforms suitable for interrogation of different parameters. For this purpose, the design of optical circuitry and the study of sensing mechanisms and interrogation techniques adequate for multiplexing should be addressed. New challenges include the design of microfluidic systems for sample distribution in the sensing chips. This project will include a collaboration with ITQB.
- Design and development of sensing chips based on photonic band gap crystals. This technology has promising characteristics for the design of complex optical circuits. Guiding conditions can be tailored by change of the lattice parameters. Combinations of these devices with polymer materials doped with luminescent or colorimetric indicator dyes are possibilities to be explored. This project is framed in a collaboration with UNCC at Charlotte.

In spite of all these possibilities, an overall evaluation of the work presented makes clear that perhaps the main difficulty encountered, which prevented faster and better developments, derived from the highly multidisciplinary character of this research area. In this regard, the collaborations established with other research laboratories were extremely valuable. Nevertheless, some

improvements are necessary in order to allow the development of a sustainable future work in the field of biochemical sensing at INESC Porto. The collaborations established should be reinforced, not only with an increased number of joint projects but also by promoting the exchange of researchers between institutions, for short periods. This strategy will allow a more fruitful collaboration, establishing a way to transfer knowledge and giving each partner a better understanding of the problems approached. Ideally, this process could result in each institution reinforcing its competencies in the other areas, thus establishing a small multidisciplinary team inside each institution. This, of course, is only possible if the necessary critical mass in terms of people and equipment is available.

6.6 List of publications resulting from this work

International journal papers

P. A. S. Jorge, M. Mayeh, R. Benrashid, P. Caldas, J. L. Santos, F. Farahi. "Quantum dots as self-referenced optical fiber temperature probes for luminescent chemical sensors". *Measurement Science and Technology*, 17, pp 1032-1038, **2006**.

P. A. S. Jorge, M. Mayeh, R. Benrashid, P. Caldas, J. L. Santos, F. Farahi. "Applications of Quantum Dots in Optical Fiber Luminescent Oxygen Sensors". *Applied Optics,* Vol. 45, Issue 16, pp 3760-3667, **2006**.

P. A. S. Jorge, P. Caldas, J. C. G. Esteves da Silva, C.C. Rosa, A.G. Oliva, J. L. Santos and F. Farahi. "Luminescence based optical fiber chemical sensors". *Fiber and Integrated Optics,* 24, issue 2-4, pp 201-225. **2005**.

P. A. S. Jorge, P. Caldas, C.C. Rosa, A.G. Oliva and J. L. Santos. "Optical fiber probes for fluorescence based oxygen sensing". *Sensors & Actuators B.* 103: pp 290-299, **2004**.

International conferences papers and presentations

Joaquim C.G. Esteves da Silva, Andreia F.G. Machado, Paula B.M. Pinheiro, Pedro A. S. Jorge, Paulo Caldas and José L. Santos. "Optical fiber pH Sensors Based on Carboxynaphtho-fluorescein and $Ru(dpp)_3$ Immobilized in sol-gel matrices". *9th International Conference on Methods and Applications of Fluorescence Spectroscopy – MAF9.* Lisbon, Portugal, 4-7 September **2005**. pp86.

Joaquim C.G. Esteves da Silva, Paula B.M. Pinheiro, Pedro A. S. Jorge, Paulo Caldas and José L. Santos. "Polypyridyl complexes of Osmium(II) as Sensors for Near Infrared fiber Optic pH Probes". In *9th International Conference on Methods and Applications of Fluorescence Spectroscopy – MAF9.* Lisbon, Portugal, 4-7 September **2005**. pp210.

P. A. S. Jorge, M. Mayeh, R. Benrashid, P. Caldas, J. L. Santos, F. Farahi. "Self-referenced intensity based optical fiber temperature probes for luminescent chemical sensors using quantum dots". In *Optical Fiber Sensors - OFS 17,* May, **2005**. Bruges, Belgium. SPIE Vol. 5855. pp42-45.

P. A. S. Jorge, M. Mayeh, R. Benrashid, P. Caldas, J. L. Santos, F. Farahi. "Intensity based luminescent optical fiber oxygen sensor using quantum dots". In *Optical Fiber Sensors - OFS 17,* May, **2005**. Bruges, Belgium. SPIE Vol. 5855. pp381-384.

Faramarz Farahi, Pedro Jorge, Mona Mayeh, Ramazan Benrashid, Paulo Caldas, José Santos. "Applications of nano-particles in optical chemical and biological sensors". Invited talk in Optics East *Sensors for Harsh Environments*, 25-28 October **2004**, Philadelphia, Pennsylvania, USA. SPIE Vol. 5590. pp 66-76.

P. A. S. Jorge, P. Caldas, C.C. Rosa, A.G. Oliva, M. B. Marques and J. L. Santos. "Optical temperature measurement configuration for fluorescence based oxygen sensors". *EWOFS'04: Second European Workshop on Optical Fiber Sensors.* June 9-11, **2004** in Santander, Spain. SPIE volume 5502. pp 279-282.

P. Caldas, P. A. S. Jorge, C.C. Rosa, A.G. Oliva, J. L. Santos. "Optical Fiber Oxygen Sensor for *in Vivo* NMR application". *Eurosensors XVII*, 21-24, September **2003**, Guimarães, Portugal. pp 556-557.

National conference papers and presentations

P. A. S. Jorge, J. C. G. Esteves da Silva, Paula B.M. Pinheiro, J. L. Santos. "Sensores de pH em fibra óptica com emissão no infravermelho e detecção no domínio das frequências". *15ª Conferência Nacional de Física, Física 2006*, Aveiro, 4 a 8 de Setembro de **2006**.

P. A. S. Jorge, P. Caldas, C. C. Rosa, J. C. G. Esteves da Silva, A. G. Oliva, J. L. Santos, F. Farahi. "Sensores luminescentes em fibra óptica para análises bioquímicas". *14ª Conferência Nacional de Física, Física 2005*, Porto, 1 a 3 de Dezembro de **2005**.

P. A. S. Jorge, M. Mayeh, R. Benrashid, P. Caldas, J. L. Santos and F. Farahi. "Luminescence Oxygen sensors with unique spectral signature for multiplexing applications". *SEON 2005*, III Symposium on Enabling Optical Networks. Aveiro, 27th June, **2005**. p126-127

P. A. S. Jorge, P. Caldas, C.C. Rosa, A.G. Oliva, J. L. Santos. "Sensores de oxigénio em fibra óptica para aplicações RMN in vivo". Conferência Física, Tecnologia e Saúde, FiTS, Lisboa, 14 e 13 de Maio, **2005**.

P. A. S. Jorge, M. Mayeh, R. Benrashid, P. Caldas, J. L. Santos and F. Farahi. "Potential Applications of Quantum Dots in Fluorescence Based Optical Oxygen sensors". *SEON 2004*, II Symposium on Enabling Optical Networks. Porto, 14th June, **2004**. p105-106.

P. Caldas, P. A. S. Jorge, Joaquim C.G. Esteves da Silva, Ricarte, J.F. Ferreira, and José L. Santos. "Fluorescent Optical Fiber Sensor for Remote Determination of pH." *SEON 2004*, II Symposium on Enabling Optical Networks. Porto, 14th June, **2004**. pp 107-108.

Joaquim C.G. Esteves da Silva, Ricarte J.F. Ferreira, Pedro A. S. Jorge, Paulo Caldas and José L. Santos. "Assessment of Immobilization Procedures for Fiber Optic Optodes." *ANALITICA'03*, 18-19 de Novembro, **2003**. Porto, Portugal.

Joaquim C.G. Esteves da Silva, José Ricardo B. Alves, Pedro A.S. Jorge, Paulo Caldas and José L. Santos. "Fiber-optic pH Fluorescent Optode Using the He-Ne Laser as Excitation Source". *ANALITICA'03*, 18-19 de Novembro, **2003**. Porto, Portugal.

Appendix

List of Abbreviations

AF	Amino fluorescein
AlGaAs	Aluminum gallium arsenide
APD	Avalanche photodiodes
AR	Anti reflection
BPB	Bromophenol blue
bpy	2,2 –bypiridyne
BSA	Bovine serum albumin
BTMOS	Isobutyltrimethoxysilane
CCD	Charge coupled device
CdS	Cadmium sulfide
CdSe	Cadmium selenide
CdTe	Cadmium-tellurium
CEC	Compound elliptical concentrator
CHC	Compound hyperbolic concentrator
CNF	5(6)-carboxynaphtofluorescein
CPC	Compound parabolic concentrator
DHLA	Dihydrolipoic acid
DMF	Dimethylformamide
DNA	Deoxyribonucleic acid
DO	Dissolved oxygen
dpp	4,7-diphenyl-1,10-phenanthrolin
EBT	Eriochrome black T
EO	Electro optic
FRET	Fluorescence resonance energy transfer
FWHM	Full width half maximum
GaAs	Gallium arsenide
GaN	Gallium nitride
GFP	Green fluorescent protein

GRIN	Graded index
HF	Hydrofluoric acid
HOMO	Highest occupied molecular orbital
HPTS	8-hydroxy-1,3,6-pyrene trisulfonic acid trisodium salt
IC	Internal conversion
InP	Indium phosphide
IS	Ionic strength
ISC	Intersystem crossing
LED	Light emitting diode
LUMO	Lowest unoccupied molecular orbital
MBE	Molecular beam epitaxy
MBP	Maltose-binding protein
MCP	Microchannel plate
MET	Methanol
MFCC	Multi frequency cross correlation
MIP	Molecular imprinted polymers
MLC	Metal ligand complex
MLCT	Metal-to-ligand charge transfer
MOCVD	Metal-organic chemical vapor phase deposition
MQW	Multiple quantum well
MTMOS	Methyltrimethoxysilane
NA	Numerical aperture
NADH	Nicotinamide adenine dinucleotide
NIR	Near infrared
NMR	Nuclear magnetic resonance
OEPK	Octaethyl-porphyrin ketones
Ormosils	Organically modified siloxanes
PAH	Polycyclic aromatic hydrocarbon
PbS	Lead sulfide
PbSe	Lead selenide
PCF	Photonic crystal fibers
PdOEP	Palladium octaethyl-porphyrin
phen	1,10-phenanthroline

Ph-TriEOS	Phenyltriethoxysilane
PLMA	Poly(lauryl methacrylate)
PMMA	Poly(methyl methacrylate)
PMT	Photomultiplier tube
PTMOS	Phenyltrimethoxysilane
PtOEP	Platinum octaethyl-porphyrin
PtTFPP	Tetrakis (pentafluorophenyl) porphyrins
PVA	Polyvinyl alcohol
PVC	Polyvinyl chloride
QD	Quantum Dot
Ru(bpy)	Tris(2,2'bipyridil) ruthenium(II) - $[Ru(bpy)_3]^{2+}$
Ru(dpp)	Tris(4,7-diphenyl-1,10-phenanthroline) ruthenium(II) - $[Ru(dpp)_3]^{2+}$
Ru(phen)	Tris(1,10-phenanthroline) ruthenium(II) - $[Ru(phen)_3]^{2+}$
RuDCbpy	Ruthenium-bis(4,7 -diphenyl, 1,10- phenantroline) 4,4-dicarboxy-2,2-bipyridine
SNARF	Semi-naphthofluorescein
SNR	Signal to noise ratio
SPT	Single photon timing
SRS	Stanford research systems
SV	Stern Volmer
TCSPC	Time-correlated single photon counting
TEOS	Tetraethoxysilane
TIR	Total internal reflection
TMC	Transition metal complexes or transition-metal-ligand complexes
TMOS	Tetramethoxysilane
TNT	Trinitrotoluene
UV	Ultra violet
ZnS	Zinc Sulfide

Faculdade de Ciências do Porto
Biblioteca do Departamento de Física